



applied sciences

Special Issue Reprint

Flow Control, Active and Passive Applications

Edited by
Josep Maria Bergada and Gabriel Bugeda Castelltort

mdpi.com/journal/applsci



Flow Control, Active and Passive Applications

Flow Control, Active and Passive Applications

Editors

Josep Maria Bergadà

Gabriel Bugada Castelltort



Basel • Beijing • Wuhan • Barcelona • Belgrade • Novi Sad • Cluj • Manchester

Editors

Josep Maria Bergadà
Fluid Mechanics
Universitat Politècnica
de Catalunya
Terrassa
Spain

Gabriel Bugada Castelltort
Civil Engineering
Universitat Politècnica
de Catalunya
Barcelona
Spain

Editorial Office

MDPI
St. Alban-Anlage 66
4052 Basel, Switzerland

This is a reprint of articles from the Special Issue published online in the open access journal *Applied Sciences* (ISSN 2076-3417) (available at: www.mdpi.com/journal/applsci/special-issues/flow_control).

For citation purposes, cite each article independently as indicated on the article page online and as indicated below:

Lastname, A.A.; Lastname, B.B. Article Title. <i>Journal Name</i> Year , <i>Volume Number</i> , Page Range.
--

ISBN 978-3-0365-8673-1 (Hbk)

ISBN 978-3-0365-8672-4 (PDF)

doi.org/10.3390/books978-3-0365-8672-4



© 2023 by the authors. Articles in this book are Open Access and distributed under the Creative Commons Attribution (CC BY) license. The book as a whole is distributed by MDPI under the terms and conditions of the Creative Commons Attribution-NonCommercial-NoDerivs (CC BY-NC-ND) license.

Contents

Josep M. Bergada and Gabriel Bugada Flow Control, Active and Passive Applications Reprinted from: <i>Appl. Sci.</i> 2023 , <i>13</i> , 9228, doi:10.3390/app13169228	1
Guijun Gao, Qingshan You, Ziming Kou, Xin Zhang and Xinqi Gao Simulation of the Influence of Wing Angle Blades on the Performance of Counter-Rotating Axial Fan Reprinted from: <i>Appl. Sci.</i> 2022 , <i>12</i> , 1968, doi:10.3390/app12041968	4
Xiaobin Xu, Ruoyu Wang, Xianjun Yu, Guangfeng An, Ying Qiu and Baojie Liu Toward the Utilization of 3D Blading in the Cantilevered Stator from Highly Loaded Compressors Reprinted from: <i>Appl. Sci.</i> 2023 , <i>13</i> , 3335, doi:10.3390/app13053335	23
Zhijun Lei, Hongrui Liu, Gang Li, Jianbo Gong, Yanfeng Zhang and Xingen Lu et al. Influence of Wake Intensity on the Unsteady Flow Characteristics of the Integrated Aggressive Interturbine Duct Reprinted from: <i>Appl. Sci.</i> 2022 , <i>12</i> , 6655, doi:10.3390/app12136655	48
Xuan Bai, Hao Zhan and Baigang Mi Unsteady Aerodynamic Design of a Flapping Wing Combined with a Bionic Wavy Leading Edge Reprinted from: <i>Appl. Sci.</i> 2023 , <i>13</i> , 1519, doi:10.3390/app13031519	68
Junyao Zhang and Baigang Mi Internal Aerodynamic Performance Enhancement for Aircraft with High Maneuver by Designing a Distributed Submerged Inlet Reprinted from: <i>Appl. Sci.</i> 2023 , <i>13</i> , 1459, doi:10.3390/app13031459	92
Youyun Shang, Kai Cheng, Qingshun Bai and Shijin Chen Drag Reduction Analysis of the Hydrostatic Bearing with Surface Micro Textures Reprinted from: <i>Appl. Sci.</i> 2022 , <i>12</i> , 10831, doi:10.3390/app122110831	110
Lorenzo Cacciatori, Carlo Brignoli, Benedetto Mele, Federica Gattere, Celeste Monti and Maurizio Quadrio Drag Reduction by Riblets on a Commercial UAV Reprinted from: <i>Appl. Sci.</i> 2022 , <i>12</i> , 5070, doi:10.3390/app12105070	128
Carlos Carbajosa, Alejandro Martinez-Cava, Eusebio Valero and Guillermo Paniagua Efficiency of Pulsating Base Bleeding to Control Trailing Edge Flow Configurations Reprinted from: <i>Appl. Sci.</i> 2022 , <i>12</i> , 6760, doi:10.3390/app12136760	145
Nil Couto and Josep M. Bergada Aerodynamic Efficiency Improvement on a NACA-8412 Airfoil via Active Flow Control Implementation Reprinted from: <i>Appl. Sci.</i> 2022 , <i>12</i> , 4269, doi:10.3390/app12094269	157
Takuto Ogawa, Kengo Asada, Makoto Sato, Tomoaki Tatsukawa and Kozo Fujii Computational Study of the Plasma Actuator Flow Control for an Airfoil at Pre-Stall Angles of Attack Reprinted from: <i>Appl. Sci.</i> 2022 , <i>12</i> , 9073, doi:10.3390/app12189073	176

Jingyi Yu and Baigang Mi A New Flow Control Method of Slat-Grid Channel-Coupled Configuration on High-Lift Device Reprinted from: <i>Appl. Sci.</i> 2023 , <i>13</i> , 3488, doi:10.3390/app13063488	197
Martí Coma, Navid Monshi Tousi, Jordi Pons-Prats, Gabriel Bugada and Josep M. Bergada A New Hybrid Optimization Method, Application to a Single Objective Active Flow Control Test Case Reprinted from: <i>Appl. Sci.</i> 2022 , <i>12</i> , 3894, doi:10.3390/app12083894	211
Xin Zhao, Zhili Tang, Fan Cao, Caicheng Zhu and Jacques Periaux An Efficient Hybrid Evolutionary Optimization Method Coupling Cultural Algorithm with Genetic Algorithms and Its Application to Aerodynamic Shape Design Reprinted from: <i>Appl. Sci.</i> 2022 , <i>12</i> , 3482, doi:10.3390/app12073482	224
Yonghong Li and Ning Qin A Review of Flow Control for Gust Load Alleviation Reprinted from: <i>Appl. Sci.</i> 2022 , <i>12</i> , 10537, doi:10.3390/app122010537	247

Flow Control, Active and Passive Applications

Josep M. Bergada ^{1,*}  and Gabriel Bugeða ^{2,3,*} 

- ¹ Department of Fluid Mechanics, Universitat Politècnica de Catalunya, 08034 Barcelona, Spain
² Department of Civil and Environmental Engineering, Universitat Politècnica de Catalunya, 08034 Barcelona, Spain
³ International Center for Numerical Methods in Engineering (CIMNE), 08034 Barcelona, Spain
* Correspondence: josep.m.bergada@upc.edu (J.M.B.); gabriel.bugeða@upc.edu (G.B.); Tel.: +34-937398771 (J.M.B.); +34-934016494 (G.B.)

1. Introduction

The Boundary Layer (BL) dynamic performance greatly affects the forces acting on any Bluff body. Ideally, the boundary layer should be attached to the surface but when separation occurs, the vortical structures and the dynamic forces' amplitude rapidly increase. In many aerodynamic applications, the Bluff bodies are shaped in such a way that the boundary separation is delayed as much as possible. Nevertheless, using novel technologies, it is possible to reattach the previously separated BL, or at least further delay its separation. One of the novel techniques which allows for the modification of the separation point of the BL is Active Flow Control (AFC). This consists of injecting/sucking fluid in pre-defined locations. In the vast majority of AFC applications, it is essential to perform an energy assessment in order to make sure that the energy saved by the reduction/increase of the forces due to the modification of the BL separation point is much larger than the energy employed for the actuation. In order to achieve this goal, it is essential to properly tune the five parameters associated to any AFC implementation, groove position, groove width, momentum coefficient, jet inclination angle and jet frequency. Such tuning can be carried out via a parametric optimization or using any optimizer. In other words, AFC is always associated with optimization methodologies; otherwise, the energy assessment cannot be successfully accomplished. The present book is based on a set of published articles that highlight some novel applications of flow control.

2. Book Contents

The articles presented in this book are related to novel flow control technologies and are divided into four main categories. The first one presents several **Passive Flow Control** (PFC) applications, which highlights the current relevance of passive methodologies. PFC is used to improve the performance of axial compressors by reducing the generation of shedding vortices at the trailing edge of a blade. This was initially investigated by Gao et al. [1]. Flow field improvements in highly loaded compressors and aeroengines are studied numerically by Xu et al. [2] and Lei et al. [3], respectively. In both cases, it was observed that appropriate three-dimensional blading resulted in an increase in static pressure and a reduction in the influence of secondary flows. A flapping bionic wavy leading edge wing is studied by Bai et al. [4], and they realized that it generated a higher lift than conventional airfoils. The passive flow-control application section is closed by the transient analysis undertaken on cruise missiles' submerged inlet by Zhang and Mi [5]. The use of a distributed submerged inlet proved to have clear advantages compared to the conventional inlet. Closely related to passive flow control applications is the section related to **surface micro-machining**, where micro-texturing is employed by Shang et al. [6], to reduce the drag and modify the cavity area in hydrostatic bearings. Micro-grooves are used by Cacciatori et al. [7], to reduce the drag in an Unmanned Aerial Vehicle's (UAV's) fixed wing. The next section presents several **Active Flow Control** (AFC) investigations. In the

Citation: Bergada, J.M.; Bugeða, G. Flow Control, Active and Passive Applications. *Appl. Sci.* **2023**, *13*, 9228. <https://doi.org/10.3390/app13169228>

Received: 1 August 2023
Accepted: 7 August 2023
Published: 14 August 2023



Copyright: © 2023 by the authors. Licensee MDPI, Basel, Switzerland. This article is an open access article distributed under the terms and conditions of the Creative Commons Attribution (CC BY) license (<https://creativecommons.org/licenses/by/4.0/>).

research by Carbajosa et al. [8], the effectiveness of a pulsating jet is compared with a steady blowing jet, aiming to control the flow on a turbine airfoil trailing edge. Several injection frequencies were evaluated, and they demonstrated that pulsating forcing is more effective than steady actuation. A parametric optimization considering three AFC parameters on an NACA-8412 airfoil at an Angle of Attack (AoA) of 15 degrees and Reynolds number of 68.5×10^3 is undertaken by Couto and Bergadà [9]. The effectiveness of using plasma actuators on an NACA 0015 airfoil at pre-stall AoA at a Reynolds number of 63000 is analyzed by Ogawa et al. [10]. An optimized design of a slat channel configuration, aiming to increase the lift of a given airfoil profile, is presented by Yu and Mi [11]. In fact, this final paper opens the door to the final chapter, which is **Optimization Techniques (OT)**. At present, in many applications and especially those involving AFC technology, it is necessary to optimize the parameters to minimize the energy used for the application while maximizing the outcome. In AFC applications, five parameters need to be optimized, and despite the fact that parametric optimizations can be quite useful, the use of optimizers based on Genetic Algorithms (GA) or gradient-based methods appear to be a much more precise way to accurately tune the required parameters. This is the direction of the work conducted by Coma et al. [12]. In this research, the performance of GA and gradient-based methods is compared when these methods applied to an SD7003 airfoil to tune the AFC parameters. A hybrid evolutionary optimization method (HCGA) in combination with a CFD solver, is presented in the work of Zhao et al. [13], as a decision-maker design tool for aerodynamic shape design. The final contribution of this book was made by Li and Qin [14], who present a review of the different flow control techniques used for gust load alleviation.

3. Concluding Remarks

The reader should consider that the present book aims to simply introduce some of the many existing flow control applications. In fact, the goal of the editors is to open a door to this rather novel technology and hopefully highlight the importance of optimization techniques in AFC applications. We sincerely hope that the reader will enjoy the different research works published here while noticing the variety of applications of flow control technologies.

As a final remark, we would like to reproduce one of Albert Einstein's quotes: **"Life is like riding a bicycle. To keep your balance, you must keep moving"**. In this way, may this book help the reader to keep moving.

Author Contributions: Both authors have contributed equally to this book. All authors have read and agreed to the published version of the manuscript.

Conflicts of Interest: The authors declare no conflict of interest.

References


1. Gao, G.; You, Q.; Kou, Z.; Zhang, X.; Gao, X. Simulation of the Influence of Wing Angle Blades on the Performance of Counter-Rotating Axial Fan. *Appl. Sci.* **2022**, *12*, 1968. [CrossRef]
2. Xu, X.; Wang, R.; Yu, X.; An, G.; Qiu, Y.; Liu, B. Toward the Utilization of 3D Blading in the Cantilevered Stator from Highly Loaded Compressors. *Appl. Sci.* **2023**, *13*, 3335. [CrossRef]
3. Lei, Z.; Liu, H.; Li, G.; Gong, J.; Zhang, Y.; Lu, X.; Xu, G.; Zhu, J. Influence of Wake Intensity on the Unsteady Flow Characteristics of the Integrated Aggressive Interturbine Duct. *Appl. Sci.* **2022**, *12*, 6655. [CrossRef]
4. Bai, X.; Zhan, H.; Mi, B. Unsteady Aerodynamic Design of a Flapping Wing Combined with a Bionic Wavy Leading Edge. *Appl. Sci.* **2023**, *13*, 1519. [CrossRef]
5. Zhang, J.; Mi, B. Internal Aerodynamic Performance Enhancement for Aircraft with High Maneuver by Designing a Distributed Submerged Inlet. *Appl. Sci.* **2023**, *13*, 1459. [CrossRef]
6. Shang, Y.; Cheng, K.; Bai, Q.; Chen, S. Drag Reduction Analysis of the Hydrostatic Bearing with Surface Micro Textures. *Appl. Sci.* **2022**, *12*, 10831. [CrossRef]
7. Cacciatori, L.; Brignoli, C.; Mele, B.; Gattere, F.; Monti, C.; Quadrio, M. Drag Reduction by Riblets on a Commercial UAV. *Appl. Sci.* **2022**, *12*, 5070. [CrossRef]
8. Carbajosa, C.; Martinez-Cava, A.; Valero, E.; Paniagua, G. Efficiency of Pulsating Base Bleeding to Control Trailing Edge Flow Configurations. *Appl. Sci.* **2022**, *12*, 6760. [CrossRef]

9. Couto, N.; Bergada, J. Aerodynamic Efficiency Improvement on a NACA-8412 Airfoil via Active Flow Control Implementation. *Appl. Sci.* **2022**, *12*, 4269. [CrossRef]
10. Ogawa, T.; Asada, K.; Sato, M.; Tatsukawa, T.; Fujii, K. Computational Study of the Plasma Actuator Flow Control for an Airfoil at Pre-Stall Angles of Attack. *Appl. Sci.* **2022**, *12*, 9073. [CrossRef]
11. Yu, J.; Mi, B. A New Flow Control Method of Slat-Grid Channel-Coupled Configuration on High-Lift Device. *Appl. Sci.* **2023**, *13*, 3488. [CrossRef]
12. Coma, M.; Tousi, N.; Pons-Prats, J.; Bugada, G.; Bergada, J. A New Hybrid Optimization Method, Application to a Single Objective Active Flow Control Test Case. *Appl. Sci.* **2022**, *12*, 3894. [CrossRef]
13. Zhao, X.; Tang, Z.; Cao, F.; Zhu, C.; Periaux, J. An Efficient Hybrid Evolutionary Optimization Method Coupling Cultural Algorithm with Genetic Algorithms and Its Application to Aerodynamic Shape Design. *Appl. Sci.* **2022**, *12*, 3482. [CrossRef]
14. Li, Y.; Qin, N. A Review of Flow Control for Gust Load Alleviation. *Appl. Sci.* **2022**, *12*, 10537. [CrossRef]

Disclaimer/Publisher's Note: The statements, opinions and data contained in all publications are solely those of the individual author(s) and contributor(s) and not of MDPI and/or the editor(s). MDPI and/or the editor(s) disclaim responsibility for any injury to people or property resulting from any ideas, methods, instructions or products referred to in the content.

Article

Simulation of the Influence of Wing Angle Blades on the Performance of Counter-Rotating Axial Fan

Guijun Gao^{1,2,3,*} , Qingshan You⁴, Ziming Kou^{1,2,3}, Xin Zhang^{1,2,3} and Xinqi Gao⁵

¹ College of Mechanical and Vehicle Engineering, Taiyuan University of Technology, Taiyuan 030024, China; zmkou@163.com (Z.K.); zxin0109@163.com (X.Z.)

² National-Local Joint Laboratory of Mining Fluid Control Engineering, Taiyuan 030024, China

³ Shanxi Research Center of Mining Fluid Control Engineering, Taiyuan 030024, China

⁴ Chongqing Vocational Institute of Engineering, Chongqing 402260, China; youqingshan@163.com

⁵ School of Design, South China University of Technology, Guangzhou 510006, China; gao_stark@163.com

* Correspondence: gaogj161@163.com; Tel.: +86-138-0343-2565

Abstract: We took the mining counter-rotating fan FBD No.8.0 as the research object, used orthogonal test and numerical simulation to study the influence of wing angle blade on fan performance, and simulated and analyzed its aerodynamic noise. The results show that the pressure distribution of the optimal blade angle blade fan on the pressure surface of the secondary blade is stronger than that of the prototype blade, and the maximum pressure at the blade height of 25%, 50%, and 75% is increased by 2.3%, 9.3%, and 8.1%, respectively, than original blade. Compared with the prototype blade; wing angle blades can effectively reduce the generation of shedding vortices at the trailing edge of the blade, and reduce the strength of shedding vortices, so that the entropy production of the optimal wing angle blade fan is 1.55% lower than that of the prototype fan. Compared with the prototype fan, the full pressure and efficiency of the angle blade fan under the rated flow have increased by 7.24% and 1.76%, and the average increase of 11.32% and 3.88%, respectively, under the full flow condition. Compared with the prototype fan, the maximum sound power of the wing blade fan in the first and second blade trailing edge regions is reduced by 0.17% and 1.62%, respectively.

Keywords: counter-rotating axial fan; orthogonal experiment; numerical simulation; wing angle blade

Citation: Gao, G.; You, Q.; Kou, Z.; Zhang, X.; Gao, X. Simulation of the Influence of Wing Angle Blades on the Performance of Counter-Rotating Axial Fan. *Appl. Sci.* **2022**, *12*, 1968. <https://doi.org/10.3390/app12041968>

Academic Editors: Josep Maria Bergadà and Gabriel Bugeđa Castelltort

Received: 5 January 2022

Accepted: 1 February 2022

Published: 14 February 2022

Publisher's Note: MDPI stays neutral with regard to jurisdictional claims in published maps and institutional affiliations.



Copyright: © 2022 by the authors. Licensee MDPI, Basel, Switzerland. This article is an open access article distributed under the terms and conditions of the Creative Commons Attribution (CC BY) license (<https://creativecommons.org/licenses/by/4.0/>).

1. Introduction

The blade is the main working component of the counter-rotating axial fan for mining, and its shape and structure will directly affect the overall performance of the fan. However, the traditional counter-rotating fan has the problems of low efficiency and high aerodynamic noise. Therefore, studying the shape of the blade has important reference value for improving the performance of the counter-rotating axial flow fan.

Jin Yongping et al. [1] used response surface method and three-dimensional flow field analysis method to optimize the swept parameters of the two-stage blades of the contra-rotating axial flow fan for mines, which increased the fan efficiency by 1.64% and improved the flow of internal fluid. Chen et al. [2,3] perforated the trailing edge of the primary blade and the leading edge of the secondary blade of a small counter-rotating axial fan, and found that the blade perforation reduced the overall noise of the fan by 6–7 dB (A). Wu et al. [4] used numerical calculation software to simulate three types of counter-rotating fans with a primary impeller hub ratio of 0.72 and a secondary impeller hub ratio of 0.72, 0.67, and 0.62. The highest efficiency was observed when the secondary impeller hub ratio was 0.62. Mistry et al. [5] studied the effect of two-stage impeller spacing on the axial flow fan, and pointed out that when the impeller spacing is 0.9 times the chord length, the performance of the fan is optimal.

In recent years, with the development of biomimetic technology, living organisms with excellent flow field characteristics in nature have attracted more and more attention.

Since the blade is the main working component of the fan, the bionic research is mostly carried out around the blade. Tian et al. [6] improved the NACA4412 airfoil based on their study of the wing structure of swallows, and the lift coefficient and lift-drag ratio of the bionic blade were improved compared to the original blade. Inspired by the non-smooth leading edge of the long-eared owl's wings, Sun et al. [7] designed a bionic blade with such a leading edge and introduced this type of blade into an axial fan. The noise of the fan was significantly reduced to the range of 500–2000 Hz, and the maximum noise reduction was about 2.52%. Liang et al. [8] improved the performance of the fan by applying a sawtooth structure on the edge of the fan blade based on the silent principle of bird flight. Under ideal conditions, the bionic blade reduced the noise by 2.2 dB (A). The noise reduction rate was about 2.5%, and the fan efficiency was increased by 5.3%. Xu et al. [9,10], based on the low-noise feature of the owl's flight, installed a bionic serrated structure on the trailing edge of the SD 2030 airfoil blade, and explored the aerodynamics of the blade at different angles of attack and with different sizes of the serrated structures. The analysis showed that the blade trail expansion speed increases with the increase of the size of the saw tooth structure.

Studies have shown that the use of bionic methods to optimize the blades can effectively improve the aerodynamic performance of the blades, thereby improving the internal flow field of the fan. However, in the past, the optimal design of counter-rotating fans was mostly the application of conventional methods, while the bionic methods were mostly concentrated on single blade or single-stage axial flow fans, and there were few bionic researches on blades of counter-rotating axial flow fans for mining. Therefore, this paper takes the FBD No.8.0 mine counter-rotating fan as the research object. Inspired by the wing angle structure of migratory birds that will improve the external flow field of the wings during the long-term evolution of migratory birds, the wing angle bionic design of the fan blade was carried out. At the same time, orthogonal experiments and numerical calculations were used to simulate the performance and noise of the modified fan, and a static analysis was carried out. The results were compared with the performance of the prototype fan, providing a design idea and data processing method for the optimal design of similar fans.

2. Numerical Calculation Model and Calculation Method

2.1. Numerical Calculation Model

This article takes a FBD No.8.0 mine counter-rotating fan as the research object. When modeling the wind turbine, in order to facilitate the numerical calculation, its internal structure was appropriately simplified. The final wind turbine model is shown in Figure 1. The entire fan model is composed of six parts: primary and secondary impellers, collector, deflectors and air ducts. The specific parameters of each part are shown in Table 1.

The wind turbine model was imported into ICEM CFD, and the two-stage impeller and the air duct area were meshed separately using a more adaptable unstructured grid. When the impeller was meshed, the flow field in this area was relatively complex and was the main area of the research, so the mesh was encrypted. The mesh size of the blade surface was controlled at 2 mm. Set 5 layers of boundary layer grids on the solid surface of the fan, and the first layer of boundary layer grids was set to 0.05 mm, so that the fan wall grid $y^+ = 30$. Finally, the two parts were superimposed to form a complete computational domain grid model. The independence of the grid is tested. The results are shown in Table 2. It is found that when the number of cells are 2 million, the efficiency basically remains unchanged, so the number of cells finally selected is 2 million.

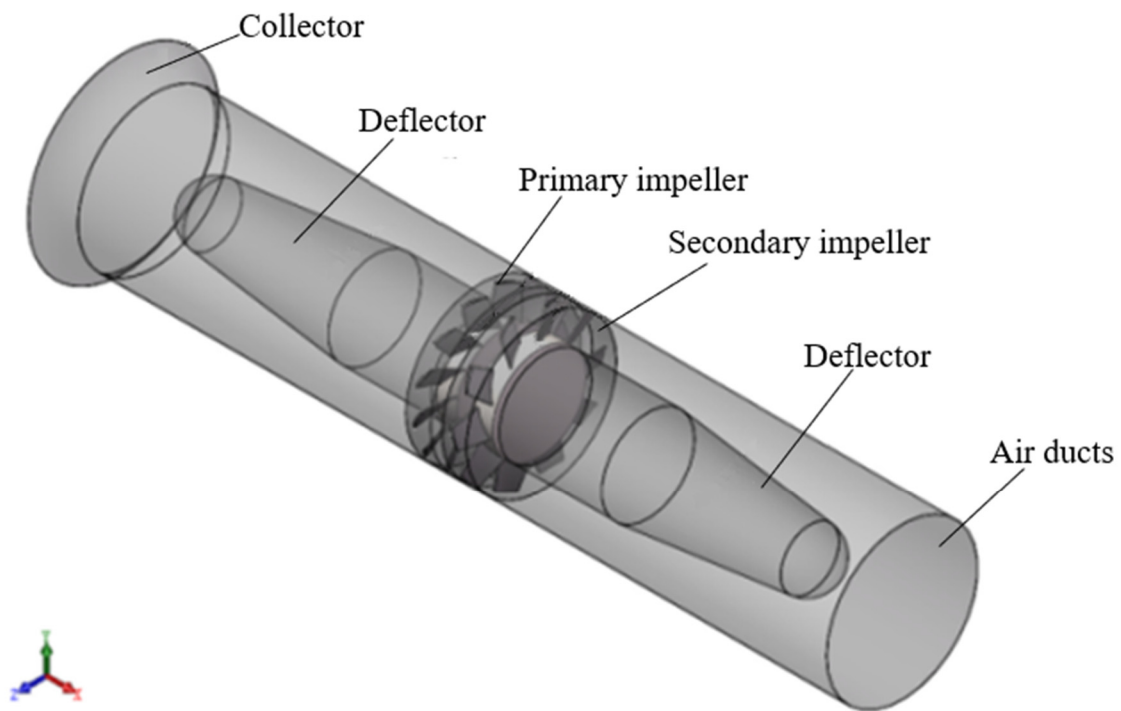


Figure 1. Three-dimensional model of wind turbine.

Table 1. Design parameters of FBD No.8.0 mine cyclone machine.

Design Parameters	Value
Number of blades of first-stage impeller	14
Number of blades of second-stage impeller	10
One, two leaf height (H/mm)	150
Chord length of first and second stage blade tip (L/mm)	111
One, two wheel hub ratio	0.6
One, two stage tip clearance(mm)	2
One, two rated speed/(rad/min)	± 2900
Mounting Angle of first-stage blade ($^{\circ}$)	46
Mounting Angle of two-stage blade ($^{\circ}$)	30

Table 2. Grid independence test.

The Number of Cells (Million)	The Efficiency (%)	The Number of Cells (Million)	The Efficiency (%)
1.34	72.23	1.70	71.98
1.79	73.25	2.02	74.62
3.22	74.50	3.64	74.56

2.2. Calculation Method and Solver Settings

Numerical simulation of the wind turbine model was carried out with ANSYS Flunet numerical calculation software. The settings were as follows:

- (1) Solver setting: Choose the RNG k- ϵ turbulence model [11] that can better reflect the rotation of the fan impeller, and ignore the influence of gravity on the fan flow field. The standard wall function was used near the wall, and the pressure and velocity coupling selected the SIMPLE algorithm, and each difference format used the second-order accuracy [12].
- (2) Setting of regional conditions: The calculation of the flow field adopted the moving coordinate system method, and the two-stage impeller part was set as the rotating zone, the speed was ± 2900 rad/min, and the fan part was the static zone [13].

- (3) Boundary condition setting: Define the inlet end face of the collector as the velocity inlet, and the velocity direction was the normal direction of the inlet end face. The turbulence intensity and hydraulic diameter method were selected to control the turbulence; the outlet end face of the air duct was set as a free outlet; define the interface between the two-stage impeller and the air duct area for coupling and data transmission; the two-stage blade and the wall of the hub were set with a rotating wall, and the rotation speed remained relatively static with the region of adjacent cells. The other walls were set as static walls. All walls adopted the wall condition without slippage and considering the surface roughness.
- (4) Convergence conditions: When the residual values of turbulent kinetic energy k , dissipation rate ε , and velocities in various directions were less than 1×10^{-4} , the calculation was considered to be convergent.

2.3. Statics Settings

During the static analysis of the blade, mesh the hub and blade with an unstructured grid, and ensure that the mesh size on the blade is the same as the mesh size of the first boundary layer of the blade in the fluid calculation, so as to reduce the transmission error in the fluid–solid coupling process. The materials of the hub and blades were steel. Import the blade surface pressure data in the fluid simulation into the ANSYS statics analysis module as the surface pressure load, and apply ± 2900 rad/min centrifugal force load and gravity field load to the primary and secondary impellers, respectively.

2.4. Experimental Verification

Since the counter-rotating fan for mining was a press-in fan, the GB/T 1236–2000 Type B device was selected to collect data related to the total pressure P_t and efficiency η of the fan, and then the accuracy of the numerical calculation results was experimentally verified.

Figure 2 is a test platform for a counter-rotating axial flow fan. The wind resistance of the fan can be changed by adjusting the distance between the cone-shaped restrictor in Figure 2b and the outlet of the test air tube to achieve the purpose of imposing different loads on the fan, and then it provided conditions for testing the fan under full flow conditions.

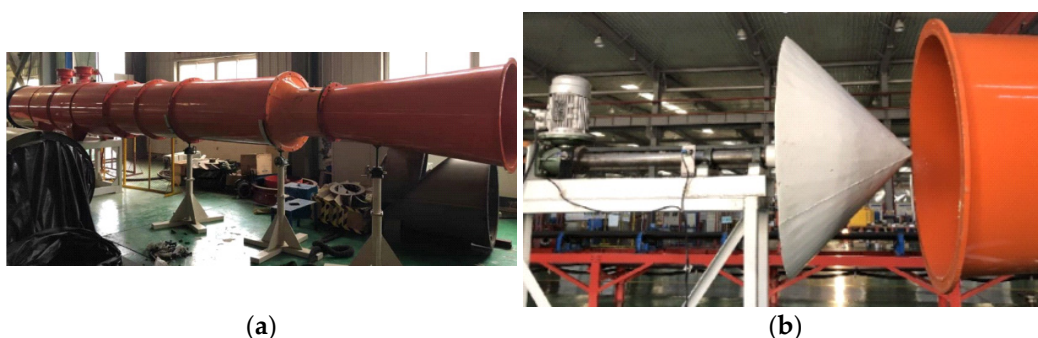


Figure 2. Test platform for contra-rotating axial fan. (a) Counter-rotating fan and test air duct; (b) tapered restrictor.

As shown in Figure 3, the collected results were compared with the numerical calculation results. It can be seen from the figure that the trends of the full pressure P_t and efficiency η curves of the simulation and experiment were basically the same. Additionally, the average deviations of the total pressure P_t and efficiency η of simulation and experiment were 1.75% and 0.60%, respectively; the relative deviations at the rated flow point were about 1.44% and 0.01%, and both were within 5%. This showed that the reliability of modeling, meshing and calculation method settings was high, and the numerical calculation results could reflect the actual operation of the wind turbine.

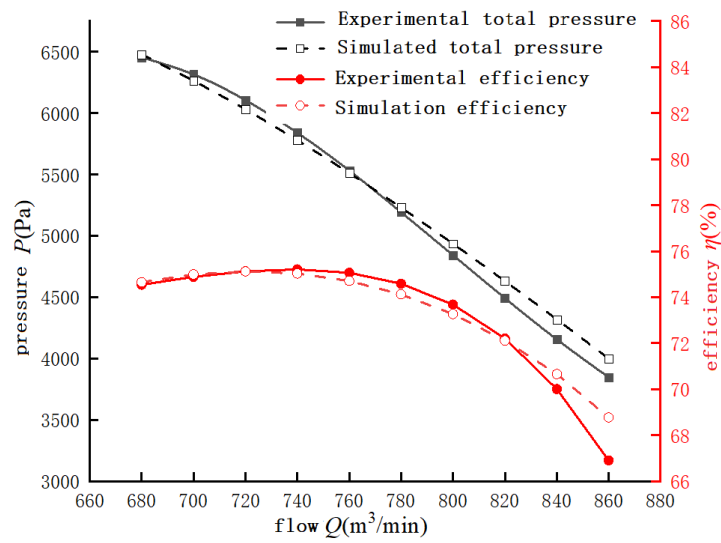


Figure 3. Comparison of fan experiment and simulation data.

3. Wing Angle Blade Model and Orthogonal Test

3.1. Wing Angle Blade Design

The blade is the main working component of the fan, and its function is to convert the mechanical energy of the rotating blade into fluid pressure energy and kinetic energy. Therefore, the shape and structure of the blades play a decisive role in the performance of the fan.

As shown in Figure 4 [14], during the flight of large migratory birds, the leading edge of their wings has wing angle structure, which helps improve the flow field near the wing during long-distance flight. Inspired by this, bionic design of two-stage fan blades was carried out by applying only a certain range of wing angle structure on the blade without changing the parameters of the prototype blade, such as airfoil, twist angle α and blade height H , as shown in Figure 5. The wing angle position s was the distance from the deflection of the upper wing angle to the blade root in the direction of the blade height. The tip offset distance a was the offset distance of the wing angle blade relative to the prototype blade at the tip of the blade upward from the chord of the blade.

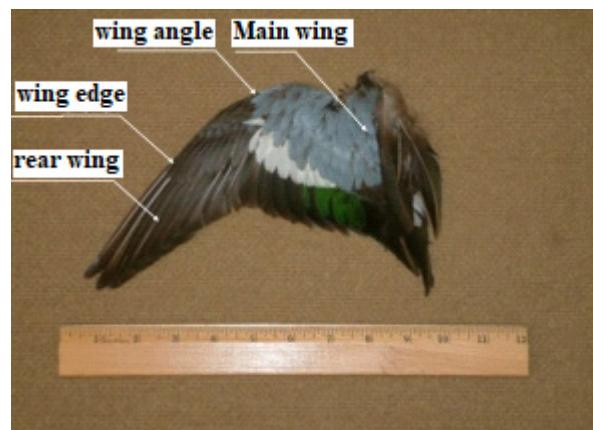


Figure 4. Wing angle structure of bird wing.

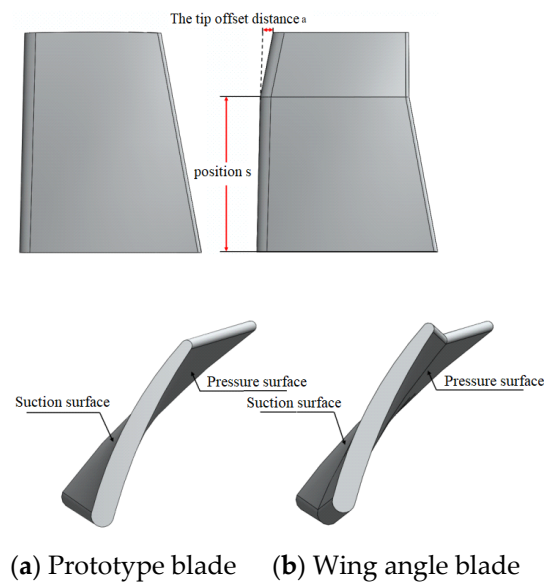


Figure 5. Blade model.

3.2. Orthogonal Experiment Design

According to the key dimensions of the wing angle blades and in order to reduce the number of tests, an orthogonal test was designed to select the wing angle position s and tip offset distance a of the first and second stage blades [15]. Among them, factor A was the position s_1 of first-stage blade tip, factor B was the tip offset distance a_1 of first-stage blade, factor C was the position s_2 of second-stage blade tip, and factor D was the tip offset distance a_2 of second-stage blade. According to relevant fan studies, the main work area of the blade was the upper middle part of the blade, and the maximum static pressure coefficient was the largest at the pressure front edge at 75% of the blade height [16]. Therefore, the position s of the wing Angle was selected in this area. The tip offset distance was selected from 10 mm to 20 mm to ensure that the blade strength will not be reduced due to excessive structural deformation. Finally, an orthogonal test with four factors and three levels was determined, as shown in Table 3.

Table 3. Orthogonal experiment factors level table.

Test Serial Number	Position of First-Stage Blade Angle A/mm	Tip Offset Distance of First-Stage Blade B/mm	Position of Second-Stage Blade Angle C/mm	Offset Distance of Blade Tip of Second-Stage Impeller D/mm
1	100	10	100	10
2	110	15	110	15
3	120	20	120	20

3.3. Optimal Wing Angle Blade Fan

Range analysis was conducted on the efficiency of rated flow points, and the efficiency values of each test were shown in Table 4. According to the principle of orthogonal test, factors with larger range values had greater influence on efficiency. Therefore, the degree of influence of each factor on efficiency was A (s_1 of first-stage blade angle), C (s_2 of second-stage blade angle), B (a_1 of first-stage blade tip offset), and D (a_2 of second-stage blade tip offset) in descending order. It could also be concluded that compared with the prototype fan ($\eta = 75.18\%$), the fan efficiency of nine experimental schemes was improved at the rated flow point. The degree of influence of the corresponding factors of the first stage impeller was greater than that of the second stage impeller, which was mainly because in the cyclone machine, the number of blades of the first-stage impeller was more than that of the second-stage impeller, and the flow velocity into the first-stage impeller was lower

than that into the second-stage impeller, and the rotational speed of the two-stage impeller was the same. Therefore, in a unit time, the effect of the first-stage impeller on the flow was stronger than that of the second stage impeller.

Table 4. Design flow point efficiency data processing and range analysis.

Test Serial Number	Position of First-Stage Blade Angle A/mm	Tip Offset Distance of First-Stage Blade B/mm	Position of Second-Stage Blade Angle C/mm	Tip Offset Distance of Second-Stage Blades B/mm	Efficiency $\eta/\%$
1	100	10	100	10	76.69
2	100	15	110	15	76.36
3	100	20	120	20	76.94
4	110	10	110	20	76.53
5	110	15	120	10	76.45
6	110	20	100	15	76.38
7	120	10	120	15	76.51
8	120	15	100	20	76.32
9	120	20	110	10	76.31
k_1	77.66	76.58	76.46	76.48	
k_2	76.45	76.38	76.40	76.42	
k_3	76.38	76.54	76.63	76.60	
Range	0.28	0.20	0.23	0.18	

k_i in the table represents the average efficiency of test parameters at the level of i , and the level corresponding to the maximum k_i is the optimal level of this factor. In conclusion, the optimal level combination of the orthogonal test is $A_1B_1C_3D_3$.

4. Analysis of Optimization Results

In order to further study the influence of wing angle blades on the internal flow field of the fan, the prototype fan was compared with the optimal wing angle blade fan in orthogonal test. For the convenience of the analysis, the orthogonal experiment optimal vane fan is referred to as wing blade fan in the following.

4.1. Total Pressure Distribution on Blade Surface

The pressure distribution on the blade surface can effectively reflect the power capacity of the fan blade. Figure 6 shows the total pressure distribution curves of the first and second blades of the wing angle blade fan and prototype fan at the rated flow point. The prototype blades and wing angle blades are, respectively, analyzed at 25%, 50% and 75% relative blade heights. The relative position $R = x/L$ is defined, where x is the distance from any point on the blade to the leading edge of the blade [16], and L is the chord length of the blade, mm. To the left of the black dotted line is the leading edge of the blade.

In Figure 6a, as the relative blade height increases, the pressure of the pressure surface also increases, which also reflects that the upper half of the blade is the main working area. The total pressure distribution of the wing angle blade and the prototype blade on the suction surface and pressure surface is roughly the same. Additionally, the maximum pressure is located at the front edge of the blade. At a relative blade height of 75%, the maximum pressure of the angle blade is 6082.19 Pa, which is an increase of 22.15% compared to the maximum pressure of the prototype blade of 4979.35 Pa.

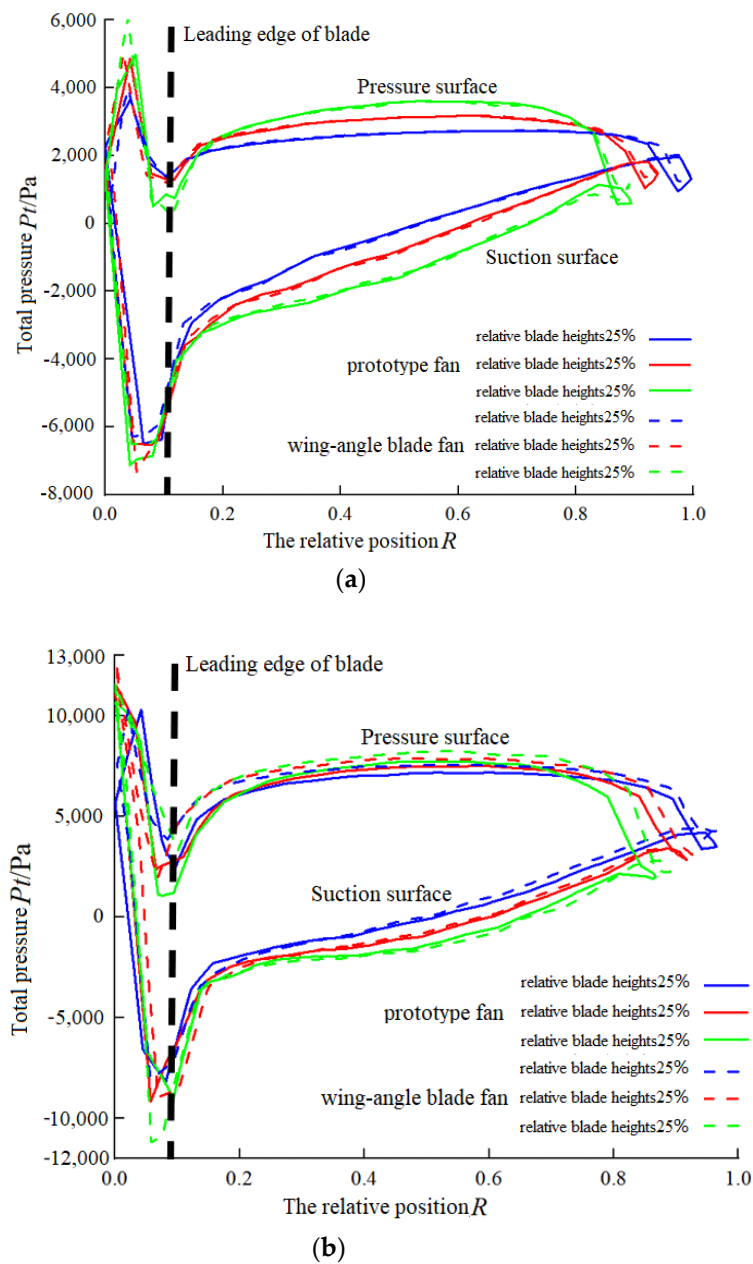


Figure 6. Total pressure distribution on blade surface. (a) Total pressure distribution of the first-stage blade; and (b) total pressure distribution of the second-stage blades.

From Figure 6b, it can be seen that the total pressure of the secondary stage impeller blade at the pressure surface of the blade is stronger than that of the prototype blade at the same blade height, which indicates that the functional force of the blade angle blade is better than that of the prototype blade, and the maximum total pressure is also located at the pressure surface of the leading edge of the blade. The maximum pressures at 25%, 50%, and 75% of the blade height are 10,289.05 Pa, 12,575.33 Pa, 11,613.50 Pa, respectively, which are 2.3%, 9.3% and 8.1% higher compared to the prototype blade at the same height.

4.2. *Q* Isosurface Analysis

Due to the relatively complex flow field in the fan wheel area, there are a large number of vortices near the blades, and the vortices will reduce the efficiency of the fan and increase the noise. Therefore, this paper uses the *Q* isosurface method to discriminate the flow

field in the two-stage impeller area of the fan, and observe the distribution of the vortex core position.

The research on vortices is in the process of continuous exploration, and a variety of vortex identification technologies have been developed. At present, the Q criterion and the Λ_2 criterion are commonly used. Indeed, Λ_2 is a very powerful tool in the comparison between the different configurations in terms of vortical structures as done, e.g., in Mariotti et al. [17], Alavi Moghadam et al. [18], and Rocchio et al. [19]. I think Q criterion is more suitable for the analysis of fan impeller flow field in this paper.

The definition of Q isosurface is:

$$Q = \frac{1}{2}(\Omega_{ij}\Omega_{ij} - \sigma_{ij}\sigma_{ij}) \quad (1)$$

Ω_{ij} represents the vorticity tensor; σ_{ij} represents the strain rate tensor, and the expressions are as follows:

$$\Omega_{ij} = \frac{1}{2}\left(\frac{\partial u_i}{\partial x_j} - \frac{\partial u_j}{\partial x_i}\right) \quad (2)$$

$$\sigma_{ij} = \frac{1}{2}\left(\frac{\partial u_i}{\partial x_j} + \frac{\partial u_j}{\partial x_i}\right) \quad (3)$$

The equation that reduces Equation (1) to 3D Cartesian coordinates is:

$$Q = -\frac{1}{2}\left[\left(\frac{\partial u}{\partial x}\right)^2 + \left(\frac{\partial v}{\partial y}\right)^2 + \left(\frac{\partial w}{\partial z}\right)^2\right] - \frac{\partial u}{\partial y} \cdot \frac{\partial v}{\partial x} - \frac{\partial u}{\partial z} \cdot \frac{\partial w}{\partial x} - \frac{\partial v}{\partial z} \cdot \frac{\partial w}{\partial y} \quad (4)$$

In Formula (4): u, v, w are the velocity components of the velocity v in the $x, y,$ and z directions, m/s. When $Q > 0$, it means that the rotation of the fluid mass is dominant.

Figure 7 shows the Q isosurface distribution of the blade angle blade fan and the prototype fan in the first-stage and second-stage impeller regions. The Q isosurface of the first-stage and second-stage impellers are about $2.5 \times 10^5 \text{ s}^{-2}$ and $8.5 \times 10^4 \text{ s}^{-2}$, respectively. It can be seen from the figure that the vortices near the blade are mainly divided into the tip leakage vortex, the tip separation vortex and the blade shedding vortex. From the comparison between the prototype fan and the blade angle blade fan, it is found that compared with the prototype fan blade, although the blade angle structure has no obvious effect on the improvement of the vortex core distribution of the tip separation vortex and the tip leakage vortex, it improves the core distribution of the vortex at the trailing edge of the blade.

The generation mechanism of the blade shedding vortex is the same as that of the Karman vortex street [20]. The formation of the Karman vortex street is due to the interaction of the inertia and viscosity of the fluid on the back of the cylinder after the fluid contacts the solid surface. A periodic vortex is formed, and the vortex will periodically fall off behind the solid with the flow of the airflow. The size of the period is related to the Reynolds number Re of the fluid and the shape of the solid. The blade shedding vortex will also produce periodic vortices in the area of the trailing edge and pressure surface of the blade. When the frequency of the shedding vortex coincides with the natural frequency of the blade rotation, resonance will occur, causing the blade to vibrate violently, which will lead to damage or failure of the blade. Therefore, in the actual design and use of the fan, the generation of blade shedding vortices should be avoided as much as possible.

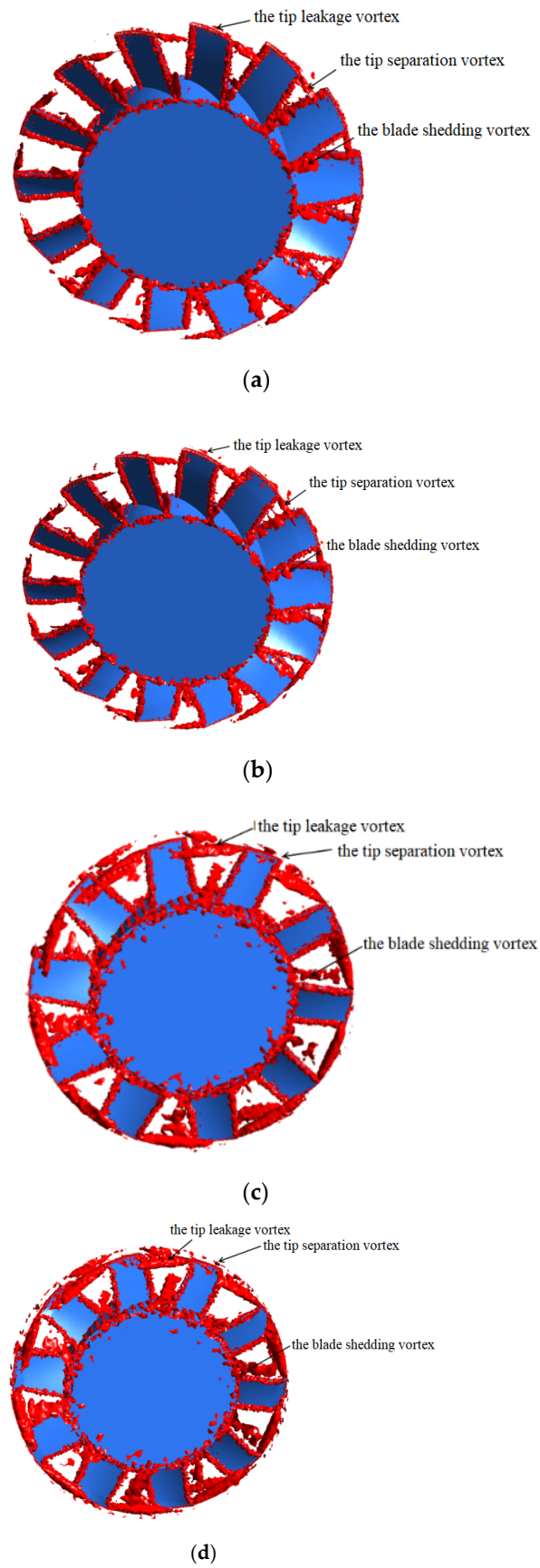


Figure 7. Q isosurface distribution. (a) First-stage blade of prototype fan; (b) first-stage blade of wing angle fan; (c) second-stage blade of the prototype fan; and (d) second-stage blade of wing angle fan.

Since the Q isosurface method can only observe the distribution of the core position of the blade vortex, it cannot obtain the strength of the vortex. For this reason, this paper uses the analysis method provided by Inoue [21] to determine the magnitude of the vortex intensity. The method found through experiments that the vortex intensity is inversely related to the static pressure, that is, the lower the static pressure at the trailing edge of the blade, the higher the vortex intensity. Additionally, the lowest area of its static pressure is the core area of the vortex. In order to obtain the distribution of the blade shedding vortex intensity, take the vicinity of the trailing edge of any blade of the two-stage impeller as the starting point, and set three planes A, B, and C at equal intervals from near to far, as shown in Figure 8, where the interval between two adjacent planes is $0.25L$. By observing the static intensity distribution cloud diagrams of these three planes, the strength of the shedding vortex at the trailing edge of the blade can be seen.

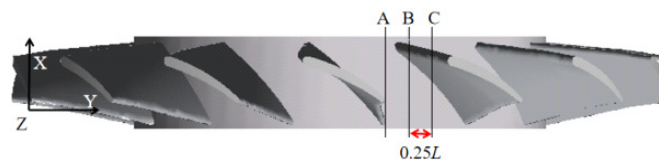


Figure 8. Distribution of plane A, B, and C positions.

Figure 9 shows the static pressure distribution of planes A, B, and C in the first and second blade trailing edge regions of the prototype fan and the angle blade fan, respectively. The arrows in the figure indicate the direction of rotation of the impeller, and the dashed lines indicate the trajectory of the blade shedding vortex. The contours are discontinuous in both figures, which is caused by errors in the interface surface during data transmission. It can be seen from the figure that the static pressure intensity distribution of the prototype blade in section A is significantly smaller than that of the angle blade, and the range of the lowest static pressure zone at section C is also larger than that of the angle blade, which indicates both the strength and range of the shedding vortex of the prototype blade are greater than those of the angle blades. This is because the wing angle structure divides the blade into upper and lower parts at the wing angle position, and the leading edge of the upper half is at a certain angle to the incoming flow direction. This causes the airflow passing through the upper half of the blade to flow toward the tip of the blade after reaching the leading edge of the blade during the rotation of the blade. This destroys the conditions for generating the tail shedding vortex, thereby reducing its vortex intensity and range.

4.3. Entropy Production Analysis of Fan

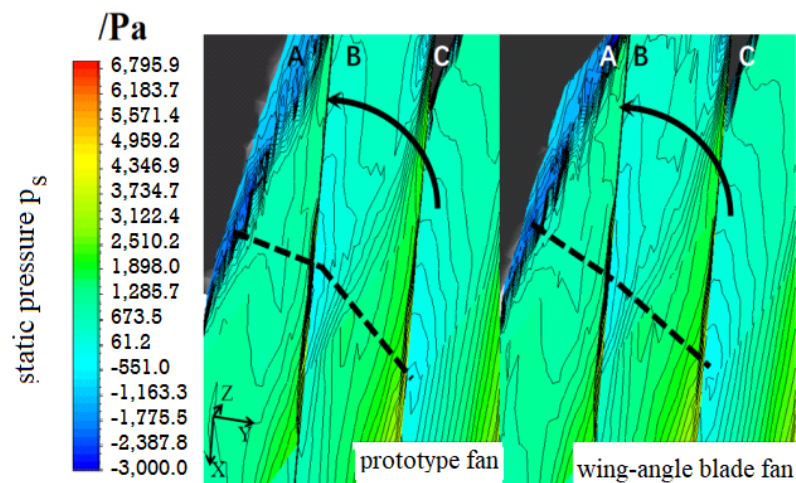
For axial fans, the existence of a vortex structure in the internal flow field will inevitably increase the entropy production of the system, which in turn will cause the internal energy loss of the fan. Entropy generation theory can evaluate the energy dissipation inside the fan, so more and more scholars use entropy generation analysis to study the internal efficiency of the fan [22–24]. As the internal temperature change of the axial flow fan is very small during operation, the entropy production caused by the temperature change is ignored. Therefore, the total entropy production rate S is composed of two parts, namely, the time-averaged entropy production rate $S_{PRO,D}$ produced by the turbulent dissipation of the time-averaged flow field, and the pulsating entropy production rate $S_{PRO,D'}$ caused by the pulsating velocity. Among them, the pulsating entropy generation rate $S_{PRO,D'}$ cannot be directly calculated due to the use of the RANS equation in the numerical calculation, but Kock found that $S_{PRO,D'}$ is related to the turbulent dissipation rate ϵ through verification [25]. Therefore, the final time average entropy production rate $S_{PRO,D}$, the pulsating entropy production rate $S_{PRO,D'}$ and the total entropy production formula are shown as Equations (5)–(7), respectively.

$$S_{PRO,D} = \frac{\mu}{T} \left\{ 2 \left[\left(\frac{\partial \bar{u}}{\partial x} \right)^2 + \left(\frac{\partial \bar{v}}{\partial y} \right)^2 + \left(\frac{\partial \bar{w}}{\partial z} \right)^2 \right] + \left(\frac{\partial \bar{u}}{\partial y} + \frac{\partial \bar{v}}{\partial x} \right)^2 + \left(\frac{\partial \bar{u}}{\partial z} + \frac{\partial \bar{w}}{\partial x} \right)^2 + \left(\frac{\partial \bar{v}}{\partial z} + \frac{\partial \bar{w}}{\partial y} \right)^2 \right\} \quad (5)$$

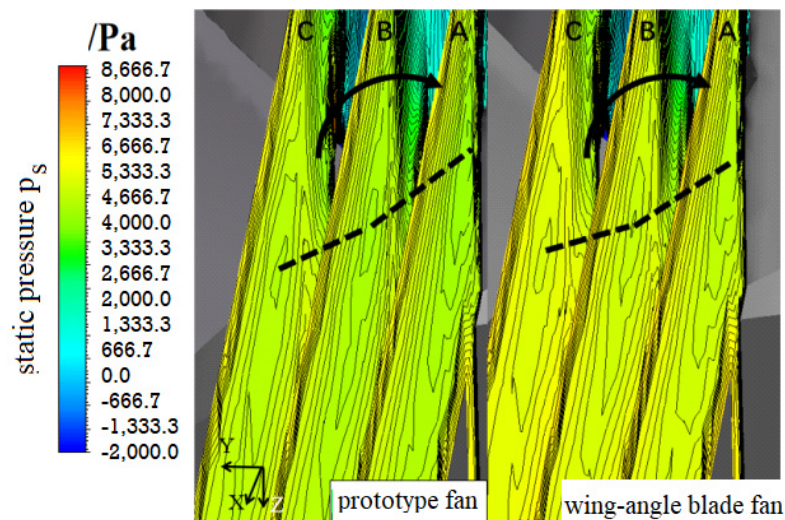
$$S_{PRO,D'} = \frac{\rho \varepsilon}{\bar{T}} \tag{6}$$

$$\dot{S} = \int_V S_{PRO,D} dV + \int_V S_{PRO,D'} dV \tag{7}$$

In the formula above, \bar{u} , \bar{v} , and \bar{w} are the time-average velocity components of velocity in the x , y , and z directions, m/s; \bar{T} is the time-average temperature, K, because the numerical calculation ignores the influence of temperature changes on the flow field, $\bar{T} = 300$ K; ρ is the density, kg/m³; ε is the turbulent dissipation rate, the formula is $\varepsilon = 1.5 (0.16U \cdot Re - 0.125) 1.5, m^{-2} \cdot s^{-3}$, where U is the average velocity of the target fluid, m/s, Re is the Reynolds number; V is the volume of the control body, m³.



(a)

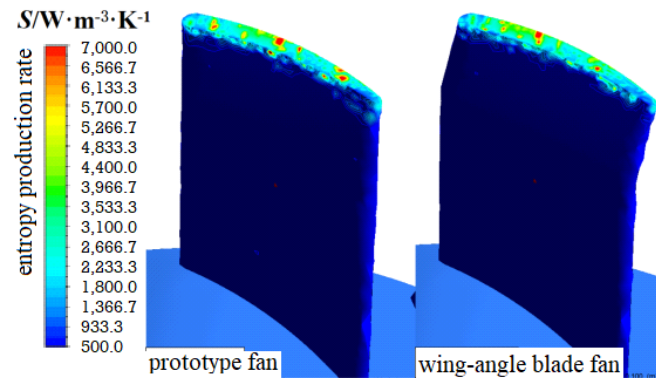


(b)

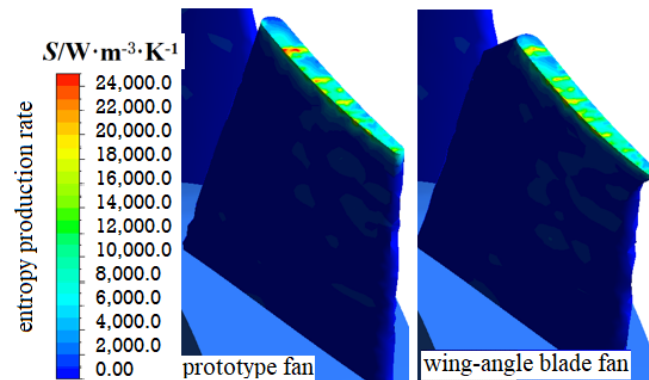
Figure 9. Static pressure distribution on plane A, B, and C. (a) Static pressure distribution at the section of the first-stage impeller; and (b) static pressure distribution at the section of the second-stage impeller.

Figure 10 shows the distribution of the total entropy production rate S in the primary and secondary blades. From the figure, it can be seen that the total entropy production rate S of the secondary leaves is greater than that of the primary leaves, and the entropy production rate of the tip part is the highest. This is because after the fluid enters the

secondary impeller through the pressurization of the primary impeller, its flow velocity must be greater than that of the primary impeller, and the fluid velocity at the tip of the blade is the largest. It can be seen from Formula (4) and Formula (5) that the time-averaged entropy production rate $S_{PRO,D}$ and the pulsating entropy production rate $S_{PRO,D'}$ are both positively correlated with the flow velocity, and the flow field at the tip clearance is relatively complicated. Therefore, under the combined effect of the above factors, the entropy generation rate in the tip area of the secondary blade is higher than that in other positions of the fan.



(a)



(b)

Figure 10. S distribution of total entropy production on the blade surface. (a) S distribution of total entropy yield in the first-stage blade; and (b) S distribution of total entropy yield in the second-stage blade.

From Table 5, it can be seen that the time-average entropy production $\dot{S}_{PRO,D}$ of the prototype fan and the angle blade fan is much smaller than the pulsating entropy production $\dot{S}_{PRO,D'}$, which also verifies the conclusion in the literature [22]. Entropy production is arranged in the order of two-stage impeller, first-stage impeller, and air duct. The air duct has the least entropy production because it has a current collector and a rectifier, so it has a relatively favorable aerodynamic shape, which causes minimal loss of entropy production. The total entropy production of the two-stage impeller is greater than that of the first-stage impeller, which is similar to the results of the previous analysis. It can also be seen from the table that the total entropy production of the angle blade fan is 1.55% lower than that of the prototype fan.

Table 5. Entropy production in each area of the angle blade fan and the prototype fan.

Type	Entropy Production	Wind Tube	Primary Impeller	Secondary Impeller	Total
Prototype fan	$\dot{S}_{PRO,D}$	0.1186	2.2784	4.1418	6.5388
	$\dot{S}_{PRO,D'}$	1.1334	29.7861	41.4495	72.3690
	\dot{S}	1.2520	32.0645	45.5913	78.9078
Wing angle blade fan	$\dot{S}_{PRO,D}$	0.1150	2.2760	4.2264	6.6174
	$\dot{S}_{PRO,D'}$	1.0972	29.6556	40.3174	71.0702
	\dot{S}	1.2122	31.9316	44.5438	77.6876

4.4. Full Flow Field Analysis

In order to analyze the full flow field characteristics of the wing blade fan, the performance of the wing blade fan under full flow conditions was simulated through numerical calculation and compared with the prototype fan. Figure 11 shows the analysis of total pressure P_t and efficiency η . The optimal wing angle blade fan has a rated flow point of $740 \text{ m}^3/\text{min}$, and the rated flow point of the prototype fan is $730 \text{ m}^3/\text{min}$. The efficiency of the angle blade fan at the rated flow point is 77.10%. At the rated flow point of the prototype fan, the total pressure and efficiency of the optimal angle blade fan are increased by 7.24% and 1.76%, respectively. Under full flow conditions, the total pressure and efficiency have increased by 11.32% and 3.88% on average.

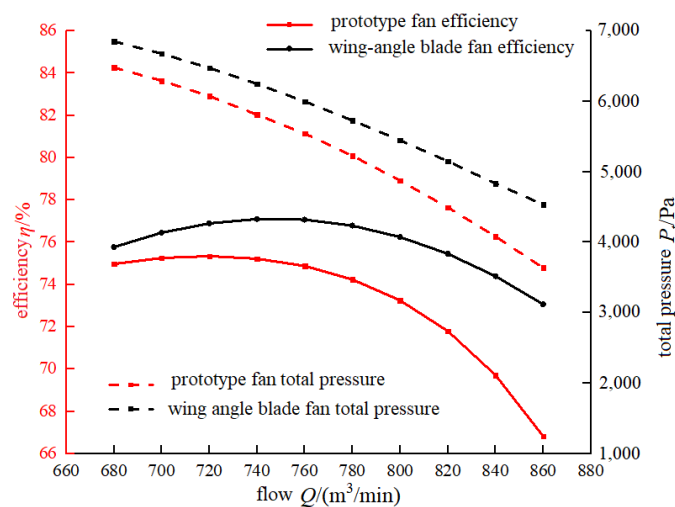
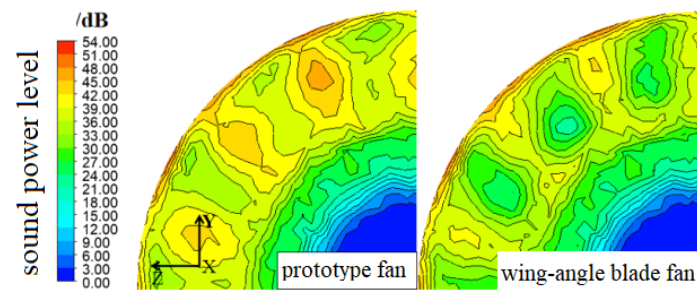


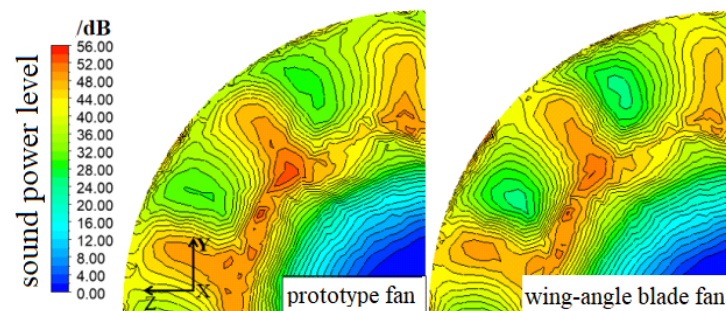
Figure 11. Full flow analysis.

4.5. Noise Estimation

The noise sources of the counter-rotating axial fans for mines are mainly aerodynamic noise and mechanical noise. Aerodynamic noise is generated by the rotation and eddy currents of the airflow inside the fan [26]. As demonstrated above, the wing blade fan can effectively reduce the strength of the blade shedding vortex, so we analyzed the section of the trailing edge 1 L of the two-stage impeller blade here. Figure 12 shows the sound power distribution in the trailing edge area of the first and second stage blades of the wing blade fan and the prototype fan. Compared to the prototype fan, the sound power distribution of the wing blade fan at the trailing edge of both the first and second stage blades has been reduced. The maximum sound power level of the wing blade fan at the trailing edge of the first-stage blade is 50.95 dB, which is 0.17% lower than that of the prototype fan. The maximum sound power level in the trailing edge area of the two-stage blade is 53.32 dB, which is reduced by 1.62% compared to the prototype fan.



(a)



(b)

Figure 12. Sound power distribution in the trailing edge area of the first and second stage blades. (a) Sound power distribution in the trailing edge area of the first-stage blade; and (b) sound power distribution in the trailing edge area of the second-stage blade.

5. Static Analysis

To analyze the partial load distribution of the angle blade fan blade, the finite element software was used to analyze the fluid–structure coupling of the impeller area of the wing angle blade fan and the prototype fan. As shown in Figure 13, the highest stress on the pressure surface of the blade is concentrated at the leading edge blade root. Additionally, as the blade height increases, the equivalent stress gradually decreases. At the suction surface of the blade, the highest equivalent stress is concentrated at the lower half of the leading edge of the blade and the root, and gradually decreases toward the tip of the blade. As summarized in Table 6, the maximum equivalent stress of the first-stage angle blade is reduced by 13.94% compared to the prototype fan. This is mainly because the air flowing through the upper half of the blade is directed by the angle structure to flow in the direction of the tip, resulting in the reduced airflow at the pressure surface of the leading edge of the blade root, thereby reducing the load in this area. Consequently, the maximum equivalent stress of the angle blade relatively is smaller than that of the prototype blade.

Figure 14 shows the deformation of the prototype fan and the angle blade fan at the first and second blades. Deformation of the first and second blades mainly occurs in the upper middle area of the leading edge of the blade, due to the stronger airflow impact on the leading edge than other parts of the blade, and the largest centrifugal force at this location. As summarized in Table 7, the deformation of the wing angle blade is lower than that of the prototype fan.

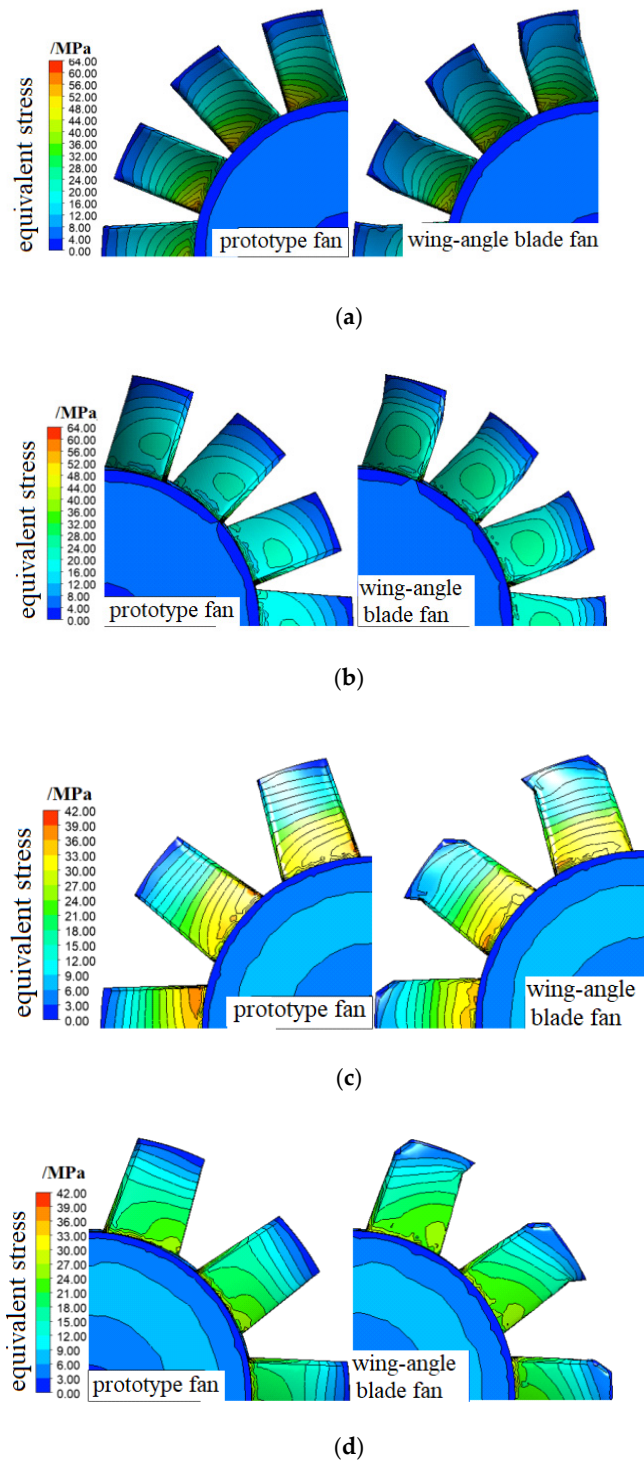


Figure 13. Comparison of equivalent distribution of wing angle blades and prototype wind turbines. (a) Equivalent stress on pressure surface of the first-stage blade; (b) equivalent stress on the suction surface of the first-stage blade; (c) equivalent stress on pressure surface of the second-stage blade; and (d) equivalent stress on the suction surface of the second-stage blade.

Table 6. Equivalent stress of blade.

Blade Stage	Prototype Fan		Wing Angle Blade Fan	
	Minimum Equivalent Stress/MPa	Maximum Equivalent Stress/MPa	Minimum Equivalent Stress/MPa	Maximum Equivalent Stress/MPa
First-stage blade	0.0008	61.8577	0.0011	53.2365
Second-stage blade	0.0048	40.0064	0.0046	40.4835

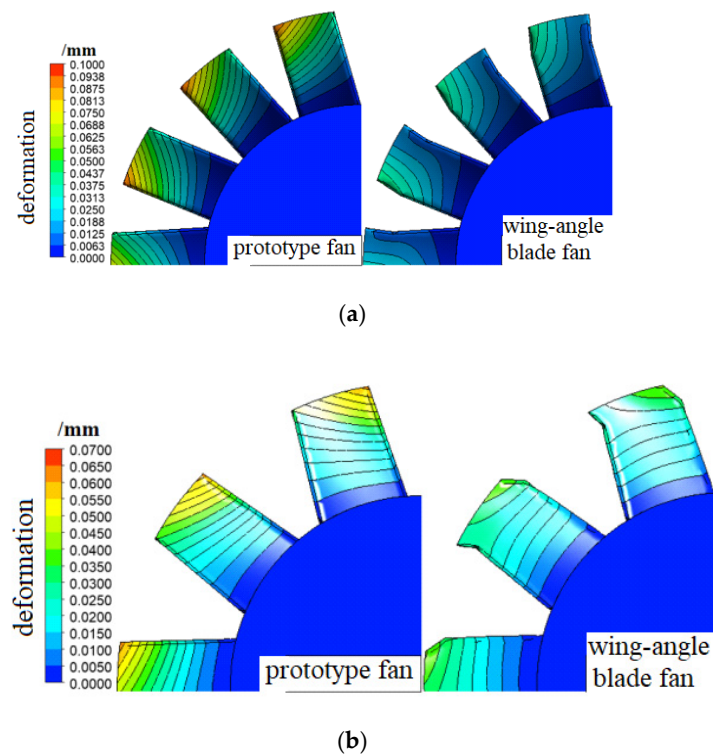


Figure 14. Deformation distribution of wing angle blades and prototype blades. (a) First-stage blade deformation distribution; and (b) second-stage blade deformation distribution.

Table 7. Maximum deformation of the blade.

Blade Stage	Maximum Deformation/mm	
	Prototype Fan	Wing Angle Blade Fan
First-stage blade	0.0969	0.0463
Second-stage blade	0.0624	0.0411

6. Conclusions

The following conclusions can be drawn from this study:

- (1) The pressure distribution on the pressure surface of the secondary blade of the optimal wing angle blade fan is stronger than that of the prototype blade. Additionally, the maximum pressures at blade heights of 25%, 50%, and 75% are increased by 2.3%, 9.3%, and 8.1%, respectively, compared with the prototype blades at the same blade height.
- (2) The angle blade can effectively reduce the generation of shedding vortices at the trailing edge of the blade, and reduce the strength of the shedding vortex, so that the entropy production of the optimal angle blade fan in the orthogonal experiment is reduced by 1.55% compared with the prototype fan.
- (3) Compared with the prototype fan, the total pressure and efficiency of the optimal wing angle blade fan are increased by 7.24% and 1.76% at the rated flow, and the total

pressure and efficiency are increased by 11.32% and 3.88% on average under the full flow condition.

- (4) In the orthogonal experiment, the maximum sound power levels of the first and second blade trailing edge regions of the optimal wing angle blade fan were reduced by 0.17% and 1.62%, respectively, compared with the prototype fan.

Author Contributions: Conceptualization, G.G., Z.K. and Q.Y.; methodology, X.Z.; software, X.Z.; validation, G.G., Z.K. and X.Z.; formal analysis, X.Z.; investigation, G.G., X.Z.; resources, Z.K.; data curation, G.G., X.Z.; writing—original draft preparation, G.G., X.Z., X.G.; writing—review and editing, G.G., X.G.; visualization, G.G., X.Z.; supervision, Z.K., Q.Y.; project administration, Z.K., Q.Y. All authors have read and agreed to the published version of the manuscript.

Funding: This research received no external funding.

Institutional Review Board Statement: This studies do not involve humans or animals.

Informed Consent Statement: No involving humans.

Data Availability Statement: Not applicable.

Acknowledgments: The authors gratefully acknowledge the financial support of Nature fund of Chongqing Science and Technology Bureau (No. cstc2020jcyj-msxmX0793) and the Research plan project of Chongqing Education Committee (No. KJQN202003402).

Conflicts of Interest: The authors declare no conflict of interest.

References

- Jin, Y.P.; Liu, D.S.; Wen, Z.J. Optimization design for skew and sweep parameters of mine contra-rotation two-stage blades. *J. China Coal Soc.* **2010**, *35*, 1754–1759.
- Wang, C.; Huang, L. Passive Noise Reduction for a Contrarotating Fan. *J. Turbomach.* **2014**, *45578*, V01AT10A011. [CrossRef]
- Wang, C. Trailing Edge Perforation for Interaction Tonal Noise Reduction of a Contra-Rotating Fan. *J. Vib. Acoust.* **2018**, *140*, VIB-17-1296. [CrossRef]
- Wu, Y.; Jin, Y.; Jin, Y.; Wang, Y.; Zhang, L. Effect of Hub-Ratio on Performance of Asymmetric Dual-Rotor Small Axial Fan. *Open J. Fluid Dyn.* **2013**, *3*, 81–84. [CrossRef]
- Mistry, C.; Pradeep, A. Effect of variation in axial spacing and rotor speed combinations on the performance of a high aspect ratio contra-rotating axial fan stage. *Proc. Inst. Mech. Eng. Part A J. Power Energy* **2013**, *227*, 138–146. [CrossRef]
- Tian, W.; Liu, F.; Cong, Q.; Liu, Y.; Ren, L. Study on aerodynamic performance of the bionic airfoil based on the swallow's wing. *J. Mech. Med. Biol.* **2013**, *13*, 1340022. [CrossRef]
- Sun, S.M.; Xu, C.Y.; Ren, L.Q.; Zhang, Y.Z. Experimental research on noise reduction of bionic axial fan blade and mechanism analysis. *J. Jilin Univ. (Eng. Technol. Ed.)* **2009**, *39*, 382–387.
- Liang, G.Q. Experimental Research on Noise Reduction of Bionic for Axial Flow Fan. *Mach. Des. Res.* **2010**, *26*, 132–137.
- Xu, K.; Qiao, W.; Ji, L.; Chen, W. An experimental investigation on the near-field turbulence for an airfoil with trailing-edge serrations at different angles of attack. *J. Acoust. Soc. Am.* **2014**, *135*, 2376.
- Xu, K.; Qiao, W.; Ji, L.; Chen, W. An experimental investigation on the near-field turbulence for an airfoil with trailing-edge serrations and an owl specimen. *J. Acoust. Soc. Am.* **2013**, *133*, 3589. [CrossRef]
- Yakhot, V.; Smith, L.M. The renormalization group, the ϵ -expansion and derivation of turbulence models. *J. Sci. Comput.* **1992**, *7*, 35–61. [CrossRef]
- Guo, P.; Cao, S.G.; Zhang, Z.G.; Li, Y.; Liu, Y.B.; Li, Y. Analysis of solid-gas coupling model and simulation of coal containing gas. *J. China Coal Soc.* **2012**, *37*, 330–335.
- Xin, Z.H.; Gui, G.A.; Yu, Q.; Li, X. The Influence of Serrated Leading Edge Blade on Aerodynamic Performance of Counter-rotating Axial Fan. *Chin. Hydraul. Pneum.* **2020**, *9*, 87–92.
- Liu, T.; Kuykendoll, K.; Rhew, R.; Jones, S. Avian Wing Geometry and Kinematics. *AIAA J.* **2006**, *44*, 954–963. [CrossRef]
- Dong, J.Y.; Yang, J.H.; Yang, G.X.; Wu, F.Q.; Liu, H.S. Research on similar material proportioning test of model test based on orthogonal design. *J. China Coal Soc.* **2012**, *37*, 44–49.
- Li, C.; Zhang, C.; Zhang, R.; Ye, X. Effects of Gurney Flap on the Performance of a Variable Pitch Axial Flow Fan. *J. Chin. Soc. Power Eng.* **2020**, *40*, 404–411.
- Mariotti, A.; Buresti, G.; Salvetti, M.V. Separation delay through contoured transverse grooves on a 2D boat-tailed bluff body: Effects on drag reduction and wake flow features. *Eur. J. Mech. B Fluids* **2019**, *74*, 351–362. [CrossRef]
- Alavi Moghadam, S.M.; Loosen, S.; Meinke, M.; Schröder, W. Reduced-order analysis of the acoustic near field of a ducted axial fan. *Int. J. Heat Fluid Flow* **2020**, *85*, 108657. [CrossRef]

19. Rocchio, B.; Mariotti, A.; Salvetti, M.V. Flow around a 5:1 rectangular cylinder: Effects of upstream-edge rounding. *J. Wind Eng. Ind. Aerodyn.* **2020**, *204*, 104237. [CrossRef]
20. Son, J.S.; Hanratty, T.J. Numerical solution for the flow around a cylinder at Reynolds numbers of 40, 200 and 500. *J. Fluid Mech.* **2006**, *35*, 369–386. [CrossRef]
21. Inoue, M.; Kurooumaru, M. Structure of tip clearance flow in an isolated axial compressor rotor. *J. Turbomach.* **1989**, *111*, 250–256. [CrossRef]
22. Wang, S.; Zhang, L.; Ye, X.; Wu, Z. Performance Optimization of Centrifugal Fan Based on Entropy Generation Theory. *Proc. Chin. Soc. Elect. Eng.* **2011**, *31*, 86–91.
23. Liu, H.; Ye, X.; Fan, F.; Li, C. Effects of Guide Vane Installation Angle on Performance and Static Structure of Twin-stage Variable-pitch Axial Fan. *J. North China Electr. Power Univ. (Nat. Sci. Ed.)* **2019**, *46*, 92–100.
24. Chen, X.; Cao, L.; Yan, P.; Wu, P.; Wu, D. Effect of meridional shape on performance of axial-flow fan. *J. Mech. Sci. Technol.* **2017**, *31*, 5141–5151. [CrossRef]
25. Kock, F.; Herwing, H. Local entropy production in turbulent shear flows: A high-Reynolds number model with wall functions. *Heat Mass Transf.* **2004**, *47*, 2205–2215. [CrossRef]
26. Liu, G.; Wang, L.; Liu, X. Numerical investigation on effects of blade tip winglet on aerodynamic and aero acoustic performance of axial flow fan. *J. Xi'an Jiaotong Univ.* **2020**, *54*, 104–112.

Article

Toward the Utilization of 3D Blading in the Cantilevered Stator from Highly Loaded Compressors

Xiaobin Xu ^{1,2}, Ruoyu Wang ^{2,3,*}, Xianjun Yu ^{2,3} , Guangfeng An ^{2,3} , Ying Qiu ⁴ and Baojie Liu ^{2,3}¹ School of Energy and Power Engineering, Beihang University, Beijing 100083, China² National Key Laboratory of Science & Technology on Aero-Engine Aero-Thermodynamics, Beihang University, Beijing 100083, China³ Research Institute of Aero-Engine, Beihang University, Beijing 102206, China⁴ China United Gas Turbine Technology Co., Ltd., Beijing 100016, China

* Correspondence: wry392003711@126.com

Abstract: Three-dimensional blading is an efficient technique in compressor aerodynamic design, and its function mechanism in the cantilevered stator needs to be addressed. This paper focuses on the sweep and dihedral in the cantilevered stator and seeks to expose their effects through detailed flow field analysis. Results show that the forward sweep could alleviate the corner flow separation by preventing the accumulation of the secondary flow toward the corner region, resulting in stronger flow separation at the blade trailing edge; in summary, forward sweep with appropriate parameters could increase static pressure rise by 14.3%. The positive dihedral will carry the endwall flow to the upper-span sections, thereby reducing blade corner separation; hence, as much as 23.5% improvement in static pressure rise could be obtained with the appropriate dihedral. Moreover, the combination of a relatively large sweep height and a moderate sweep angle with a low dihedral height and a moderate sweep angle provides optimum aerodynamic performance; the static pressure rise coefficient sees an increment of 25.5% at the near stall point. An experiment is then performed to further validate the theory, which shows a 2% improvement in efficiency of 3D blading at small mass flow rates. However, the secondary leakage should be given attention at high mass flow coefficients, while the corner separation needs further elimination at small mass flow rates.

Keywords: cantilevered stator; 3D blading; leakage flow; secondary flow

Citation: Xu, X.; Wang, R.; Yu, X.; An, G.; Qiu, Y.; Liu, B. Toward the Utilization of 3D Blading in the Cantilevered Stator from Highly Loaded Compressors. *Appl. Sci.* **2023**, *13*, 3335. <https://doi.org/10.3390/app13053335>

Academic Editor: Francesca Scargiali

Received: 21 February 2023

Revised: 3 March 2023

Accepted: 3 March 2023

Published: 6 March 2023



Copyright: © 2023 by the authors. Licensee MDPI, Basel, Switzerland. This article is an open access article distributed under the terms and conditions of the Creative Commons Attribution (CC BY) license (<https://creativecommons.org/licenses/by/4.0/>).

1. Introduction

The cantilevered stator is signified by its simple structure and low weight and hence is a promising configuration in the high-performance compressor. However, the leakage flow created by the radial gap at the stator root substantially complicates the endwall flow, necessitating a thorough understanding and advanced design techniques. Dean stated in the 1950s that the cantilevered stator could obtain better aerodynamic performance than the shrouded stator [1]. His conclusion was then verified experimentally by Lakshminarayana and Horlock, who also pointed out the existence of an optimum clearance size [2–4]. Although the leakage flow could, in a way, benefit endwall flow, it will at the same time introduce flow blockage and mixing loss; thus, studies have been conducted to reveal the flow mechanisms in the corner region. For example, Singh and Ginder, Lee et al., and George et al. believe the leakage flow weakens the corner separation by suppressing the endwall flow [5–7], whereas Gbadebo et al. argue that it is the suppression of the horseshoe vortex in the leading edge that causes removal of the corner separation [8]. Dong et al. state that the suppression of corner separation is mainly caused by the mixing of the high-energy leakage flow with the low-energy corner flow [9]. In terms of the clearance size, Lakshminarayana et al. proposed that the optimum choice is when the strengths of the leakage flow and the secondary flow are identical [2,4], whereas Gbadebo et al. revealed that the clearance flow tends to strengthen the corner separation when the

clearance size is very small [8]. While George et al. proposed an optimum hub clearance of 1% blade height [5], the optimum stator clearance remains in question [9–13]. Tanwar et al. investigated the hub clearance height and found that the interaction of hub leakage and passage vortex leads to mitigation of overall secondary flow adverse effects [14].

Three-dimensional blading can improve the compressor aerodynamic performance through reorganization of the flow field and hence is widely used in axial compressors. In general, 3D blading can be classified as sweep and dihedral. It is well known that the forward sweep of the rotor blade tip can reduce the local inlet Mach number, thereby weakening the shock wave and reducing the loss [7,13,15–20]. The sweep of the blade can also be used to control the corner flow in the subsonic compressor. As for the dihedral, it is recognized that the positive dihedral can construct a radial pressure gradient in the blade passage, thereby weakening the accumulation of the boundary layer at the corner region and inhibiting the occurrence of flow separation. According to the research of Breugelmans et al. and Weingold et al., the positive dihedral at both ends of the blade can reduce the endwall loss but will increase the loss in the midspan areas [21,22]. Sasaki further notes that the beneficial effect of positive dihedral on the near-wall region is mainly related to the dihedral angle, whereas the negative effect at the midspan is determined by the dihedral height [23]. More information on 3D blading can be found in references [24,25].

Although the application of 3D blading is quite common in conventional rotors/stators, there are few reports about its utilization in the cantilevered stator. Lange et al. attributed the beneficial effect of dihedral to the improvement of the rotor flow according to their experimental measurements [26]. Tweedt et al. found that the forward sweep can draw the high-momentum flow to the corner region of the suction surface, thereby suppressing the thickening of the viscous flow [20]. Lu et al. performed a numerical investigation of the effect of the forward sweep in the cantilevered stator, indicating that a reasonable sweep can not only reduce the shock wave at the stator hub but also reduce the loading near the blade leading edge [27]. Gunn and Hall found that the loss of the non-axisymmetric cantilevered stator with undistorted inflow could be 10% lower than conventional stator [28]. From the above analysis, it can be seen the application of 3D blading in the cantilevered stator is prospective in further improving the compressor aerodynamic performance, and the current attempt is limited to individual sweep or dihedral. To further optimize the cantilevered stator, a comprehensive understanding of the 3D blading mechanism is required, and guidelines for the compound sweep and dihedral design are necessary.

The present paper seeks to shed light on the utilization of 3D blading in the cantilevered stator; it is organized as follows: Section 2 gives an introduction of the investigation methods. Section 3 numerically investigates the effect of the sweep, dihedral, and compound sweep and dihedral, through which the flow mechanisms are revealed, and recommendations of the different parameters are provided. The theory is then validated by an experiment, which consists of the redesign of a cantilevered stator and a detailed comparison of the flow field with the datum scheme, as shown in Section 4. The main conclusions are summarized in Section 5.

2. Research Object and Investigation Methodology

The effects of the 3D blading are investigated both numerically and experimentally in the present work. An introduction of the 3D modeling parameters will be given in this section, followed by details of the research methodology.

2.1. Geometric Definition of the 3D Blading

This paper employs the widely used Sweep-Dihedral Coordinates to define the 3D blading parameters [25,29,30]. As shown in Figure 1, the displacement of the blade section in the chordwise direction is called “sweep”. Meanwhile, an obtuse angle between the endwall and leading-edge stacking line in the meridional plane is defined as a forward sweep. On the other hand, the displacement of the blade section in the direction perpendicular to the blade chordwise is called “dihedral”. Similarly, an obtuse angle between the

endwall and blade stacking line in the meridional plane designates a positive dihedral, and vice versa.

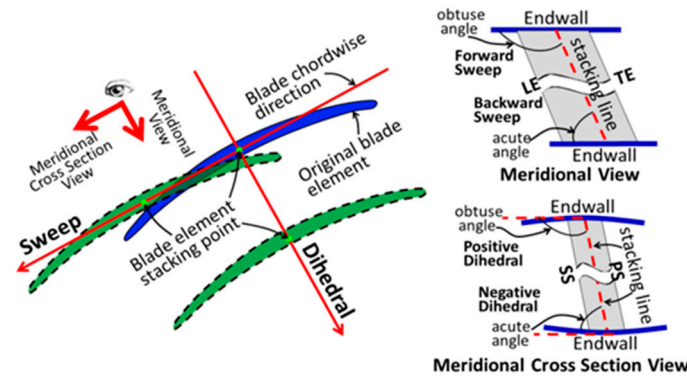


Figure 1. Definitions of 3D blade design in the orthogonal coordinates.

2.2. Numerical Simulation Method

The cantilevered stator to be investigated comes from the aft stage of a highly loaded high-pressure compressor, whose hub clearance is constant at 1% blade height. As shown in Figure 2, The numerical simulation is performed under the stage environment, with the simulation domain containing three blade rows: the IGV, the rotor, and the stator. The domain inlet is 2.0 times the chord length upstream of the IGV, while the domain outlet is 3.5 times the chord length downstream of the stator blade. The structured grid was generated using NUMECA Autogrid5; the main blade region and the clearances adopt the O4H topology and the H-O topology, respectively. Moreover, the grid is clustered at the near-wall region to satisfy the requirements of the turbulent model; y^+ of the first grid off wall is about 2.5 in the region close to the transition position, and the number is smaller near the trailing edge. After grid independence analysis with grid density, the total grid number for the rotor and stator blade rows was 1.28 million and 1.45 million, respectively [31,32]. For a 1.5-times finer mesh, the variation of the loss, the static pressure rise coefficient, and the flow angle compared with the selected mesh is less than 0.1%.

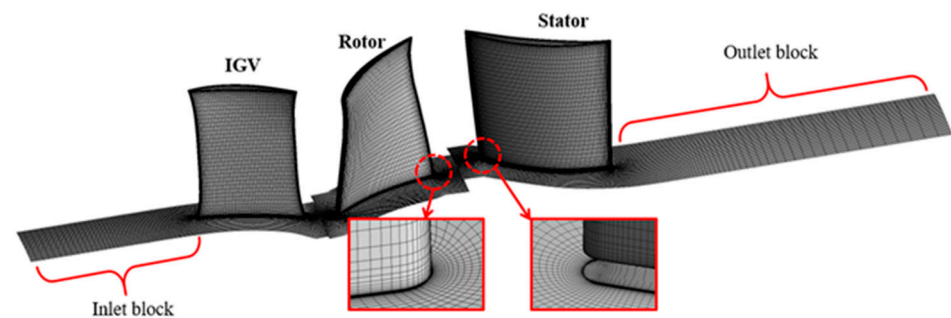


Figure 2. Model configuration and simulation grid.

This paper uses the commercial software ANSYS CFX 18.0 to explore the effects of the 3D blading techniques; previous studies have found that the two-equation eddy-viscosity models could simulate the complex vortex flows in the low-speed compressor with satisfying accuracy [33,34]. As a low-speed compressor ($Ma \sim 0.2$), the atmospheric condition (101,325 Pa, 288.15 K) was imposed at the domain inlet, where the total pressure was specified using a circumferential averaged radial profile obtained from experimental results. The mass flow rate was given at the outlet. Rotational periodic conditions were applied to the side walls, whereas the solid walls were defined as the adiabatic non-slip walls. The rotating speed of the rotor was 1100 rpm, and the interface between the rotor and the stator was modeled as the mixing plane. As for the turbulent model, the standard $k-\omega$ model was chosen, as it can capture more accurate 3D flow details than the standard

k-ε model, while obtaining a better convergence than the SST model [19,35]. A combination of the second-order spatial and temporal numerics are selected for the transport equations.

To ensure calculation accuracy, in addition to the default parameters, self-defined parameters, including the compressor pressure ratio, efficiency, and the inlet/outlet mass flow rate, were monitored during the simulation process. The flow field was considered converged when the mass flow discrepancy at the domain inlet and outlet was smaller than 0.1%.

2.3. Experimental Method

To check the effect of the 3D blading technique, a cantilevered stator in the existing test facility was redesigned and measured experimentally to reveal the variations of the flow field. The experiment was conducted in the low-speed large-scale axial compressor (LSLSAC) test facility at Beihang University. As shown in Figure 3a, the LSLSAC, whose hub-to-tip ratio is 0.75, adopts the 1.5 stage configuration, with a row of inlet guide vanes. The rotor and stator blades are nearly radially stacked by the controlled diffusion airfoil (CDA). The rotating speed is 1100 rpm, which is the same as the numerical simulation. At the design point, the stage loading coefficient is approximately 0.46 (based on midspan velocity), whereas the nominal rotor tip clearance and stator hub clearance are 1.5% and 1.0% blade height, respectively.

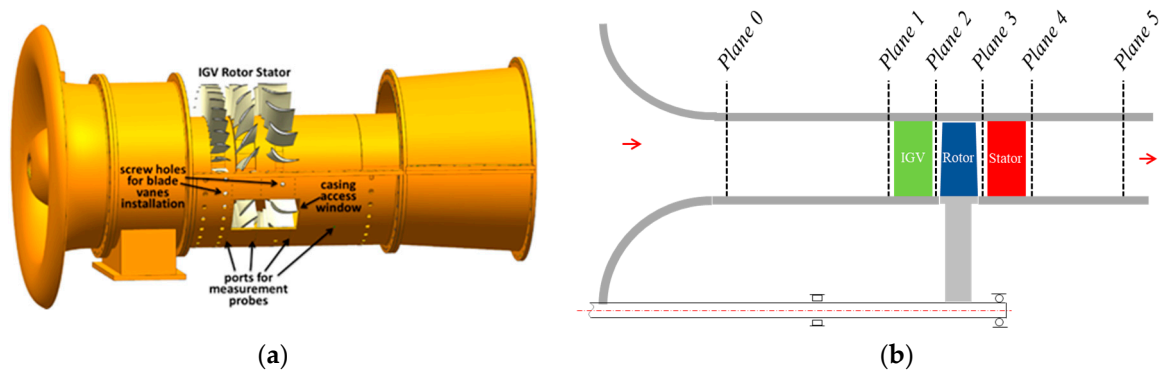


Figure 3. Schematics of the LSLSAC. (a) Geometry configuration; (b) measurement locations.

As shown in Figure 3b, five measurement planes are arranged along the axial direction, where multiple static pressure taps are installed on the casing wall. The mass flow coefficient is monitored by the four circumferential static pressure taps at Plane 0, while the static pressure rise of the compressor is measured by circumferential static pressure taps at Plane 1 and Plane 5. The outlet total pressure is measured by the pitot probes at Plane 5. It should be mentioned that the inlet total pressure is the ambient pressure, which is measured by an atmospheric pressure gauge. Moreover, a torque meter is used to measure the input shaft power to the compressor, which is utilized to calculate the efficiency of the compressor. The torque efficiency is calculated as follows:

$$\eta = \frac{30}{\pi} \frac{kR}{k-1} \frac{m_0 T_0^* \left[(p_5^*/p_2^*)^{(k-1)/k} - 1 \right]}{Mn}, \quad (1)$$

where M denotes the torque, n is the rotating speed, and m_0 and T_0^* are the mass flow rate and the total temperature at the compressor inlet (Plane 0), respectively.

To obtain the 3D velocity and pressure profiles at the stator inlet and outlet, measurement at Planes 3 and 4 was executed using an L-shaped five-hole probe. In the radial direction, the nearest measurement point to the hub and the shroud wall was 2.0% and 2.5% blade height, respectively. Moreover, a novel zonal method was utilized to process the pressure data, through which the measurement angle range was extended to $\pm 60^\circ$ [36]. The pressure was acquired by the Rosemount pressure transducers, whose measurement range and uncertainty were ± 6.22 KPa and 0.025% FS, respectively. Error analysis demonstrated

that the measurement uncertainties of the five-hole probe were 0.5° for the flow angles, 1% (normalized by the flow dynamic pressure) for the total pressure, 2% (normalized by the flow dynamic pressure) for the static pressure, and 1% for the flow velocity [36].

In the present study, oil-flow visualization tests were conducted to exhibit the flow patterns in the stator blade passage. The material used to make the skin-friction lines was a mixture of industrial silicone. The running time of each test was between 5 and 10 min.

3. Effects of 3D Blading on the Cantilevered Stator

To reveal the effect of 3D blading on the cantilevered stator, a parametric investigation of the 3D modeling parameters was first conducted. Numerical simulation was employed to evaluate the various design schemes.

3.1. Effects of the Blade Sweep

In the present work, the forward sweep was employed to control the corner flow. To determine the sweep height and the sweep angle, the effect of these two parameters are discussed. As specified in Table 1, the sweep height is varied between 30% and 70% of the total blade height, whereas the sweep angle is between 120° and 150° . The modeling schemes are named by the following rule: “parameter type + index + parameter type + index”. For example, scheme “A1B1” designates a sweep starting from 30% blade span with a sweep angle of 120° .

Table 1. Modeling scheme for blade sweep.

Parameter Type	1	2	3
A: Sweep height	30% span	60% span	70% span
B: Sweep angle	120°	135°	150°

3.1.1. Effects of the Sweep Height

The influence of sweep height is first compared using the control variate method. As shown in Figure 4, the design schemes are A1B2, A2B2, and A3B2. A slight forward sweep is also adopted at the tip region to balance the pressure gradient in the radial direction (135° , 70% span). Results are compared to the orthogonal/straight blade (Orth.). Note that no dihedral is utilized in this section.

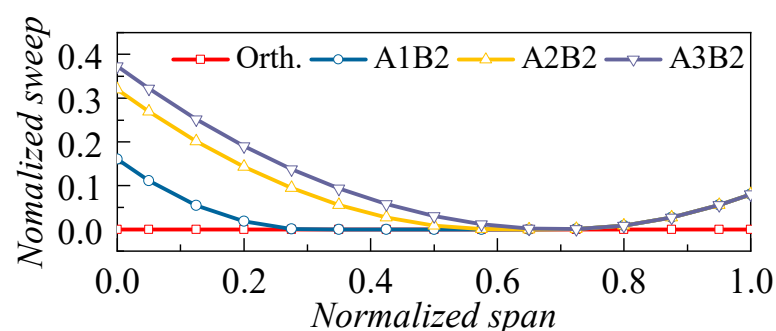


Figure 4. Radial distribution of blade sweep for the cases with different sweep heights.

The pressure rise and loss characteristics of the cantilevered stators are demonstrated in Figure 5. Results show that, except for the near-stall condition of A1B2, the utilization of the forward sweep could always improve the stator aerodynamic performance in comparison to the baseline case. Moreover, the comparison of different schemes indicates that the 60% sweep height (A2B2) outperforms the other designs. At the near-stall condition, the static pressure rise coefficient and the total pressure loss coefficient in A2B2 are increased and decreased by 14.3% and 5.4%, respectively.

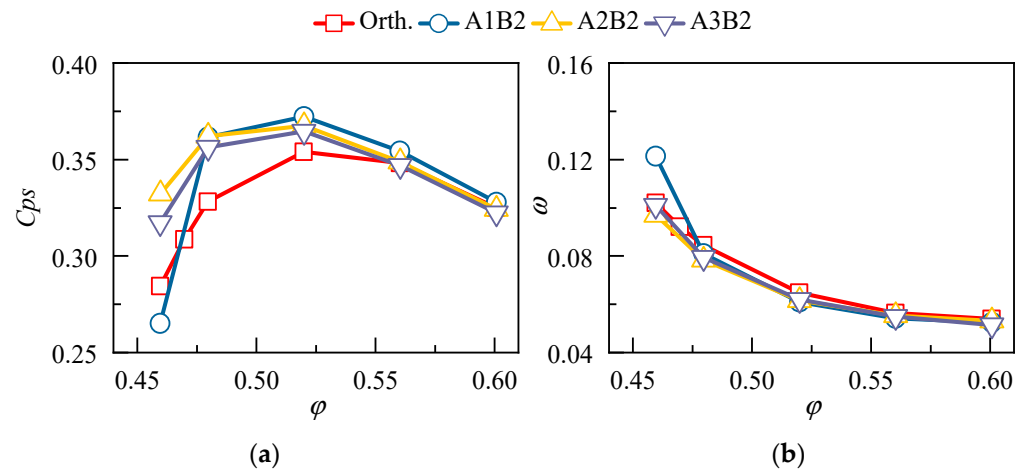


Figure 5. Pressure rise and loss characteristics for the stator with different sweep heights. (a) Pressure rise and (b) loss.

Figure 6 illustrates the flow field distribution for the cases with different sweep heights. Both the leakage streamlines and the surface streamlines are depicted. Results show that the forward sweep moves the hub leakage flow upstream, thus enhancing the hindrance to the secondary flow and attenuating the accumulation of the low-energy fluid toward the corner region. Consequently, the blockage at the corner region of the suction surface witnesses a remarkable shrink. However, the forward sweep will incur the radial expansion of the suction surface flow separation; hence, the wake is broadened in the upper span areas. Moreover, under the same mass flow ratio, the sweep height exhibits little effect on the leakage flow but will influence the trailing edge separation significantly. At the sweep height of 60% blade span (A2B2), the trailing edge separation tends to be uniform along the radial direction, thus bringing optimum aerodynamic performance.

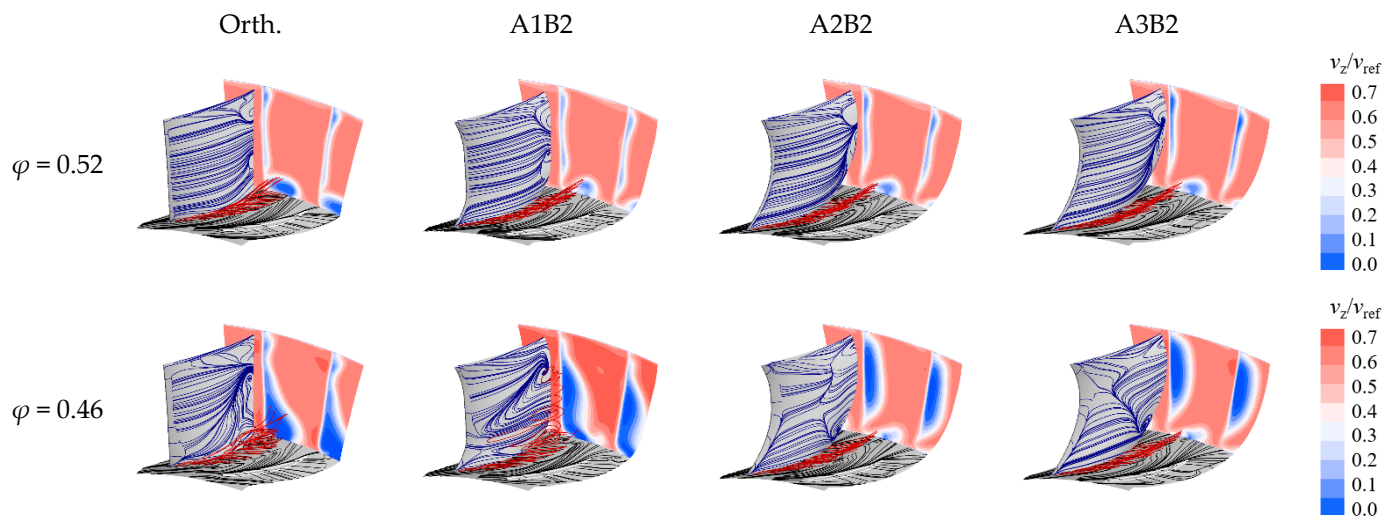


Figure 6. Flow field distribution for the cases with different sweep heights.

To evaluate the aerodynamic performance of the cantilevered stator quantitatively, the radial distribution of the aerodynamic parameters is given in Figure 7. The variation of the mass flow coefficient suggests that the forward sweep is able to improve the flow capacity in the hub region, whereas the alleviation of corner separation flow brings a reduction in the deviation angle. The effect of the forward sweep is more pronounced at small mass flow ratios (i.e., the conditions with higher loading). By comparing different blading schemes, it can be seen that the larger sweep height adds to the beneficial effect. Nevertheless, when the sweep height is greater than 60% (A3B2), the performance improvement at the

corner region by further increasing the sweep height becomes less significant, yet the upper span performance starts to deteriorate; hence, the 60% sweep height is suitable for the present case.

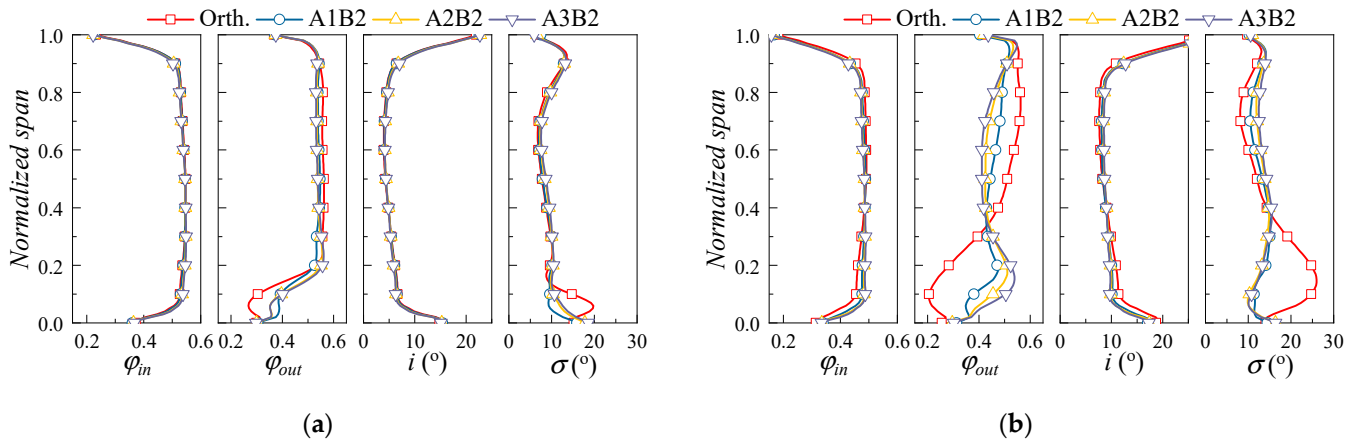


Figure 7. Radial distribution of aerodynamic performance for the cases with different sweep heights. (a) $\varphi = 0.52$; (b) $\varphi = 0.46$.

To reveal the effect of sweep height on the leakage flow, the variation of the mass flow rate of the leakage flow is presented in Figure 8. Results indicate that the leakage flow rate first decreases in the areas between 0~20% blade chord and then continues to increase toward the trailing edge. The increase in the mass flow rate of the leakage flow will enhance the removal of low-energy fluid in the corner region of the blade suction surface, thus confirming the former analysis. Additionally, although increasing the sweep will enhance the 3D blading effect, the leakage characteristics of the A2B2 case and the A3B2 case exhibit similar patterns; hence, further increasing the sweep height will result in less benefit.

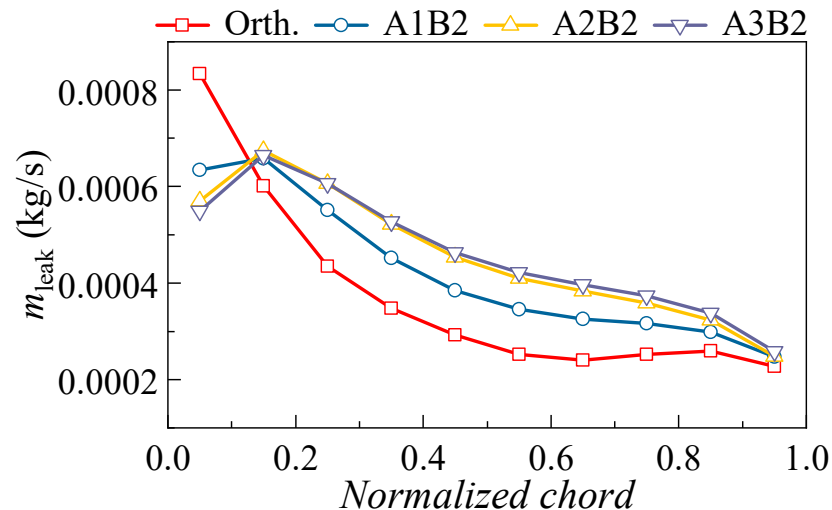


Figure 8. The comparison of the streamwise leakage mass flow rate under different sweep heights ($\varphi = 0.46$).

3.1.2. Effects of the Sweep Angle

To investigate the influence of the sweep angle, the design schemes A2B1, A2B2, and A2B3 are compared in this section, as illustrated in Figure 9. A tip region of each case employs the forward sweep at the 70% span with the same sweep angle as the hub. The orthogonal/straight blade works as the benchmark of comparison.

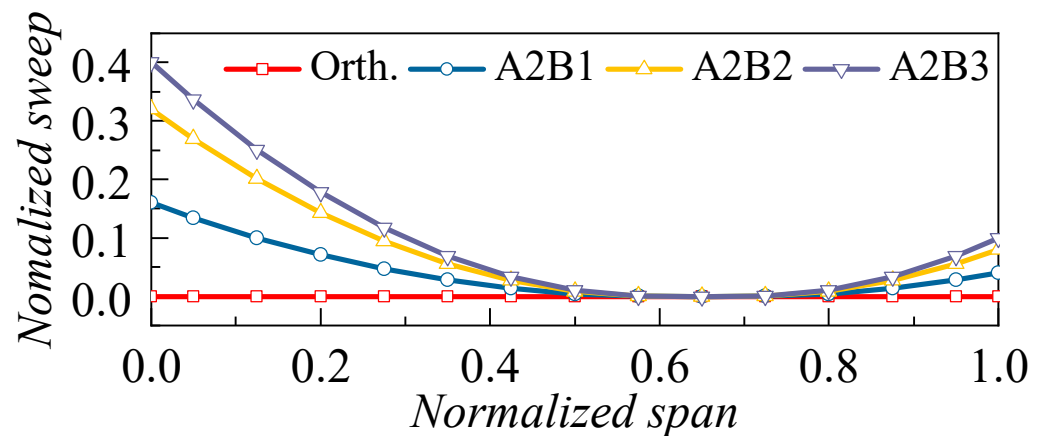


Figure 9. Radial distribution of blade sweep for the cases with different sweep angles.

Figure 10 presents the pressure rise and loss characteristics of the cantilevered stators. It can be seen that the aerodynamic performances of different design schemes share similar trends; except for the near-stall condition, the pressure rise coefficients are enhanced significantly in comparison with the orthogonal blade. Observation of the near-stall condition indicates that the sweep angle should be controlled within a proper range, as a too-large sweep angle (A2B3, 150°) will deteriorate the blade pressure rise coefficient; however, the performance remains better than that of the straight blade.

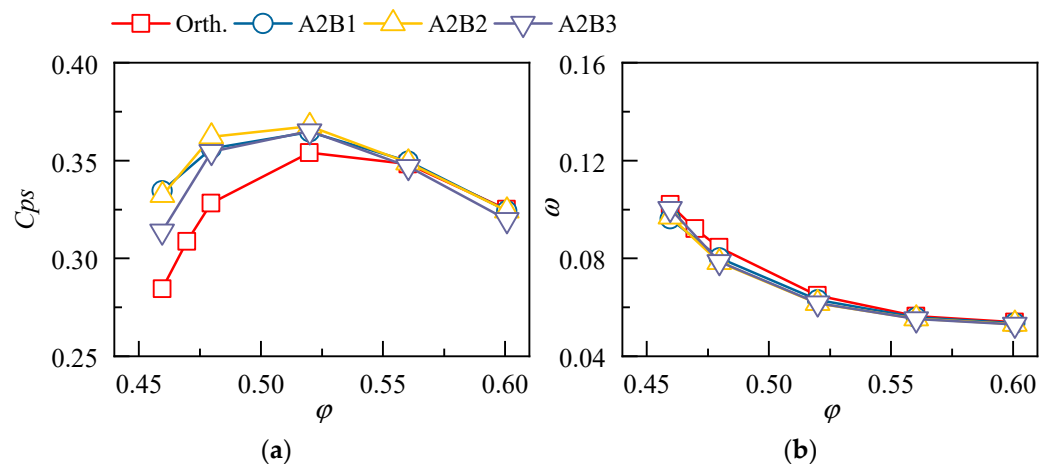


Figure 10. Pressure rise and loss characteristics for the stator with different sweep angles. (a) Pressure rise and (b) loss.

The flow field distributions for the design schemes with different sweep angles are given in Figure 11. Similar to the previous conclusions, the forward sweep will weaken the flow separation in the blade corner region, but at the same time enhance the flow separation at the midspan. With the increase of the sweep angle, the leakage flow tends to move toward the pressure surface of the adjacent blade, thus increasing the traveling distance to the outlet. Consequently, the mixing of the leakage flow with the corner flow is improved, and the radial dimension of the low-speed area at the blade outlet shrinks. It should be noted that excessively large sweep angle will lead to a significant increase in the suction surface flow separation (A2B3), thereby weakening the aerodynamic performance gains brought by the forward sweep; thus, the sweep angle should be appropriately selected when at the design stage.

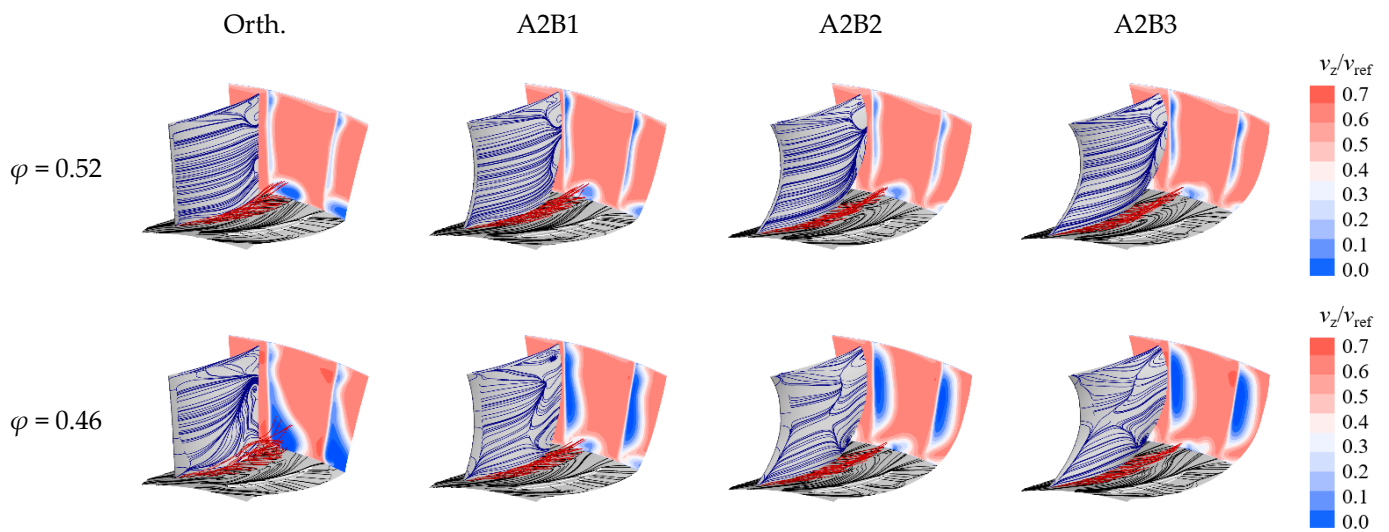


Figure 11. Flow field distribution for the cases with different sweep angles.

The radial distribution of the aerodynamic parameter for the cases with different sweep angles is given in Figure 12. Results of both the $\varphi = 0.52$ and the $\varphi = 0.46$ conditions are provided. With the increase of sweep angle, the flow coefficient at the hub region increases, resulting in the improvement of the flow capacity. On the contrary, the flow capacity at the upper span parts is decreased, corresponding to the widening of the blade wake in Figure 11. The influence of the sweep angle on the radial flow of the blade is more significant at small mass flow rates. Considering the influence of the sweep angle on the corner flow and the blade separation flow, a moderate sweep angle (approximately 135° for the present study) is appropriate for the cantilevered stator.

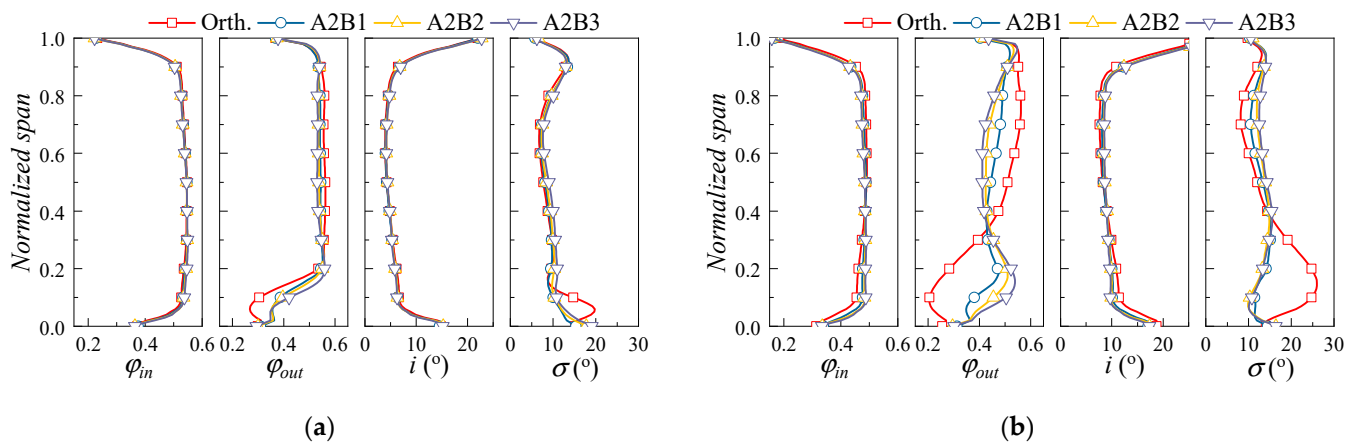


Figure 12. Radial distribution of aerodynamic performance for the cases with different sweep angles. (a) $\varphi = 0.52$; (b) $\varphi = 0.46$.

Figure 13 presents the variation of the mass flow rate for the stator leakage flow along the streamwise direction. Increasing the sweep angle tends to reduce the leakage flow at the blade leading edge, yet it will enhance the leakage flow in the other regions. The total mass flow rate of the leakage flow will be increased upon the utilization of the forward sweep, thus strengthening the interaction of different corner flow structures.

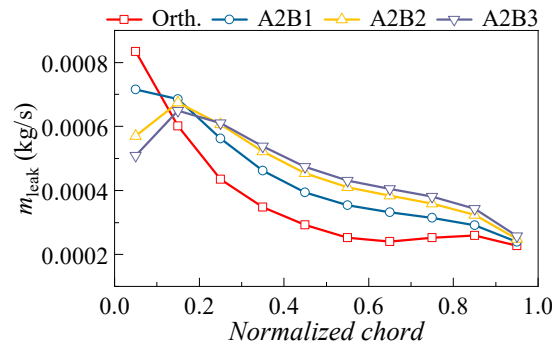


Figure 13. The comparison of the streamwise leakage mass flow rate under different sweep angles ($\varphi = 0.46$).

Hence, the forward sweep could inhibit the transverse flow near the hub endwall and alleviate the flow separation at the corner region. Increasing the sweep height facilitates a uniform separation along the span without changing the endwall flow significantly.

3.2. Effects of the Blade Dihedral

3.2.1. Effects of the Dihedral Height

Except for the forward sweep, the positive dihedral is also adopted in the present study to optimize the stator performance. Therefore, the effects of the dihedral height and dihedral angle need to be clarified. As shown in Table 2, the dihedral height is varied between 20% and 60% of the total blade height, whereas the dihedral angle is between 120° and 150° . The modeling schemes are named following the same rule as that of the sweep (e.g., scheme “C1D1” corresponds to a dihedral starting from 30% blade span with a dihedral angle of 120°).

Table 2. Modeling scheme for blade dihedral.

Parameter Type	1	2	3
C: Dihedral height	20% span	40% span	60% span
D: Dihedral angle	120°	135°	150°

Likewise, the influence of dihedral height is first compared using the control variate method. As shown in Figure 14, the design schemes are C1D3, C2D3, and C3D3. A slight positive sweep is also adopted at the tip region (150° , 90% span). Simulation results are compared to the orthogonal/straight blade (Orth.); note that no sweep is utilized in this section.

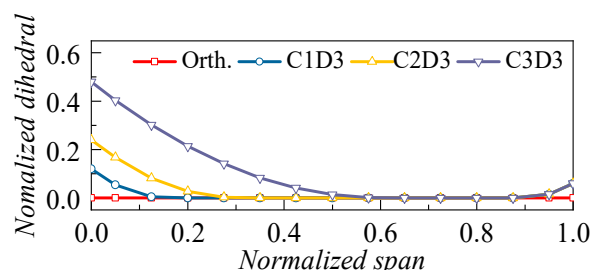


Figure 14. Radial distribution of blade dihedral for the cases with different dihedral heights.

Figure 15 presents the pressure rise and loss characteristics for the design schemes with different dihedral heights. Compared with the orthogonal blade, the scheme with a small dihedral height (C1D1) could improve the diffusing capacity of the cantilevered stator without increasing its total pressure loss, thus improving the aerodynamic performance of the cantilevered stator. However, with the increase of the dihedral height (C2D3 and

C3D3), the blade loss will start to rise, and the pressure rise capacity is reduced remarkably, thus eliminating the advantages of the positive dihedral.

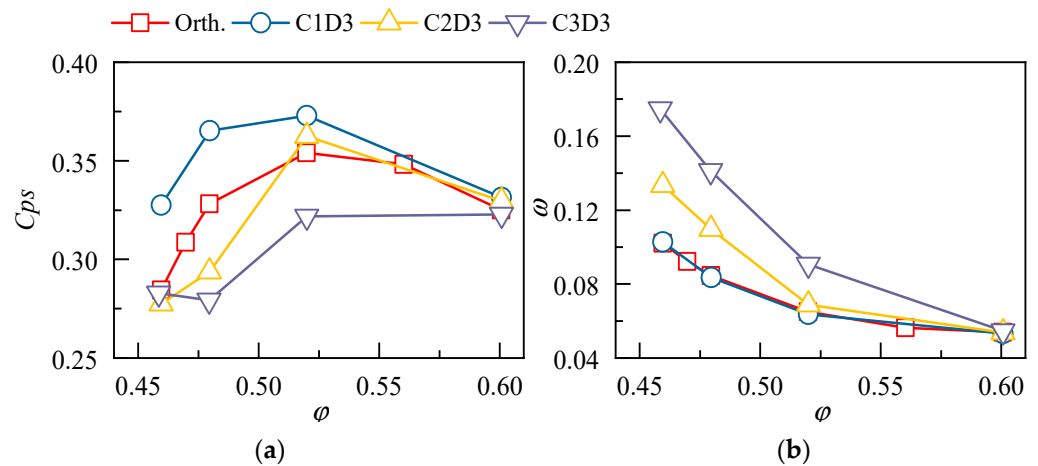


Figure 15. Pressure rise and loss characteristics for the stator with different dihedral heights. (a) Pressure rise and (b) loss.

To determine the reason why increasing the dihedral height will reduce the stator performance, the flow field distribution was established for the cases with different dihedral heights, as presented in Figure 16. Results at the mass flow coefficient of 0.52 demonstrate that the positive dihedral will not only push the trajectory of the leakage vortex away from the blade suction surface but also promote the radial migration of the low-energy fluid. In scheme C1D3, the dihedral height is relatively low, and the accumulation of low-energy fluid at the corner region of the blade suction surface is reduced by the circumferential migration of the leakage flow. Therefore, the blockage at the blade outlet is alleviated significantly. With the increase of the dihedral height (C2D3), although the corner separation at the stator hub is weakened effectively, the wake in the lower and middle parts of the blade is elongated and widened remarkably, which is detrimental to the comprehensive aerodynamic performance of the cantilevered stator. Moreover, if the dihedral height is further increased to 60% (C3D3), the leakage flow will undergo an obvious radial migration under the strong blade force. As a result, the separation at the blade trailing edge will be significantly enhanced, and the performance of the cantilever stator will further deteriorate. Note that with the decrease of the mass flow coefficient, the influence of the dihedral amplifies substantially.

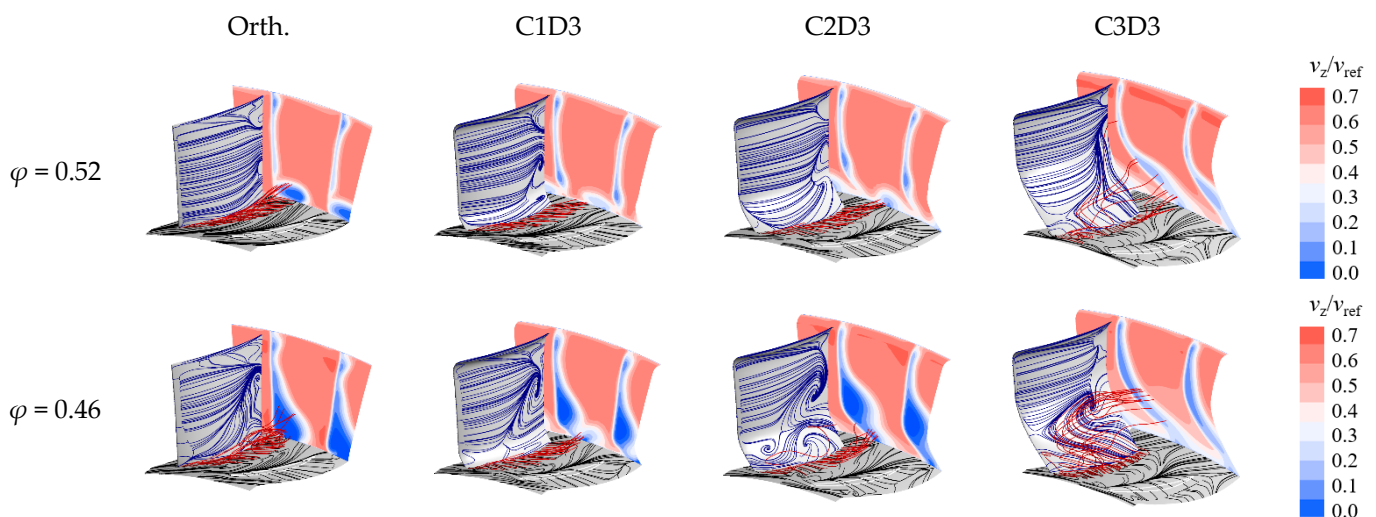


Figure 16. Flow field distribution for the cases with different dihedral heights.

The radial distribution of the aerodynamic parameter for the cases with different dihedral heights is given in Figure 17 to evaluate the stator performance quantitatively. The increase of incidence angle at the hub region indicates that the positive dihedral will restrict the flow capacity at the blade inlet, while increasing the dihedral height will amplify the effect. On the other hand, the mass flow coefficient at the outlet of the cantilevered stator distributes differently with the variation of the dihedral height. For scheme C1D3, the flow capacity below 20% blade height is increased significantly due to the weakening of the corner separation flow, Meanwhile, the mass flow coefficient in the areas above 20% span witnesses a slight reduction owing to the enhancement of the trailing edge separation, the deviation angle also rises correspondingly. With the increase of the dihedral height (C2D3 and C3D3), the flow capacity above 20% blade height suffers from a significant reduction because of the strengthening of the radial flow migration in the blade channel, thus bringing adverse effects to the aerodynamic performance of the cantilevered stator.

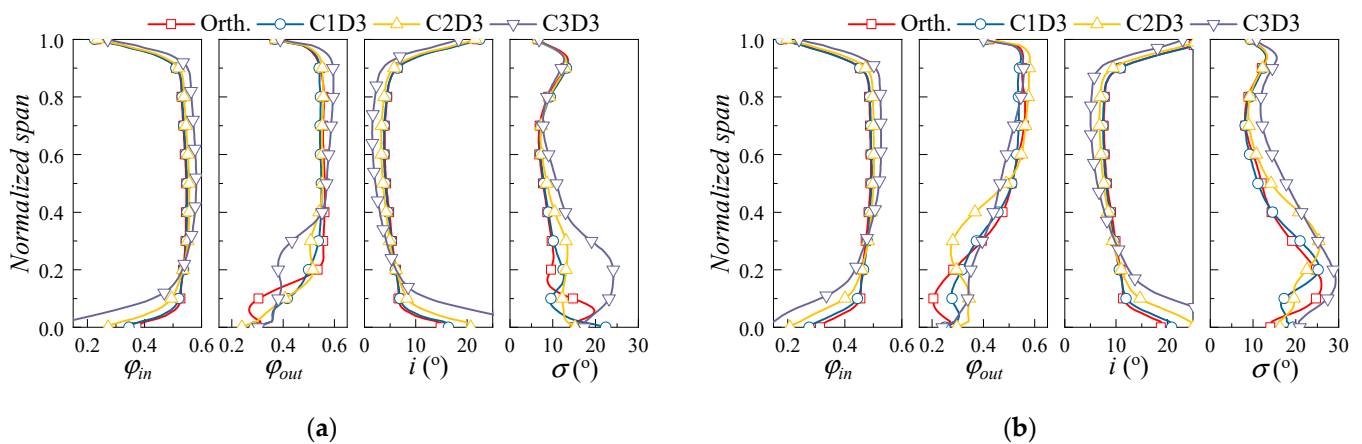


Figure 17. Radial distribution of aerodynamic performances for the cases with different dihedral heights. (a) $\varphi = 0.52$; (b) $\varphi = 0.46$.

Figure 18 presents the variation of the leakage mass flow rate. An interesting phenomenon is that increasing the dihedral height will first increase and then decrease the leakage mass flow rate at the blade leading edge. Consequently, the uniformity of the leakage flow characteristic along the blade chord is first decreased and then increased. Moreover, although the slight positive dihedral (C1D3) could increase the mass flow rate of the leakage flow along the axial direction, increasing the dihedral height will incur a significant reduction of leakage flow at the blade leading edge, thus weakening the effect of the 3D blading technique.

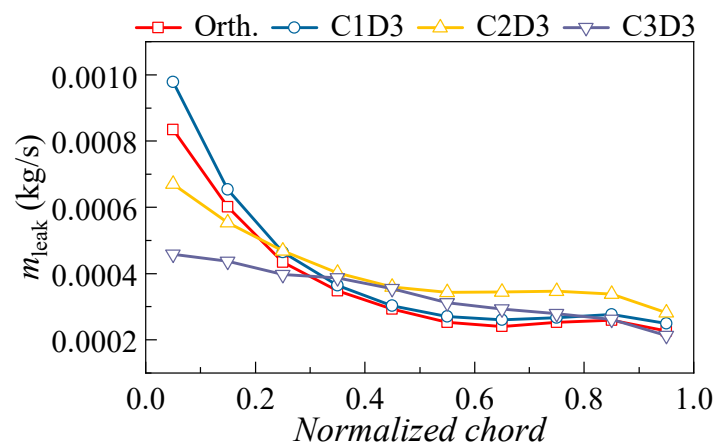


Figure 18. Comparison of the streamwise leakage mass flow rate under different dihedral heights ($\varphi = 0.46$).

3.2.2. Effects of the Dihedral Angle

To investigate the influence of the dihedral angle, under the optimum dihedral height, the stator performances with different dihedral angles are inspected. As illustrated in Figure 19, the cases to be investigated are C1D1, C1D2, and C1D3; note that the blade tip also adopts positive dihedrals (at 80% span with the same dihedral angle as the hub) to balance the pressure gradient in the radial direction.

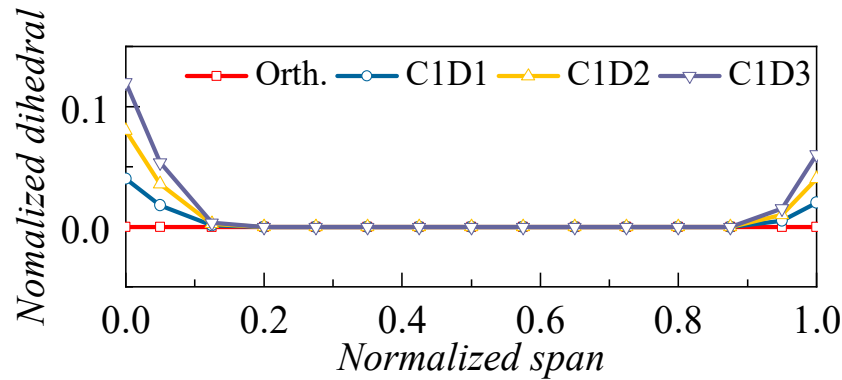


Figure 19. Radial distribution of blade dihedral for the cases with different dihedral angles.

The pressure rise and loss characteristics for the design schemes with different dihedral heights are demonstrated in Figure 20. The influence of the dihedral is more pronounced in terms of pressure rise coefficient and at small mass flow ratios. In comparison to the orthogonal blade, the positive dihedral will always improve the blade static pressure coefficient, whereas the increment will first increase and then decrease with the increase of the dihedral angle. The optimum dihedral angle in the present study is 135° , where the value of C_{ps} is improved by 23.5% at the near-stall condition.

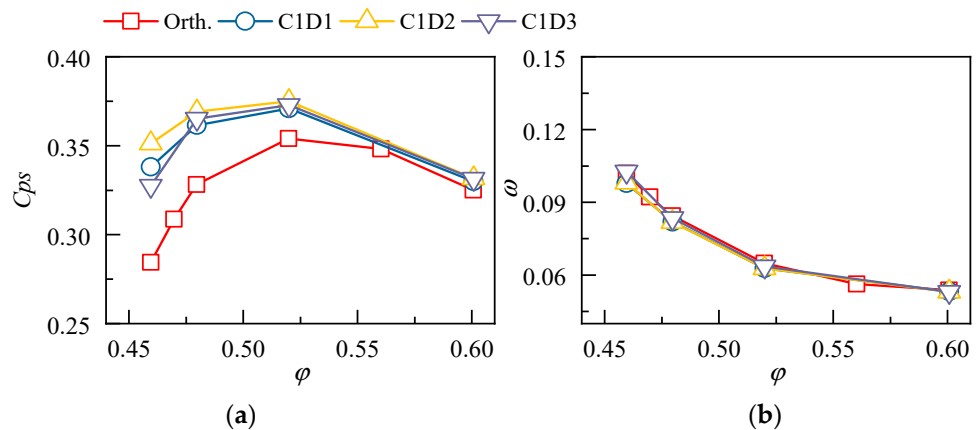


Figure 20. Pressure rise and loss characteristics for the stator with different dihedral angles. (a) Pressure rise and (b) loss.

The flow field distributions at the mass flow coefficients of 0.52 and 0.46 are given in Figure 21. It is apparent that the leakage flow will deviate from the blade suction surface with the increase of the dihedral angle. As a result, the mixing of the leakage flow with the mainstream is more sufficient, and the blockage at the outlet alleviates. However, the increase of the dihedral angle will also enhance the radial migration of the blade corner flow, thus strengthening the flow separation on the suction surface. Of all the design schemes, C1D2 could not only suppress the secondary flow at the hub endwall but also avoid excessive flow separation on the blade suction surface, hence obtaining the optimum aerodynamic performance.

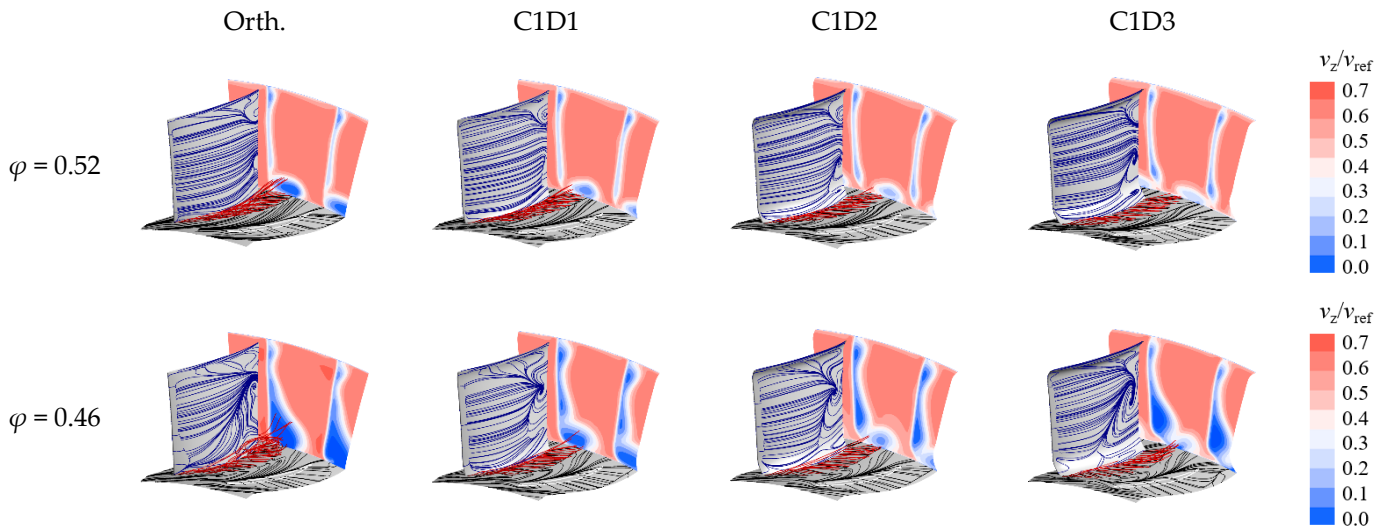


Figure 21. Flow field distribution for the cases with different dihedral angles.

As shown in Figure 22, the influence of the dihedral angle on the performance of the cantilevered stator is illustrated clearly. Results show that the current dihedral angles barely influence the distribution of the mass flow coefficient at the stator inlet; however, the mass flow distribution at the stator outlet is altered. To be specific, at the $\varphi = 0.52$ condition, the mass flow coefficient in the lower and upper regions of the 20% blade height is increased and decreased, respectively, which echoes the flow field characteristics in Figure 21. The comparison of different design schemes indicates that with the increase of the dihedral angle, the enhancement of flow capacity at the stator hub will become inconspicuous, yet the worsening of aerodynamic performance at the upper span becomes more significant, which consequently weakens the total beneficial effect. The above phenomenon is more significant at small mass flow ratios.

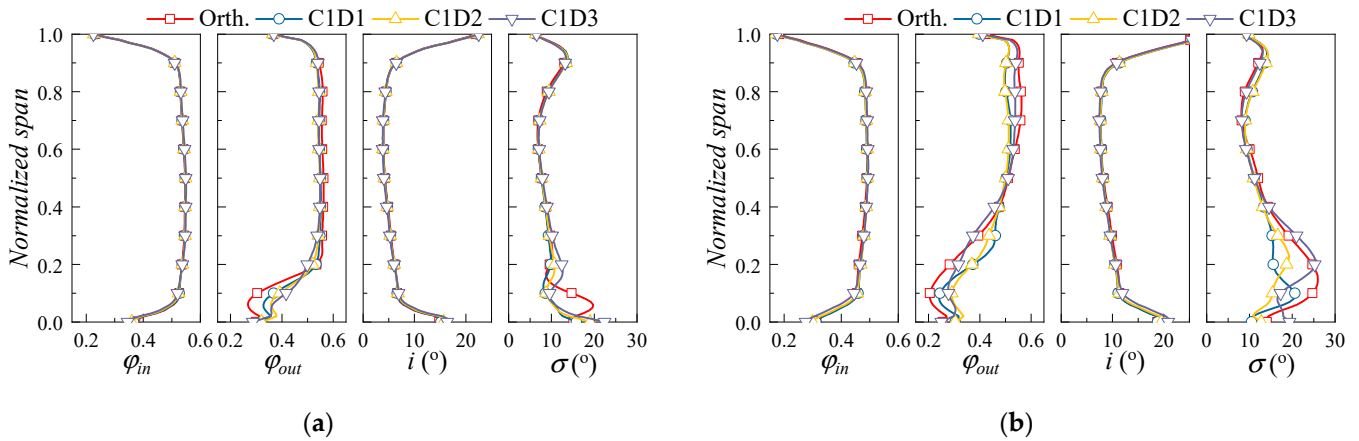


Figure 22. Radial distribution of aerodynamic performances for the cases with different dihedral angles. (a) $\varphi = 0.52$; (b) $\varphi = 0.46$.

Figure 23 presents the variation of the leakage mass flow rate. Results demonstrate that although the mass flow rate of the leakage flow is increased slightly in comparison with the orthogonal blade, the current range of the dihedral angle barely influences the axial distribution of the leakage flow, and the absolute mass flow rates for different blading schemes are approximately identical.

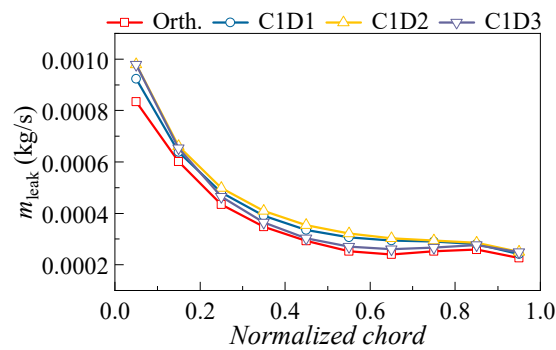


Figure 23. Comparison of the streamwise leakage mass flow rate under different dihedral angles ($\varphi = 0.46$).

Hence, the positive dihedral will not only push the trajectory of the leakage vortex away from the blade suction surface but also promote the radial migration of the low-energy fluid at the hub corner. A large dihedral height will elongate the blade wake and induce the radial transportation of the leakage flow.

3.3. Effects of the Compound Sweep and Dihedral

According to the former analysis, the mechanism of 3D blading in the cantilevered stator is summarized in Figure 24. The forward sweep can enhance the hindrance of the leakage flow on the low-energy fluid near the endwall, while flow separation on the blade suction side is exaggerated slightly. Increasing the sweep height facilitates a uniform separation along the span without changing the endwall flow significantly, whereas excessively large sweep angles lead to a large-scale separation on the blade suction surface and harm the total effect. On the other hand, as shown in Figure 24b, the positive dihedral will not only push the trajectory of the leakage vortex away from the blade suction surface but also promote the radial migration of the low-energy fluid at the hub corner. The utilization of large dihedral heights will elongate the blade wake and induce the radial transportation of the leakage flow, while the excessive dihedral angle will damage the performance at the midspan.

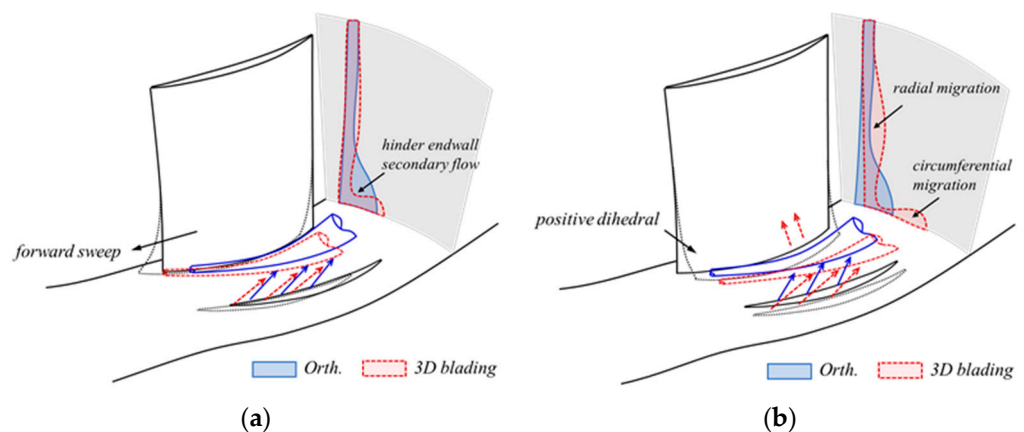


Figure 24. The mechanisms of sweep and dihedral on the cantilevered stator: (a) sweep; (b) dihedral.

In consideration of the effects above, a novel cantilevered stator with comprehensive sweep and dihedral is designed, whose aerodynamic performance is evaluated via numerical simulation. As shown in Figure 25, the 3D cantilevered stator employs a relatively high sweep height with a moderate sweep angle, and the dihedral is designed to have a low height and a moderate angle. Note that the blade tip also adopts a forward sweep to balance the radial pressure gradient.

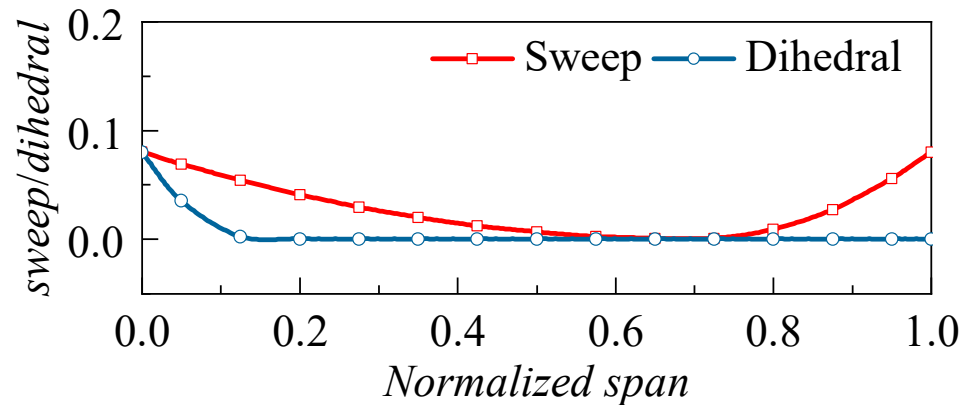


Figure 25. Radial distribution of sweep and dihedral for the 3D cantilevered stator.

Figure 26 presents the pressure rise and loss characteristics of the 3D cantilevered stator; results of the orthogonal blade, the bare sweep scheme (no dihedral), and the bare dihedral scheme (no sweep) are also provided for the convenience of comparison. Figure 26 implies that the combination of the sweep and dihedral will intensify the beneficial effects, as the “sweep + dihedral” scheme has the highest static pressure ratio and the lowest total pressure loss over the whole operating range. At the near-stall point, the static pressure rise coefficient and the total pressure loss coefficient are increased and decreased by 25.5% and 11.1%, respectively. Given the remarkable improvement over the baseline case, it is safe to say that the working mechanism summarized above is correct, and the redesign is successful. The following section will outline the experimental methods used to validate the conclusions.

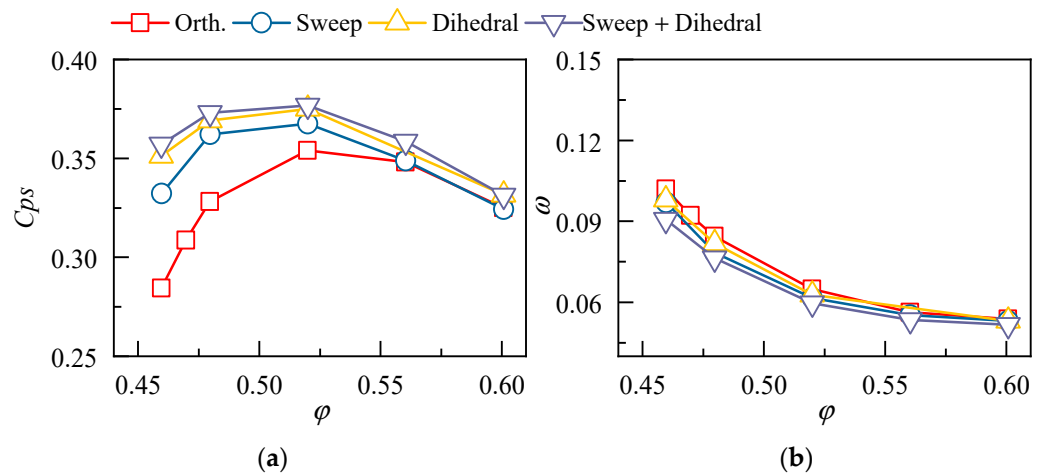


Figure 26. Pressure rise and loss characteristics for the 3D cantilevered stator. (a) Pressure rise; (b) loss.

4. Application of 3D Blading in a Cantilevered Stator

4.1. The Redesign of the Cantilevered Stator

The design parameters of the datum stator are shown in Table 3, with the diffusion factor varying from 0.58 to 0.35 from hub to tip. Moreover, the stator hub clearance occupies 1% of the blade height, which proved beneficial for the stator aerodynamic performance in a previous study [37]. Since the datum stator was comparable to the orthogonal cantilevered stator in the former study, the 3D blading strategy in Figure 25 is adopted for the redesign scheme.

Table 3. Design parameters for the highly loaded cantilevered stator.

	Hub	Midspan	Tip
Diffusion factor (-)	0.58	0.33	0.35
Incidence (°)	8	1	0
Solidity (-)	1.75	1.6	1.5
Stagger angle (°)	18	22	25
Turning angle (°)	49	45	42
Hub-tip ratio (-)		0.75	
Aspect ratio (-)		1	
Hub clearance (% span)		1%	
Blade profile type		CDA	

Figure 27 presents the comparison of the aerodynamic performances of the datum and redesigned cantilevered stators. To improve the simulation accuracy, the numerical simulation considers the stator blade row separately and imposes the experimentally measured flow fields at the stator inlet according to the specific operating conditions. In the datum case, the pressure rise capability of the cantilevered stator will drop significantly once the mass flow coefficient is below 0.53, due to the deterioration of flow conditions at the hub corner (Figure 28). On the other hand, the stator with 3D blading can overcome the above problem efficiently, as the C_{ps} is increased by 71.8% at the mass flow coefficient of 0.45 (P1). The total pressure loss coefficient for the redesigned case is reduced remarkably as well, implying the effectiveness of the 3D blading scheme.

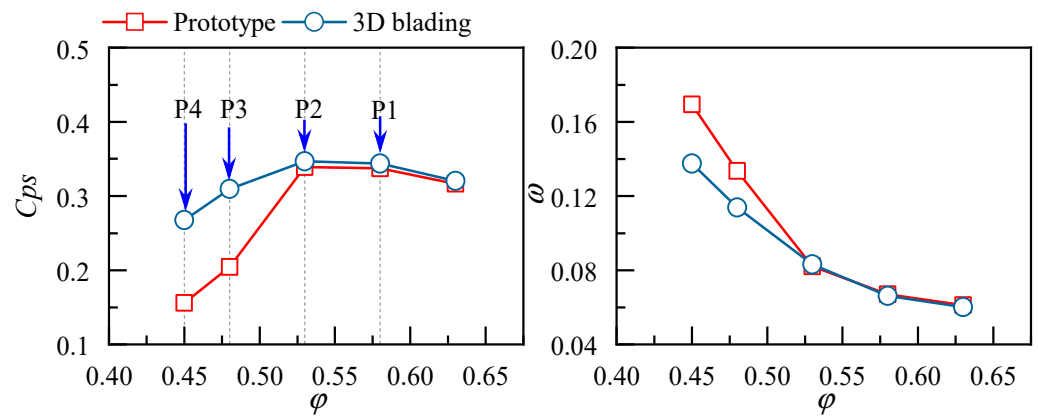


Figure 27. Comparison of pressure rise and loss characteristics of the cantilevered stators.

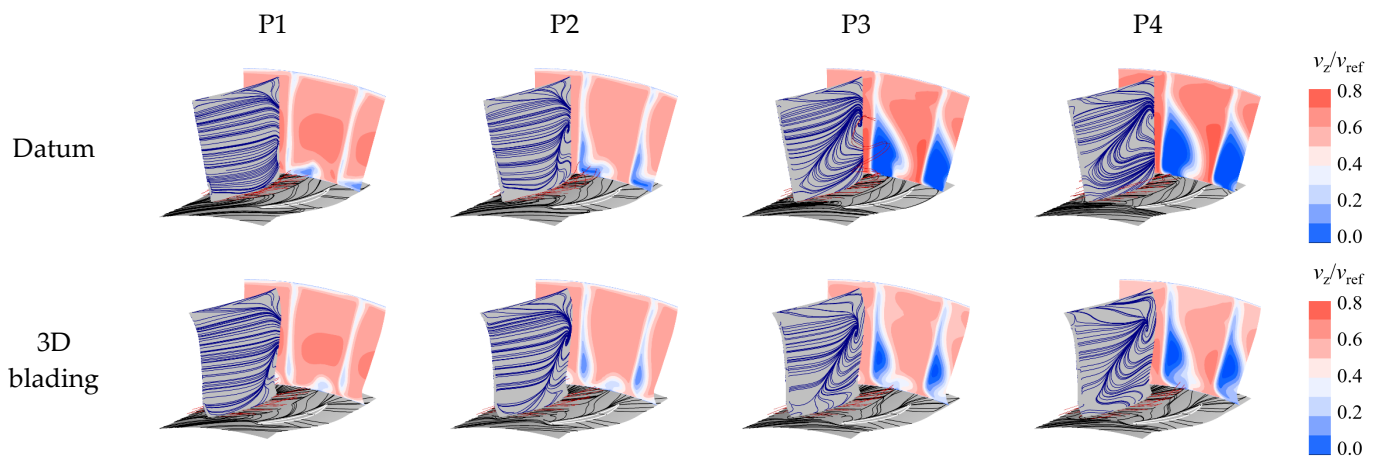


Figure 28. The comparison of field distribution between the datum and the redesigned stator.

As shown in Figure 28, the comparison of the flow field under different operating conditions (P1~P4, see Figure 27) indicates that the datum stator suffers from severe corner flow separation at the near-stall condition, leading to the sudden drop of the pressure rise capacity. Meanwhile, the utilization of compound sweep and dihedral reorganizes the flow field; hence, the accumulation of low-energy fluid at the hub corner is relieved significantly, corresponding to the performance improvement in Figure 27. Note that the flow separation in the upper span areas is intensified in comparison with the datum scheme, which is due to the radial migration of the low-energy fluid from the positive dihedral.

The radial distribution of the aerodynamic parameters is given in Figure 29 to illustrate the effect of 3D blading quantitatively. Results show that the 3D blading can enhance the through flow capacity at the hub region over a wide operating range, as the mass flow distribution is more uniform along the radial direction. The beneficial effect extends from 15% to 50% span as the operating point moves from P1 to P4, which is consistent with the former analysis. Moreover, the total pressure loss demonstrates the advantage of 3D blading in reducing the near-stall loss, yet the effect is less remarkable under larger mass flow coefficients when the flow field is naturally healthy. The following section will outline the experimental methods used for further validation.

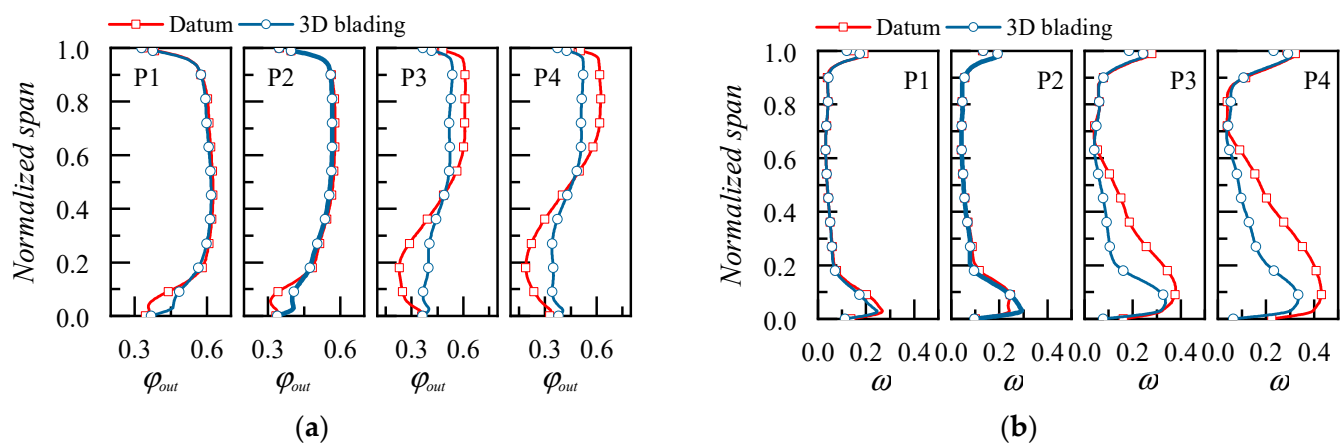


Figure 29. The radial distribution of mass flow coefficient and loss under different operating conditions: (a) outlet mass flow coefficient; (b) total pressure loss.

4.2. Discussion of the Experimental Results

4.2.1. Effect of 3D Blading on the Aerodynamic Performance

To start, the overall aerodynamic performance of the compressor stage is compared, as shown in Figure 30. Results highlight that the 3D blading on the cantilevered stator could significantly improve the performance of the compressor stage at small mass flow conditions; at the near stall condition (P4), the total pressure rise coefficient and the efficiency are increased by 3% and 2%, respectively. However, as the operating point moves to the right, the 3D blading will start losing its advantage, and the stage efficiency at $\varphi > 0.51$ will even drop by 0.7%. As only stator blades have been changed, Figure 31 shows the loss characteristics of the cantilevered stators, in which the CFD results are also plotted to present the deviation between the experiment result and the CFD result. Figure 31 indicates the CFD results have high reference value, so the above numerical analysis results are credible.

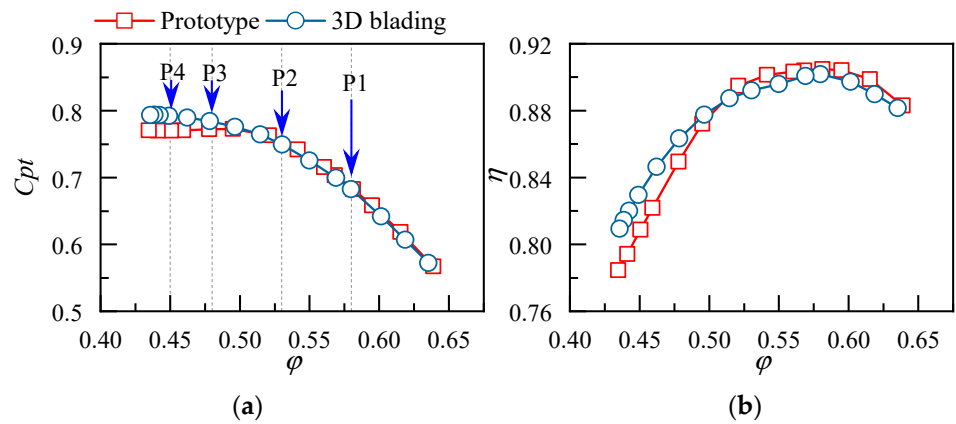


Figure 30. Comparison of performance characteristics of the compressor stage: (a) total pressure rise coefficient; (b) efficiency.

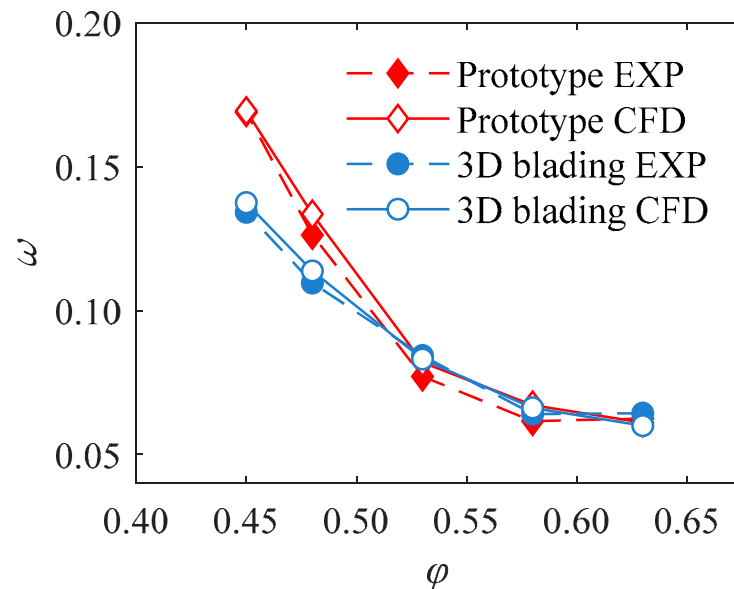


Figure 31. Comparison of loss characteristics of the cantilevered stators between experiment and CFD.

Turning to the stator blade row, Figure 32a presents the variation of the stator total pressure loss coefficient with the stage mass flow coefficient. In comparison with the datum scheme, the total pressure loss of the 3D cantilevered stator is reduced significantly; the absolute reduction reaches 0.035 at the near-stall point (P4), or 20.5%. However, the loss of the cantilevered stator will increase slightly at higher mass flow conditions; the maximum increment is 0.008 at $\phi = 0.53$, which is acceptable in consideration of its advantage under other conditions. Additionally, the variation of the stator loss coincides with the trend on the stage level, thus implying that the variation of compressor stage performance in Figure 30 is attributed mainly to the 3D bladed stator. In order to further quantify the impact of 3D blading on different regions of the cantilevered stator, the total loss is decomposed along the blade span, as shown in Figure 32b–d. The blade is classified into three regions according to the mass flow, i.e., the hub region (0~25% total mass flow), the middle region (25~75% total mass flow), and the tip region (75~100% total mass flow). Results show that the loss reduction of the 3D stator stems mainly from the hub and midspan regions, which is consistent with the weakening of corner flow separation in these areas. Moreover, the utilization of the forward sweep turns out to improve the tip region over the whole operating range, which signifies the necessity of balancing radial flow in the design process.

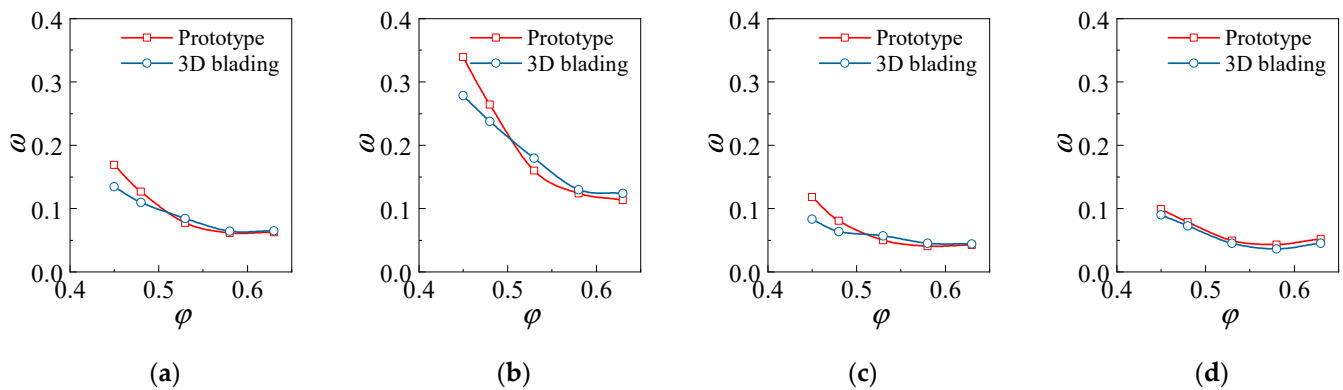


Figure 32. Comparison of loss characteristics of the cantilevered stator: (a) total loss, (b) hub loss, (c) midspan loss, and (d) tip loss.

The radial distribution of the mass flow coefficient for the cantilevered stator is illustrated in Figure 33. Results show that the 3D blading barely influences the mass flow distribution at the stator inlet, whereas it could improve the throughflow capacity at the hub region over a wide operating range. The distribution of mass flow coefficient at the stator outlet exhibits a similar pattern to that in Figure 29, which proves the accuracy of the numerical simulation. On the other hand, the mass flow coefficient in the lower span areas of the stator outlet sees a remarkable increment at P2~P4 conditions, implying the flow capacity near the endwall is enhanced via the combination of the forward sweep and dihedral. It should be noted that at the P1 condition, the mass flow coefficient of a 10~40% span is reduced for the 3D blading scheme, which indicates the flow capacity is weakened in these regions. The mass flow at the midspan areas is first increased and then decreased as the operating point moves from P1 to P4, owing to the redistribution of radial flow. The effect of 3D blading is more pronounced at small mass flow coefficients, thus confirming the former investigation.

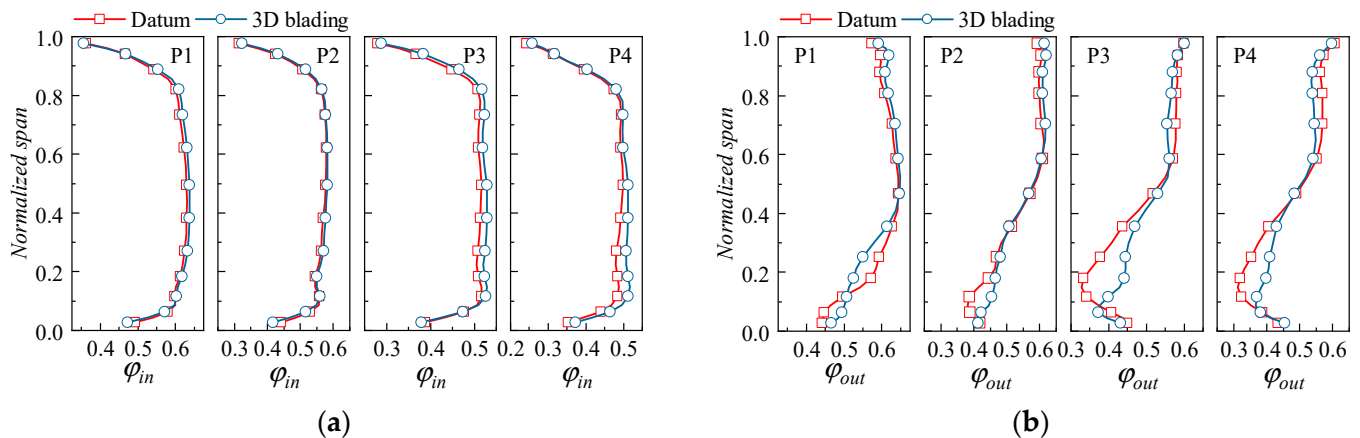


Figure 33. The radial distribution of mass flow coefficients under different operating coefficients: (a) inlet mass flow coefficient; (b) outlet mass flow coefficient.

Figure 34 presents the distributions of the blockage coefficient and the total pressure loss coefficient. The variation of the blockage denotes that the 3D blading could generally relieve the flow blockage at the hub corner, thereby creating a healthier flow field. However, the blockage coefficient of a 10~40% span is increased at the P1 condition, which corresponds to the reduction of mass flow ratio in Figure 33b. As for loss characteristics, large amounts of loss reduction are brought by the 3D blading at small mass flow conditions (P3 and P4), whereas the beneficial effect is less distinctive at large mass flow ratios (P1 and P2).

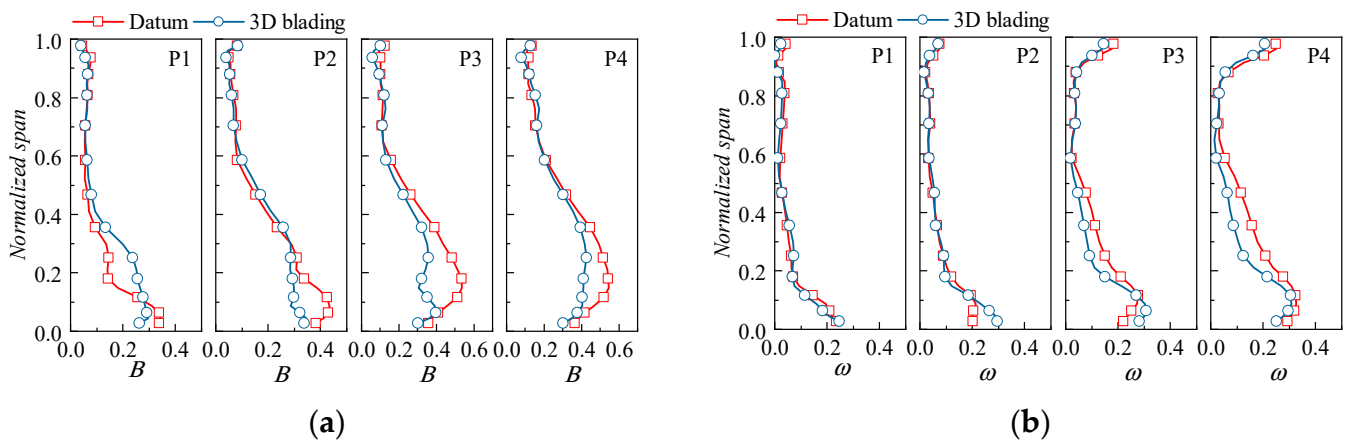


Figure 34. The radial distribution of blockage and loss under different operating coefficients: (a) blockage; (b) total pressure loss.

4.2.2. Effect of 3D Blading on the Flow Field Distribution

To obtain an overview of the flow structures in the cantilevered stator, Figure 35 presents the oil-flow results of the datum stator. The separation line (SL) is denoted by the red solid line, the attachment line (AL) is denoted by the red dotted line, the spiral node is denoted by the letter F, and the saddle point is denoted by the letter S. It can be seen that at the P1 condition, under the blowing effect of the endwall leakage flow, the corner separation at the stator hub starts from the saddle point S1 and separates into S1-F1 and S1-F3 along the radial direction; the tip region also suffers corner flow separation. The upper and lower separation areas bounded by S1 are approximately symmetrical and located close to the blade trailing edge, whereas the separation region at the blade tip is independent of the hub corner separation. With the decrease of the mass flow coefficient, the corner flow separation first enlarges its radial scale at P2 and then changes the topology at P3: the separation line S1-F1 heads upstream, pushing F1 to the endwall and incurring the corner stall. According to Figure 35, the stator hub is severely blocked at the P3 condition, represented by the large-scale low-speed zone at the outlet. Further observation of the tip flow shows that at the near-stall conditions (P3, P4), the separation region at the stator hub and the tip will gradually merge at the trailing edge, which is also demonstrated in Figure 35. Finally, under the cantilevered geometry, the occurrence of the corner stall will only induce local separation flow at SL2, which is distinctively different from the conventional shrouded stator (represented by the large-scale endwall separation and a rapid expansion of the separation zone) [37–39].

Figure 36 presents the flow field distribution at the stator outlet, where the results of both the datum stator and the 3D bladed stator are demonstrated. It can be observed that the 3D blading can effectively push the leakage flow away from the blade suction surface, yet it will incur secondary leakage at the large flow conditions (in P1 and P2, the leakage flow moves into adjacent blade channel). As a result, the flow separation at the blade trailing edge is enhanced slightly. With the decrease of mass flow rate, both the leakage flow and the transverse secondary flow will be enhanced by the increase of the circumferential pressure gradient, while the difference in their variation rate makes the leakage flow approach the blade suction surface and finally accumulate toward the hub corner of the blade suction surface (P3 and P4). In fact, it is only at the near-stall conditions when the 3D blading manifests its advantage: at P3 and P4, the flow separation is weakened in the middle and lower part of the stator, thereby alleviating the blockage in the middle and lower span areas. Moreover, the forward sweep at the stator tip turns out to improve the flow field in the meantime, as the wake is narrowed correspondingly.

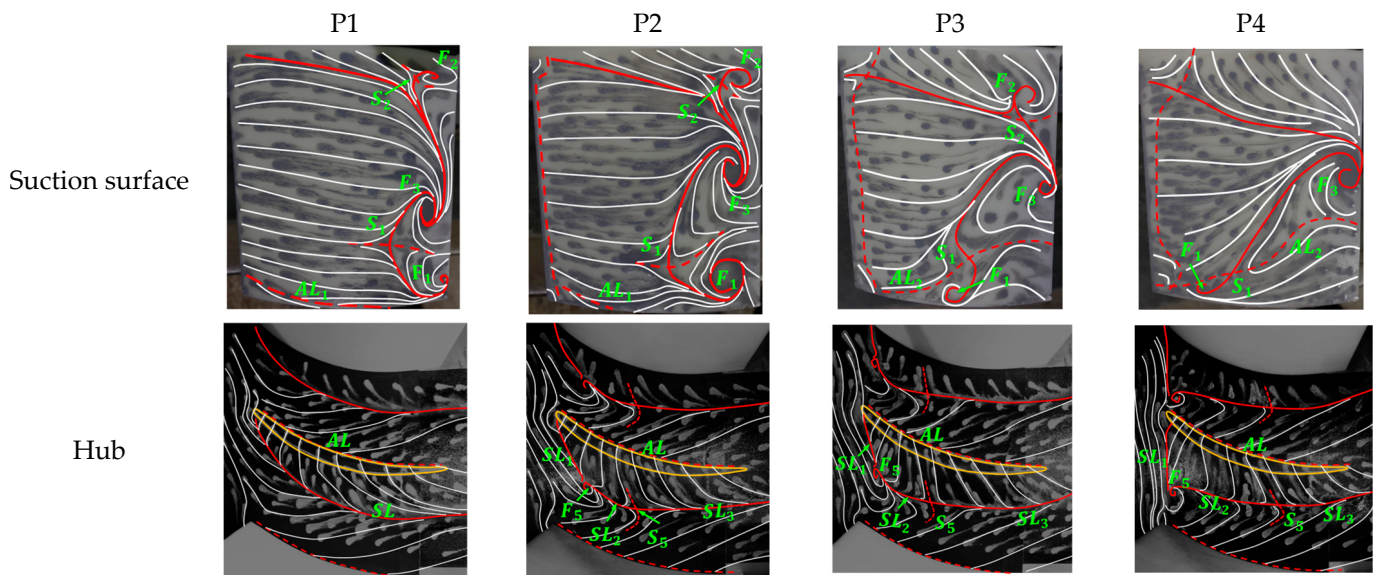


Figure 35. Oil-flow results on the blade suction surface and hub wall for the datum stator.

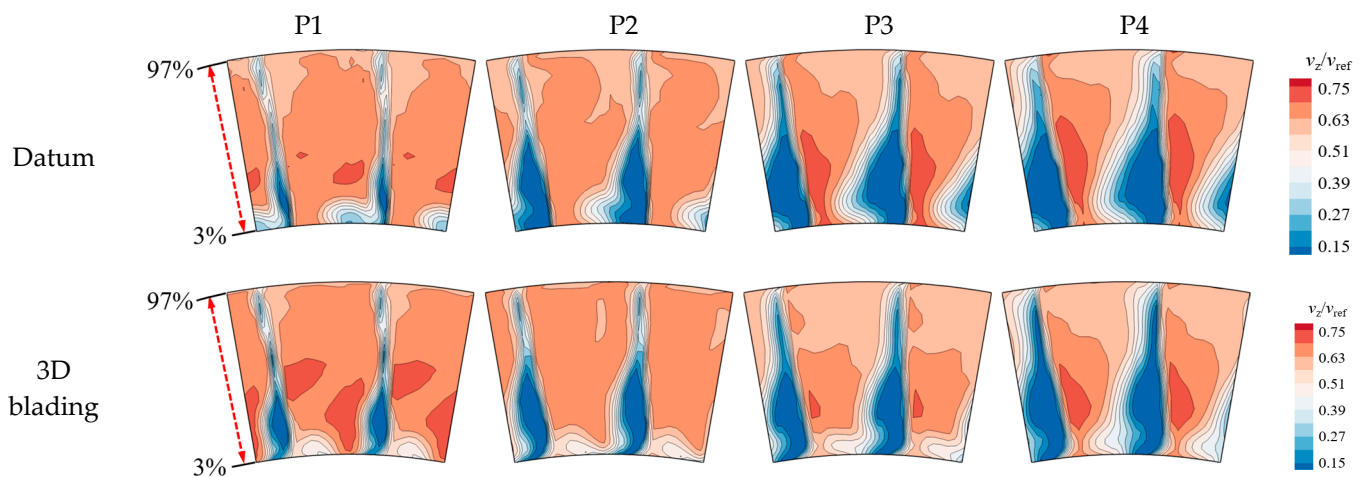


Figure 36. The distribution of the normalized axial speed at the stator outlet.

To further reveal the mechanism of 3D blading in the corner flow in the cantilevered stator, Figure 37 presents the comparison of the secondary flow velocity vector at the stator outlet. Traces of the secondary flow (CF) and the leakage flow (LF) are depicted to demonstrate the flow structures with better clarity. Apparently, the leakage flow that travels from the blade pressure surface to the suction pressure surface could hinder the circumferential migration of the secondary flow. In the datum scheme, the CF travels through the bottom of the LF and climbs to the blade suction surface, inducing a counterclockwise vortex on its left side and a clockwise vortex on its right side. Upon the utilization of 3D blading, the strengthening of the leakage flow enhances the inhibition effect of the LF on the CF, leading to secondary leakage at the P1 and P2 conditions. As for P3 and P4 conditions, the flow separation in the corner region is reduced, owing to the weakening of the secondary flow.

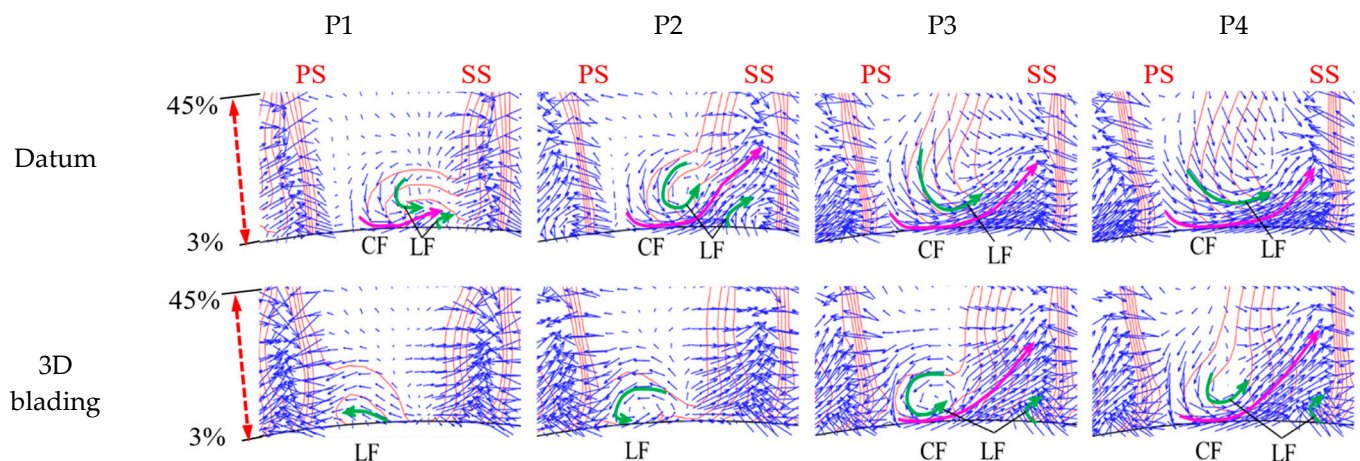


Figure 37. Distribution of secondary flow velocity vector at the stator outlet.

To sum up, the interaction between the endwall leakage flow and the transverse secondary flow determines the effect of the 3D blading. For the present cantilevered stator, at large mass flow rates, the experimental results demonstrate that the 3D blading pushes the leakage flow too close to the pressure side of the adjacent blade, thereby inducing secondary leakage. However, at small mass flow rates, the inhibition of the leakage flow to the endwall secondary flow is not strong enough; hence, the corner separation requires further elimination. The above results also imply that the design of 3D blading needs to optimize the evolution of corner flow structures at different operating conditions.

5. Conclusions

This study focuses on the utilization of 3D blading in the cantilevered stator and seeks to reveal its mechanism in improving the compressor aerodynamic performance. The main conclusions are drawn as follows:

1. The forward sweep can inhibit the transverse flow near the hub endwall and alleviate the flow separation at the corner region, while flow separation on the blade suction side was exaggerated slightly. Increasing the sweep height facilitates a uniform separation along the span without changing the endwall flow significantly, whereas excessively large sweep angles lead to a large-scale separation on the blade suction surface and harm the total effect;
2. The positive dihedral not only pushes the trajectory of the leakage vortex away from the blade suction surface but also promotes the radial migration of the low-energy fluid at the hub corner. The utilization of large dihedral heights elongates the blade wake and induces the radial transportation of the leakage flow, while the excessive dihedral angle damages the performance at the midspan;
3. The compound forward sweep and positive dihedral can combine the advantages of both strategies and provide better aerodynamic performance for the cantilevered stator, the benefit extends over the whole operating range and is more significant at lower mass flow ratios. In comparison to the orthogonal stator, the static pressure rise coefficient and the total pressure loss coefficient of the 3D bladed stator are increased and decreased by 25.5% and 11.1%, respectively;
4. The compound sweep and dihedral were utilized to redesign a cantilevered stator in a low-speed compressor test facility. Experimental results demonstrate that the total pressure loss of the 3D cantilevered stator is reduced by 20.5% at the near-stall point, thus proving the effectiveness of the 3D blading technique. The advantage of 3D blading is more pronounced at small mass flow coefficients;
5. The performance enhancement of the 3D blading stems mainly from the hub and lower span areas. At large mass flow ratios, the leakage flow leaks into the adjacent blade channel and causes secondary loss, yet at small mass flow rates, the inhibition

of the leakage flow to the endwall secondary flow is not strong enough; hence, the corner separation needs further elimination. The design of the 3D cantilevered stator needs to optimize the evolution of corner flow structures over the operating range.

The validation of the 3D blading is conducted in the low-speed compressor test facility under the single-stage environment in the present study, and it would be meaningful if experiments could be implemented in high-speed and multi-stage environments in the future to reveal more flow mechanisms while validating the present conclusions.

Author Contributions: Conceptualization, G.A. and X.Y.; methodology, X.X., R.W. and G.A.; software, G.A.; validation, Y.Q., G.A. and X.Y.; formal analysis, X.X., R.W. and G.A.; investigation, X.X., Y.Q., R.W., B.L., G.A. and X.Y.; resources, Y.Q. and G.A.; data curation, Y.Q., X.X., R.W. and G.A.; writing—original draft preparation, X.X. and R.W.; writing—review and editing, R.W.; visualization, Y.Q., X.X. and R.W.; supervision, B.L.; project administration, B.L. and X.Y.; funding acquisition, B.L. All authors have read and agreed to the published version of the manuscript.

Funding: This research was funded by National Natural Science Foundation of China (Grant Nos. 52276025, 52206038), the National Science and Technology Major Project (J2019-II-0004-0024, J2019-II-0003-0023), the Advanced Jet Propulsion Innovation Center/AEAC (funding number HKCX2022-01-008), and the Fundamental Research Funds for the Central Universities.

Data Availability Statement: Not applicable.

Conflicts of Interest: The authors declare no conflict of interest. The funders had no role in the design of the study; in the collection, analyses, or interpretation of data; in the writing of the manuscript; or in the decision to publish the results.

References

1. Dean, R.C. Secondary Flow in Axial Compressors. Ph.D. Thesis, Massachusetts Institute of Technology, Cambridge, MA, USA, 1954.
2. Lakshminarayana, B. Methods of Predicting the Tip Clearance Effects in Axial Flow Turbomachinery. *J. Basic Eng.* **1970**, *92*, 467–480. [CrossRef]
3. Lakshminarayana, B.; Horlock, J. *Tip-Clearance Flow and Losses for an Isolated Compressor Blade*; Her Majesty's Stationery Office: London, UK, 1962.
4. Lakshminarayana, B.; Horlock, J. *Leakage and Secondary Flows in Compressor Cascades*; Her Majesty's Stationery Office: London, UK, 1967.
5. George, K.K.; Agnimitra Sunkara, S.N.; George, J.T.; Joseph, M.; Pradeep, A.M.; Roy, B. Investigations on Stator Hub End Losses and its Control in an Axial Flow Compressor. In Proceedings of the ASME Turbo Expo 2014: Turbine Technical Conference and Exposition, Dusseldorf, Germany, 16–20 June 2014.
6. Singh, U.K.; Ginder, R.B. The Effect of Hub Leakage Flow in a Transonic Compressor Stator. In Proceedings of the ASME 1998 International Gas Turbine and Aeroengine Congress and Exhibition, Stockholm, Sweden, 2–5 June 1998; p. V001T001A099.
7. Lee, C.; Song, J.; Lee, S.; Hong, D. Effect of a Gap Between Inner Casing and Stator Blade on Axial Compressor Performance. In Proceedings of the ASME Turbo Expo 2010: Power for Land, Sea, and Air, Glasgow, UK, 14–18 June 2010; pp. 203–210.
8. Gbadebo, S.A.; Cumpsty, N.A.; Hynes, T.P. Three-Dimensional Separations in Axial Compressors. *J. Turbomach.* **2005**, *127*, 331–339. [CrossRef]
9. Dong, Y.; Gallimore, S.J.; Hodson, H.P. Three-Dimensional Flows and Loss Reduction in Axial Compressors. *J. Turbomach.* **1987**, *109*, 354–361. [CrossRef]
10. Wennerstrom, A.J. Experimental Study of a High-Throughflow Transonic Axial Compressor Stage. *J. Eng. Gas Turbines Power* **1984**, *106*, 552–560. [CrossRef]
11. McDougall, N. A Comparison Between the Design Point and Near-Stall Performance of an Axial Compressor. *J. Turbomach.* **1990**, *112*, 109–115. [CrossRef]
12. An, G.; Fan, Z.; Qiu, Y.; Wang, R.; Yu, X.; Liu, B. Numerical Investigation of the Effect of Hub Gaps on the 3D Flows Inside the Stator of a Highly Loaded Axial Compressor Stage. *Energies* **2022**, *15*, 6993. [CrossRef]
13. Gbadebo, S.A.; Cumpsty, N.A.; Hynes, T.P. Interaction of Tip Clearance Flow and Three-Dimensional Separations in Axial Compressors. *J. Turbomach.* **2007**, *129*, 679–685. [CrossRef]
14. Singh Tanwar, B.P.; Singh, A.; Mistry, C.S. Numerical Investigations on Application of Cantilever Stator on Aerodynamic Performance of Tandem Bladed Axial-Flow Compressor. In Proceedings of the ASME Turbo Expo 2021: Turbomachinery Technical Conference and Exposition, Online, 7–11 June 2021.
15. Horlock, J.H.; Louis, J.F.; Percival, P.M.E.; Lakshminarayana, B. Wall Stall in Compressor Cascades. *J. Basic Eng.* **1966**, *88*, 637–648. [CrossRef]
16. Peacock, R.E. A review of turbomachinery tip gap effects: Part 1: Cascades. *Int. J. Heat Fluid Flow* **1982**, *3*, 185–193. [CrossRef]

17. Peacock, R.E. A review of turbomachinery tip gap effects: Part 2: Rotating machinery. *Int. J. Heat Fluid Flow* **1983**, *4*, 3–16. [CrossRef]
18. Tweedt, D.L.; Okiishi, T.H.; Hathaway, M.D. Stator Endwall Leading-Edge Sweep and Hub Shroud Influence on Compressor Performance. *J. Turbomach.* **1986**, *108*, 224–232. [CrossRef]
19. Storer, J.A.; Cumpsty, N.A. Tip Leakage Flow in Axial Compressors. *J. Turbomach.* **1991**, *113*, 252–259. [CrossRef]
20. Yamaguchi, N.; Tominaga, T.; Hattori, S.; Mitsuhashi, T. IGTC-8 Secondary-loss reduction by forward-skewing of axial compressor rotor blading. In Proceedings of the 1991 Yokohama International Gas turbine Congress, Yokohama, Japan, 27 October–1 November 1991; pp. 61–68.
21. Breugelmans, F.; Carels, Y.; Demuth, M.N. Influence Of Dihedral on the Secondary Flow in a Two-Dimensional Compressor Cascade. *J. Eng. Gas Turbines Power* **1984**, *106*, 578–584. [CrossRef]
22. Weingold, H.D.; Neubert, R.J.; Behlke, R.F.; Potter, G.E. Bowed Stators: An Example of CFD Applied to Improve Multistage Compressor Efficiency. *J. Turbomach.* **1997**, *119*, 161–168. [CrossRef]
23. Sasaki, T.; Breugelmans, F. Comparison of Sweep and Dihedral Effects on Compressor Cascade Performance. *J. Turbomach.* **1998**, *120*, 454–463. [CrossRef]
24. Vad, J. Aerodynamic effects of blade sweep and skew in low-speed axial flow rotors at the design flow rate: An overview. *Proc. Inst. Mech. Eng.* **2008**, *222*, 69–85. [CrossRef]
25. Xu, P.; Yu, X.; Liu, B. The Effects of Blade 3D Designs in Different Orthogonal Coordinates on the Performance of Compressor Cascades. *Int. J. Turbo Jet-Engines* **2014**, *31*, 329–345. [CrossRef]
26. Lange, M.; Vogeler, K.; Mailach, R.; Gomez, S.E. An experimental verification of a new design for cantilevered stators with large hub clearances. *J. Turbomach.* **2013**, *135*, 041022. [CrossRef]
27. Lu, H.; Li, Q.; Pan, T. Using forward end-sweep to reduce transonic cantilevered stator losses to improve compressor performance. *Eng. Appl. Comput. Fluid Mech.* **2018**, *12*, 293–307. [CrossRef]
28. Gunn, E.J.; Hall, C.A. Nonaxisymmetric Stator Design for Boundary Layer Ingesting Fans. *J. Turbomach.* **2019**, *141*, 071010. [CrossRef]
29. Gallimore, S.J.; Bolger, J.J.; Cumpsty, N.A.; Taylor, M.J.; Wright, P.I.; Place, J.M.M. The Use of Sweep and Dihedral in Multistage Axial Flow Compressor Blading—Part I: University Research and Methods Development. *J. Turbomach.* **2002**, *124*, 521–532. [CrossRef]
30. Pullan, G.; Harvey, N.W. Influence of Sweep on Axial Flow Turbine Aerodynamics at Midspan. *J. Turbomach.* **2007**, *129*, 591–598. [CrossRef]
31. An, G. Studies of the Unsteady Flow Behaviors for the Tip Leakage Flow and the Modeling of the Flow Blockage and Loss. Ph.D. Thesis, Beihang University, Beijing, China, 2016.
32. Fu, D. Theoretical and Experimental Study on the Highly Loaded Compressor with Tandem Blades. Ph.D. Thesis, Beihang University, Beijing, China, 2019.
33. Menter, F.R. Two-equation eddy-viscosity turbulence models for engineering applications. *AIAA J.* **1994**, *32*, 1598–1605. [CrossRef]
34. Liu, B.; An, G.; Yu, X. Assessment of curvature correction and reattachment modification into the shear stress transport model within the subsonic axial compressor simulations. *Proc. Inst. Mech. Eng.* **2015**, *229*, 910–927. [CrossRef]
35. Menter, F.R. Review of the shear-stress transport turbulence model experience from an industrial perspective. *Int. J. Comput. Fluid Dyn.* **2009**, *23*, 305–316. [CrossRef]
36. Liu, B.; Qiu, Y.; An, G.; Yu, X. Utilization of Zonal Method for Five-Hole Probe Measurements of Complex Axial Compressor Flows. *J. Fluids Eng.* **2020**, *142*, 061504. [CrossRef]
37. Liu, B.; Qiu, Y.; An, G.; Yu, X. Experimental Investigation of the Flow Mechanisms and the Performance Change of a Highly Loaded Axial Compressor Stage with/without Stator Hub Clearance. *Appl. Sci.* **2019**, *9*, 5134. [CrossRef]
38. Lei, V.M.; Spakovszky, Z.S.; Greitzer, E.M. A Criterion for Axial Compressor Hub-Corner Stall. *J. Turbomach.* **2008**, *130*, 031006. [CrossRef]
39. Taylor, J.V.; Miller, R.J. Competing Three-Dimensional Mechanisms in Compressor Flows. *J. Turbomach.* **2016**, *139*, 021009. [CrossRef]

Disclaimer/Publisher’s Note: The statements, opinions and data contained in all publications are solely those of the individual author(s) and contributor(s) and not of MDPI and/or the editor(s). MDPI and/or the editor(s) disclaim responsibility for any injury to people or property resulting from any ideas, methods, instructions or products referred to in the content.

Article

Influence of Wake Intensity on the Unsteady Flow Characteristics of the Integrated Aggressive Interturbine Duct

Zhijun Lei ^{1,2}, Hongrui Liu ^{1,2,*}, Gang Li ^{1,2,*}, Jianbo Gong ^{1,2}, Yanfeng Zhang ^{1,2}, Xingen Lu ^{1,2}, Gang Xu ^{1,2} and Junqiang Zhu ^{1,2}

¹ Key Laboratory of Light-Duty Gas Turbine, Institute of Engineering Thermophysics, C.A.S., Beijing 100190, China; leizhijun@iet.cn (Z.L.); gongjianbo@iet.cn (J.G.); zhangyanfeng@iet.cn (Y.Z.); luxg@iet.cn (X.L.); xug@iet.cn (G.X.); zhujq@iet.cn (J.Z.)

² School of Aeronautics and Astronautics, University of Chinese Academy of Sciences, Beijing 100049, China

* Correspondence: liuhongrui@iet.cn (H.L.); ligang@iet.cn (G.L.)

Abstract: The interturbine transition duct (ITD), located between the high-pressure (HP) and low-pressure (LP) turbines of aeroengines, tends to be designed as an aggressive ITD integrated with wide-chord struts to meet the requirements of civil aeroengines for high bypass ratios and thrust-weight ratios. This paper presents a detailed unsteady numerical investigation of the effects of the HP rotor trailing-edge radius on the unsteady flow characteristics in the integrated aggressive interturbine transition duct (AITD), including the transport and dissipation of HP rotor wakes, the control mechanism of HP rotor wakes on flow separation and the influence of wake parameters. A sweeping rod, with a nondimensional diameter ranging from $d/s = 0.056\text{--}0.143$ (based on the pitch (s) of wide-chord struts at the midspan) and a reduced frequency (f) of 1.07, is used to simulate the HP rotor wake to decouple its influence from other secondary flows. Using the $k\text{-}\omega$ SST turbulence model and gamma-theta transition model, a structured grid with 6.3 million nodes can achieve similar global results. The wake in the lower part of the AITD channel dissipates rapidly because of the stretching between its own circumferential motion and the radial upward secondary flow, especially for a small d/s . Only the residual wake in the upper part can reach wide-chord struts in the case with large d/s . A sweeping rod with a large d/s can reduce the radial pressure gradient in the AITD, inhibit the internal secondary flow to a certain extent, reduce the dissipation rate of the wake, enhance its suppression effect on flow separation on a wide-chord strut, and decrease the flow loss. However, the wake can also enhance the passage vortex due to the increasing circumferential pressure gradient in the wide-chord strut channel, resulting in increasing blade profile loss. In the scope of this study, the aerodynamic gain of the wake is still not enough to compensate for its loss increment (including its own dissipation loss). Therefore, selecting a small trailing-edge radius of the HP rotor is conducive to improving the aerodynamic performance of the integrated AITD.

Keywords: interturbine transition duct; sweeping rods; boundary layer transition; unsteady flow

Citation: Lei, Z.; Liu, H.; Li, G.; Gong, J.; Zhang, Y.; Lu, X.; Xu, G.; Zhu, J. Influence of Wake Intensity on the Unsteady Flow Characteristics of the Integrated Aggressive Interturbine Duct. *Appl. Sci.* **2022**, *12*, 6655. <https://doi.org/10.3390/app12136655>

Academic Editors: Gabriel Bugeđa Castellort and Josep Maria Bergada

Received: 26 May 2022

Accepted: 27 June 2022

Published: 30 June 2022

Publisher's Note: MDPI stays neutral with regard to jurisdictional claims in published maps and institutional affiliations.



Copyright: © 2022 by the authors. Licensee MDPI, Basel, Switzerland. This article is an open access article distributed under the terms and conditions of the Creative Commons Attribution (CC BY) license (<https://creativecommons.org/licenses/by/4.0/>).

1. Introduction

The interturbine transition duct (ITD) is an annular S-shaped diffuser between the high-pressure turbine (HPT) and low-pressure turbine (LPT), as shown in Figure 1. With the increase in the bypass ratio of a high-performance engine, designers often use an aggressive interturbine transition duct (AITD) to raise the LPT passage to reduce the low-pressure rotor speed and improve the LPT output power. The larger outlet-to-inlet area ratio, shorter axial length and/or larger HP-to-LP radial offset of the AITD make the axial, circumferential and radial pressure gradients more complex, which in turn affects the internal secondary flow development and loss mechanisms of the AITD.

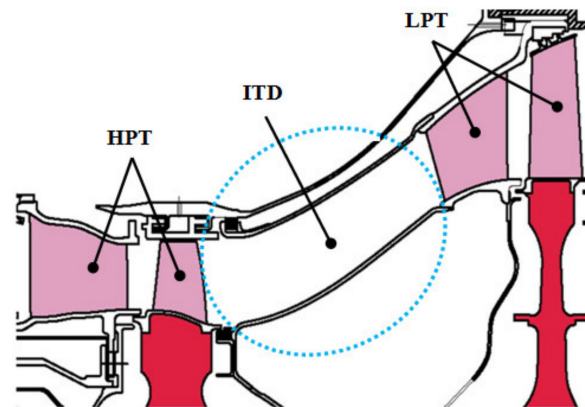


Figure 1. Typical ITD in a turbobfan aeroengine.

Dominy et al. [1,2], as early investigators of the ITD, indicated that although the simulated HPT steady wake and swirl did not result in large changes in the overall loss, they were important factors that affected the structure of the secondary flow and the distribution of loss in the ITD. They also found that because of the pressure gradient inside the ITD, the simulated HPT wakes interacted with the boundary layer of the end wall, and a pair of counter vortices were generated at the hub and the casing, which affected the distribution of loss and the outlet flow angle. Zhang et al. [3] improved the understanding of the formation mechanism of the vortex pairs near the hub and shroud: the low momentum fluid near the ITD hub forms the pair of vortices driven by the radial pressure gradient, while the migrated low momentum fluid forms a three-dimensional boundary layer on the shroud and develops into a pair of vortices. Miller et al. [4] indicated that the radial migration and mixing of the flow between the midspan and the shroud caused by the radial pressure gradient was the main source of loss in it. By comparing two ITDs with different axial lengths and the same area ratio and radial offset, Norris et al. [5] found that the changes in ITD end wall curvature and diffusion rate caused by the decreased axial length were the main factors affecting the internal secondary flow in ITDs. Based on the detailed measurement data of an ITD, Zhang et al. [6] concluded that an increased mean rise angle and area ratio aggravated the flow separation on the shroud by enhancing the inverse streamwise pressure gradient. Axelsson [7–9], Göttlich [10] and Marn [11–13] studied the influence of the upstream HPT leakage flow on the internal flow of an ITD and indicated that the increase in tangential flow angle near the shroud caused by the increasing tip clearance helped to suppress the boundary layer separation of the shroud but led to an increase in the overall loss. Dominy [14], Hu [15], Zhang [16] and Bailey [17] investigated the influence of inlet swirls on the ITD flow. They found that the inlet swirl could increase the effective fluid motion path in an ITD to suppress the influence of wall curvature on its internal pressure gradient, while the increasing inlet swirl near the shroud inhibited the boundary layer separation on the shroud. Schennach et al. [18] studied the effect of the potential flow of the low-pressure turbine guide vane (LPT-GV) on the ITD flow and believed that an optimal circumferential position of the LPT-GV maximized the system performance for a specific ITD system.

Norris [19,20], Miller [21], and Walker [22] indicated that the built-in strut in an ITD changed the area distribution of flow passage, which forced the pipeline to expand, resulting in worse boundary layer separation, significantly enhanced unsteady flow, and greatly increased losses. Lengani [23,24] found that the interaction between the wakes and vortex structure of struts and the LPT rotor not only caused fluctuations in flow velocity and flow angle but also greatly affected the pressure fluctuation peak downstream. On the basis of their proposed integrated design concept of an ITD and strut, Marn et al. [25] used 18 wide-chord struts to replace 48 LPT-GVs in the original ITD, which not only ensured the outlet flow quality of the ITD but also reduced the weight of the guide vane by 20–39%. The integrated design of a wide-chord strut and ITD can enhance the secondary flow

in the ITD, resulting in a deterioration in the uniformity of the outlet flow. Therefore, Spataro [26] arranged two zero-loading splitter blades between adjacent wide-chord struts, effectively improving the uniformity of ITD outlet flow. Bader [27] and Faustmann [28] further indicated that a small splitter blade could break the large passage vortices in the passage of wide-chord struts into small passage vortices, thereby improving the outlet flow uniformity at the expense of increasing flow losses. Du [29], Wang [30], Liu [31], Xu [32] and Liu [33] carried out design and flow mechanism research of the integrated AITD and noted that the convergence passage of a wide-chord strut can effectively inhibit the three-dimensional separation on the shroud and suppress the passage vortices around the blade tip by improving the radial and circumferential pressure gradient, which is conducive to reducing the flow loss in the AITD.

In an integrated AITD, the distance between the LPT-GV and the upstream HPT rotor is greatly shortened so that the wake of the HPT rotor can reach the LPT-GV before dissipation, which provides an opportunity to use the upstream sweeping wakes to inhibit its boundary layer separation. The inhibition mechanism of upstream sweeping wakes on the flow separation of high-loading LPT blades in cascade wind tunnels [34–38] has been studied systematically. However, different from the linear cascade flow, the AITD is an S-shaped annular passage with a strong axial reverse pressure gradient and radial pressure gradient, which inevitably affects the transport and dissipation of the HP rotors' wakes in AITD. There were only a few studies [18,23,24] on the influence of sweeping wake on ITD flow, and most of them were generally coupled with the influence of inlet swirl or tip leakage flow, so the impact of a decoupled wake is still not particularly clear. Liu et al. [33,39,40] studied the transport mechanism of the decoupled wake in AITD and the influence of Re and FSTI (free stream turbulence intensity) on its propagation. They found that with the shortening of the axial length of AITD, the upstream wake almost existed in the full channel range, and could periodically suppress the separation bubble on the suction surface of LPT-GV. Based on their works, the effects of sweeping wakes with different HPT rotor trailing-edge radii on the internal flow field of an AITD and the boundary layer of an integrated LPT-GV will be studied in this paper.

2. Numerical Methods

This paper employed the commercial ANSYS CFX solver, a fully implicit solver coupled algebraic multigrid technique, to solve three-dimensional Reynolds-averaged Navier–Stokes (RANS) equations. The high-resolution upwind discrete scheme was used for convective and diffusive terms, and the second-order backward difference method was used for time terms. Turbulence closure was achieved through the shear stress transport (SST) k - ω two-equation turbulence model coupled with the gamma–theta transition model, since this approach can model flow structures with high-curvature endwall geometry and high turbulent dissipation in freestreams [3].

2.1. Integrated AITD

As shown in Figure 2a,b, the integrated AITD, which was designed based on the original ITD of a turbofan engine, includes the aggressive intermediate-turbine duct and the integrated LPT-GV. For the AITD, its inlet aspect ratio ($R_{\text{hub}}/R_{\text{tip}}$) was 0.656, and the inlet channel height (H) was 85 mm. The nondimensional duct length (L/H , ITD axial length/inlet annulus height) was 1.97, and the mean rise angle (θ) was 28.08° with an outlet-to-inlet area ratio (AR) of 1.34. Based on the above parameters, the red dot in Figure 3 shows the comparison between the design parameters of this AITD and those of other turbofan engines, where cp^* is the best AR Line of ITD for the given L/h_{in} , and cp^{**} is the best L/h_{in} line for the given AR. The design parameters of the conventional ITD are generally located between these two lines, while the ITD (with small L/h_{in} and large AR) studied in this paper is marked by the red dot on the left side of the cp^* line, which indicates that it is in the category of an AITD. The design parameters in Table 1 of the integrated LPT-GV refer to the prototype guide vane of the turbofan engine with its inlet and outlet

metal angles unchanged. Figure 2b shows the geometric model of the integrated LPT-GV and the blade profiles for sections in the spanwise direction.

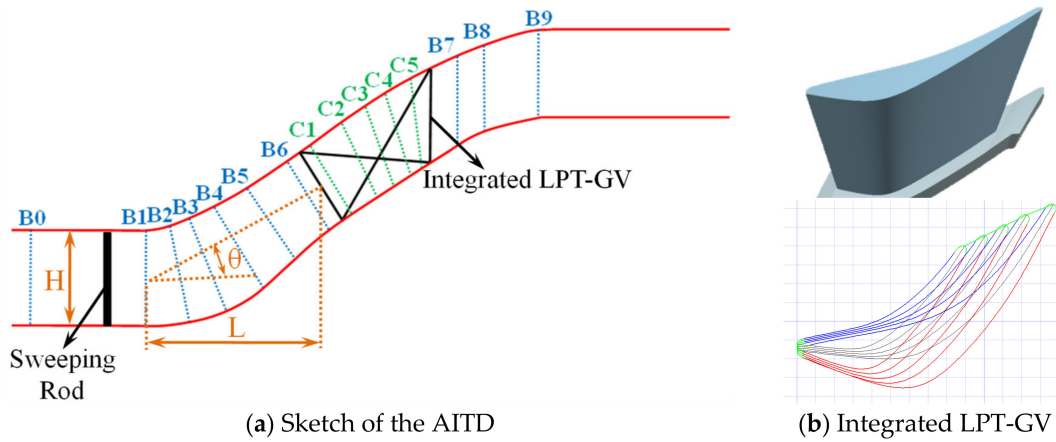


Figure 2. Cross section of the integrated AITD and measurement locations.

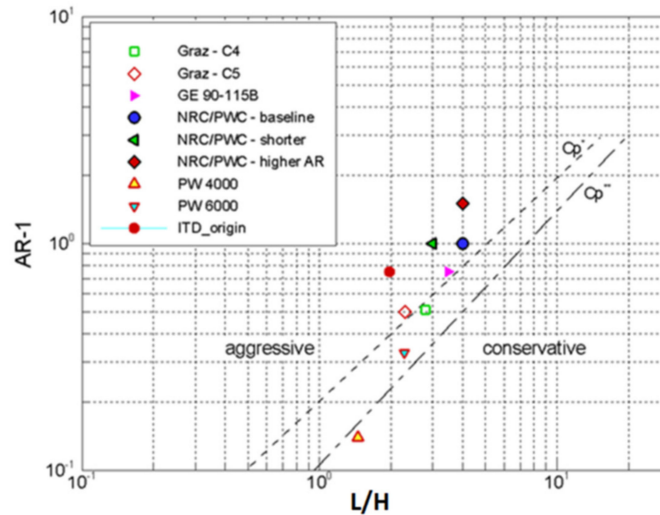


Figure 3. ITD design parameters of some turbofan engines [30].

Table 1. Design parameters of the integrated LPT-GV.

	Chord (mm)	Leading-Edge Radius (mm)	Trailing-Edge Radius (mm)	Stagger Angle (°)	Inlet Metal Angle (°)	Outlet Metal Angle (°)	Tmax/Chord	Throat/Pitch	Solidity
Root	74.5	3.5	2.5	35°	−6°	62°	0.200	0.444	1.348
Midspan	94.1	3.5	2.5	35°	−6°	62°	0.197	0.427	1.457
Tip	112.8	3.5	2.5	35°	−6°	62°	0.194	0.410	1.566

To decouple the sweeping wakes from other secondary flows, such as the tip leakage flow, sweeping rods were used to simulate the wakes of HPT rotors to isolate the effects of the sweeping wakes. Previous studies have demonstrated that when the flow resistance of the rod is the same as that of the blade, the structure of the rod’s wake is the same as that of the blade [34]. As shown in Figure 2, the sweeping rod was arranged 0.4H upstream of the AITD inlet, and its diameter (*d*) was calculated according to the measured airfoil loss (*Y*) of the HPT rotor by the following equation:

$$Y = C_d \frac{d}{S_b} Z \left[1 - \left(0.25 C_d \frac{d}{S_b} Z - 1 \right) (Z^2 - 1) \right] \tag{1}$$

where C_d represents the resistance coefficient of the rod (approximately 1.05 in the range of Re values studied in this paper), S_b is the rod spacing, and Z is the cosecant of the relative flow angle at the HPT outlet. Under the design conditions, the diameter of the sweeping rod is 4.6 mm ($d/s = 0.10$) with a rotating speed of 220 RPM, which is equivalent to a reduced frequency of $f = f_{HPT}C_x/u_e = 1.07$. To study the wake effect of the HPT rotor with different trailing-edge radii, this paper also carried out unsteady simulations for d/s values of 0.056, 0.078, 0.122 and 0.143.

As shown in Figure 2a, fifteen sections (B0–B9, C1–C5) in the streamwise direction were selected for characterizing the flow field in the integrated AITD. Section B0 is located at an inlet of the computational domain and would be used as a reference plane; Section B1 is located at the AITD inlet; Sections B2–B6 are located inside the AITD, roughly perpendicular to the shroud and hub; Sections C1–C5 are located in the passage of the integrated LPT-GV; Sections B7–B9 are located at 25% C_x , 50% C_x and 100% C_x (C_x is the axial chord of the LPT-GV midspan) downstream of the LPT-GV, respectively.

2.2. Boundary Conditions and Grid Independence

The computational domain consisted of a rotating domain of the sweeping rod and a static domain of the integrated AITD, as shown in Figure 4. Its inlet, located 1.5H upstream of the sweeping rod, was prescribed as $Re = 7.16 \times 10^4$ (based on the inlet annulus height) and $FSTI = 3\%$. The outlet, located 2.5 C_x downstream of the integrated LPT-GV, was set at uniform atmospheric pressure. No-slip and no-heat transfer conditions were imposed at the solid boundaries. The rotation speed of the sweeping rod was set to 220 RPM, and the reduced frequency was 1.07. In the unsteady calculation, the total duration was 0.389 s, and the minimum physical time step ($\Delta t = 6.5 \times 10^{-5}$ s) was set to 20 times the Karman vortex street frequency downstream of the round rod calculated by classical boundary layer theory.

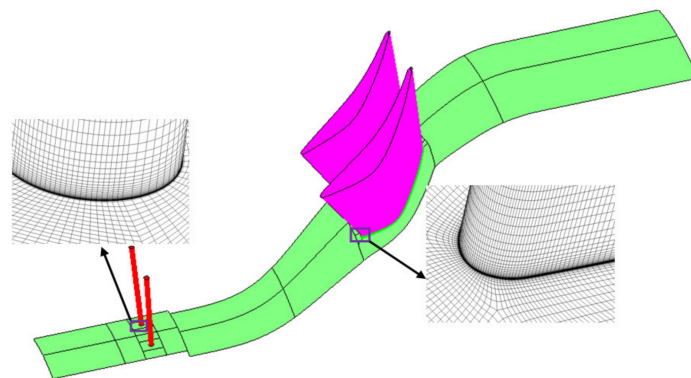


Figure 4. Calculation domain and grid of the integrated AITD.

Using the commercial software Numeca/AutoGrid, the computational domain of the integrated AITD was meshed with an HOH-type structured grid. Numerical simulations with 12.2, 6.3 and 3.1 million nodes were conducted to investigate the grid independence. As the results with 12.2 million nodes were only slightly different from those with 6.3 million nodes, the latter grid was chosen for further calculations. In the chosen grid, the numbers of circumferential, spanwise and streamwise nodes were 73, 133 and 552, respectively, and the numbers of O-type nodes around the LPT-GV and rod were 369 and 81, respectively. In the boundary layer, the grid thickness of the first layer was 0.002 mm, and the growth ratio was 1.15, which ensured that $y^+ < 1$ for all cases studied in this paper.

2.3. Validation

To verify the numerical method used in this paper, confirmatory calculations were carried out for the AITD model (Figure 5) experimentally studied in the paper [32]. Figure 6 compares the predicted limiting streamlines and the oil flow visualization on the surface of the shroud and hub. The bending position and the trend of the limiting streamlines

driven by the circumferential pressure gradient were in good agreement with the oil flow visualization. Figure 7a shows the total pressure coefficient (C_{p0}) contour on Sections C1 and C2, and the measurement boundary of each section is marked with the dotted line. The predicted C_{p0} distribution had good similarity with the experimental results, especially in the freestream region. However, the measured total pressure in the regions of wake and passage vortices was lower than the predicted value, and the range of this low total pressure region was larger than that of the numerical result. Figure 7b shows the radial distribution of the predicted pitchwise-averaged static pressure coefficient (C_{ps}) and flow angle at the AITD outlet (Section C3) and compares them with the experimental results. The predicted C_{ps} was in good agreement with the experimental result in Section C3. The trend of the predicted flow angle was basically consistent with the experimental results, especially in the middle region. However, the measured flow angle in the regions with large velocity gradients (such as the endwall region and passage vortices) was larger than the predicted flow angle. The reasons for the above differences might be that for the seven-hole probe with a diameter of 2.5 mm, its different measuring holes would be in different velocity zones in the regions with large velocity gradients (such as the wake, boundary layer, and passage vortices), and this velocity difference was interpreted as the flow angle when solving the measured flow field, resulting in the measured flow angle being larger than the actual value and the measured total pressure being lower. Therefore, the numerical method used in this paper could accurately model the flow field of an AITD with a high-curvature geometry.

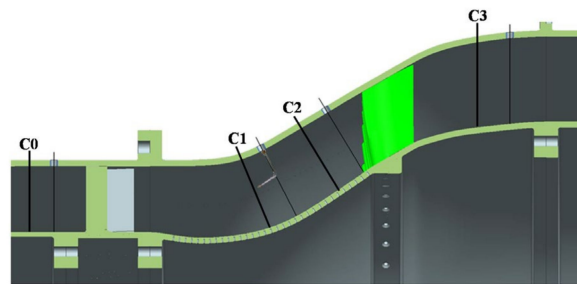


Figure 5. Sketch and grid of the AITD.

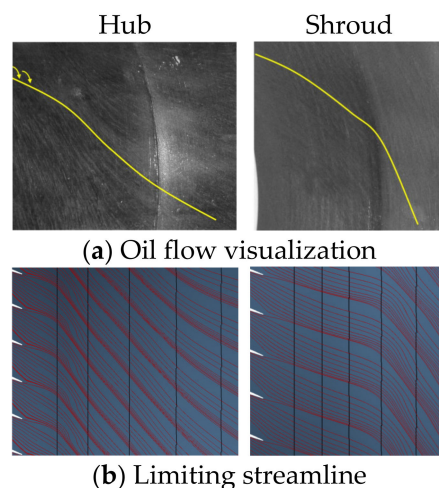


Figure 6. Flow visualization and computed limiting streamline on the ITD.

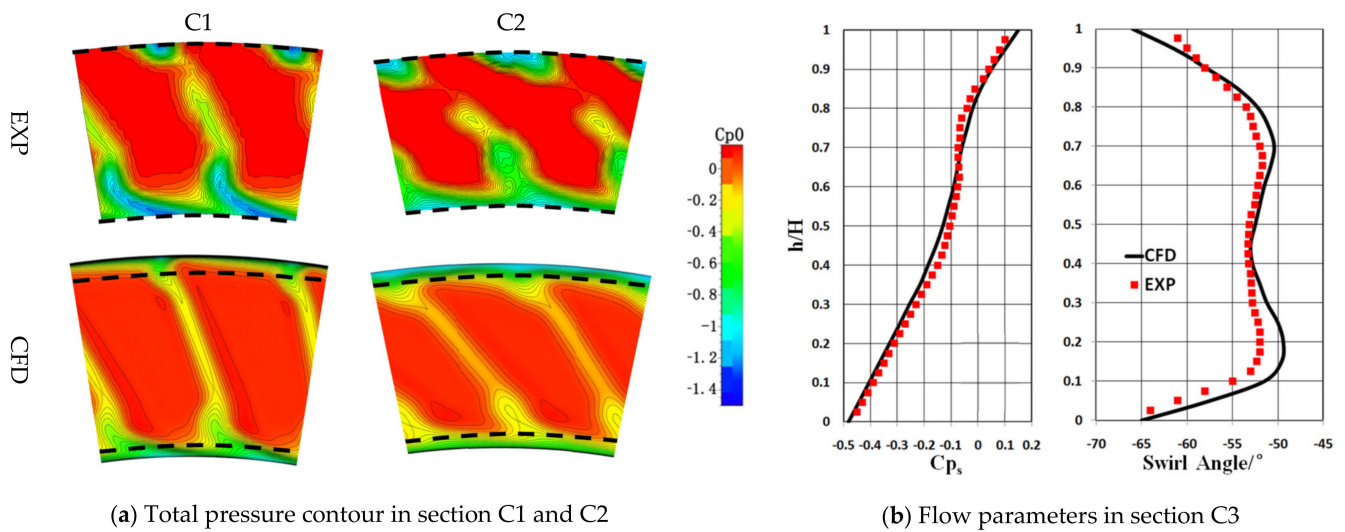


Figure 7. Comparison between experimental and numerical results.

3. Results and Discussion

In this paper, unsteady calculations were carried out for five conditions with the diameter of the sweeping rod ranging from $d/s = 0.056\sim 0.143$. Typical cases with $d/s = 0.078, 0.10$ and 0.122 are adopted to elaborate on the influence of the trailing-edge radius of the HPT on the unsteady wake transportation and the internal flow mechanism in the integrated AITD.

3.1. Influence on Unsteady Wake Transport in AITD

Figure 8 shows the circumferential distribution of the turbulence intensity (T_u) at the midspan of different streamwise sections inside the AITD. As shown in Section B1, the width and intensity of the wakes increased significantly with increasing d/s value. Taking the case of $d/s = 0.122$ as an example, the wake width ($w/s = 0.464$) and the peak turbulence intensity (18.86%) increased by 28.9% and 42.8% compared with the case of $d/s = 0.078$ in this section, respectively. With the transport inside the AITD, the wakes moved downstream in a clockwise direction (as viewed in the flow direction), as shown by the red and black straight arrow lines in Figure 8, because of the tangential velocity due to the rotation of the sweeping rod. Meanwhile, they were also diffusing continuously, as shown by their increasing width and decreasing peak turbulence intensity in Sections B2-B6 of Figure 8. In comparison, the high turbulence intensity of the wake when d/s was large often meant faster energy exchange with the surrounding fluid, which made its diffusion speed and dissipation rate greater than the cases with a small d/s . Compared with the case of $d/s = 0.078$, the wake width was increased by 36.4% and the reduction of peak turbulence intensity was increased by 2.5% in Section B6 of Figure 8 when $d/s = 0.122$. When $d/s \geq 0.10$, the adjacent swept wakes in the AITD diffused to contact each other at a certain position upstream of Section B5, the interaction between wakes occurred, and the dissipation of their turbulence intensity was further enhanced. This behavior was another reason for the increasing dissipation rate of the wake peak turbulence intensity in the case of a large d/s .

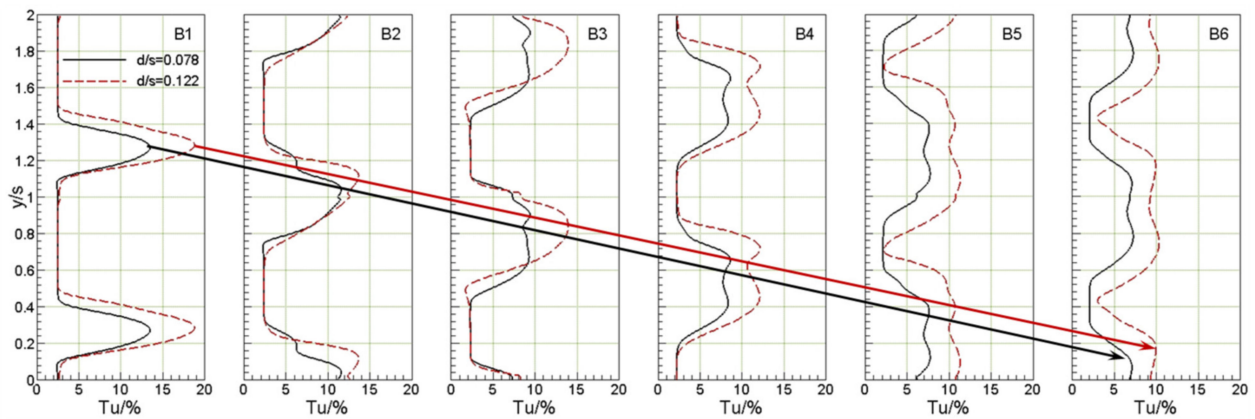


Figure 8. Circumferential distribution of turbulence intensity at the midspan of different passages inside the AITD.

Figure 9 shows the distribution of the time-averaged static pressure coefficient on the hub and shroud of the AITD for different d/s values. The sweeping wake, which blocked the effective flow area of the AITD as a low-energy fluid mass, not only led to a decrease in total pressure but also caused an increase in velocity (constant flow) by blocking the flow area, which inevitably resulted in a decrease in static pressure in the AITD. With the increase in d/s , the increasing width and intensity of the sweeping wakes further enhanced their blockage effect, resulting in a greater reduction in the static pressure coefficient. As shown in Figure 9, the static pressure coefficients on the AITD shroud and hub decreased with increasing d/s in all cases, which supported the above inference. However, the different surfaces in the AITD had different responses to the wake blocking effect: (1) At the first bend of the AITD ($x/C_x = 0 \sim 1.8$), the static pressure coefficient on the hub decreased more than that of the shroud with increasing d/s , which reduced the radial pressure gradient from the hub to the shroud. The differential C_{p_s} was 0.62, 0.61 and 0.57 at $x/C_x = 0.4$ when d/s was 0.078, 0.10 and 0.122, respectively. (2) In contrast, at the second bend of the AITD ($x/C_x = 2.0 \sim 3.0$), the static pressure coefficient on the shroud decreased more than that of the hub with increasing d/s , which reduced the radial pressure gradient from the shroud to the hub. The differential C_{p_s} was 0.84, 0.84 and 0.83 at $x/C_x = 2.8$ when the d/s values were 0.078, 0.10 and 0.122, respectively. Under the different sweeping wake conditions, the change in the radial pressure gradient in the AITD would affect the development of internal secondary flow and the vortex migration and interaction process, which will be analyzed in detail below.

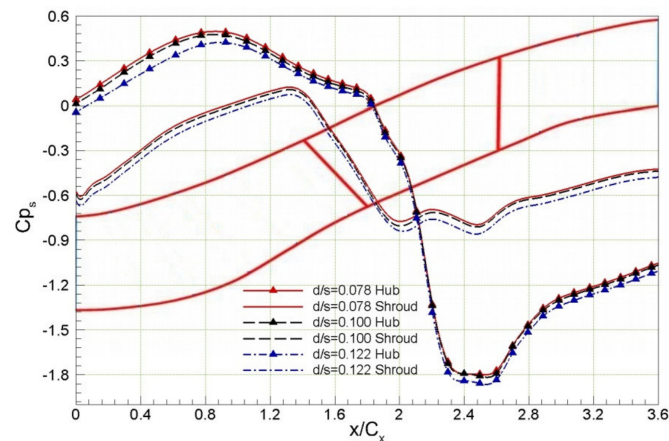


Figure 9. Time-averaged wall static pressure coefficient on the hub and shroud of the AITD.

Figure 10 shows the time-averaged streamwise vorticity contour at different streamwise sections of the AITD under the different sweeping wake conditions. Comparing the wake shapes of different sections shows that the inclination of the wake increased continuously with its diffusion in the AITD. This increase occurred because the tangential velocity at the hub and shroud did not decrease proportionally with the rise of the AITD's passage, where it decreased more at the shroud than at the hub. This tangential velocity difference also led to the circumferential stretching of the wake vortices, especially in the middle and lower regions of the AITD passage, as shown by the significantly stretched vortices (marked as "Str V") in Sections B3–B5 in Figure 10. This stretching effect was conducive to promoting the mixing and dissipation of the wake vortices, resulting in the streamwise vorticity in the corresponding regions of Sections B3–B5 in Figure 10 being significantly smaller than that in its upper half region. Meanwhile, the stretching shape and dissipation rate of the wake vortices in this region were not consistent in the cases with different d/s , which indicated that these processes were also affected by the factors related to the wake intensity. Based on the analysis conclusion of Figure 9, the AITD passage between Sections B1 and B6 was always subject to a radial pressure gradient from the hub to the shroud, which could drive the low momentum fluid from the hub to the shroud along the wake. In the lower half region of the AITD passage, this radial secondary flow drove the wake vortices to move upward, coupling with the abovementioned clockwise circumferential stretching effect, resulting in the wake vortices showing an obvious stretching phenomenon, as shown by "Str V" in Sections B3–B5 in Figure 10. This radial pressure gradient in the AITD passage decreased with increasing d/s , which suggested that the radial pressure gradient was larger and the radial secondary flow was more significant under the condition of a small d/s (e.g., $d/s = 0.078$). Therefore, compared with the condition of a large d/s (e.g., $d/s = 0.122$), the wake vortex shown by "Str V" in Figure 10 was longer, and its dissipation was also faster under the corresponding condition of a small d/s (e.g., $d/s = 0.078$). In Figure 10, the wake had no obvious vortex core in Section B5 when $d/s = 0.078$, while a relatively clear vortex core remained in this section when $d/s = 0.122$. The wake vortices in the upper half region moved upward and gradually converged because of the radial upward secondary flow, as shown by 'Con V' in Figure 10. This phenomenon was even conducive to accelerating the dissipation of wake vortices, especially in the case of a small d/s : (1) When $d/s = 0.078$, the wake vortices (as shown by 'Con V') had gathered together in Section B2, began to squeeze and merge in Section B3, and were almost exhausted in Section B5; (2) in the case of $d/s = 0.122$, the wake vortices did not converge until Section B3, the squeezing and merging occurred in Section B4, and an obvious vortex structure remained in the upper region of Section B5. For a large d/s , the decrease in the radial pressure gradient weakened the radial secondary flow and delayed the dissipation process of the wake vortices, resulting in an obvious wake vortex structure at the inlet of the LPT nozzle (Section B6), which provided an opportunity to use the sweeping wake of HPT to suppress the flow separation on the suction surface of LPT-GV.

Figure 11 shows the radial distribution of the pitchwise mass-averaged total pressure coefficient and its contour in Section B6. For a small d/s , the strong radial secondary flow led to the accumulation of low-energy fluid masses (such as wake vortices) near the shroud. Taking the condition of $d/s = 0.078$ as an example, a large range of low total pressure coefficient regions were near the shroud ($h/H > 0.7$) in the total pressure contour, and the pitchwise mass-averaged Cp_0 in the corresponding region was also significantly lower than that in other regions. As d/s increased to 0.1, the accumulation of low-energy fluid in the upper region ($h/H > 0.7$) decreased with the radial pressure gradient, and the wake dissipation did not increase much, so the pitchwise mass-averaged Cp_0 from $h/H = 0.7\sim 0.9$ in this case was greater than that of $d/s = 0.078$. When d/s was large (i.e., $d/s > 0.10$), the radial and circumferential distribution range of the low momentum region was significantly larger, and the pitchwise mass-averaged Cp_0 was also lower than that in the cases of a small d/s because of the strong dissipation of wake vortices. On the other hand, because of the weakening radial transport process of wake vortices when the d/s

was large, the low-energy fluid in the AITD passage gathering toward the shroud was not as obvious as in the cases of a small d/s but was almost evenly distributed in the radial range of $h/H = 0.2 \sim 1.0$. However, the transport of the radial secondary flow still existed, some low-energy fluids accumulated in the upper region ($h/H > 0.6$), and the pitchwise mass-averaged C_{p0} also decreased in this region compared with the other regions in these cases.

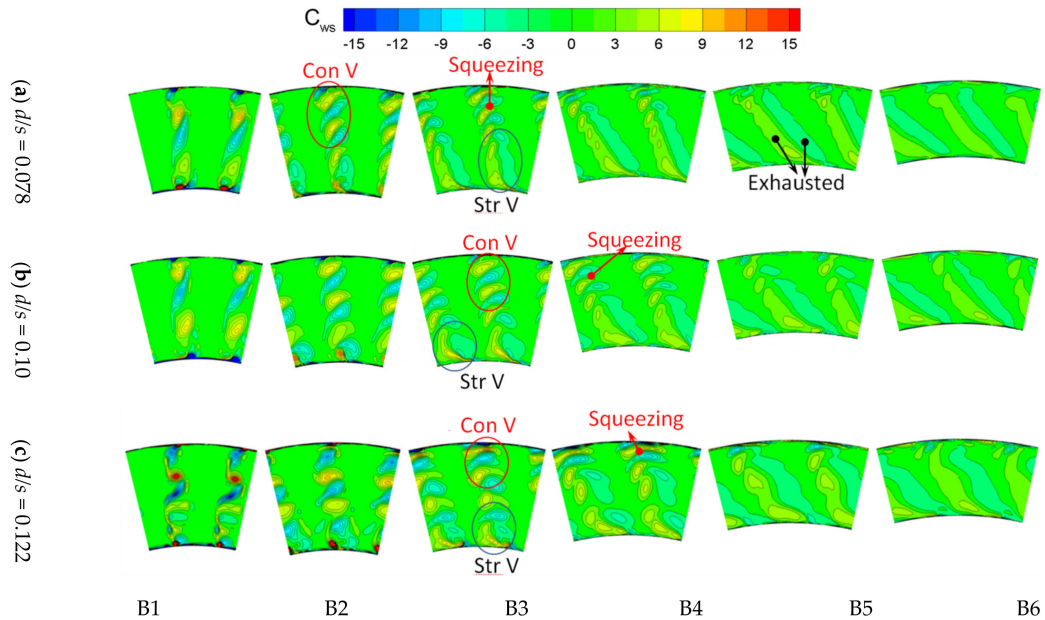


Figure 10. Time-averaged streamwise vorticity contour in different sections of the AITD.

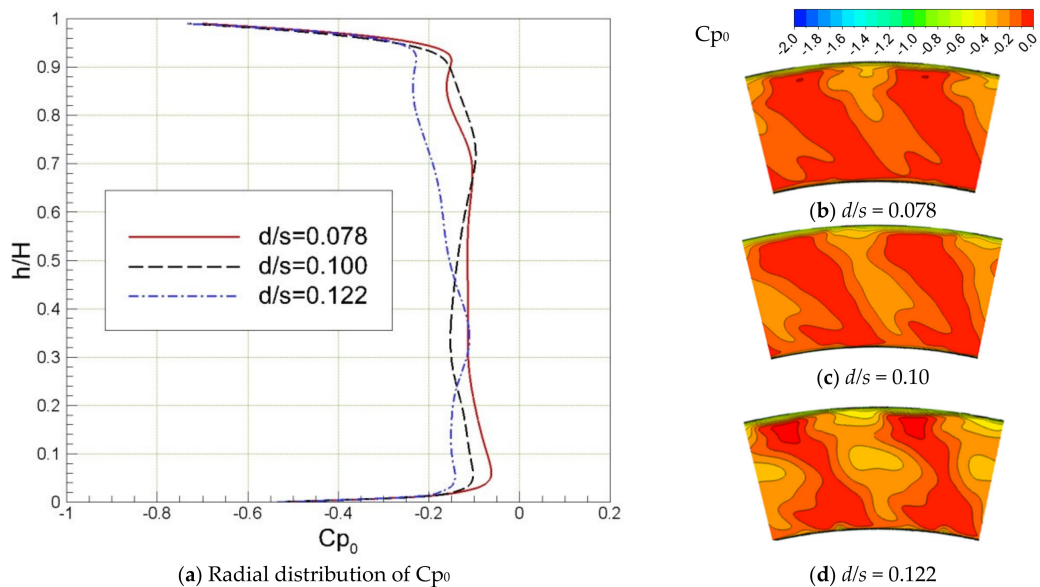


Figure 11. Distribution of the pitchwise mass-averaged total pressure coefficient and its contour in Section B6.

3.2. Effect of Wake on the Integrated LPT-GV

Based on the above analysis conclusions about the transport mechanism of sweeping wakes with different d/s values and their influence on the internal flow of the AITD, the effect of the remaining wake on the flow characteristics of the integrated LPT-GV, especially the boundary layer separation, viscosity loss and vortex structure in blade passages, is described in detail below.

Figure 12 shows the distribution of the time-averaged static pressure coefficient on the integrated LPT-GV in the AITD under different sweeping wake conditions. A pressure plateau appeared on the C_{p_s} curve of the suction surface in all cases, and the area of the plateau decreased with increasing d/s . This result meant that the residual wakes still could not completely suppress the flow separation on the suction surface, but the stronger wake in the case of a larger d/s had a better suppressing effect on the separation bubble. The reduction in separation bubbles increased the effective flow area of the LPT-GV passage to a certain extent, which improved the static pressure coefficient of the LPT-GV. As the mass flow rate was constant, the wake blockage effect increased the velocity in the LPT-GV passages, resulting in a decrease in the static pressure coefficient. In the case of $d/s = 0.10$, the static pressure coefficients at the three sections were almost the same as those when $d/s = 0.078$ because the flow passage blockage caused by the enhanced wake in this case could offset its effect of increasing the flow area by suppressing separation. When $d/s = 0.122$, the static pressure coefficient was significantly lower than that of the other two cases, as shown in Figure 12, which indicated that the reduction in the flow area caused by the blockage effect of the strong wake was significantly greater than the increase in the flow area caused by its inhibition of the flow separation bubble in this case. Moreover, in this case, the decrease in the static pressure coefficient on the suction surface was larger than that on the pressure surface, which indicated that the pressure gradient from the pressure surface to the suction surface increased, especially in the section of a 15% span.

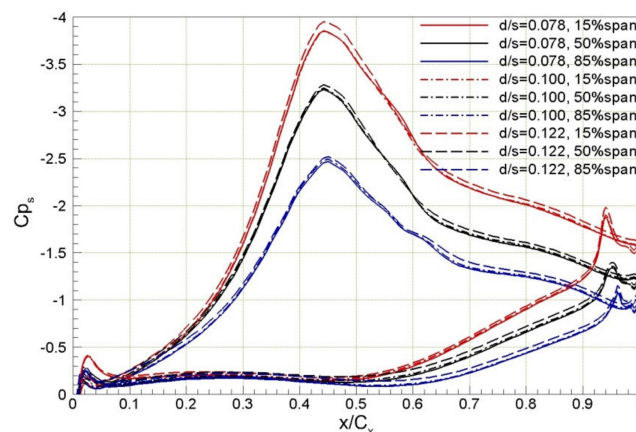


Figure 12. Distribution of the time-averaged static pressure coefficient on the integrated LPT-GV in the AITD.

Figure 13 shows the limiting streamline and static pressure coefficient contour on the suction surface of the integrated LPT-GV when $d/s = 0.078$, 0.10 and 0.122. A passage vortex, marked by 'PV@C' in Figure 13, appeared on the upper part of the LPT-GV suction surface in all cases, and this vortex disappeared on the suction surface as it broke away from the wall downstream (discussed in detail below). Comparing the cases with different d/s values, the area of these passage vortices decreased with increasing d/s . The area of PV@C was significantly smaller when $d/s = 0.122$ compared to the other two cases, as shown in the figure where $t = 0.2T$. This difference arose because when d/s was large due to the reduced radial pressure gradient from the hub to the shroud, the accumulation of low-energy fluid near the shroud and the horseshoe vortex at the leading edge of the LPT-GV were weakened, and the passage vortex developed by the horseshoe vortices entraining low-energy fluids was bound to be reduced. At the midspan of the LPT-GV, the residual wake could well inhibit the boundary layer separation on the suction surface in all cases, and the stronger wake could inhibit the flow separation earlier and more persistently in the cases with larger d/s . For example, the midspan flow separation was completely suppressed from $t = 0.15T$ to $t = 0.75T$ when $d/s = 0.122$, while the separation bubble was not completely inhibited until $t = 0.30T$ and recovered at $t = 0.54T$ when $d/s = 0.078$. In the

lower region of the LPT-GV, a passage vortex (marked by PV@H in Figure 13) was near the hub even during the sweeping wake cycle in all cases. Because of the radial secondary flow from the AITD shroud to the hub, this passage vortex hardly expanded in the radial direction downstream. For the same reason, the decrease in the radial pressure gradient also led to the weakening of this passage vortex, which could also be proven because the passage vortex at the lower part of the LPT-GV was smallest when $d/s = 0.122$.

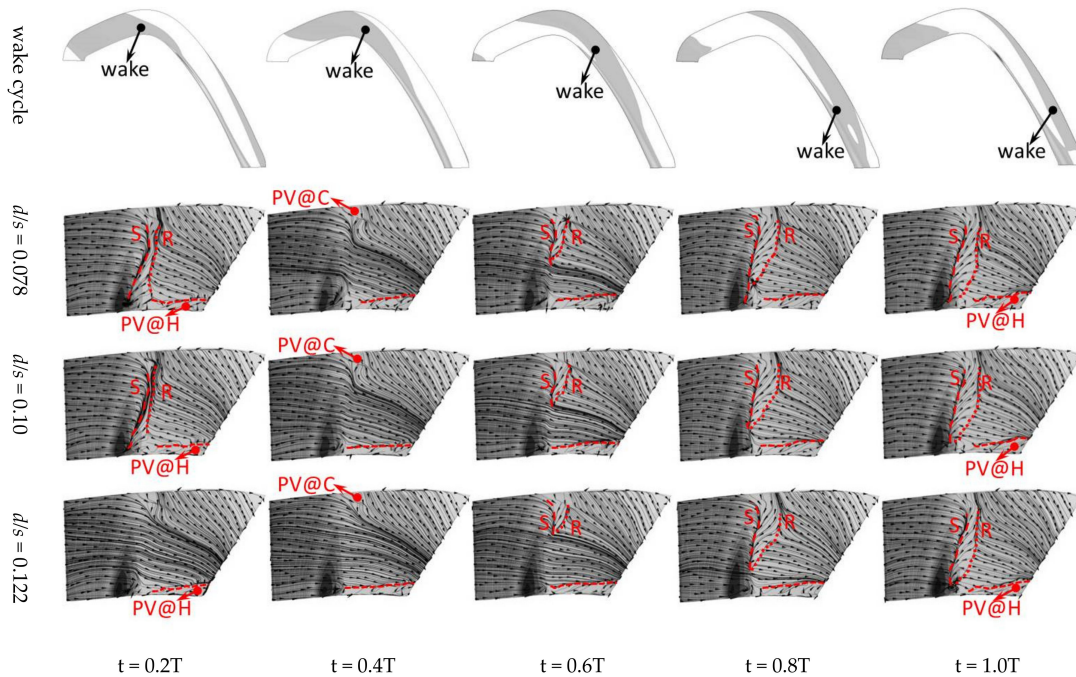


Figure 13. Limited streamline and static pressure coefficient contour on the suction surface of the integrated LPT-GV.

As the midspan was the most significant region of the integrated LPT-GV affected by the sweeping wakes, its boundary layer was analyzed in detail below to reveal the influence of unsteady wakes. Figure 14 shows the space-time diagram of the boundary layer shape factor (H_{12}) and loss coefficient (ξ) at the midspan of the integrated LPT-GV when $d/s = 0.078, 0.10$ and 0.122 . The leading edge/centerline/trailing edge of the wake (Lines A, L and B, respectively), the boundary of the calm zone (Line C) and the transition position (Line T) induced by the wake are also shown in Figure 14 according to the empirical judgment criterion. The shape factor was the ratio of the displacement thickness of the boundary layer to its momentum thickness: the lower the shape factor was, the fuller the velocity profile of the boundary layer; in contrast, the velocity profile was concave, which often indicated that flow separation might have occurred in the boundary layer. Based on the conclusions verified by the experiment, when the shape factor was greater than 3.5, boundary layer separation of the LPT blade often occurred [34]. In all cases, the shape factor was relatively small ($H_{12} < 3.5$) in the wake sweeping cycle, as shown by the blue area between Line A and Line C in the space-time diagram of the shape factor, indicating that the sweeping wake could well inhibit the flow separation at the midspan of LPT-GV. With the increase in d/s , the width and turbulence intensity of the sweeping wake increased, as did its influence range. When d/s increased from 0.078 to 0.122, the area between Line A and Line C, representing the influence range of the sweeping wake, increased from $0.24T$ to $0.5T$ at $x = 0.55C_x$ in the upper row of Figure 14. This prolongation of wake inhibition apparently helped to reduce losses due to flow separation on LPT-GVs. In the gap of the sweeping wake, the shape factor increased and exceeded 3.5 in all cases, as shown in the area circled by the isoline of $H_{12} = 3.5$ in the upper row of Figure 14, which meant that the boundary layer separation bubble recovered again. With increasing d/s , the separation

bubble zone delineated by the isoline of $H_{12} = 3.5$ not only significantly reduced the time range (due to the increased influence range of the wake) but also continuously reduced its axial range (representing the size of the separation bubble) and peak value (representing the thickness of the separation bubble). This result was obtained for the following reason: although in the wake gap, the mixing and dissipation of the wake upstream enhanced the turbulence intensity of the main flow at the inlet of LPT-GV to a certain extent, with increasing d/s , the further enhanced turbulence intensity was conducive to promoting energy exchange between the boundary layer and the main flow and induced the boundary layer transition earlier, resulting in better suppression of the size and thickness of the boundary layer separation bubble.

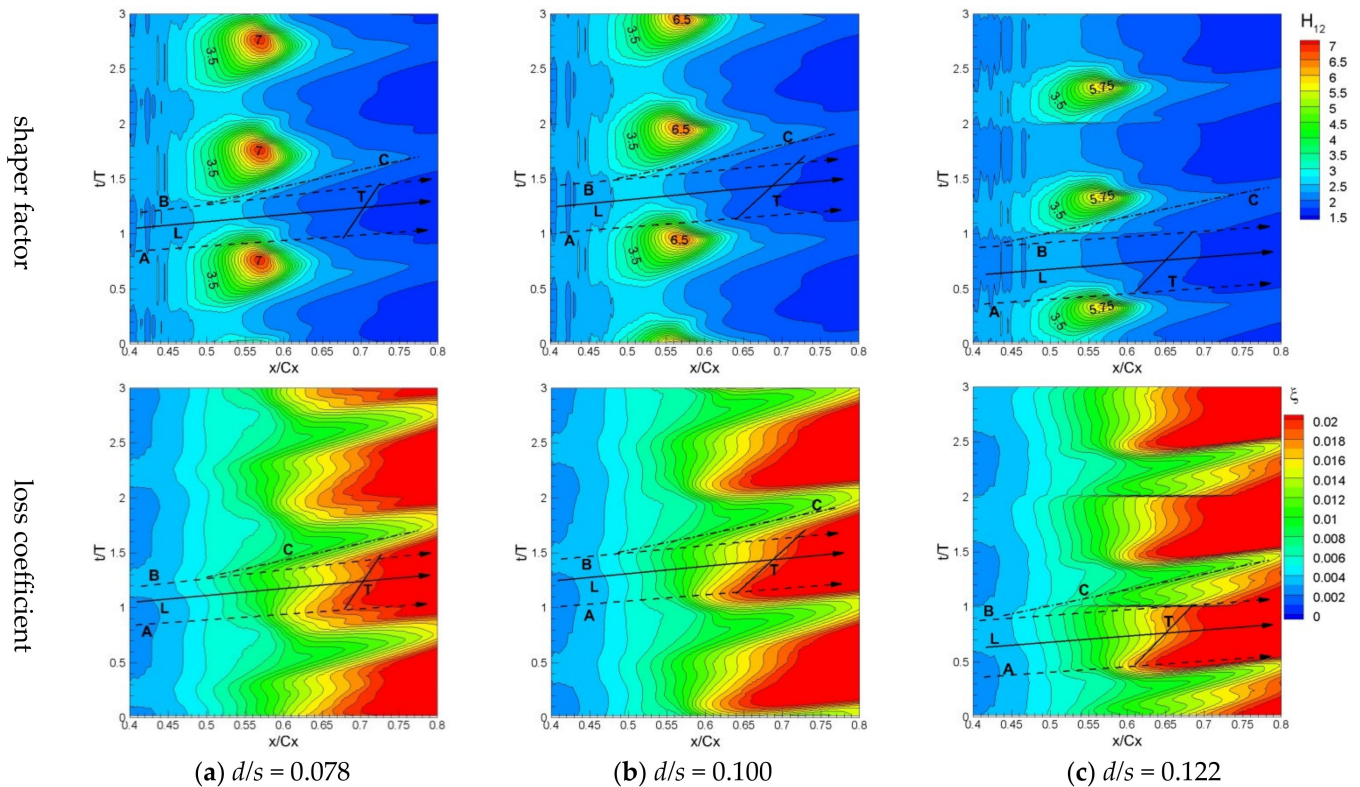


Figure 14. Space-time diagram of the boundary layer shape factor and loss coefficient when $d/s = 0.078, 0.10$ and 0.122 .

The loss coefficient of the boundary layer represented the viscosity loss in the boundary layer. Because of the wake dissipation and the interaction between the roll-up vortex induced by wake vortices [34] and the boundary layer, the boundary layer loss coefficient was high in the wake sweeping cycle, especially after the wake-induced transition (Line T), as shown in the green and red color blocks between Line A and Line B in the lower row of Figure 14. Comparing the different cases, with increasing d/s , the enhanced wake promoted the early transition of the boundary layer, and the wet area of the turbulent boundary layer with a high boundary layer loss coefficient (the red block behind Line T) expanded in the lower row of Figure 14. For example, when $d/s = 0.122$, the front point of the boundary layer transition was $0.065C_x$ earlier than that of the $d/s = 0.078$ case. Overall, wakes could not only reduce the losses by suppressing separation bubbles but also increase viscosity loss due to the increasing wet area of the turbulent boundary layer, which indicated that a comprehensive balance of these two factors was the key to the effective use of sweeping wakes.

Before discussing the influence of the upstream wake on vortices, its origin and distribution in the integrated LPT-GV passage must be briefly introduced. Figure 15 shows the vortex distribution in the LPT-GV passage when $d/s = 0.078$. The upstream boundary

layer rolled up at the leading edge of the LPT-GV and moved downstream along the blade, resulting in a horseshoe vortex in the upper and lower regions. This vortex with a small scale was generally confined in the boundary layer of the hub or shroud. In the upper-end region of LPT-GV, the pressure surface branch of the horseshoe vortex moved toward the suction surface under the circumferential pressure gradient, continuously entrained the low momentum fluid in the end region, and then developed into a passage vortex. After reaching the suction surface, because of the radial secondary flow from the shroud to the hub at the rear of the LPT-GV, this passage vortex moved down radially and finally split into two vortices: one of the vortices moved down radially, as shown by PV3 in Figure 15; the other vortex continued to move downstream along the blade root and then split into two vortices again by the pull of radial secondary flow when it grew large enough, as shown by PV1 and PV2 in Figure 15. Because of the weakening radial pressure gradient, this passage vortex only split once when $d/s \geq 0.10$, resulting in PV1 and PV3 vortices in Figure 15. A small-scale corner vortex was near the shroud. In the lower end region, there was also a passage vortex based on the same formation mechanism mentioned above. Under the radial pressure gradient at the rear of the LPT-GV, this passage vortex did not grow upward radially but concentrated around the blade root. There were also two small-scale vortices—the counter vortex and the corner vortex—as shown in Figure 15. For the interaction and mixing process between different vortices, the readers can refer to [32,39,41].

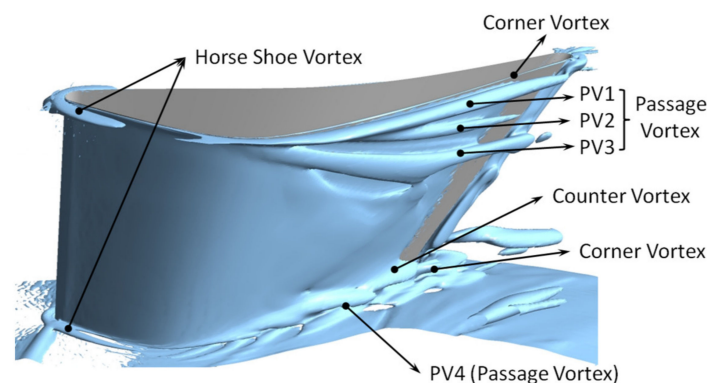


Figure 15. Vortices in the integrated LPT-GV passage when $d/s = 0.078$.

Figure 16 shows the total pressure coefficient contour of five streamwise sections in the LPT-GV channel when $d/s = 0.078, 0.10$ and 0.122 . When $d/s \leq 0.10$, due to the abovementioned radial upward secondary flow, the low-energy fluid was enriched near the shroud (as shown in Figure 11b,c), resulting in a thick boundary layer on the shroud, as shown by ‘TBL’ in Sections C1 and C2 in Figure 16. In contrast, when $d/s > 0.10$, because the radial pressure gradient was weakened by the stronger sweeping wake, the boundary layer of the shroud (as shown by ‘BL’ in Sections C1 and C2 in Figure 16) was thinner than that of the case with a small d/s , but the total pressure coefficient near the shroud ($h/H = 0.7\sim 1.0$) still decreased because of the dissipation of strong wakes. In the tip region of the LPT-GV, the passage vortices (marked by ‘PV’ in Section C3 of Figure 16) entrained a large amount of low momentum fluid in the boundary layer of the end wall, resulting in the boundary layer of Section C3 being thinner than that of Section C2 in all cases. Comparing these passage vortices in different cases, the PV area in Section C3 decreased with increasing d/s . This result was obtained because the boundary layer thickness of the end wall and radial pressure gradient, which are two important factors for the formation of passage vortices, decreased with increasing d/s . Similarly, the strength and range of PV3 split from the passage vortices downstream of Section C3 and decreased with increasing d/s . Unlike PV3, the influence range of the residual passage vortex increased with d/s , as shown by the yellow contour marked by ‘PV1’ in Figure 15. This result was obtained mainly because many low momentum fluids were in the region around the shroud, which could be entrained by PV1, due to the dissipation of the residual wake vortices (as shown in

Section B6 of Figure 10) when d/s was large. This result also showed that the influence of wake on the vortices in the LPT-GV's tip region had an obvious two-sidedness: (1) it could weaken the passage vortices by reducing the radial pressure gradient; (2) the low-momentum fluid could enhance the passage vortices in the LPT-GVs' tip region due to its own strong dissipation.

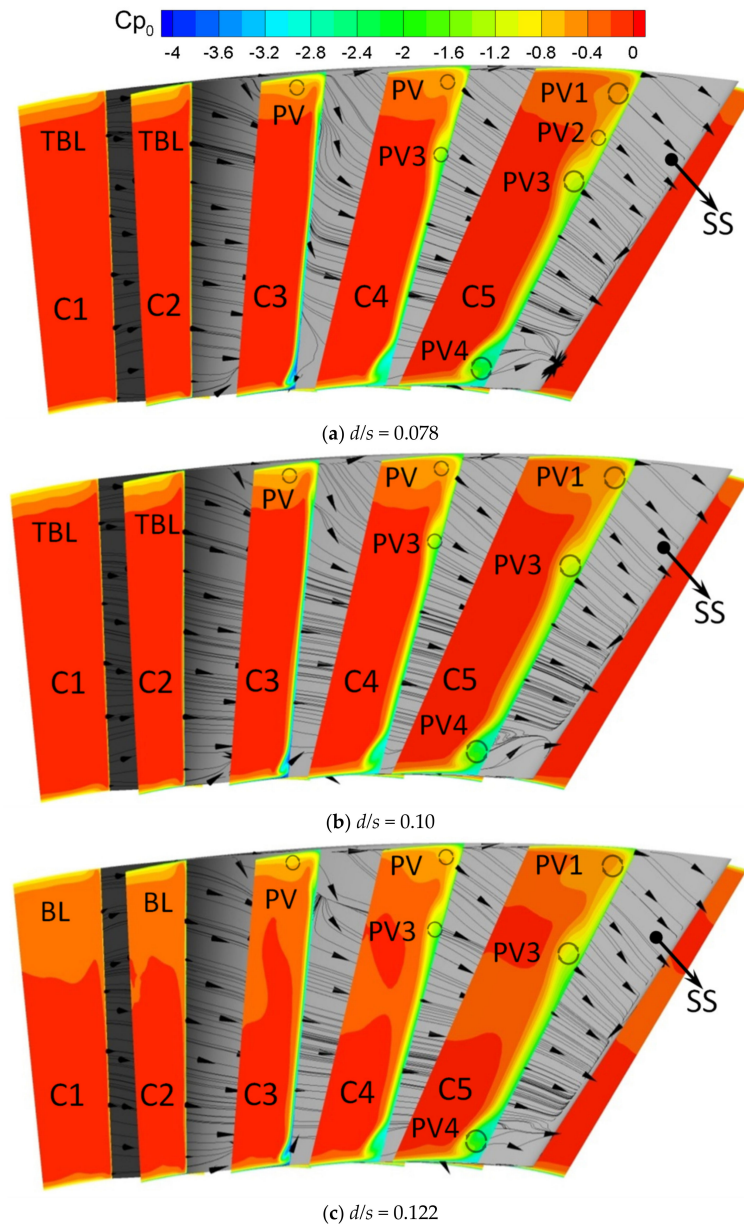


Figure 16. Total pressure coefficient contour of the integrated LPT-GV passages.

In the midspan of the LPT-GV, the boundary layer of the suction surface continuously thickened from Section C3 to Section C5 in Figure 16 because of the inverse pressure gradient (as shown in Figure 16). Moreover, with increasing d/s , the boundary layer thickness of the suction surface increased in the same axial section. This result was obtained because the wake could trigger the earlier transition of the boundary layer with increasing d/s , which increased the growth time of the turbulent boundary layer under an inverse pressure gradient. At the root of the LPT-GV with increasing d/s , the decreasing radial pressure gradient, as mentioned above, also weakens the passage vortices in this region (as shown by 'PV4' in Figure 16), which is conducive to reducing the total pressure loss in the corresponding regions.

Figure 17 shows the radial distribution of the pitchwise mass-averaged total pressure coefficient at the integrated AITD outlet. From the general trend, the total pressure coefficient decreased with increasing d/s , but the mechanism of flow loss differed between regions: (1) Near the hub ($h/H < 0.1$), the wake dissipated rapidly in all cases and was exhausted before reaching the inlet of LPT-GV, so the loss in this region was hardly affected by the sweeping wake, as shown by the coincident total pressure coefficient curves of this region in Figure 17. (2) In the middle region ($h/H = 0.2\sim 0.7$), the loss mainly came from wake dissipation and boundary layer separation. Although the sweeping wake could further inhibit the time and space range of separation bubbles when d/s was large, the aerodynamic income was still insufficient to compensate for the total pressure loss caused by the wake dissipation. Therefore, the total pressure coefficient in this region decreased with increasing d/s . (3) Near the shroud ($h/H > 0.7$), the loss mainly came from the passage vortex and the wake mixing. Based on the above conclusions, strong residual wake vortices were still in this region at the inlet of the LPT-GV, which can bring total pressure gain by suppressing the passage vortex and separation bubble, and this aerodynamic profit was significantly greater than that in the middle region, so the total pressure coefficient in this region was higher than that in the middle region. However, when d/s was large, the total pressure coefficient was still smaller than that in the case of a small d/s , which indicated that the aerodynamic benefit brought by increasing the intensity of wakes was still insufficient to offset the total pressure loss caused by its dissipation near the shroud. Given this situation, to improve the aerodynamic performance of AITD by using the sweeping wake, the authors believed that the following methods could be adopted: (1) Reduce the blade loading of the LPT-GV by increasing the number of blades, thereby suppressing the size of the passage vortex near the hub and separation bubble in the middle of the blade section, reducing the loss of the LPT-GV's middle and lower sections; then, use the HPT wakes with a small trailing-edge radius to control the separation bubble on the blades' middle section to suppress the loss of the separation bubble when reducing the loss caused by the wake dissipation. (2) Further shorten the axial distance between the HPT and LPT-GV so that the wakes of the HPT can reach the LPT-GV before being completely dissipated to make full use of the HPT wake with a small trailing-edge radius to suppress flow separation and passage vortices, reduce the wake dissipation loss and improve the aerodynamic gain brought by the flow control using HPT wakes.

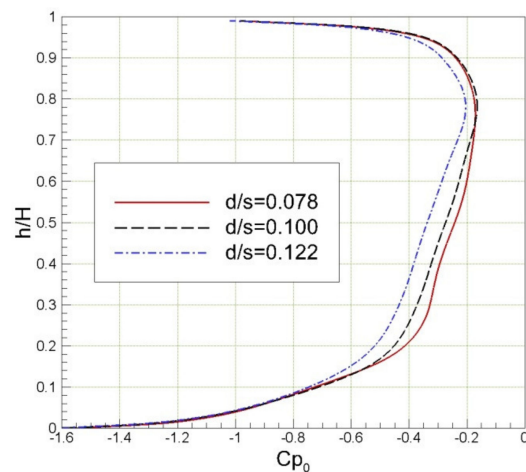


Figure 17. Radial distribution of the pitchwise averaged total pressure coefficient at the outlet of the AITD.

Figure 18 shows the total pressure loss of the integrated AITD and its components in all cases. The total pressure loss of AITD increased with increasing d/s , and the loss of the integrated LPT-GV was the main loss source, accounting for more than 82.9% (@ $d/s = 0.144$). If the design condition with $d/s = 0.10$ was used as a benchmark, then reducing the d/s

value of the sweeping rod helped to decrease the total pressure loss of the integrated AITD, which indicated that the radius of the HPT trailing edge should be minimized to reduce the additional loss caused by the wake dissipation within the scope of this paper. When $d/s \leq 0.078$, the loss of the integrated LPT-GV remained basically unchanged, which indicated that the aerodynamic gain of wakes could offset their dissipation. Whether a further reduction of the d/s value can lead to the reverse overshoot of aerodynamic gain needs to be further studied. When $d/s > 0.078$, the aerodynamic gain of the sweeping wake was obviously insufficient to compensate for its dissipation, resulting in increased loss of the integrated LPT-GV with increasing d/s . For the AITD upstream of the LPT-GV, the loss mainly included the wall friction loss and the wake dissipation loss and increased with increasing d/s .

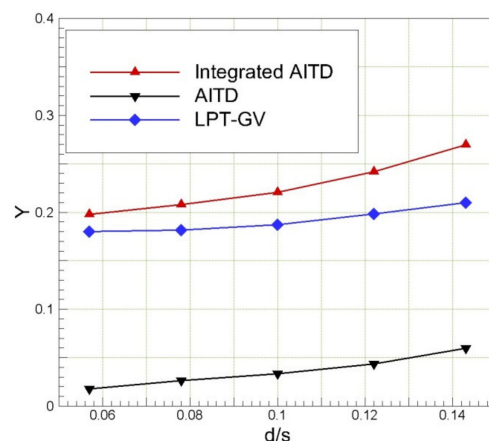


Figure 18. Total pressure loss of the integrated AITD and its components in all cases.

4. Conclusions

A detailed unsteady numerical study was carried out to investigate the effects of the HP rotor trailing-edge radius on the unsteady flow characteristics in the integrated AITD. The HP rotor wake was simulated by a sweeping rod to decouple its influence from other secondary flows. The radial pressure gradient in the integrated AITD passage decreased with increasing rod diameter (d/s), especially at its first bend. The wake in the lower part of the AITD channel was exhausted rapidly before reaching the LPT-GV inlet because of the stretching between its own circumferential motion and the radial upward secondary flow for all values of d/s , especially when d/s was small. For the upper part of the AITD channel, the wake vortices were gathered, squeezed and dissipated because of the stronger radially upward secondary flow when d/s was small. When d/s was large, these processes were delayed because of the stronger wake that reduced the radial pressure gradient, and some residual wake vortices in the upper part of the channel could reach the LPT-GV.

For the LPT-GV, the pressure gradient from the pressure surface to the suction surface was enhanced with increasing d/s , especially in the lower region of the blade passage. In the blade tip region, the passage vortices were significantly enhanced in the small d/s cases because of the enrichment of low momentum fluid and the stronger radial pressure gradient. In the blade root region, the difference between the passage vortices was small because the wake vortices had been dissipated upstream of the LPT-GV in all cases. In the midspan of the blade, the length, thickness and existence time of the separation bubble decreased with increasing d/s , resulting in a reduction in the loss of the separation bubble; however, the strong wake induced the boundary layer transition to occur earlier, increasing the wet area of the turbulent boundary, which in turn led to an increase in losses.

The flow loss in the integrated AITD was dominated by wake dissipation, passage vortices and boundary layer separation and increased with increasing d/s . In the scope of this study, as the aerodynamic gain of the wake was still not enough to compensate for its

loss increment, the authors suggested that selecting a small trailing-edge radius of HPT is conducive to improving the aerodynamic performance of the integrated AITD.

Author Contributions: Conceptualization, Z.L.; validation, H.L. and G.L.; formal analysis, J.G. and Y.Z.; writing-original draft preparation, Z.L.; writing-review and editing H.L. and G.L.; project administration, X.L.; supervision, G.L., G.X. and J.Z. All authors have read and agreed to the published version of the manuscript.

Funding: This research was funded by “the National Natural Science Foundation of China, grant number 51906242” and “the National Science and Technology Major Project, grant number J2019-II-0007-0027 and J2019-III-0020-0064”.

Conflicts of Interest: The authors declare no conflict of interest.

Nomenclature

AR: outlet-to-inlet area ratio

AITD: aggressive Interturbine transition duct

C_d : resistance coefficient of the sweeping rod

$C_{p0} = (P_0 - P_{s,ref}) / (P_{0,ref} - P_{s,ref})$: total pressure coefficient

$C_{ps} = (P_s - P_{s,ref}) / (P_{0,ref} - P_{s,ref})$: static pressure coefficient

$C_{\omega s} = (v_x \omega_x + v_y \omega_y + v_z \omega_z) \cdot H / (u_e \cdot \sqrt{v_x^2 + v_y^2 + v_z^2})$: streamwise vorticity coefficient

C_x : axial chord

d : diameter of the sweeping rod

d/s : nondimensional diameter of the sweeping rod

f : reduced frequency

f_{HPT} : passing frequency of the HPT rotor

FSTI: free stream turbulence intensity

h : height relative to hub

H : annulus height of the ITD inlet

H_{12} : shape factor

HP: high pressure

HPT: high pressure turbine

ITD: Interturbine transition duct

L : axial length of ITD

L/H : nondimensional axial length of ITD

LP: low pressure

LPT: low pressure turbine

LPT-GV: low pressure turbine-guide vane

R_{hub} : radius of hub at the ITD's inlet

R_{tip} : radius of casing at the ITD's inlet

ref : reference plane (Plane B0)

s : pitch of LPT-GV at midspan

s_b : the sweeping rod spacing at midspan

T : the time of full cycle sweeping wake

T_{II} : turbulence intensity

u_e : mass-averaged exit velocity

w : width of wake

w/s : nondimensional width of wake

Y : total pressure loss

y^+ : nondimensional thickness of the first layer grid on the wall

Z : cosecant of the relative flow angle at HPT outlet

θ : mean rise angle/momentum thickness

β_e : the exit flow angle

$\zeta = 2\theta / (s \cdot \cos(\beta_e))$: loss coefficient

Δt : the minimum physical time step

References

1. Dominy, R.G.; Kirkham, D.A. The Influence of Blade Wakes on the Performance of Inter-turbine Diffusers. *J. Turbomach.* **1996**, *118*, 347–352. [CrossRef]
2. Dominy, R.G.; Kirkham, D.A.; Smith, A.D. Flow Development through Inter-turbine Diffusers. *J. Turbomach.* **1998**, *120*, 298–304. [CrossRef]
3. Zhang, X.; Hu, S.; Benner, M.; Gostelow, P.; Vlastic, E. Experimental and Numerical Study on an Inter-turbine Duct. In Proceedings of the ASME 2010 International Mechanical Engineering Congress and Exposition, Vancouver, BC, Canada, 12–18 November 2010; Paper No.: IMECE2010-37322; pp. 679–690.
4. Miller, R.J.; Moss, R.W.; Ainsworth, R.W.; Harvey, N.W. The Development of Turbine Exit Flow in a Swan-Necked Inter-stage Diffuser. In Proceedings of the ASME Turbo Expo 2003: Power for Land, Sea, and Air, Atlanta, GA, USA, 16–19 June 2003; Paper No.: GT2003-38174; pp. 863–875.
5. Norris, G.; Dominy, R.G. Diffusion Rate Influences on Inter-Turbine Diffusers. *Proc. Inst. Mech. Eng. Part A J. Power Energy* **1997**, *211*, 235–242. [CrossRef]
6. Zhang, Y.; Hu, S.; Mahallati, A.; Zhang, X.; Vlastic, E. Effects of Area Ratio and Mean Rise Angle on the Aerodynamics of Inter-Turbine Ducts. *J. Turbomach.* **2018**, *140*, 091006. [CrossRef]
7. Axelsson, L.U.; Osso, C.A.; Cadrecha, D.; Johansson, T.G. Design, Performance Evaluation and Endwall Flow Structure Investigation of an S-shaped Intermediate Turbine Duct. In Proceedings of the ASME Turbo Expo 2007: Power for Land, Sea, and Air, Montreal, QC, Canada, 14–17 May 2007; Paper No.: GT2007-27650; pp. 693–701.
8. Axelsson, L.U.; Johansson, T.G. Experimental Investigation of the Time-Averaged Flow in an Intermediate Turbine Duct. In Proceedings of the ASME Turbo Expo 2008: Power for Land, Sea, and Air, Berlin, Germany, 9–13 June 2008; Paper No.: GT2008-50829; pp. 1313–1322.
9. Axelsson, L.U.; George, W.K. Spectral Analysis of the Flow in an Intermediate Turbine Duct. In Proceedings of the ASME Turbo Expo 2008: Power for Land, Sea, and Air, Berlin, Germany, 9–13 June 2008; Paper No.: GT2008-51340; pp. 1419–1426.
10. Göttlich, E.; Marn, A.; Pecnik, R.; Malzacher, F.; Schennach, O.; Pirker, H. The Influence of Blade Tip Gap Variation on the Flow through an Aggressive S-Shaped Intermediate Turbine Duct Downstream a Transonic Turbine Stage: Part II—Time-Resolved Results and Surface Flow. In Proceedings of the ASME Turbo Expo 2007: Power for Land, Sea, and Air, Montreal, QC, Canada, 14–17 May 2007; Paper No.: GT2007-28069; pp. 843–853.
11. Marn, A.; Göttlich, E.; Pecnik, R.; Malzacher, F.; Schennach, O.; Pirker, H. The Influence of Blade Tip Gap Variation on the Flow through an Aggressive S-Shaped Intermediate Turbine Duct Downstream a Transonic Turbine Stage: Part I—Time-Averaged Results. In Proceedings of the ASME Turbo Expo 2007: Power for Land, Sea, and Air, Montreal, QC, Canada, 14–17 May 2007; Paper No.: GT2007-27405; pp. 575–585.
12. Göttlich, E.; Heitmeir, F.; Malzacher, F.; Marn, A. Comparison between the Flow through an Aggressive and a Super-Aggressive Intermediate Turbine Duct. In Proceedings of the International Symposium on Air Breathing Engines, Montreal, QC, Canada, 7–11 September 2009. Paper No.: ISABE-2009-1259.
13. Marn, A.; Göttlich, E.; Malzacher, F.; Pirker, H. The Effect of Rotor Tip Clearance Size onto the Separated Flow through a Super-Aggressive S-Shaped Intermediate Turbine Duct Downstream of a Transonic Turbine Stage. *J. Turbomach.* **2012**, *134*, 051019. [CrossRef]
14. Dominy, R.G.; Kirkham, D.A. The Influence of Swirl on the Performance of Inter-Turbine Diffusers. *VDI Berichte.* **1995**, *1186*, 107–122.
15. Hu, S.; Zhang, Y.; Zhang, X.; Vlastic, E. Influences of Inlet Swirl Distributions on an Inter-Turbine Duct: Part I—Casing Swirl Variation. In Proceedings of the ASME Turbo Expo 2011: Power for Land, Sea, and Air, Vancouver, BC, Canada, 6–10 June 2010; Paper No.: GT2011-45554; pp. 619–630.
16. Zhang, Y.; Hu, S.; Zhang, X.; Vlastic, E. Influences of Inlet Swirl Distributions on an Inter-Turbine Duct: Part II—Hub Swirl Variation. In Proceedings of the ASME Turbo Expo 2011: Power for Land, Sea, and Air, Vancouver, BC, Canada, 6–10 June 2010; Paper No.: GT2011-45555; pp. 631–641.
17. Bailey, D.W.; Carrotte, J.F. The Influence of Inlet Swirl on the Flow within an Annular S-Shaped Duct. In Proceedings of the International Gas Turbine and Aeroengine Congress and Exhibition, Birmingham, UK, 10–13 June 1996. Paper No.: 96-GT-060.
18. Schennach, O.; Pecnik, R.; Paradiso, B.; Göttlich, E.; Marn, A.; Woisetschläger, J. The Effect of Vane Clocking on the Unsteady Flow Field in a One-and-a-Half Stage Transonic Turbine. *J. Turbomach.* **2008**, *130*, 031022. [CrossRef]
19. Norris, G.; Dominy, R.G.; Smith, A.D. Strut Influences within a Diffusing Annular S-Shaped Duct. In Proceedings of the International Gas Turbine and Aeroengine Congress and Exhibition, Stockholm, Sweden, 2–5 June 1998. Paper No.: 98-GT-425.
20. Norris, G.; Dominy, R.G.; Smith, A.D. Flow Instability within a Diffusing, Annular S-Shaped Duct. In Proceedings of the International Gas Turbine and Aeroengine Congress and Exhibition, Indianapolis, IN, USA, 7–10 June. Paper No.: 99-GT-070.
21. Miller, R.J.; Moss, R.W.; Ainsworth, R.W.; Harvey, N.W. The Effect of an Upstream Turbine on a Low-Aspect Ratio Vane. In Proceedings of the ASME Turbo Expo 2004: Power for Land, Sea, and Air, Vienna, Austria, 14–17 June 2004; Paper No.: GT2004-54017; pp. 1417–1428.
22. Walker, A.D.; Barker, A.G.; Mariah, I.; Peacock, G.L.; Northall, R. An Aggressive S-Shaped Compressor Transition Duct with Swirling Flow and Aerodynamic Lifting Struts. In Proceedings of the ASME Turbo Expo 2014: Power for Land, Sea, and Air, Düsseldorf, Germany, 16–20 June 2014. Paper No.: GT2014-25844.

23. Lengani, D.; Santner, C.; Spataro, R.; Paradiso, B.; Göttlich, E. Experimental Investigation of the Unsteady Flow Field Downstream of a Counter-Rotating Two-Spool Turbine Rig. In Proceedings of the ASME Turbo Expo 2012: Power for Land, Sea, and Air, Copenhagen, Denmark, 11–15 June 2012; Paper No.: 2545-2554; pp. 2545–2554.
24. Lengani, D.; Santner, C.; Spataro, R.; Ttlich, E.G. Analysis Tools for the Unsteady Interactions in a Counter-Rotating Two-Spool Turbine Rig. *Exp. Therm. Fluid Sci.* **2012**, *42*, 248–257. [CrossRef]
25. Marn, A.; Göttlich, E.; Cadrecha, D.; Pirker, H.P. Shorten the Intermediate Turbine Duct Length by Applying an Integrated Concept. In Proceedings of the ASME Turbo Expo 2008: Power for Land, Sea, and Air, Berlin, Germany, 9–13 June 2008; Paper No.: GT2008-50269; pp. 1041–1051.
26. Spataro, R.; Santner, C.; Lengani, D.; Göttlich, E. On the Flow Evolution through a LP Turbine with Wide-Chord Vanes in an S-Shaped Channel. In Proceedings of the ASME Turbo Expo 2012: Turbine Technical Conference and Exposition, Copenhagen, Denmark, 11–15 June 2012; Paper No.: GT2012-68178; pp. 1011–1020.
27. Bader, P.; Sanz, W.; Spataro, R.; Göttlich, E. Flow Evolution through a Turning Mid Turbine Frame with Embedded Design. In Proceedings of the ASME Turbo Expo 2014: Power for Land, Sea, and Air, Düsseldorf, Germany, 16–20 June 2014. Paper No.: GT2014-25009.
28. Faustmann, C.; Zerobin, S.; Spataro, R.; Marn, A.; Heitmeir, F.; Göttlich, E. On the Acoustics of a Turning Mid Turbine Frame with Embedded Design in a Two-Stage Test-Turbine. *Proc. Inst. Mech. Eng. Part A J. Power Energy* **2015**, *229*, 529–538. [CrossRef]
29. Du, Q.; Wang, P.; Gong, J.; Zhu, J. Design Performance Evaluation and Vortex Structure Investigation of Different S-Shaped Intermediate Turbine Ducts. *Sci. China Technol. Sci.* **2012**, *55*, 3510–3520. [CrossRef]
30. Wang, P. *Design and Flow Mechanism of Integrated Aggressive Intermediate Turbine Duct*; Institute of Engineering Thermophysics, C.A.S.: Beijing, China, 2014.
31. Liu, J.; Wang, P.; Du, Q.; Liu, G.; Zhu, J. Effects of Rising Angle on Upstream Blades and Intermediate Turbine Duct. *J. Therm. Sci.* **2016**, *25*, 293–301. [CrossRef]
32. Xu, Q.; Wang, P.; Du, Q.; Liu, J.; Liu, G. Effects of Axial Length and Integrated Design on the Aggressive Intermediate Turbine Duct. *Proc. IMechE Part A J. Power Energy* **2018**, *233*, 443–456. [CrossRef]
33. Liu, H.; Liu, J.; Ji, L.; Du, Q.; Liu, G.; Wang, P. Influence of Reynolds Number on the Unsteady Aerodynamics of Integrated Aggressive Intermediate Turbine Duct. *J. Therm. Sci.* **2018**, *27*, 294–303. [CrossRef]
34. Mahallati, A. Aerodynamics of a Low Pressure Turbine Airfoil Under steady and Periodically Unsteady Conditions. Ph.D. Thesis, Carleton University, Ottawa, ON, Canada, 2004.
35. Meyer, R.J. The Effect of Wakes on the Transient Pressure and Velocity Distributions in Turbomachines. *ASME J. Basic Eng.* **1958**, *80*, 1544–1552. [CrossRef]
36. Stieger, R.D. The Effects of Wakes on Separating Boundary Layers in Low Pressure Turbines. Ph.D. Thesis, Cambridge University, Cambridge, UK, 2002.
37. Zhong, S.; Kittichaikarn, C.; Hodson, H.P.; Ireland, P. A study of unsteady wake-induced boundary layer transition with thermochromic liquid crystals. *Proc. Inst. Mech. Eng. Part G J. Aerosp. Eng.* **1999**, *213*, 163–171. [CrossRef]
38. Roberts, S.K.; Yaras, M.I. Large-Eddy Simulation of Transition in a Separation Bubble. *ASME J. Fluids Eng.* **2006**, *128*, 232–238. [CrossRef]
39. Liu, H.; Liu, J.; Du, Q.; Liu, G.; Wang, P. Unsteady Flow Mechanism of the integrated Aggressive Inter-turbine Duct in Low Reynolds number condition. *Proc. Inst. Mech. Eng. Part G J. Aerosp. Eng.* **2020**, *234*, 1507–1517. [CrossRef]
40. Liu, H.; Liu, J.; Du, Q.; Liu, G.; Wang, P. Impact of Turbulence Intensity on the Unsteady Flow Characteristics of the integrated Aggressive Inter-turbine Duct. *Proc. Inst. Mech. Eng. Part A J. Power Energy* **2020**, *234*, 490–499. [CrossRef]
41. Jeon, W.; Shin, C.B. Design and Simulation of Passive Mixing in Microfluidic Systems with Geometric Variations. *Chem. Eng. J.* **2009**, *152*, 575–582. [CrossRef]

Article

Unsteady Aerodynamic Design of a Flapping Wing Combined with a Bionic Wavy Leading Edge

Xuan Bai, Hao Zhan and Baigang Mi *

School of Aeronautics, Northwestern Polytechnical University, Xi'an 710072, China

* Correspondence: mibaigang@163.com

Abstract: Based on the bionic design of the humpback whale fin, a passive flow control method is proposed to obtain greater flapping lift by applying the wavy leading edge structure to the straight symmetrical flapping wing. The leading edge of the conventional flapping wing is replaced by the wavy shape represented by regular trigonometric function to form a special passive flow control configuration imitating the leading edge of the humpback whale fin. The dynamic aerodynamic performance and flow field characteristics of straight wing and wavy leading edge flapping wing with different parameters are compared and analyzed by CFD numerical simulation. The simulation results show that the wavy leading edge structure changes the flow field of the baseline flapping wing and reduces the pressure on the upper surface of the flapping wing during the process of downward flapping, thereby increasing the pressure difference between the upper and lower surfaces of the flapping wing and increasing the lift. The sensitivity analysis of the design parameters shows that in order to obtain the maximum lift coefficient while losing the least thrust, the smaller amplitude should be selected on the premise of selecting the smaller wavelength. Among the configurations of different design parameters calculated in this paper, the optimal wavy leading edge flapping wing configuration increases the time average lift coefficient by 32.86% and decreases the time average thrust coefficient by 14.28%. Compared with the straight wing, it has better low-speed flight and can withstand greater take-off weight.

Keywords: flapping wing; wavy leading edge; flow control; bionics; computational fluid dynamics (CFD)

Citation: Bai, X.; Zhan, H.; Mi, B. Unsteady Aerodynamic Design of a Flapping Wing Combined with a Bionic Wavy Leading Edge. *Appl. Sci.* **2023**, *13*, 1519. <https://doi.org/10.3390/app13031519>

Academic Editors: Josep Maria Bergada and Gabriel Bugeđa Castellort

Received: 27 December 2022

Revised: 18 January 2023

Accepted: 19 January 2023

Published: 24 January 2023



Copyright: © 2023 by the authors. Licensee MDPI, Basel, Switzerland. This article is an open access article distributed under the terms and conditions of the Creative Commons Attribution (CC BY) license (<https://creativecommons.org/licenses/by/4.0/>).

1. Introduction

Flapping wing aircraft generates lift to overcome gravity and thrust to fly forward by imitating birds flapping and twisting wings. This flight mode has the unique characteristics such as small size, high maneuverability, good flexibility, and strong concealment. It has shown broad development prospects in military, civilian, detection, earthquake relief and other industries. Therefore, flapping wing aircraft has become an important direction and hot issue in the research and development of UAV aircraft.

Because the geometric size of the flapping wing is relatively small, the chord length is usually less than 15 cm, and it is often in the low Reynolds number range (10^4 – 10^6), the flapping wing flight principle is complex. In addition, it exhibits a highly unsteady nonlinear flow phenomenon. In order to realize the efficient and stable flight of flapping wing aircraft, it is necessary to study on its aerodynamic characteristics and influencing factors based on the biological knowledge of bird flight. The main influencing factors include the static geometric shape of the flapping wing [1,2], multi-degree of freedom flapping [3], dynamic flexible deformation [4], wing tip slit [5,6], leading/trailing edge serrations [7,8], leading edge alula [9,10], and other small-scale flow control structures. In the process of the preliminary design and flow control of the flapping wing aircraft, it is very important and effective to improve its flow field and aerodynamic performance by referring to the biological structure of nature.

In 1995, Fish et al. [11] observed the cross section of the whale fins and studied the hydrodynamic performance of the convex structure of the fin limb of the humpback whale for the first time. They pointed out that the wavy leading edge can play a role like the lifting device. Since then, the leading edge wavy configuration has been tried to apply to the study of flow control under various scenarios and conditions. Sudhakar et al. [12] took a typical UAV as the research object and pointed out that compared with the straight wing, the wavy leading edge wing can increase lift and reduce drag and the lift-drag ratio increased by 25%. In addition, by using the oil flow method and PIV technique, they found that the wavy leading edge also makes the height and length of the laminar separation bubble on the straight wing change significantly under the condition of low angle of attack ($\alpha = 6^\circ$) [13]. Wei et al. [14] studied the effect of wavy leading edge on the aerodynamic performance of swept conical SD7032 wing by experiment. The results show that the wavy leading edge can slightly improve the stall performance, and the stall angle of attack can be delayed by 2–4 degrees. However, when the angle of attack is in the range of 7–20 degrees, it makes the lift drag ratio of the original wing decrease by 0–40%. Abdelrahman et al. [15] adopted an infinite span rectangular wing with a high radian S1223 airfoil to numerically study the influence of leading edge wavys on its performance and concluded that the wavy structure can completely change the flow structure on the airfoil. The flow separation on the wing surface is limited to the trough of the wavy leading edge, which plays a role in flow control. Seyhan et al. [16] verified the feasibility of flow control of NACA0015 airfoil by wavy leading edge under low Reynolds number conditions. Gopinathan et al. [17] compared the effect of wavy leading edge structure on swept wings of two different airfoils by numerical and experimental methods, and pointed out that this method has great development potential. In addition to extensive researches on wings [12–20], as a flow control method, wavy leading edge has also been tried to apply in the design of rotor [21], hydraulic turbine cascade and steam turbine cascade [22–24], wind turbine blade [25–28], hydrofoil [29–32], etc., to improve mechanical efficiency. However, their motion mode and flow field characteristics are far different from those of flapping wings. Flapping wings have a complex flight principle and highly unsteady nonlinear flow phenomenon, which brings difficulty to flow control. Anwar et al. [33] numerically simulated the aerodynamic performance of six wavy leading edge flapping wing with different design parameters similar to insect flapping motion. The results show that the lift-to-drag ratio of the best performed wavy leading edge wing decreases by 0.34%, and the efficiency decreases by 0.35%. It concluded that the wavy leading edge wing is not better than the straight wing in insect flapping motion with azimuth rotation. However, the flapping mode of imitation bird flapping wings is different from that of insects, and the influence of wavy leading edge on its aerodynamic performance remains to be further studied. The studies on the bionic wavy leading edge are summarized as shown in Table 1.

In this paper, based on bionics, a passive flow control method is proposed to solve the problem that the average lift force of the straight symmetrical flapping wing is difficult to improve. The passive flow control method is applied to the flapping wing by applying the wavy leading edge which imitating the fin structure of the humpback whale. The aerodynamic performance parameters of the straight wing and the wavy leading edge flapping wing with different design parameters are calculated and compared, and the flow field characteristics and control mechanism are analyzed. At the same time, the sensitivity of the design parameters is analyzed, and the basis for selecting the optimal design parameters of the wavy leading edge flapping wing configuration is given. It brings new inspiration for flapping wing to obtain flapping lift and unsteady flow control under a low Reynolds number.

Table 1. Studies on flow control using bionic wavy leading edge.

Author	Object	Method	Reynolds Number	Aerodynamic Performance Change
Fish et al. [11]	NACA63	Experiment	6×10^6	The stall angle of attack is delayed by more than 5° .
Sudhakar et al. [12]	A high aspect-ratio UAV	Experiment	1.8×10^5 2.7×10^5	The lift-drag ratio is increased by up to 25%.
Sudhakar et al. [13]	NACA 4415	Experiment	1.2×10^5	The separation bubble on the upper wing surface is obviously reduced.
Wei et al. [14]	Swept conical SD7032 wing	Experiment	2.2×10^5	The stall attack angle is delayed by 2–4 degrees.
Abdelrahman et al. [15]	S1223	Simulation	1×10^5 3×10^5 1.5×10^6	No considerable difference occurs in lift and drag before the stall.
Seyhan et al. [16]	NACA 0015	Experiment	6.3×10^4	Lift coefficients have increased by at least 26.2% after stall angles.
Gopinathan et al. [17]	NACA 0015NACA 4415	Experiment/Simulation	1.83×10^5	The t/c ratio of the HW flipper is strategically reduced to 0.15.
Torró et al. [18]	NACA0021	Simulation	1.2×10^5	The lift coefficient increased by 0.064 and the drag coefficient decreased by 0.045.
Ikeda et al. [19]	Serrated single-feather wing	Experiment	5.9×10^3 9.8×10^3	The lift and lift-to-drag ratio decrease at AoAs $< 15^\circ$, and the aerodynamic performance of the two is basically the same at AoAs $> 15^\circ$.
Ramachandiran et al. [20]	NACA 0015NACA 4415	Simulation	1.83×10^5	The lift increases at the angle of attack of 11–15 degrees, and the stall angle of attack is delayed by about three degrees.
Rostamzadeh et al. [30]	NACA 0021	Simulation	1.2×10^5 1.5×10^6	The lift loss is delayed at 18–25° angle of attack.
Anwar et al. [33]	insect-like flapping wing	Simulation	400	The lift-drag ratio is reduced by 0.34%.

2. Aerodynamic Characteristics Analysis of Baseline Flapping Wing

2.1. Flapping Wing Motion Model

The flapping wing motion can be decomposed into two basic motion forms: flapping and pitching, as shown in Figure 1. The cross-sections of bird's wing like thin and cambered airfoil. NACA0014 airfoil has been experimented [34] and numerically simulated [34,35] as a flapping wing. Therefore, the flapping wing model adopted in this paper is a rectangular straight wing with a finite span and the wing section of NACA0014 airfoil. The chord length of the wing is c , the span length is L and aspect ratio is $AR = \frac{L}{c}$. The set flapping wing motion law is expressed as Equation (1) [35], where, f is the flapping frequency, $\psi(t)$ represents the flapping motion, ψ_1 is the amplitude of the flapping motion, $\alpha(t)$ represents the pitching motion, α_0 is the pre-installation angle of the wing, α_1 is the amplitude of the pitching motion, ϕ is the phase difference, and the center of the pitching motion is

the quarter chord length of each section of the wing. Figure 2 shows the time history plot corresponding to Equation (1).

$$\begin{cases} \psi(t) = \psi_1 \cos(2\pi ft) \\ \alpha(t) = \alpha_0 + \alpha_1 \cos(2\pi ft + \phi) \end{cases} \quad (1)$$

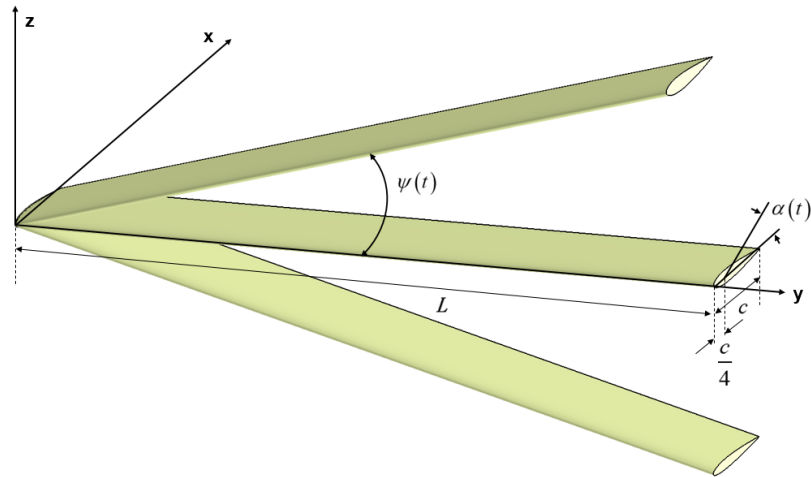


Figure 1. Motion of flapping wing.

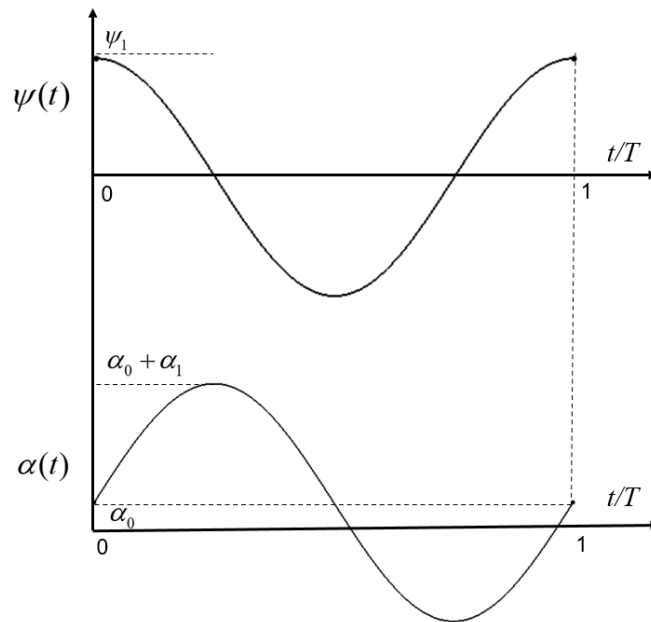


Figure 2. The time history plot corresponding to Equation (1).

According to the flight speed and flapping frequency of small birds such as pigeons, the approaching velocity U_∞ is 15 m/s, the flapping frequency f is 8 Hz, the chord length $c = 0.12\text{m}$, the aspect ratio $AR = 8$, the Reynolds number is $Re = \frac{\rho U_\infty c}{\mu} = 1.2 \times 10^5$, the reduced frequency is $k = \frac{\pi f c}{U_\infty} = 0.2$. The specific values of each parameter are shown in Table 2.

Table 2. Relevant parameters of flapping wing.

Parameter	Value	Parameter	Value
Reynolds number Re	1.2×10^5	Plunging amplitude ψ_1 ($^\circ$)	15
Wing chord length c (m)	0.12	Plunging motion equation ($^\circ$)	$\psi(t) = 15 \cos(16\pi t)$
Wing aspect ratio AR	8	Pitching amplitude α_1 ($^\circ$)	15
Approaching velocity U_∞ (m/s)	15	Setting angle of wing α_0 ($^\circ$)	0
Mach number Ma	0.0435	Pitching axis location (m)	0.25c
Flapping frequency f (Hz)	8	Phase difference ϕ ($^\circ$)	90
Reduced frequency k	0.2	Pitching motion equation ($^\circ$)	$\alpha(t) = 15 \cos(16\pi t + 90)$

2.2. Calculation Method and Verification

Flapping wing has flight characteristics of low speed and low Reynolds number. The numerical calculation in this paper is based on the three-dimensional unsteady Reynolds-averaged N-S Equation, which based on the finite volume method. The second-order up-wind scheme is used in the convection direction, the central difference is used in the diffusion term, and the Coupled algorithm is used to solve [36].

The two-Equation shear stress ($k - \omega$ SST) turbulence model [37] modified by the low Reynolds number is used for calculation. The turbulence model simulates the transition process with the damping function in the low Reynolds number eddy viscosity model, which has wide applicability. The $k - \omega$ SST turbulence model Equation can be expressed as the following Equation (2):

$$\begin{aligned} \mu_t &= \frac{\rho a_1 k}{\max(a_1 \omega; \Omega F_2)} \\ \frac{\partial(\rho k)}{\partial t} + u_i \frac{\partial(\rho k)}{\partial x_i} &= P_k - \beta_k \rho k \omega + \frac{\partial}{\partial x_i} \left[\left(\mu_l + \frac{\mu_t}{\sigma_k} \right) \frac{\partial k}{\partial x_i} \right] \\ \frac{\partial(\rho \omega)}{\partial t} + u_i \frac{\partial(\rho \omega)}{\partial x_i} &= C_\omega P_\omega - \beta_\omega \rho \omega^2 + \frac{\partial}{\partial x_i} \left[\left(\mu_l + \frac{\mu_t}{\sigma_\omega} \right) \frac{\partial \omega}{\partial x_i} \right] + 2\rho(1 - F_1) \frac{1}{\sigma_{\omega 2}} \frac{1}{\omega} \frac{\partial k}{\partial x_i} \frac{\partial \omega}{\partial x_i} \end{aligned} \quad (2)$$

The low Reynolds number-corrected $k - \omega$ SST turbulence model constructs the mode coefficient α^* in the eddy viscosity coefficient $\mu_t = \alpha^* \rho \kappa / \omega$ of the $k - \omega$ Equation as Equation (3) [38], where $Re_t = \rho \kappa / \mu \omega$ represents the turbulent Reynolds number:

$$\alpha^* = \alpha_\infty^* \left[\frac{\alpha_0^* + \frac{Re_t}{R_k}}{1 + \frac{Re_t}{R_k}} \right] \quad (3)$$

In order to verify the reliability of the numerical simulation, the rectangular straight wing of NACA0014 airfoil with aspect ratio of $AR = 8$ is selected. The mode of motion is sinusoidal oscillation, as shown in Equation (4). $z(t)$ is the wing displacement in the vertical direction at time t , amplitude $h = 0.4c$, reduction frequency $k = 0.2$, and Reynolds number $Re = 1 \times 10^6$ [34].

$$z(t) = h \cos(kt) \quad (4)$$

The boundary conditions of the calculation model are referred to [34]. Since the overset grid method is used in the subsequent calculation, the surrounding and far field of the wing are divided into two parts during grid division. Figures 3 and 4 show the comparison of the average lift coefficient and the average thrust coefficient of the flapping wing in one period calculated by using the overset grid method, and the results calculated by Jones [34]. The two have good consistency, indicating that the numerical simulation method used in this paper is reliable.

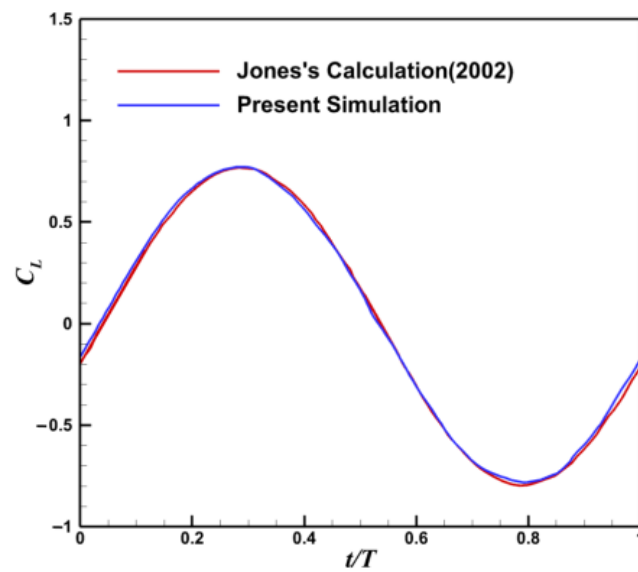


Figure 3. Comparison of average lift coefficient.

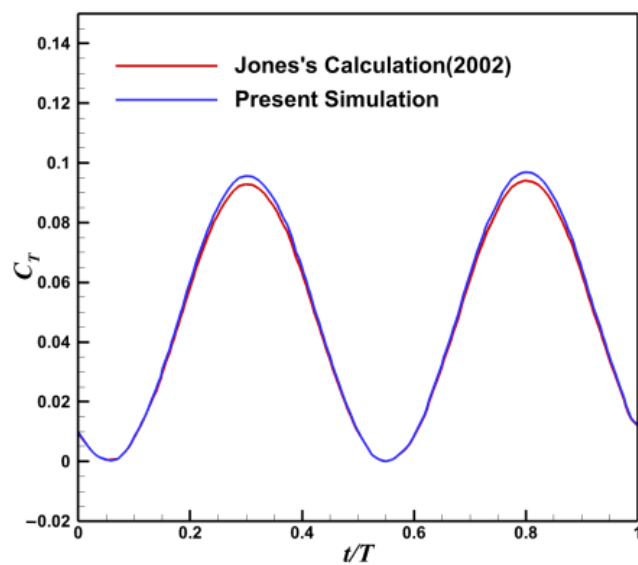


Figure 4. Comparison of average thrust coefficient.

2.3. Grid and Time Step Independence Verification

Overset grid method is used in this paper, where the component grid is fluid domain grid including flapping wing. The boundary layer is set on the surface of the flapping wing to ensure $y^+ < 1$. The background grid is a cylindrical area with a radius of $25c$ and a height of $10c$, and it is locally refined to ensure that the mesh size at the junction of the background grid and the component grid is close. The component and background grid are divided by polyhedral unstructured grids. The computational domain grids and boundary conditions are shown in Figure 5. And Figure 6 shows the y^+ contours of baseline case.

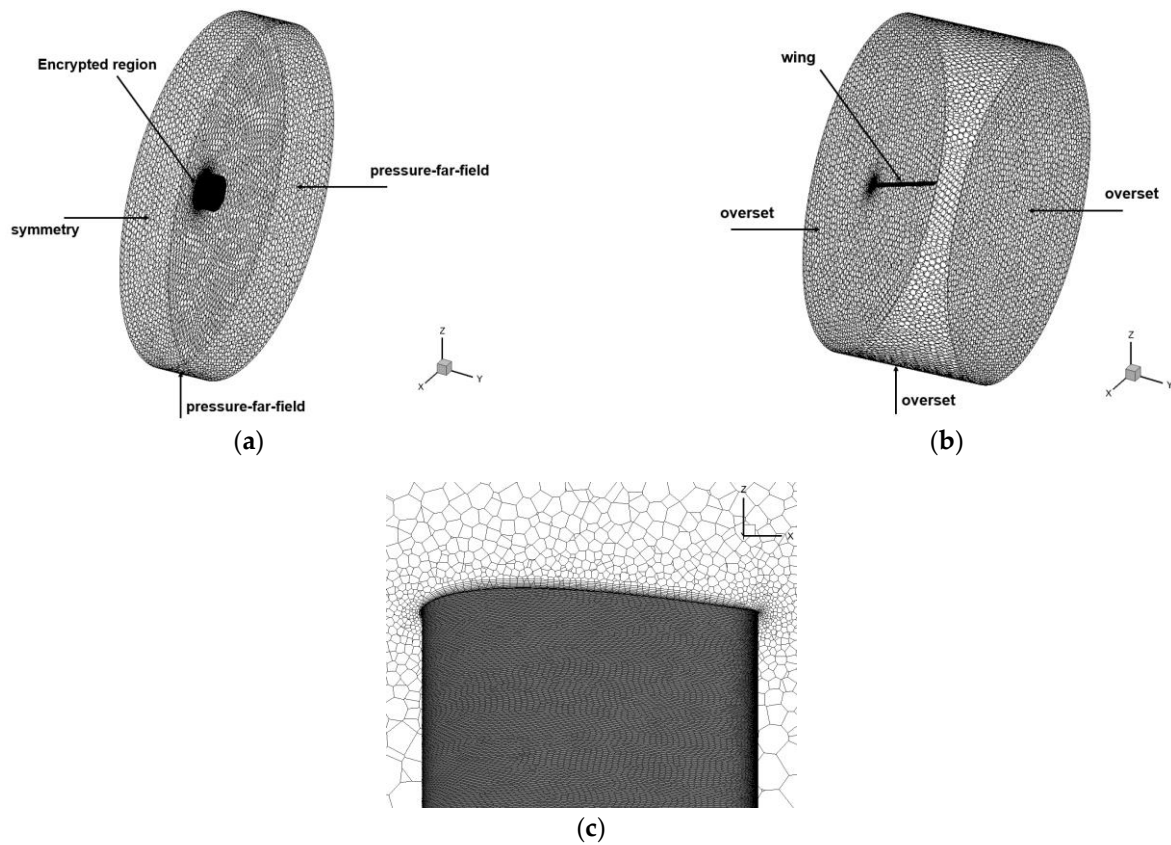


Figure 5. Grid and boundary conditions. (a) Background grid; (b) Component grid; (c) Boundary layer and surface mesh.

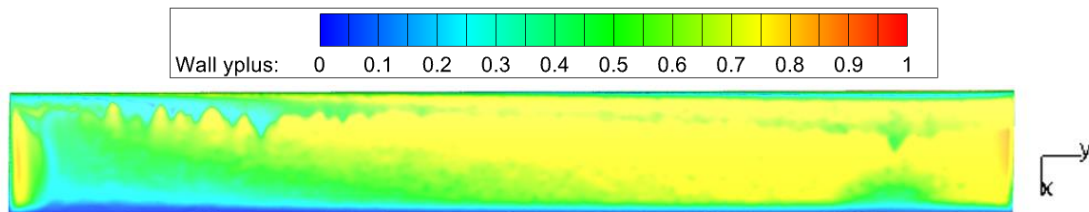


Figure 6. The y^+ contours of baseline case.

In order to ensure the accuracy of numerical calculation and save computational cost, the independence of computational mesh and time step is verified by the straight flapping wing model. The fifth flapping cycle is selected for comparison, and the calculation results are stable. The lift and trust coefficient time history of the fifth and sixth cycles is compared in Figure 7. Firstly, three groups of overset grids with different number of grids are selected as shown in Table 3 to calculate. The calculation results are shown in Figure 8. As can be seen, the grid solution results of Case2 and Case3 tend to coincide, which can be considered that the grid has reached the grid independence requirements. Therefore, the grid division scheme of Case2 is selected for subsequent calculation. Secondly, to verify the independence of the time step, three different time steps for calculation are taken; the unit is s, and the result is shown in Figure 9. When the time step is 0.0025 s and 0.001 s, the relative error between the time average lift coefficient, and the time average trust coefficient is less than 2%, which meets the requirement of independence. Therefore, in the subsequent calculation, the time step is set to 0.0025 s.

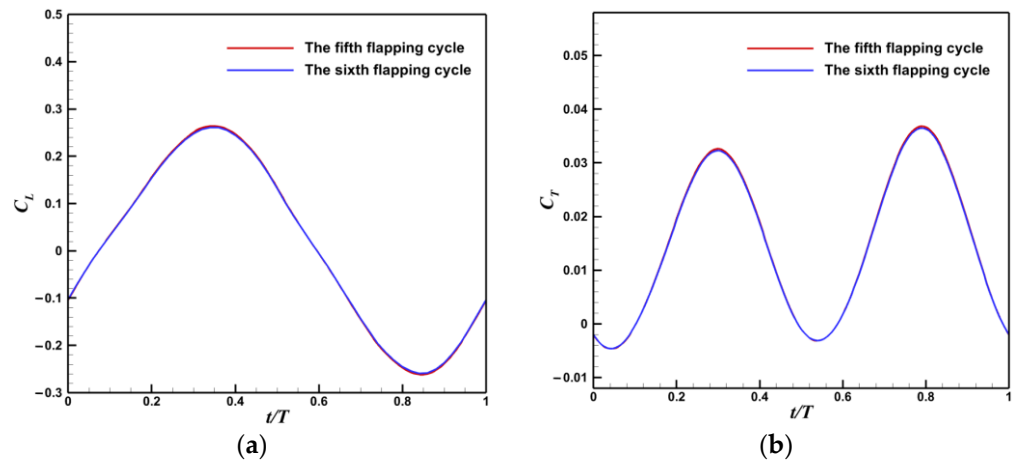


Figure 7. The comparison of time history of lift and thrust coefficient. (a) Lift coefficient; (b) Thrust coefficient.

Table 3. Grid independence verification.

Case	Number of Background Grid (w)	Number of Component Grids (w)	Total Number of Grids (w)	Total Faces (w)	Total Nodes (w)
Case1	70	562	632	3612	2565
Case2	135	706	841	4554	3150
Case3	289	836	1125	6908	4816

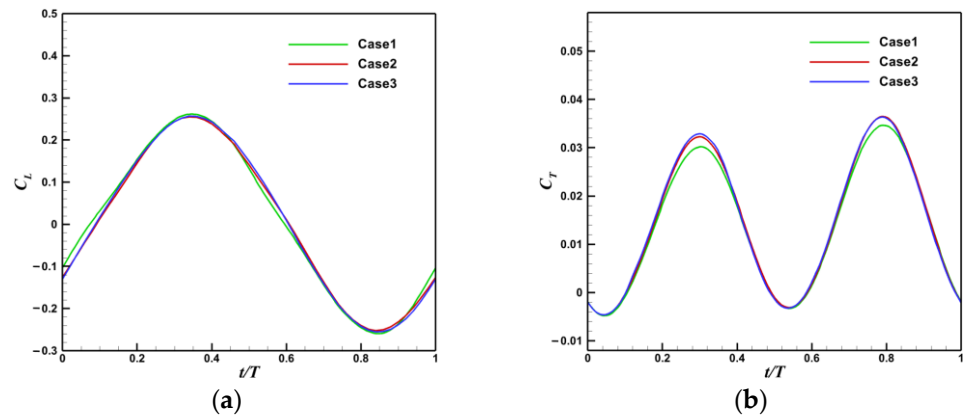


Figure 8. Grid independence verification. (a) Lift coefficient; (b) Thrust coefficient.

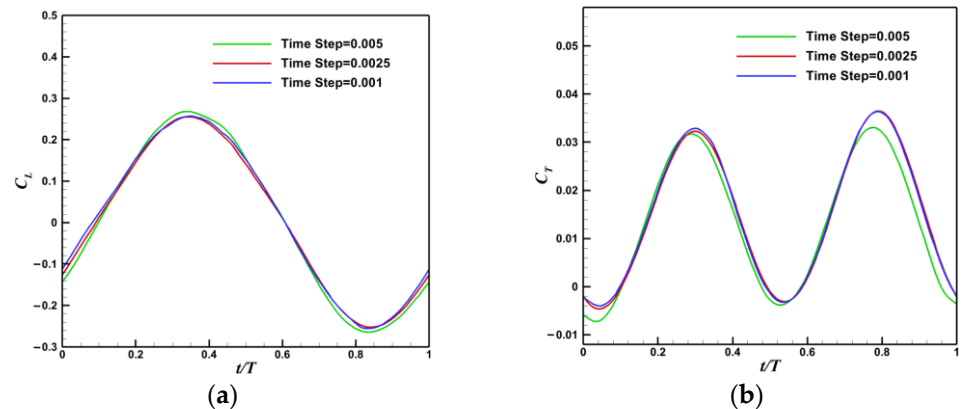


Figure 9. Time step independence verification. (a) Lift coefficient; (b) Thrust coefficient.

2.4. Flow Field Structure Characteristics of Baseline Flapping Wing

The baseline flapping wing used in this paper is a straight symmetrical flapping wing. As shown in Figure 9, it produces positive lift during the downstroke, and negative lift during the upstroke. Many studies have shown that for this type of flapping wing, the flapping frequency increases can increase the peak value of positive and negative lift and increase the thrust, but the average lift in the cycle cannot increase much. The time-averaged lift coefficient is small and difficult to improve, and therefore, the takeoff weight of aircraft with straight symmetrical flapping wing is generally small, and the flight performance is hard to improve [39,40].

The flapping wing flutters downward from the highest position ($t/T = 0$), forming the leading edge vortex at the leading edge of the upper surface and the wing tip vortex at the wing tip. When the flapping wing flaps down to the horizontal position ($t/T = 0.25$), the vortex intensity of leading edge vortex and tip vortex reaches the maximum, as shown in Figure 10; the left side is the wing tip direction. The inner part of the red circle is the vortex. As the flapping continues downward, the flapping wing begins to decelerate, the leading edge vortex and the wing tip vortex begin to diffuse, the intensity is weakened. The asymmetry of the up and down flapping process and the strong leading edge vortex attached to the upper surface during the down flapping process are the important mechanisms of lift generation.

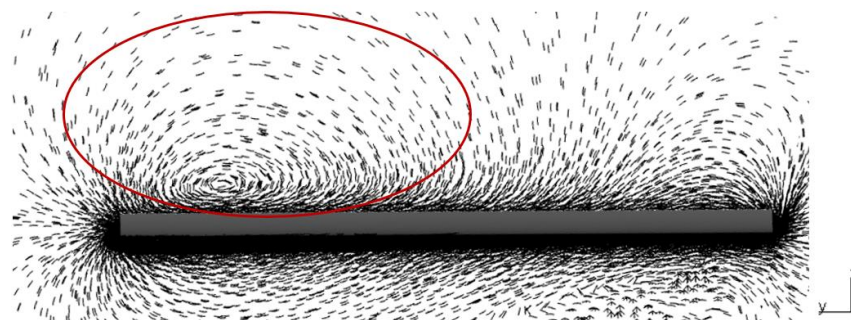


Figure 10. Velocity vector diagram of 1% chordwise section at $t/T = 0.25$.

3. Design of Wavy Leading Edge Flapping Wing

3.1. Flow Control Mechanism of Wavy Leading Edge

Figure 11 shows that the leading edge of the flippers of the humpback whale has special nodular structures. These wavy bulges can maintain lift at a high angle of attack and provide higher maneuverability during the predation process [11].

Many scholars have studied and analyzed the flow control mechanism of wavy leading edge structure on the wing or other blades. The numerical results of Abdelrahman et al. [15] show that the wavy leading edge changes the flow field, and the flow separation on the upper surface of the wing is suppressed at the wavy leading edge, which has the effect of delaying stall. Torró et al. [18] found that the unsteady aerodynamic force of the airfoil at the periodic vortex shedding frequency is reduced by the wavy leading edge through the large eddy simulation method. In the study of hydrofoil, Rostamzadeh et al. [30] pointed out that the effect of wavy leading edge structure on the flow field is similar to the principle of vortex generator. By generating shedding vortex, the pressure difference between the upper and lower surfaces of the wing is increased to achieve the effect of increasing lift and reducing drag. The longitudinal vortex also causes the downwash velocity at the peak position of the leading edge of the wing, which changes the flow state of the fluid. Under the condition of low angle of attack, flow separation will also occur at the leading edge of the wavy shape, and the vortex structure presents the “bi-periodic” state [13,31]. The bi-periodic state means that when the fluid flows through the wavy leading edge, a pair of backflows will be formed at the trough, as shown in Figure 12. Therefore, under the influence of unsteady effect and vortex generated by wavy leading edge, even if the

flapping wing does not exceed the stall angle of attack, its flow field characteristics will change.



Figure 11. Flipper’s front structure of humpback whale [41].

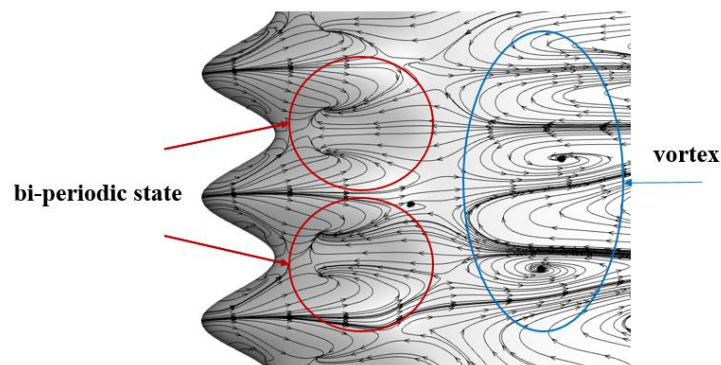


Figure 12. Upper surface limit streamline of wavy leading edge wing.

3.2. Characteristic Parameters of Wavy Leading Edge

Based on the above analysis, the aerodynamic performance of the wavy leading edge flapping wing with NACA0014 as the base section in the unsteady flapping state is studied. The structure of the wavy leading edge wing is shown in Figure 13. The sinusoidal wavy is defined by the two parameters of amplitude A and wavelength W and varies along the wing wingspan according to Equation (5). In addition, x is the spanwise length from any section to the wing root. The average chord length and projection area of the wavy leading edge flapping wing are the same as those of the reference flapping wing.

$$Y(x) = \frac{A}{2} \sin\left(\frac{2\pi}{W}x\right) \tag{5}$$

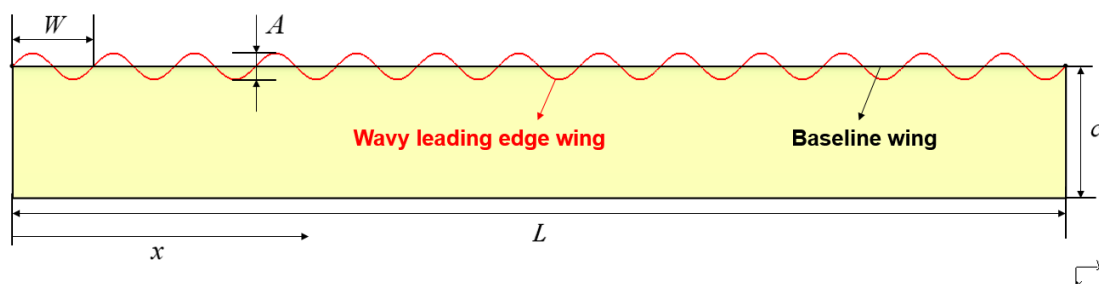


Figure 13. Wavy leading edge wing.

A sinusoidal wave is generated by five sections along the spanwise direction, as shown in Figure 14a. The airfoil data for each section are defined by Equation (6), and the airfoil at the middle is the same as the airfoil of the baseline wing.

$$\begin{cases} x_{wavy} = \begin{cases} \frac{x_{baseline}}{x_{max}} [x_{max} + (Y(x) - c)] - [Y(x) - c] & x_{wavy} < x_{max} \\ x_{baseline} & x_{wavy} \geq x_{max} \end{cases} \\ z_{wavy} = z_{baseline} \end{cases} \quad (6)$$

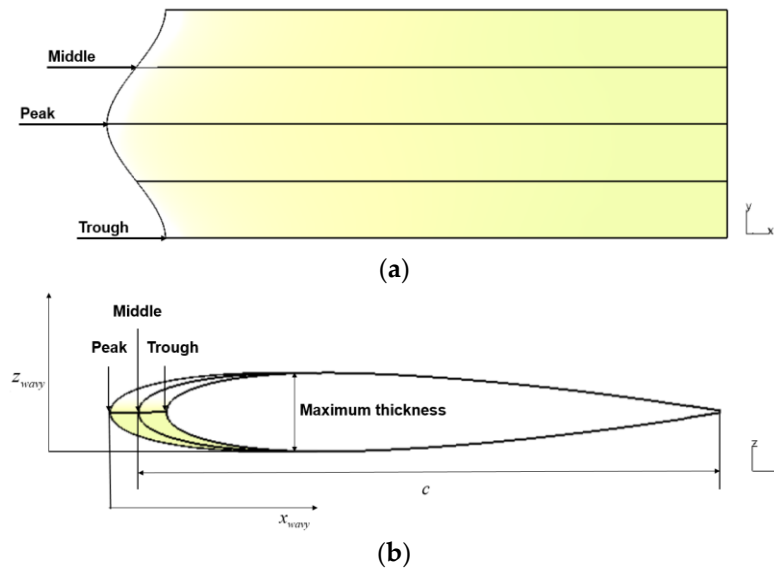


Figure 14. Construction method of wavy leading edge wing. (a) Wing spanwise section of wavy leading edge wing; (b) Airfoil of wavy leading edge wing.

The $x_{baseline}$ and x_{wavy} represent the abscissas of the baseline wing and the wavy leading edge wing, respectively, and x_{max} represents the abscissa at the maximum thickness of the baseline wing. The $z_{baseline}$ and z_{wavy} represent the ordinates of the baseline wing and the wavy leading edge wing, respectively. When generating spanwise section airfoil data, only the geometry from the leading edge to the maximum thickness is changed, while the geometry from the maximum thickness to the trailing edge is kept unchanged. The baseline airfoil is stretched or compressed according to the chord length at different spanwise positions, as shown in Figure 14b.

For purpose of further clarifying the influence of design parameters on the aerodynamic performance and flow control effect of the bionic wavy leading edge flapping wing, dimensionless processing was carried out for amplitude and wavelength, as shown in Equation (7). Twelve different flapping wing configurations composed of three amplitudes and four wavelengths are selected for calculation and comparison. The specific parameters of the configurations are shown in Table 4, and the values of these parameters are within the range of protuberances found on the humpback whale’s pectoral fin in nature [42]. Figure 15 shows the schematic diagrams of all twelve configurations. The comparison of different design parameters of the wavy leading edge wing configurations can be seen through Figure 15.

$$\begin{cases} \bar{A} = \frac{A}{c} \\ \bar{W} = \frac{W}{L} \end{cases} \quad (7)$$

Table 4. Wavy leading edge flapping wing configuration.

Configuration	\bar{A}	\bar{W}	Configuration	\bar{A}	\bar{W}	Configuration	\bar{A}	\bar{W}
1-1	0.05	0.1	2-1	0.1	0.1	3-1	0.2	0.1
1-2	0.05	0.05	2-2	0.1	0.05	3-2	0.2	0.05
1-3	0.05	0.02	2-3	0.1	0.02	3-3	0.2	0.02
1-4	0.05	0.01	2-4	0.1	0.01	3-4	0.2	0.01

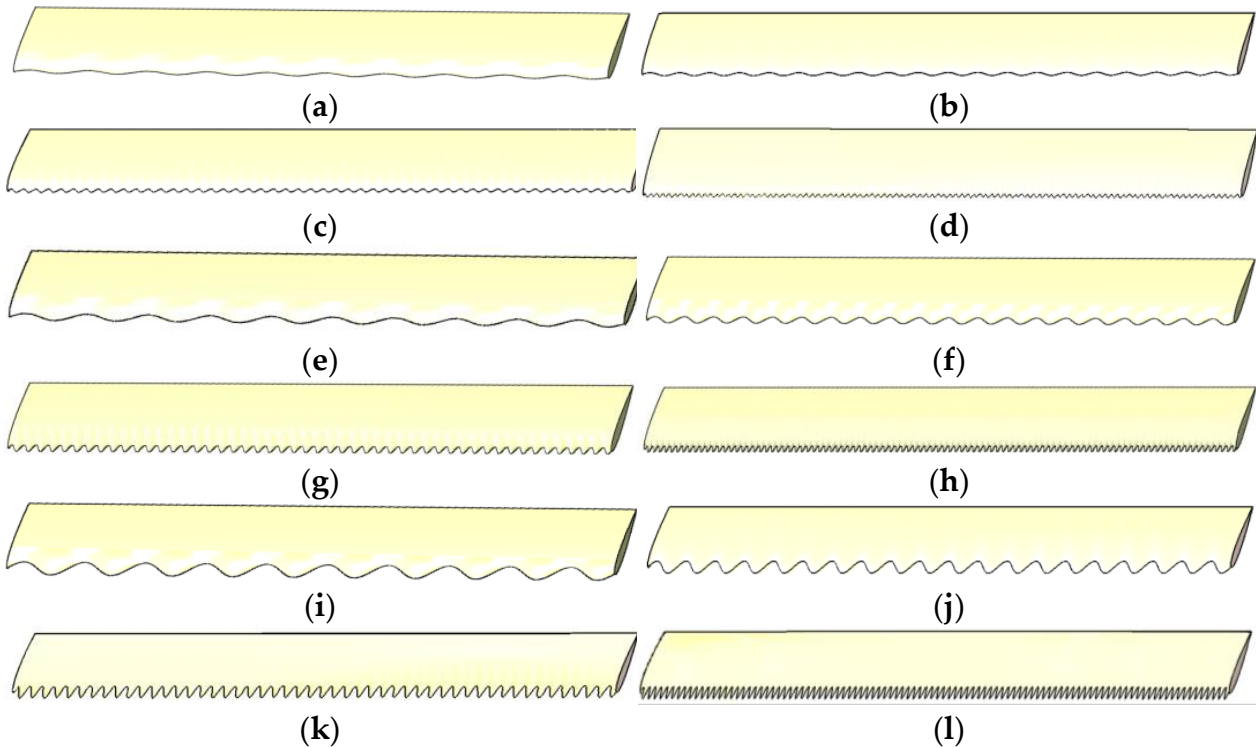


Figure 15. Wavy leading edge flapping wing configuration. (a) Configuration 1-1; (b) Configuration 1-2; (c) Configuration 1-3; (d) Configuration 1-4; (e) Configuration 2-1; (f) Configuration 2-4; (g) Configuration 1-3; (h) Configuration 2-4; (i) Configuration 3-1; (j) Configuration 3-2; (k) Configuration 3-3; (l) Configuration 3-4.

3.3. Grid Independence Verification

Due to the difference between the wavy leading edge flapping wing and the baseline wing in the model, Configuration 1-1 ($\bar{A} = 0.05$, $\bar{W} = 0.1$) and Configuration 3-4 ($\bar{A} = 0.2$, $\bar{W} = 0.01$) of the wavy leading edge are selected for grid independence verification to ensure the accuracy of the numerical simulation. The same background grid as the straight wing is used, and the number of grids is 1.35 million. The partitioning strategy of the component grid is also the same as the three cases in Section 2.3. Figures 16 and 17, respectively, show the calculation results of the lift coefficient and thrust coefficient of Configuration 1-1 and Configuration 3-4 in one period with time. It can be seen that the Case2 can meet the grid independence requirements.

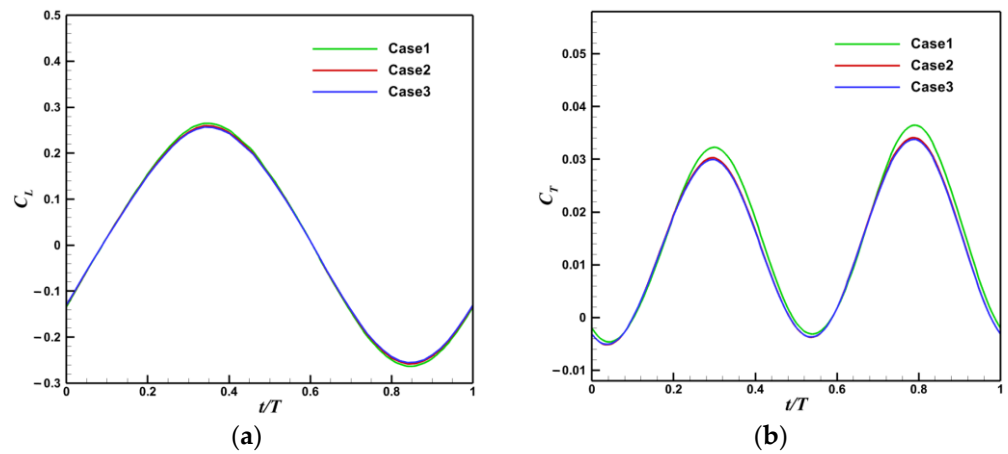


Figure 16. The time history of lift and thrust coefficient (Configuration 11). (a) Lift coefficient; (b) Thrust coefficient.

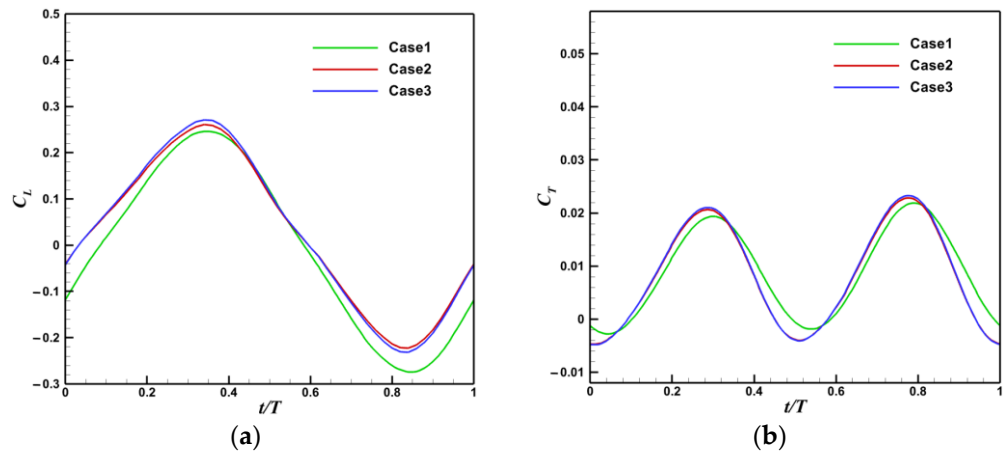


Figure 17. The time history of lift and thrust coefficient (Configuration 3-4). (a) Lift coefficient; (b) Thrust coefficient.

4. Numerical Results

In order to compare the influence of wavy leading edge on the aerodynamic performance of flapping wing more directly, the calculation results are divided into two parts according to different wavelengths and different amplitudes. The aerodynamic performance of flapping wing is measured by time averaged lift coefficient $\overline{C_L}$ and time averaged thrust coefficient $\overline{C_T}$ in a flapping cycle. The two parameters are defined as Equation (8).

$$\begin{cases} \overline{C_L} = \frac{1}{T} \int_0^T C_L(t) dt \\ \overline{C_T} = \frac{1}{T} \int_0^T -C_D(t) dt = \frac{1}{T} \int_0^T C_T(t) dt \end{cases} \quad (8)$$

4.1. Effects of Different Wavelengths on Aerodynamic Performance of Flapping Wing

Figures 18 and 19, respectively, show the time history comparison of lift coefficient and thrust coefficient of straight flapping wing and wavy leading edge flapping wing with different wavelengths in one flapping cycle. It can be seen that the lift coefficient of the flapping wing with the wavy leading edge is higher than that of the straight wing in the process of downward flapping ($t/T = 0-0.5$) and in the last quarter stage of upward flapping ($t/T = 0.875-1$). In the first three quarters of upward flapping ($t/T = 0.5-0.875$), the lift coefficient is similar to or slightly lower than that of the straight wing. The thrust coefficient is close to that of the straight wing in the whole process of the downward flapping ($t/T = 0-0.5$) and the first half of the upward flapping ($t/T = 0.5-0.75$), and it

decreases obviously in the latter half ($t/T = 0.75-1$), which has strong regularity. That is, the smaller the wavelength of the wavy leading edge flapping wing, the more the thrust coefficient decreases.

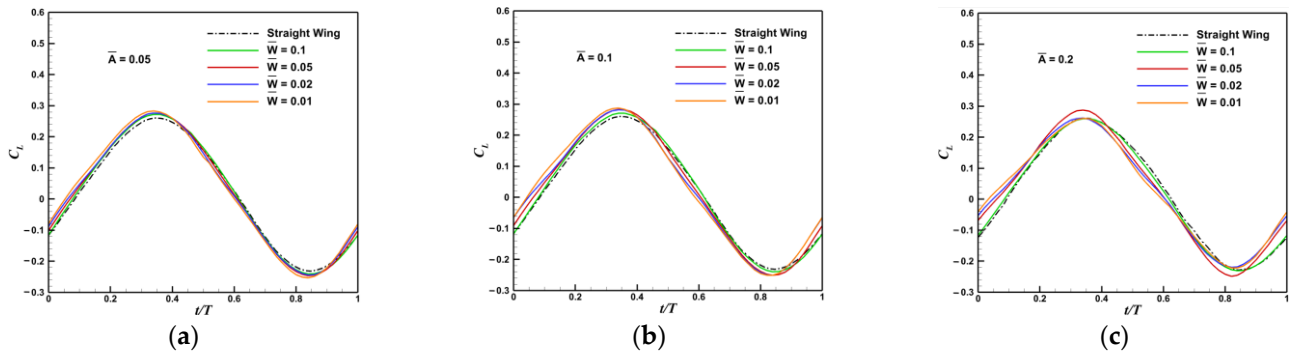


Figure 18. Time history of lift coefficient in a flapping cycle. (a) $\bar{A} = 0.05$; (b) $\bar{A} = 0.1$; (c) $\bar{A} = 0.2$.

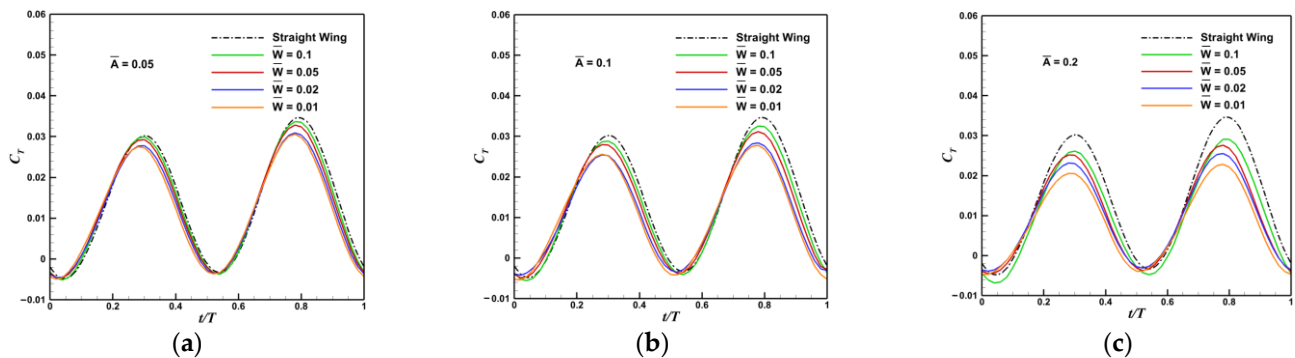


Figure 19. Time history of thrust coefficient in a flapping cycle. (a) $\bar{A} = 0.05$; (b) $\bar{A} = 0.1$; (c) $\bar{A} = 0.2$.

Figure 20 compares the time averaged lift and thrust coefficients of the straight wing and wavy leading edge wings. The wavy leading edge inevitably reduces the thrust coefficient while increasing the lift coefficient, and the smaller the wavelength, the larger the time averaged lift coefficient and the smaller the time averaged thrust coefficient. Figures 21 and 22, respectively, show the time-averaged lift coefficient and thrust coefficient during downstroke ($t/T = 0-0.5$) and upstroke ($t/T = 0.5-1$). The wavy leading edge wings mainly increases the lift in the downstroke, while the thrust decreases in both the up-and-down stroke of the flapping. Table 5 shows the average growth rate of time averaged lift coefficient relative to straight wing and the average reduction rate of time averaged thrust coefficient for flapping wing with different wavelengths. When the wavelength is $\bar{W} = 0.01$, the average lift coefficient increases the most, which is 41.04% of the straight wing, but at the same time, the average thrust coefficient decreases by 25.97%. Therefore, it is necessary to weigh the lift and thrust of the flapping wing during design, or to increase the thrust by increasing the flapping frequency. Wavy leading edge flapping wing can withstand greater take-off weight, and it has better low-speed flight ability.

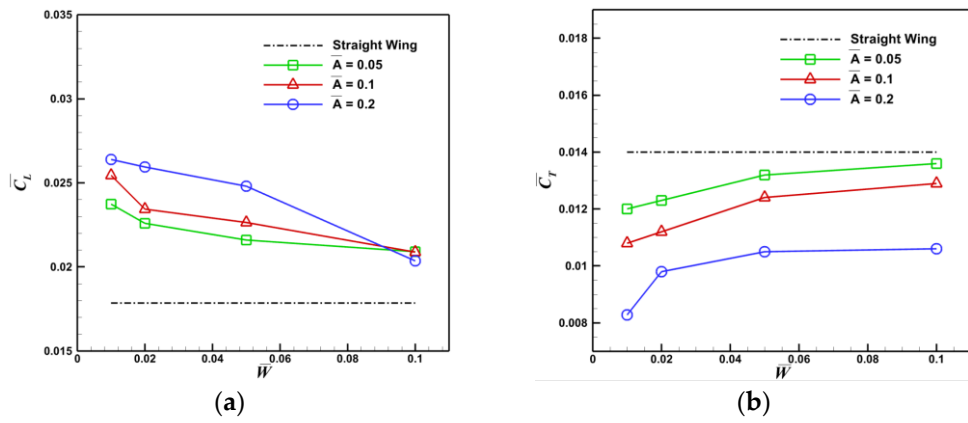


Figure 20. Comparison of average lift coefficient and thrust coefficient. (a) Time averaged lift coefficient; (b) Time averaged thrust coefficient.

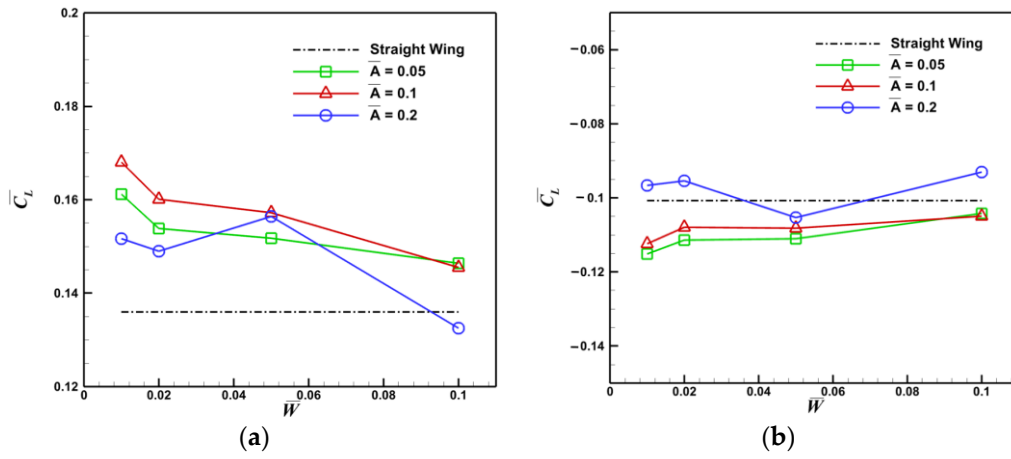


Figure 21. Comparison of average lift coefficient of downstroke and upstroke. (a) Time averaged lift coefficient of downstroke; (b) Time averaged lift coefficient of upstroke.

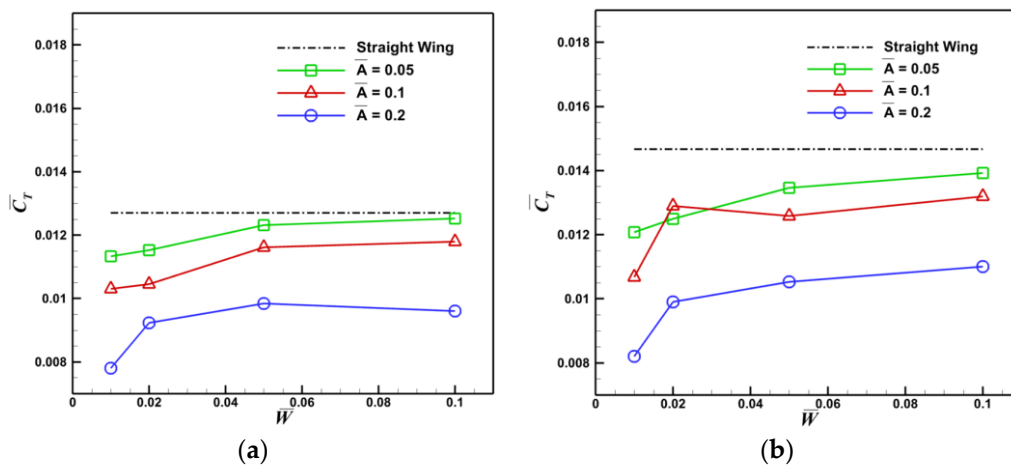


Figure 22. Comparison of average thrust coefficient of downstroke and upstroke. (a) Time averaged thrust coefficient of downstroke; (b) Time averaged thrust coefficient of upstroke.

Table 5. Average change rates of flapping wings at different wavelengths.

\bar{W}	0.1	0.05	0.02	0.01
Time averaged lift coefficient \bar{C}_L	16.01%↑	28.89%↑	34.32%↑	41.04%↑
Time averaged trust coefficient \bar{C}_T	11.66%↓	14.04%↓	20.71%↓	25.97%↓

With the purpose of further clarifying the mechanism of wavy leading edge changing the characteristics of flow field and the influence of different wavelengths, four typical moments ($t/T = 0, 0.2, 0.5$ and 0.8) in a flapping cycle are compared and analyzed by taking the straight wing ($\bar{W} = 0$) and the wavy leading edge flapping wing with $\bar{A} = 0.1$ as an example. Figure 23 shows the pressure contours of the upper surface of the flapping wing, and the unit of pressure is Pa. In the downward stage ($t/T = 0$ and 0.2), the pressure on the upper surface of the wavy leading edge flapping wing decreases, while in the upward stage ($t/T = 0.5$ and 0.8), the pressure on the upper surface increases. The change of pressure is mainly reflected in the position above 60% of the wingspan, and the change of the pressure difference between the upper and lower surfaces will cause the change of lift. Figure 24 compares the pressure coefficients of the straight wing and the wavy leading edge wing with different wavelengths at 80% wingspan section. When $t/T = 0$ and 0.2 , the pressure of the upper surface of the wavy leading edge flapping wing decreases compared with the straight wing, and the pressure of the lower surface increases. The pressure difference between the upper and lower surfaces increases, and the lift increases. Although Figure 24a is similar to Figure 24c, and Figure 24b is similar to Figure 24d, it can be seen from the pressure contours that the pressure on the upper surface of the flapping wing is greater than that on the lower surface. Therefore, after the wavy leading edge causes the pressure difference to increase, the downward force on the flapping wing is further increased. That is, the lift is reduced.

Figure 25 shows the pressure coefficient contours and streamlines of the 50% spanwise section of the flapping wing when $t/T = 0$. As the wavelength decreases, the vortex generated by the wavy leading edge decreases the pressure coefficient on the upper surface of the wing section and increases the pressure coefficient on the lower surface, resulting in an increase in the lift coefficient. In addition, the pressure coefficient on the trailing edge decreases with the decrease of the wavelength, which leads to a decrease in the thrust coefficient of the flapping wing.

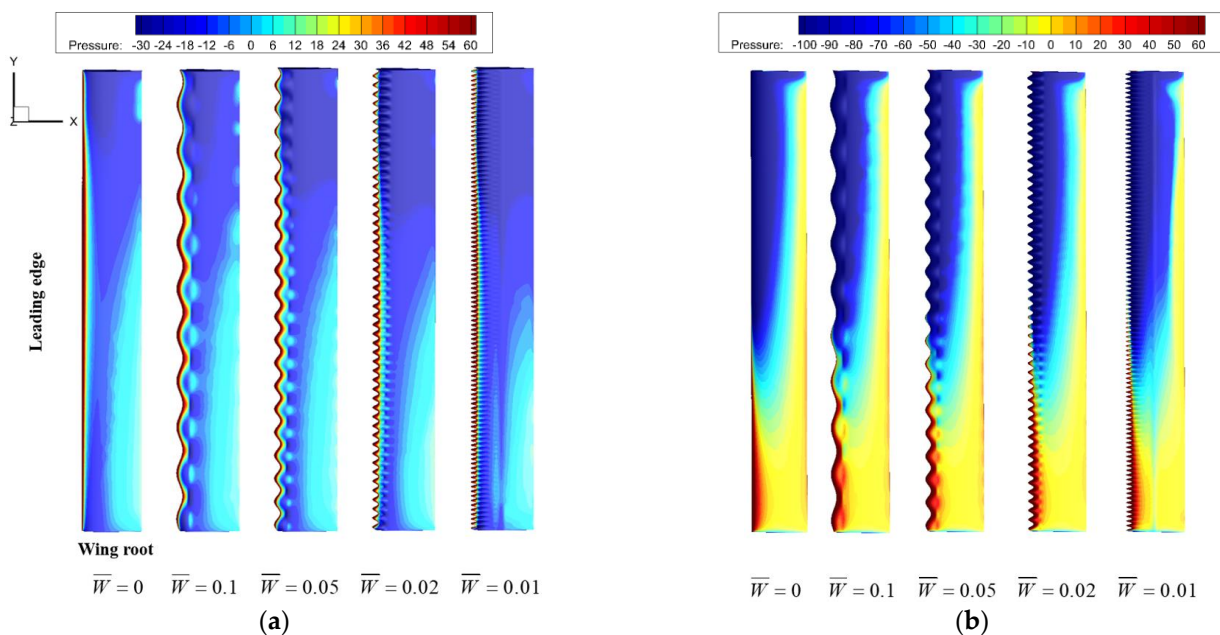


Figure 23. Cont.

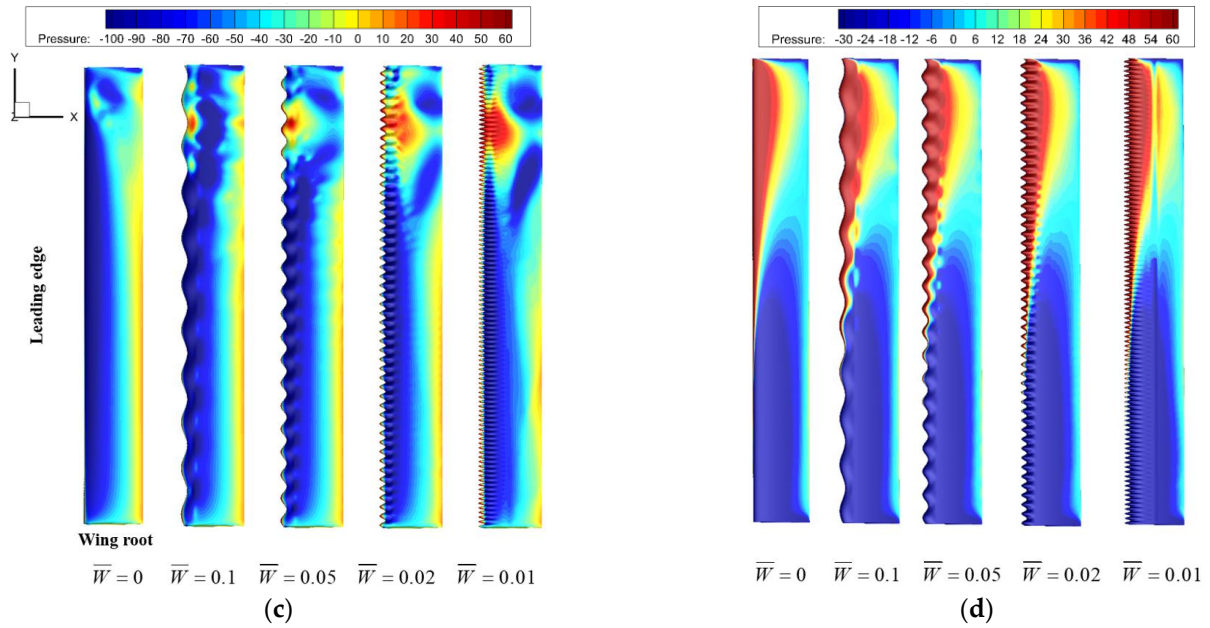


Figure 23. Pressure contours of the upper surface of flapping wing (Pa). (a) $t/T = 0$; (b) $t/T = 0.2$; (c) $t/T = 0.5$; (d) $t/T = 0.8$.

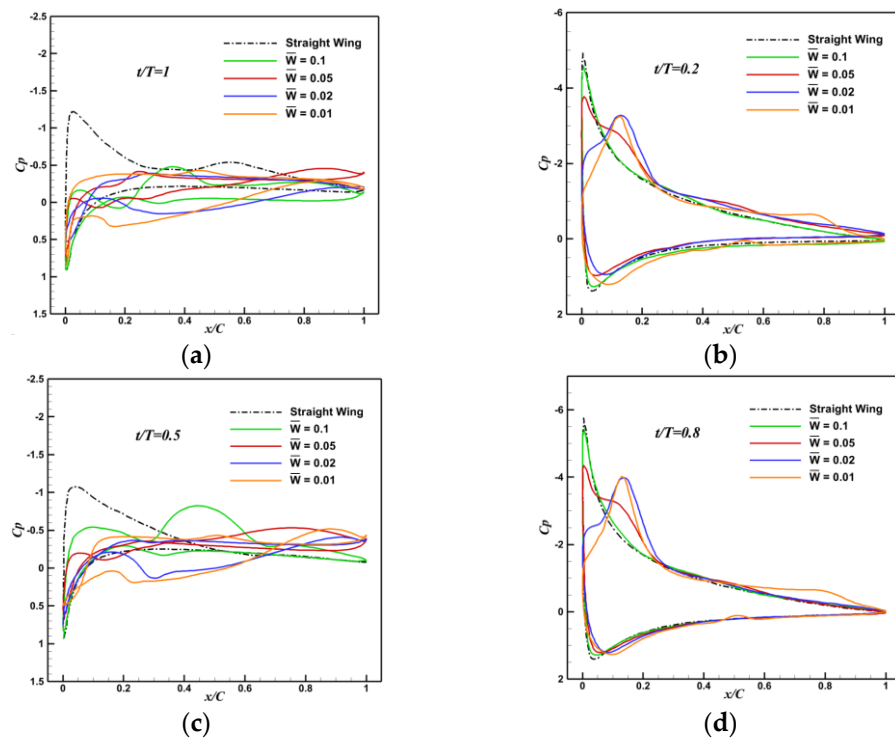


Figure 24. Pressure coefficient of 80% wingspan section. (a) $t/T = 1$; (b) $t/T = 0.2$; (c) $t/T = 0.5$; (d) $t/T = 0.8$.

4.2. Effects of Different Amplitudes on Aerodynamic Performance of Flapping Wing

Figures 26 and 27, respectively, show the time history comparison of lift coefficient and thrust coefficient of straight flapping wing and wavy leading edge flapping wing with different amplitudes in one flapping cycle. When the wavelength is large, the change of amplitude has little effect on the lift coefficient, and at the same wavelength, the larger the amplitude, the more the thrust coefficient decreases.

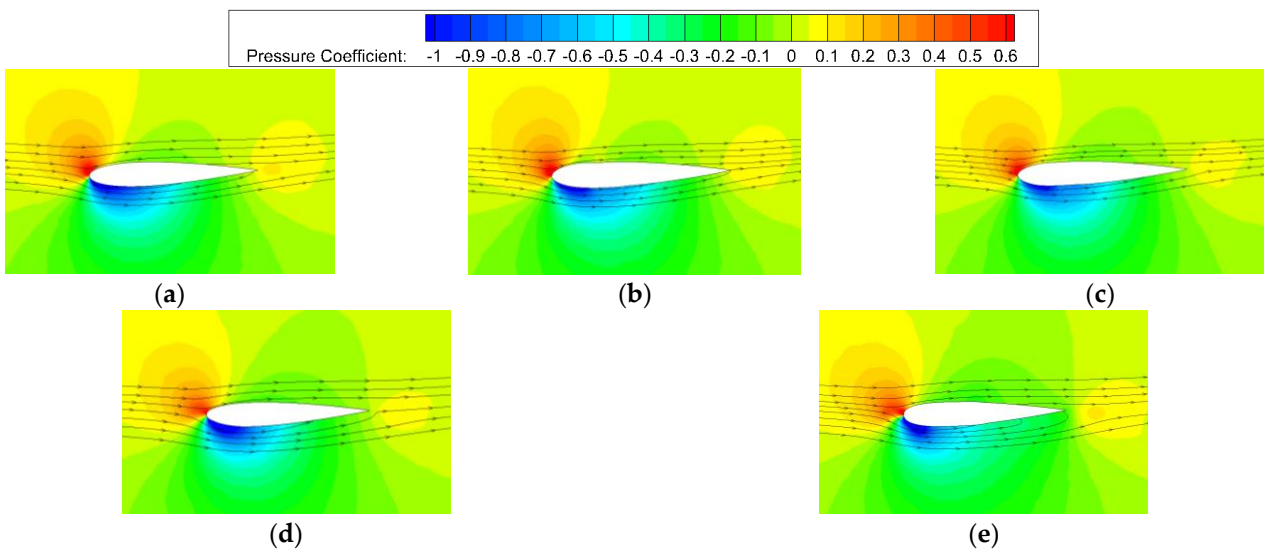


Figure 25. Pressure contours and streamlines of 50% spanwise section of flapping wing at $t/T = 0$. (a) Straight Wing; (b) $\bar{W} = 0.1$; (c) $\bar{W} = 0.05$; (d) $\bar{W} = 0.02$; (e) $\bar{W} = 0.01$.

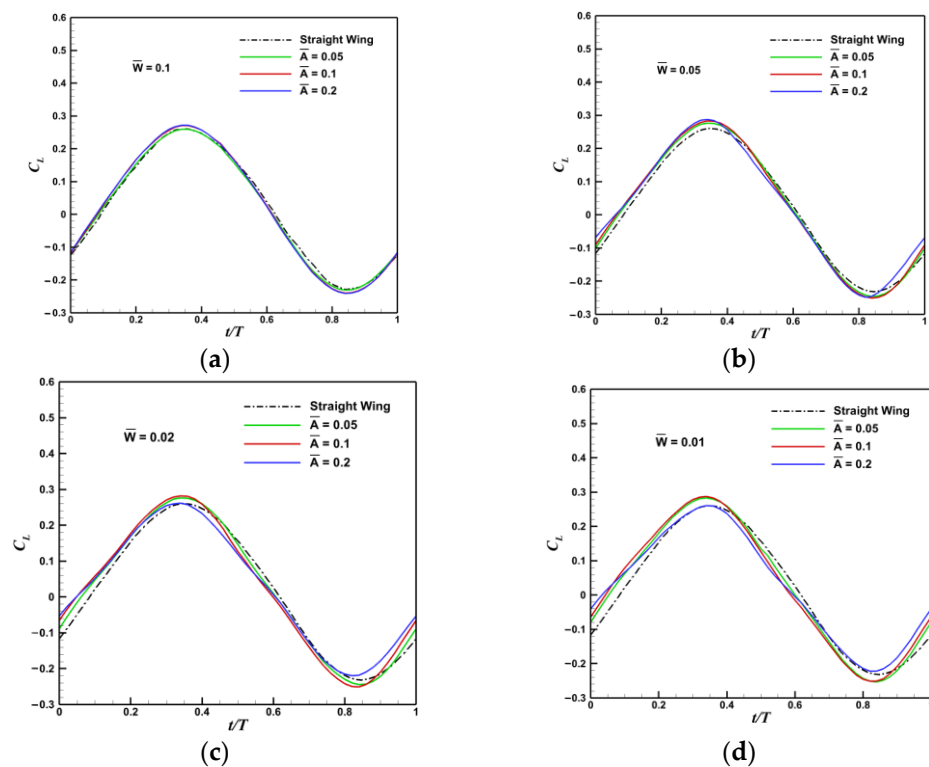


Figure 26. Time history of lift coefficient in a flapping cycle. (a) $\bar{W} = 0.1$; (b) $\bar{W} = 0.05$; (c) $\bar{W} = 0.02$; (d) $\bar{W} = 0.01$.

Figure 28 compares the time averaged lift and thrust coefficients of the straight wing and wavy leading edge wings with different amplitudes, and Figures 29 and 30, respectively, show the time-averaged lift coefficient and thrust coefficient during downstroke ($t/T = 0-0.5$) and upstroke ($t/T = 0.5-1$). Table 6 shows the average growth rate of time averaged lift coefficient and the average reduction rate of time averaged thrust coefficient of them. As can be seen, at the same wavelength, the larger the amplitude, the higher the average lift coefficient and the more the time-averaged thrust coefficient decreases.

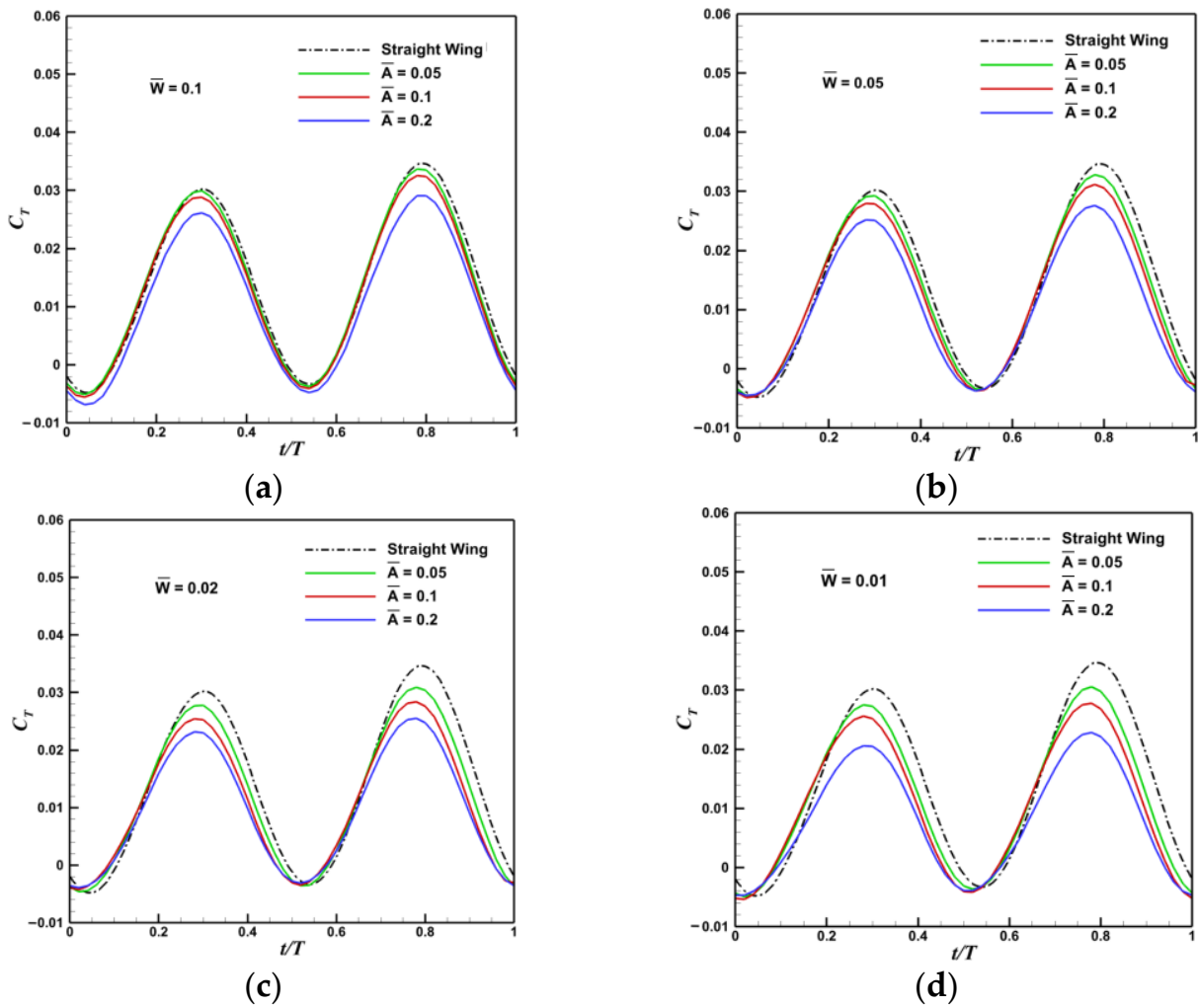


Figure 27. Time history of thrust coefficient in a flapping cycle. (a) $\bar{W} = 0.1$; (b) $\bar{W} = 0.05$; (c) $\bar{W} = 0.02$; (d) $\bar{W} = 0.01$.

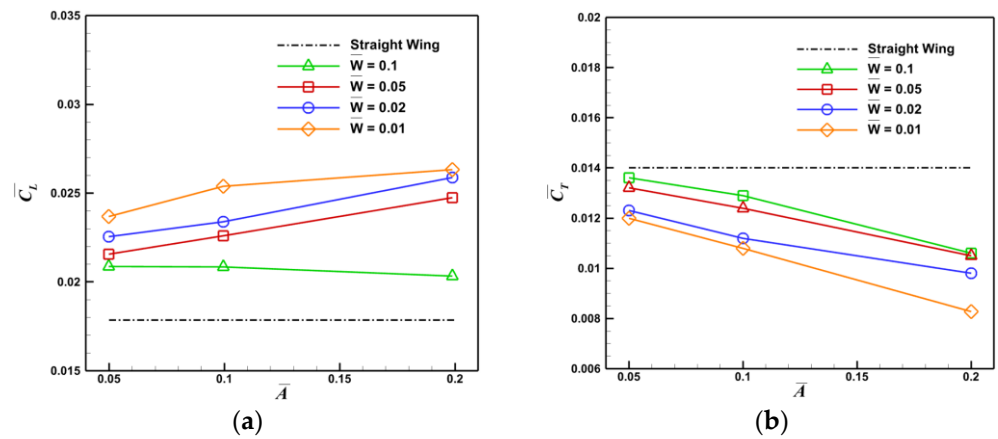


Figure 28. Comparison of average lift coefficient and thrust coefficient. (a) Time averaged lift coefficient; (b) Time averaged thrust coefficient.

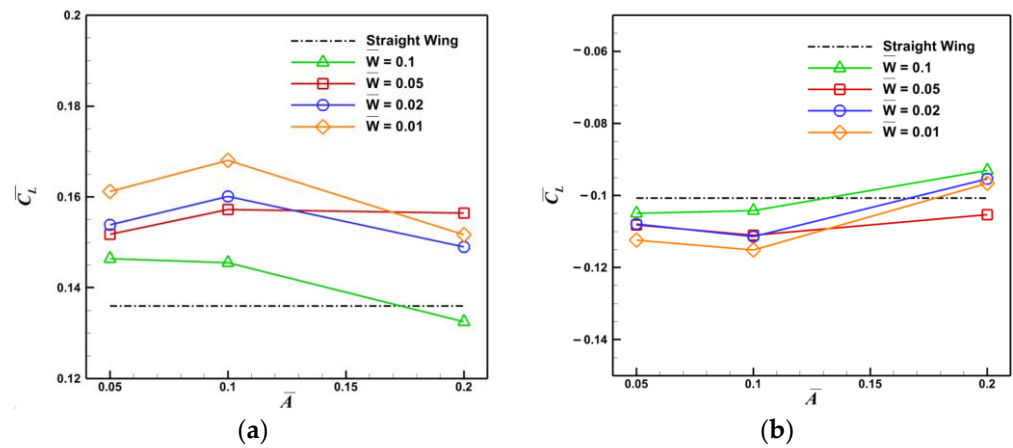


Figure 29. Comparison of average lift coefficient of downstroke and upstroke. (a) Time averaged lift coefficient of downstroke; (b) Time averaged lift coefficient of upstroke.

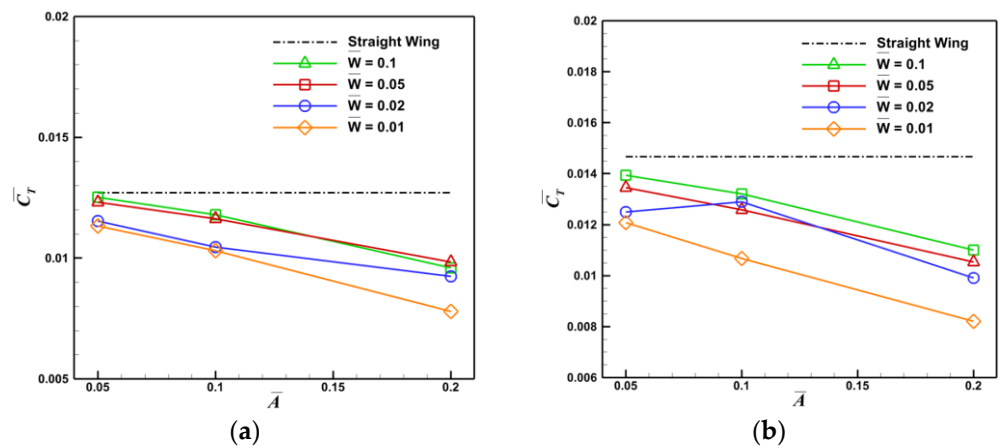


Figure 30. Comparison of average thrust coefficient of downstroke and upstroke. (a) Time averaged thrust coefficient of downstroke; (b) Time averaged thrust coefficient of upstroke.

Table 6. Average change rates of flapping wings at different amplitudes.

\overline{A}	0.05	0.1	0.2
Time averaged lift coefficient $\overline{C_L}$	24.34%↑	29.33%↑	36.52%↑
Time averaged thrust coefficient $\overline{C_T}$	8.75%↓	15.53%↓	29.03%↓

Taking the straight wing ($\overline{A} = 0$) and the wavy leading edge flapping wing with different amplitudes at wavelength $\overline{W} = 0.02$ as an example, the four typical moments in a flapping cycle ($t/T = 0, 0.2, 0.5,$ and 0.8) are compared and analyzed. The pressure contours of the upper surface of the flapping wing are shown in Figure 31; the unit of pressure is Pa. It can be seen that the wavy leading edge changes the pressure distribution on the flapping wing. In the downward flapping stage, the larger the amplitude, the smaller the pressure behind the trough, the smaller the pressure on the upper surface of the flapping wing, the larger the pressure difference between the upper and lower surfaces, and the higher the lift.

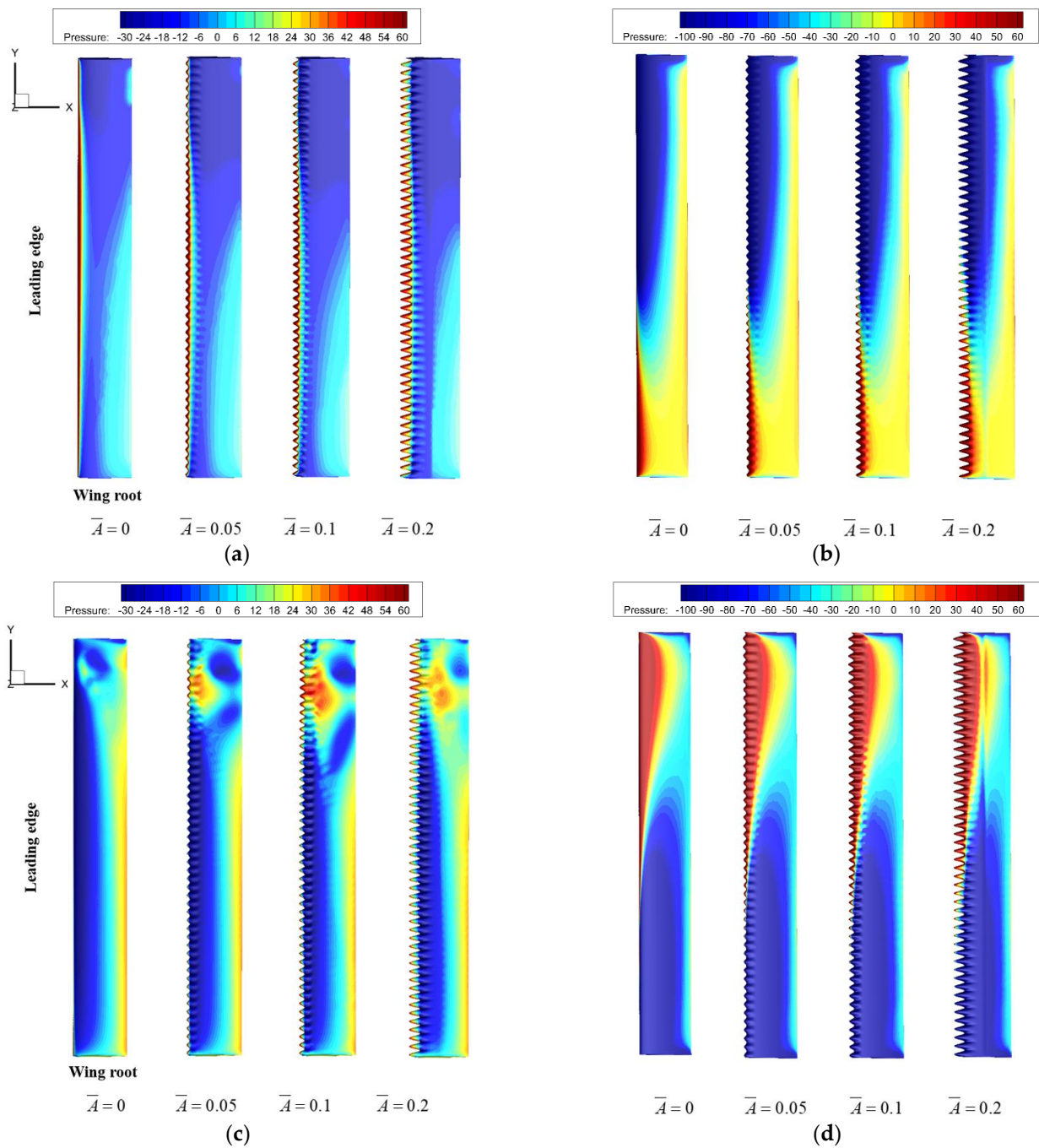


Figure 31. Pressure contours of the upper surface of flapping wing. (a) $t/T=0$; (b) $t/T = 0.2$; (c) $t/T = 0.5$; (d) $t/T = 0.8$.

Figure 32 shows the Mach number contours at 50% spanwise section of the straight wing and the wavy leading edge flapping wing with different amplitudes when $t/T = 0$, where is the trough position. When the gas flows through the wavy leading edge, the airflow on the upper surface of the wing accelerates, and the airflow on the lower surface decelerates. Moreover, the larger the amplitude, the more obvious the change in velocity, so the greater the lift increase.

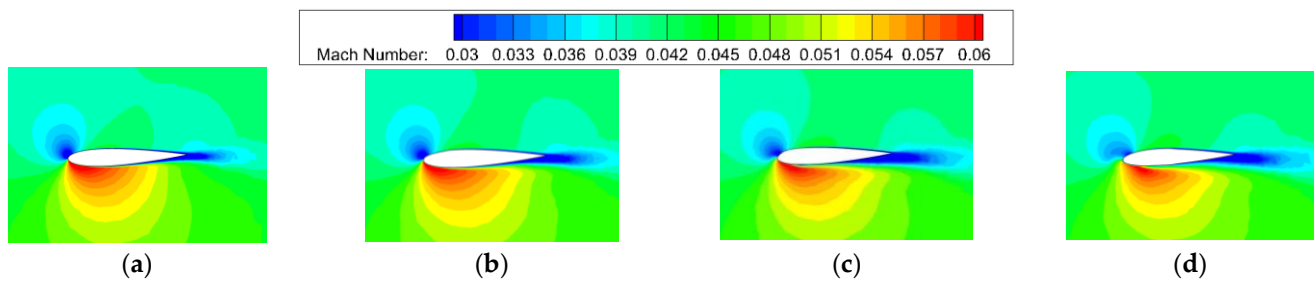


Figure 32. Mach number contours of 50% spanwise section of flapping wing at $t/T = 0$. (a) Straight Wing; (b) $\bar{A} = 0.05$; (c) $\bar{A} = 0.1$; (d) $\bar{A} = 0.2$.

4.3. Sensitivity Analysis of Design Parameters

In order to further analyze the influence of design parameters of wavy leading edge flapping wing on its aerodynamic performance, the sensitivities of time averaged lift coefficient and thrust coefficient to wavelength and amplitude are calculated, respectively, as shown in Table 7. At the same amplitude, the larger the wavelength of the wavy leading edge flapping wing, the smaller the time averaged lift coefficient and the larger the time averaged thrust coefficient. At the same wavelength, the larger the amplitude, the larger the time averaged lift coefficient and the smaller the time averaged thrust coefficient.

Table 7. Sensitivity of design parameters.

	Wavelength \bar{W}	Amplitude \bar{A}
Time averaged lift coefficient \bar{C}_L	−77.4%	22.6%
Time averaged trust coefficient \bar{C}_T	52.9%	−47.1%

To obtain the maximum lift coefficient while losing the least thrust, the minimum wavelength and the smallest amplitude should be selected. That is, in the configuration calculated in this paper, the configuration with wavelength $\bar{W} = 0.01$ and amplitude $\bar{A} = 0.05$ is optimal. Compared with the straight wing, the time averaged lift coefficient is increased by 32.86%, and the time averaged thrust coefficient is reduced by 14.28%.

5. Conclusions

In this paper, a flow control method is proposed to apply the wavy leading edge structure to the straight symmetrical flapping wing to improve the average flapping lift. The aerodynamic performance and flow field characteristics of straight flapping wing and wavy leading edge flapping wing with different design parameters are calculated and compared by numerical simulation method. The mechanism of improving average lift is analyzed, and the sensitivity of the design parameters of wavy leading edge is carried out. The calculation results show that:

1. The wavy leading edge separates the airflow, which reduces the pressure on the upper surface of the flapping wing, increases the pressure difference between the upper and lower surfaces, and increases the lift. Moreover, the different velocity distributions at the peak and trough also changes the aerodynamic performance of the flapping wing. The wavy leading edge wing loses part of the trust while gaining flapping lift.
2. The calculated amplitude is $\bar{A} = 0.05\text{--}0.2$, and the wavelength is $\bar{W} = 0.01\text{--}0.1$. At the same amplitude, the larger the wavelength of the wavy leading edge flapping wing, the smaller the time averaged lift coefficient and the larger the time averaged thrust coefficient. At the same wavelength, the larger the amplitude, the larger the time averaged lift coefficient and the smaller the time averaged thrust coefficient.
3. In order to obtain the maximum lift coefficient while losing the least thrust, the wavelength and amplitude should be selected as small as possible in the design, and the wavelength has the greatest influence on the time averaged lift coefficient. In

the configuration calculated in this paper, the configuration 1–4 with wavelength $\bar{W} = 0.01$ and amplitude $\bar{A} = 0.05$ is the best. Compared with the straight wing, this configuration can increase the average lift coefficient by 32.86% and reduce the average thrust coefficient by 14.28%.

Author Contributions: Conceptualization, B.M.; methodology, X.B.; data curation, X.B.; writing—original draft, X.B.; writing—review & editing, B.M.; supervision, H.Z.; project administration, H.Z. All authors have read and agreed to the published version of the manuscript.

Funding: National Natural Science Foundation of China (Grant No. 12202363); Natural Science Basic Research Program of Shaanxi (Program No. 2021JQ-084).

Institutional Review Board Statement: Not applicable.

Informed Consent Statement: Not applicable.

Data Availability Statement: The relevant information of numerical calculation has been reflected in the manuscript in the form of pictures, charts, etc.

Acknowledgments: The authors would like to acknowledge the support of National Natural Science Foundation of China (Grant No. 12202363) and the support of Natural Science Basic Research Program of Shaanxi (Program No. 2021JQ-084).

Conflicts of Interest: The authors declare no conflict of interest.

References

1. Thielicke, W.; Stamhuis, E. The influence of wing morphology on the three-dimensional flow patterns of a flapping wing at bird scale. *J. Fluid Mech.* **2015**, *768*, 240–260. [CrossRef]
2. Shahzad, A.; Mumtaz Qadri, M.N.; Ahmad, S. Numerical analysis of high aspect ratio flexible wings in flapping motion. *J. Appl. Fluid Mech.* **2019**, *12*, 1979–1988. [CrossRef]
3. Ajanic, E.; Feroskhan, M.; Mintchev, S.; Noca, F.; Floreano, D. Bioinspired wing and tail morphing extends drone flight capabilities. *Sci. Robot.* **2020**, *5*, eabc2897. [CrossRef] [PubMed]
4. Kang, C.-K.; Aono, H.; Cesnik, C.E.S.; Shyy, W. Effects of flexibility on the aerodynamic performance of flapping wings. *J. Fluid Mech.* **2011**, *689*, 32–74. [CrossRef]
5. Kleinheerenbrink, M.; Johansson, L.C.; Hedenström, A. Multi-cored vortices support function of slotted wing tips of birds in gliding and flapping flight. *J. R. Soc. Interface* **2017**, *14*, 20170099. [CrossRef]
6. Lynch, M.; Mandadzhiev, B.; Wissa, A. Bioinspired wingtip devices: A pathway to improve aerodynamic performance during low Reynolds number flight. *Bioinspiration Biomim.* **2018**, *13*, 036003. [CrossRef]
7. Avallone, F.; Pröbsting, S.; Ragni, D. Three-dimensional flow field over a trailing-edge serration and implications on broadband noise. *Phys. Fluids* **2016**, *28*, 3818–3831. [CrossRef]
8. Rao, C.; Liu, H. Aerodynamic robustness in owl-inspired leading-edge serrations: A computational wind-gust model. *Bioinspiration Biomim.* **2018**, *13*, 056002. [CrossRef]
9. Lee, S.I.; Choi, H. Characteristics of the alula in relation to wing and body size in the Laridae and Sternidae. *Anim. Cells Syst.* **2017**, *21*, 63–69. [CrossRef]
10. Linehan, T.; Mohseni, K. Investigation of a sliding alula for control augmentation of lifting surfaces at high angles of attack. *Aerosp. Sci. Technol.* **2019**, *87*, 73–88. [CrossRef]
11. Fish, F.E.; Battle, J.M. Hydrodynamic design of the humpback whale flipper. *J. Morphol.* **1995**, *225*, 51–60. [CrossRef] [PubMed]
12. Sudhakar, S.; Karthikeyan, N.; Venkatakrisnan, L. Influence of leading edge tubercles on aerodynamic characteristics of a high aspect-ratio UAV. *Aerosp. Sci. Technol.* **2017**, *69*, 281–289. [CrossRef]
13. Sudhakar, S.; Karthikeyan, N.; Suriyanarayanan, P. Experimental Studies on the Effect of Leading-Edge Tubercles on Laminar Separation Bubble. *AIAA J.* **2019**, *57*, 1–11. [CrossRef]
14. Wei, Z.Y.; New, T.H.; Cui, Y.D. Aerodynamic performance and surface flow structures of leading-edge tubercled tapered swept-back wings. *AIAA J.* **2018**, *56*, 423–431. [CrossRef]
15. Abdelrahman, A.; Emam, A.; Adam, I.; Hassan, H.; Ookawara, S.; El-Wardany, A. A Numerical Study Into the Influence of Leading Edge Tubercles on the Aerodynamic Performance of a Highly Cambered High Lift Airfoil Wing at Different Reynolds Numbers. In Proceedings of the ASME 2020 International Mechanical Engineering Congress and Exposition, Virtual, 16–19 November 2020.
16. Seyhan, M.; Sarioglu, M.; Akansu, Y.E. Influence of Leading-Edge Tubercle with Amplitude Modulation on NACA 0015 Airfoil. *AIAA J.* **2021**, *59*, 3965–3978. [CrossRef]
17. Gopinathan, V.T.; Rose, J. Aerodynamic performance investigation of sweptback wings with bioinspired leading-edge tubercles. *Int. J. Mod. Phys. C* **2022**, *33*, 3. [CrossRef]

18. Pérez-Torró, R.; Kim, J.W. A Large-eddy Simulation on a Deep-stalled Aerofoil with a Wavy Leading edge. *J. Fluid Mech.* **2017**, *813*, 23–52. [CrossRef]
19. Ikeda, T.; Ueda, T.; Nakata, T.; Noda, R.; Tanaka, H.; Fujii, T.; Liu, H. Morphology Effects of Leading-edge Serrations on Aerodynamic Force Production: An Integrated Study Using PIV and Force Measurements. *J. Bionic Eng.* **2018**, *15*, 661–672. [CrossRef]
20. Ramachandiran, V.; Vt, G. On the role of leading-edge tubercles in the pre-stall and post-stall characteristics of airfoils. In Proceedings of the Emerging Trends in Engineering, Science and Technology for Society, Energy and Environment, Thrissur, India, 18–20 January 2018.
21. Ferreira, P.H.; Brondani, L.M.; Scarpari, J.R.; Corrêa, F.L.; de Paula, A.A.; da Silva, R.G. Evaluation of wavy leading edge for rotary-wing applications. In Proceedings of the 2018 Flow Control Conference, Atlanta, Georgia, 25–29 June 2018.
22. Shi, W.; Atlar, M.; Norman, R.; Aktas, B.; Turkmen, S. Numerical optimization and experimental validation for a tidal turbine blade with leading-edge tubercles. *Renew. Energy Int. J.* **2016**, *96*, 42–55. [CrossRef]
23. Chen, T.; Xie, D.; Yang, C.; Zhang, H.; Xiong, Y.; Haifen, D.U.; Zhang, J.; Turbine, D. Application of Biologically Inspired Wavy Leading Edge in Nuclear Steam Turbine Cascade. *Proc. Chin. Soc. Electr. Eng.* **2018**, *38*, 3605–3612.
24. Tu, B.; Wang, H.; Hu, J. Investigation on the aerodynamic performance of high camber turning angle cascade with tubercle leading edge. *Proc. Inst. Mech. Eng. Part A J. Power Energy* **2021**, *235*, 29–43. [CrossRef]
25. Abate, G.; Mavris, D.N. Performance analysis of different positions of leading-edge tubercles on a wind turbine blade. In *AIAA Journal, Proceedings of the 2018 Wind Energy Symposium, Kissimmee, FL, USA, 8–12 January 2018*; AIAA: Sterling, TX, USA, 2018; pp. 1–11.
26. Abate, G.; Mavris, D.N.; Sankar, L.N. Performance effects of leading-edge tubercles on the NREL phase V wind turbine blade. *J. Energy Resour. Technol.* **2019**, *141*, 051206.1–051206.9. [CrossRef]
27. Ke, W.; Hashem, I.; Zhang, W.; Zhu, B. Influence of leading-edge tubercles on the aerodynamic performance of a horizontal-axis wind turbine: A numerical study. *Energy* **2022**, *239*, 122186. [CrossRef]
28. Roy, S.; Das, B.; Biswas, A. A comprehensive review of the application of bio-inspired tubercles on the horizontal axis wind turbine blade. *Int. J. Environ. Sci. Technol.* **2022**, 1–28. [CrossRef]
29. Wei, Z.; Zang, B.; New, T.; Cui, Y. A proper orthogonal decomposition study on the unsteady flow behaviour of a hydrofoil with leading-edge tubercles. *Ocean. Eng.* **2016**, *121*, 356–368. [CrossRef]
30. Rostamzadeh, N.; Kelso, R.M.; Dally, B. A numerical investigation into the effects of Reynolds number on the flow mechanism induced by a tubercled leading-edge. *Theor. Comput. Fluid Dyn.* **2016**, *31*, 1–32. [CrossRef]
31. Zhao, M.; Zhang, M.M.; Xu, J.Z. Numerical simulation of flow characteristics behind the aerodynamic performances on an airfoil with leading-edge protuberances. *Eng. Appl. Comput. Fluid Mech.* **2017**, *11*, 193–209. [CrossRef]
32. Pendar, M.R.; Esmailifar, E.; Roohi, E. LES Study of Unsteady Cavitation Characteristics of a 3-D Hydrofoil with Wavy Leading Edge. *Int. J. Multiph. Flow* **2020**, *132*, 103415. [CrossRef]
33. Anwar, M.B.; Shahzad, A.; Qadri, M. Investigating the effects of leading-edge tubercles on the aerodynamic performance of insect-like flapping wing. *Proc. Inst. Mech. Eng. Part C J. Mech. Eng. Sci.* **2021**, *235*, 330–341. [CrossRef]
34. Jones, K.; Castro, B.; Mahmoud, O.M.K.M.; Pollard, S.; Platzer, M.; Neef, M.; Gonet, K.; Hummel, D. A collaborative numerical and experimental investigation of flapping-wing propulsion. In Proceedings of the 40th Aerospace Sciences Meeting and Exhibit, Reno, NV, USA, 14–17 January 2002.
35. Lin, S.Y.; Hu, J.J. *Numerical Study of Flapping Wing*; AIAA: Sterling, TX, USA, 2003; pp. 2003–3448.
36. ANSYS Inc ANSYS FLUENT 2022 (Theory Guide). Available online: <http://WWW.Fluent.com> (accessed on 1 October 2022).
37. Menter, F.R. Two-equation eddy-viscosity turbulence models for engineering applications. *AIAA J.* **1994**, *32*, 8. [CrossRef]
38. Wilcox, D.C. *Turbulence Modeling for CFD*; DCW Industries, Inc.: La Canada, CA, USA, 1993.
39. Lai, J.C.S.; Platzer, M.F. The jet characteristics of a plunging airfoil. *AIAA J.* **1998**, *37*, 12.
40. Delaurier, J.D. An ornithopter wing design. *Can. Aeronaut. Space J.* **1999**, *40*, 1.
41. Whale and Dolphin Conservation. Available online: <https://uk.whales.org/whales-dolphins/species-guide/humpback-whale/> (accessed on 1 November 2022).
42. Johari, H.; Henoch, C.; Custodio, D.; Levshin, A. Effects of leading-edge protuberances on airfoil performance. *AIAA J.* **2007**, *45*, 2634–2642. [CrossRef]

Disclaimer/Publisher’s Note: The statements, opinions and data contained in all publications are solely those of the individual author(s) and contributor(s) and not of MDPI and/or the editor(s). MDPI and/or the editor(s) disclaim responsibility for any injury to people or property resulting from any ideas, methods, instructions or products referred to in the content.

Article

Internal Aerodynamic Performance Enhancement for Aircraft with High Maneuver by Designing a Distributed Submerged Inlet

Junyao Zhang  and Baigang Mi *

School of Aeronautics, Northwestern Polytechnical University, Xi'an 710072, China

* Correspondence: mibaigang@nwpu.edu.cn

Abstract: Submerged inlet has been widely used in UAVs and cruise missiles due to its good stealth characteristics, but it also brings the disadvantage of poor aerodynamic characteristics. Especially in large maneuvering flight, the flow field near the fuselage has a strong unsteady effect, and the total pressure recovery coefficient and distortion characteristics have deteriorated sharply. In order to investigate the steady and transient aerodynamic characteristics of the submerged inlet in large maneuver flight and improve its maneuver envelope, a design scheme of a distributed submerged inlet for large maneuver flight is proposed in this paper. Taking a cruise missile as the research object, the steady and transient analysis of the conventional submerged inlet and the distributed submerged inlet is carried out using CFD numerical method. The results show that the distributed submerged inlet can significantly improve the inlet performance and enhance the sideslip limit of the submerged inlet during large sideslip maneuver flight. When the sideslip angle is 30° , compared with the conventional submerged inlet configuration, the outlet total pressure recovery coefficient of the distributed submerged inlet configuration is increased by 44.2%, and the total pressure distortion index is reduced by 66.3%.

Keywords: submerged inlet; large maneuver state; nested mesh; total pressure distortion index; distortion characteristics; hysteresis effect

Citation: Zhang, J.; Mi, B. Internal Aerodynamic Performance Enhancement for Aircraft with High Maneuver by Designing a Distributed Submerged Inlet. *Appl. Sci.* **2023**, *13*, 1459. <https://doi.org/10.3390/app13031459>

Academic Editors: Josep Maria Bergada and Gabriel Bugeda Castellort

Received: 29 December 2022

Revised: 13 January 2023

Accepted: 18 January 2023

Published: 22 January 2023



Copyright: © 2023 by the authors. Licensee MDPI, Basel, Switzerland. This article is an open access article distributed under the terms and conditions of the Creative Commons Attribution (CC BY) license (<https://creativecommons.org/licenses/by/4.0/>).

1. Introduction

The 4S standards of the fourth-generation fighter (called the fifth generation by Russia) refer to Stealth, Supersonic, Super sensor, and Super mobility. Among them, super maneuverability refers to the ability of aircraft to significantly change its flight speed, flight altitude, and flight direction within a certain period of time. It is an important tactical and technical indicator of aircraft. The excellent maneuverability is conducive to the advantages of the fighter in close combat and breaking through the flight-restricted area, so the maneuverability is very important for the fighter. In order to achieve large maneuver flight, it is necessary to consider not only aerodynamic layout design and aerodynamic configuration design, but also excellent inlet and engine matching. When the aircraft maneuvers rapidly, strong unsteady effects appear in the fuselage flow field, such as the flow parameters at the inlet, the total pressure recovery coefficient at the outlet, and the total pressure distortion. Especially in the maneuvering state of high angle of attack and high sideslip angle, the inlet distortion characteristics deteriorate rapidly, which can very easily cause engine surge or even engine shutdown and poses a serious threat to flight safety. Therefore, if the aircraft wants to obtain excellent maneuverability, it is necessary to find out the aerodynamic characteristics of the inlet during maneuvers at high angles of attack and high sideslip angles. Common maneuvers include circling, rolling, diving, somersault, battle turning, and rapid ascent. These maneuvers are characterized by large changes in flight angle of attack/sideslip angle, large three-axis angular rate, and large changes in velocity/direction/altitude. At the same time, there are strong unsteady characteristics in the internal flow of the inlet that pose a great challenge to theoretical research, computational simulation, test technology, verification means, etc.

Walsh K R et al. used experimental and numerical simulation methods to study the influence of the high angle of attack maneuver flight on the aerodynamic characteristics of the inlet. The research results showed that the increase of the angle of attack from 10° to 60° would lead to an increase in the range of low-pressure area at the inner side of the inlet bottom and showed a more obvious pressure gradient on the engine inlet section [1]. In the F/A-18A project, SMITH CF et al. carried out a numerical simulation of an aircraft inlet under multiple working conditions in order to explore the difference in inlet aerodynamic characteristics between rapid maneuver flight and steady flight. The research results show that the static pressure in the numerical calculation results is in good agreement with the flight data [2]. In order to judge whether the results obtained under stable conditions are sufficient to describe the distortion level generated by the inlet during the rapid maneuver of the aircraft, Yuhas A J used experimental means to study the aerodynamic characteristics of the inlet. The research results show that the transient high angle of attack maneuver conditions will not improve the distortion of the inlet [3]. Steenken W G compared the steady inlet data with the inlet data during the transient rapid maneuver, and the results showed that the total pressure recovery of the rapid maneuver inlet was very consistent with the total pressure recovery coefficient obtained under the equivalent stable angle of attack [4]. In order to explore whether the inlet can provide stable and uniform airflow for the engine during flight outside the normal maneuvering envelope, Steenken W G et al. used wind tunnel experiments to explore the inlet during maneuvering flight. In the experiments, engine surges were encountered in the process of nose left deviation and nose right deviation, while the total pressure distortion level did not exceed the maximum limit during the stable attitude experiment, which indicates that the aircraft's position. The rapid change of attitude may cause the increase of total pressure distortion in the inlet and even cause engine surge [5]. In order to predict the total pressure recovery and distortion at the engine inlet section, PODLESKI used the numerical simulation method to study the forebody/inlet model of F/a-18 at $M_e = 0.20$, $\alpha = 60^\circ$ and $\beta = 10^\circ$. The research results show that the calculation program used in the article tends to underestimate the total pressure recovery at the engine inlet section and overestimate the distortion level [6]. In order to accurately predict the performance of aircraft inlet under extreme flight conditions, Bruns J E et al. used numerical simulation methods to explore the inlet. The results showed that the calculated results were in good agreement with the surface static pressure of the precursor in the wind tunnel test results, and the calculated results were slightly lower than the experimental data. This difference may be partly due to the low mesh resolution at the inlet lip [7]. Wu Chaojun and others developed a maneuvering inlet test device based on dual torque motor synchronous drive, simulated the rapid pitching and other maneuvering processes of the fighter and different working conditions of the inlet, and established the unsteady test method of the fighter inlet. The basic law of inlet performance change during a fast pitch maneuver of a fighter model is studied by means of the test [8]. Yang Yingkai conducted a wind tunnel test study on the dynamic characteristics of the bump inlet on both sides and explored the aerodynamic characteristics of the inlet within a certain angle of attack. The research results show that the total pressure recovery coefficient and distortion index have a strong unsteady hysteresis effect, which is significantly different from the steady-state results at the same angle of attack [9]. Xiang Huan et al. applied the dynamic nested mesh technology to study the dynamic aerodynamic characteristics of the fighter's inlet under a rapid pitch maneuver and verified it with flight data. They captured the unsteady hysteresis effect in the inlet during the fighter's maneuver flight and analyzed its influencing factors and mechanism [10–13]. However, most of the current research on the unsteady flow characteristics in the inlet during maneuvering flight is carried out for the conventional inlet with a windward surface, and it is difficult to find the relevant information of the submerged inlet in the domestic and foreign open literature.

The design of the submerged inlet integrated with the aircraft body has many advantages. In addition to significantly reducing the windward surface of the aircraft and reducing the wind resistance, it can also reduce the radar scattering area and improve

the survivability of the aircraft [14–17]. At present, the submerged inlet is widely used in cruise missiles and UAVs, such as the cruise missile AGM-129 and the whaling fork of the United States [18,19]. Researchers from various countries have also carried out a series of research on the submerged inlet. As early as 1945, Axelson J A et al. designed a NACA submerged inlet and carried out a lot of experiments on it. The submerged inlet uses a long inclined plate with a very small angle of inclination (about 7°) to introduce air into the inlet, but the intake volume of the inlet is small and the total pressure recovery coefficient is low [20–25]. Subsequently, a large number of researchers carried out in-depth research on the intake mechanism [26,27], optimization design method [28–30], internal flow characteristics [31–33], and flow control method [34–37] of the submerged inlet. Now the performance of the submerged inlet can basically meet the engineering application requirements. However, the research on the submerged inlet is only limited to the steady numerical simulation or ground wind tunnel experiment when the angle of attack and sideslip of the aircraft are constant. The research on the unsteady flow characteristics of the submerged inlet in the process of large maneuvering flight is still blank, and the research on the optimization and flow control method of the submerged inlet in the process of large maneuvering flight is impossible.

In this paper, a new configuration of the submerged inlet based on the distributed design concept is proposed creatively to solve the problem of the low efficiency of submerged inlets during flight in a large maneuver state. Taking a cruise missile as the research object, the CFD numerical method is used to analyze the steady flow characteristics of the conventional submerged inlet and the distributed submerged inlet under the condition of stable aerodynamic angle, and then the transient flow characteristics during the large maneuver flight are analyzed. The unsteady aerodynamic characteristics of the distributed submerged inlet and the conventional submerged inlet during the large maneuver movement are compared to improve their adaptability in the large maneuver flight.

2. Distributed Submerged Inlet Design

2.1. Flow Characteristics Analysis of Submerged Inlet

In order to avoid the engine surge or even engine shutdown caused by the sharp deterioration of the inlet distortion characteristics of the submerged inlet at high angle of attack and large sideslip angle maneuver, it is necessary to discuss the intake mechanism of the submerged inlet under different flight conditions. Figure 1 is a schematic diagram of the mechanism of submerged air intake under different flight conditions. From Figure 1a, it can be seen that when the angle of attack and the sideslip angle are small, the external airflow is mainly driven into the inlet by the entrainment vortices generated by the side edge. As the sideslip angle gradually increases, the side edge with the same direction of the incoming flow can no longer produce a suction vortex that is beneficial to the intake. Although the side edge opposite to the incoming flow can still produce a suction vortex that is beneficial to the intake, the effect of driving the external airflow into the inlet is weakened a lot because the airflow changes the angle of the side edge during the flow around the body, as shown in Figure 1b.

It can be seen from Figure 1c that the submerged inlet has a windward surface during the flight at a positive angle of attack, which is conducive to improving the inlet efficiency, and the airflow directly flows into the inlet, which experiences less drag from the boundary layer on the surface of the projectile, and the total pressure loss of the airflow is less. It can be seen from Figure 1d that the submerged inlet also has a windward surface during the flight with a negative angle of attack, which is beneficial to improve the intake efficiency, but there is certain energy loss when the airflow is dragged by the boundary layer on the surface of the projectile when it bypasses the surface of the projectile. At the same time, the angle of airflow around the body changes, so the effect of driving the external airflow into the inlet is somewhat weakened.

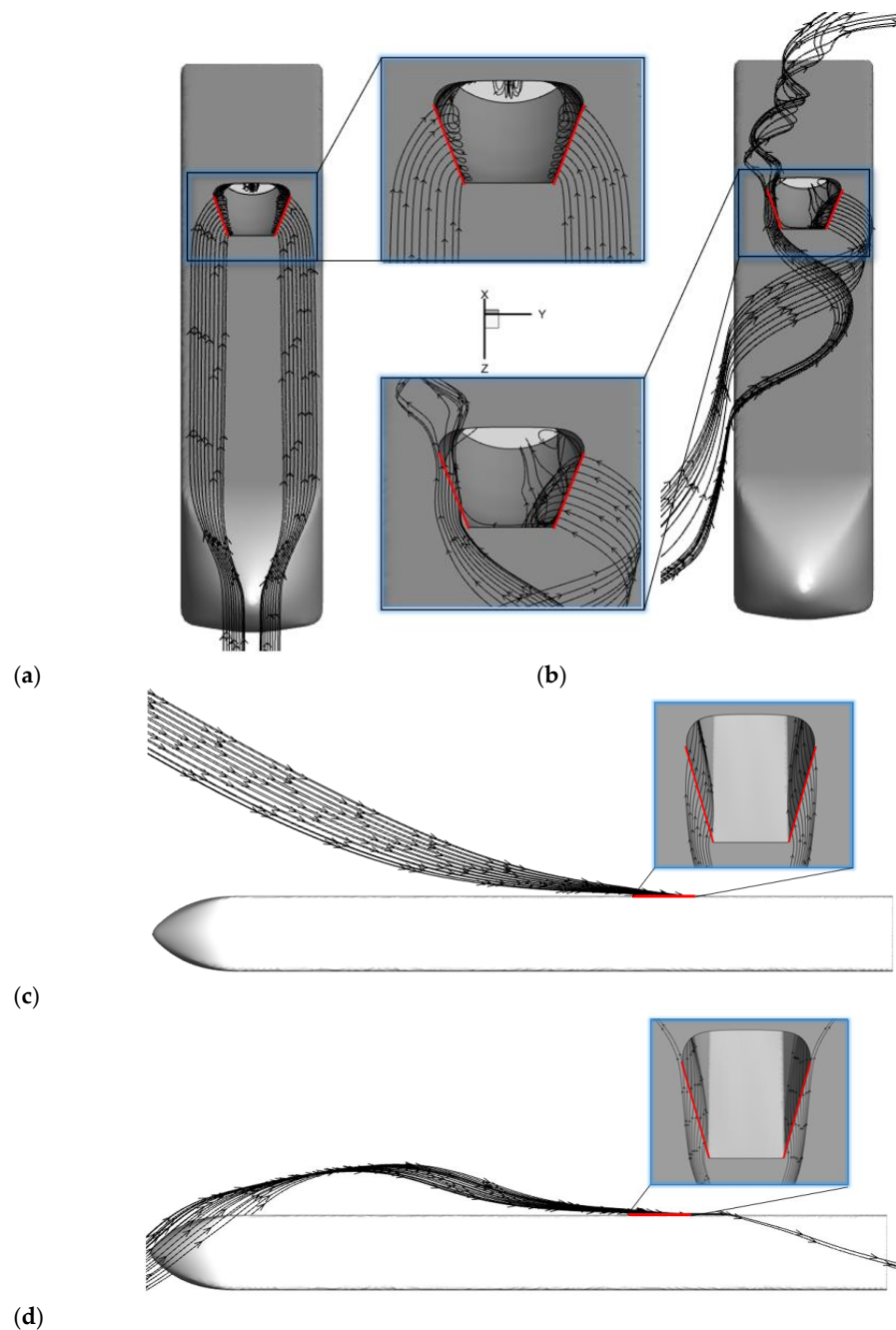


Figure 1. Intake mechanism intention of submerged inlet under different flight conditions. ((a) Intake mechanism intention when sideslip angle and angle of attack are small, (b) Intake mechanism intention when sideslip angle is large and angle of attack is small, (c) Intake mechanism intention when the sideslip angle is small and the angle of attack is positive and large, (d) Intake mechanism intention when sideslip angle is small, angle of attack is negative and large).

From the above analysis, it can be seen that the inlet efficiency of the submerged inlet is low when the sideslip angle and attack angle are large, and some flow control measures should be adopted to improve its inlet performance. However, the use of commonly used passive flow control methods, such as ridge vortex generators, will increase the projected area of the incoming flow direction and increase the resistance while destroying the stealth performance. If the commonly used active flow control methods, such as jet, blowing, and suction flow control methods, are used, they will need to consume additional mass and energy, and need an external drainage pump and other equipment, which is more complex.

Therefore, according to the characteristics of the submerged inlet and the characteristics of the large sideslip maneuver flight, the distributed submerged inlet configuration applied to the large maneuver state is proposed in this paper.

2.2. Distributed Submerged Inlet Design

The inlet efficiency of the submerged inlet is high when there is a windward surface, so an inlet layout that will produce an additional windward surface in the flight state of a large sideslip maneuver is designed. Its three views and main parameters are shown in Figure 2. A submerged inlet, called auxiliary inlet, is arranged on both sides of the submerged inlet. The submerged auxiliary inlet is connected with the main inlet, and its main function is to create an additional windward surface for the inlet during sideslip maneuver, so as to improve the low intake efficiency of the conventional submerged inlet during a large sideslip maneuver. The auxiliary inlet is designed according to the design method of submerged inlet, and then the designed auxiliary inlet and main inlet are trimmed and the intersection line is smoothed. In Figure 2, gray is the part that needs to be retained after the trim, and yellow is the part that needs to be deleted after the trim.

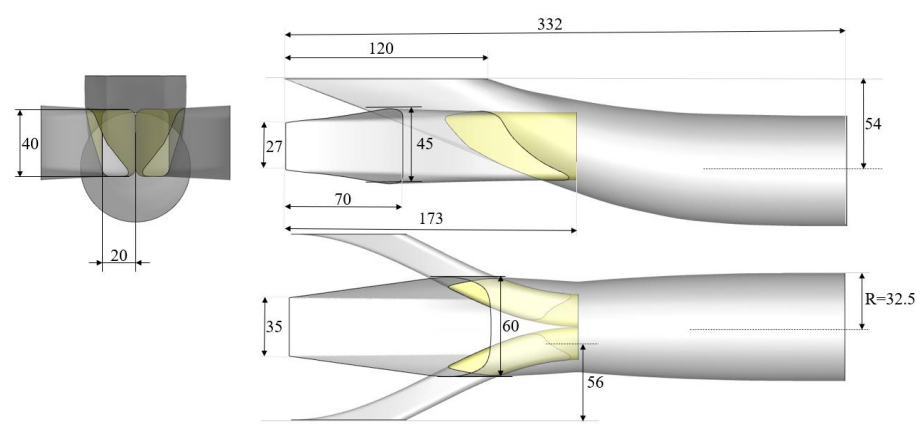


Figure 2. Three views and main parameters of the distributed submerged inlet.

The main research object of this paper is the conventional submerged inlet configuration and the distributed inlet configuration with additional auxiliary inlets on both sides of the body. For ease of reading, the former is referred to as the conventional submerged inlet configuration, and the latter is referred to as the distributed inlet configuration. The conventional submerged inlet configuration, the distributed inlet configuration, and the projectile body are shown in Figure 3. The cross-section shape of the projectile body is a filleted rectangular shape. The inlet opening is located on the lower belly plane of the missile body, and the upper and lower surfaces of the missile body are inverted for easy observation (the upper and lower surfaces are inverted in the subsequent relevant pictures).

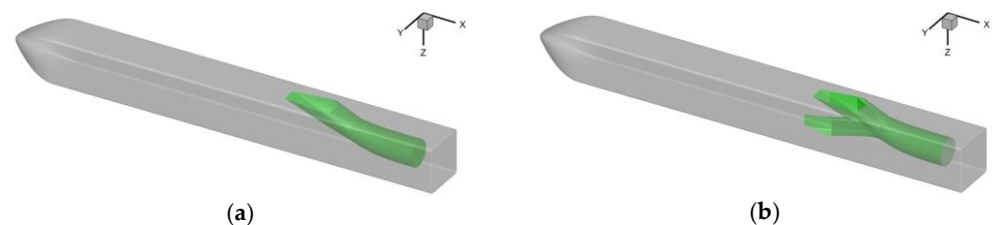


Figure 3. Two configurations of inlet and missile body. ((a) Conventional inlet configuration, (b) Distributed inlet configuration).

3. Calculation Mesh and Boundary Condition Setting

3.1. Steady-State Mesh and Boundary Condition Setting

Figure 4 shows the surface mesh of the missile, inlet, and far field. The mesh form adopts unstructured polyhedral mesh. The far-field calculation domain of the conventional submerged inlet configuration and the distributed submerged inlet configuration are identical. Both are cuboids with length, width, and height of 40 m, 10 m, and 10 m respectively. The two configurations of the inlet and the body model body surface mesh size are the same. The minimum size of the body surface mesh is 1 mm and the maximum size is 5 mm; the minimum size of the inlet surface mesh is 1 mm, the maximum size is 3 mm.

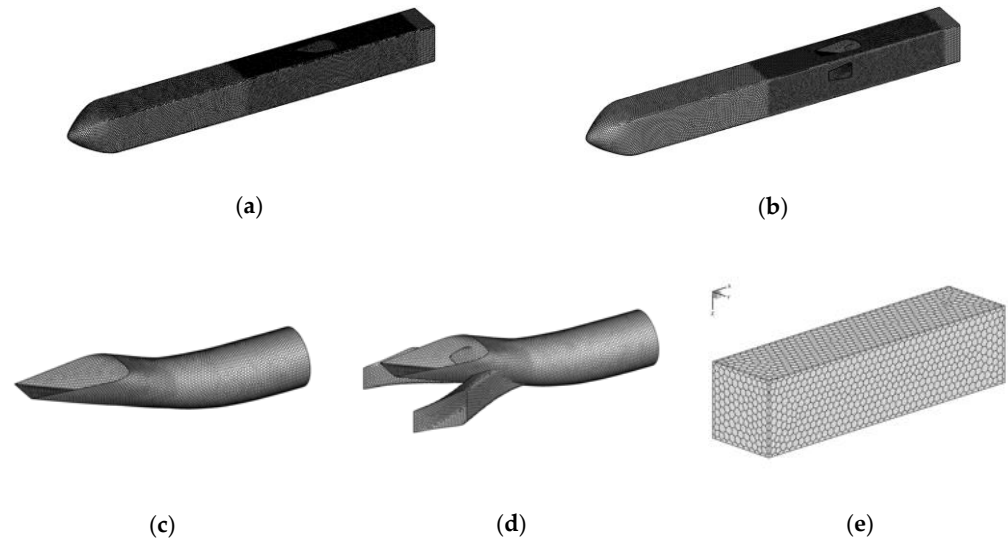


Figure 4. Surface mesh of projectile body, inlet, and far-field. ((a) Surface mesh of missile body in the conventional inlet, (b) Surface mesh of missile body in the distributed inlet, (c) Surface mesh of the conventional inlet, (d) Surface mesh of the distributed inlet, (e) Surface mesh of far-field).

The Spalart–Allmaras turbulence model is mainly used in the numerical simulation in this paper. The S-A turbulence model is a single equation model, which can directly solve the modified turbulent viscosity. It is often used in the flow around the aviation field and is characterized by high accuracy and small amount of calculation. In order to capture the complex flow on the surface of the missile and inlet as well as possible, enhanced wall treatment (EWT) is required, which requires that the near-wall mesh is very dense, and y^+ is close to 1. However, considering that too dense near-wall mesh will lead to low mesh quality, the boundary layer mesh shall be properly adjusted without reducing the calculation accuracy. The final number of boundary layers is 10, the first layer of mesh height is 0.01 mm, and the growth rate is 1.2. In order to make the calculation results more accurate and reliable, an encryption area is set around the missile body, the maximum size of the encryption area is not more than 30 mm, and an encryption area is also set near the inlet, the maximum size of the encryption area is not more than 3 mm, as shown in Figure 5. The number of volume mesh of the conventional submerged inlet configuration is about 0.9 million, of which the boundary layer prismatic mesh accounts for 0.4 million and the polyhedral mesh away from the wall accounts for 0.5 million. The number of the distributed inlet configuration volume mesh is about 1.2 million, of which the boundary layer prismatic mesh accounts for 0.5 million and the polyhedral mesh away from the wall accounts for 0.7 million.

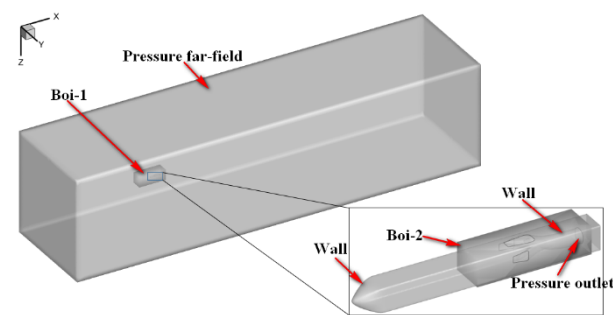


Figure 5. Setting of Steady State Boundary Conditions.

Figure 5 shows the setting of steady-state boundary conditions. The pressure far-field boundary is used for the far-field, and the freestream parameters are given according to the atmospheric conditions at 5 km altitude, $M_0 = 0.7$; The outlet of the inlet adopts the pressure outlet boundary condition, and the pressure is set to the corresponding pressure when $M_e = 0.4$; the body and inlet adopt non-slip adiabatic wall boundary.

3.2. Transient State Mesh and Boundary Condition Setting

In the transient calculation, the dynamic nested mesh technology is used to establish the calculation domain of two concentric spheres, which are the external flow field of the flight airspace and the internal flow field, including the aircraft. The external flow field domain is stationary during the simulation of large maneuvering flight, and the internal flow field mesh, including the aircraft body rotates around the center of gravity along with the aircraft. The mesh size of the body and inlet surface is consistent with that of the steady state. An encryption area shall be set near the inlet, and the maximum size of the encryption area shall not exceed 3 mm, as shown in Figure 6. The mesh boundary layer settings are consistent with the steady state. The number of volume meshes of the conventional submerged inlet configuration is about 1.4 million, of which the boundary layer prismatic meshes account for 0.8 million and the polyhedral mesh away from the wall accounts for 0.6 million; The number of the distributed inlet configuration volume meshes is about 1.6 million, of which the boundary layer prismatic meshes account for 0.9 million and the polyhedral meshes away from the wall account for 0.7 million.

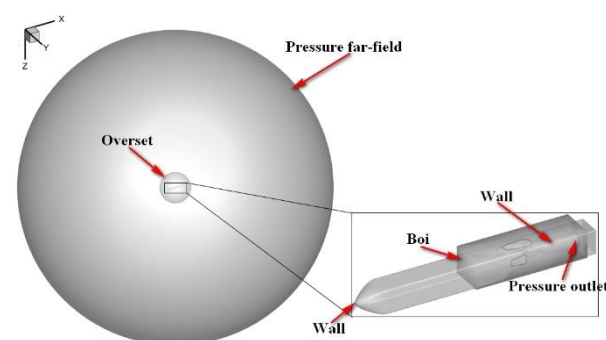


Figure 6. Setting of Transient Boundary Conditions.

Figure 6 shows the setting of transient boundary conditions. The pressure far-field boundary is used for the far-field, and the free-flow parameters are given according to the atmospheric conditions at 5 km altitude, $M_0 = 0.7$; the outlet of the inlet adopts the pressure outlet boundary condition, and the pressure is set to the corresponding pressure when $M_e = 0.4$; the interface between dynamic and static domains is set as the overset boundary condition; the body and inlet adopt non-slip adiabatic wall boundary.

3.3. Independence Analysis

3.3.1. Mesh Independence Analysis

The mesh-independence analysis takes the conventional submerged inlet as an example. In order to minimize the impact of the number of meshes on the accuracy of the results, four sets of mesh are finally obtained by adjusting the density of mesh nodes. The number of volume meshes is 0.9 million, 1.2 million, 3 million, and 5 million, respectively. The numerical simulation results and experimental results of four sets of mesh are shown in Table 1. Compared with the experimental results, the error of the calculated results is less than 0.65%, which indicates that the accuracy of the numerical solution of the flow field is basically independent of the number of meshes after the meshes are larger than 0.9 million. In order to save calculation time, this paper uses the node density of mesh scheme 1 to calculate.

Table 1. Comparison of different mesh schemes and experimental results.

Mesh Scheme	Number of Mesh (Million)	Total Pressure at outlet of the Inlet (Pa)	Error
1	0.9	68,696.44	0.00639
2	1.2	68,872.64	0.00384
3	3	69,108.51	0.00043
4	5	69,097.21	0.00059
experimental result [38]	/	69,138.49	/

It should be noted that the computational mesh used in this paper is unstructured polyhedral mesh. At the same density, the number of polyhedral meshes is much lower than that of conventional unstructured tetrahedral mesh. Taking the polyhedral mesh with a mesh number of about 0.9 million as an example, using the same face mesh, the same boundary layer setting, and the same volume mesh growth rate, the total volume mesh number when dividing the tetrahedral mesh is about 3.7 million, of which the boundary layer prism mesh accounts for about 0.7 million, and the tetrahedral mesh far from the wall accounts for about 3 million. The geometry of the submerged inlet and projectile studied in [34,38] is similar to that in this paper. The number of calculation mesh is 0.9 million, so the calculation mesh used in this paper can meet the requirements of calculation accuracy.

3.3.2. Time Step Independence Analysis

The full name of the CFL condition is the Courant–Friedrich–Lewy condition. The CFL condition is an important parameter for the stability and convergence of numerical calculation, so it is a very important condition in computational fluid dynamics [39]. In the three-dimensional case, the CFL condition is:

$$C = \frac{u_x \Delta t}{\Delta x} + \frac{u_y \Delta t}{\Delta y} + \frac{u_z \Delta t}{\Delta z} \leq C_{\max} \quad (1)$$

In the formula, u_x , u_y , and u_z are the velocities in the x , y , and z directions during the mesh movement; Δt is the time step; Δx , Δy , and Δz are the minimum mesh size of the calculation mesh in the x , y , and z directions. Generally, the value of C_{\max} is 1, which physically means that the displacement of fluid in unit time step cannot exceed the unit length of the calculation mesh, otherwise the calculation may diverge.

In this paper, two time steps of 0.001 s and 0.0001 s are selected for transient calculation, which can meet the CFL condition.

At the same time, in order to give consideration to the computational efficiency of the flow field simulation, two time steps of 0.001 s and 0.0001 s are used to analyze the step independence, taking the pitching maneuver of the conventional submerged inlet as an example. Let the mesh in the internal rotation domain conduct a simple pitching maneuver around the y -axis. The pitching angle changes in a sine motion. The average angular velocity of the sine motion is $60^\circ/\text{s}$ and the amplitude is 30° .

Figure 7 shows the calculation results of the total pressure recovery coefficient at the outlet of the inlet under two time steps of 0.2 to 0.5 s. It can be seen from Figure 7 that the calculation results of the two step sizes are almost the same.

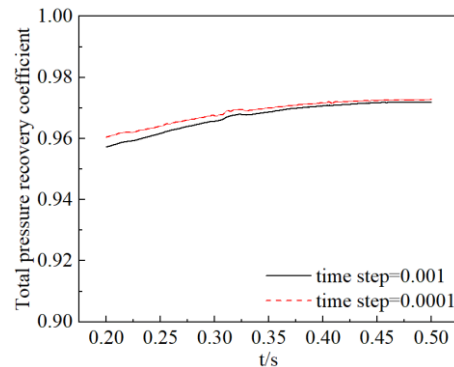


Figure 7. Calculation results of total pressure recovery coefficient at outlet of the inlet in two time steps of 0.2 to 0.5 s.

The average total pressure recovery coefficient in 0.2~0.5 s is shown in Table 2. When the step length is 0.001 s, the average total pressure recovery coefficient during 0.2 to 0.5 s is 0.966. When the step length is 0.0001 s, the average total pressure recovery coefficient is 0.968 during 0.2 to 0.5 s. Based on the calculation result with a step of 0.0001 s, the error of the calculation result with a step of 0.001 s is only 0.2%, which means that a step of 0.001 s is sufficient to accurately capture the flow field details. Considering the computational efficiency and accuracy, the step size used in the transient calculation is 0.001 s.

Table 2. Average total pressure recovery coefficient in 0.2~0.5 s.

Time Step (s)	Average σ in 0.2~0.5 s	Error
0.001	0.966	0.2%
0.0001	0.968	/

3.4. Example Verification

In order to verify the accuracy of the numerical simulation method in this paper, the flow field of the missile body and the submerged inlet in the literature [40] was simulated and compared with the relevant experimental data. The calculation model is shown in Figure 8.

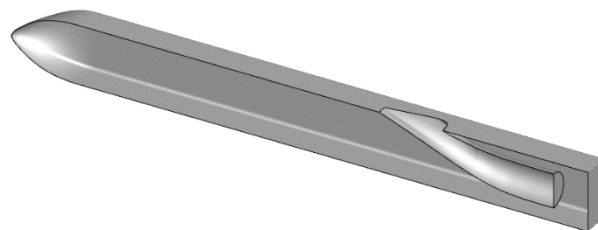


Figure 8. Reference [40] Submerged inlet.

In the case of no sideslip, the flow field is symmetrical, so the half model is used for mesh generation to reduce the computational cost. Unstructured polyhedral mesh is adopted, and the far field is in the shape of a cuboid, with the length, width, and height of 40 m, 10 m, and 10 m, respectively. The local mesh of the missile body surface and inlet is shown in Figure 9. The total number of meshes in the computational domain is 0.5 million, the number of boundary layers is 10, the height of the first layer is 0.01 mm, and the growth rate is 1.2.

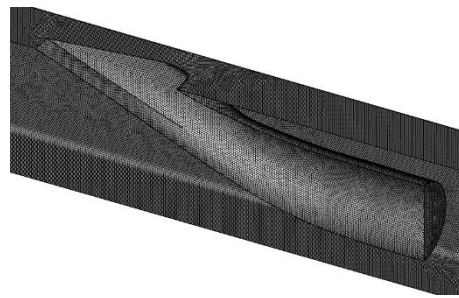


Figure 9. Local mesh of missile body surface and inlet.

The calculation conditions are set according to the experimental conditions in the literature, $M_0 = 0.73$, and the altitude is 5 km. The pressure far-field boundary condition is adopted in the far field of the computational domain, and the outlet of the inlet is set as the pressure outlet. The inlet and missile body walls are set as non-sliding walls.

The experimental results show that σ of the missile body and the submerged inlet is 0.9220 when $M_0 = 0.73$ and $M_e = 0.4$. In the calculation results, σ at the outlet of the inlet is 0.9244, and the error between the numerical simulation results and the experimental results is only 0.26%. Figure 10 shows the total pressure distribution at the outlet of the inlet, which is also in good agreement with the experimental results. Therefore, the accuracy of the numerical simulation method in this paper is verified.

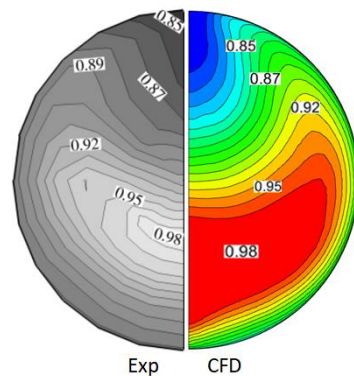


Figure 10. Total pressure distribution at the outlet of the inlet.

4. The Flow Characteristics of Two Inlet Configurations under High Maneuver Condition

In order to simplify the problem, the change of inlet flow characteristics caused by the change of α when $\beta = 0^\circ$ and the change of inlet flow characteristics caused by the change of β when $\alpha = 0^\circ$ are considered respectively in the calculation.

The total pressure recovery coefficient at outlet of the inlet and total pressure distortion index are commonly used to evaluate the inlet aerodynamic performance. This paper also uses the total pressure recovery coefficient and total pressure distortion index to evaluate the inlet performance.

The total pressure recovery coefficient is defined as the ratio of the average total pressure at the outlet of the inlet to the total pressure the of free flow, expressed as σ . The calculation formula is as follows:

$$\sigma = \frac{P_{AIP}}{P_0} \quad (2)$$

In the formula, P_{AIP} is the average total pressure at the AIP section at the outlet of the inlet, and P_0 is the total pressure of freestream.

The total pressure distortion index is the main parameter used to evaluate the airflow uniformity at the outlet of the inlet, expressed as D_1 . The calculation formula is as follows:

$$D_1 = \frac{P_{AIP,max} - P_{AIP,min}}{P_{AIP,max}} \quad (3)$$

where $P_{AIP,max}$ is the maximum total pressure of the AIP section at the outlet of the inlet and $P_{AIP,min}$ is the minimum total pressure of the AIP section at the outlet of the inlet.

4.1. Analysis of Steady Flow Characteristics

During the steady state calculation, the attitude of the missile body and the incoming flow conditions remain unchanged. The total pressure recovery coefficient and total pressure distortion index on the outlet of the inlet section are shown in Figure 11. Configuration I represents the conventional submerged inlet, and configuration II represents the distributed inlet. It can be seen from Figure 11a,b that the σ of the two inlet configurations has a very similar trend with the α . In the range of -30° to 30° , α first rises, then decreases, and then rises. α is above 0.88. The total pressure distortion indices of the two inlet configurations are also very similar with the angle of attack, showing a trend of first rising and then declining in the range of -30° to 30° , and the total pressure distortion indices are below 0.2. The σ of the conventional submerged inlet is slightly higher than that of the distributed inlet, and D_1 of the conventional submerged inlet is slightly lower than that of the distributed inlet. This is because there is a certain airflow mixing phenomenon at the intersection of the auxiliary inlet and the main inlet in the distributed submerged inlet configuration, which brings a certain energy loss. In addition, the auxiliary inlet located on both sides of the missile body in the distributed submerged inlet configuration will cause low-energy gas in the boundary layer on both sides of the missile body to flow into the inlet, which will also lead to a decrease in total pressure and an increase in total pressure distortion.

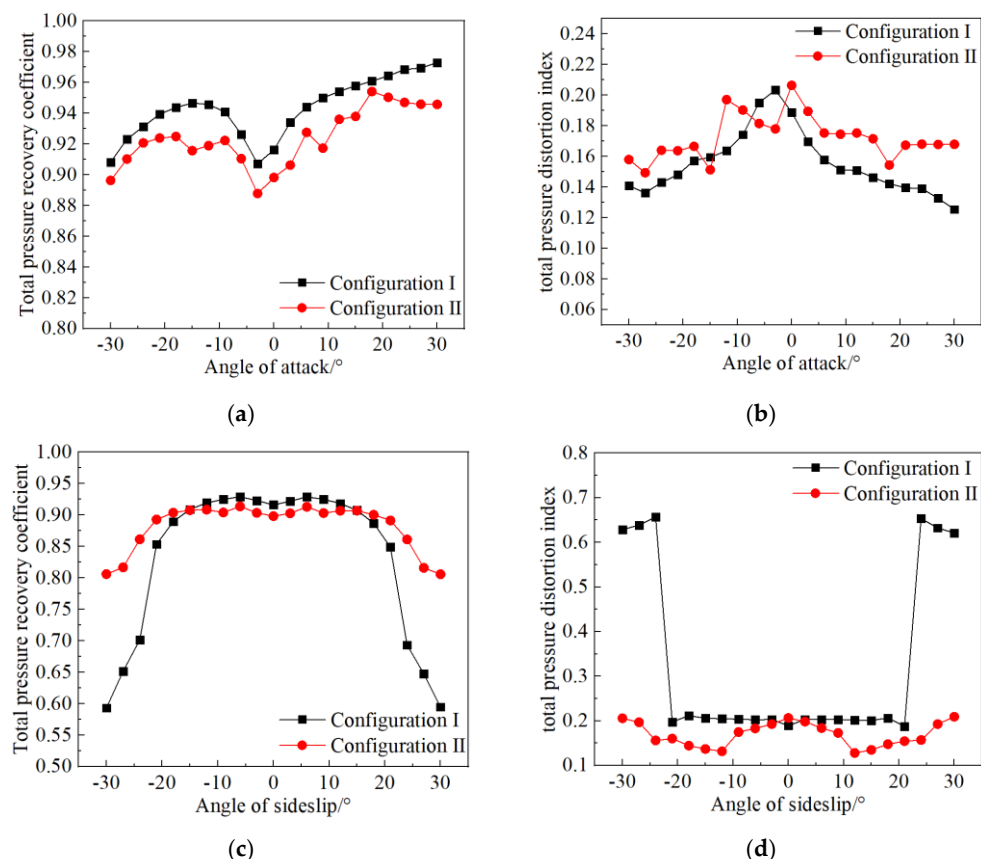


Figure 11. Steady State Calculation Results. (a) Total pressure recovery coefficient versus angle of attack, (b) Total pressure distortion index versus angle of attack, (c) Total pressure recovery coefficient versus angle of sideslip, (d) Total pressure distortion index versus angle of sideslip.

It can be seen from Figure 11c,d that the limit of sideslip angle of conventional submerged inlet configuration is $\pm 20^\circ$. When the absolute value of β is greater than 20° , σ at the outlet drops sharply; when β reaches $\pm 30^\circ$, σ is less than 0.6. When β is within

$\pm 20^\circ$, D_1 of the conventional submerged inlet is about 0.22, and when the β reaches $\pm 30^\circ$, the D_1 suddenly increases to 0.7. This is because the submerged inlet mainly relies on the entrainment vortices generated by the side edges to drive the external airflow into the inlet. When the absolute value of the β is less than 20° , the side edges on both sides of the inlet can generate the entrainment vortices that are beneficial to the inlet to drive the external airflow into the inlet. When the absolute value of the β is greater than 20° , the side edge with the same direction as the incoming flow can no longer generate the entrainment vortices beneficial to the air inlet. Although the side ribs opposite to the incoming flow can still produce entrainment vortices that are conducive to the intake, the effect of driving the external airflow into the inlet is greatly weakened because the airflow changes the angle of the airflow through the side ribs during the flow around the body.

When the β is greater than $\pm 20^\circ$, the σ at the outlet of the distributed submerged inlet also decreases to some extent, but the decrease is small. When β reaches $\pm 30^\circ$, the σ at the outlet of the distributed inlet is still greater than 0.80. D_1 of the distributed inlet is always kept within 0.2. When β is $\pm 10^\circ$, the D_1 is about 0.12. In the large sideslip flight state, compared with the conventional submerged inlet configuration, σ at the outlet of the distributed submerged inlet configuration is increased by 44.2%, and D_1 is reduced by 66.3%.

In order to better reveal the formation and development mechanism of flow in the submerged inlet under large sideslip condition, and Figure 12 lists the main flow characteristics in the inlet under typical sideslip angles. It can be seen from Figure 12a that when $\beta = -21^\circ$, the side edges on both sides of the inlet of the conventional submerged inlet can generate entrainment vortices. However, due to the different angles of the airflow passing through the side edges on both sides, the intensity of the entrainment vortices generated by the side edges with the same direction as the incoming flow is weak, and part of the airflow is not drawn into the inlet. With the further increase of β , the intensity of the entrainment vortices generated by the side edges with the same direction of the incoming flow gradually weakens. It can be seen from the Figure 12b–d that when the absolute value of β is greater than 24° , the entrainment vortices beneficial to the intake cannot be generated, and at the same time, there is obvious air separation. An obvious low total pressure area can be observed at the outlet of inlet. The area of the low total pressure area accounts for about one third of the total area. The same problem is also encountered at the side edges of the main inlet of the distributed inlet configuration. However, since the auxiliary inlets on both sides have a certain windward surface during sideslip maneuver flight, which can provide high energy airflow for the intake system to make up for the deficiencies of the inlet during large sideslip flight, no obvious low-pressure area is observed at the outlet of the inlet, and σ is above 0.8.

4.2. Analysis of Transient Flow Characteristics

In order to simplify the problem, only the internal flow characteristics of the inlet during pitch maneuver and yaw maneuver are investigated [41–43]. In the course of pure pitch maneuver with constant incoming flow conditions, the angle of attack of the aircraft is equal to the angle of pitch; The angle of attack of the aircraft is equal to the sideslip angle during the simple yaw maneuver with the inflow conditions unchanged. In order to be consistent with the description in the steady-state analysis, the pitch angle in the periodic pitch maneuver is called the angle of attack, and the yaw angle in the periodic yaw maneuver is called the sideslip angle.

The background mesh remains stationary, and the given internal rotation domain mesh rotates along with the aircraft around the center of gravity in a single-axis, and the law is a sine function. In order to study the effect of pitch rate on the dynamic characteristics of the inlet, two motion laws shown in Figure 13 are applied to the mesh in the rotating domain. Due to the characteristics of the chord function, the angular velocity at different angles in the process of motion is different. The velocity is low near the peak or trough, and high away from the peak or trough. Therefore, the angular velocity marked in the figure is the average angular velocity.

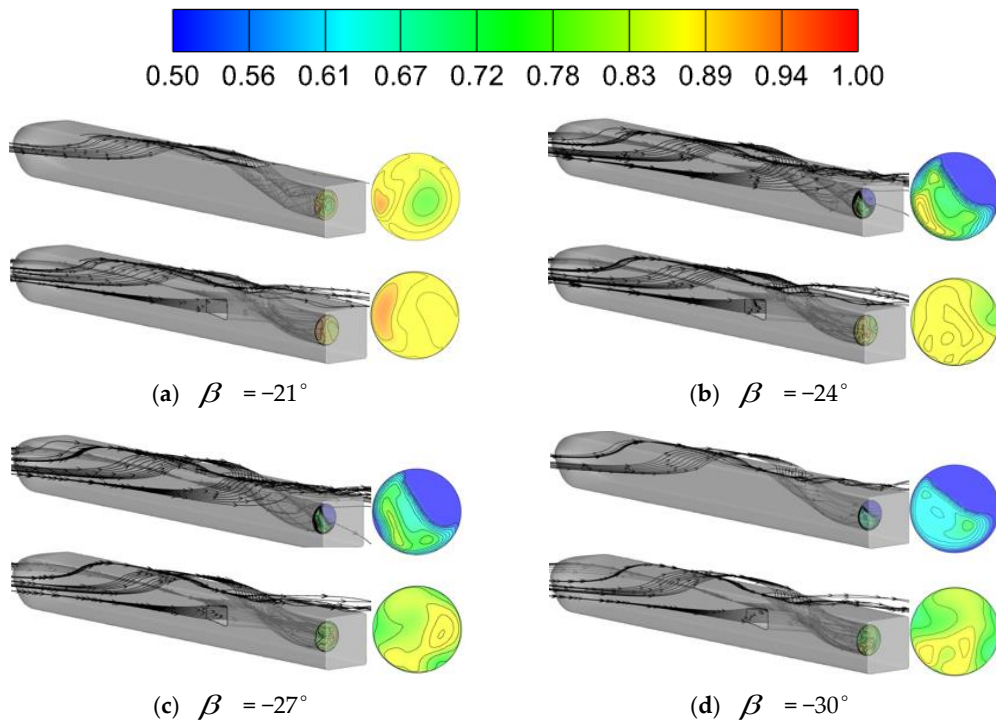


Figure 12. Flow characteristics of inlet under typical sideslip angles.

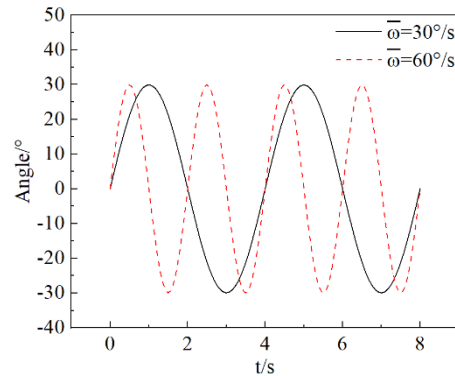


Figure 13. Two Motion Laws of Transient Maneuver.

The two equations of motion law are:

$$A_1 = \frac{\pi}{6} \sin\left(\frac{\pi}{2}t\right) \tag{4}$$

$$\omega_1 = \frac{\pi^2}{12} \cos\left(\frac{\pi}{2}t\right) \tag{5}$$

$$A_2 = \frac{\pi}{6} \sin(\pi t) \tag{6}$$

$$\omega_2 = \frac{\pi^2}{6} \cos(\pi t) \tag{7}$$

4.2.1. Flow Characteristics of the Submerged Inlet with the Rapid Pitch Maneuver

Let the mesh in the internal rotating region conduct a simple pitching maneuver around the y-axis at two angular velocities, and the calculated total pressure recovery coefficient of the outlet of the inlet is shown in Figure 14.

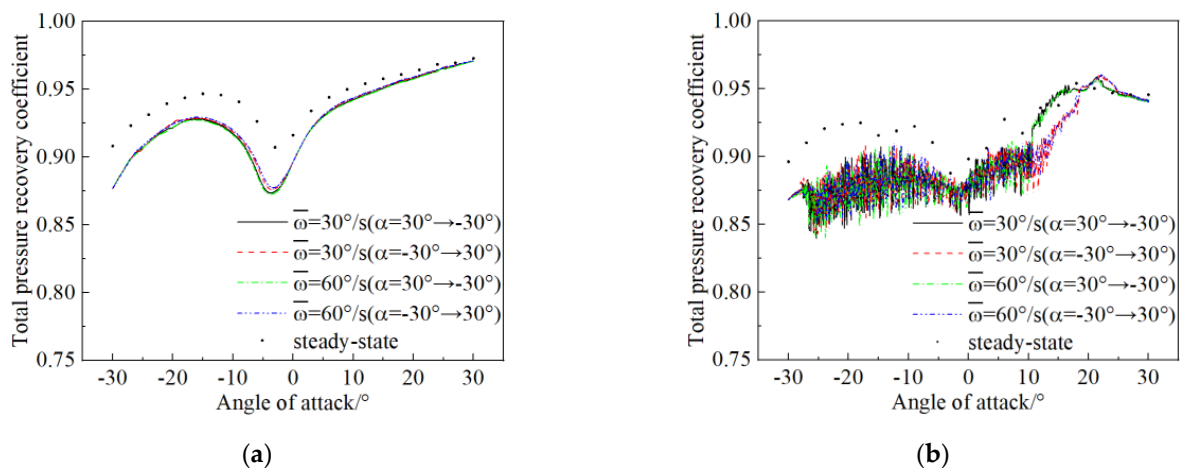


Figure 14. Total pressure recovery coefficient versus angle of attack. (a) Conventional submerged inlet, (b) Distributed submerged inlet.

It can be seen from Figure 14 that the instantaneous total pressure recovery coefficient of two configurations of the inlet during pitching maneuver shows a trend of first increasing, then decreasing and then increasing with the increase of α , which is consistent with the trend of equivalent steady state calculation results. However, the value of σ calculated in the steady state is slightly higher than that calculated in the transient state. When the $\alpha = -30^\circ$, the difference between the results calculated in the steady state and the results calculated in the transient state is the largest, about 0.05. The difference decreases with the increase of α . When α reaches 30° , there is almost no difference between the steady-state and transient results.

It can be seen from Figure 14a that there is a certain hysteresis phenomenon in the pitching maneuver cycle. In the pitching up process (in the process of α from -30° to 30°), the total pressure recovery coefficient is slightly lower than that in the pitching down process (in the process of α from 30° to -30°), and the hysteresis phenomenon is obvious in the range of -10° to 0° .

It can be seen from Figure 14b that σ of the distributed inlet configuration fluctuates significantly during the pitching maneuver period. In the range of α from 10° to 20° , it can be clearly observed that σ of the pitching up maneuver (in the process of α from -30° to 30°) is significantly lower than that of pitching down maneuver (in the process of α from 30° to -30°). This is because the submerged inlet is located in the belly of the missile, and the airflow has an upward velocity relative to the missile in the process of pitching down, which increases the included angle between the airflow and the plane where the submerged inlet opening is located, thus increasing the windward surface of the inlet to facilitate air intake. In contrast, the airflow has a downward velocity relative to the missile in the process of pitching up, which reduces the angle between the airflow and the plane of the submerged inlet opening, and thus reduces the windward surface of the inlet, which is not conducive to air intake.

The hysteresis of the conventional submerged inlet configuration is more obvious in the range of -10° to 0° , while the hysteresis of the distributed submerged inlet configuration is more obvious in the range of 10° to 20° . The reason for this difference is the different intake mechanism of the two configurations. Specifically, the conventional submerged inlet mainly relies on the suction vortex generated by the side edge at the inlet to drive the airflow into the inlet, so it is more sensitive to the angle between the airflow and the side edge when the airflow passes through the side edge. In addition to the entrained vortex generated by the side edges of the main inlet, the side edges of the auxiliary inlet distributed on both sides of the missile body are also generating entrained vortex beneficial to the intake. In the process of angle of attack change, the entrainment vortices intensity of the main inlet

and the entrainment vortices intensity of the auxiliary inlet are not synchronized, so the angle of hysteresis of the two configurations is different.

4.2.2. Flow Characteristics of Submerged Inlet with Rapid Yaw Maneuver

Let the mesh in the internal rotating region perform a simple yaw maneuver around the z-axis at two angular velocities, and the calculated total pressure recovery coefficient of the outlet of the inlet plane is shown in Figure 15.

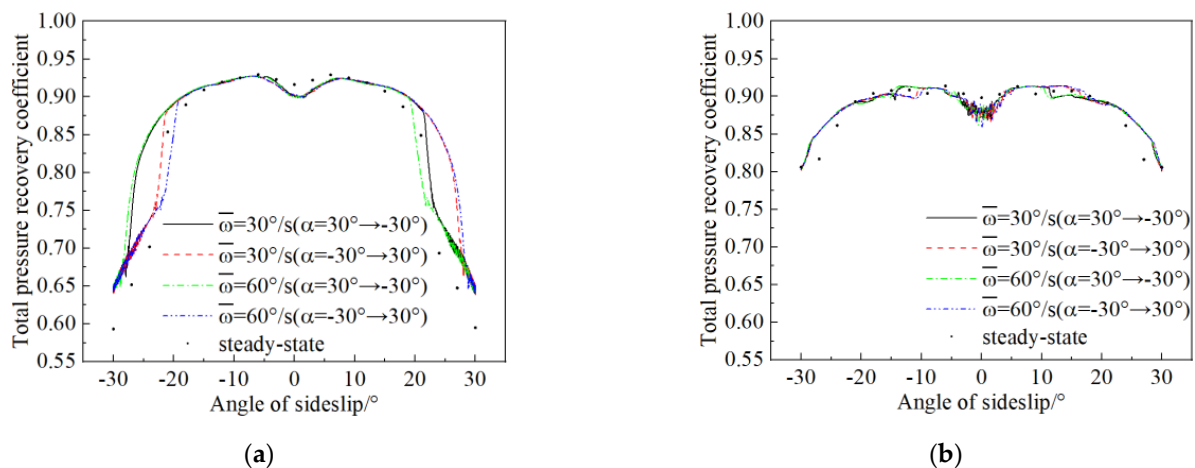


Figure 15. Total pressure recovery coefficient versus angle of sideslip. (a) Conventional submerged inlet, (b) Distributed submerged inlet.

It can be seen from Figure 15 that in the range of β from -30° to 30° during the yaw maneuver of the inlet of two configurations, the σ first increases, then decreases, then increases, and then decreases with the increase of β , which is consistent with the trend of equivalent steady state calculation. When the absolute value of the β is less than 20° , the transient and steady calculation results are almost consistent. When the β is close to $\pm 30^\circ$, the transient calculation result is slightly higher than the steady calculation result.

It can be seen from Figure 15a that the σ of the conventional submerged inlet drops sharply when the absolute value of β is greater than 20° , and σ is less than 0.65 when the $\beta = \pm 30^\circ$. $\beta = 0^\circ$ is considered as the equilibrium position. In the process of deviating from the equilibrium position, the σ is higher than that of approaching the equilibrium position. This phenomenon is particularly obvious in the range of $\beta -30^\circ$ to -20° and 20° to 30° . This is due to the hysteresis effect of the flow field. Specifically, in the case of large sideslip flight, the side edge on the same side of the incoming flow can no longer produce entrainment vortices that are conducive to air intake, and the side edge on the opposite side of the incoming flow play a major role. In the process of deviating from the equilibrium position, the relative motion of the missile increases the angle between the airflow and the opposite side edge, thus increasing the intensity of the entrainment vortices, which is conducive to improving the intake efficiency. At the same time, it can be observed that the greater the angular velocity, the more obvious the hysteresis phenomenon.

From Figure 15b, it can be seen that the distributed submerged inlet configuration also has a significant decrease when the absolute value of the β is greater than 20° , but the decrease is smaller than that of the conventional submerged inlet configuration. When the absolute value of the β is 30° , σ is still greater than 0.8. This is because the special structure of the distributed submerged inlet creates additional intake conditions, so that it is no longer overly dependent on the entrainment vortices generated by the side edge to drive the external airflow into the inlet. There is an obvious hysteresis phenomenon near the sideslip angle of 12° . In the process of deviating from the equilibrium position, σ is higher than that near the equilibrium position. This is mainly because the auxiliary inlet on the opposite side of the incoming flow plays a major role in the large sideslip maneuver

flight. In the process of deviating from the equilibrium position, the angle between the airflow and the inlet plane of the distributed inlet on the opposite side of the incoming flow is increased, which in turn increases the windward surface and leads to a higher total pressure recovery coefficient. At the same time, it can be observed that the greater the angular velocity, the more obvious the hysteresis phenomenon.

5. Conclusions

In this paper, based on the flow characteristics of the submerged inlet, the distributed submerged inlet configuration applied to the large maneuvering state is proposed. Firstly, the accuracy of the numerical simulation method is verified. Then, the flow characteristics of the conventional submerged inlet and the distributed submerged inlet are analyzed respectively in the steady and transient large maneuvering states, and the following conclusions can be obtained:

1. The trend of transient and equivalent steady state calculation results of the two configurations of inlet during pitching maneuver is consistent, but the value of σ calculated in steady state is slightly higher than that calculated in transient state. When $\alpha = -30^\circ$, the difference between the steady-state and transient results is the largest, which decreases with the increase of α . When $\alpha = 30^\circ$, there is almost no difference between the steady and transient results. In the course of the yaw maneuver, the trend of transient and equivalent steady state calculation results of σ is consistent, but the value of σ calculated in steady state is slightly lower than that calculated in transient state. When the absolute value of β is less than 20° , the transient and steady calculation results are almost consistent. When β is close to $\pm 30^\circ$, the transient calculation result is slightly higher than the steady calculation result.
2. When flying at a high angle of attack, the σ and D_1 of the distributed submerged inlet and conventional submerged inlet have little difference. Compared with the conventional submerged inlet configuration, σ at the outlet of the distributed submerged inlet configuration is increased by 44.2% and D_1 is reduced by 66.3% in the case of high sideslip flight, which greatly improves the performance of the inlet in the case of high sideslip maneuver flight, and significantly improves the sideslip limit of the submerged inlet.
3. In the transient calculation results of the large maneuver flight state, the two submerged inlet configurations show an obvious hysteresis effect, which is more obvious with the increase of angular velocity.

Author Contributions: Conceptualization, J.Z.; methodology, J.Z.; software, J.Z.; validation, J.Z.; formal analysis, J.Z.; investigation, J.Z.; resources, J.Z.; data curation, J.Z.; writing—original draft preparation, J.Z.; writing—review and editing, B.M.; visualization, J.Z.; supervision, B.M.; project administration, B.M.; funding acquisition, B.M. All authors have read and agreed to the published version of the manuscript.

Funding: This research was funded by [the National Natural Science Foundation of China] grant number [12202363] and [the Natural Science Basic Research Program of Shaanxi] grant number [2021JQ-084].

Institutional Review Board Statement: Not applicable.

Informed Consent Statement: Not applicable.

Data Availability Statement: Not applicable.

Acknowledgments: Not applicable.

Conflicts of Interest: The authors declare no conflict of interest.

Nomenclature

D_1	total pressure distortion index
P	mass-average total pressure
P_{AIP}	mass-average total pressure over the aerodynamic interface plane, Pa
P_0	freestream total pressure, Pa
$P_{AIP,max}$	maximum total pressure over the aerodynamic interface plane, Pa
$P_{AIP,min}$	minimum total pressure over the aerodynamic interface plane, Pa
M	Mach number
M_e	Mach number at the exit
M_0	freestream Mach number
α	angle of attack, °
β	angle of sideslip, °
A	instantaneous angle in sinusoidal motion, °
ω	instantaneous angular velocity in sinusoidal motion, °/s
$\bar{\omega}$	average angular velocity of sinusoidal motion, °/s
Subscripts	
0	freestream
e	exit
AIP	the aerodynamic interface plane
AIP, max	maximum value on the aerodynamic interface plane
AIP, min	minimum value on the aerodynamic interface plane

References

- Walsh, K.R.; Yuhas, A.J.; Williams, J.G.; Steenken, W.G. *Inlet Distortion for an F/A-18A Aircraft during Steady Aerodynamic Conditions up to 60 Deg Angle of Attack*; National Aeronautics and Space Administration, Dryden Flight Research Center: Edwards, CA, USA, 1997.
- Smith, C.F.; Podleski, S.D.; Barankiewicz, W.S.; Zeleznik, S.Z. Comparison of the F/A-18A inlet flow analysis with flight data. II. *J. Aircr.* **1996**, *33*, 457–462. [CrossRef]
- Yuhas, A.J.; Steenken, W.G.; Williams, J.G.; Walsh, K.R. *F/A-18A Inlet Flow Characteristics During Maneuvers with Rapidly Changing Angle of Attack: NASA-TM-104327[R]*; NASA: Washington, DC, USA, 1997.
- Steenken, W.G.; Williams, J.G.; Walsh, K.R. *Inlet Flow Characteristics During Rapid Maneuvers for an F/A-18A Airplane: NACA-TM-206587[R]*; NASA: Washington, DC, USA, 1999.
- Steenken, W.G.; Williams, J.G.; Yuhas, A.J.; Walsh, K.R. *An Inlet Distortion Assessment During Aircraft Departures at High Angle of Attack for an F/A-18A Aircraft: NACA-TM-206587[R]*; NASA: Washington, DC, USA, 1997.
- Podleski, S. Installed F/A-18 inlet flow calculations at 60 deg angle-of-attack and 10 deg side slip. In Proceedings of the 29th Joint Propulsion Conference and Exhibit, Monterey, CA, USA, 28–30 June 1993.
- Bruns, J.E.; Smith, C.F. Installed F/A-18 inlet flow calculations at a high angle of attack. *J. Propuls. Power* **1971**, *10*, 110–115. [CrossRef]
- Wu, C.J.; Nie, B.W.; Kong, P. Test Technology on Unsteady Characteristics of Inlet Flow during Fighter Plane Maneuvers. *J. Exp. Fluid Mech.* **2013**, *27*, 39–42. (In Chinese)
- Yang, Y.K. The study on bump inlet dynamic characteristics under aircraft fast pitching maneuver. *J. Exp. Fluid Mech.* **2013**, *27*, 39–42.
- Xiang, H. The use of URANS algorithm based on overset mesh in aircraft inlet engineering. In Proceedings of the 5th Engine Inlet and Nozzle Conference, Nanjing, China, 19–21 January 2017; pp. 371–379. (In Chinese)
- Xiang, H. The calculation of inlet dynamic characteristics under aircraft rapid pitching maneuver. In Proceedings of the 6th National Inlet and Nozzle Conference, Xining, China, 16–19 October 2018; pp. 633–640.
- Xiang, H. The inlet dynamic characteristics under aircraft rapid pitching maneuver. In Proceedings of the Chinese Society of Aeronautics and Astronautics Aircraft Branch 14th Academic Forum and Exchange, Chengdu, China, 21–23 November 2018; pp. 563–570. (In Chinese)
- Xiang, H.; Yang, Y.K.; Xie, J.R.; Wu, Y. Inlet aerodynamic characteristics of fighter under high angle of attack and post-stall maneuver. *Acta Aeronaut. Sin.* **2020**, *41*, 523460. (In Chinese)
- Jia, G.; Yin, P.; Shao, S.; Wang, J. Review of RCS measurement and imaging methods of stealth aircraft. *J. Natl. Univ. Def. Technol.* **2022**, *44*, 93–103.
- Zheng, R.; Qi, N.; Zhang, Q.; Xiao, Z. Integrated Investigation of Aerodynamic Shape and Stealth Performance for Supersonic Vehicle with “X” Sawtooth Lip Inlet. *J. Propuls. Technol.* **2017**, *38*, 8.
- Yu, X.; Zhao, Y. A Study on Stealth Technology in UAV Inlet Design. *Flight Dynamics* **2007**, *25*, 69–72.
- Shi, L.; Guo, R. Electromagnetic Scattering of a Submerged Inlet. *Acta Aeronaut. Et Astronaut. Sin.* **2008**, *29*, 1098–1104.
- Anderson, B.H.; Reddy, D.R.; Kapoor, K. Study on computing separating flows within a diffusion inlet S-duct. *J. Propuls. Power* **1994**, *10*, 661. [CrossRef]

19. Harloff, G.J.; Smith, C.F.; Bruns, J.E.; DeBonis, J.R. Navier-Stokes analysis of three-dimensional S-ducts. *J. Aircr.* **1993**, *30*, 526–533. [CrossRef]
20. Axelson, J.A.; Taylor, R.A. *Preliminary Investigation of the Transonic Characteristics of an NACA Submerged Inlet*; Technical Report Archive & Image Library: Kingston, Ontario, Canada, 1950.
21. Hall, C.F.; Frank, J.L. *Ram-Recovery Characteristics of NACA Submerged Inlets at High Subsonic Speeds*; Technical Report Archive & Image Library: Kingston, Ontario, Canada, 1948.
22. Mossman, E.A.; Randall, L.M. *An Experimental Investigation of the Design Variables for NACA Submerged Duct Entrances*; Technical Report Archive & Image Library: Kingston, Ontario, Canada, 1948.
23. Frank, J.L. *Pressure-Distribution and Ram-Recovery Characteristics of NACA Submerged Inlets at High Subsonic Speeds*. [R]. NACA RM-A50E02; NASA: Washington, DC, USA, 1950.
24. Anderson, W.E.; Frazer, A.C. *Investigation of an NACA Submerged Inlet at Mach Numbers from 1.17 to 1.99*; Technical Report Archive & Image Library: Kingston, ON, Canada, 1952.
25. Seddon, J.; Goldsmith, E.L. *Intake Aerodynamics*; American Institute of Aeronautics and Astronautics, 1985.
26. Guo, R.W.; Liu, S.Y. Design of submerged inlet. *J. Nanjing Univ. Aeronaut. Astronaut.* **2002**, *33*, 8–12.
27. Yang, A. An Investigation on Design and Performance for a Submerged Air Intake. *Acta Aerodyn. Sin.* **1998**, *16*, 154.
28. Taskinoglu, E.; Knight, D. Design Optimization for Submerged Inlets. In Proceedings of the 41st Aerospace Sciences Meeting and Exhibit, Reno, NV, USA, 6–9 January 2003.
29. Yu, A.; Le, J.; Guo, R. A study of the design method and an investigation of high speed experiments for a submerged inlet under a stealthy shaped fuselage. *Acta Aerodyn. Sin.* **2007**, *25*, 150–156.
30. Wang, Y.G.; Wang, C.H.; Xiao, Y.C.; Chen, B.; Zhou, S.; Guo, J.T.; Sun, M.W. Construction methodology for lip surface of a submerged inlet. *Aerosp. Sci. Technol.* **2016**, *54*, 340–352. [CrossRef]
31. Sun, S.; Guo, R. Experimental Research of Effects of Entrance Parameters on Performance of Submerged Inlet. *Acta Aeronaut. Et Astronaut. Sin.* **2005**, *26*, 268–275.
32. Cheng, D.S.; Sun, S.; Wen, Y.F.; Tan, H.J. Submerged inlet performance improvement with blowing on fuselage. *J. Aerosp. Power* **2012**, *27*, 1131–1138.
33. Cheng, D.S.; Tan, H.J.; Sun, S.; Tong, Y. Computational Study of a High-Performance Submerged Inlet with Bleeding Vortex. *J. Aircr.* **2012**, *49*, 852–860. [CrossRef]
34. Xie, W.Z.; Yang, S.Z.; Zeng, C.; Liao, K.; Ding, R.; Zhang, L.; Guo, S. Effects of forebody boundary layer on the performance of a submerged inlet. *Aeronaut. J.* **2021**, *125*, 1260–1281. [CrossRef]
35. Saheby, E.B.; Huang, G.; Qiao, W.; Tang, W. Highly Integrated Inlet Design Based on the Ridge Concept. *J. Propuls. Power* **2016**, *32*, 1505–1515. [CrossRef]
36. Huang, G.; Saheby, E.B.; Akhlaghi, M.; Yu, Z. Effects of Ridge Configuration on the Performance of Integrated inlets. In Proceedings of the Aiaa/SAE/ASAE Joint Propulsion Conference, Salt Lake City, UT, USA, 25–27 July 2016.
37. Perez, C.C.; Ferreira, S.B.; Silva, L.; De Jesus, A.B.; Oliveira, G.L. Computational Study of Submerged Air Inlet Performance Improvement Using Vortex Generators. *J. Aircr.* **2007**, *44*, 1574–1587. [CrossRef]
38. Sun, S.; Guo, R.; Wu, Y. Characterization and Performance Enhancement of Submerged Inlet with Flush-Mounted Planar Side Entrance. *J. Propuls. Power* **2007**, *23*, 987–995. [CrossRef]
39. Parent, B.; Shneider, M.N.; Macheret, S.O. Detailed Modeling of Plasmas for Computational Aerodynamics. *Aiaa J.* **2016**, *54*, 898–911. [CrossRef]
40. Sun, S.; Guo, R.W. Numerical Analysis and Experimental Validation of a Submerged Inlet on the Plane Surface. *Chin. J. Aeronaut.* **2005**, *18*, 199–205. [CrossRef]
41. Karasu, I.; Tumse, S.; Tasci, M.O.; Sahin, B.; Akilli, H. Near-surface particle image velocimetry measurements over a yawed slender delta wing. *Proc. Inst. Mech. Eng. Part G J. Aerosp. Eng.* **2021**, *235*, 2466–2478. [CrossRef]
42. Tasci, M.O.; Pektas, M.C.; Tumse, S.; Karasu, I.; Sahin, B.; Akilli, H. The impact of the pitching motion on the structure of the vortical flow over a slender delta wing under sideslip angle. *J. Vis.* **2021**, *24*, 437–442. [CrossRef]
43. Tumse, S.; Tasci, M.O.; Karasu, I.; Sahin, B. Effect of ground on flow characteristics and aerodynamic performance of a non-slender delta wing. *Aerosp. Sci. Technol.* **2021**, *110*, 106475. [CrossRef]

Disclaimer/Publisher’s Note: The statements, opinions and data contained in all publications are solely those of the individual author(s) and contributor(s) and not of MDPI and/or the editor(s). MDPI and/or the editor(s) disclaim responsibility for any injury to people or property resulting from any ideas, methods, instructions or products referred to in the content.

Article

Drag Reduction Analysis of the Hydrostatic Bearing with Surface Micro Textures

Youyun Shang ^{1,*}, Kai Cheng ^{2,†}, Qingshun Bai ¹ and Shijin Chen ¹¹ School of Mechatronics Engineering, Harbin Institute of Technology, Harbin 150001, China² Department of Mechanical and Aerospace Engineering, Brunel University London, Uxbridge UB8 3PH, UK

* Correspondence: shangyy@alu.hit.edu.cn

† These authors contributed equally to this work.

Abstract: Surface microtexturing has been widely used due to its good hydrophobic or drag reduction characteristics, and become an effective method to improve product performance and reduce energy consumption. This paper mainly discusses the improvement of microtextures on the dynamic pressure characteristics of hydrostatic bearings, and explores the effects of texture parameters on carrying capacity, macroscopic wall two-plane shear force, cavity area and other factors. In the oil film model calculation of the smooth wall surface of the radial hydrostatic bearing under the action of high speed and large external load, the oil film divergent wedge often has a negative pressure area, which is obviously not in line with the actual situation, so the cavitation effect needs to be considered. The CFD analysis method of the “gas-oil” two-phase flow model was carried out by using the mixture model to seek the optimal texture model scheme and thus to improve the load carrying capacity (LCC) and reduce the wall shear force. The effects of the texture area arrangement and geometric parameters on the lubrication characteristics were compared and analyzed. It is found that the carrying capacity of local texture is better than that of global texture, and different texture arrangements can achieve better drag reduction rates. The work presented in this paper studies the lubrication of the surface texture of a hydrostatic bearing. Taking the oil film carrying capacity and shear force as the target parameters, the factors, such as texture morphology, geometric parameters, texture distribution and cavitation phenomenon, are investigated through simulation and experimental methods. The surface textured hydrostatic bearing is expected to obtain the maximum oil film carrying capacity and the minimum friction resistance. The analysis results show that by arranging the partial streamwise texture at the rear end of the diverging wedge, the maximum shear force of the wall can be reduced by about 15%, and the LCC can be increased by about 18%.

Keywords: CFD method; cavitation effects; drag reduction; microtexture; hydrostatic bearing

Citation: Shang, Y.; Cheng, K.; Bai, Q.; Chen, S. Drag Reduction Analysis of the Hydrostatic Bearing with Surface Micro Textures. *Appl. Sci.* **2022**, *12*, 10831. <https://doi.org/10.3390/app122110831>

Academic Editors: Josep Maria Bergada and Gabriel Bugeda Castellort

Received: 9 August 2022

Accepted: 17 October 2022

Published: 26 October 2022

Publisher's Note: MDPI stays neutral with regard to jurisdictional claims in published maps and institutional affiliations.



Copyright: © 2022 by the authors. Licensee MDPI, Basel, Switzerland. This article is an open access article distributed under the terms and conditions of the Creative Commons Attribution (CC BY) license (<https://creativecommons.org/licenses/by/4.0/>).

1. Introduction

Surface microtexturing has gradually attracted attention due to its good hydrophobicity and drag reduction properties, which has become an effective way to improve the performance of new products and reduce energy consumption. Since Hamilton and Halavit [1] first proposed to process the microstructure on the surface of the friction pair to obtain the dynamic pressure effect, many scholars have carried out research in this area. The effects of texture morphology, geometric parameters, texture distribution and environmental factors on the lubricating performance were investigated by simulation and experiment. Rahmani et al. [2] combined the Reynolds equation and surface discontinuity of the hydrostatic bearing to establish a model and studied the influence of various forms of surface texture on the friction and carrying capacity of the hydrostatic bearing and believed that the form of texture has a significant impact on the bearing lubrication performance; waist triangle, right triangle and rectangular microtextures significantly improved the lubricating performance. Sinanoğlu et al., used experimental methods to verify that the

trapezoid has a higher load-carrying capacity than the zigzag texture, and the maximum pressure value is reduced by 36% compared to the smooth journal. In terms of pit-like textures, Tala-Ighil et al. [3] analyzed the effects of spherical, cylindrical and parallelepiped textures on the minimum oil film thickness, maximum pressure, axial flow velocity and friction force on the shaft diameter surface under the condition of stable flow field by using the finite element method, and the cylindrical texture performance improved more. Wang [4] found through experiments that with a reasonable design of geometric shapes and distributions, micropits can obtain nearly 2.5 times the carrying capacity of smooth surfaces.

Rahmani's [2] research shows that texture height has a greater impact on tribological properties than texture area ratio. Through experimental comparison, Sinanoğlu [5] found that reducing the texture height and inclination would reduce the LCC. Cupillard [6] applied numerical methods to study the effect of microgrooves on the axial direction of the bearing pad wall on the lubricity of radial hydrostatic bearings when cavitation effects were considered. It shows that the microgrooves can increase the minimum oil film thickness and reduce the frictional resistance under the condition of small depth and low load (eccentricity $\varepsilon < 0.15$); under the condition of large depth and high load ($\varepsilon > 0.15$), the microgrooves can reduce the friction force, but simultaneously, the thickness of the oil film is reduced. In terms of thrust hydrostatic bearing research, Wang [4] used the load capacity/friction coefficient transition point to measure the performance of the bearing, and studied the effects of the ratio of the area of the crater, the depth of the crater and the diameter of the crater in the transition point of the LCC and obtained the best result. Zhang [7] optimized the geometrical parameters of the fan-shaped straight groove texture on the bearing surface and considered that the microtexture had different optimal parameters under different constraints and objectives. He analyzed the effect of groove texture on the fluid thrust lubrication mechanism of thrust washers and found that the width and number of grooves have optimal values for load carrying capacity.

Regarding the location of texture distribution, Cupillard [6] simulation found that the microtexture model arranged in the maximum pressure region can reduce friction and oil film thickness compared with the smooth wall model. Liu Hongbin's numerical study found that there is a reasonable density and distribution for the oil film LCC. Brizmer [8,9] found in the micropit texture research that the global texture model cannot effectively improve the LCC, but it is suitable for mechanical seals.

Hamilton [1] proposed the "lubrication effect of microbumps", which believes that the microbumps on the surface hinder the movement of the fluid. When the fluid flows through the microbumps, the pressure rises rapidly and cavitation causes the pressure asymmetry, resulting in additional LCC. Cupillard's [10,11] numerical analysis of textured slider bearings found a "reflow phenomenon". When the texture depth increases to a certain value, backflow will occur, and the backflow will reduce the pressure gradient and LCC. Lo [12] found that the pit-textured surface lubricating fluid penetrates into the surrounding area to reduce friction and wear. Wang experimentally verified this phenomenon and summarized it as "secondary lubrication effect". Fowell [4] discovered the phenomenon of "inlet suction" when studying low-convergence textured wall bearings: unlike the classical shear force that entrains the lubricating oil to form hydrodynamic pressure, the phenomenon is that the textured area at the bearing inlet produces a lower pressure than the outside air. The high pressure causes the lubricating oil to be squeezed into the bearing, thereby increasing the LCC of the bearing. Tauviqueerahman et al. [13] believed that the surface microstructure affects the slip length of the fluid-solid surface, the journal bearings lubricated by Newtonian fluid and non-Newtonian fluid are compared, and it is concluded that non-Newtonian fluid is more effective in improving the load-carrying capacity in the case of high eccentricity.

Numerous studies have shown that applying a reasonable surface texture can lead to better tribological performance than smooth surfaces, but some issues still need to be investigated [14]. Whether there are some special textures that can achieve the best results

performance in any situation; how different calculation models used affect the accuracy of the calculation results.

2. Analysis of Smooth-Walled Radial Bearing Ignoring Cavitation Effects

2.1. Governing Equations

In the process of high-speed rotation of hydrostatic bearings, the oil film of journal bearings will form negative pressure under the action of oil wedge. This cavitation phenomenon has been considered by a large number of scholars, and the most common is the half-Sommerfeld method. However, it is more practical to explain this phenomenon through gas-liquid two-phase flow [13,15]. Therefore, the conservation of momentum and energy are formulated as follows:

Mass conservation equation:

$$\nabla \cdot \vec{V} = 0 \tag{1}$$

Momentum equation:

$$\rho \frac{D\vec{V}}{Dt} = -\nabla p + \rho \vec{g} + \mu \nabla^2 \vec{V} \tag{2}$$

We can see that the momentum equation is related to the density, viscosity and the volume velocity of the micro element, extending Equation (2):

$$\frac{\partial}{\partial x_j} (\rho u_i u_j) = -\frac{\partial p}{\partial x_i} + \frac{\partial}{\partial x_j} \left(\mu \left(\frac{\partial u_i}{\partial x_j} + \frac{\partial u_j}{\partial x_i} \right) \right) + \frac{\partial}{\partial x_j} (-\rho \overline{u'_i u'_j}) \tag{3}$$

Energy equation:

$$\frac{\partial}{\partial t} (\rho E) + \nabla \cdot [\vec{v}(\rho E + p)] = \nabla \cdot [k_{eff} \nabla T] + S_h \tag{4}$$

The two-dimensional schematic diagram of a radial hydrostatic bearing, shown in Figure 1.

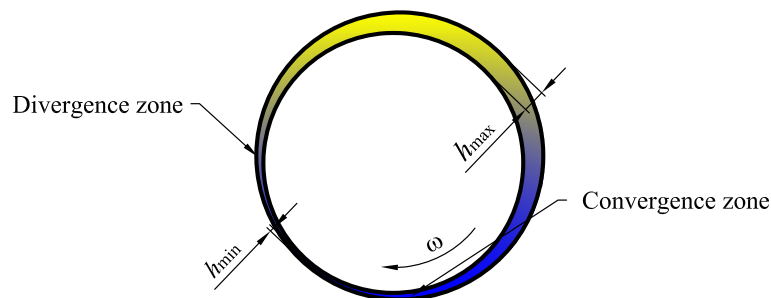


Figure 1. Schematic diagram of a radial hydrostatic bearing.

The main parameters of oil are: density 810 kg/m³; specific heat capacity 2000 J/(kg · K); thermal conductivity 0.37 W/(m · K); dynamic viscosity of lubricating oil is 3.85 × 10⁻³ Pa · s (temperature T = 293 K). Analysis parameters are shown in Table 1.

Table 1. Calculation parameters for radial hydrostatic bearing.

Journal Diameter	Bearing Length	Radius Clearance	Eccentricity	Lubricant	Rotating Speed
20 mm	20 mm	0.02 mm	0.7	Mobil Velocite oil No. 2	5000 r/min

According to the Reynolds number calculation formula:

$$Re = \frac{\rho v d}{\mu} \tag{5}$$

where d is length scale, and v is reference velocity. Based on the maximum oil film thickness, let $d = 2h_{max}$, the Reynolds number calculated as about 75, which is much lower than the range of 1000 to 2000, which can generate turbulent flow. Therefore, this problem can be calculated according to the laminar flow theory, and the obtained pressure distribution in the oil film is shown in Figure 2.

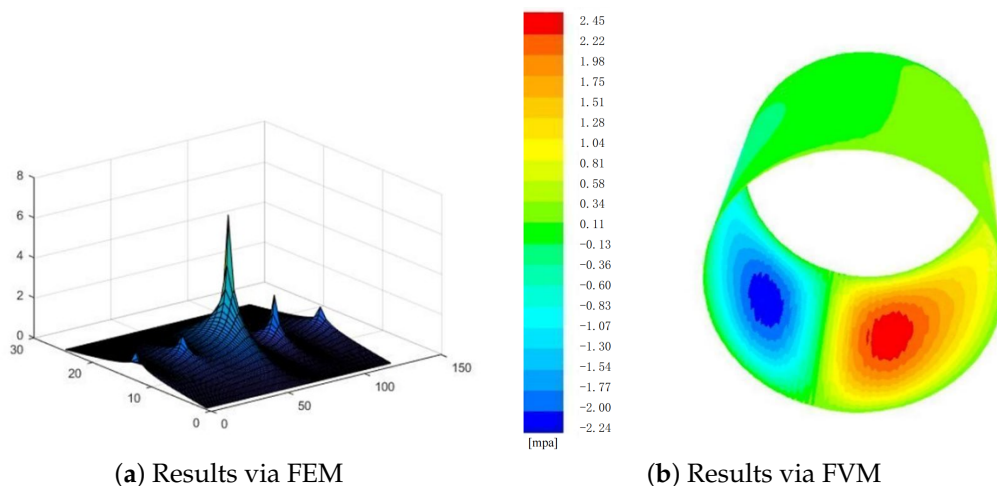


Figure 2. Pressure distribution of oil film on the journal hydrostatic bearing: oil pressure (MPa).

Based on the maximum oil film thickness, the Reynolds number is calculated as about 75, which is much lower than the range of 1000 to 2000, which can generate a turbulent flow. Therefore, this problem can be calculated according to the laminar flow theory, and the obtained pressure distribution in the oil film is shown in Figure 2.

In order to verify mesh independence, three different proportions of mesh number are compared with the FEM method. As shown in Table 2.

Table 2. Mesh independence verification.

Calculation Scheme	Mesh Number	LCC	Error
FEM	61,500	853.1 N	
Scheme 1	20,364	847.6 N	0.65%
Scheme 2	61,179	853.6 N	0.05%
Scheme 3	114,260	850.9 N	0.26%

It can be seen that without considering the cavitation effect, the minimum pressure may be negative pressure, which is obviously inconsistent with the actual situation. Therefore, the cavitation effect must be considered to obtain reasonable results. At the same time, the number of the mesh has little influence on the calculation results, which proves the independence of the mesh.

The process of generating, compressing, expanding and collapsing of tiny bubbles in a liquid is called cavitation. Several scholars have made outstanding contributions to the mathematical theory of cavitation effects. It was first predicted by the physicist Reynolds in 1873 that the high-speed relative motion between the propeller and the water would create a vacuum cavity that affects the performance of the propeller during the travel of the ship. Later, S.W. Barnaby et al. [16]. However, cavitation is not the only disadvantage. Along with the cavitation process, the bubbles generated by the fluid and the moving wall reduce the macroscopic shear force during the movement. For example, supercavitation

technology is used to generate cavitation on the surface of the torpedo, so that the resistance of the torpedo can be reduced by 90% [17], among which the “full cavitation model” was studied by Singhal et al. It accounts for phase change, bubble dynamics, turbulent pressure fluctuations, and noncondensable gases. It is able to take into account multiphase flows or flows with multiphase transport of matter, the effect of sliding velocity between liquid and gas phases, as well as the thermal effects and compressibility of liquid and gas phases, establishing the Rayleigh–Plesset equation, also known as the Porisky equation, which is also a widely used cavitation model [18].

Since the negative pressure problem in the diverging wedge region needs to be solved in combination with the cavitation phenomenon, the bearing oil film model is divided into two simplified slider bearings, the convergent wedge and the diverging wedge, which are analyzed separately.

With the multiphase cavitation modeling approach, a basic two-phase cavitation model consists of using the standard viscous flow equations governing the transport of mixture phases. In cavitation, the liquid–vapor mass transfer equation has the following form:

$$\frac{\partial}{\partial t}(\alpha\rho_v) + \nabla \cdot (\alpha\rho_v\vec{v}_v) = R_e - R_c \quad (6)$$

In the equations mentioned above, t is time, α is volume fraction, ρ_v is vapor density, \vec{v}_v is vapor velocity, R_e and R_c are mass transfer source terms connect to the growth and collapse of the vapor bubbles. For different cavitation models, the definition of α or other assumptions are different, resulting in different calculation methods of R_e and R_c . However, several cavitation models can be written as similar formulas with different calculation methods of coefficients C_{vap} and C_{cond} .

$$\begin{cases} R_e = C_{vap}\rho_v\rho_l\sqrt{\frac{2}{3}\frac{(p_v-p)}{\rho_l}} \\ R_c = C_{cond}\rho_v\rho_l\sqrt{\frac{2}{3}\frac{(p-p_v)}{\rho_l}} \end{cases} \quad (7)$$

The saturation pressure p_v is corrected by an estimation of the local values of the turbulent pressure fluctuations:

$$p_v = p_{sat} + \frac{1}{2}(0.39\rho k) \quad (8)$$

where k is kinetic energy.

2.2. Method Selection for Cavitation Effect Calculation

To account for cavitation in oil film CFD calculations, a multiphase flow model needs to be enabled. There are three commonly used multiphase flow models, namely the VOF model, the mixture model and the Eulerian model, and their characteristics are as follows.

- The VOF (Volume of Fluid) model is used in situations where the interface between two or more incompatible fluids needs to be obtained. It is used in slug flow, liquid flow, sloshing, free surface flow, and CFD calculation of stratified flow and dam collapse.
- The mixture model is used for the calculation of two-phase flow or multi-phase flow. It is a simplification of the Eulerian model based on the assumption that the Stokes number is very small. The result of this assumption is that the size and direction of the particle phase and the main phase are basically the same. Applications include bubbly flow, settling, and agitators.
- The Eulerian model establishes a continuity equation and a momentum equation for each phase, so the solution process is the most complicated among the three equations. Applications include sedimentation, bubble columns, fluidized beds, suspended particles, etc.

For the bearing oil film model where the gas phase and liquid phase are mixed and the gas phase volume ratio is much greater than 10%, the VOF model mainly used to calculate the stratified flow or free surface flow is obviously not suitable. Therefore, the calculation

model needs to compare the mixture model and the Eulerian model. Pull the model to make trade-offs. The selection of the mixture model and Eulerian model is mainly based on the following principles.

- The mixture model is used when the gas phase is widely distributed, and the Eulerian model is used when the gas phase is concentrated in a local area.
- The mixture model is used when the stability and efficiency of the calculation are pursued, and the Eulerian model is used when the calculation accuracy is pursued.
- When choosing the Eulerian model, the influence of the interphase drag force needs to be considered. If the interphase drag force rule is unknown, the mixture model is used.

For the bearing oil film model with micro-texture on the wall surface, the flow field is more complicated. In order to improve the stability of the calculation, the mixture model is used to calculate the cavitation phenomenon.

2.3. Simulation of Smooth-Walled Radial Bearing Considering Cavitation Effects

The pressure distribution of the smooth wall radial bearing calculate d in this paper is singular because cavitation effect is not considered. Here, the model considering cavitation effect is adopted, and the calculated pressure distribution is shown in Figure 3. The analysis results show that the results after considering the cavitation effect are more in line with the real situation, and the maximum pressure also increased.

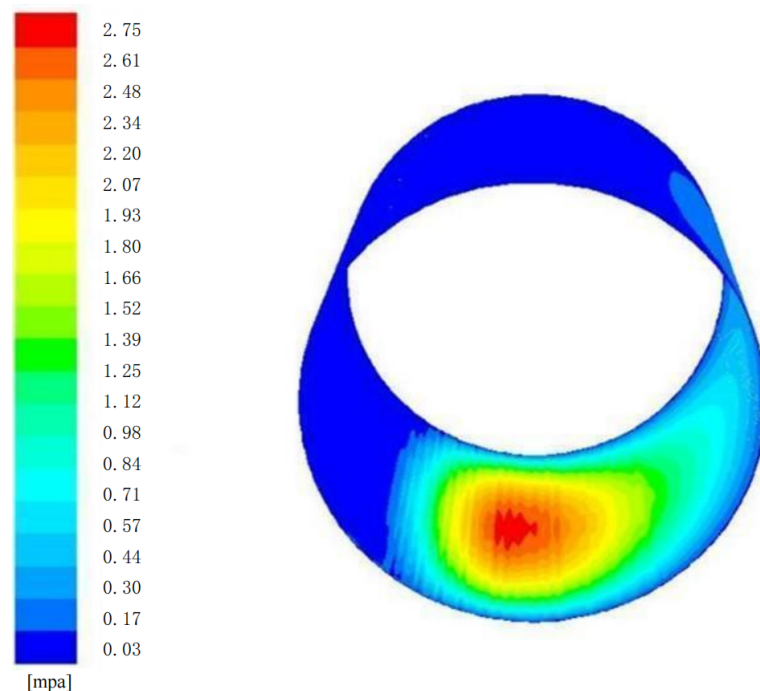


Figure 3. Oil film pressure distribution considering cavitation effect: Oil pressure (MPa).

Figure 4 shows the cloud diagram of gas phase volume fraction distribution. The dark blue area indicates that the gas phase volume fraction is 0, that is, this area only contains oil, while other warm tone areas indicate that this area is a cavitation area. Obviously, the cavitation area is distributed in the bearing divergence wedge area. From the volume fraction of the gas phase in the cavitation area, it can be seen that the volume fraction of the gas phase increases gradually from the minimum oil film thickness to the maximum oil film thickness along the circumference. The area with less volume fraction of the gas phase corresponds to the initial stage of the cavitation. With the rotation of the journal, the cavitation is brought to the area with large oil wedge thickness and developed, and finally collapses and disappears in the area near the maximum oil film thickness.

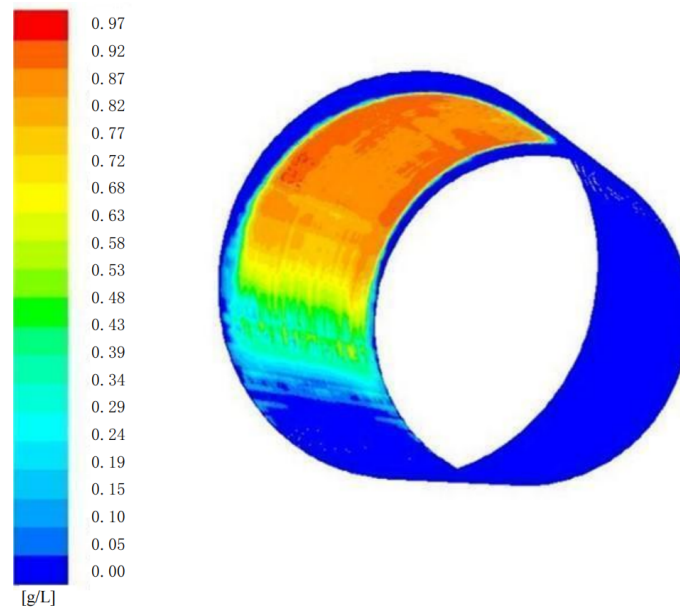


Figure 4. Gas phase volume fraction distribution considering cavitation effect: Volume fraction (g/L).

The results show that the maximum velocity of the gas phase and the liquid phase are almost the same, and about 70% of the bubbles are distributed in units with a gas volume fraction of less than 9.71%.

3. Analysis of Iubrication Characteristics of Converging Wedge Slider Bearing Surface Texture

3.1. Pressure Distribution Simulation of Non-Textured Convergent Wedge Slide Bearing

The slider bearing is a simplification of the convergent area and the divergent area of the radial hydrostatic bearing, so that the calculation can be more refined. The size of the slider bearing is selected as shown in Figure 5.

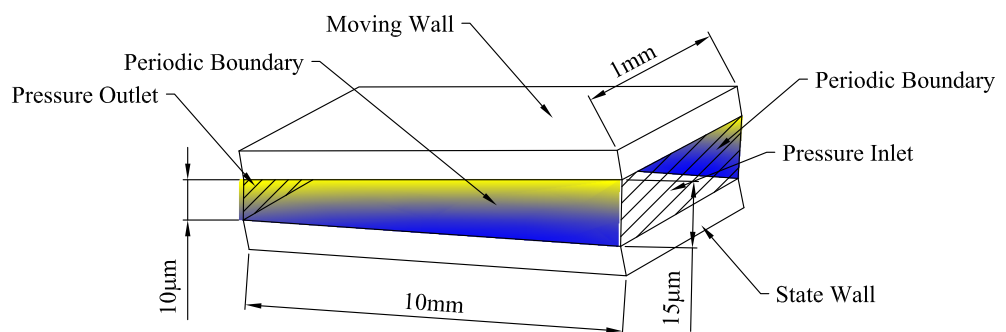


Figure 5. Schematic diagram of slider bearing dimensions.

The lubricating oil is Mobil Velocite oil No 2, and the oil temperature is 293.15 K. The moving speed of the upper wall (Moving Wall) is $v = 20$ m/s, and the lower wall (state wall) is stationary. In order to ignore the influence of the two side walls facing the flow, the periodic boundary conditions are set in the analysis. The processing of periodic boundary conditions from the finite element analysis theory has the characteristics of accelerating the convergence, so it will not adversely affect the analysis results.

For the untextured smooth surface, applying CFD analysis, the flow velocity variation along the oil film thickness direction at the inlet position, the center position and the outlet position is obtained as shown in Figure 6.

In the figure, $x = 5$ mm is the entrance position, $x = 0$ mm is the center position, and $x = -5$ mm is the exit position.

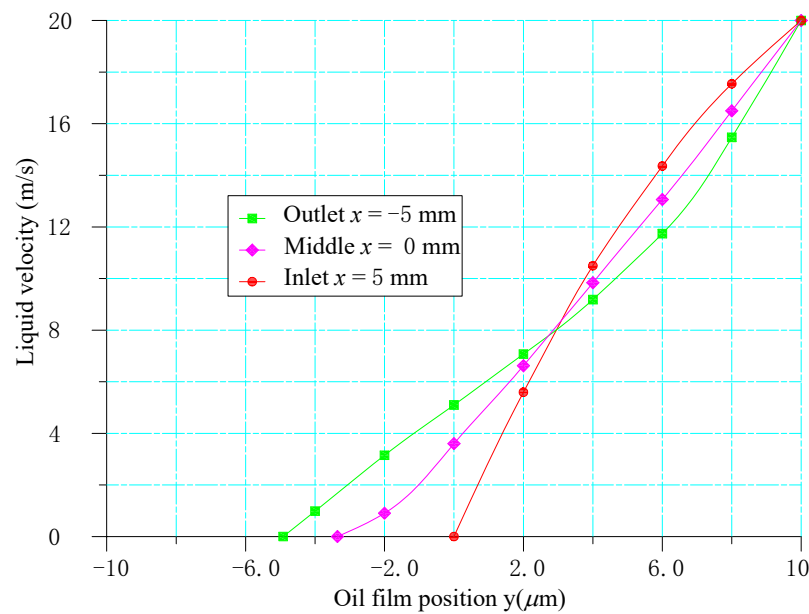


Figure 6. Velocity distribution along the thickness of the oil film.

3.2. Simulation of Convergence Wedge-Slide Bearing Pressure Distribution on the Streamwise and Transverse Textured Surfaces

Figure 7 shows two microtexture models (streamwise and transverse) selected to analyze the effects of texture orientation on bearing performance.

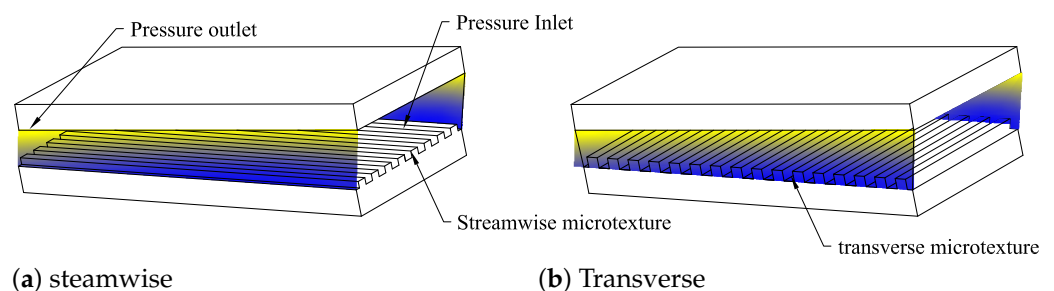


Figure 7. Schematic diagram of slider bearing microtexture.

The micro-texture topography only considers the rectangular cross-section, and the micro-texture is uniformly distributed, with a micro-textured surface in the whole area on the state wall.

The dimensionless depth h_0 is defined as the ratio of the texture depth to the minimum oil film thickness. The minimum oil film thickness is set to $10 \mu\text{m}$ and the texture groove width is $50 \mu\text{m}$. The effect of the dimensionless depth on the carrying capacity is calculated. As shown in Figure 8.

Figure 8 shows that the dimensionless LCC decreases with the increase of the dimensionless depth. The transverse texture has better LCC than the streamwise texture. With the increasing dimensionless texture depth, the dimensionless relative LCC of the transverse texture shows a decreasing trend, but it is not a rapid linear decrease like the streamwise texture, but is basically stable at around 0.78, that is, the transverse texture decreases. Compared with the smooth surface, the LCC of the structural model is reduced by about 22%.

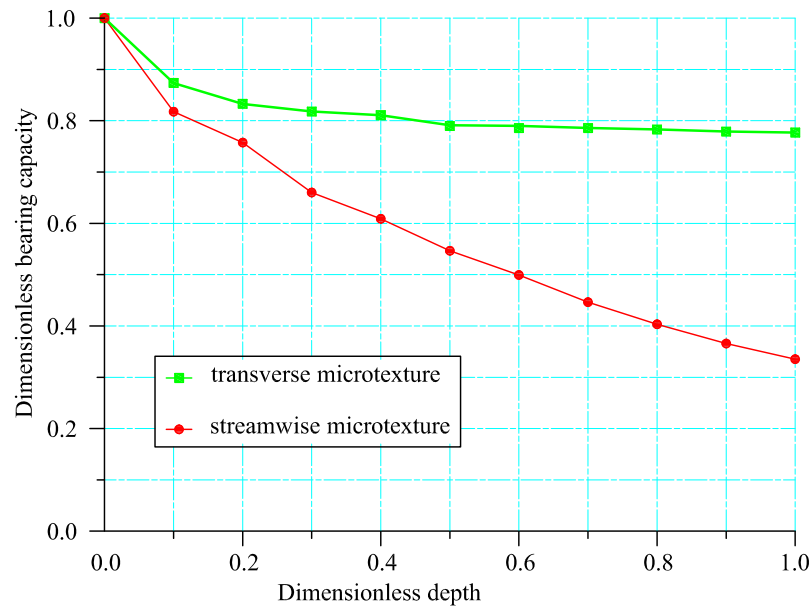


Figure 8. Effects of dimensionless depth of microtexture on carrying capacity.

The variation of shear force on the fixed wall and moving wall of the streamwise and transverse microtextures with the dimensionless texture depth is obtained through analysis. Figure 9 shows the variation trend of the dimensionless shear force of the streamwise texture model.

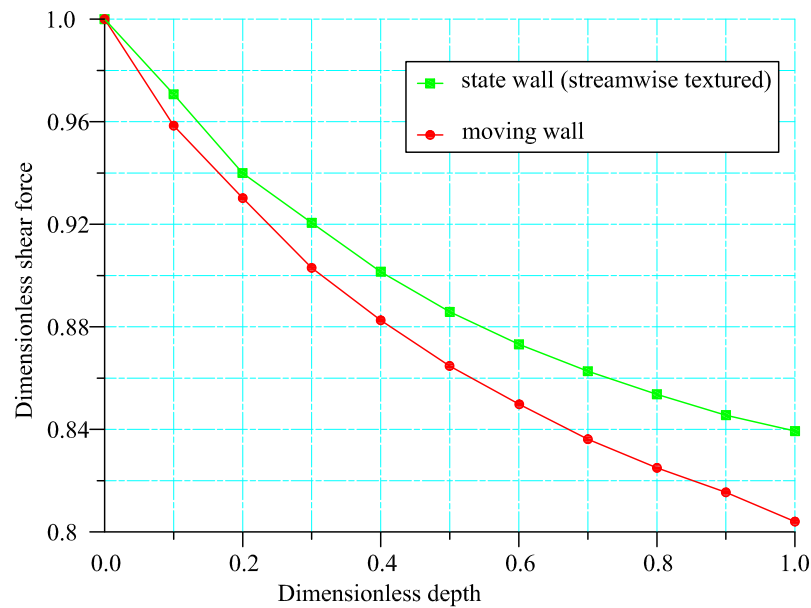


Figure 9. Influence of dimensionless depth of microtexture on wall shear force in streamwise texture model.

Figure 10 shows that compared with the smooth model without texture, the wall shear force of the streamwise textured model is significantly reduced. The shear force of the moving wall is slightly lower than that of the fixed textured wall. When the dimensionless texture depth is 1, the dimensionless shear force of the upper plate wall is close to 0.8, that is, the drag reduction rate is about 20%.

Figure 10 shows the variation trend of dimensionless shear force of the transeverse texture model.

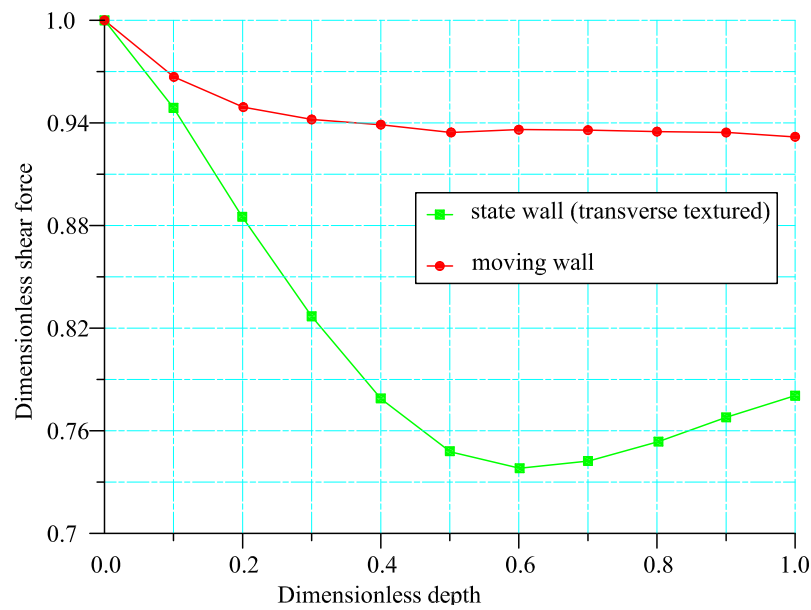


Figure 10. Influence of dimensionless depth of microtexture on wall shear force in transverse texture model.

Figure 10 shows that when the transverse micro-textured slider bearing is applied, the shear force between the moving wall and the fixed wall is quite different. The dimensionless depth is about 0.6 close to the minimum value, and then the shear force increases gradually. The dimensionless shear force of the moving wall is basically between 0.93 and 0.94. Usually, the drag reduction of hydrostatic bearings has no meaning for fixed walls, so the drag reduction characteristics reflected by the transverse texture are not obvious.

3.3. Lubrication Characteristic Analysis of Local Texture Model

No matter what texture type is used, the above analysis shows that the LCC is lower than that of the untextured smooth wall model, which obviously does not meet the lubrication goals of improving LCC and reducing wall friction. Therefore, the loss caused by changing the full texture model needs to be considered.

First of all, it is determined that only suitable microtextures are produced in the required bearing parts, the length of the slider bearing is set as L , and two parameters α and β are defined to describe the size and entrance distance of the microtextures. The length of the microtexture is $l = \alpha \times L$ and the entrance distance $d = \beta \times L$. Combining α and β , the wall shear force and pressure distribution of the slider bearing were analyzed. Among them, the dimensionless shear force on the wall surface of the streamwise texture is shown in Table 3.

Table 3. Dimensionless shear forces for the streamwise local texture state wall.

β	α	Texture Area from Entrance	Texture Area from Exit	Dimensionless Shear Force
0.1	0.8	0.1 L	0.1 L	0.853
0.2	0.7	0.2 L	0.1 L	0.862
0.3	0.6	0.3 L	0.1 L	0.875
0.4	0.5	0.4 L	0.1 L	0.886
0.5	0.4	0.5 L	0.1 L	0.898
0.6	0.3	0.6 L	0.1 L	0.905
0.7	0.2	0.7 L	0.1 L	0.914

The analysis shows that with the same value of α , the texture distribution on the inlet side can obtain a higher drag reduction rate.

Figure 11 calculates the pressure distribution of the smooth surface, transverse textured and streamwise textured slider bearings for setting $\alpha = 0.1, \beta = 0.9$.

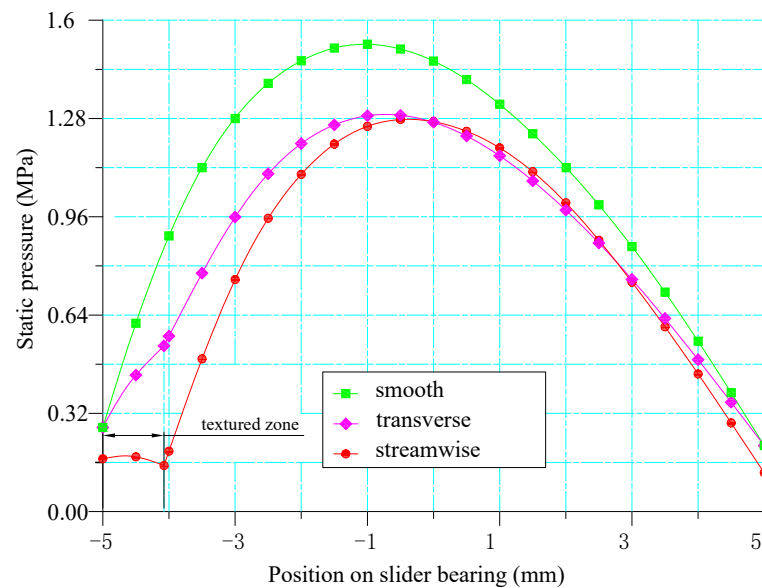


Figure 11. Influence of local texture on oil film pressure distribution.

It can be seen from the figure that the introduction of microtexture not only affects the small area of the texture distribution, but also affects the size and shape of the pressure distribution of the entire bearing. However, the maximum load-carrying capacity of a smooth bearing cannot be reached regardless of the distribution.

4. Analysis of Bearing Lubrication Characteristics under Cavitation Effect

4.1. Analysis of Lubrication Characteristics of Divergent Wedge Slider Bearing Based on Full Texture Model

In the analysis of a convergent wedge texture model, CFD calculation can be completed only by using a pressure-based solver. For the divergent wedge texture model, the influence of cavitation should be considered.

Figure 12 shows the distribution of oil film pressure on the moving wall before and after considering the cavitation effect when the streamwise dimensionless texture depth is 0.5. The abscissa -5 mm point in the figure corresponds to the oil film inlet, and $+5$ mm corresponds to the oil film outlet. The figure on the left shows the situation without considering the cavitation effect. The oil film pressure distribution is similar to a parabola. When the x -axis coordinate is about -1 mm, there is a minimum pressure of -0.9 MPa (absolute pressure); the picture on the right shows the case considering the cavitation effect. On the moving wall, the oil film pressure in the middle of the wall is equal to the cavitation pressure. There is a sudden change in the pressure value at the inlet and outlet of the oil film, and the oil film pressure at the inlet. The strength first increases to 0.038 MPa and then decreases to the cavitation pressure, while the oil film pressure at the outlet surges from the cavitation pressure to about 0.082 MPa. The upper part of the left figure shows the pressure position of cavitation pressure, showing the huge difference between considering and not considering cavitation.

According to the previous analysis, the arrangement of the micro-texture at the inlet will lead to the reduction of LCC, while at the outlet, due to the consideration of cavitation effect, the negative pressure strength obtained without considering cavitation effect is corrected, which improves the LCC. Therefore, it can be imagined that if the cavitation effect is strengthened by using a micro-texture at the exit, the LCC may be improved. Figure 13 shows the corresponding dimensionless bearing capacities from the analysis of different dimensionless texture depths for a fully textured diverging wedge slider bearing.

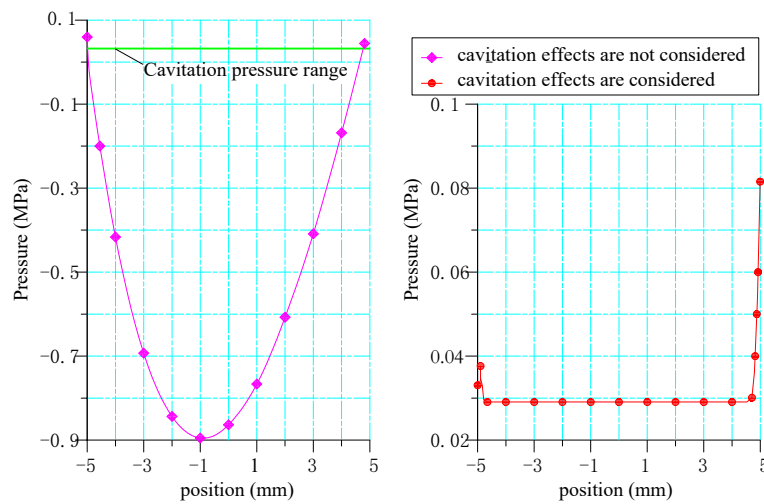


Figure 12. Pressure distribution on moving wall before and after considering cavitation effect in streamwise texture.

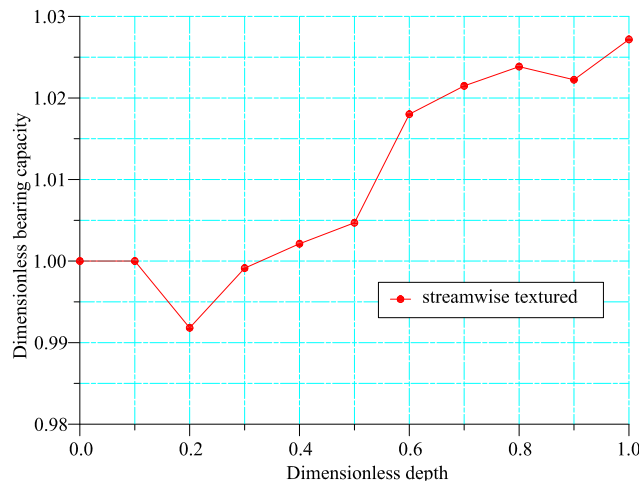


Figure 13. The influence of the depth of streamwise texture on the dimensionless LCC.

Figure 13 shows that changing the depth of the texture has no obvious effect on improving the LCC, but it usually does not reduce the LCC. Figure 14 shows the dimensionless shear force obtained by changing the dimensionless texture depth analysis.

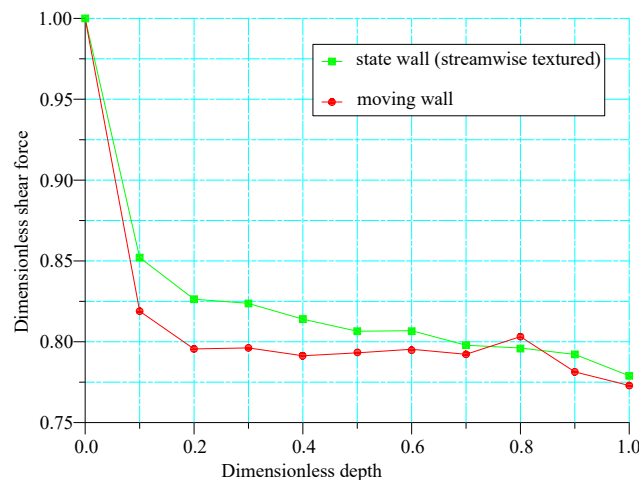


Figure 14. The effect of the depth of streamwise texture on the dimensionless shear force.

It can be seen from Figure 14 that increasing the texture depth is very effective in reducing the wall shear force, and its maximum drag reduction rate is likely to reach 22%.

In order to compare the two different directions of micro texture used in the previous convergent wedge, the oil film pressure analysis, dimensionless LCC and dimensionless shear force analysis of the divergent wedge with a transverse micro-texture are carried out. The characteristics of oil film pressure are almost the same as those in the streamwise micro-texture pressure distribution in Figure 12, but the LCC and shear force are quite different. Figure 15 shows the dimensionless LCC obtained by changing the dimensionless texture depth analysis.

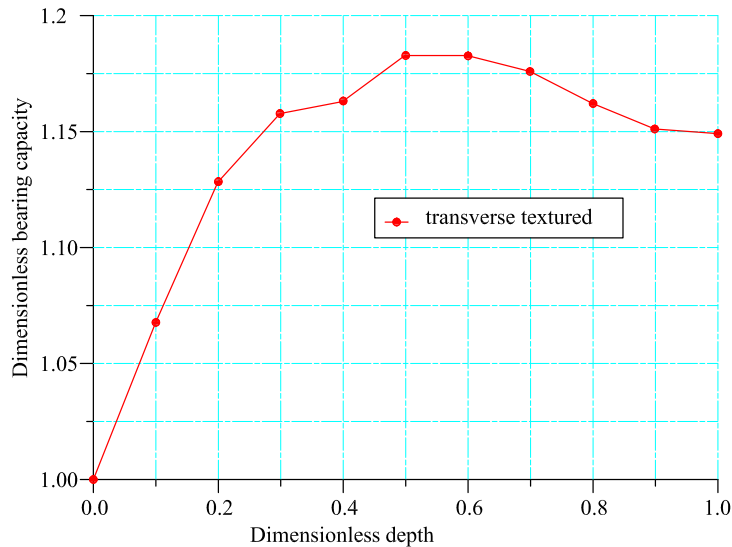


Figure 15. Influence of transverse texture depth on dimensionless LCC.

Figure 15 shows that the LCC of the transverse texture model is greater than that of the smooth model. The dimensionless LCC first increases rapidly with increasing dimensionless texture depth, and when the dimensionless texture depth is 0.6, the maximum dimensionless LCC is 1.18, and then the dimensionless LCC decreases slowly.

The variation of transverse wall dimensionless shear force with dimensionless texture depth is shown in Figure 16.

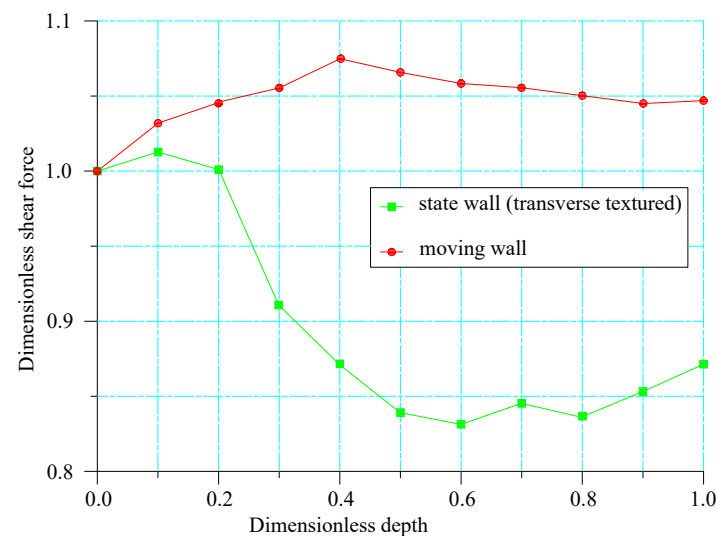


Figure 16. Influence of transverse texture depth on dimensionless shear force.

Transverse texture can effectively reduce the dimensionless shear force on the fixed wall, that is, the shear force lower than that of the smooth wall model can be obtained. When the dimensionless texture depth is 0.6, the minimum dimensionless shear force can be obtained as about 0.85, and the corresponding drag reduction rate is about 12%. However, while reducing the shear force on the state wall, the transverse texture model increases the dimensionless shear force on the moving wall. For example, when the dimensionless texture depth is 0.6, the shear force increases by 6.5% compared with the smooth wall. For the divergent wedge, the increase of the LCC of the moving wall and the increase of the shear force are unfavorable factors for lubrication.

4.2. Simulation of Drag Reduction Effect of Local Texture Model of Divergent Wedge Slider

Dimensionless parameters are defined in the same way as in the previous convergence wedge α and β to represent the length of the texture area and the distance from the exit, that is, when β at 0, the local texture is arranged at the exit. For the streamwise texture model, the dimensionless shear force of the moving wall obtained from the simulation analysis is consistent with β , and the relationship is shown in Figure 17.

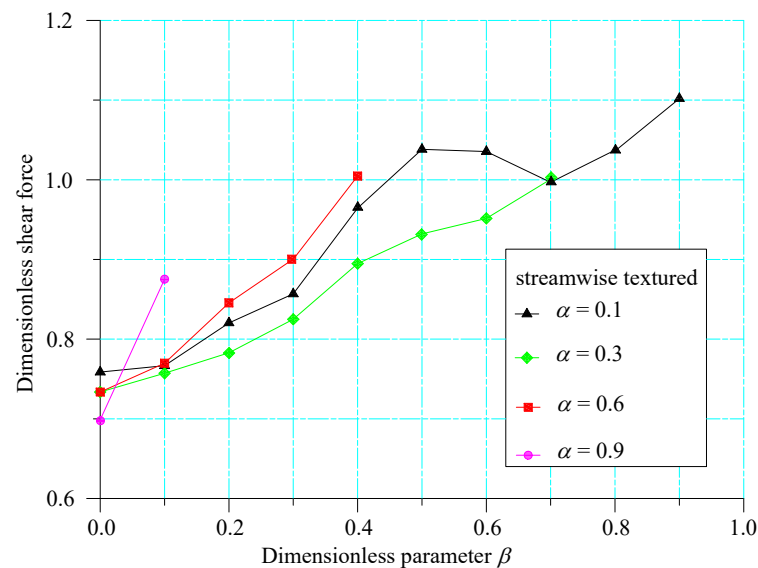


Figure 17. The influence of the position of the streamwise texture on the dimensionless shear force on the moving wall.

Figure 17 shows that the texture arrangement at the oil film outlet of the divergent wedge can obtain a lower wall shear force, for example $\alpha = 0.3$ and β at 0, the dimensionless wall shear force of the moving wall can be reduced to left and right, respectively. As the distance from the outlet increases, the shear force will increase, and the texture is arranged in an inappropriate area. Compared with the smooth surface, the shear force can be increased. For example, from the pressure distribution, if $\alpha \leq 0.3$, and if the texture is arranged at the entrance, it will be higher than the smooth wall by about 20%, because the texture area is in the pressure rise area of the oil film, and the corresponding texture boundary position just corresponds to the peak point.

By analyzing the hydrostatic block bearing with transverse local texture, the dimensionless shear force on the moving wall and β . The relationship is shown in Figure 18.

It can be seen from the figure that if the transverse micro-texture arrangement is adopted, it is possible to reduce the shear force only if it is arranged in a very narrow area at the outlet.

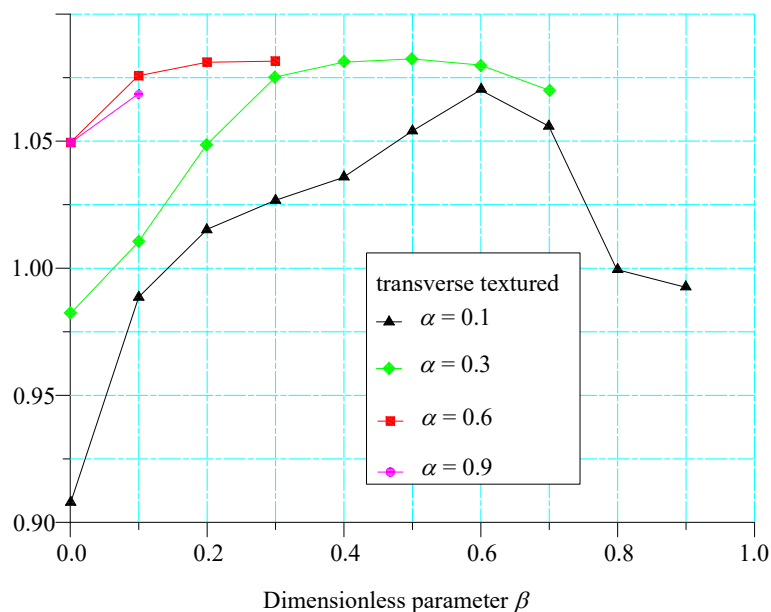


Figure 18. Influence of transverse texture position on dimensionless shear force on moving wall.

5. Verification Test of Micro Texture Drag Reduction Characteristics

To verify the drag reduction effect of the streamwise micro-texture, half of the bearing bush is made of brass material, and the other half of the smooth bearing bush is used as the test reference, as shown in Figure 19, and the bearing test bench is on the right.

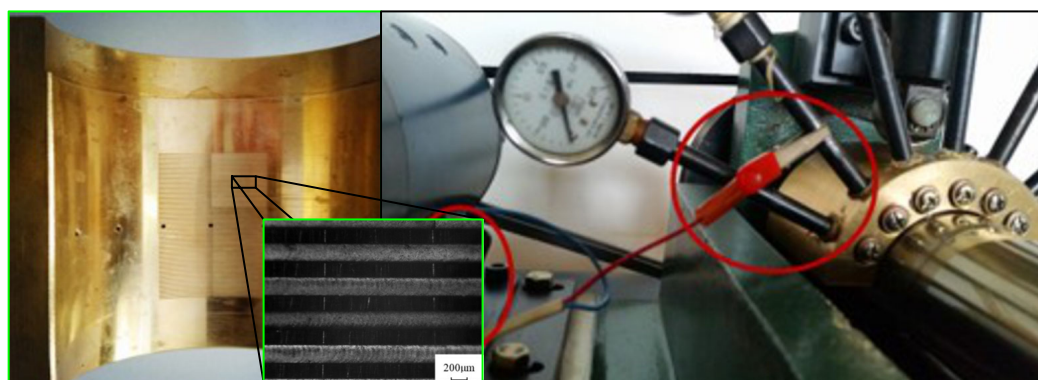


Figure 19. Bearing bush and test bench with streamwise texture.

The inner radius of the bearing bush is 30 mm, the total axial length is 72 mm, the axial length of the micro texture is 52 mm, the width of the micro texture is 200 μm , the depth is 100 μm , and the micro texture envelope angle is 22.5° and is set at the outlet of the divergent wedge according to the loading conditions.

The experimental loads are 650 N, 750 N and 1150 N, respectively, and the average speed of the bearing speed is 50 r/min, 75 r/min, 100 r/min, 125 r/min, 150 r/min, 175 r/min and 200 r/min, respectively. The lubricating oil used in the experiment is 45 # lubricating oil.

Theoretically, the viscosity changes with the change of pressure and temperature. However, because half of the bearing bush is used in the experiment, and the other half of the journal is immersed in an open oil groove, the temperature change is small, and the dynamic viscosity is approximately a constant, which is taken as $\eta = 0.34 \text{ Pa} \cdot \text{s}$. Figure 20 shows the measured friction coefficient of smooth bearing shells under different loads and different rotating speeds.

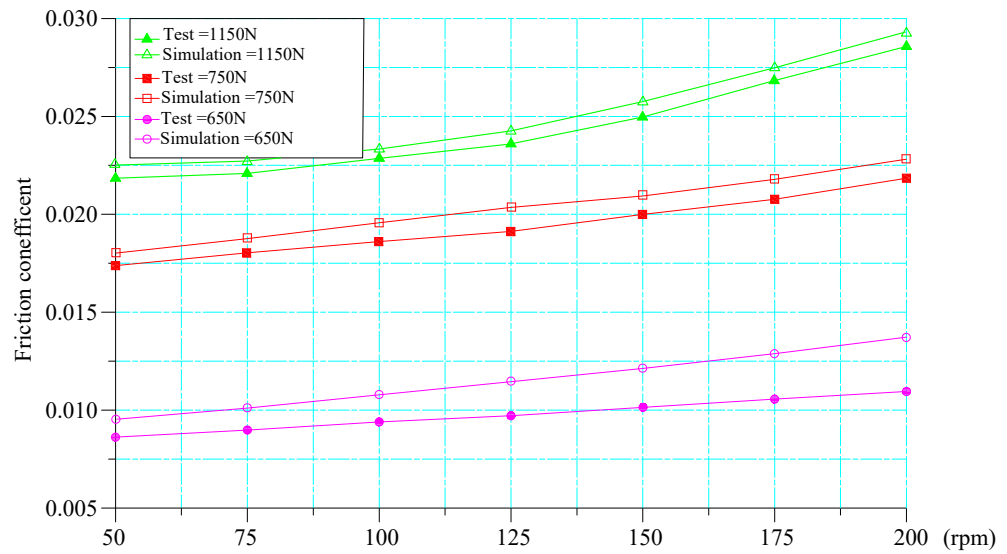


Figure 20. Comparison between friction coefficient and simulation results under smooth bearing test conditions.

Since the friction coefficient is the ratio of shear force to a corresponding load, the variation law of the shear force and friction coefficient is basically the same. With the increase of rotating speed, the wall friction coefficient tend to increase; in addition, increasing the load will increase the wall shear force and friction coefficient. Figure 21 shows the friction coefficient measured by the streamwise textured bearing bush under different loads and different rotating speeds.

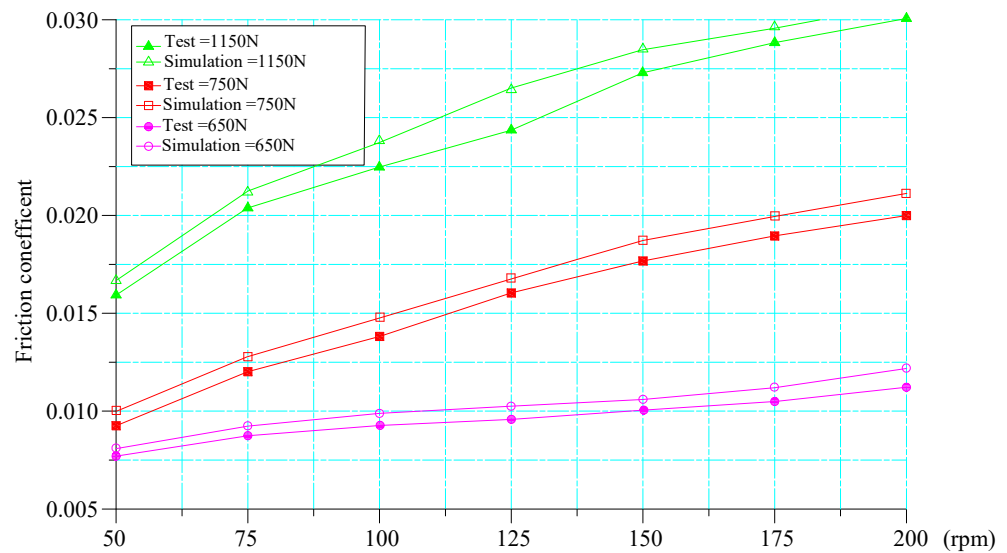


Figure 21. Comparison between friction coefficient and simulation results under test conditions of axial bearing with flow direction texture.

It can be seen from the test data that the shear force and friction coefficient of the bearing bush with local streamwise micro-texture are smaller than those of the smooth bearing. Taking the smooth bearing test data as a reference, the dimensionless shear force is calculated as shown in Figure 22.

From Figure 22, the dimensionless shear force in the whole region is less than 1, that is, the textured bearing bush can obtain a wall shear force lower than that of the smooth bearing bush, and the drag reduction rate is better than that of the high-speed state at low speed. However, the relationship with the load did not show up.

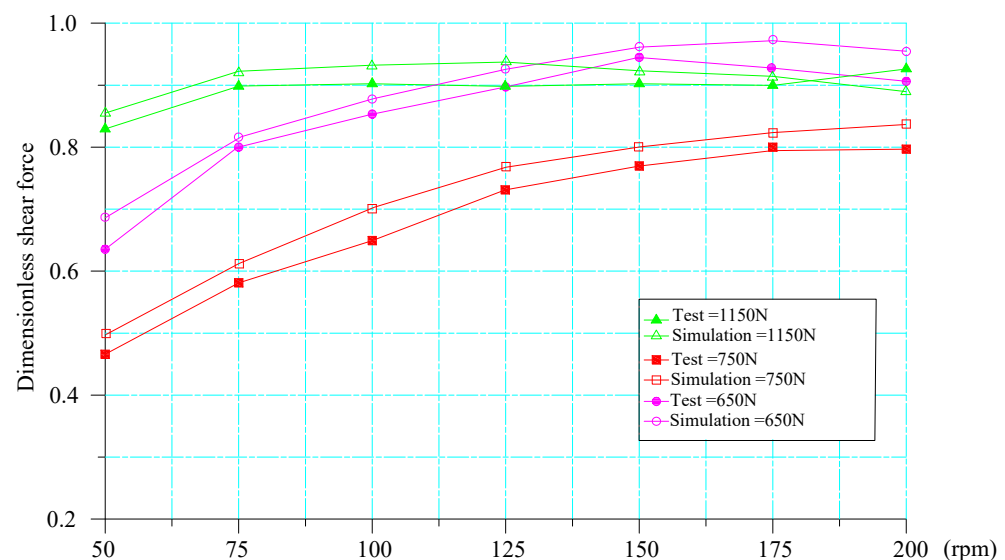


Figure 22. Comparison between dimensionless shear force and simulation results in different working conditions.

Compared with the simulation results, the friction force and friction coefficient of the surface texture are slightly lower in the experimental results, because the ideal airtight state cannot be achieved due to the limitation of experimental conditions, and part of the friction loss is carried away by the oil. Additionally, shear force is higher than the experimental measurement results, this is because the calculation of the shear stress is associated with speed, without considering energy loss and under the influence of external factors, with the increase of rotational speed, the simulation for the shear stress calculation results is slightly higher than that of the experimental results, but the overall trend, which verifies the correctness and effectiveness of the simulation method.

6. Discussion

By analyzing the LCC and dimensionless shear force of convergent wedge and divergent wedge with rectangular cross-section micro texture, it can be basically determined that in general, the use of a streamwise texture has a better drag reduction effect, and the possible reason is that the collapse position of bubbles is changed. The effect of local micro-textured surfaces is better than that of full micro-textured surfaces. From Figures 17 and 18, when the micro-texture is arranged at the exit of the converging wedge or the entrance of the spreading wedge, it will lead to the reduction of the load capacity and the increase of the wall shear force, which proves that the arrangement of the micro-texture at the minimum oil film thickness of the journal bearing has no benefit to the performance improvement. The experimental results also prove the correctness of the numerical simulation. In the analysis of the divergent wedge considering cavitation, it is found that there is a region where the pressure almost does not change. The pressure in this region may be modified by the micro-textured surface to meet the requirements of the bearing performance.

There is no obvious direct relationship between load and dimensionless shear force from the experiment, because only a kind of micro-textured surface is used for experimental research, and it is impossible to draw a conclusion. However, further research may explore the optimal corresponding relationship between micro-textures for different loads and different speeds.

The initial convergence wedge analysis does not consider the cavitation model, so it cannot be directly determined that micro texture technology cannot be used in the convergence wedge to improve the LCC under special conditions and reduce the shear force.

When the high-speed fluid flows through the micro-textured surface, it will produce a bubble generation and collapse process, which will produce a periodic impact on the moving wall. There is no effective means to analyze the impact process on the rotation

accuracy of the bearing. At present, most of the research content focuses on the use of CFD software for simulation, and the research on the residence time of bubbles on the micro-textured surface and the research on the boundary slip length are relatively few. For high-precision hydrostatic bearings, further research is needed on the effect of the microtextured surface on the axial drift.

Author Contributions: Conceptualization, Y.S. and K.C.; methodology, Y.S.; software, Y.S.; validation, Q.B., S.C. and K.C.; formal analysis, S.C.; investigation, Y.S.; resources, Q.B.; data curation, Q.B.; writing—original draft preparation, Y.S.; writing review and editing, Y.S.; visualization, S.C.; supervision, K.C.; project administration, K.C.; All authors have read and agreed to the published version of the manuscript.

Funding: This research received no external funding.

Institutional Review Board Statement: Not applicable.

Informed Consent Statement: Not applicable.



Data Availability Statement: Not applicable.

Conflicts of Interest: The authors declare no conflict of interest.

References

1. Hamilton, D.B.; Walowit, J.A.; Allen, C.M. A Theory of Lubrication by Microirregularities. *J. Basic Eng.* **1966**, *88*, 177–185. [CrossRef]
2. Rahmani, R.; Mirzaee, I.; Shirvani, A.; Shirvani, H. An analytical approach for analysis and optimisation of slider bearings with infinite width parallel textures. *Tribol. Int.* **2010**, *43*, 1551–1565. [CrossRef]
3. Tala-Ighil, N.; Maspeyrot, P.; Fillon, M.; Bounif, A. Hydrodynamic effects of texture geometries on journal bearing surfaces. In Proceedings of the 10th International Conference on Tribology ROTRIB'07, Bucharest, Romania, 8–10 November 2007.
4. Wang, X.; Kato, K.; Adachi, K.; Aizawa, K. Loads carrying capacity map for the surface texture design of SiC thrust bearing sliding in water. *Tribol. Int.* **2003**, *36*, 189–197. [CrossRef]
5. Sinanoğlu, C.; Nair, F.; Karamış, M.B. Effects of shaft surface texture on journal bearing pressure distribution. *J. Mater. Process. Technol.* **2005**, *168*, 344–353. [CrossRef]
6. Cupillard, S.; Cervantes, M.; Glavatskih, S. A CFD study of a finite textured journal bearing. In Proceedings of the Symposium on Hydraulic Machinery and Systems, IAHR 24, Foz do Iguassu, Brazil, 27–31 October 2008.
7. Zhang, J.; Meng, Y. Optimal Design of Surface Texture in Parallel Trust Bearings. *J. Mech. Eng.* **2012**, *48*, 91–99. [CrossRef]
8. Liu, H.; Meng, Y. Hydrodynamic Lubrication Analysis of Textured Surfaces with the Domain Decomposition Method-effect of Texture Distribution Patterns. *Tribology* **2007**, *27*, 555–561.
9. Liu, H.; Niu, R. Hhe Effect of Surface Tetures on Loading Capacity of Journal Bearing Lubricating Film. *Lubr. Eng.* **2010**, *35*, 18–22.
10. Cupillard, S.; Cervantes, M.; Glavatskih, S. Pressure buildup mechanism in a textured inlet of a hydrodynamic contact. *J. Tribol.* **2008**, *130*, 1–10. [CrossRef]
11. Cupillard, S.; Glavatskih, S.; Cervantes, M.J. 3D thermohydrodynamic analysis of a textured slider. *Tribol. Int.* **2009**, *42*, 1487–1495. [CrossRef]
12. Lo, S.W.; Horng, T.C. Lubricant permeation from micro oil pits under intimate contact condition. *J. Tribol.* **1999**, *121*, 633–638. [CrossRef]
13. Tauviqirrahman, M.; Jamari, J.; Susilowati, S.; Pujiastuti, C.; Setiyana, B.; Pasaribu, A.H.; Ammarullah, M.I. Performance Comparison of Newtonian and Non-Newtonian Fluid on a Heterogeneous Slip/No-Slip Journal Bearing System Based on CFD-FSI Method. *Fluids* **2022**, *7*, 225. [CrossRef]
14. Jiao, F.; Saravi, S.S.; Cheng, K. Investigation on an integrated approach to design and micro fly-cutting of micro-structured riblet surfaces. *Proc. Inst. Mech. Eng. Part C J. Mech. Eng. Sci.* **2017**, *231*, 3291–3300. [CrossRef]
15. Xu, R.s.; Wang, J.j.; Chen, X.w.; Ju, S.s. Numerical simulation of two-phase air/oil flow characteristic in bearing chamber. International Conference on Electric Information and Control Engineering, *Wuhan, China*, **2011**, 2412–2415.
16. Thornycroft, J.I.; Barnaby, S.W. Torpedo-boat destroyers.(Including appendix and plate at back of volume). In *Minutes of the Proceedings of the Institution of Civil Engineers*; Institution of Civil Engineers: London, UK, 1895; Volume 122, pp. 51–69.
17. Kuklinski, R. Experimental studies in the control of cavitating bodies. In Proceedings of the AIAA Guidance, Navigation, and Control Conference and Exhibit, Keystone, CO, USA, 21–24 August 2006; p. 6443.
18. Singhal, A.K.; Athavale, M.M.; Li, H.; Jiang, Y. Mathematical basis and validation of the full cavitation model. *J. Fluids Eng.* **2002**, *124*, 617–624. [CrossRef]

Drag Reduction by Riblets on a Commercial UAV

Lorenzo Cacciatori ^{1,†}, Carlo Brignoli ^{1,†}, Benedetto Mele ², Federica Gattere ¹ , Celeste Monti ³
and Maurizio Quadrio ^{1,*} 

- ¹ Department of Aerospace Science and Technologies, Politecnico di Milano, 20133 Milan, Italy; lorenzo.cacciatori@mail.polimi.it (L.C.); carlo.brignoli@mail.polimi.it (C.B.); federica.gattere@polimi.it (F.G.)
² Department of Industrial Engineering, University of Naples Federico II, 80138 Napoli, Italy; benmele@unina.it
³ Sky Eye Systems, 56021 Pisa, Italy; c.monti@skyeyesystems.it
* Correspondence: maurizio.quadrio@polimi.it
† These authors contributed equally to this work.

Abstract: Riblets are micro-grooves capable of decreasing skin-friction drag, but recent work suggests that additional benefits are possible for other components of aerodynamic drag. The effect of riblets on a fixed-wing, low-speed Unmanned Aerial Vehicle (UAV) on the total aerodynamic drag are assessed here for the first time by means of RANS simulations. Since the microscopic scale of riblets precludes their direct representation in the geometric model of the UAV, we model riblets via a homogenised boundary condition applied on the smooth wall. The boundary condition consists in a suitably tuned partial slip, which assumes riblets to be locally aligned with the flow velocity, and to possess optimal size. Several configurations of riblets coverage are considered to extract the potential for drag reduction of different parts of the aircraft surface. Installing riblets with optimal size over the complete surface of the UAV leads to a reduction of 3% for the drag coefficient of the aircraft. In addition to friction reduction, analysis shows a significant additional form of drag reduction localised on the wing. By installing riblets only on the upper surface of the wing, total drag reduction remains at 1.7%, with a surface coverage that is only 29%, thus yielding a significant improvement in the cost–benefit ratio.

Keywords: riblets; drag reduction; slip length

Citation: Cacciatori, L.; Brignoli, C.; Mele, B.; Gattere, F.; Monti, C.; Quadrio, M. Drag Reduction by Riblets on a Commercial UAV. *Appl. Sci.* **2022**, *12*, 5070. <https://doi.org/10.3390/app12105070>

Academic Editors: Gabriel Bugeđa Castellort and Josep Maria Bergada

Received: 14 April 2022

Accepted: 16 May 2022

Published: 18 May 2022

Publisher's Note: MDPI stays neutral with regard to jurisdictional claims in published maps and institutional affiliations.



Copyright: © 2022 by the authors. Licensee MDPI, Basel, Switzerland. This article is an open access article distributed under the terms and conditions of the Creative Commons Attribution (CC BY) license (<https://creativecommons.org/licenses/by/4.0/>).

1. Introduction

The growing concern over energy efficiency and environmental pollution is furthering the appeal of transport vehicles, particularly aircraft, that produce less aerodynamic drag. One of the most interesting passive drag reduction techniques is the use of riblets, i.e., streamwise-aligned micro-grooves that are known to reduce turbulent skin-friction drag (see, for example, the review paper [1] and the many references therein), and are approaching usability in aeronautics.

Early studies, spurred by the oil crisis of the 1970s, were performed at NASA [2], and important experiments were carried out in the Berlin oil tunnel by Bechert and coworkers [3,4]. They evidenced the crucial importance of the riblet shape, their size, and—most importantly—the sharpness of their tip; optimal configurations empirically determined at the time yield up to 6–8% and possibly higher reductions in skin friction for low-*Re* flat plate-boundary layers studied in laboratory conditions. The theoretical understanding of the riblets working mechanism is due to Luchini [5], who quantified the different resistance offered by a grooved wall to the parallel flow and the cross-flow. He also explained [6] how skin-friction drag reduction is equivalent to an upward shift of the logarithmic portion of the turbulent velocity profile. This important argument, later taken up again by [7], implies that it is incorrect to describe riblets performance simply as a percentage change of the skin-friction coefficient, as this simplistic figure depends on the Reynolds number of the flow. However, the value of the upward shift, once measured in

viscous units, is Reynolds independent and should be used to characterize the ability of riblets (and other techniques) to reduce turbulent friction; in fact, recently this concept has been extended [8] to other strategies of skin-friction reduction.

To capture, in a numerical simulation, the complex physics of the interaction between turbulence and a solid wall covered by riblets, and to properly measure friction reduction, direct numerical simulations (DNS) or wall-resolved large eddy simulations (LES) are required. Such computations are unfeasible for complex aeronautical configurations at high Reynolds numbers, where numerical simulations based on the Reynolds-Averaged Navier–Stokes equations (RANS) equipped with a turbulence model are the standard approach. Owing to their microscopic dimensions, however, riblets on an aircraft cannot be included directly in a RANS simulation. Even if they could, it is unclear to what extent a standard RANS model would be able to represent the physics of drag reduction.

Bridging the gap between drag reduction by riblets in turbulent flows and the need to incorporate it into RANS-type flow solvers has led to the development of computational models for riblets. Aupoix et al. [9] modified the Spalart–Allmaras turbulence model to account for riblets by using smooth-wall geometry. Along similar lines, Mele et al. [10] introduced a modified boundary condition for the $k - \omega$ turbulence model, and Koepplin et al. [11] extended the Aupoix model to describe riblets locally misaligned with the mean flow, and to account for mean pressure gradients.

How riblets affect a turbulent boundary layer with a non-zero pressure gradient is a debated subject [12–14]. In 2018, Mele and Tognaccini [15] developed a new model based on a slip-length concept, whose results provided an interesting view on the riblets drag reduction mechanism in presence of pressure gradients. In addition to friction reduction, they found that riblets alter the pressure distribution, and may provide additional pressure drag reduction. This indirect effect was also observed for other friction-reduction devices: Banchetti et al. [16] used spanwise forcing to reduce turbulent friction on a wall with a bump, and found in their incompressible DNS study that a reduced friction drag is accompanied by a reduced pressure drag. Similarly, using DNS, Quadrio et al. [17] studied the compressible flow over a wing, and observed how spanwise forcing affects the shock wave to yield large reduction of the total drag of the aircraft. The availability of a boundary condition to faithfully simulate in a RANS the presence of riblets on the surface of a solid body of complex shape is thus becoming extremely attractive.

The standard no-slip condition at a solid wall can be extended to a partial-slip one, which is useful to describe specific physical situations (e.g., flow over superhydrophobic surfaces). Riblets are amenable to such a description; their slip length is related to the protrusion height concept [3–5]. In particular, Luchini in [5] defined the longitudinal and transverse protrusion heights, which identify the virtual origin for the streamwise and spanwise velocity profiles, and realised that the only meaningful non-arbitrary quantity is their difference. Later, he also introduced [18] a linearised boundary condition for generic roughness and the protrusion heights for various roughness types to be adopted in DNS. He also demonstrated that the difference Δh between the two riblets protrusion heights corresponds to the slip length λ . Gomez de Segura et al. [19] later discussed how the slip length λ^+ expressed in viscous units is equivalent to the upward displacement ΔU^+ of the mean velocity profile in the logarithmic region; here, $\lambda^+ = \lambda u_\tau / \nu$, where ν is the kinematic viscosity, $u_\tau = \sqrt{\tau_w / \rho}$ is the friction velocity, ρ is the density, and τ_w is the (local) shear stress.

The value of the slip length λ depends upon the shape and size of the riblets cross-section. Bechert et al. [4] found that the largest drag reduction for riblets of different shapes was obtained when s^+ , the spanwise period of the riblets, is in the range 10–20. García-Mayoral and Jiménez [1] tested alternative scalings to find whether drag reduction can be linked to a single geometric parameter that captures the importance of riblet spacing and their cross-sectional shape as well. Data for different riblets were found to best collapse when plotted against a dimensionless length scale l_g^+ derived from the cross-sectional area A_g of the groove, and defined as $l_g^+ = (A_g^+)^{1/2}$. For riblets of various geometries, the best

performance was consistently found at $l_g^+ \approx 10.5$. For optimal triangular riblets, $l_g^+ = 10.5$ corresponds to a unitary shift ΔU^+ , which coincides with the one reported in previous studies [15,20,21]. Recently, Zhang et al. [22] have been able to compute the slip length for other riblets shapes, i.e., with trapezoidal and blade cross-sections.

The goal of this paper is to present the implementation of a slip-length boundary condition for riblets, and to use it in a set of RANS simulations to assess the drag reduction capabilities of riblets when installed on a fixed-wing UAV, for which endurance is of capital importance. Indeed, over the years, riblets have been studied either at low speed over plane walls, or in transonic flow conditions for aeronautical applications, especially for medium- or long-range commercial passenger aircraft. Such studies, carried out both numerically [10,23] and experimentally [24–28], provide interesting results for aircraft operating in a range of chord-based Reynolds numbers up to $Re_\infty = 3 \times 10^7$. In contrast, the low-speed aircraft considered in the present work has a cruise speed of 22 m/s with $Re_\infty = 5 \times 10^5$.

This paper describes the implementation into an incompressible CFD solver of a slip-length wall boundary condition, similar to that described in ref. [21], to compute the drag reduction achievable with riblets of optimal dimensions. The computational model is validated against configurations of increasing complexity, and eventually applied to a realistic use case. We also consider selective deployment of riblets to different parts of the aircraft to show that drag reduction is not trivially proportional to the surface area covered by riblets. The structure of the work is as follows. After this introduction, Section 2 describes our model and the computational setup; Section 3 contains the results of preliminary simulations intended for validation; the actual results are described in Section 4, and Section 5 contains a concluding discussion.

2. Methods

2.1. Slip Length Boundary Condition

Both theory and experiments [3–5] suggest that the physics involved in drag reduction by riblets acts through a local mechanism. Indeed, since riblets are small compared to the turbulent structures of the near-wall cycle, far enough from the wall, the turbulent flow perceives the presence of riblets only as a homogeneous effect: the upward shift $\Delta U^+ > 0$ of the logarithmic portion of the mean velocity profile:

$$U^+ = \frac{1}{\kappa} \log(y^+) + A + \Delta U^+ \quad (1)$$

where $\kappa = 0.392$ is the von Kármán constant, and $A = 4.48$ is the near wall intercept for smooth surfaces (these constants are set after [29], but their numerical value does not affect the outcome of the study). The dimensionless vertical shift ΔU^+ equals the virtual shift in wall units of the non-slipping wall [4], i.e., the slip length λ^+ . We exploit this shift to account for the presence of riblets via a slip boundary condition, which linearly relates the wall value of the longitudinal component of the velocity u_w (the subscript w indicates quantities evaluated at the wall) to the wall shear rate $(\partial u / \partial y)_w$ through the slip length λ :

$$u_w = \lambda \left(\frac{\partial u}{\partial y} \right)_w, \quad (2)$$

thus effectively recovering the no-slip condition when $\lambda = 0$. The discrete counterpart of Equation (2), where the derivative is approximated with a finite difference, reads:

$$u_w = \lambda \frac{u_1 - u_w}{d}, \quad (3)$$

where u_1 is the longitudinal velocity at the first inner mesh point, and d is its distance from the wall. Hence, the velocity at the wall is:

$$u_w = u_1 \frac{\lambda}{\lambda + d}. \quad (4)$$

In this work, we always set the shift of the mean velocity profile at $\Delta U^+ = 1$, which corresponds [15,20,21] to the best-performing riblets with triangular cross-section. These riblets have a square root of the cross-sectional area of $l_g^+ = 10.5$, and provide a drag reduction of 7% when measured in the lab under controlled conditions and at low Re . Using $\Delta U^+ = 1$ implies setting $\lambda^+ = 1$, whence the physical size of the riblets varies along the body with the friction velocity of the flow. In other words, riblets are assumed to be locally optimal everywhere, and the corresponding physical dimensions are computed as a result of the simulation.

It is worth noticing that the present boundary condition can be used to simulate, besides riblets, any other drag reduction method whose effect reduces to a shift in the mean velocity profile. To this purpose, only the slip-length value must be adjusted.

2.2. Computational Setup

The boundary condition described above has been implemented in OpenFOAM [30], an open-source finite-volumes CFD library widely used in engineering and science, both in commercial and academic studies. Before considering the UAV, the boundary condition has been validated on flow cases of increasing complexity where at least partial information is available for comparison: a flat plate and a NACA 0012 airfoil.

The selected flow solver is SimpleFOAM, which uses the SIMPLE (Semi-Implicit Method for Pressure-Linked Equations) algorithm to solve the incompressible steady RANS equations. The $k - \omega$ SST turbulence model [31] has been adopted in this work, where standard values for the coefficients and no transition model have been used. For all the simulations, we adopt a freestream ratio between eddy and laminar viscosity equal to 0.001, together with free-stream turbulence intensity of $TU_\infty = 5\%$, with the only exception of the flat plate case, for which $TU_\infty = 0.5\%$. The spatial discretization used for the divergence, gradient, and Laplacian operators is second-order accurate. All the results have been checked to be fully converged in integral quantities (drag and lift) and in the residuals, by ensuring that the L_1 norm reduced to 10^{-8} times the initial value of the residual.

The study considers three geometries of increasing complexity. The first case is a two-dimensional flat plate boundary layer of length $L = 2$ m is considered, where $Re = U_\infty L / \nu = 10^6$. With air as working fluid, and a free-stream velocity of $U_\infty = 5$ m/s, the computational domain is rectangular and extends for 2.3 m in length and 1 m in height. The flat plate sits along the lower boundary of the computational domain. The domain extends 0.3 m upstream of the flat plate, and a symmetry boundary condition is used to simulate a free stream approaching the plate in this region. A suitable volume mesh is designed with the BlockMesh utility available in OpenFoam, and checked to yield mesh-independent results with a mesh sensitivity study. The final mesh, which provides a local friction coefficient that does not vary with further refinements, consists of 125,000 hexahedral elements, with 250 cells in the wall-normal direction and 500 cells in the wall-parallel direction, of which 400 are distributed over the flat plate. Non-uniform grid spacing is adopted to obtain more resolution in the near-wall and in the leading-edge regions, to better capture the boundary-layer development. Transition is adequately described, and the distance y_1 of the first cell from the wall is always below unity when expressed in wall units, i.e., $y_1^+ < 1$.

The second case is a two-dimensional NACA 0012 airfoil, at a chord-based Reynolds number of $Re_\infty = 10^6$. The airfoil chord c is taken of unitary length at 1 m, and the far-field boundary is located approximately $50c$ away from the airfoil surface. A mesh sensitivity study is carried out on a number of C-type grids by observing changes in the drag coefficient after successive mesh refinements. The chosen grid consists of 450 hexahedral cells in the chord-normal and 725 in the chord-tangent directions, and provides a repeatable transition

location. The mesh spacing near the airfoil is sufficient to ensure $y^+ < 1$ over the airfoil surface. Stretching of the grid is used to improve resolution in the wake region. To further validate the mesh accuracy, the solution has also been checked as a function of the angle of attack α . Hence, a number of preliminary runs at various values of α have been performed, without riblets, by replicating the flow conditions used in [32]. The outcome in terms of lift and drag coefficients is in very good agreement with the results reported by [32], as well as with the experimental measurements described in [33].

The final and most important case is the UAV. With a total length of 2.4 m and wing span of 3.6 m; its (simplified) geometry is described in some detail in Section 2.3. Simulations are carried out first on the isolated UAV wing, to understand to what extent the indirect beneficial effects of riblets noticed for the NACA 0012 carry forward to three dimensions, and the complete UAV is then considered. In both cases, the computational domain is made by a hemisphere, with a radius of 50 m that surrounds the wing half-span and the UAV half-span mounted on the $x - z$ plane, respectively. Symmetry is used to reduce computational cost. In this case, a commercial mesher is used to create unstructured meshes made by hexahedral and tetrahedral cells, with refinements boxes to capture the flow development near the body and in the wake. The grids possess 24 additional layers of hexahedral and tetrahedral elements aligned to the boundary surface, to guarantee that $y_1^+ < 1$, thus satisfying the requirements for an accurate computation inside the boundary layer within a low- Re formulation that does not resort to wall functions or other models of the near-wall region. A suitable mesh density is determined by observing changes in the drag coefficient, and robustness in predicting transition. The final mesh is designed with 4 million elements for the wing and 9.6 million elements for the full UAV.

2.3. The UAV Model

The considered UAV belongs to the family of Mini and Light Tactical UAV, with a MTOW (maximum take-off weight) ranging from 25 to 50 kg. The UAVs of this class are designed to integrate multiple payloads with different capabilities, e.g., EO/IR sensors, multi/hyperspectral cameras, LiDAR, transmitters, and radars. Flexibility is ensured by the fuselage modularity and by the possibility of changing the onboard systems configuration to achieve an optimised aircraft balance.

In this work, we consider a simplified geometric model of the UAV, as plotted in Figure 1, where small-scale geometric details and the propeller are omitted. The motivation is two-fold: such a simplified geometry, while remaining representative of the actual aircraft and retaining its essential qualitative features and dimensional characteristics, is free from intellectual property constraints; moreover, the lack of small-scale details allows some savings of computational effort. The simplified UAV is 2.4 m long and it has a span $b = 3.6$ m. It has a swept wing with a chord length of 0.3 m at the root with winglets at the tips of 0.22 m and dihedral angle of 21.5° . The considered reference surface area is $S = 1$ m². The UAV is characterised by a reverse V tail made by a symmetric four-digit NACA airfoil with a span of 1.05 m and a chord of 0.23 m. The tail is directly connected to the lower surface of the wing by two booms of 1.05 m with a circular cross-sectional area of radius 0.015 m. The fuselage is 1.41 m long and its cross-section originates from a rectangular shape, 0.29 m high and 0.23 m wide, with rounded edges. The drone cruise speed is 22 m/s, leading to a chord-based Reynolds number $Re_\infty = 5 \times 10^5$. The UAV weight of 25 kg and the cruise speed of 22 m/s, together with the geometrical information mentioned above, imply a lift coefficient in cruise of $C_L = 0.8322$.

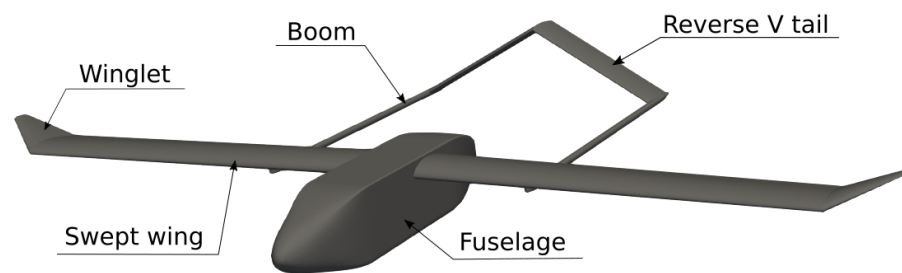


Figure 1. CAD model of the simplified UAV.

2.4. Dimensionless Force Coefficients

In this paper, the aerodynamic coefficients, i.e., the ratio of a force component and the reference quantity $1/2\rho U_\infty^2$, are the lift coefficient C_L and the total drag coefficient C_D . The latter can be decomposed into friction $C_{D,f}$ and pressure $C_{D,p}$ drag coefficients; the former describes the resistance to the relative motion between the fluid and the solid boundary due to viscous effects, the latter quantifies the net drag force arising from pressure variation around the body. When a wing of finite span is considered, the drag coefficient can alternatively be decomposed into induced and profile drag coefficients. The former, defined as $C_{D,i} = C_L^2 / (\pi b^2 / S)$ describes the additional drag due the three dimensional effects cause by the lift, and the latter, defined as $C_{D,pr} = C_D - C_{D,i}$ describes the same quantity due to all the other types of drag except that which is lift induced. Profile drag can further be decomposed in friction drag $C_{D,f}$ and form drag $C_{D,form} = C_{D,pr} - C_{D,f}$. Lastly, the local skin-friction and pressure coefficients are defined as $C_f = 2\tau_w / \rho U_\infty^2$ and $C_p = 2p / \rho U_\infty^2$ (in the coefficient subscripts, capital letters indicate global quantities and small letters indicate local quantities).

Changes between clean and riblets configurations are computed as $\Delta C_x = C_{x,0} - C_x$, where the subscript 0 refers to the clean configuration and x is the quantity of interest. The drag reduction rate, i.e., the change in drag normalised with the drag of the clean configuration is defined as $\Delta C_D / C_{D,0}$.

3. Validation

The boundary condition used to model riblets is first tested on simple two-dimensional flows, where available information allows a quantitative check of the outcome.

3.1. Flat Plate

The first application example is the zero-pressure gradient boundary layer developing over a flat plate. Optimal V-shape riblets, with $l_g^+ = 10.5$ corresponding to $h^+ = \sqrt{2}l_g^+$, are placed everywhere along the plate, immersed in a uniform external flow.

Figure 2 (left) shows how riblets influence the streamwise evolution of the friction coefficient, demonstrating the correct amount of drag reduction. On the entire plate, the integrated percentage drag reduction is $\Delta C_D / C_{D,0} = 6.5\%$, in agreement with existing experimental [3] information. Local changes of C_f , descending from the imposed slip, are consistent with those by ref. [15]. The evolution of the physical dimensions of the grooves is shown in Figure 2 (right), together with the analogous evolution of the slip length. Once the boundary layer becomes fully turbulent, i.e., for $Re_x > 10^5$, changes of the slip length with the streamwise coordinate are rather mild: there is a small increase with Re_x to reach the largest value of 50 microns at the downstream end of the plate. By construction, as explained earlier in Section 2, this corresponds to one viscous length. At the plate end, the predicted size of optimal riblets is approximately $h = 0.8$ mm.

The correctness of the model is directly checked in Figure 3, which provides graphical evidence that, regardless of the streamwise location, the upward shift of the mean velocity profile is of unitary value, confirming that $\Delta U^+ = \lambda^+ = 1$.

3.2. NACA 0012 Airfoil

Testing progresses to consider the two-dimensional flow around a NACA 0012 airfoil; this test case remains highly simplified, but brings in pressure drag, and thus lends itself to studying the effect of riblets on this non-frictional drag component. Unfortunately, little information is available for validation.

Once again, the airfoil is assumed to be fully covered by riblets of locally optimal size, i.e., ensuring $l_g^+ = 10.5$ everywhere. Figure 4 shows the mean velocity profile on the upper surface of the airfoil at $x/c = 0.5$, for two different angles of attack, namely 0 and 4 degrees. The expected unitary upward shift ΔU^+ due to the grooves is consistently observed. At $\alpha = 4^\circ$, experimental data are available from ref. [34], and the present results appear to agree with them. However, the agreement is less satisfactory at other incidences. It must be mentioned that experiments were carried out with riblets of constant physical size, with a size that is about 10 viscous lengths. The percentage total drag reduction at $\alpha = 0^\circ$ is measured to be 7%, which is in agreement with the experimental data from ref. [34,35], as well as with CFD results obtained by Mele and Tognaccini in [32]. Our data indicate only a mild variation of drag reduction with the angle of attack, while ref. [35] mentions an increase beyond 16% at $\alpha = 0^\circ$ and a sudden drop to zero at $\alpha = 10^\circ$. The lower part of Figure 4 compares the evolution of the skin-friction coefficient along the airfoil, and shows very good agreement with the same quantity taken from ref. [32] (except for the precise location of the transition region).

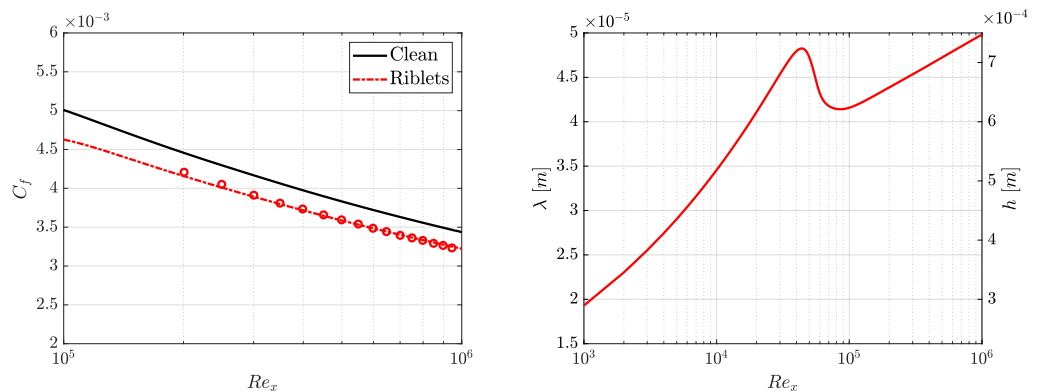


Figure 2. Zero-pressure-gradient boundary layer over a flat plate. **Left:** evolution of the skin-friction coefficient with/without riblets, and comparison with data from ref. [15]; **right:** change along the plate of the slip length (left y axis) and riblets height (right y axis), in dimensional units.

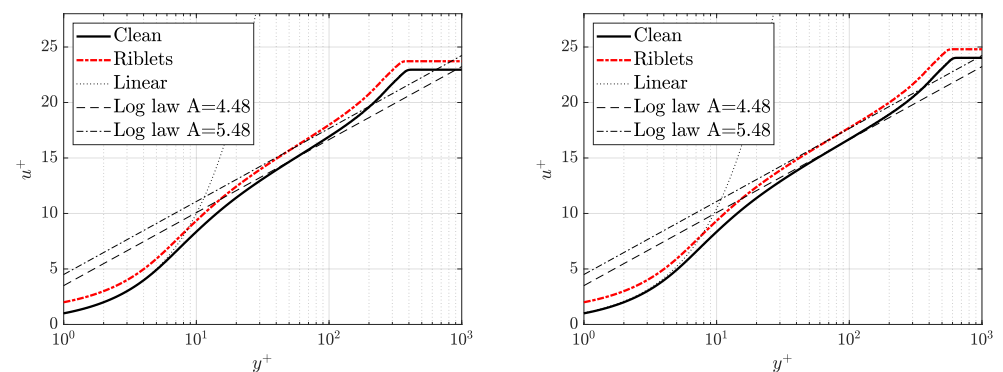


Figure 3. Mean velocity profile with/without riblets over the flat plate, at $Re_x = 5 \times 10^5$ (left) and $Re_x = 9 \times 10^5$ (right). The riblets profile consistently shows the upward shift of $\Delta U^+ = 1$ on the logarithmic region.

The pressure coefficient C_p and the difference $\Delta C_p = C_{p,0} - C_p$ at $\alpha = 4^\circ$ are shown in Figure 5. Changes are visible, to attest once again the effect of riblets on the pressure

distribution along the airfoil. Changes in the expansion peak at the leading edge and on the pressure recovery at the trailing edge due to riblets provide a significant additional contribution to drag reduction; form drag is reduced by 7.7%, adding to the friction reduction of 6.7%. These results agree with several findings by Mele and Tognaccini [15], who interpreted the reduced form drag by observing that riblets change the flow field by making it more similar to the inviscid solution, where the slip length is infinite, and form drag is exactly zero. Moreover, the altered pressure distribution leads to a larger lift in all tested incidences; this effect, which will be discussed later when discussing the full aircraft, is important for the reduction of the total drag: since the aircraft in cruise always needs the same lift, increased aerodynamic efficiency implies a reduced angle of attack in cruise, thus bringing in an additional contribution to drag reduction.

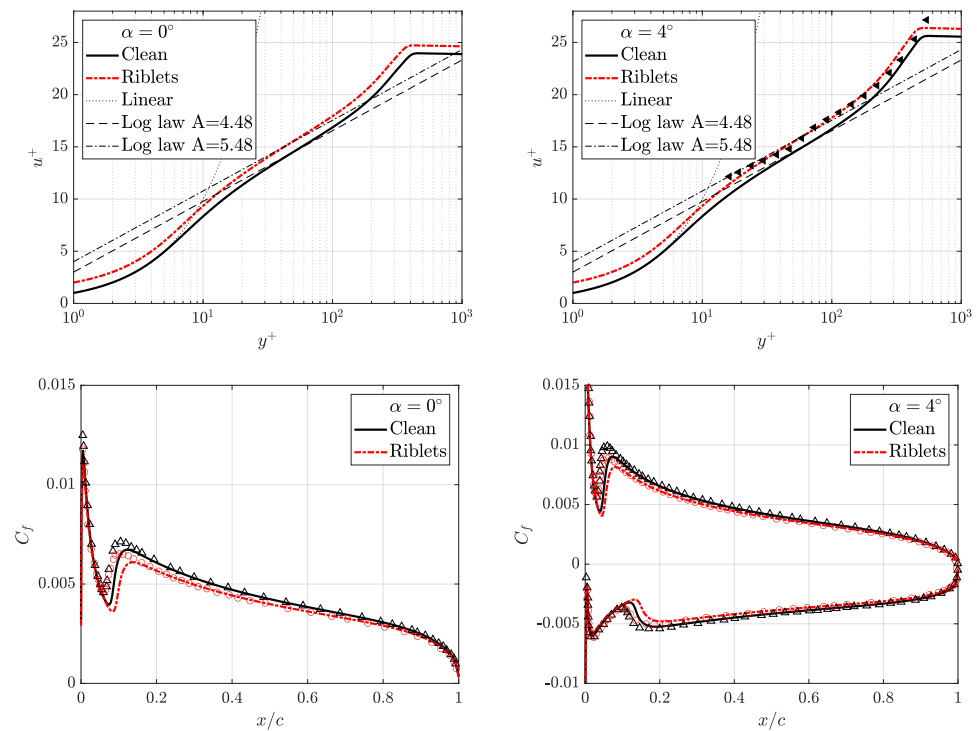


Figure 4. Mean velocity profiles (top) and skin-friction coefficient (bottom) for the NACA0012 airfoil, at an incidence of $\alpha = 0^\circ$ (left) and $\alpha = 4^\circ$ (right). The top row shows the mean profile over the suction side in law-of-the-wall form at $x/c = 0.5$, and compares with data from ref. [34]. The bottom row plots the evolution of the friction coefficient along the chord, and compares with data from ref. [32], represented with symbols.

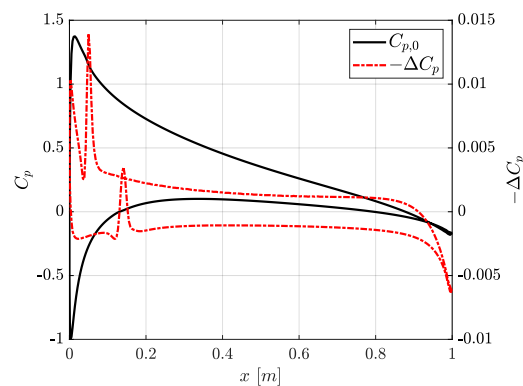


Figure 5. Pressure coefficient on the pressure and suction sides of the NACA0012 airfoil at $\alpha = 4^\circ$ for the clean case (black line), and difference with the riblets case (red dashed line).

4. Results

4.1. The Isolated UAV Wing

The UAV wing is considered first, to focus on the presence of indirect drag reduction effects in three dimensions, but without the geometrical complexities implied by the interaction between wing and fuselage. The UAV finite isolated wing is considered at the cruise flight condition of $Re_\infty = 5 \times 10^5$. As always, locally optimal riblets with $l_g^+ = 10.5$ are placed over the entire wing surface.

Figure 6 shows how drag reduction induced by riblets changes with the angle of attack. The friction component of the total drag reduction is nearly constant at 6.3%, whereas pressure and total drag change with α . At $\alpha = 0^\circ$, the total drag reduction rate is 3.7%, and diminishes at larger incidences. Clearly, the diminished total drag reduction goes hand in hand with the diminished pressure drag reduction. As already observed for the NACA 0012 airfoil in Section 3.2, riblets tend to modify the pressure distribution in such a way that lift is increased; this is confirmed here for the UAV wing. This phenomenon causes an increase in the lift-induced drag, which is not seen in two dimensions. This should not be regarded as a negative effect of riblets, since the aircraft has to achieve the same lift, and increased aerodynamic efficiency is always beneficial.

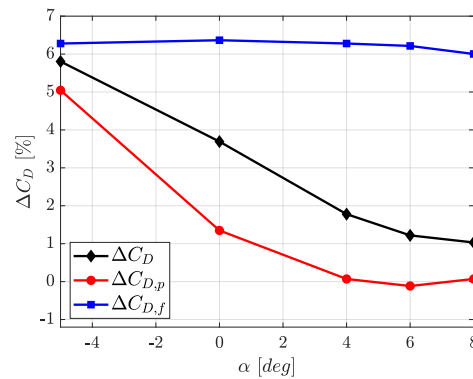


Figure 6. Riblets drag reduction vs. angle of attack for the UAV wing.

In fact, riblets' performance should be measured by adjusting α in such a way that the lift coefficient is unchanged. In Table 1, we compare the clean case and the riblets case at the same angle of attack, and at the same lift coefficient as well. Two configurations are considered, at a nominal angle of attack of $\alpha = 0^\circ$ and $\alpha = 4^\circ$. Total drag is split into friction $C_{D,f}$ and pressure $C_{D,p}$ drag, as well as induced $C_{D,i}$ and profile $C_{D,pr}$ drag. As expected, comparing at the same C_L provides larger drag reduction than comparing at the same α . At the same angle of attack, riblets produce a larger lift coefficient, and hence, a larger induced drag. It is worth noticing that the decrease in $C_{D,pr}$ is almost the same for the cases at constant α and constant C_L , whereas the induced drag is larger when compared at the same α .

Table 1. Aerodynamic coefficients for the isolated UAV wing. Comparison between clean and riblets configurations is carried out at the same angle of attack and at the same lift coefficient for nominal angle of attack of $\alpha = 0^\circ$ and $\alpha = 4^\circ$.

	Clean		Riblets		Clean		Riblets	
	$\alpha = 0^\circ$	$\alpha = 0^\circ$	$\alpha = -0.0626^\circ$	$\alpha = 4^\circ$	$\alpha = 4^\circ$	$\alpha = 4^\circ$	$\alpha = 3.885^\circ$	$\alpha = 3.885^\circ$
C_L	0.4996	0.5055 (+1.2%)	0.4996 (-)	0.8719	0.8828 (+1.8%)	0.8719 (-)	0.8719 (-)	0.8719 (-)
C_D	0.0227	0.0219 (-3.7%)	0.0217 (-4.5%)	0.0386	0.0380 (-1.8%)	0.0374 (-3.3%)	0.0374 (-3.3%)	0.0374 (-3.3%)
$C_{D,p}$	0.0121	0.0119 (-1.4%)	0.0118 (-2.8%)	0.0280	0.0280 (-)	0.027 (-2.2%)	0.027 (-2.2%)	0.027 (-2.2%)
$C_{D,f}$	0.0106	0.0099 (-6.4%)	0.0099 (-6.4%)	0.0106	0.0100 (-6.3%)	0.0100 (-6.3%)	0.0100 (-6.3%)	0.0100 (-6.3%)
$C_{D,i}$	0.0077	0.0079 (+2.4%)	0.0077 (-)	0.0235	0.0241 (+2.5%)	0.0235 (-)	0.0235 (-)	0.0235 (-)
$C_{D,pr}$	0.0150	0.0140 (-6.8%)	0.0140 (-6.8%)	0.0151	0.0138 (-8.4%)	0.0138 (-8.5%)	0.0138 (-8.5%)	0.0138 (-8.5%)

Drag breakdown is graphically shown at various α in Figure 7: the focus is on the total, induced, and profile drag on the left panel, and on the contributions to profile drag on the right panel. From the left panel, riblets are seen to mainly act on the profile drag, while the lift-induced drag is essentially unchanged. The right panel of Figure 7 focuses on the decomposition of profile drag, and shows that, besides the obvious reduction of friction drag, riblets additionally act upon form drag in a significant way. Depending on the angle of attack, the benefit of riblets in reducing $C_{D,pr}$ is in the 5–10% range. This is linked to the modifications on the pressure distribution on the wing, already observed in the NACA 0012 validation tests; see Figure 5. The pressure distribution at $2y/b = 0.52$ for the UAV wing is shown in Figure 8, and confirms the larger pressure recovery and the increased expansion peak induced by riblets that are at the root of form drag reduction.

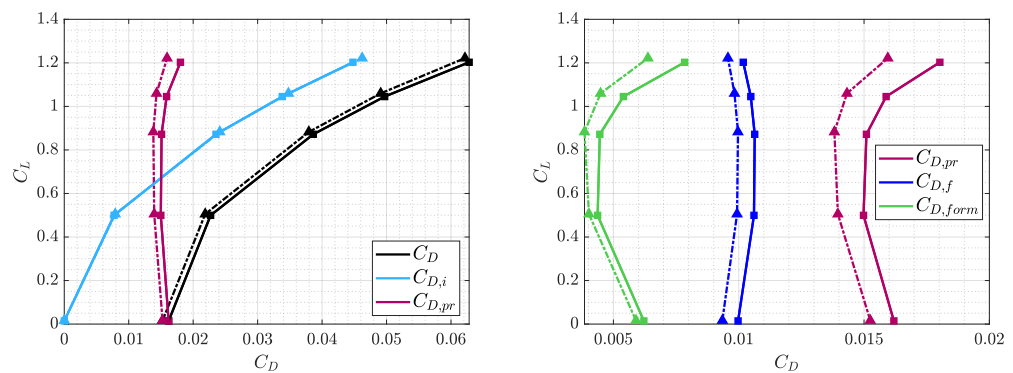


Figure 7. Drag breakdown for the isolated UAV wing (left), and focus on the profile drag (right). Solid lines with square markers indicate the clean configuration; dashed lines with triangular markers indicate the configuration with riblets.

Finally, Figure 9 plots the skin friction distribution at the spanwise station $2y/b = 0.52$ of the wing, and compares clean and riblets configurations at different angles of attack. A decrease in the skin friction across the entire chord is observed. In particular, on the suction side friction is mainly reduced in the fore portion; at large angles of attack, friction reduction vanishes in the aft part. On the lower surface, the reduction in friction is almost constant when α is varied.

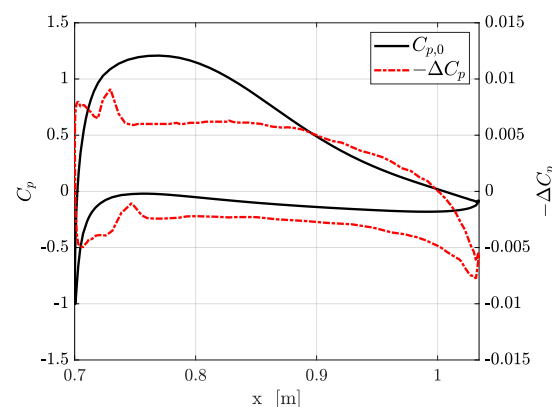


Figure 8. Pressure coefficient on the pressure and suction sides of the isolated UAV wing at $2y/b = 0.52$, at $\alpha = 4^\circ$, for the clean case (black line) and difference with the riblets case (red dashed line).

4.2. The UAV

The complete UAV is now considered in the configuration described above and shown in Figure 1. Consistently with the rest of this study, riblets are assumed to be locally optimal,

with $l_g^+ = 10.5$ and unitary slip length $\lambda^+ = 1$. The spatial distribution of the optimal riblet size, i.e., l_g (which, for a given cross-sectional shape, leads immediately to the geometric dimensions of the riblets) is retrieved as a result of the simulations. It should be remarked, however, that previous work [10] indicates how the size of locally optimal riblets does not vary much, so that the drag reduction obtained adopting riblets with constant physical size is quite near to the maximum drag reduction.

A series of simulations with/without riblets is carried out to provide data points to build the polar of the aircraft (Figure 10). Owing to the already highlighted lift increase provided by riblets, the angle of attack necessary to provide the required lift in cruise conditions slightly decreases from $\alpha = 2.85^\circ$ to 2.81° . The drag reduction obtained for the entire aircraft is an interesting 3%, which derives from a combination of a (less important) friction drag reduced by 6.1% and a (more important) pressure drag reduced by 1.5%.

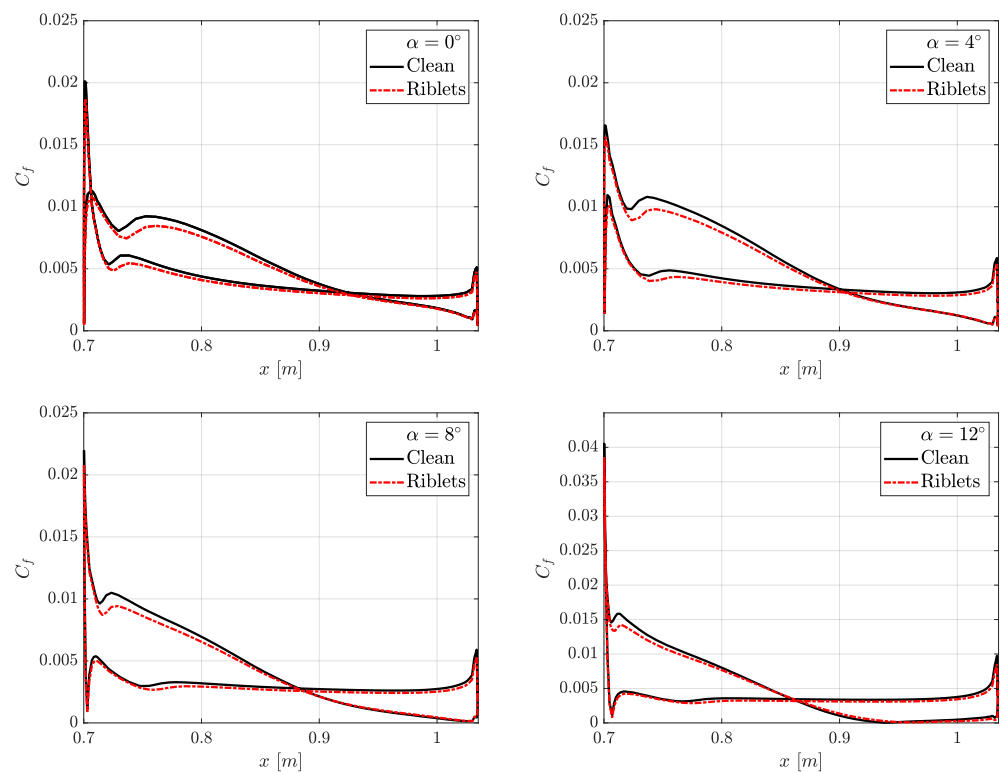


Figure 9. Friction coefficient for the isolated UAV wing, at spanwise location $2y/b = 0.52$ and four angles of attack.

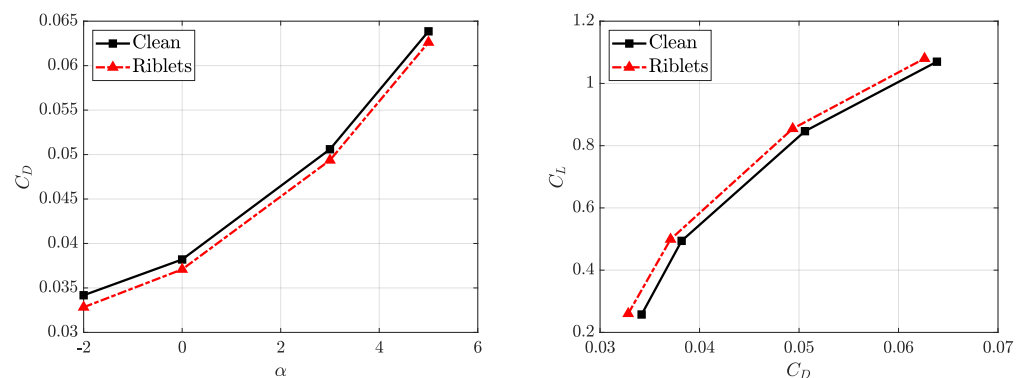


Figure 10. $C_D(\alpha)$ and polar curves of the UAV, in clean/riblets configurations.

Figure 11 helps determining where the largest percentage changes of the skin friction take place over the surface of the aircraft. $\Delta C_f / C_{f,0}$ is about 6% almost everywhere, roughly

as expected for a flat plate at this value of Re , except for the region near the trailing edge and for the aft part of the fuselage: here, the absolute value of C_f approaches zero, and its percentage variations become less meaningful.

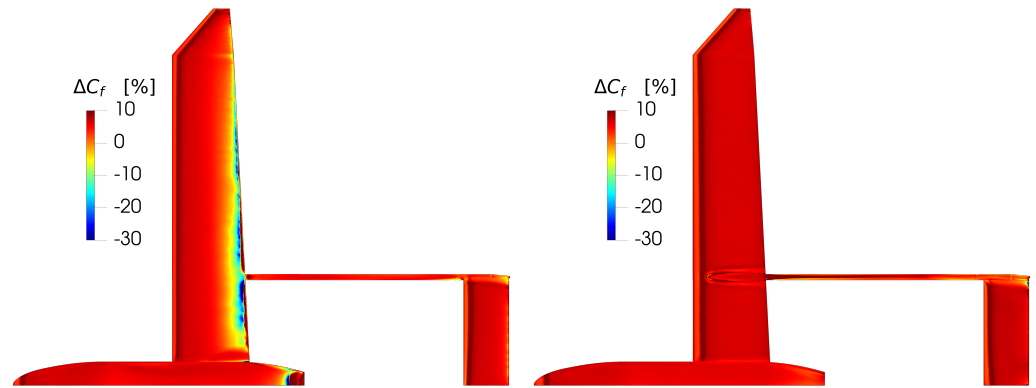


Figure 11. Percentage of skin friction reduction on the upper (left) and lower (right) parts of the aircraft in cruise condition.

Figure 12 shows the computed height distribution for the locally optimal riblets, by assuming that the cross-sectional riblet shape is a standard V groove, for which $s^+ = h^+ = \sqrt{2}l_g^+$. The optimal riblets height is about 0.2 mm nearly everywhere, except for the trailing edge of the wing, and for the aft part of the fuselage. This provides graphical evidence for the previous statement that riblets of properly chosen constant physical height would provide drag reduction that is very close to the maximum.

Riblets are then tested in off-design situations, i.e., at various incidences different from the cruise angle of attack, to check for robustness and to verify that riblets do not cause unwanted effects on the UAV aerodynamics during manoeuvres or the climb/descent phases of a typical mission. As already noted for the UAV wing, Figure 13 shows that, although drag reduction is maximum in cruise, the performance degrades only mildly when the angle of attack differs from the cruise value. Again, it is confirmed that friction drag reduction remains nearly constant when α ranges from -2° to 5° .

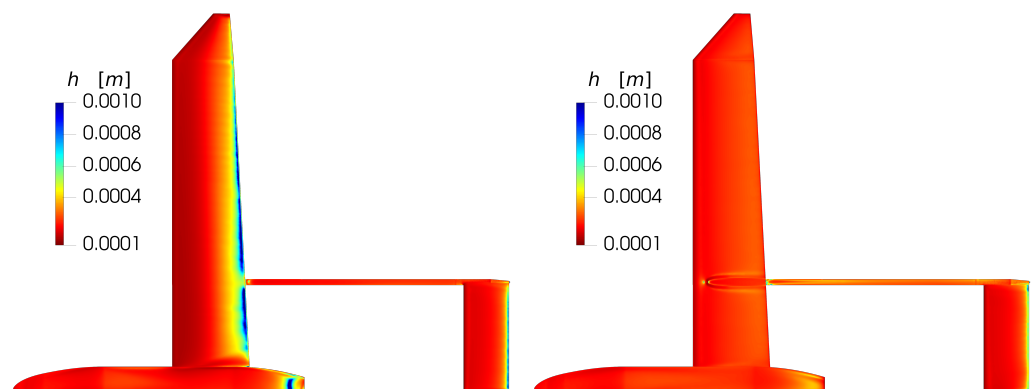


Figure 12. Spatial distribution of the computed optimal riblets height in physical units, for symmetric V groove riblets. **Left:** upper part of the aircraft in cruise conditions; **right:** lower part.

Finally, the aerodynamic drag is broken down into profile drag and induced drag in the left plot of Figure 14, while the right plot decomposes further profile drag into friction and form drag. The most obvious difference between clean and riblets configurations is the reduced profile drag, which derives from a sizable reduction in the friction component, joint with a comparable contribution from the form drag.

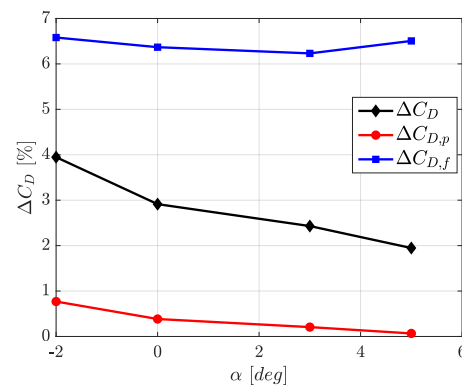


Figure 13. Drag reduction rate vs. angle of attack. The largest drag reduction is achieved in cruise condition.

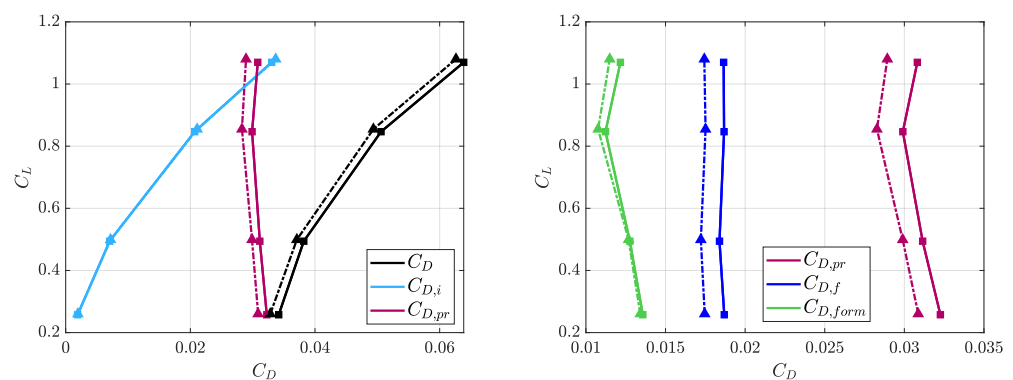


Figure 14. Drag breakdown (left) and decomposition of profile drag (right). Solid lines with square markers refer to clean configuration; dashed lines with triangular markers refer to riblets configuration.

4.3. Partial Coverage

Perhaps the most interesting consequence of the availability of a simple yet accurate boundary condition to model riblets within RANS simulations is the ability to carry out quick numerical studies to address practical problems related to their use. For example, since riblets produce limited benefits and imply costs and penalties, an elementary cost/benefit analysis should start by addressing the simple question of which area of the aircraft surface would yield the largest benefits after riblets installation. To this aim, we have designed a further set of simulations to explore partial coverage of the aircraft surface with riblets. The amount of coverage is quantified by the ratio β between the riblets-covered area and the total area, with $\beta = 1$ indicating total coverage. In these simulations, the full aircraft is considered, but riblets coverage varies according to Table 2, where case I is the full-coverage case described above. Outcomes of the simulations are shown in Table 3 and graphically represented in Figure 15. Figure 16 schematically illustrates where riblets are applied on the surface of the UAV.

Table 2. Coverage configurations.

	Riblets Deployment	β
I	Full coverage	1.000
II	No wing TE	0.953
III	No booms	0.935
IV	Only wing	0.524
V	Only wing, suction side	0.289

Table 3. Drag breakdown for the UAV in cruise condition, for different configurations of riblets coverage, and percentage changes with the clean case.

	C_D	$\Delta C_D/C_{D,0}\%$	$C_{D,p}$	$\Delta C_{D,p}/C_{D,p0}\%$	$C_{D,f}$	$\Delta C_{D,f}/C_{D,f0}\%$
Clean	0.0508	-	0.0338	-	0.0170	-
I	0.0493	3.0	0.0333	1.5	0.0160	6.1
II	0.0493	3.0	0.0333	1.5	0.0160	6.1
III	0.0493	2.9	0.0333	1.5	0.0160	5.8
IV	0.0498	2.0	0.0333	1.4	0.0165	3.3
V	0.0499	1.7	0.0333	1.5	0.0167	2.2

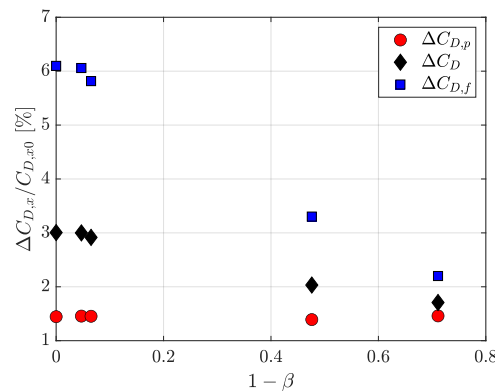


Figure 15. Drag reduction contributions for different configurations of riblets coverage from highest (I-full coverage) to lowest (V-wing only, suction side) coverage.

Since, at the trailing edge of the wing, riblets do not provide significant reductions in skin friction (Figure 11) while locally enforcing a substantial change from the optimal size, in configuration II riblets are removed from the trailing edge of the entire wing. The reduction of the riblets-covered surface is minimal (less than 5%) but, as expected, there is no appreciable decrease in terms of performance. Configuration III has riblets removed from the booms that connect the wing to the tail. Again, the overall drag reduction is essentially unchanged, with 6.5% savings in covered areas: pressure drag reduction remains unchanged since the boom is not an aerodynamic body, whereas friction reduction decreases, but minimally so, because the surface of the boom is small. Together, cases II and III suggest that removing riblets from both the trailing edge and the booms would avoid difficult areas, and save over 10% of application surface without incurring insignificant performance degradation.

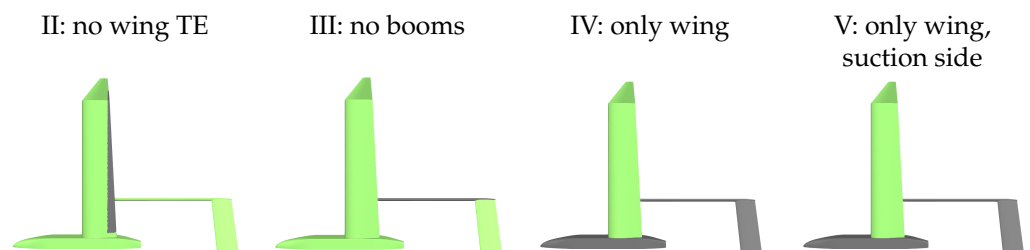


Figure 16. Schematic drawing of various riblets coverage configurations, cases II–V.

Configuration IV has riblets applied on the wing only, and is motivated by the observation that, in this application, pressure drag is approximately 2/3 of the whole drag, and that riblets placed on the wing produce pressure drag reduction in addition to friction drag reduction. With configuration IV, performance indeed degrades from 3% to 2%, but the saving in coverage area is more than proportional, with riblets surface shrinking down to one half at $\beta = 0.524$. As expected, pressure drag reduction remains almost unchanged at

1.4%, and friction drag reduction is seen to diminish from 6.1% to 3.3%: indeed, the area of the wing is approximately one half of the total area. Perhaps the most interesting configuration is configuration V, where only the suction side of the wing (and the entire winglet) is equipped with riblets, leading to $\beta = 0.289$. In contrast, the riblets-induced benefit remains more than one half, i.e., 1.7% instead of 3.0%.

5. Conclusions

The drag reduction potential of riblets deployed on a fixed-wing, low-speed Unmanned Air Vehicle (UAV) has been assessed with RANS simulations, with the aim of determining an optimal coverage policy. While riblets are fully characterised in low-speed flows over plane walls, and studies are available for aeronautical configurations in transonic flow (commercial mid- or long-range passenger aircraft), a low-speed aircraft such as the present one (for which the cruise speed is only 22 m/s) is considered here for the first time. Since the friction component of the aerodynamic drag of the UAV is modest, the effectiveness of riblets in this specific application needs to be assessed.

The RANS simulations, which employ a standard OpenFOAM setup, are unable to describe riblets directly. Thus, the presence of riblets is accounted for via a suitable slip condition enforced at the planar wall. The chosen amount of slip is constant in viscous units, and corresponds to riblets that locally possess optimal size in viscous wall units. The slip length model has been validated in the simple flows over a flat plate and around a subsonic airfoil, where results agree with available information.

Once applied to the UAV, the simulated riblets have brought out indirect and favourable effects, which go beyond the local reduction of friction drag, and also render the deployment of a friction-reduction device definitely interesting in such a low-speed application. Indeed, riblets significantly change the pressure distribution across the wing of the aircraft, which translates into an additional reduction of form drag, and in a lift increment as well. Although the latter obviously causes an increase in lift-induced drag, the requirement for the aircraft in cruise to fly at a given lift leads to a reduced angle of attack, and thus, to a further contribution to drag reduction. In the end, riblets provide up to 3% reduction of the total drag of the aircraft at cruise speed: a noticeable result, especially when the low-flight Reynolds number of the UAV is considered.

Once a cheap computational model is available to reliably compute the global effect of riblets on the aerodynamic drag, varying the riblets coverage policy becomes a computationally affordable task; relatively inexpensive simulations can help determine what drag benefit can be achieved with a given extent and location of the coverage of the aircraft surface. Thanks to the importance of secondary effects on pressure drag reduction induced by riblets, as a consequence of the significant pressure drag component, up to 1.7% of total drag reduction is achieved by placing riblets on the upper surface of the wing only. In this configuration, the total drag reduction is almost 2/3 of the maximum obtained with full coverage, but it is obtained with a coverage of less than 1/3 of the total area. Since riblets costs (for application and maintenance) are directly linked to the amount of riblets-covered surface, the wing-only configuration offers a reduced cost–benefit ratio, and does not touch the UAV fuselage, where systems (sensors, cameras, and transmitters) are designed to be installed. Further analysis can determine the practicality of riblets removal from high-wear areas (e.g., the leading edge), which would further add to the practical appeal of riblets in this application. Such calculations are made possible by the simplicity of the slip-length model, whose validity goes beyond riblets, since it can be used to simulate a generic drag-reducing device which locally reduces the skin friction.

Author Contributions: Conceptualization and methodology, C.M. and M.Q.; software and validation, C.B., L.C. and B.M.; writing—original draft preparation, C.B. and L.C.; writing—review and editing, F.G. and M.Q.; data curation, F.G.; supervision, M.Q.; project administration, C.M. All authors have read and agreed to the published version of the manuscript.

Funding: This research received no external funding.

Data Availability Statement: The data presented in this study are available on request from the corresponding author.

Conflicts of Interest: The authors declare no conflicts of interest.

References

- García-Mayoral, R.; Jiménez, J. Drag Reduction by Riblets. *Philos. Trans. R. Soc. A* **2011**, *369*, 1412–1427. [CrossRef] [PubMed]
- Walsh, M.J.; Weinstein, L.M. Drag and Heat-Transfer Characteristics of Small Longitudinally Ribbed Surfaces. *AIAA J.* **1979**, *17*, 770–771. [CrossRef]
- Bechert, D.; Bruse, M.; Hage, W.; Hoeven, J.V.D.; Hoppe, G. Experiments on Drag-Reducing Surfaces and Their Optimization with an Adjustable Geometry. *J. Fluid Mech.* **1997**, *338*, 59–87. [CrossRef]
- Bechert, D.; Bartenwerfer, M. The Viscous Flow on Surfaces with Longitudinal Ribs. *J. Fluid Mech.* **1989**, *206*, 105–209. [CrossRef]
- Luchini, P.; Manzo, F.; Pozzi, A. Resistance of a Grooved Surface to Parallel Flow and Cross-Flow. *J. Fluid Mech.* **1991**, *228*, 87–109. [CrossRef]
- Luchini, P. Reducing the Turbulent Skin Friction. In *Computational Methods in Applied Sciences 1996*; Wiley: Hoboken, NJ, USA, 1996.
- Spalart, P.; McLean, J. Drag Reduction: Enticing Turbulence, and Then an Industry. *Philos. Trans. R. Soc. A* **2011**, *369*, 1556–1569. [CrossRef] [PubMed]
- Gatti, D.; Quadrio, M. Reynolds-Number Dependence of Turbulent Skin-Friction Drag Reduction Induced by Spanwise Forcing. *J. Fluid Mech.* **2016**, *802*, 553–558. [CrossRef]
- Aupoix, B.; Pailhas, G.; Houdeville, R. Towards a General Strategy to Model Riblet Effects. *AIAA J.* **2012**, *50*, 708–716. [CrossRef]
- Mele, B.; Tognaccini, R.; Catalano, P. Performance Assessment of a Transonic Wing-Body Configuration with Riblets Installed. *J. Aircr.* **2016**, *53*, 129–140. [CrossRef]
- Koepplin, V.; Herbst, F.; Seume, J.R. Correlation-Based Riblet Model for Turbomachinery Applications. *J. Turbomach.* **2017**, *139*, 071006. [CrossRef]
- Nieuwstadt, F.T.M.; Wolthers, W.; Leijdens, H.; Krishna Prasad, K.; Schwarz-van Manen, A. The Reduction of Skin Friction by Riblets under the Influence of an Adverse Pressure Gradient. *Exp. Fluids* **1993**, *15*, 17–26. [CrossRef]
- Debisschop, J.; Nieuwstadt, F. Turbulent Boundary Layer in an Adverse Pressure Gradient: Effectiveness of Riblets. *AIAA J.* **1996**, *34*, 932–937. [CrossRef]
- Boomsma, A.; Sotiropoulos, F. Riblet Drag Reduction in Mild Adverse Pressure Gradient: A Numerical Investigation. *Int. J. Heat Fluid Flow* **2015**, *56*, 251–260. [CrossRef]
- Mele, B.; Tognaccini, R. Slip Length-Based Boundary Condition for Modeling Drag Reduction Devices. *AIAA J.* **2018**, *56*, 3478–3490. [CrossRef]
- Banchetti, J.; Luchini, P.; Quadrio, M. Turbulent Drag Reduction over Curved Walls. *J. Fluid Mech.* **2020**, *896*, 1–23. [CrossRef]
- Quadrio, M.; Chiarini, A.; Gatti, D.; Banchetti, J.; Memmolo, A.; Pirozzoli, S. Drag Reduction on a Transonic Airfoil. *J. Fluid Mech.* **2022**, *in press*. [CrossRef]
- Luchini, P. Linearized No-Slip Boundary Conditions at a Rough Surface. *J. Fluid Mech.* **2013**, *737*, 349–367. [CrossRef]
- Gomez-de-Segura, G.; Fairhall, C.; MacDonald, M.; Chung, D.; Garcia-Mayoral, R. Manipulation of Near-Wall Turbulence by Surface Slip and Permeability. *J. Phys.* **2018**, *1001*, 012011. [CrossRef]
- Walsh, M. Drag Characteristics of V-Groove and Transverse Curvature Riblets. In *Symposium on Viscous Flow Drag Reduction*; GR Hough American Institute of Aeronautics and Astronautics: New York, NY, USA, 1980.
- Mele, B.; Tognaccini, R.; Catalano, P.; de Rosa, D. Effect of Body Shape on Riblets Performance. *Phys. Rev. Fluids* **2020**, *5*, 124609. [CrossRef]
- Zhang, Z.; Zhang, M.; Cai, C.; Kang, K. A General Model for Riblets Simulation in Turbulent Flows. *Int. J. Comput. Fluid Dyn.* **2020**, *34*, 333–345. [CrossRef]
- Catalano, P.; de Rosa, D.; Mele, B.; Tognaccini, R.; Moens, F. Performance Improvements of a Regional Aircraft by Riblets and Natural Laminar Flow. *J. Aircr.* **2020**, *57*, 29–40. [CrossRef]
- Walsh, M.J.; Sellers, L.W.; McGinley, C.B. Riblet Drag at Flight Conditions. *J. Aircr.* **1989**, *26*, 570–575. [CrossRef]
- McLean, J.; George-Falvy, D.; Sullivan, P. Flight Test of Turbulent Skin-Friction Reduction by Riblets. In *Proceedings of the RAeS International Conference on Turbulent Drag Reduction by Passive Means*; Royal Aeronautical Society: London, UK, 1987; Volume RAeS 2, pp. 408–424.
- Szodruch, J. Viscous Drag Reduction on Transport Aircraft. In *Proceedings of the 29th Aerospace Sciences Meeting*, Reno, NV, USA, 7–10 January 1991; Aerospace Sciences Meetings; American Institute of Aeronautics and Astronautics: Reston, VA, USA, 1991. [CrossRef]
- Kurita, M.; Nishizawa, A.; Kwak, D.; Iijima, H.; Iijima, Y.; Takahashi, H.; Sasamori, M.; Abe, H.; Koga, S.; Nakakita, K. Flight Test of a Paint-Riblet for Reducing Skin Friction. In *Proceedings of the AIAA 2018 Applied Aerodynamics Conference*, Atlanta, GA, USA, 25–29 June 2018; pp. 1–7. [CrossRef]
- Kurita, M.; Iijima, H.; Koga, S.; Nishizawa, A.; Kwak, D.; Iijima, Y.; Takahashi, H.; Abe, H. Flight Test for Paint Riblets. In *Proceedings of the AIAA Scitech 2020 Forum*, Orlando, FL, USA, 6–10 January 2020. [CrossRef]
- Luchini, P. Universality of the Turbulent Velocity Profile. *Phys. Rev. Lett.* **2017**, *118*, 224501. [CrossRef] [PubMed]

30. Weller, H.; Tabor, G.; Jasak, H.; Fureby, C. A Tensorial Approach to Computational Continuum Mechanics Using Object-Oriented Techniques. *Comput. Phys.* **1998**, *12*, 620–631. [CrossRef]
31. Menter, F. Two-Equation Eddy-Viscosity Turbulence Models for Engineering Applications. *AIAA J.* **1994**, *32*, 1598–1605. [CrossRef]
32. Mele, B.; Tognaccini, R. Numerical Simulation of Riblets on Airfoils and Wings. In Proceedings of the 50th AIAA Aerospace Sciences Meeting including the New Horizons Forum and Aerospace Exposition, Nashville, TN, USA, 9–12 January 2012; American Institute of Aeronautics and Astronautics: Reston, VA, USA, 2012.
33. Ladson, C.L. *Effects of Independent Variation of Mach and Reynolds Numbers on the Low-Speed Aerodynamic Characteristics of the NACA 0012 Airfoil Section*; NASA TM 4074; NASA: Washington, DC, USA, 1988.
34. Sundaram, S.; Viswanath, P.; Rundrakumar, S. Viscous Drag Reduction Using Riblets on NACA 0012 Airfoil to Moderate Incidence. *AIAA J.* **1996**, *34*, 676–682. [CrossRef]
35. Viswanath, P. Aircraft Viscous Drag Reduction Using Riblets. *Prog. Aerosp. Sci.* **2002**, *38*, 571–600. [CrossRef]

Article

Efficiency of Pulsating Base Bleeding to Control Trailing Edge Flow Configurations

Carlos Carbajosa ¹, Alejandro Martinez-Cava ^{2,*}, Eusebio Valero ^{1,3} and Guillermo Paniagua ³

- ¹ Center of Computational Simulation, Universidad Politécnica de Madrid, Plaza Cardenal Cisneros 3, E-28040 Madrid, Spain; c.carbajosa@alumnos.upm.es (C.C.); eusebio.valero@upm.es or evaleros@purdue.edu (E.V.)
- ² Instituto Universitario de Microgravedad “Ignacio da Riva”, Universidad Politécnica de Madrid (IDR/UPM), E-28223 Madrid, Spain
- ³ Maurice J. Zucrow Laboratories, Purdue University, 500 Allison Road, West Lafayette, IN 47907-2014, USA; gpaniagua@purdue.edu
- * Correspondence: alejandro.martinezcava@upm.es

Abstract: As high-pressure-turbines operate at extreme temperature conditions, base bleed can be applied at the trailing edge of the airfoils, enhancing the thermal protection along the trailing edge surface, but also disrupting the trailing edge flow and altering the overall aerodynamic pressure losses. The current work explores the potential use of base bleed as a flow control tool to modulate the flow between turbine blade rows. Through the numerical analysis of a symmetric airfoil immersed in a subsonic flow, the effects that trailing edge ejection has on the base region properties and the downstream flow are evaluated. In particular, previous research constrained to steady blowing is now extended to consider an unsteady pulsating base bleed injection. Three injection frequencies are investigated, covering a wide range of base bleed intensities. The results presented herein demonstrate that pulsating bleed flow is more efficient than its steady counterpart in terms of reducing pressure losses and controlling the primary frequency of the downstream oscillations for the same mass flow injection.

Keywords: flow control; aerodynamics; trailing edge flow; unsteady flow characteristics; computational fluid dynamics

Citation: Carbajosa, C.; Martinez-Cava, A.; Valero, E.; Paniagua, G. Efficiency of Pulsating Base Bleeding to Control Trailing Edge Flow Configurations. *Appl. Sci.* **2022**, *12*, 6760. <https://doi.org/10.3390/app12136760>

Academic Editors: Josep Maria Bergada and Gabriel Bugada Castellort

Received: 31 May 2022

Accepted: 28 June 2022

Published: 4 July 2022

Publisher’s Note: MDPI stays neutral with regard to jurisdictional claims in published maps and institutional affiliations.



Copyright: © 2022 by the authors. Licensee MDPI, Basel, Switzerland. This article is an open access article distributed under the terms and conditions of the Creative Commons Attribution (CC BY) license (<https://creativecommons.org/licenses/by/4.0/>).

1. Introduction

In pursuing higher performance, the architecture of aircraft engines evolves towards lighter and more compact designs. Compactness can be achieved using counter-rotating subsonic turbines [1], transonic turbines [2], or supersonic turbines with pressure gain combustion [3]; but those configurations normally increase the unsteadiness and flow detachment of the boundary layer downstream of the trailing edge, which significantly contributes to the profile losses [4].

To illustrate the problem, Figure 1 depicts a representative trailing edge flow topology. As the flow approaches the trailing edge, the boundary layers from the pressure and suction sides of the turbine airfoils separate into two alternate shear layers, rolling into vortical structures. Eventually, the two periodic shear layers merge downstream at a confluence point, forming a confined region of low pressure and momentum, known as the base region [5]. The flow structures that form downstream of the turbine blade and their behavior are strongly affected by the base region properties, in particular the intermittent shear layer detachment that generates one or more pairs of vortexes that roll downstream. Both the rear suction side of the airfoil and the trailing edge must be carefully designed as they are prime contributors to aerodynamic drag and a source of forcing to downstream blade rows.

One way of mitigating both the losses and the source of unsteady forcing is to add momentum to this region, disrupting the base pressure, wake, and the downstream vortical pattern [6]. As high-pressure-turbines work in extreme temperatures environments, they require continuous airfoil cooling. In particular, the trailing edge of the airfoils is refrigerated by the redirection of coolant flow constantly ejected through holes or slots. When ejected at the trailing edge, this mass flow may be exploited to control the flow topology of the base region [6,7]. In recent years, the use of trailing edge or base bleed coolant ejection has proven to be effective in the mitigation and modulation of wake flow structures [8–10], or, when high velocities are involved, the trailing edge shock wave [11–14]. Available results in the literature mostly consider a constant mass flow ejection. Towards a more efficient use of this flow actuation, the modulation of the base bleed flow by means of intermittent trailing edge injection instead of a constant mass flow can be considered. This topic was numerically and experimentally covered in the low supersonic regime [15–17], with interesting results. While part of the published numerical data suggests that employing intermittent base bleed actuation would not offer significant gains when compared to constant actuation [16], empirical results indicate the contrary. It has been shown that forcing base bleed to actuate by pulses may enhance blade cooling and reduce associated losses, as the modulation of the trailing edge flow could alter the impingement of the trailing edge shock wave on the suction side of downstream blades [17].

However, trailing edge coolant injection may lead to the onset of unintuitive flow configurations. Saracoglu et al. [14] reported for the first time the onset of non-symmetric trailing edge flows when the flow is ejected in symmetric supersonic turbine blade configurations. A hydrodynamic stability analysis of the former configuration performed by Martinez-Cava et al. [18] demonstrated that a global instability may become dominant for specific blowing intensities, eventually breaking the symmetry of the base bleed jet. The flow topology at the base region may yield flow perturbations, whose properties depend on the ejected flow intensity and may tend to grow, eventually introducing a source of asymmetry, developing a *Coanda* effect produced by local pressure gradients. While this effect was present only at certain base bleed intensities, its link with the vortex detachment could affect the downstream flow structures and the aerodynamic forces developed on the airfoil [19].

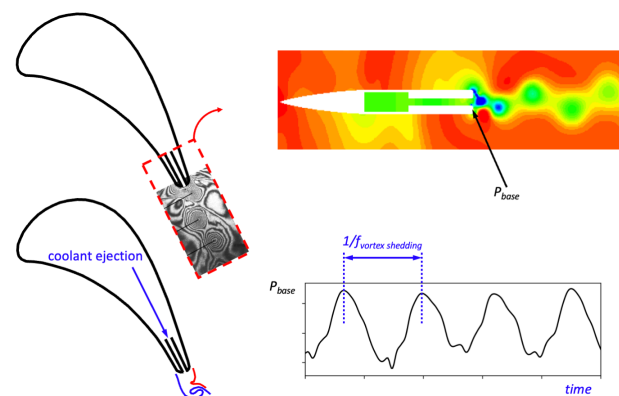


Figure 1. Representational scheme of trailing edge base region flow, together with static pressure contours and static pressure time series. Image partially reproduced from Martinez-Cava et al. [19]. Copyright © 2021, published by Elsevier Masson SAS. All rights reserved.

The current work further explores the effects of base bleed on subsonic conditions, considering a pulsating coolant flow base ejection to verify if unsteady blowing is more efficient than a continuous and steady trailing edge injection. A large set of numerical flow calculations covering a range of base bleed intensities and injection frequencies is compared against constant blowing conditions at the same maximum flow rate. Wake structure,

pressure loss, angle of the jet, and a detailed energy balance are evaluated. Despite having an apparent lower effect on the base region than constant base bleed, notable changes in the ejected jet angle, pressure losses, and measured forces are found when pulsating base bleed is employed, with significant gains on the energy costs required to reduce the aerodynamic pressure drag.

2. Computational Set-Up

The geometry considered in this work is the same studied by Martinez-Cava et al. [19] that we reproduce here for clarity.

A simplified trailing edge flow is achieved through a zero-cambered airfoil of 160 mm chord (c), with an aspect ratio value of 8 (defined as c/D , $D = 0.020$ m being the trailing edge thickness). Boundary layer separation at the leading edge has been avoided using a smooth Haack Series [20] nose shape. The mass flow employed on the base bleed is first discharged in a stagnation plenum inside the airfoil, which is connected to the base region by a thinner passage covering a third of its width ($b = 0.3D$). The model is confined between two parallel walls separated by 230 mm, and the inlet and outlet boundaries are placed at enough distance to avoid any interference of the boundary conditions. Subsonic conditions are imposed to recover a Mach and Reynolds number of $M = 0.34$ and $Re_c = 1.53 \times 10^6$, respectively. As no thermal aspects are covered in this analysis, a total temperature of 257 K is set at the free stream and a static temperature of 250 K is imposed on the base bleed flow.

Without any flow actuation, pairs of vortices would detach from the trailing edge with an associated frequency related to the incoming flow velocity and the trailing edge thickness, under a characteristic Strouhal number of $St = 0.287$. These vortices separate in an alternating manner from upper and lower sides, producing an oscillating behavior of the wake and the base region (Figure 1).

Flow calculations in this work are computed with the Finite Volume DLR-TAU Code [21] (TAU). Based on a three-dimensional finite volume scheme approach, TAU is a state-of-the-art compressible flow solver used on the aerospace industry to accurately calculate flow solutions from the low subsonic to the hypersonic flow regime. On time-dependent solutions, such as TAU, employ a dual time-stepping scheme coupled with a multigrid acceleration. Due to its performance in compressible flow, turbulent fluxes are modeled with the Menter's 2003 Shear Stress Transport version of the $k-\omega$ closure model [22]. The flow is considered to be fully turbulent from the leading edge, according to the suggestions of the high-pressure turbine community. The spatial discretization of the domain is done using a non-structured quadrilateral mesh (Figure 2), with localized refinements on the areas of interest, keeping y^+ values below unity so the boundary layer is fully resolved. Both mesh sensitivity and influence of the inlet turbulence intensity were evaluated in previous works [19], ensuring spatial discretization independence on the results and discarding sensitive results to changes in the turbulent inlet conditions. Furthermore, convergence of the periodic unsteady flowfield was ensured following the recommendations established by Clark and Grover [23].

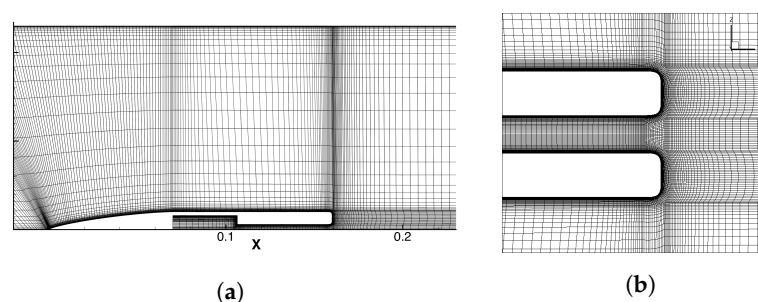


Figure 2. Detail of the grid spatial discretization used on the numerical analysis. General view (a) and trailing edge mesh details (b). Image partially reproduced from Martinez-Cava et al. [19]. Copyright © 2021, published by Elsevier Masson SAS. All rights reserved.

Actuation Details

Trailing edge flow actuation is modeled using TAU native boundary conditions, allowing control of the ejected mass flow and modulating its timing. The mass flow used on the trailing edge flow actuation is first discharged within a stagnation chamber and connected through a straight passage to the base region.

To keep a consistent nomenclature with previous works on trailing edge actuation of the literature, the mass flow ejected on the base bleed actuation is non-dimensionalized as:

$$C_b = \dot{m} / \rho_\infty U_\infty h, \tag{1}$$

\dot{m} being the imposed mass flow rate, $h = 0.9D$ the width of the base bleed stagnation chamber, with ρ_∞ and U_∞ as the free stream density and flow velocity. In this work, the non-dimensional parameter C_b is varied from 0 to 1, evaluating the different effects on the trailing edge flow encountered when varying the total ejected mass flow.

The base bleed flow is modulated in frequency and smoothed to avoid sudden changes, ramping up and down from constant blowing velocity to zero-mass flow during one actuation cycle, as depicted in Figure 3. The actuation time period is defined as $T = T_{act} + T_z$, T_{act} being the time where the flow is injected per period and T_z the zero flow rate actuating time. A duty cycle value of $D_c = T_{act} / T = 0.5$ is considered for all the studied cases.

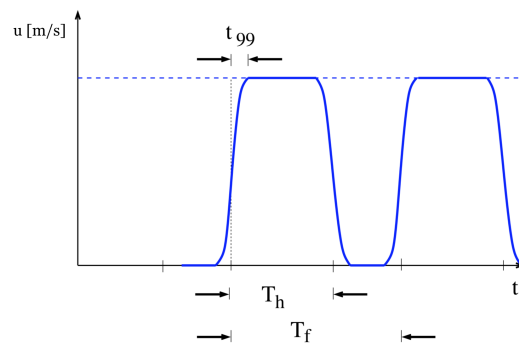


Figure 3. Illustration of the actuating boundary condition for periodic base bleed.

All configurations are tested for constant and pulsating blowing at the same maximum flow rate and at a range of frequencies varying from 100 to 200 Hz, the expected periodicity caused by the blade passing on high pressure turbines. The downstream flow topologies, the influence of the *Coanda* effect, and the energy gains due to the trailing edge flow injection are herein investigated. Furthermore, numerical monitors are employed to monitor static pressure at specific regions that, together with the calculated viscous forces, are time averaged to evaluate the changes produced during the pulsating trailing edge actuation.

3. Results and Discussion

3.1. Trailing Edge Steady Actuation

The effects of steady base bleed on the base pressure and the characteristic Strouhal number of the wake flow structures were studied in Martinez-Cava et al. [19] and are summarized in Figure 4. The evidence obtained from numerical analyses suggested to divide the trailing edge flow behavior in four distinctive phases:

Phase I. $C_b \simeq 0$. Vortices shed in an alternate manner from the trailing edge when no base bleed is applied. We refer to this stage as a non-blowing configuration.

Phase II. $C_b < 0.38$. Base pressure increases due to an initial “filling” effect, raising the maximum base pressure value to $P_{base} / P_\infty \approx 1.1$, with a slight increment in the frequency associated to the vortices. Under these conditions, the base bleed introduces a source of asymmetry on the wake downstream, followed by a neutralization of the vortex shedding.

Phase III. $0.38 < C_b < 0.8$. At this stage, the base pressure rapidly decays, almost eliminating the observed gains produced by a lower intensity trailing edge actuation. These changes are also accompanied by a reduction of the dominant wake flow frequency. While the trailing edge flow initially behaves as symmetric when it is time averaged, higher blowing intensities promote the onset of a non-symmetric flow topology.

Phase IV. $C_b > 0.8$. Elevated ejected mass flows eventually force a symmetric trailing edge flow, weakening any oscillation and increasing the base pressure towards a final plateau of $P_{base}/P_\infty \approx 1.07$. Further increments in the base bleed intensity do not produce significant changes in the flow topology.

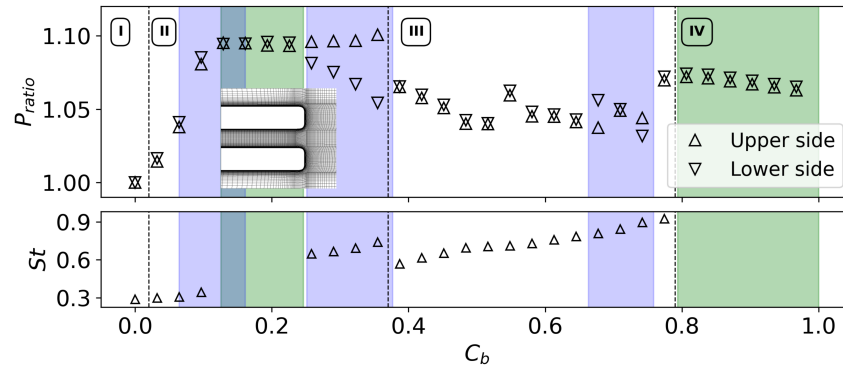


Figure 4. Evolution of the temporal averaging of the static base pressure ratio ($P_{ratio} = P_{base}/P_{baseNB}$) and the Strouhal number ($St = fD/U_\infty$) when the base bleed intensity is increased. Those mass flows related to non-symmetrical trailing edge flows are highlighted in blue, while those associated with the disappearance of vortex shedding are marked in green. Reproduced from Martinez-Cava et al. [19]. Copyright © 2021, published by Elsevier Masson SAS. All rights reserved.

3.2. Trailing Edge Pulsating Actuation

To evaluate the influence of a pulsating injection, the analysis of the considered base bleed configurations targets the evolution of four aerodynamic aspects:

1. Airfoil drag force.
2. Airfoil lift force, monitoring characteristic frequencies and extreme values.
3. Onset of a base region *Coanda* effect.
4. Energy efficiency of the trailing edge actuation.

Results are compared against those obtained with non-blowing and steady base bleeding configurations.

3.2.1. Airfoil Drag Force

To track the evolution of the viscous drag forces with respect to the base bleed intensity, a relative non-dimensional coefficient for the aerodynamic drag forces, $\overline{C_{d,R}}$, is defined as:

$$\overline{C_{d,R}} = \frac{C_d}{C_{d_{NB}}}, \quad (2)$$

where C_d is the drag force coefficient for a specific configuration and $C_{d_{NB}}$ is the corresponding drag coefficient for a non-blowing configuration. Its dependency with the non-dimensional base bleed rate, C_b , is depicted in Figure 5 for different pulsating base bleed frequencies. Increasing the values of C_b , the drag force coefficient initially decreases until it reaches a minimum at $\simeq C_b = 0.13$, approximately 17% lower than the reference value. However, higher values of C_b imply a further increment of the drag force coefficient, this being more pronounced for a steady base bleed. This increment of the drag force coefficient is related to a decrease in the base pressure value, as the ejected mass flow evacuates flow from the base region, hence increasing the pressure drag. Nevertheless, this

trend is more pronounced for a steady base bleed actuation, indicating that a pulsating injection may be more beneficial in terms of aerodynamic drag than its steady counterpart.

In the evaluated injection frequency range of 100–200 Hz, the drag forces appear to be quite insensitive to the frequency of the bleeding. Lower frequency ejections (below 100 Hz) may show a smooth transition from the numbers observed on a steady actuation to those shown herein for a pulsating actuation, but that remains out of the scope of the present analysis.

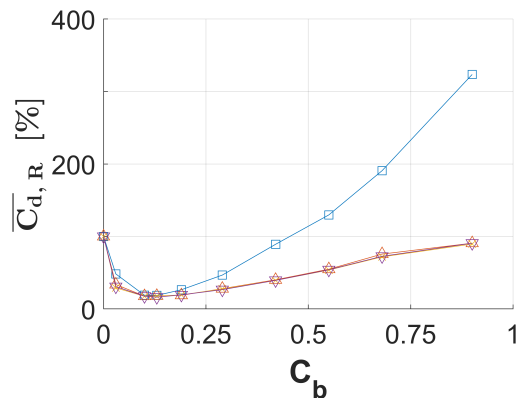


Figure 5. Mean drag coefficient relative to a non-blowing configuration against non-dimensional base bleed rate for constant (-□-) [19] and pulsating base bleeds at 100 Hz (-△-), 150 Hz (-×-) and 200 Hz (-▽-).

For illustration, snapshots of instantaneous pressure coefficient contours obtained from an URANS solution at $C_b = 0.13$ and $C_b = 0.90$ for a pulsating base bleed frequency of $f = 100$ Hz are depicted in Figure 6. The pulsation of base bleed modulates the pattern of trailing edge vortex shedding but does not neutralize it for high values of the non-dimensional base bleed rate, as observed in steady base bleed actuation [19].

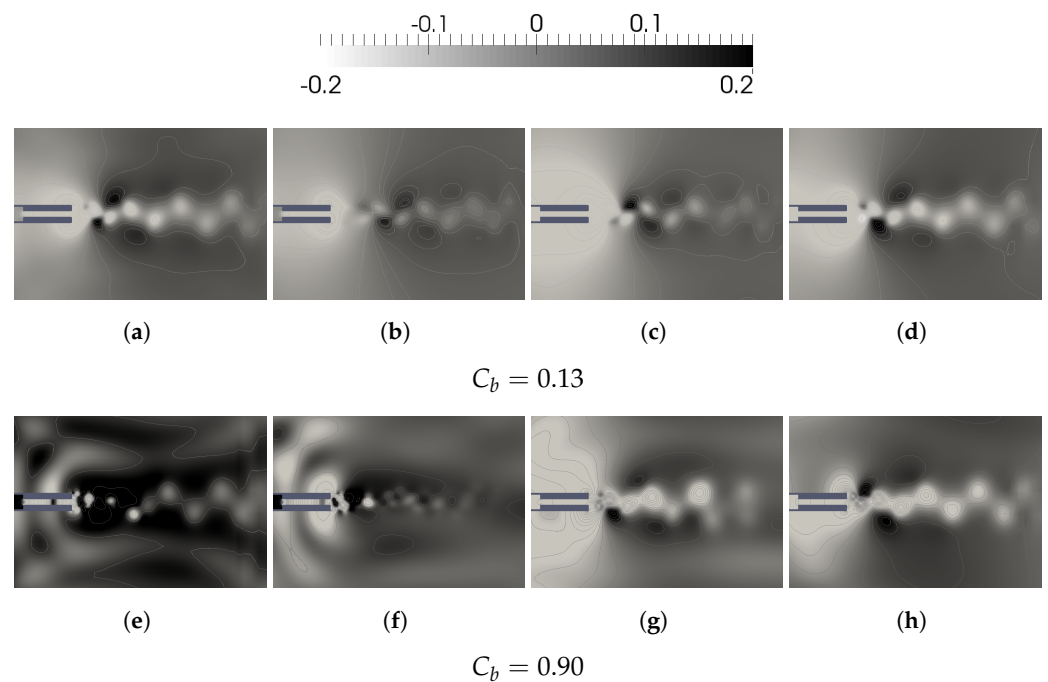


Figure 6. Snapshots of instantaneous pressure coefficient contours for a pulsating base bleed of $f = 100$ Hz and non-dimensional base bleed rates of $C_b = 0.13$ and $C_b = 0.90$. (a) $t = 0.1T$. (b) $t = 0.4T$. (c) $t = 0.7T$. (d) $t = T$. (e) $t = 0.1T$. (f) $t = 0.4T$. (g) $t = 0.7T$. (h) $t = T$.

3.2.2. Airfoil Lift Force

In this Section, the effect of the pulsating base bleed on the frequency and amplitude of the oscillations of the lift force coefficient is discussed. The definition of the Strouhal number considered for the interpretation of the results shown herein follows the definition:

$$St = \frac{fD}{U}, \tag{3}$$

where U is the velocity of the incident flow, D is the thickness of the considered airfoil at the trailing edge, and f is the lift force main oscillation frequency. The reference value for the Strouhal number is associated with a non-blowing configuration, $St = 0.287$. According to the underlying physics, there are three main possible contributions to the lift force oscillations:

1. Vortex shedding phenomenon
2. Oscillations of the jet angle
3. Injection frequency

The characteristic frequency is determined through a Fast Fourier Transform (FFT) of the time series obtained from the URANS simulations, which have been ensured to have reached convergence by showing periodic flow tendencies. Figure 7 depicts the Strouhal number obtained of the most energetic frequency plotted against the non-dimensional base bleed rate. The injection has a strong impact on the frequency of the lift oscillations, and despite the fact that there is no clear relation between St and C_b , certain conclusions can be extracted.

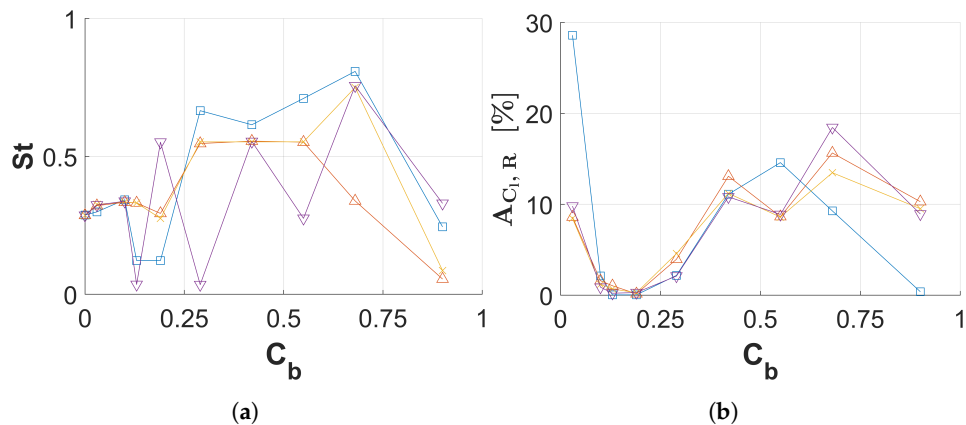


Figure 7. Strouhal number (a) and relative lift coefficient amplitude (b), $A_{C_l, R} = A_{C_l} / A_{C_l, NB}$, against non-dimensional base bleed rate. Results for constant (\square) [19] and pulsating base bleeds at 100 Hz (\triangle), 150 Hz (\times) and 200 Hz (∇).

The dependency of the associated frequencies with the base bleed rate follows the observed trend for steady base bleed [19], peaking as C_b increases. At certain ranges of base bleed intensities ($C_b = 0.1-0.3$ and $C_b > 0.8$), the oscillations are so small that it can be assumed that vortex shedding has been suppressed. The use of base bleed generally reduces the amplitude of the oscillations when compared to the non-blowing configuration, but the effect of the pulsating injection appears to be less evident than a steady actuation. For each injection cycle, the flow patterns at the base region are modulated with the *duty cycle*. Although base bleed mostly affects the base region area, the downstream region flow topology is also severely altered. A probe located downstream of the injection channel is used to monitor flow variables over time (point F_w on Figure 8). In Figure 9, spectrograms based on pressure time series of four actuation cycles are gathered for a non-blowing configuration and two different base bleed intensities. As the profiling point is located in the symmetry plane of the model, the first shows a clear dominance of a frequency value that doubles the frequency corresponding to the natural vortex shedding. However, the other two frequencies appear modulated by the actuation cycle, with the

former showing a disappearance of the vortex shedding related oscillations as the strength of the base bleed jet generates a symmetric flow topology.

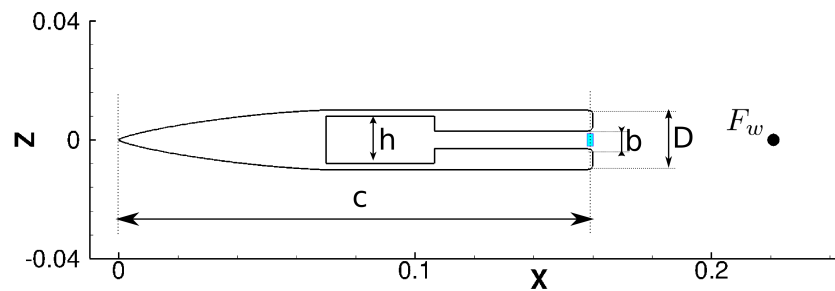


Figure 8. Main dimensions of the model and location of numerical probes for flow monitoring. Regions for jet flow analysis are highlighted in blue, and the location of the wake analysis probe is named F_w .

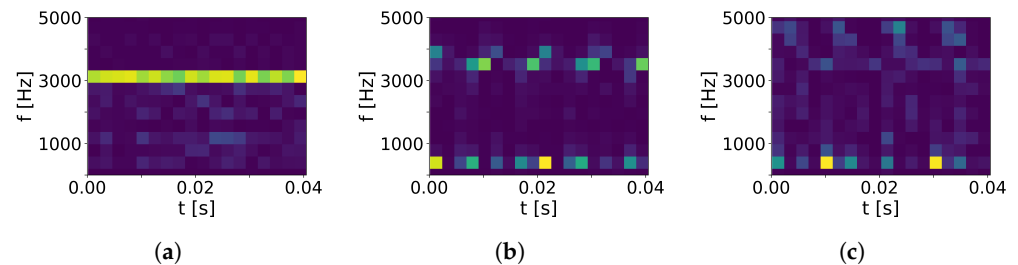


Figure 9. Frequency spectrograms taken at location F_w (see Figure 8) during four actuation cycles, for a pulsating base bleed of $f = 100$ Hz and different non-dimensional base bleed rates. (a) $C_b = 0.00$. (b) $C_b = 0.13$. (c) $C_b = 0.90$.

3.2.3. Base Region *Coanda* Effect

The evolution of non-symmetrical perturbations at the end of the base bleed injection channel develops the interaction of the upper and lower recirculation regions, eventually causing a deflection of the trailing edge jet following a so called “weak *Coanda*” effect [18]. This asymmetry in the base region is evaluated herein by means of two interrelated variables: the injection jet angle, β , and the averaged value of the lift coefficient, $\bar{C}_l = \bar{l}/q_\infty c$, l being the transversal aerodynamic force.

The base region flow properties are modified over time as a combination of the shear layer oscillations, vortex shedding, and the behavior of the base bleed jet. The jet angle, β , indicates the direction of the injected base bleed flow with respect to the symmetry plane. In this regard, several probes are located at the end of the injection channel, monitoring the different velocity components. An oscillation of β is expected when vortices are shed from the base region, while steady deviations of the injection flow, with respect to the horizontal, are caused by the onset of the aforementioned *Coanda* effect. Averaged values of the absolute value of the jet angle, $|\beta|$, are depicted in Figure 10, indicating that a *Coanda* effect appears for mid and low values of C_b , in a similar behavior to that obtained for a steady blowing, and its magnitude increases with the frequency of the pulsating injection. However, as opposed to steady base bleed configurations, where the deviation in the jet remains constant, now an oscillation in the direction of the jet linked to the intermittent flow injection appears, causing a further increment of the absolute value of the average jet angle. It can be argued that this phenomenon is related to the ramping-down effect of the jet intensity when the *duty cycle* is on its low stage, as the ejected mass flow decreases and acquires values for which a *Coanda* effect might develop. Finally, in a similar way to the observed trends during a steady actuation, at higher values of the injection rate, the *Coanda* effect is negligible.

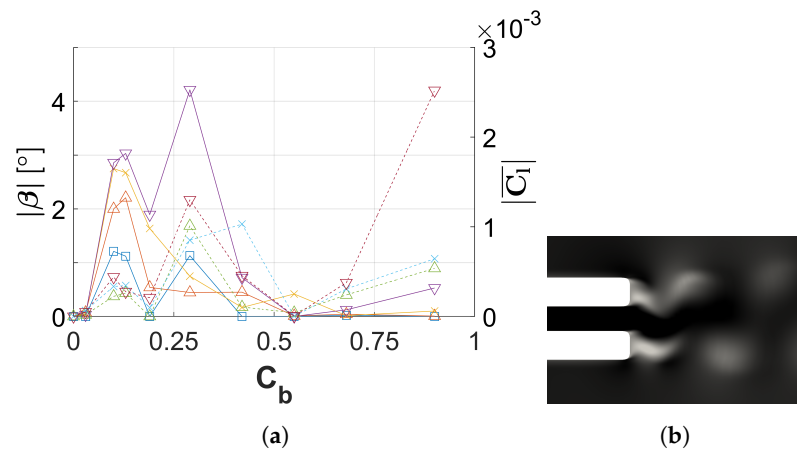


Figure 10. (a) Absolute value of the jet angle, $|\beta|$, (continuous lines) and averaged lift coefficient, $\overline{C_l}$, against non-dimensional base bleed rate (dashed lines). Results for constant (–□–) [19] and pulsating base bleeds at 100 Hz (–△–), 150 Hz (–×–), and 200 Hz (–▽–). (b) Snapshot of base region velocity contours, illustrating base bleed jet angle variations.

In absence of trailing edge injection, the mean value of the lift force is zero despite the flow oscillations. However, the *Coanda* effect induced by certain base bleed intensities introduces a non-symmetric flow topology, causing transversal loads with a non-zero average value. This effect is reflected in the results gathered in Figure 10, where the averaged lift force as a function of the injected mass flow rate is depicted. For illustration, lift forces are compared with those obtained with a non-blowing configuration. As expected, low values of the jet angle are linked to near zero averaged values of the lift force. Lift values increase with low C_b values, this effect being more pronounced for higher injection rates. Without contradicting the aforementioned results of the jet angle analysis, it appears that, despite the low jet angle for high C_b values, the large mass flow injected at the trailing edge has a non-negligible effect on the aerodynamics forces.

It may be argued that the global effect on the aerodynamic loads over a symmetric airfoil as the one analyzed here is relatively low. However, this effect could gain relevance on cambered airfoils with different trailing edge shapes, possibly causing circulation alterations and thus lift variations.

3.2.4. Efficiency Gain

A last analysis is performed herein, evaluating the energy requirements for each bleeding strategy. For a particular pulsating base bleed frequency, f , the total amount of mass flow injected per actuating period yields $m = \dot{m}D_c/f$. Hence, we may express the total energy needed to inject an amount of mass, m , at a certain flow speed, V , during a time period, T , as:

$$E_{Injection} = \frac{1}{2}mV^2 = \frac{1}{2}\dot{m}\frac{D_c}{f}V^2. \tag{4}$$

The injection power, $P_{Injection}$, defined as the energy required per unit of time, here expressed as a certain number of injection periods, $N_{periods}$, with respect to an actuation time, t , is then enunciated as:

$$P_{Injection} = \frac{E_{Injection}N_{periods}}{t} = \frac{1}{2}\dot{m}D_cV^2. \tag{5}$$

An important conclusion drawn from the aforementioned formulation is that, in the analytical approach performed, the injection power for a given base bleed rate is independent of the injection frequency and only depends on the *duty cycle*. The injection power for steady base bleed configurations can be recovered when $M = T$, while the injection power required for pulsating base bleed results from taking $D_c = M/T = 0.5$.

Given the two-dimensional nature of the analyses, the dissipated power per unit depth, $P_{Dissipated}$, can be defined as the product of the dimensional aerodynamic drag per unit depth and the inflow velocity:

$$P_{Dissipated} = q_{\infty} U_{\infty} \overline{C_d}, \quad (6)$$

with the corresponding values of for the dynamic pressure, q_{∞} , and the free stream velocity, U_{∞} , calculated from the inlet conditions described in Section 2.

The dissipated power is depicted in Figure 11, where the benefits of pulsed injection are clearly visible. It is interesting to note that, despite the variation on the ejected total mass flow and the subsequent variations on the base pressure, the gains in the averaged pressure drag of the most efficient configuration ($C_b \approx 0.13$) are nearly the same as those obtained for a steady trailing edge actuation. Increasing the injection intensity, a pulsed injection results in a more efficient use of the energy compared to constant bleeding, this effect being more accused for higher injection powers.

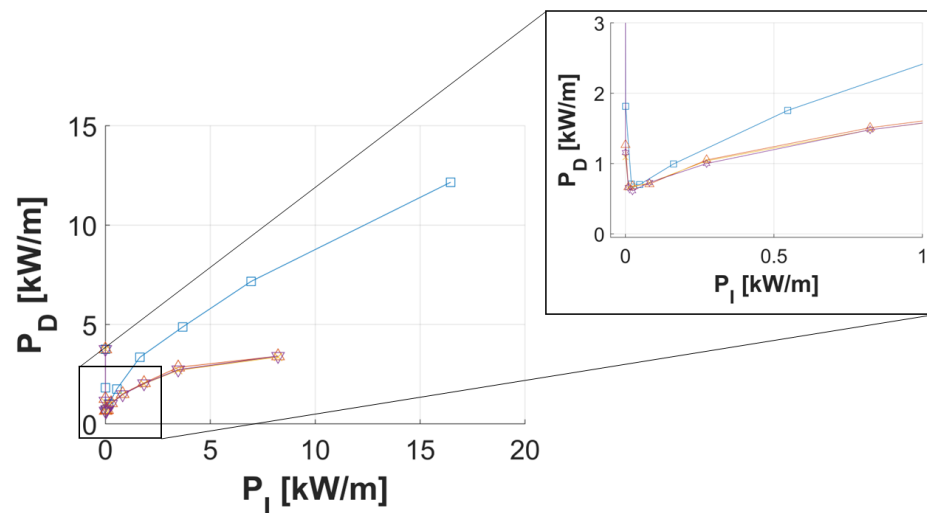


Figure 11. Dissipated power, P_D , against injection power, P_I , for constant (\square) [19] and pulsating base bleeds at 100 Hz (\triangle), 150 Hz (\times), and 200 Hz (∇).

4. Conclusions

In this work, a thorough numerical analysis on the effects and gains caused by pulsating flow actuation applied at an airfoil trailing edge has been conducted and compared with previous results obtained for constant base bleed and configurations without flow control at subsonic inflow speeds. In particular, actuation frequencies linked to the periodicity of the flow that may be caused by the blade passing on high pressure turbines is investigated. The potential capabilities of pulsating bleeding at the trailing edge as an active flow control methodology are notable, with proven effectiveness on the modulation of downstream flow structures, reducing the overall drag and controlling the frequency of the vortex detachment and transversal forces.

Considering the injected mass flow and the frequency of the injection as critical parameters, the results show a drag reduction of almost 85% for a non-dimensional injected mass flow of $C_b = 0.13$. While this gain is comparable to that obtained with steady blowing, a pulsed injection results in a more efficient use of the energy compared with constant bleeding, with this effect being more pronounced for higher injection powers.

The use of base bleed reduces the amplitude of the force oscillations when compared to the non-blowing configuration, but the effect of the pulsating injection on the lift force associated frequencies is less evident. While relatively low ($C_b \approx 0.13$) and high ($C_b > 0.8$) values of the non-dimensional base bleed mass flow are still related to a drastic reduction of the wake perturbations, indicating a vortex shedding neutralization, intermediate values

behave more erratically and seem to be more dependent on the pulsating frequency than expected. Further investigation is needed in this regard. However, the obtained frequency spectrograms for the trailing edge downstream flow show a clear modulation of the perturbations and a coupling with the frequency of actuation. Interestingly, a *Coanda* effect appears for mid and low values of C_b , in a similar behavior to that obtained for a steady blowing, and its magnitude (measured through the angle of the base bleed jet angle) increases with the frequency of the pulsating injection. Contrary to the cases with constant base bleed, where the deviation in the jet remains constant, now an oscillation in the direction of the jet linked to the intermittent flow injection appears, causing an increment of the absolute value of the average jet angle.

As coolant flow ejected at the trailing edge is currently employed on the enhancement of airfoil performance through base pressure modulation, the results shown herein present the use of pulsating flow actuation as a more efficient flow modulating tool to be considered on cooling flow systems. Additionally, intermittent flow actuation allows for modulate the airfoil wake structures, coupling it to the employed actuating frequencies and allowing for further exploitation of these methodologies.

Author Contributions: Conceptualization, A.M.-C. and G.P. and E.V.; Methodology, C.C. and A.M.-C.; Validation, C.C. and A.M.-C.; Writing, C.C., A.M.-C., E.V. and G.P.; Funding Acquisition, E.V. and G.P. All authors have read and agreed to the published version of the manuscript.

Funding: This research has received funding from the Ministerio de Ciencia, Innovation e Universidades of Spain under the project SIMOPAIR (Ref: RTI2018-480 097075-B-I00). This work has received funding from the European Union's Horizon 2020 research and innovation programme under the project FLOWCID, grant agreement No 101019137.

Institutional Review Board Statement: Not Applicable.

Informed Consent Statement: Not Applicable.

Data Availability Statement: Not Applicable.

Acknowledgments: The authors gratefully acknowledge the Universidad Politécnica de Madrid for providing computing resources on Magerit Supercomputer.

Conflicts of Interest: The authors declare no conflict of interest.

References

1. Paniagua, G.; Szokol, S.; Kato, H.; Manzini, G.; Varvill, R. Contra-rotating turbine aero-design for an advanced hypersonic propulsion system. *J. Propuls. Power* **2008**, *24*, 1269–1277. [CrossRef]
2. Sieverding, C.H.; Heinemann, H. The influence of boundary layer state on vortex shedding from flat plates and turbine cascades. *ASME J. Turbomach.* **1990**, *112*, 181–187. [CrossRef]
3. Sousa, J.; Paniagua, G.; Collado, E. Supersonic turbine design suitable for detonation based engines. *Chin. J. Aeronaut.* **2022**, *in press* [CrossRef]
4. Denton, J.D. Loss Mechanisms in Turbomachinery. *ASME J. Turbomach.* **1993**, *115*, 621–656. [CrossRef]
5. Nash, J.F. A Review of Research on Two-Dimensional Base Flow. *ARC R&M* **1963**, 1–25.
6. Sieverding, C.H. The influence of trailing edge ejection on the base pressure in transonic turbine cascades. *Proc. ASME Turbo Expo* **1983**, *105*, 215–222. [CrossRef]
7. Motallebi, F.; Norbury, J. The effect of base bleed on vortex shedding and base pressure in compressible flow. *J. Fluid Mech.* **1981**, *110*, 273–292. [CrossRef]
8. Barigozzi, G.; Armellini, A.; Mucignat, C.; Casarsa, L. Experimental investigation of the effects of blowing conditions and Mach number on the unsteady behavior of coolant ejection through a trailing edge cutback. *Int. J. Heat Fluid Flow* **2012**, *37*, 37–50. [CrossRef]
9. Rehder, H.J. Investigation of trailing edge cooling concepts in a high pressure turbine cascade-aerodynamic experiments and loss analysis. *J. Turbomach.* **2012**, *134*, 51029-1–51029-11. [CrossRef]
10. Li, Y.; Xu, H.; Wang, J.; Zhu, J.; Su, H. Numerical study of unsteady flow and cooling characteristics of turbine blade cutback trailing edges integrated with pin fins and film holes. *Aerosp. Sci. Technol.* **2022**, *126*, 107604. [CrossRef]
11. Kost, F.H.; Holmes, A.T. Aerodynamic effect of coolant ejection in the rear part of transonic rotor blades. In *AGARD Heat Transfer and Cooling in Gas Turbines (SEE N86-29823 21-07)*; AGARD: Neuilly Sur Seine, France, 1985.

12. Raffel, M.; Kost, F. Investigation of aerodynamic effects of coolant ejection at the trailing edge of a turbine blade model by PIV and pressure measurements. *Exp. Fluids* **1998**, *24*, 447–461. [CrossRef]
13. Yang, Z.; Hu, H. An experimental investigation on the trailing edge cooling of turbine blades. *Propuls. Power Res.* **2012**, *1*, 36–47. [CrossRef]
14. Saracoglu, B.H.; Paniagua, G.; Sanchez, J.; Rambaud, P. Effects of blunt trailing edge flow discharge in supersonic regime. *Comput. Fluids* **2013**, *88*, 200–209. [CrossRef]
15. Saracoglu, B.H.; Paniagua, G.; Salvadori, S.; Tomasoni, F.; Duni, S.; Yasa, T.; Miranda, A. Trailing edge shock modulation by pulsating coolant ejection. *Appl. Therm. Eng.* **2012**, *48*, 1–10. [CrossRef]
16. Bernardini, C.; Salvadori, S.; Martelli, F.; Paniagua, G.; Saracoglu, B.H. Pulsating Coolant Ejection Effects Downstream of Supersonic Trailing Edge. *Eng. Appl. Comput. Fluid Mech.* **2013**, *7*, 250–260. [CrossRef]
17. Saavedra, J.; Paniagua, G.; Saracoglu, B.H. Experimental Characterization of the Vane Heat Flux Under Pulsating Trailing-Edge Blowing. *J. Turbomach.* **2017**, *139*, 061004. [CrossRef]
18. Martinez-Cava, A.; Wang, Y.; de Vicente, J.; Valero, E. Pressure Bifurcation Phenomenon on Supersonic Blowing Trailing Edges. *AIAA J.* **2019**, *57*, 153–164. [CrossRef]
19. Martinez-Cava, A.; Rodríguez, D.; Valero, E.; Paniagua, G. Characterization of base bleed effects on subsonic trailing edge flows. *Aerosp. Sci. Technol.* **2021**, *113*, 106730. [CrossRef]
20. Perkins, E.W.; Jorgensen, L.H.; Sommer, S.C. *NACA-TR-1386: Investigation of the Drag of Various Axially Symmetric Nose Shapes of Fineness Ratio 3 for Mach Numbers from 1.24 to 7.4*; Technical Report; National Advisory Committee for Aeronautics; Ames Aeronautical Lab.: Moffett Field, CA, USA, 1958.
21. Schwamborn, D.; Gerhold, T.; Heinrich, R. The DLR Tau-code: Recent applications in research and industry. In Proceedings of the ECCOMAS CFD 2006: European Conference on Computational Fluid Dynamics, Egmond aan Zee, The Netherlands, 5–8 September 2006; Delft University of Technology: Edmond aan Zee, The Netherlands, 2006.
22. Wilcox, D.C. Formulation of the k- ω Turbulence Model Revisited. *AIAA J.* **2008**, *46*, 2823–2838. [CrossRef]
23. Clark, J.P.; Grover, E.A. Assessing convergence in predictions of periodic-unsteady flowfields. In *Turbo Expo: Power for Land, Sea, and Air*; Paper No: GT2006-90735; International Gas Turbine Institute: Barcelona, Spain, 2006; pp. 1831–1841. [CrossRef]

Article

Aerodynamic Efficiency Improvement on a NACA-8412 Airfoil via Active Flow Control Implementation

Nil Couto ¹  and Josep M. Bergada ^{2,*} 

¹ Politecnico di Milano, School of Industrial and Information Engineering, Campus Bovisa La Masa, 20156 Milan, Italy; nil.couto@mail.polimi.it

² Fluid Mechanics Department, Universitat Politècnica de Catalunya, 08034 Barcelona, Spain

* Correspondence: josep.m.bergada@upc.edu; Tel.: +34-937398771

Abstract: The present paper introduces a parametric optimization of several Active Flow Control (AFC) parameters applied to a NACA-8412 airfoil at a single post-stall Angle of Attack (AoA) of 15° and Reynolds number $Re = 68.5 \times 10^3$. The aim is to enhance the airfoil efficiency and to maximize its lift. The boundary layer separation point was modified using Synthetic Jet Actuators (SJA), and the airfoil optimization was carried on by systematically changing the pulsating frequency, momentum coefficient and jet inclination angle. Each case has been evaluated using Computational Fluid Dynamic (CFD) simulations, being the Reynolds Averaged Navier–Stokes equations (RANS) turbulence model employed the Spalart Allmaras (SA) one. The results clarify which are the optimum AFC parameters to maximize the airfoil efficiency. It also clarifies which improvement in efficiency is to be expected under the operating working conditions. An energy balance is presented at the end of the paper, showing that for the optimum conditions studied the energy saved is higher than the one needed for the actuation. The paper clarifies how a parametric analysis has to be performed and which AFC parameters can be initially set as constant providing sufficient previous knowledge of the flow field is already known. A maximum efficiency increase versus the baseline case of around 275% is obtained from the present simulations.

Keywords: Computational Fluid Dynamics (CFD); Active Flow Control (AFC); synthetic jet; boundary layer; aerodynamic efficiency

Citation: Couto, N.; Bergada, J.M. Aerodynamic Efficiency Improvement on a NACA-8412 Airfoil via Active Flow Control Implementation. *Appl. Sci.* **2022**, *12*, 4269. <https://doi.org/10.3390/app12094269>

Academic Editor: Wei Huang

Received: 13 March 2022

Accepted: 20 April 2022

Published: 23 April 2022

Publisher's Note: MDPI stays neutral with regard to jurisdictional claims in published maps and institutional affiliations.



Copyright: © 2022 by the authors. Licensee MDPI, Basel, Switzerland. This article is an open access article distributed under the terms and conditions of the Creative Commons Attribution (CC BY) license (<https://creativecommons.org/licenses/by/4.0/>).

1. Introduction

The Active Flow Control (AFC) technology applied to airfoils is beginning to be of common use, then a considerable number of recent papers tackle this matter [1–3]. Parametric analysis is still the most common methodology employed to evaluate the effect of the AFC on airfoils, yet the use of optimizers is becoming popular to obtain the most appropriate AFC parameters in any given application [4,5]. Some initial studies analyzed the performance when using continuous and pulsating actuations, and it was soon discovered that pulsating flow was coupling with the boundary layer natural instabilities and so being more energetically efficient [6–8].

Airfoil aerodynamic efficiency decisively effect fuel consumption, and AFC can improve it. Briefly, the AFC technology adds or subtracts momentum to/from the main flow with the aim of interacting with the boundary layer and delaying or advancing its separation. One of the advantages over passive flow control is that it is not creating drag increase when operating outside the design conditions. Cattafesta and Sheplak [9] divided the AFC techniques into three categories. (1) Moving body actuators, they do not add or subtract mass and induce local fluid motion [10]. (2) Plasma actuators, they generate high frequency ionized jets of fluid [11–14]. (3) Fluidic actuators (FA), create pulsating flow and in some configurations no moving parts are required. In some particular FA designs, the origin of the self-sustained oscillations was recently unveiled in [15–17].

From the different sorts of FA, Zero Net Mass Flow Actuators (ZNMFA) also called Synthetic Jet Actuators (SJA), have gained particular attention in the scientific community due to their high capabilities in controlling boundary layer separation [18–21]. Another advantage of SJAs is that do not require external fluid supply.

When considering the implementation of SJAs, two parameters are particularly relevant: the non-dimensional frequency $F^+ = fC/U_\infty$, where f is the dimensional frequency, C the airfoil chord and U_∞ the free-stream velocity, and the momentum coefficient (C_μ). C_μ is defined as $C_\mu = (h\rho_{jet}(U_j^2) \sin \theta) / (C\rho_\infty(U_\infty^2))$, where h is the jet width, ρ_{jet} is the jet density and ρ_∞ is the far field one, U_j characterizes the jet maximum velocity, the parameter θ defines the inclination angle of the jet versus the adjacent surface.

Amitay et al. [22] and Amitay and Glezer [23] studied the SJA frequency, position and C_μ when applied to a symmetric airfoil and observed that when locating the actuator near to the boundary layer separation point, the momentum coefficient needed to reattach the flow was smaller. Regarding the actuation frequency, they found that when it was an order of magnitude higher than the vortex shedding one ($F^+ \mathcal{O}(10)$), the flow was completely reattached.

SJAs on a NACA-0015 airfoil at $Re = 8.96 \times 10^5$ were experimentally studied by Gilarranz et al. [24]. They increased the stall angle from 12° to 18° and observed that for $AoA > 10^\circ$, the effectiveness of the actuation considerably increased. At $AoA > 25^\circ$, considerably high actuation frequencies were needed to observe large flow variations. The same airfoil and Reynolds number was studied by You and Moin [25] using Large Eddy Simulation (LES). A lift increase of 70% was obtained when using $C_\mu = 0.0123$, $F^+ = 1.284$ and $\theta = 30.2^\circ$. The same airfoil at $Re = 3.9 \times 10^4$ was experimentally studied by Tuck and Soria [26]. The optimum momentum coefficient and actuation frequencies were respectively, $C_\mu = 0.0123$ and $F^+ = 0.7$ and 1.3 , being the highest frequency the most effective one. When using these forcing conditions, an improvement of the stall AoA from 10° to 18° was observed. Kitsios et al. [27] numerically studied the same airfoil and Reynolds number via LES simulations. They observed that the optimal frequencies coincided with the vortex shedding one obtained from the baseline case (f_{wake}) and its first harmonic ($2f_{wake}$). Buchmann et al. [28] reached the same conclusion through experimental tests. Flow control using SJAs on a NACA-23012 at $Re = 2.19 \times 10^6$ was numerically investigated by Kim and Kim [29], Monir et al. [30]. Maximum lift was obtained when the jet was placed nearby the boundary layer separation point and $F^+ = 1$. When applying SJA tangentially, clear advantages were observed than when injecting/sucking fluid perpendicular to the surface.

The separation control generated by SJA on a NACA-0025 airfoil at $Re = 10^5$ and $AoA = 5^\circ$ were experimentally studied by Goodfellow et al. [31]. Momentum coefficient was found to be the primary control parameter, a drag decrease of nearly 50% was obtained when C_μ was higher than a certain threshold value. The same Reynolds number and wing profile, but at $AoA = 10^\circ$ was evaluated by Feero et al. [32]. They observed that the momentum coefficient needed C_μ to keep the flow reattached, was an order of magnitude lower when the excitation frequencies happened to be around the vortex shedding one. The same Reynolds number and wing profile but at $AoA = 12^\circ$ was analyzed in [33], where the jet position effectiveness in controlling the flow separation was evaluated. The optimum results were obtained when locating the jet groove nearby (whether downstream or upstream) the boundary layer separation point, a small improvement was observed in the upstream location. The NACA-0018 profile at $AoA = 10^\circ$ and at $Re = 1000$, was evaluated using direct numerical simulation (3D-DNS) by Zhang and Samtaney [34]. Three non-dimensional frequencies ($F^+ = 0.5, 1$ and 4) were considered. The optimum frequency was $F^+ = 1$ although improvement was observed in all of them. In Rodriguez et al. [35], the SD7003 airfoil at $Re = 6 \times 10^4$ and under three $AoA = 4^\circ, 11^\circ$ and 14° was numerically studied. At $AoA = 14^\circ$ they obtained an aerodynamic efficiency increase of 124%. The same Reynolds number and wing profile but at $AoA = 14^\circ$, and $AoA = 13^\circ$ & 16° was studied by [4,5], respectively. Due to the fact that in these studies optimization processes were employed, the maximum efficiency increase was obtained to be 280% and 591%, respectively.

The airfoil chosen for the present study is the NACA-8412, a Reynolds number of $Re = 68.5 \times 10^3$ and $AoA = 15^\circ$ were considered. According to the authors knowledge no previous studies for this airfoil and Re configuration have been found in the literature. The usage of the NACA-8412 airfoil was motivated by its large curvature, which in combination with the high AoA used will produce a separation of the flow close to the leading edge. This early separation will remark the effects of introducing SJA, and enable a clearer comparison of the results with the baseline case. Furthermore, the methodology employed in the present manuscript, which is based on a previous knowledge of the flow field and consist in initially fixing some AFC parameters, is proven to be very useful in obtaining good results while saving computational resources.

The rest of the manuscript is structured as follows. The formulation of the problem, the numerical methods employed and the mesh independence study are presented in Section 2. The definition of the AFC parameters and their implementation are introduced in Section 3. The Results section is introduced in Section 4 and the summary of the work is presented in Section 5.

2. Numerical Method

2.1. Governing Equations and Turbulence Model

Due to the unsteadiness of the problem, three possible turbulence models arose: Direct Numerical Simulation (DNS), Large Eddy Simulations (LES) and Unsteady Reynolds Averaged Navier–Stokes (URANS). Due to the large computational power required to perform both DNS and LES simulations, URANS was selected as the turbulence model used. More specifically, the Spalart–Allmaras model was chosen to perform all the simulations involved in the present study because of its suitability for low Reynolds cases and its easy convergence when the Courant–Friedrichs–Levy number $CFL < 1$. The Navier–Stokes equations for incompressible flow, take the form:

$$\frac{\partial u_i}{\partial x_i} = 0 \tag{1}$$

$$\frac{\partial u_i}{\partial t} + \frac{\partial u_i u_j}{\partial x_j} = -\frac{1}{\rho} \frac{\partial p}{\partial x_i} + \nu \frac{\partial^2 u_i}{\partial x_j \partial x_j} \tag{2}$$

Substituting each variable ϕ by the average $\bar{\phi}$ and fluctuation ϕ' terms.

$$\phi = \bar{\phi} + \phi' \tag{3}$$

Being $\phi(x, t)$ a generic flow variable, it can be written as the sum of its mean $\bar{\phi}(x, t)$ and fluctuating components $\phi'(x, t)$, being $\phi(x, t) = \bar{\phi}(x, t) + \phi'(x, t)$. By substituting it in the Navier–Stokes equations and taking the time average, it results in the following Reynolds-averaged Navier–Stokes equations,

$$\frac{\partial \bar{u}_i}{\partial x_i} = 0 \tag{4}$$

$$\frac{\partial \bar{u}_i}{\partial t} + \frac{\partial \bar{u}_i \bar{u}_j}{\partial x_j} = -\frac{1}{\rho} \frac{\partial \bar{p}}{\partial x_i} + \nu \frac{\partial^2 \bar{u}_i}{\partial x_j \partial x_j} - \frac{\partial \overline{u'_i u'_j}}{\partial x_j} \tag{5}$$

where the term $\overline{u'_i u'_j}$ is the Reynolds stress tensor denoted by R_{ij} and was approximated using Boussinesq hypothesis. The deviatoric part of the tensor is given as follows,

$$R_{ij} - \frac{1}{3} R_{kk} \delta_{ij} = -2\nu_t \bar{S}_{ij} \tag{6}$$

where ν_t is the kinematic eddy viscosity that needs to be modeled using one of the RANS models.

As it has been previously mentioned, the turbulence model selected was the Spalart–Allmaras (S-A). The model proposed by [36] solves a single transport equation for the modified form of the turbulent kinetic energy called $\tilde{\nu}$. This new parameter is identical to ν_t except in the viscous-affected region nearby the wall.

$$\nu_t = \tilde{\nu} \left(\frac{\chi^3}{\chi^3 + C_{v1}^3} \right) \tag{7}$$

The transport equation of $\tilde{\nu}$ is given as:

$$\frac{\partial \tilde{\nu}}{\partial t} + u_j \frac{\partial \tilde{\nu}}{\partial x_j} = \frac{1}{\sigma} \left[\frac{\partial}{\partial x_j} \left((\nu + \tilde{\nu}) \frac{\partial \tilde{\nu}}{\partial x_j} \right) + C_{b2} \frac{\partial \tilde{\nu}}{\partial x_i} \frac{\partial \tilde{\nu}}{\partial x_i} \right] + C_{b1} (1 - f_{t2}) \tilde{S} \tilde{\nu} - \left[C_{w1} f_w - \frac{C_{b1}}{\kappa^2} f_{t2} \right] \left(\frac{\tilde{\nu}}{d} \right)^2 \tag{8}$$

where:

$$\begin{aligned} f_w &= g \left[\frac{1 + C_{\omega 3}^6}{g^6 + C_{\omega 3}^6} \right]^{1/6}, \quad g = r + C_{\omega 2} (r^6 - r), \quad r = \min \left[\frac{\tilde{\nu}}{5 \kappa^2 d^2}, 10 \right] \\ \tilde{S} &= \Omega + \frac{\tilde{\nu}}{\kappa^2 d^2} f_{v2}, \quad f_{t2} = C_{t3} \exp(-C_{t4} \chi^2), \quad f_{v2} = 1 - \frac{\chi}{1 + \chi f_{v1}} \\ f_{v1} &= \frac{\chi^3}{\chi^3 + C_{v1}^3}, \quad \chi = \frac{\tilde{\nu}}{\nu} \end{aligned} \tag{9}$$

Being d the distance from a given point to the nearest wall, and Ω the magnitude of the vorticity. The model constants have the following default values:

$$\begin{aligned} C_{b1} &= 0.1355, \quad C_{b2} = 0.622, \quad \sigma = \frac{2}{3}, \quad C_{\omega 1} = \frac{C_{b1}}{\kappa^2} + \frac{(1 + C_{b2})}{\sigma} \\ C_{\omega 2} &= 0.3, \quad C_{\omega 3} = 2.0, \quad C_{v1} = 7.1, \quad \kappa = 0.4187, \quad C_{t3} = 1.2 \\ C_{t4} &= 0.5 \end{aligned} \tag{10}$$

2.2. Numerical Domain and Boundary Conditions

The NACA-8412 airfoil’s leading edge (LE) was located at the origin of the coordinate system, and the airfoil was fixed at zero degree angle with respect to the x -axis. The post-stall angle of attack of 15° was introduced by decomposing the freestream velocity in the corresponding x and y components. Note that all distances have been expressed as function of the airfoil chord C (see Figure 1). The distance between the inlet and the LE following the x -axis was set at $10C$, while the distance between the trailing edge (TE) and the outlet was set at $18C$. The height of the domain is $16C$, symmetrically distributed with respect to the airfoil. An almost identical computational domain was recently employed in [4].

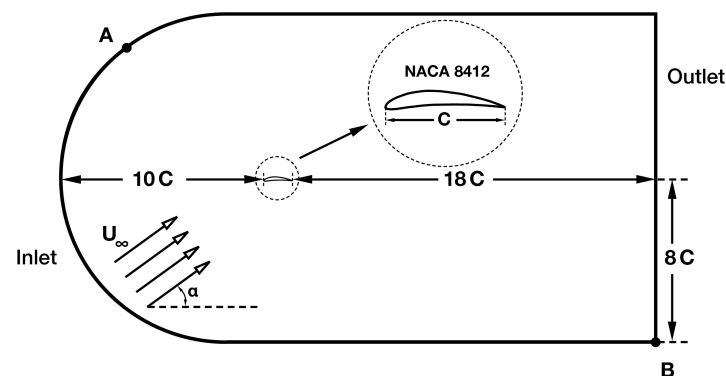


Figure 1. Sketch of the computational domain. The inlet and outlet boundaries have their limits in the points defined by the letters A and B.

The inlet was defined by the line connecting points A and B (see Figure 1) in a counter-clockwise direction, while the outlet was defined by the line connecting A and B in clockwise direction. At the inlet, Dirichlet boundary conditions for velocity were set by imposing the decomposition of the freestream velocity as it has been previously mentioned. Regarding pressure, Neumann boundary conditions were used. At the outlet, Neumann boundary conditions for velocity and Dirichlet boundary conditions for pressure were imposed. Over the airfoil’s surface Dirichlet boundary conditions for velocity were imposed in order to guarantee the non-slip condition, Neumann boundary conditions for pressure were considered.

The point A represented in Figure 1, which corresponds to one of the connecting points between the inlet and the outlet, had to guarantee that the angle formed by its tangent was larger than the angle of attack studied (AoA = 15°). For the present configuration, the tangent line to the inlet curve at the point A and the horizontal form an angle of 36.87°, complying with the mentioned restriction. Figure 2 introduces some AFC parameters as the jet position, jet width and jet inclination angle. The International Standard Atmosphere (ISA) model at sea level was used to select the air density, the pulsating flow fluid density, as well as the fluid dynamic viscosity. A relatively low Reynolds number was selected in order to have proportionally low mesh computational requirements and computational time. The values of the physical parameters involved in the present study are summarized in Table 1.

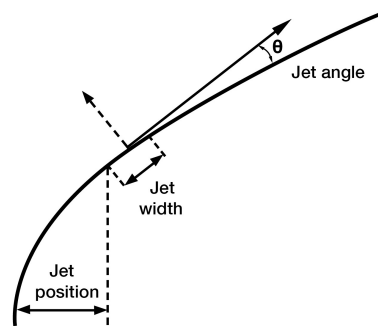


Figure 2. Sketch of the groove location and injection angle over the airfoil.

Table 1. Physical conditions.

Reynolds number (Re)	68.5×10^3
Freestream velocity (U_∞)	1 m/s
Kinematic Viscosity (ν)	$1.4599 \times 10^{-5} \text{ m}^2/\text{s}$
Density (ρ)	1.225 kg/m^3
Pulsating flow fluid density (ρ_j)	1.225 kg/m^3
Angle of attack (α)	15°
Chord length (C)	1 m

2.3. Non-Dimensional Parameters

In this section the non dimensional groups used along the paper are introduced.

Reynolds number

$$Re = \frac{U_\infty C}{\nu} \quad (11)$$

where U_∞ is the free-stream velocity, C the chord length and ν the fluid kinematic viscosity.

Lift coefficient

$$C_l = \frac{2F_l}{\rho C U_\infty^2} \quad (12)$$

where ρ is the free-stream fluid density, and F_l the dimensional lift force.

Drag coefficient

$$C_d = \frac{2F_d}{\rho C U_\infty^2} \tag{13}$$

where F_d is the dimensional drag force. Note that the lift and drag coefficients are a function of the angle of attack (AoA) and Reynolds number.

Aerodynamic efficiency

$$E = \frac{F_l}{F_d} = \frac{C_l}{C_d} \tag{14}$$

Pressure coefficient

$$C_P = \frac{P - P_\infty}{\frac{1}{2}\rho U_\infty^2} \tag{15}$$

The parameter P is the generic static pressure and P_∞ is the free-stream one.

Friction coefficient

$$C_F = \frac{\tau_w}{\frac{1}{2}\rho U_\infty^2} \tag{16}$$

where τ_w are the wall shear stresses.

Dimensionless wall distance

$$y^+ = \frac{u_\tau y}{\nu} \tag{17}$$

With:

$$u_\tau = \sqrt{\frac{\tau_w}{\rho}} \tag{18}$$

u_τ characterizes the friction velocity and y is the dimensional distance with respect to the wall.

Jet momentum coefficient

$$C_\mu = \frac{h(\rho U_{max}^2)\sin\theta_j}{C(\rho U_\infty^2)} \tag{19}$$

where h characterizes the jet width, U_{max} is the maximum jet velocity and θ_j stands for the jet inclination angle measured versus the airfoil surface (see Figure 2).

Non-dimensional forcing frequency, (Strouhal number)

$$Strouhal = F^+ = \frac{fC}{U_\infty} \tag{20}$$

The non-dimensional forcing frequency is often given as:

$$F_*^+ = \frac{f}{f_0} \tag{21}$$

The variable f is a generic frequency and f_0 is the vortex shedding frequency obtained from the baseline case. As in the preset study $C = 1$ and $U_\infty = 1$, the relation between F^+ and F_*^+ becomes, $F^+ = F_*^+ f_0$.

Courant–Friedrichs–Levy number

$$CFL = \frac{u\Delta t}{\Delta x} \tag{22}$$

where u is the generic fluid velocity, Δt is the time step and Δx the generic mesh cell length.

2.4. Mesh Assessment

Due to the fact that no previous experimental or numerical studies are available in the literature, it is essential to validate the numerical model. In order to study the baseline case and the later AFC configurations, a mesh independence test was performed to guarantee independence between the mesh resolution and the simulated results. A hybrid mesh configuration, composed by a rectangular structured and a triangular unstructured

mesh region, was implemented in order to capture the boundary layer while saving computational power required on the outer regions of the domain. The surrounding region of the airfoil consists on two body-fitted structured sub-meshes with a progressive growth of 1% for the one closest to the airfoil and 3% for the one surrounding the first sub-mesh. The remaining portion of the domain was filled with an unstructured mesh, the resolution was particularly high on the wake region. An overall view of the computational domain is presented in Figure 3, a close up view of the regions surrounding the airfoil for the baseline case and for the corresponding AFC mesh implementation is shown in Figure 4 and Figure 5, respectively.

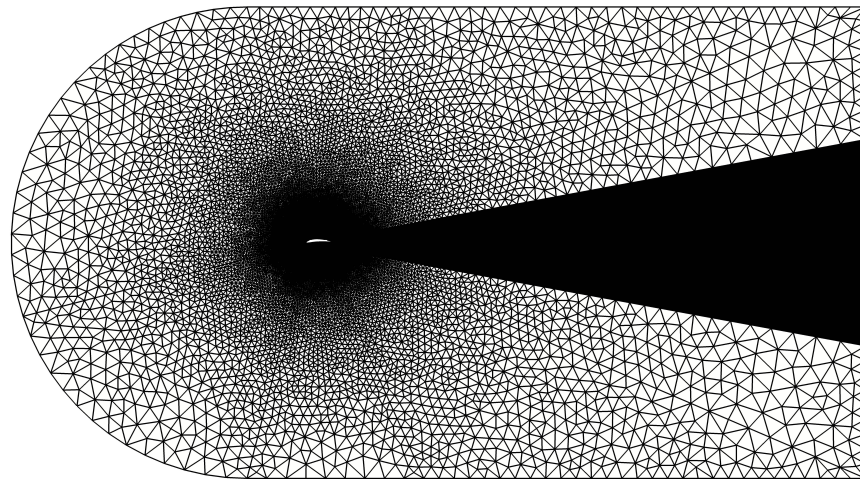
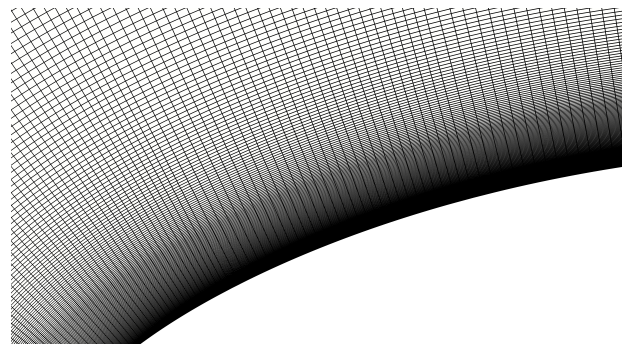
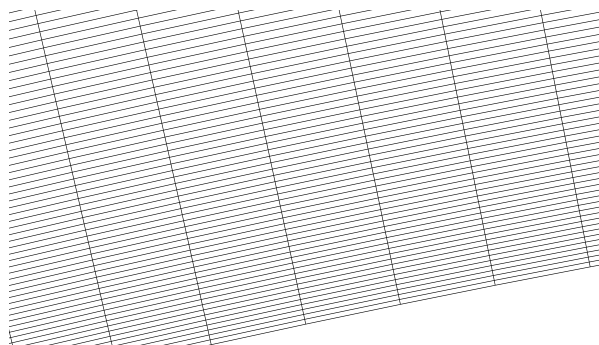


Figure 3. Overall view of the computational domain.



(a)



(b)

Figure 4. Detailed view of the near-wall region of the mesh. (a) Close up view of the structured sub-mesh. (b) Close up view of the LE region structured sub-mesh.

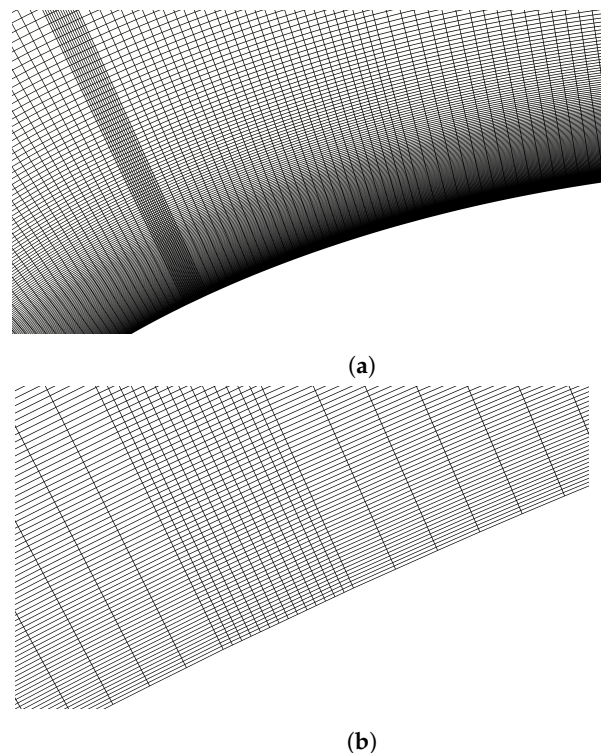


Figure 5. Mesh modification for the AFC jet implementation. (a) Close up view of the structured sub-mesh. (b) Close up view of the jet area.

Four mesh candidates were designed according to four decreasing y^+ values, and consequently an increasing mesh resolution, as it can be observed in Table 2 from the number of mesh cells N_{cell} employed in the CFD models. Due to the lack of experimental data for the NACA-8412 airfoil at $Re = 68.5 \times 10^3$, the evaluation of the proper mesh could not be based on the relative error between experimental and computational data. Alternatively, the strategy followed was to study the temporal averaged C_l and C_d , as well as C_p and C_f distributions along the chord for each mesh candidate, and to compare them to observe for which y^+ the results did not significantly change. This approach was also applied to evaluate whether the relative error between the results compensated in terms of computational cost. A baseline case simulation was performed for each mesh candidate for a computational time of 30 s, which was determined based on the evaluation of the velocity and pressure residuals. The time step was of 2×10^{-4} s. In order to avoid the transient phase, the resulting time averaged for the lift C_l and drag C_d coefficients were computed considering the last 10 s of each simulation. The resulting averaged aerodynamic coefficients together with the relative error $C_l Error$, $C_d Error$ given in percentage are presented in Table 2. Calculated y^+ values were assessed on the upper side of the airfoil due to its importance in the later AFC implementation, and its maximum value obtained for each case is also included in Table 2. The resulting pressure and friction coefficients are introduced in Figures 6 and 7, respectively.

Table 2 shows that the time averaged aerodynamic coefficients stabilize as y^+ decreases. For instance, the relative error between $y^+ = 0.3$ and $y^+ = 1$ is 14.93% for C_l and 9.14% for C_d . On the other hand, the relative error between $y^+ = 0.3$ and $y^+ = 0.5$ is 3.35% for C_l and 1.97% for C_d . As the difference among the aerodynamic coefficients for $y^+ = 0.3$ and $y^+ = 0.5$ can be considered relatively small ($\Delta C_l = -0.0425$ and $\Delta C_d = 4.8 \times 10^{-3}$, with reference values corresponding to the $y^+ = 0.3$ results), and the computational time for the $y^+ = 0.3$ resulted in nearly the double than the one required for $y^+ = 0.5$, the results corresponding to the mesh with an estimated $y^+ = 0.5$ were considered acceptable for the present simulations. It is relevant to highlight that the calculated maximum y^+ values on the airfoil upper surface were slightly lower than the estimated ones used to determine

the first cell height, which certifies that the mesh was properly designed and ensured the condition of $y^+ < 1$ necessary to evaluate the boundary layer.

Table 2. Mesh candidates for the Mesh Independence Test.

y^+	N_{cell}	C_l	C_d	$C_l Error$ %	$C_d Error$ %	Calculated Maximum y^+
1	120,879	1.0797	0.2218	14.93	9.14	0.9127
0.7	139,551	1.1153	0.2267	12.12	7.13	0.6544
0.5	160,557	1.2267	0.2393	3.35	1.97	0.4728
0.3	183,897	1.2692	0.2441	-	-	0.2887

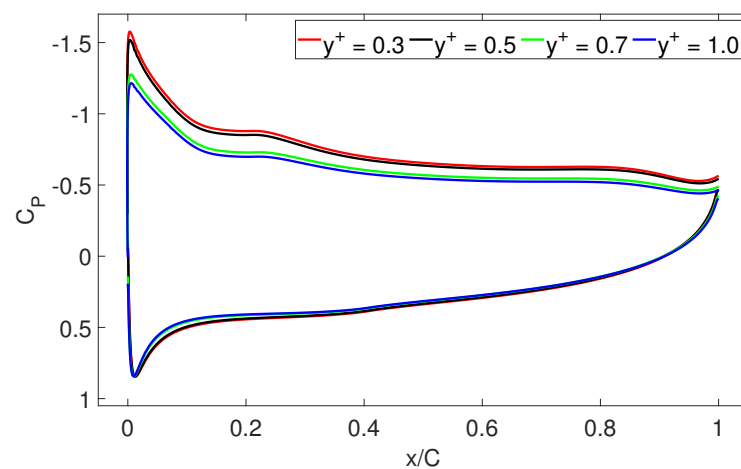


Figure 6. Baseline case pressure coefficient comparison.

In order to further check the mesh to be employed, the pressure coefficient C_p evaluated at each point of the airfoil surface and for all y^+ studied is presented in Figure 6. The C_p distribution along airfoil lower surface showed a very similar behaviour for every mesh candidate, despite that $y^+ = 1$ and $y^+ = 0.7$ showed a slightly lower C_p value for approximately the 80% of the chord. A more notable difference can be observed in the airfoil upper surface, where C_p progressively grows as y^+ decreases. It can be observed how C_p in the airfoil upper surface for $y^+ = 0.3$ and $y^+ = 0.5$ are very similar along the whole chord, only showing a minor difference between the leading edge of the airfoil and $x/C = 0.3$. When considering the friction coefficient, see Figure 7, no notable differences can be noticed between the C_f distribution for the different meshes studied. The separation point is well predicted by all meshes evaluated, while small differences are observed in the reattachment point. After analyzing the C_p , C_f , C_l and C_d coefficients, we can conclude that the results obtained for the mesh with an estimated $y^+ = 0.5$ are representative and almost mesh independent. This mesh was selected for the baseline case evaluation as well as for the later AFC implementation simulations. In addition, selecting this mesh exploited the fact that the computational time required to complete the simulations was drastically lower than for the most dense mesh, without compromising the solution in a great extent. To conclude with the baseline case analysis, the streamlines of the averaged flow field are presented in Figure 8. A huge separation bubble is generated very close to the airfoil LE, as indicated in Figure 7, and it extends up to the vicinity of the TE, where a counter rotating vortical structure is generated. Notice that the boundary layer separation point is observed to be at about 10% of the chord, $x/C = 0.1045$. The objective of the AFC implementation is to postpone the boundary layer separation, breaking this large vortical

structure onto smaller ones, or even completely suppressing it. This will reduce the drag generated by the large vortex and increase the lift generated by the airfoil.

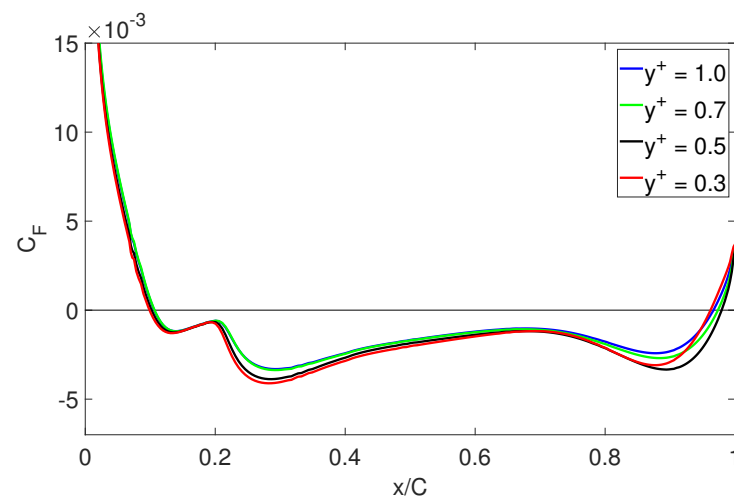


Figure 7. Baseline case friction coefficient comparison.

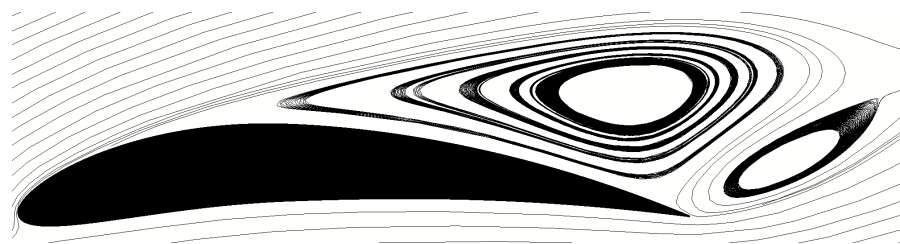


Figure 8. Averaged streamlines of the baseline case.

3. AFC Implementation

3.1. Jet Location and Mesh Modification

In order to evaluate the influence of AFC on aerodynamic efficiency, three design variables have been studied: the jet inclination angle θ , the jet momentum coefficient C_{μ} and the non-dimensional forcing frequency F_*^+ . In the present study, the groove width h and location were kept constant. The design of the AFC synthetic jet begins by studying its location over the airfoil. According to [33] among others, the optimum location is just upstream of the boundary layer separation point, which can clearly be seen in Figures 7 and 8. The separation point is located at $x/C = 0.1045$, considerably close to the LE. This is a consequence of the high AoA used (15°) and of the geometry of the airfoil selected, as it shows a pronounced curvature near the leading edge. At the separation point C_F begins to adopt negative values due to the adverse pressure gradient, leading to flow separation. Based on what it was defined in reference [4], the synthetic jet has been placed at a location of $0.01C$ upstream of the flow separation point, with a slot width of $0.01C$ (1% of the chord), from $x/C = 0.08$ to $x/C = 0.09$. The next step is to design the AFC velocity signal, which must be time periodic as the jet corresponds to the ZNMF typology. Thus, in the following subsections, the frequency, amplitude and jet inclination angle will need to be evaluated. The mesh was further refined in the slot region due to the quick variation of the flow properties close to the jet. For this reason, the number of partitions at the vicinity of the jet have been increased as it can be seen in Figure 5. The total number of mesh cells increased to 162,789 for the cases where AFC was considered. Regarding the instantaneous velocity along the groove it was decided to use a top hat velocity distribution.

3.2. AFC Velocity Input

Synthetic jets, also called ZNMF actuators, are characterized by transporting the same quantity of fluid in the blowing and suction phases. For this reason, a sinusoidal velocity input as in Equation (23) must be designed with the objective of extracting and injecting moment from the boundary layer. An initial approach must be carried out to estimate a reference value for the velocity input frequency f and amplitude A .

$$U_{jet}(t) = A \sin(2\pi ft) \quad (23)$$

The introduction of periodic forcing is aimed to modify the airfoil vortex shedding frequency and amplitude. The vortex shedding natural frequency for the baseline case must be assessed by analyzing its frequency spectrum. Following the methodology presented in [37], a Fast Fourier Transform for the lift coefficient of the baseline case was performed. The resulting vortex shedding frequency was $f_0 = 0.6965$ Hz. The amplitude A of the velocity signal corresponds to the maximum velocity of the jet U_{max} when sucked/injected from/to the boundary layer. The parametric study presented in this paper is designed as follows: the groove position and width were kept constant, and the natural vortex shedding frequency was selected as input frequency. Then, for a given jet inclination angle, CFD simulations were performed for a set of momentum coefficients C_μ ranging between $0.0001 \leq C_\mu \leq 0.1$. The process was performed for three different jet inclination angles of $\theta = 20^\circ, 30^\circ$ and 40° . Via following this procedure the optimum momentum coefficient and jet injection angle (from the range chosen) were obtained. As a final step, a set of jet pulsating frequencies ranging between $0.5 \leq F_*^+ \leq 7$ were evaluated for the optimum C_μ and θ configuration previously obtained.

4. Results

Three jet inclination angles θ have been studied ($20^\circ, 30^\circ$ and 40°). For each θ , twelve momentum coefficients C_μ have been evaluated to obtain the optimal θ and C_μ configuration among those studied. The rest of the parameters were kept constant. The range of C_μ values have been selected based on previous validated studies [38].

4.1. Optimal θ and C_μ Configuration

Figure 9 introduces the different values of the temporal averaged C_l , C_d and aerodynamic efficiency $E = C_l/C_d$ as a function of the different jet injection angles θ and momentum coefficients C_μ studied. Observing Figure 9a, it can be stated that regardless of the injection angle studied, high C_l are obtained for momentum coefficients ranging between $0.0005 \leq C_\mu \leq 0.05$. In general the optimum jet inclination angle is $\theta = 40^\circ$, although two maximum lift coefficients are obtained at $\theta = 40^\circ$ $C_\mu = 0.0005$ and $\theta = 20^\circ$ $C_\mu = 0.001$, respectively. Regarding the results at $\theta = 30^\circ$, the graphic presents a much flatter shape than for $\theta = 20^\circ$, with an efficiency maximum at about $C_\mu = 0.005$. In fact, regardless of the injection angle studied, the maximum lift coefficients are obtained for momentum coefficients in the range $0.0005 \leq C_\mu \leq 0.001$.

For C_μ values larger than 0.015, regardless of the injection angle, the lift coefficient values significantly decrease. Finally, the C_l curve obtained for $\theta = 40^\circ$ is the most flat one, indicating the lift obtained at this inclination angle is good and pretty stable for a large range of momentum coefficients. Note that as θ increases, C_l tends to be more stable in the range of C_μ between 0.0005 and 0.015, indicating that the effectiveness of C_μ is higher for growing θ values. When considering the drag coefficient in Figure 9b, minimum values are obtained for $\theta = 40^\circ$, although for $\theta = 30^\circ$ relatively low drag coefficients are observed. The minimum C_d is obtained at $\theta = 40^\circ$ and $C_\mu = 0.003$. Comparing Figure 9a with Figure 9b it can be concluded that to maximize lift and minimize drag the optimum jet injection angle is $\theta = 40^\circ$, yet, the momentum coefficient to maximize lift is $C_\mu = 0.0005$ while the one minimizing drag needs to be $C_\mu = 0.003$. In order to solve this dilemma the airfoil efficiency must be considered.

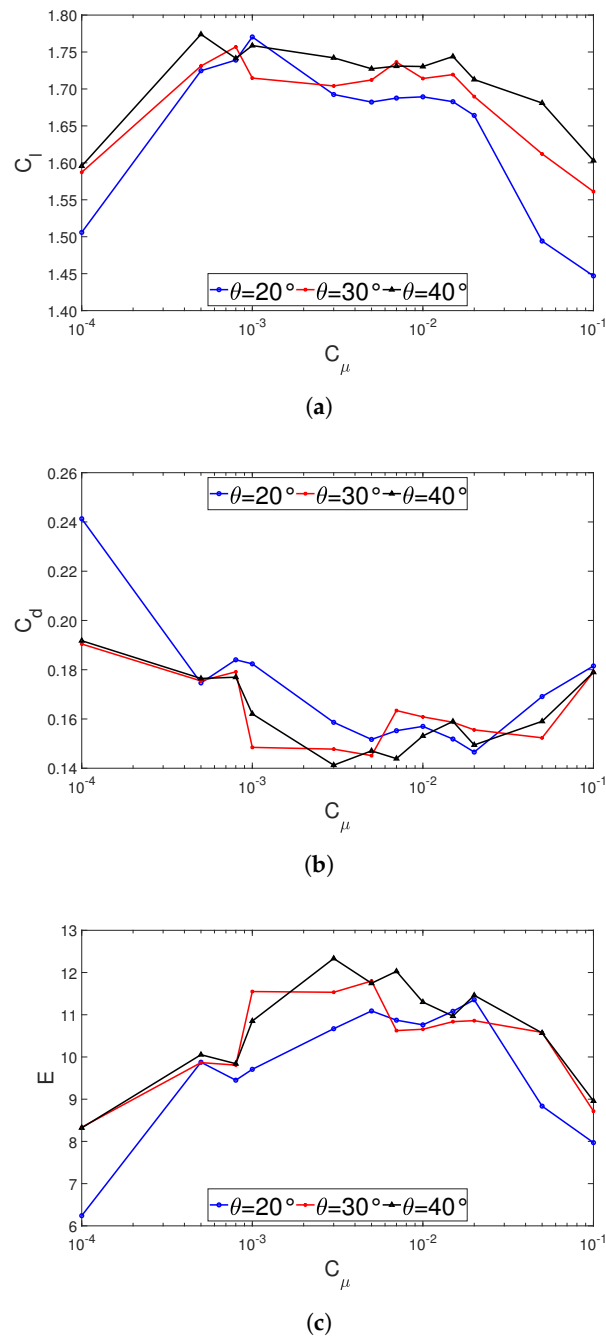


Figure 9. Aerodynamic coefficients comparison for the different C_μ and θ studied. (a) Lift coefficient comparison for the different C_μ and θ studied. (b) Drag coefficient comparison for the different C_μ and θ studied. (c) Aerodynamic efficiency comparison for the different C_μ and θ studied.

Airfoil efficiency E is presented in Figure 9c. Maximum aerodynamic efficiencies are obtained for $\theta = 40^\circ$ followed by $\theta = 30^\circ$. The maximum aerodynamic efficiency has been obtained for $\theta = 40^\circ$ and $C_\mu = 0.003$, with $E = 12.3291$. Comparing this case with the baseline case, it supposes a $\Delta C_l = 0.51154$, $\Delta C_d = -0.098$, and $\Delta E = 7.2043$. Consequently, these results have been considered satisfactory in order to proceed with the frequency study.

For completeness, Table A1 is presented in Appendix A, where the results obtained from the different simulations previously introduced in Figure 9 are presented. Note that all values presented in this table correspond to the time averaged values obtained during the last 10 seconds of each simulation.

4.2. Forcing Frequency Analysis

As it has been previously mentioned, maintaining constant the groove position and width as well as the AFC parameters optimized in Section 4.1 ($\theta = 40^\circ$ and $C_\mu = 0.003$), a set of different F_*^+ values ($0.5 \leq F_*^+ \leq 7$) have been applied in the present subsection. After simulating each F_*^+ case for a computational time of 30 s, the resulting time averaged C_l and C_d values, as well as the airfoil efficiency are presented in Table 3. The optimum case corresponds to $F_*^+ = 4$, with a resulting $C_l = 1.8147$, $C_d = 0.0942$ and $E = 19.2649$. It can be concluded that the modification of the pulsating flow frequency has brought an efficiency improvement of around 56% versus the one obtained with the optimum C_μ and θ . The increase in lift and decrease in drag corresponds to $\Delta C_l = 0.0726$ and $\Delta C_d = -0.0471$, respectively. When comparing the final AFC optimum properties with the baseline case ones, it is observed an airfoil efficiency increase of 275.8%, being the lift increase and drag decrease respectively of $\Delta C_l = 0.588$ and $\Delta C_d = -0.1451$. From Table 3 there is another condition which is worth to report, this is the maximum lift condition, which happens for $F_*^+ = 3$. It is interesting to note that the AFC parameters to obtain maximum efficiency and maximum lift are almost the same, just the pulsating frequency is slightly different, being four times and three times the natural vortex shedding frequency, respectively.

Table 3. Time averaged aerodynamic coefficients and efficiency obtained for the set of F_*^+ studied.

C_μ	F_*^+	C_l	C_d	E
0.003	0.5	1.6473	0.2063	7.9853
	1	1.7421	0.1413	12.3331
	2	1.8075	0.1289	14.0214
	3	1.8272	0.1120	16.3160
	4	1.8147	0.0942	19.2649
	5	1.8220	0.1054	17.2829
	7	1.7724	0.1190	14.8941

The drastic increase in airfoil efficiency is clearly understood when observing the evolution of the pressure coefficient over the airfoil when the optimized AFC parameters are considered. In Figure 10, the pressure coefficient distribution along the chord is presented for the baseline, maximum efficiency and maximum lift cases. For both maximum conditions, a substantial increase of C_p is observed along the airfoil. From $x/C = 0$ up to $x/C = 0.6$, a huge decrease of the pressure coefficient is seen on the airfoil upper surface, while on the last 40% of the chord the pressure is a bit higher than the one obtained in the baseline case.

To further understand the flow structure around the airfoil, streamlines of the averaged flowfield for the maximum efficiency and maximum lift cases are presented in Figure 11a,b, respectively. A drastic reduction of the vorticular structure generated over the airfoil upper surface with respect to the baseline case solution (see Figure 8) can be observed for both configurations presented. Clearly, for the maximum efficiency condition vortical structures have nearly disappeared over the airfoil. Just a small laminar bubble which appears at about $x/C = 0.7$ and disappears before $x/C = 0.8$ can be observed, indicating a corresponding boundary layer separation and reattachment at these points. The separation of the boundary layer is delayed to about $x/C = 0.7$ for the case of maximum lift, reattaching close to the trailing edge. An elongated vortical structure is therefore generated around the airfoil trailing edge.

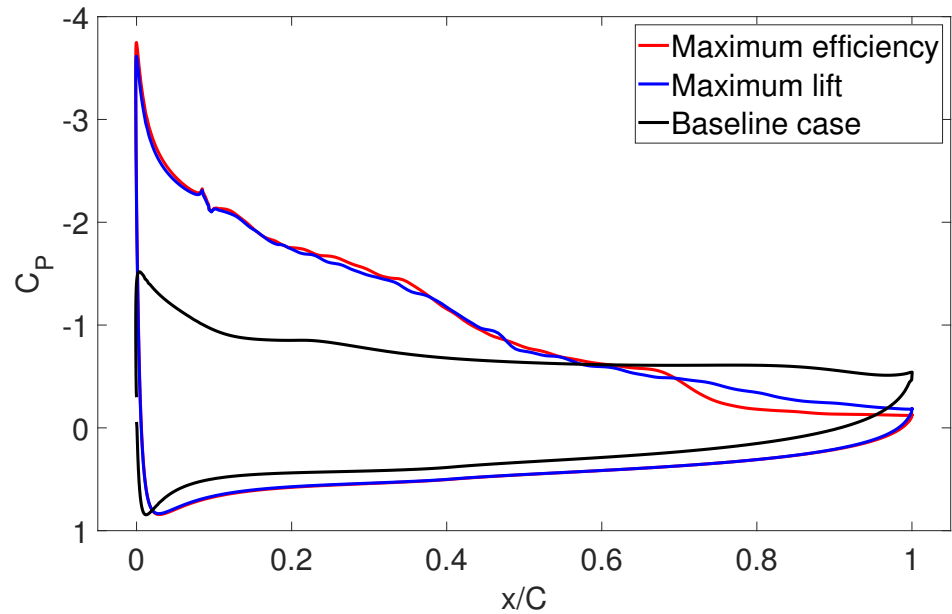


Figure 10. Pressure coefficient comparison for the baseline case and maximum efficiency and maximum lift configurations.

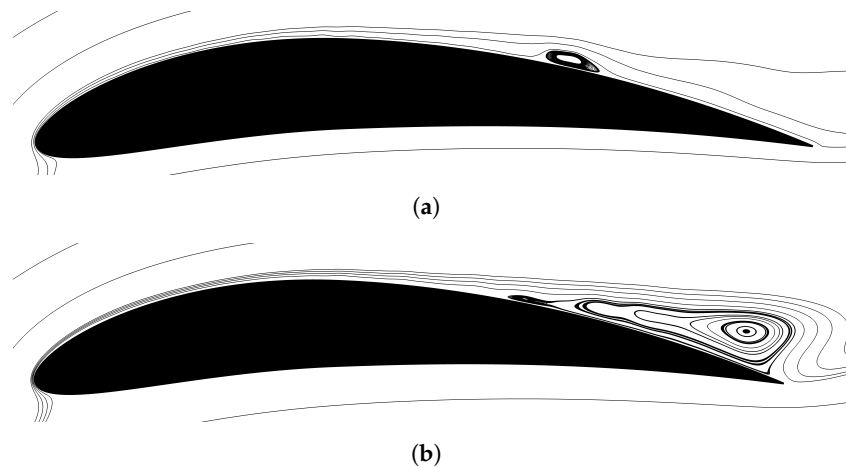
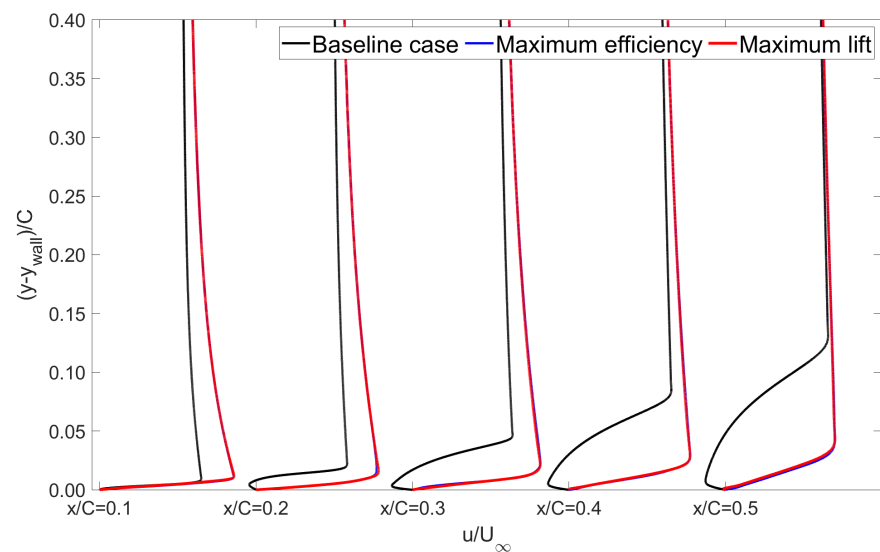


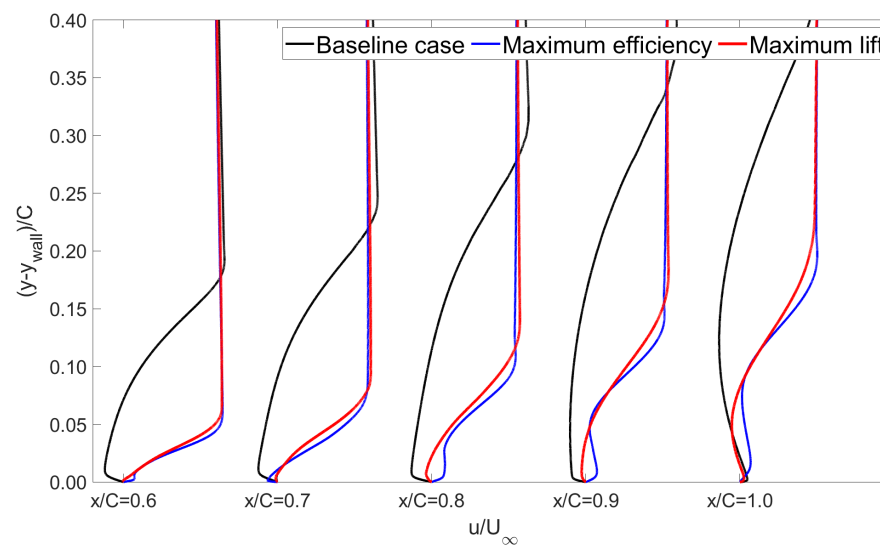
Figure 11. Streamlines of the averaged flowfield for the optimal and maximum lift configurations. (a) Streamlines of the averaged flowfield for the optimal configuration. (b) Streamlines of the averaged flowfield for the maximum lift configuration.

A good method to understand the flow evolution over the airfoil is via plotting the boundary layer thickness along the airfoil chord. For the baseline, maximum efficiency and maximum lift cases, this is presented in non-dimensional form and every 10% of the chord in Figure 12. The set of profiles for both the maximum efficiency and maximum lift cases show only positive velocity values up to around $x/C = 0.7$, entitling no boundary layer separation appears until this streamwise position. For the maximum efficiency case, at around $x/C = 0.7$, negative averaged velocities start appearing close to the wall, returning to a completely positive profile at $x/C \approx 0.8$, which matches perfectly well with the small laminar bubble observed in Figure 11a. A slightly different behaviour is observed for the maximum lift case, where Figure 12 shows how the averaged velocities close to the wall become negative for the streamwise positions ranging from $x/C = 0.7$ and $x/C = 1$. A direct connection between the boundary layer thickness just presented and what it is observed in Figure 11b can be made, the elongated and downstream growing vortex is clearly observed in both figures. When observing the negative velocity distributions associated

to the maximum lift case from Figure 12b, and when comparing them with the velocity distributions corresponding to the baseline case, it can be concluded that the intensity associated to the maximum lift case vortex is much smaller than the one corresponding to the baseline case, therefore the maximum lift vortex must rotate with a low angular velocity. The vortex generated for the maximum efficiency configuration at around $x/C = 0.7$ has a larger vorticity magnitude than the maximum lift one, but still lower than the vorticity associated to the baseline case vortex. For the baseline case, negative averaged velocity values can be observed from the streamwise position $x/C = 0.1$ up to $x/C = 1$, indicating a rapid separation of the boundary layer that extends for the whole airfoil. In reality, the negative averaged velocities cannot be clearly seen at streamwise position $x/C = 0.1$ in Figure 12a, but the separation point can be easily localized around $x/C = 0.1$ in Figure 12a. At $x/C = 1$, slightly positive averaged velocities can be observed close to the wall due to the appearance of a counter rotating vortex generated at the trailing edge, as observed in Figure 8.



(a)



(b)

Figure 12. Mean velocity profiles for the baseline, maximum E and maximum L cases, from $x/C = 0.1$ to $x/C = 1$. (a) Velocity profiles of the mean velocity from $x/C = 0.1$ to $x/C = 0.5$. (b) Velocity profiles of the mean velocity from $x/C = 0.6$ to $x/C = 1$.

4.3. Energy Assessment

In order to find out how effective is the AFC approach employed for the maximum efficiency and maximum lift cases, the power per unit length required by the SJA (W_j) as well as the power saved after the actuation (W_G) have to be calculated. The power needed to drive the synthetic jet is given as:

$$W_j = \frac{1}{2} \rho_j S_j \sin(\theta) \overline{u_j^3} \tag{24}$$

where $S_j = h * l$ defines the groove cross-sectional area, due to the fact that the airfoil length is equal to unity $l = 1$, the groove and the jet width h are equivalent. The parameter θ stands for the jet inclination angle measured versus the wing profile surface.

The definition of the synthetic jet actuator time dependent velocity profile to the power three, $\overline{u_j^3}$, was taken from [6,39].

$$\overline{u_j^3} = \frac{1}{T/2} \int_0^{T/2} U_{max}^3 \sin^3(2\pi ft) dt = \frac{4}{3\pi} U_{max}^3 \tag{25}$$

where U_{max} characterizes the jet maximum velocity. The equation representing the power saved when AFC is applied and due to the drag force reduction, takes the form:

$$W_G = U_\infty (D_{baseline} - D_{actuated}) = \frac{\rho U_\infty^3 C}{2} (C_{d_{baseline}} - C_{d_{actuated}}) \tag{26}$$

where the drag force and the drag coefficient are respectively given as D and C_d . When AFC is applied, the parameter defining the power ratio P_R is represented as:

$$P_R = \frac{W_G}{W_j} \tag{27}$$

Energy saving exist for power ratio values higher than one.

The set up parameters and resulting power ratios are summarised in Table 4. Both maximum efficiency and maximum lift configurations present energy savings, with a power gain two orders of magnitude higher than the power required by the SJA.

This result confirms that the introduction of AFC in an airfoil with separated flow is capable of reducing the drag coefficient and increase the lift coefficient significantly, by keeping the boundary layer attached for a larger portion of the airfoil. Therefore, it can be sated that the implementation of the SJA is energetically efficient for the separated flow case presented.

Table 4. Power ratio values characterizing the maximum efficiency and maximum lift configurations.

Cases	α°	U_{max} [m/s]	S_j [m ²]	θ°	W_j [W]	W_G [W]	W_G/W_j
max efficiency	15	0.6832	0.01	40	5.3277×10^{-4}	0.0889	166.81
max lift	15	0.6832	0.01	40	5.3277×10^{-4}	0.0780	146.35

5. Conclusions

This paper presents a parametric analysis on a NACA-8412 airfoil with the aim to optimize three AFC parameters, momentum coefficient, jet inclination angle and pulsating frequency, associated to a SJA. The procedure followed to perform a parametric optimization of any airfoil is established and presented. A maximum airfoil efficiency increase, measured respect to the baseline case, of 276% is obtained for $C_\mu = 0.003$; $F_*^+ = 4$ and $\theta = 40^\circ$, the groove was located from $x/C = 0.08$ to $x/C = 0.09$ being its width of $0.01C$. The maximum airfoil lift was obtained for the same AFC parameters except the pulsating frequency which was of $F_*^+ = 3$. The efficiency increase with respect to the baseline case

was of around 218%. From the comparison of the AFC parameters for maximum lift and maximum efficiency cases, it is proved that the pulsating frequency is capable of highly improving the airfoil efficiency.

Author Contributions: Conceptualization, J.M.B. and N.C.; methodology, N.C. and J.M.B.; software, N.C.; validation, N.C.; formal analysis, N.C. and J.M.B.; investigation, N.C. and J.M.B.; data curation, N.C.; writing—original draft preparation, N.C. and J.M.B.; writing—review and editing, J.M.B.; visualization, N.C. and J.M.B.; supervision, J.M.B.; project administration, J.M.B. All authors have read and agreed to the published version of the manuscript.

Funding: No funding was associated to this project.

Institutional Review Board Statement: Not applicable.

Informed Consent Statement: Not applicable.

Data Availability Statement: Not applicable.

Conflicts of Interest: The authors declare no conflict of interest.

Appendix A. Lift, Drag and Efficiency Results for the Different θ and C_μ Values Studied

Table A1. AFC results comparison at different jet injection angles θ and momentum coefficients C_μ .

θ	C_μ	C_l	C_d	E
-	-	1.2267	0.2393	5.1262
20°	0.0001	1.5059	0.2413	6.2408
	0.0005	1.7246	0.1746	9.8774
	0.0008	1.7390	0.1840	9.4511
	0.001	1.7704	0.1824	9.7061
	0.003	1.6925	0.1586	10.6715
	0.005	1.6823	0.1517	11.0897
	0.007	1.6877	0.1552	10.8744
	0.01	1.6893	0.1570	10.7599
	0.015	1.6828	0.1519	11.0783
	0.02	1.6642	0.1466	11.3520
	0.05	1.4941	0.1691	8.8356
0.1	1.4470	0.1815	7.9725	
30°	0.0001	1.5872	0.1904	8.3361
	0.0005	1.7310	0.1754	9.8689
	0.0008	1.7570	0.1791	9.8102
	0.001	1.7147	0.1485	11.5468
	0.003	1.7041	0.1478	11.5298
	0.005	1.7122	0.1451	11.8001
	0.007	1.7363	0.1634	10.6261
	0.01	1.7141	0.1609	10.6532
	0.015	1.7194	0.1587	10.8343
	0.02	1.6897	0.1556	10.8593
	0.05	1.6121	0.1523	10.5850
0.1	1.5612	0.1791	8.7169	

Table A1. Cont.

θ	C_μ	C_l	C_d	E
40°	0.0001	1.5957	0.1918	8.3196
	0.0005	1.7739	0.1764	10.0561
	0.0008	1.7415	0.1770	9.8390
	0.001	1.7587	0.1621	10.8495
	0.003	1.7421	0.1413	12.3291
	0.005	1.7273	0.1471	11.7424
	0.007	1.7309	0.1439	12.0285
	0.01	1.7304	0.1531	11.3024
	0.015	1.7439	0.1590	10.9679
	0.02	1.7128	0.1495	11.4569
	0.05	1.6810	0.1590	10.5723
0.1	1.6031	0.1790	8.9559	





References

- Hochhäusler, D.; Erfort, G. Experimental study on an airfoil equipped with an active flow control element. *Wind. Eng.* **2021**. [CrossRef]
- Khalil, K.; Asaro, S.; Bauknecht, A. Active flow control devices for wing load alleviation. *J. Aircr.* **2022**, *59*, 458–473. [CrossRef]
- Mosca, V.; Karpuk, S.; Sudhi, A.; Badrya, C.; Elham, A. Multidisciplinary design optimisation of a fully electric regional aircraft wing with active flow control technology. *Aeronaut. J.* **2021**, *126*, 730–754. [CrossRef]
- Tousi, N.M.; Coma, M.; Bergada, J.M.; Pons-Prats, J.; Mellibovsky, F.; Bugada, G. Active Flow Control Optimisation on SD7003 Airfoil at Pre and Post-Stall Angles of Attack using Synthetic Jets. *Appl. Math. Model.* **2021**, *98*, 435–464. [CrossRef]
- Tadjfar, M.; Kamari, D. Optimization of Flow Control Parameters Over SD7003 Airfoil with Synthetic Jet Actuator. *J. Fluids Eng.* **2020**, *142*, 021206. [CrossRef]
- De Giorgi, M.; De Luca, C.; Ficarella, A.; Marra, F. Comparison between synthetic jets and continuous jets for active flow control: Application on a NACA 0015 and a compressor stator cascade. *Aerosp. Sci. Technol.* **2015**, *43*, 256–280. [CrossRef]
- Traficante, S.; De Giorgi, M.; Ficarella, A. Flow separation control on a compressor-stator cascade using plasma actuators and synthetic and continuous jets. *J. Aerosp. Eng.* **2016**, *29*, 04015056. [CrossRef]
- Zhang, H.; Chen, S.; Gong, Y.; Wang, S. A comparison of different unsteady flow control techniques in a highly loaded compressor cascade. *Proc. Inst. Mech. Eng. Part G J. Aerosp. Eng.* **2019**, *233*, 2051–2065. [CrossRef]
- Cattafesta, L.N.; Sheplak, M. Actuators for Active Flow Control. *Annu. Rev. Fluid Mech.* **2011**, *43*, 247–272. [CrossRef]
- Wang, L.; Tian, F.B. Numerical simulation of flow over a parallel cantilevered flag in the vicinity of a rigid wall. *Phys. Rev. E* **2019**, *99*, 053111. [CrossRef]
- Cho, Y.C.; Shyy, W. Adaptive flow control of low-Reynolds number aerodynamics using dielectric barrier discharge actuator. *Prog. Aerosp. Sci.* **2011**, *47*, 495–521. [CrossRef]
- Foshat, S. Numerical investigation of the effects of plasma actuator on separated laminar flows past an incident plate under ground effect. *Aerosp. Sci. Technol.* **2020**, *98*, 105646. [CrossRef]
- Benard, N.; Moreau, E. Electrical and mechanical characteristics of surface AC dielectric barrier discharge plasma actuators applied to airflow control. *Exp. Fluids* **2014**, *55*, 1846. [CrossRef]
- Benard, N.; Pons-Prats, J.; Periaux, J.; Bugada, G.; Braud, P.; Bonnet, J.; Moreau, E. Turbulent separated shear flow control by surface plasma actuator: Experimental optimization by genetic algorithm approach. *Exp. Fluids* **2016**, *57*, 22. [CrossRef]
- Bergadà, J.M.; Baghaei, M.; Prakash, B.; Mellibovsky, F. Fluidic Oscillators, Feedback Channel Effect under Compressible Flow Conditions. *Sensors* **2021**, *21*, 5768. [CrossRef]
- Baghaei, M.; Bergada, J.M. Fluidic Oscillators, the Effect of Some Design Modifications. *Appl. Sci.* **2020**, *10*, 2105. [CrossRef]
- Baghaei, M.; Bergada, J.M. Analysis of the Forces Driving the Oscillations in 3D Fluidic Oscillators. *Energies* **2019**, *12*, 4720. [CrossRef]
- Glezer, A.; Amitay, M. Synthetic jets. *Annu. Rev. Fluid Mech.* **2002**, *34*, 503–529. [CrossRef]
- Rumsey, C.; Gatski, T.; Sellers, W.; Vatsa, V.; Viken, S. Summary of the 2004 CFD validation workshop on synthetic jets and turbulent separation control. In Proceedings of the 2nd AIAA Flow Control Conference, Portland, OR, USA, 28 June–1 July 2004; p. 2217.
- Wynanski, I. The variables affecting the control of separation by periodic excitation. In Proceedings of the 2nd AIAA Flow Control Conference, Portland, OR, USA, 28 June–1 July 2004; p. 2505.
- Findanis, N.; Ahmed, N. The interaction of an asymmetrical localised synthetic jet on a side-supported sphere. *J. Fluids Struct.* **2008**, *24*, 1006–1020. [CrossRef]
- Amitay, M.; Smith, D.R.; Kibens, V.; Parekh, D.E.; Glezer, A. Aerodynamic flow control over an unconventional airfoil using synthetic jet actuators. *AIAA J.* **2001**, *39*, 361–370. [CrossRef]

23. Amitay, M.; Glezer, A. Role of actuation frequency in controlled flow reattachment over a stalled airfoil. *AIAA J.* **2002**, *40*, 209–216. [CrossRef]
24. Gilarranz, J.; Traub, L.; Rediniotis, O. A New Class of Synthetic Jet Actuators—Part I: Design, Fabrication and Bench Top Characterization. *J. Fluids Eng.* **2005**, *127*, 367–376. [CrossRef]
25. You, D.; Moin, P. Active control of flow separation over an airfoil using synthetic jets. *J. Fluids Struct.* **2008**, *24*, 1349–1357. [CrossRef]
26. Tuck, A.; Soria, J. Separation control on a NACA 0015 airfoil using a 2D micro ZNMF jet. *Aircr. Eng. Aerosp. Technol.* **2008**, *80*, 175–180. [CrossRef]
27. Kitsios, V.; Cordier, L.; Bonnet, J.P.; Ooi, A.; Soria, J. On the coherent structures and stability properties of a leading-edge separated aerofoil with turbulent recirculation. *J. Fluid Mech.* **2011**, *683*, 395–416. [CrossRef]
28. Buchmann, N.; Atkinson, C.; Soria, J. Influence of ZNMF jet flow control on the spatio-temporal flow structure over a NACA-0015 airfoil. *Exp. Fluids* **2013**, *54*, 1485. [CrossRef]
29. Kim, S.H.; Kim, C. Separation control on NACA23012 using synthetic jet. *Aerosp. Sci. Technol.* **2009**, *13*, 172–182. [CrossRef]
30. Monir, H.E.; Tadjfar, M.; Bakhtian, A. Tangential synthetic jets for separation control. *J. Fluids Struct.* **2014**, *45*, 50–65. [CrossRef]
31. Goodfellow, S.D.; Yarusyevych, S.; Sullivan, P.E. Momentum Coefficient as a Parameter for Aerodynamic Flow Control with Synthetic Jets. *AIAA J.* **2013**, *51*, 623–631. [CrossRef]
32. Feero, M.A.; Goodfellow, S.D.; Lavoie, P.; Sullivan, P.E. Flow Reattachment Using Synthetic Jet Actuation on a Low-Reynolds-Number Airfoil. *AIAA J.* **2015**, *53*, 2005–2014. [CrossRef]
33. Feero, M.A.; Lavoie, P.; Sullivan, P.E. Influence of synthetic jet location on active control of an airfoil at low Reynolds number. *Exp. Fluids* **2017**, *58*, 99. [CrossRef]
34. Zhang, W.; Samtaney, R. A direct numerical simulation investigation of the synthetic jet frequency effects on separation control of low-Re flow past an airfoil. *Phys. Fluids* **2015**, *27*, 055101. [CrossRef]
35. Rodriguez, I.; Lehmkuhl, O.; Borrell, R. Effects of the Actuation on the Boundary Layer of an Airfoil at Reynolds Number $Re = 60000$. *Flow Turbul. Combust.* **2020**, *105*, 607–626. [CrossRef]
36. Spalart, P.; Allmaras, S. A one-equation turbulence model for aerodynamic flows. In Proceedings of the 30th Aerospace Sciences Meeting and Exhibit, Reno, NV, USA, 6–9 January 1992; p. 439. [CrossRef]
37. Minelli, G.; Krajnovic, S.; Basara, B. Numerical Investigation of Active Flow Control Around a Generic Truck A-Pillar. *Flow Turbul. Combust.* **2016**, *97*, 1235–1254. [CrossRef] [PubMed]
38. Tuck, A.; Soria, J. Active flow control over a NACA 0015 airfoil using a ZNMF jet. In Proceedings of the 15th Australasian Fluid Mechanics Conference, Sydney, Australia, 13–17 December 2004; pp. 13–17.
39. De Giorgi, M.G.; Traficante, S.; De Luca, C.; Bello, D.; Ficarella, A. Active flow control techniques on a stator compressor cascade: A comparison between synthetic jet and plasma actuators. In Proceedings of the ASME Turbo Expo 2012: Turbine Technical Conference and Exposition, Copenhagen, Denmark, 11–15 June 2012; American Society of Mechanical Engineers: New York, NY, USA, 2012; Volume 44748, pp. 439–450.

Article

Computational Study of the Plasma Actuator Flow Control for an Airfoil at Pre-Stall Angles of Attack

Takuto Ogawa ^{1,*} , Kengo Asada ², Makoto Sato ³ , Tomoaki Tatsukawa ²  and Kozo Fujii ^{2,*} ¹ Department of Industrial Engineering, Tokyo University of Science, Tokyo 125-8585, Japan² Department of Information and Computer Technology, Tokyo University of Science, Tokyo 125-8585, Japan³ Department of Mechanical Science and Engineering, Kogakuin University, Tokyo 163-8677, Japan;

* Correspondence: 4418701@ed.tus.ac.jp (T.O.); fujii@rs.tus.ac.jp (K.F.); Tel.: +81-3-5876-1696 (T.O. & K.F.)

Abstract: Large-eddy simulations of the flows over an NACA0015 airfoil were conducted to investigate a flow control authority of a dielectric barrier discharge plasma actuator at pre-stall angles of attack. The Reynolds number was set to 63,000, and angles of attack were set to 4, 6, 8, and 10 degrees. The plasma actuator was installed at 5% chord length from the airfoil's leading edge. Good flow control authority was confirmed in terms of lift-to-drag ratio increase and drag reduction. These improvements mainly result from the reduction of the pressure drag, which is due to the change in pressure distribution accompanying the movement and shrink of the laminar separation bubble on the airfoil surface. Additionally, although flow control using a burst drive with a nondimensional burst frequency of six improves the lift-to-drag ratio at all angles of attack, the phenomena leading to the improvement differ between near-stall angles (10 and 12 degrees) and the other lower angles. At near-stall angles, the turbulent transition is rapidly promoted by PA, and the flow is reattached. Whereas, at the lower angles, the transport of two-dimensional vortex structures, which maintain their structures up to downstream and suppress the turbulent transition, makes the flow reattachment.

Citation: Ogawa, T.; Asada, K.; Sato, M.; Tatsukawa, T.; Fujii, K.

Computational Study of the Plasma Actuator Flow Control for an Airfoil at Pre-Stall Angles of Attack. *Appl. Sci.* **2022**, *12*, 9073. <https://doi.org/10.3390/app12189073>

Academic Editors: Josep Maria Bergadà and Gabriel Bugeda Castellort

Received: 9 August 2022

Accepted: 5 September 2022

Published: 9 September 2022

Publisher's Note: MDPI stays neutral with regard to jurisdictional claims in published maps and institutional affiliations.



Copyright: © 2022 by the authors. Licensee MDPI, Basel, Switzerland. This article is an open access article distributed under the terms and conditions of the Creative Commons Attribution (CC BY) license (<https://creativecommons.org/licenses/by/4.0/>).

Keywords: flow control; plasma actuator; airfoil; pre-stall angles; duty cycle; burst; computational fluid dynamics; large eddy simulation

1. Introduction

Flow control using a dielectric barrier discharge plasma actuator (PA) has been widely studied for the last 10 to 20 years because PA has the advantages of thin/light simple structures and easy to use. PA only consists of two electrodes with a dielectric layer between them (Figure 1), and can be attached to an existing body surface without changing the original shape of the body surface. PA can be attached on flat or curved surfaces, corners, or edges and flow separation is controlled [1–3]. PA is also used for the control of boundary layer flows [4–9] and many researchers have tried to reduce skin friction drag by PA. To enhance the authority of PA, studies for PA expand over wide areas of research: low-temperature plasma discharge, flow structures induced by PA, use of duty cycles, etc. Geometry of the electrodes and the layout of multiple PAs were also studied. A good review of different types of PAs was written by Wang, Choi, and others [10], where review papers for conventional use of flow control by PA were presented. Up to the present, there has been active research on the application of various types of PA in a variety of devices [11–13].

For the flow separation control over an airfoil, PA is installed near the leading edge on the suction side of the airfoil surface except for in a few cases [14]. Most of the studies used a two-dimensional spanwise electrode, which induces coherent spanwise jet flows. Some studies used effective duty cycles (so-called burst actuation compared to regular continuous actuation), where still more effective flow control is achieved by a proper choice of the PA parameters. When duty cycles are used, two-dimensional coherent discrete

vortex structures are induced at every cycle of the duty. Thus, PAs—especially in the burst actuation—have three important flow features: jet flow near the airfoil surface, two-dimensional vortex structures with the merger of these structures, and introduction of flow disturbances. Good authority of PA comes from the fact that each of these features may become dominant with proper choice of electric parameters [15]. Furthermore, in the flow control for airfoil flows, saw-tooth, serpentine spanwise electrodes, or line up of the chordwise electrodes—which create chordwise vortex structures and others—were studied by several authors [16–19].

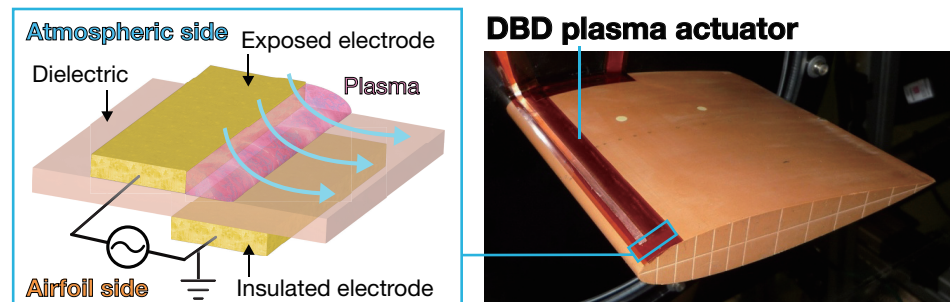


Figure 1. Schematic diagram of the DBD plasma actuator (PA) and the example of practical applications.

In either case, most of the former studies were conducted at post-stall angles of attack [4,20–22] and lift characteristics were mainly discussed since interest was in the control of the separated shear layer over an airfoil. Effective parameters of PA, such as locations, burst frequencies, and others, were discussed both computationally and experimentally. Although computational studies showed that drag reduction [23] occurred in many cases, the mechanism of the drag reduction was not well discussed. From the observation of the flow fields computationally simulated by the present authors' group, pressure drag was identified to be the main source of drag reduction for the flows at the Reynolds number of order of 10^4 to 10^5 , where laminar separation bubbles play an important role for the airfoil aerodynamic characteristics. Since laminar separation bubbles exist at angles of attack lower than the stall, we may expect a similar drag reduction even at pre-stall angles of attack. UAV or MAV would be considered for the application of flow control by PA at this Reynolds number range. Atmospheric wind would influence much for the flow conditions for these type of flight vehicles, and it is necessary to understand flow features and achieve high L/D for a wide range of angles of attack, and discuss flow control authority of PA. Several researchers investigate the flow at pre-stall angles of attack [24–26], but most of their work is aimed at evaluating aerodynamic characteristics, and analysis of the flow feature is not their major focus.

Regarding pre-stall conditions, we have conducted two types of computational studies in the past. First, we showed that better L/D (lift-to-drag ratio) is obtained at cruise conditions than that of the well-recognized airfoil geometry [27]. Here, the detailed flow structure was discussed, but for only a single angle of attack $\alpha = 6$ deg. The result indicated that burst actuation tends to keep sequential spanwise vortex structures over the upper surface and keeps flow laminar until near the trailing edge in contrast to the promotion of turbulent transition at near stall angle [15]. The resultant flow field became similar to the flow over a well-recognized high-performance airfoil at a low Reynolds number flow regime. Second, a survey of several angles of attack was carried out [28]. Here, time-averaged aerodynamic characteristics were mainly discussed, and unsteady flow features were not discussed in conjunction with the aerodynamic characteristics at each angle of attack.

The present study aims to understand the PA-controlled flow features by performing high-fidelity LESs at a broader range of pre-stall angles of attack and discuss the relation with the aerodynamic characteristics of the airfoil. The flow fields over an NACA0015 airfoil at angles of attack $\alpha = 4, 6, 8,$ and 10 deg are considered. NACA0015 airfoil flows have been investigated in many previous studies [8,23,29–31], and a wealth of experimental

and numerical data are available for comparison. The thickness of this airfoil is not practical for actual flights. However, such a thick airfoil is less restrictive in structural design and has the advantage that a large amount of fuel can be loaded inside a wing. Therefore, the range of aircraft design possibilities will expand if the flow controls can improve the aerodynamic characteristics. The Reynolds number was set to 63,000, which was considered in the previous experimental and computational studies [8,29,30,32], and reliability of the flow simulations has been well established. Previous studies [8,30] show that small fluid fluctuations such as turbulence play an important role in fluid control using PA. In the Reynolds-averaged Navier–Stokes equation (RANS) method, the small fluctuations induced by PA are immediately damped. Therefore, in the present study, wall-resolved LESs are conducted to resolve small fluid fluctuations properly. The obtained results are discussed together with the result of the post-stall condition ($\alpha = 12$).

Throughout the obtained results, the flow fields and the relationship between the aerodynamic characteristics are discussed. Focus is laid on the drag reduction, but the lift and the lift-to-drag ratio are also discussed. The results show the good flow control authority of PA for the aerodynamic characteristics of the airfoil at pre-stall angles of attack. In the cases of burst actuation, although the aerodynamic characteristics are improved at all angles of attack, the phenomena leading to the improvement are different between near-stall angles (including the post-stall angle) and lower angles. At near-stall angles, the turbulent transition is rapidly promoted by PA, and the flow is reattached. Whereas, at lower angles, the transport of two-dimensional vortex structures, which maintain their structures downstream and suppresses the turbulent transition, allow the flow reattachment. Furthermore, the strategy of parameter settings of burst actuation of PA at angles of attack less than stall is indicated.

2. PA Drive Methods and Computational Cases

The plasma actuator is installed at 5% chord length from the leading edge. This position is close to the separation point of the flow at $\alpha = 12$ and is effective for flow separation control [8]. Two PA drive methods are considered in the present study.

The continuous actuation is a standard drive method of PA. The AC voltage, which is based on a base frequency f_{base} is continuously applied to the PA. The burst actuation is the other method of driving PA. The AC voltage modulated with the duty cycle is applied to PA during the burst actuation. Figure 2 shows a schematic diagram of the AC voltage waveform for the burst actuation. Parameters of the waveform are defined as in Equation (1). f_{base} is a base frequency of the AC voltage waveform. t_{on} and t_{burst} are the driving time and burst period, respectively. f_{burst} denotes the burst frequency. F^+ , F_{base} , and BR are non-dimensional f_{burst} , non-dimensional f_{base} , and burst ratio, respectively. Previous studies [30,33] have shown that the burst actuation controls flow separations more efficiently than the continuous actuation at low Reynolds numbers ($Re \simeq 10^4$ – 10^5) at post-stall angles of attack.

The studies show that the burst actuation with $F^+ = 6$ and $BR = 0.1$, which promotes a turbulent transition, is effective for suppressing a flow separation at $\alpha = 12$. In the present study, the burst actuation with those burst parameters was employed to confirm a flow control authority of PA at pre-stall angles of attack.

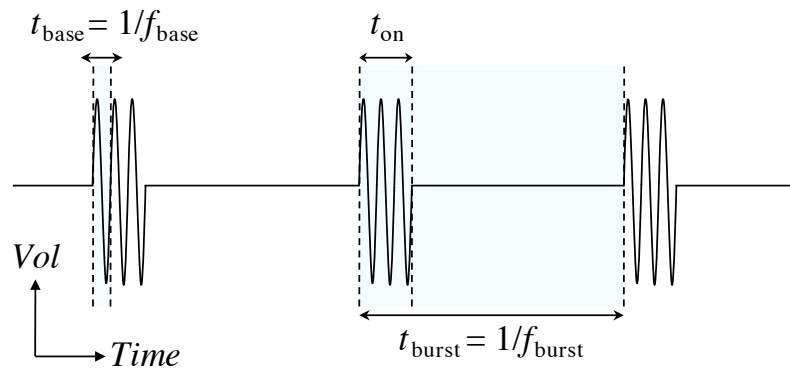


Figure 2. Alternating current (AC) voltage waveform for the burst actuation.

Hereafter, we call a computational case of the continuous drive a “Continuous” case and the burst drive a “Burst” case. In both cases, F_{base} is set to 60 according to the previous experimental and computational studies [8,31]. In addition to the computational cases with PA, Flows without PA are considered, called “PA-OFF” cases, as baseline flows. Four angles of attack $\alpha = 4, 6, 8,$ and 10 are considered. Therefore, the total number of computational cases is 12. In addition, each case at $\alpha = 12$ is used to discuss the difference in the phenomena at pre-stall and post-stall angles.

$$F^+ = \frac{f_{burst}c}{U_\infty}, \quad F_{base} = \frac{f_{base}c}{U_\infty}, \quad BR = \frac{t_{on}}{t_{burst}}. \quad (1)$$

3. Computational Approach

3.1. Governing Equations

Three-dimensional compressible Navier–Stokes equations with the source term added were solved in the present study. The equations are non-dimensionalized by the free-stream density, free-stream velocity, and chord length of the airfoil and are represented as follows:

$$\frac{\partial \rho}{\partial t} + \frac{\partial \rho u_j}{\partial x_j} = 0, \quad (2)$$

$$\frac{\partial \rho u_i}{\partial t} + \frac{\partial (\rho u_i u_j + p \delta_{ij})}{\partial x_j} = \frac{1}{Re} \frac{\partial \tau_{ij}}{\partial x_j} + D_c S_i, \quad (3)$$

$$\frac{\partial e}{\partial t} + \frac{\partial ((e + p)u_j)}{\partial x_j} = \frac{1}{Re} \frac{\partial u_k \tau_{jk}}{\partial x_j} - \frac{1}{(\gamma - 1)Pr Re M_\infty^2} \frac{\partial q_j}{\partial x_j} + D_c S_j u_j, \quad (4)$$

where $\rho, u_i, p, e, q_i, x_i, t,$ and τ_{ij} denote the non-dimensional forms of the density, velocity vector, pressure, energy per unit volume, heat flux vector, position vector, time, and stress tensor, respectively. δ_{ij} is the Kronecker delta. Equations (2)–(4) follow Einstein notation. The subscript i is a free index, and j and k are dummy indices. The indices take the value 1, 2, or 3. $Re, M_\infty,$ and Pr denote the Reynolds number, free-stream Mach number, and Prandtl number, respectively. They are defined as follows:

$$Re = \frac{\rho_\infty U_\infty c}{\mu_\infty}, \quad M_\infty = \frac{U_\infty}{a_\infty}, \quad Pr = \frac{\mu_\infty c_p}{\kappa_\infty}, \quad (5)$$

where $\rho_\infty, U_\infty, c, \mu_\infty, a_\infty, c_p,$ and κ_∞ denote the density, velocity, chord length, viscosity, sound speed, constant pressure specific heat, and heat conduction coefficient, respectively. Here, a quantity with subscript ∞ denotes the quantity in the free-stream condition. The viscosity is calculated using Sutherland’s law. $D_c S_i$ and $D_c S_j u_j$ in Equations (3) and (4) correspond to the body force and power added to the unit volume by PA, respectively. Hereinafter, $x, y, z, u, v,$ and w are used to represent the position and flow velocity of $x_1, x_2, x_3, u_1, u_2,$ and $u_3,$ respectively, for ease of discussion. In the present study, the free-stream

Mach number is set to 0.2, which reduces the computational time. The compressibility of the fluid is almost negligible although the Mach numbers in the present study and previous experimental studies [29,30] are different.

3.2. Plasma Actuator Modeling

The body force term for PA was modeled with $D_c S_i$ and $D_c u_k S_k$ in the Navier–Stokes equations, as in Equations (3) and (4). The Suzen–Huang model [34] is utilized to obtain S_i . The non-dimensional body force vector S_i is represented as follows:

$$S_i = \rho_c \left(-\frac{\partial \phi}{\partial x_i} \right) f(t)^2, \tag{6}$$

where $f(t)$ is the waveform function of the input voltage, ρ_c is the net charge density, and ϕ is the electric potential. The following equations are solved to obtain ρ_c and ϕ :

$$\frac{\partial}{\partial x_j} \left(\epsilon_r \frac{\partial \phi}{\partial x_j} \right) = 0, \tag{7}$$

$$\frac{\partial}{\partial x_j} \left(\epsilon_r \frac{\partial \rho_c}{\partial x_j} \right) = \frac{\rho_c}{\lambda_d^2}, \tag{8}$$

where ϵ_r is the relative permittivity of the medium, and λ_d is the Debye length.

The following plasma actuator was considered in the present study: The exposed electrode was 2 mm wide, and the insulated electrode was 8.75 mm wide. The electrodes were 0.1 mm thick and separated by a 0.1 mm thick dielectric. The streamwise spacing of electrodes was 0.5 mm. The dielectric was Kapton, and ϵ_r was 2.7. In the air, ϵ_r was 1.0. For λ_d , the same 1 mm as in the previous study was used [34]. These length parameters were non-dimensionalized by the reference length $c = 0.1$ m. Equations (7) and (8) were solved by the successive over-relaxation (SOR) method using a 1201×801 two-dimensional mesh. Boundary conditions for Equation (7) are given as follows:

$$\begin{aligned} \text{on outer boundaries,} & \quad \partial \phi / \partial n_i = 0, \\ \text{on exposed electrode,} & \quad \phi = 1.0, \\ \text{on insulated electrode,} & \quad \phi = 0, \end{aligned}$$

where n_i is the unit normal vector. The boundary conditions for Equation (8) are given as:

$$\begin{aligned} \text{on outer boundaries and in dielectric,} & \quad \rho_c = 0, \\ \text{on the surface of dielectric above the insulated electrode,} & \quad \rho_c = G(x'), \\ \text{on the other surface of PA,} & \quad \partial \rho_c / \partial n_i = 0. \end{aligned}$$

$G(x')$ is given by a half Gaussian distribution as follows:

$$G(x') = \exp\left(-\frac{x'^2}{2\delta^2}\right), \tag{9}$$

where x' is the chordwise length measured from the edge of the insulated electrode, and δ was $0.3l_e$ in the present study. l_e is the insulated electrode length. In the present study, the input voltage is a standard alternating current. Therefore, the waveform $f(t)$ is the sinusoidal wave:

$$f(t) = \sin(2\pi F_{\text{base}} t). \tag{10}$$

Figure 3 shows the distribution of the body force magnitude in the x direction (S_x) when $f(t) = 1$. The body force vectors are also shown in an enlarged view near PA. The length of the model region is $0.15c$ in the chordwise direction and $0.05c$ in the wall-normal direction. The body force in the spanwise direction was not implemented so that

no disturbance in the spanwise direction could be included in the plasma actuation of the present simulations. The magnitude of the body force was determined by the non-dimensional input voltage parameter, D_c , which is defined as follows:

$$D_c = \frac{\rho_{c,\max}\phi_{\max}}{\rho_{\infty}U_{\infty}^2}, \quad (11)$$

where $\rho_{c,\max}$ and ϕ_{\max} are the maximum values of ρ_c and ϕ . In the present study, $D_c = 0.04$ was used. The maximum induced velocity produced by continuous actuation with $D_c = 0.04$ in quiescent air reaches approximately 3.4 m/s if the reference velocity is $U_{\infty} = 10$ m/s [32]. This value is equivalent to the induced velocity produced by PA with a peak-to-peak applied voltage of 9 kV [31]. In the present body force model, the fluctuation is modeled by the square of the sinusoidal function. The direction of the body force produced by this fluctuation does not change within a single AC cycle, and even if the phase of the AC voltage changes, the body force in the opposite direction is not generated. This characteristic is similar to that of the “push-push type” model suggested by Font et al. [35]. F_{base} was set to 60, which corresponds to the frequency used in previous experiments [29,30]. Although the present model is simple, we validated it by comparing the LES results and the experimental results [23]. In addition, we also confirmed that the LES results using this model were not significantly different from those using a high-fidelity model [36]. Note that the flow induced by the plasma actuator in quiescent air conditions is considered to be unchanged for freestream velocities below 100 m/s [37]. In the present study, the freestream velocity is assumed to be 10 m/s. Therefore, the model equations were not solved concurrently with Navier–Stokes equations but in advance.

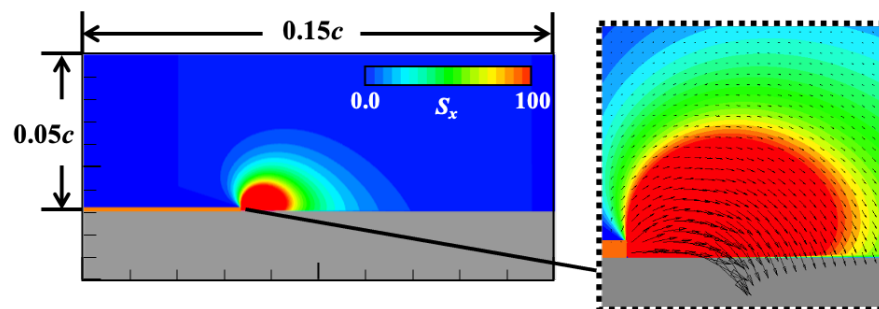


Figure 3. Distribution of body force in the x direction based on the Suzen–Huang model [34] and body force vectors near PA. Gray and orange areas represent the airfoil surface and exposed electrode, respectively.

The obtained body force is mapped to the computational grid for LES after rotating around the downstream edge of the exposed electrode to match the tangential direction of the airfoil surface.

3.3. Computational Method

We employ the flow solver LANS3D, which has been developed and verified to achieve high-fidelity simulations [38–40]. Generalized curvilinear coordinates (ξ, η, ζ) were adopted to solve the governing equations. The spatial derivatives of the convective and viscous terms, metrics, and Jacobians were evaluated using a sixth-order compact difference scheme [41]. At the first and second points off the wall boundary, a second-order explicit difference scheme was adopted. Tenth-order low-pass filtering [41,42] was used with a filtering coefficient of 0.495. A backward second-order difference formula was used for time integration, and five sub-iterations [43] were adopted to ensure time accuracy. For time integration, the lower-upper symmetric alternating direction implicit and symmetric Gauss–Seidel (ADI-SGS) [44] methods were used. The time step size nondimensionalized by the free-stream velocity and the chord length was 4×10^{-5} . The maximum Courant number was approximately 2.0. The nondimensional time step based on the wall units was lower

than 0.025 at the attached turbulent boundary layer. Choi and Moin [45] indicated that a time step of less than 0.4 is sufficient for the LES on a turbulent boundary layer. In the present study, wall-resolved LESs were conducted. The LES using the compact difference scheme with the high-order low-pass filter is well-validated and shows comparable results with standard LESs with explicit sub-grid-scale models when the computational grid resolution is fine enough [46–48]. The high-order low-pass filter adds numerical viscosity to computations at the only coarse grid region and implicitly acts as sub-grid scale models. Thus, the explicit sub-grid scale models were not used in the present study to avoid unpreferable turbulence decay. Utilized grid resolutions in the present study are explained in Section 3.4.

All variables were extrapolated from the point inside the outflow boundary into the point at the boundary. At the outflow boundary, all variables were extrapolated from the grid points next to the boundary into the grid points at the boundary, and the static pressure was fixed as the free stream value. At the wall boundary, adiabatic and no-slip conditions were applied. For the boundaries in the spanwise direction, a periodic boundary condition was adopted. At the inflow boundary, a uniform free stream condition without disturbance was employed.

All LESs were performed using the JAXA Supercomputer System Generation 2 and 3 (JSS2 and JSS3) at the Japan Aerospace Exploration Agency. Approximately 80 nodes (2560 cores) were used for each case.

The computations were conducted until the aerodynamic coefficients became quasi-steady before obtaining the time-averaged flow field and aerodynamic coefficients. The computational time in nondimensional time before obtaining the data was longer than 30. The data obtaining duration was five in nondimensional time.

3.4. Computational Grid

The computational grids and the computational domain with a schematic diagram of the inflow are shown in Figure 4. The zonal method [49] using two computational grids with different resolutions were employed to treat small fluid fluctuations induced by PA in the present LES. The computational grids consist of a C-type grid around the airfoil (zone1: blue and red) and a fine grid around PA (zone 2: green). The body force of the Suzen–Huang model was obtained in advance and mapped to zone 2. Equations (2)–(4) were solved for zones 1 and 2, and physical values were exchanged with each other at every time step.

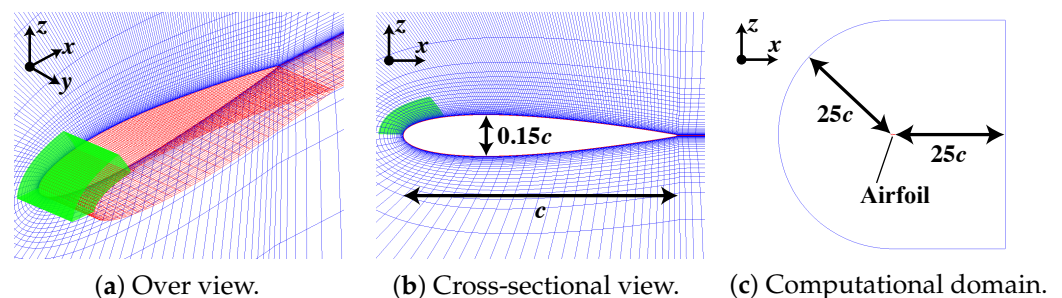


Figure 4. Computational grids and domain. The grids were visualized for every four points.

The distance from the airfoil surface to the outer boundary was $25c$, and the width of the span-wise computational domain was $0.2c$. The grid points of zone 1 and zone 2 were approximately 1.8×10^7 and 2.0×10^6 , respectively, as shown in Table 1. The minimum grid spacing in the wall-normal direction was $0.00012c$. The maximum grid sizes based on the wall unit were $(\Delta\xi^+, \Delta\eta^+, \Delta\zeta^+) \lesssim (8, 9, 1)$ at the attached turbulent boundary layer region. The present grid resolution and the computational methods were validated in the previous study [23].

Table 1. Number of computational grid points.

	ξ	η	ζ	Total Point
Zone 1	759	134	179	18,205,374
Zone 2	149	134	111	2,216,226

4. Results and Discussion

4.1. Validation

Here, the present LESs are validated by comparing them with the experimental results. The experimental data were acquired using the same facility at the Institute of Space and Astronautical Science, Japan Aerospace Exploration Agency (JAXA), utilized in the previous study [30]. The test section size of the wind tunnel was 100 mm in width, 400 mm in height, and 700 mm in length. The turbulence intensity at the center of the tunnel was verified to be approximately 0.08% at a freestream velocity of 6.6 m/s. A two-dimensional NACA0015 wing model with a chord length of 100 mm and a span length of 100 mm was used. The model surface had a total of 29 pressure ports, and the time-averaged pressure measurements were conducted, but the pressure around $x/c = 0.05$ could not be measured due to the PA installation on the airfoil surface. The freestream velocity was set to 10 m/s, corresponding to the Reynolds number of approximately 63,000, based on the chord length and the freestream velocity, which is the same as the present LES. The applied voltage of PA was 3.5 kV_{pp} (peak-to-peak voltage). The details may be found in the literature [30]. It should be noted that the experimental results include the effect of the wind tunnel’s side walls and the freestream disturbance.

Figure 5 compares pressure coefficient (C_p) distributions at $\alpha = 6, 8,$ and 10 obtained by the LESs and experiments. The shape of the NACA0015 airfoil is shown in gray on the background. Table 2 shows mean absolute errors (MAE) between the C_p distributions obtained by the LESs and the experiments.

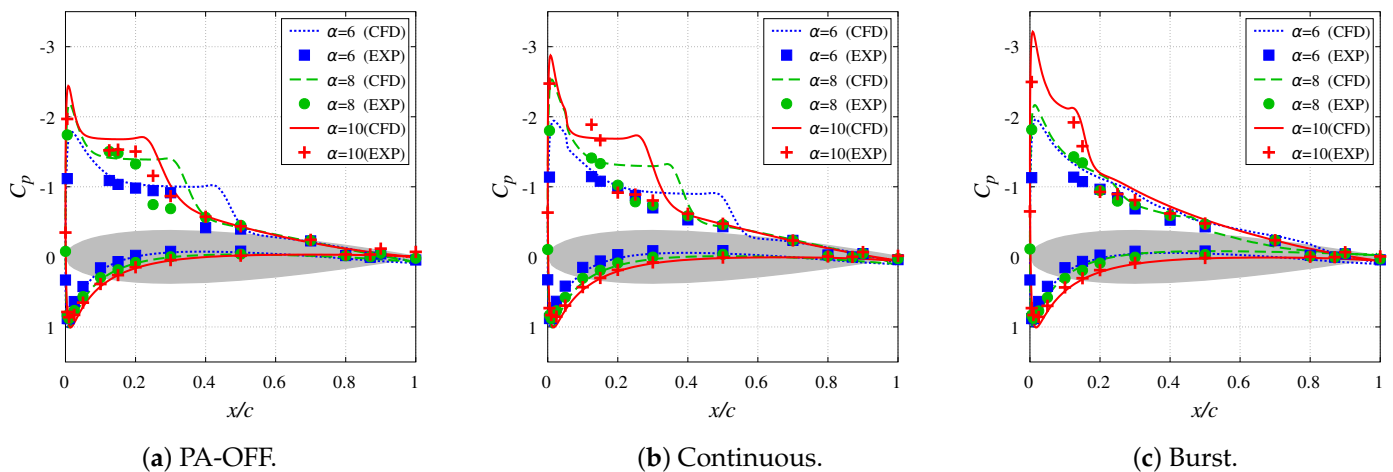


Figure 5. Pressure coefficient (C_p) distributions around the airfoil in each case of the computations (CFDs) and experiments (EXPs).

Table 2. Mean absolute errors (MAE) between the C_p distributions obtained by the LESs and the experiments.

	α [deg]		
	6	8	10
PA-OFF	0.076	0.078	0.064
Continuous	0.115	0.098	0.097
Burst	0.094	0.059	0.078

In the PA-OFF case at $\alpha = 10$ (Figure 5a) and the Burst cases (Figure 5c), the LES results show quantitative agreement with the experimental results at all angles of attack. The MAE values are relatively low in these case. On the other hand, in the PA-OFF case at $\alpha = 6$ and 8 and the Continuous case, the LESs overestimate the plateau region of C_p distribution. This discrepancy between the LESs and experiments is probably because of a tripping effect of the PA electrodes on the airfoil surface and a freestream disturbance [30]. These disturbances would make the Continuous case's flow of experiments close to that of the Burst case. The parameter D_c uncertainty, which is set to match the maximum value of the PA-inducing velocity, also might affect the computational results. Although a discussion of the Continuous case needs to be conducted carefully; we consider that the LES results are reliable enough to discuss the effectiveness of PA because the LESs can predict the quantitative agreement of the Burst cases and the qualitative tendency that the plateau region in each case becomes smaller as the angle of attack increases. In addition, the computational method and the PA model used in the present study have been validated even at the angle of attack after stall [8,23].

4.2. Aerodynamic Characteristics

Figure 6 shows the average value of the lift-to-drag ratio (L/D) with the minimum and maximum values in each case. The Continuous and Burst cases show the L/D value superior to the PA-OFF cases except for the Burst case at $\alpha = 4$. This result indicates that the flow control using PA helps the improvement in the aerodynamic characteristics even at lower angles of attack than the stall angle.

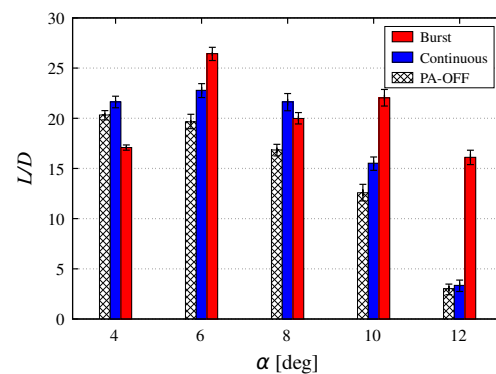


Figure 6. Lift-to-drag ratio (L/D) versus angle of attack (α).

Figure 7 shows the lift coefficient (C_L) and drag coefficient (C_D) in each case. The C_L of the Continuous case was higher than the PA-OFF case in all cases, while C_L of the Burst case at $\alpha = 4$ and 8 was lower than PA-OFF. The C_D values of Continuous and Burst cases were more stable than the PA-OFF case at any angle of attack and control method, and the fluctuation was slight. At the post-stall angles of attack, L/D improved by a C_L increase and a C_D decrease [23]. However, at $\alpha = 8$, which is a pre-stall angle of attack, C_L of the Burst case was lower than the PA-OFF case. On the other hand, the C_D of the Burst case was lower than the PA-OFF case, and as a result, L/D was higher than the PA-OFF case. In other words, at the pre-stall angle of attack, the reduction of C_D contributes more to the improvement of L/D than the improvement of C_L .

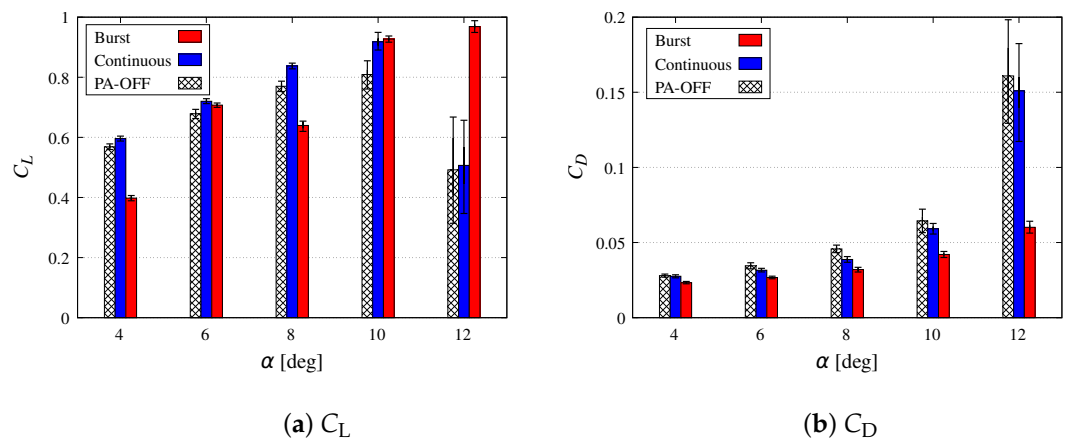


Figure 7. Lift coefficient (C_L) and drag coefficient (C_D) versus angle of attack (α).

Figure 8 shows the breakdown of C_D : viscous drag (C_{D_v}) and pressure drag (C_{D_p}) in each case. Although there was no significant change in C_{D_v} by using PA, C_{D_p} decreased in both pre-stall and post-stall angles. In particular, the reduction in C_{D_p} was more remarkable in the Burst cases than in the Continuous cases. The C_{D_p} reduction effect of the Burst cases is discussed in detail in the following section (Section 4.3).

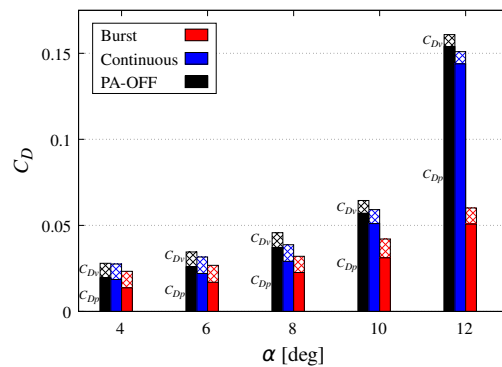


Figure 8. Pressure drag coefficient (C_{D_p}) versus angle of attack (α).

4.3. Averaged Flow Feature

In this section, we discuss what flow changes with the PA control cause an aerodynamic characteristic change. In the following discussion, the results at $\alpha = 4$ are omitted because their overall tendency is similar to that at $\alpha = 6$, and arguments will be made with the results at $\alpha = 6, 8$, and 10.

Figure 9 shows the pressure coefficient (C_p) distribution around the airfoil obtained in each case. The shape of the NACA0015 airfoil is drawn in gray on the background. The black up- and down-pointing triangle symbols indicate the highest and lowest airfoil surface positions at each angle of attack, respectively. The characteristic changes in the C_p distribution with the PA control are mainly observed on the airfoil's upper surface. In the Continuous cases, the C_p value at the suction peak near the leading edge lowered, and the plateau region moved toward the trailing edge and slightly shrunk. In the Burst cases, the C_p plateau region was significantly reduced, and the C_p value at the suction peak became low at $\alpha = 6$ and 10. The local variation of C_p seen at $0.2 \lesssim x/c \lesssim 0.5$ in the Burst cases at $\alpha = 6$ and 8 was due to the merging of the two-dimensional vortex structures. The details are discussed in Section 4.4. Additionally, at $\alpha = 8$, the pressure on the underside of the airfoil was slightly lower than that of the PA-OFF and Continuous cases.

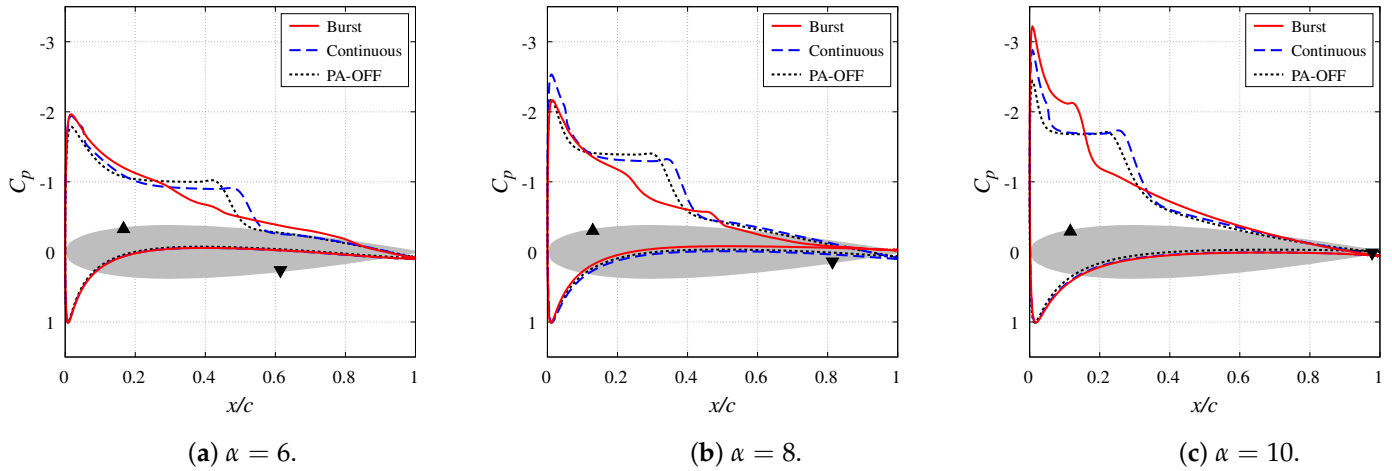


Figure 9. Pressure coefficient (C_p) distributions around the airfoil.

We discuss the C_p distribution in more detail from the perspective of reducing C_{D_p} . Since the force due to the surface pressure acts perpendicularly to the airfoil surface, the force contribution direction (thrust or drag) depends on the orientation of the airfoil surface. When there is no inflection point on the suction side, such as the NACA0015 airfoil, the surface pressure at the front half region from the highest point of the airfoil contributes to thrust, while the surface pressure at the back half part from the highest point contributes to drag increase. In Figure 9, since the suction peak exists upstream from the highest point in each case, the lower the pressure at the peak position, the more significant the contribution to thrust and the lower C_{D_p} . On the contrary, in the PA-OFF case shown in Figure 9, most of the plateau region caused by the separation bubbles exists downstream from the highest point; thus, the negative pressure contributes to the drag.

Figure 10 shows the distribution of the skin-friction coefficient (C_f) on the airfoil's upper surface in each case. In the PA-OFF case at $\alpha = 6$, C_f is negative in the range of $0.1 \lesssim x/c \lesssim 0.5$, indicating that the flow is separated and forms separation bubbles. The negative C_f region coincides with the plateau region in Figure 9a. In the Continuous cases in Figure 9, the pressure of the suction peak is reduced at any angle of attack. On the other hand, as shown in Figure 10, the plateau region in Figure 9 is moved to the trailing edge side due to the movement of the separation bubble position (the area where C_f is negative) to the downstream. The movement of this plateau region to the downstream contributes to the C_{D_p} increase. However, since the contribution of the C_{D_p} decrease because the pressure decrease in the suction peak is larger and C_{D_p} slightly decreases at any angle of attack, as shown in Figure 8. In the Burst cases, the suction peak value of C_p near the leading edge is lower than the other cases at $\alpha = 6$ and 10 (Figure 9a,c). In addition, the plateau region is reduced at all angles of attack, and therefore, C_{D_p} value becomes lower than the Continuous cases.

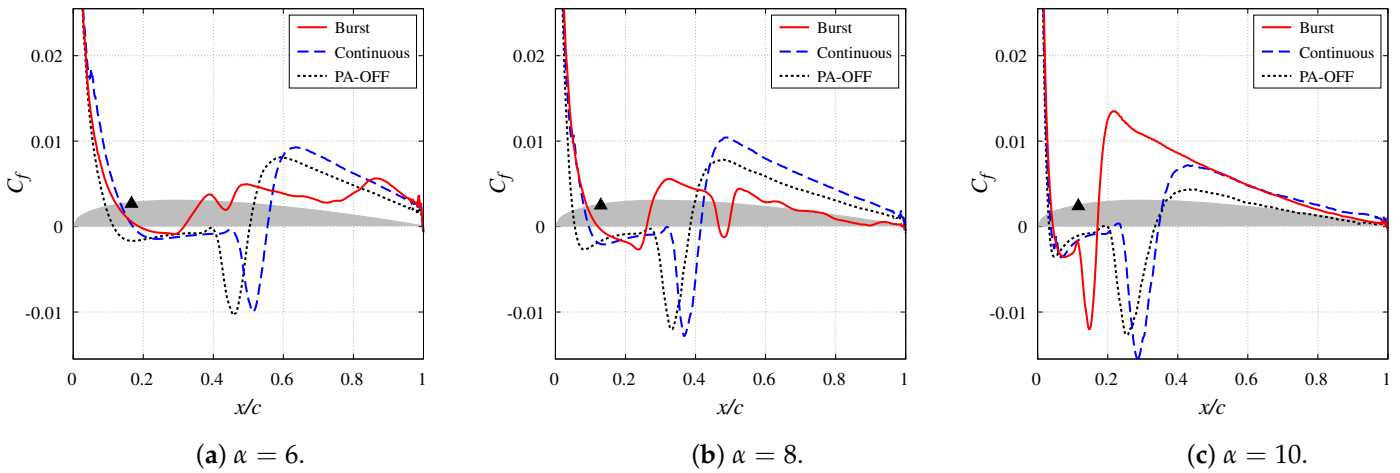


Figure 10. Skin friction coefficient (C_f) distributions on the airfoil's upper surface.

The relationship between the flow field and the pressure distribution on the airfoil surface is discussed in more detail. Figure 11 shows time- and spanwise-averaged flows colored with the chordwise velocity normalized by the freestream velocity (u/U_∞) for each case, and Figure 12 shows the displacement thickness (δ^*) on the airfoil's upper surface. Figures 11 and 12 are helpful in understanding the separation bubble size in the wall-normal direction of the airfoil. The displacement thickness is nondimensionalized by the chord length. The NACA0015 airfoil is shown in the background to the same scale as the displacement thickness. In all cases, the flow separates from around $x/c \simeq 0.1$, forming a separation bubble, although it is difficult to see in the Burst cases.

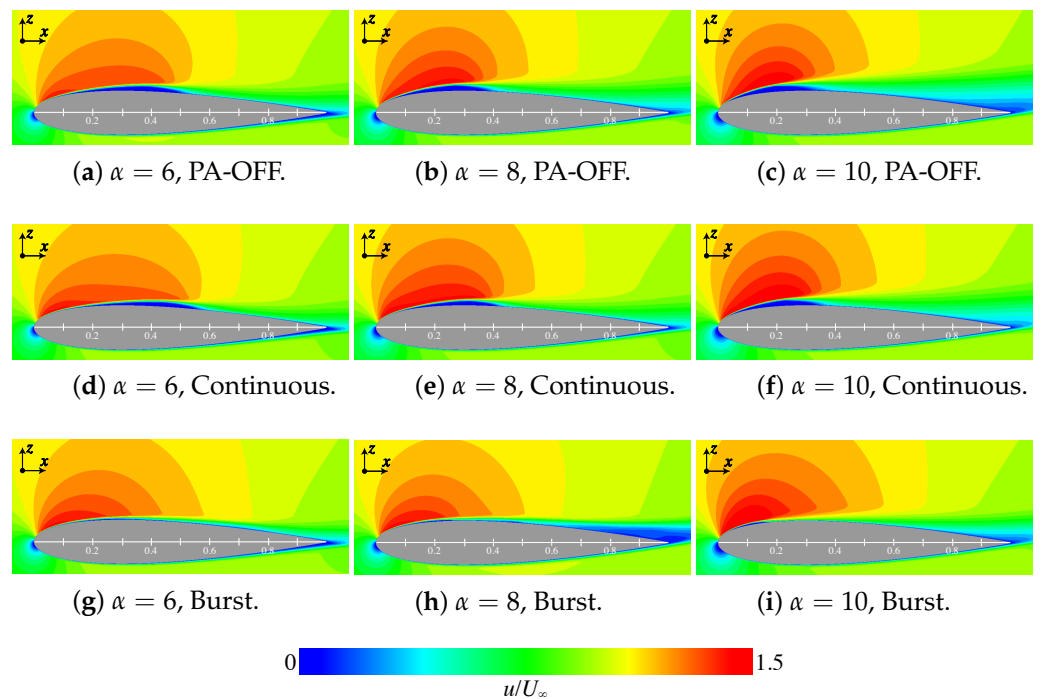


Figure 11. Time- and spanwise-averaged flows colored with the chordwise velocity (u/U_∞).

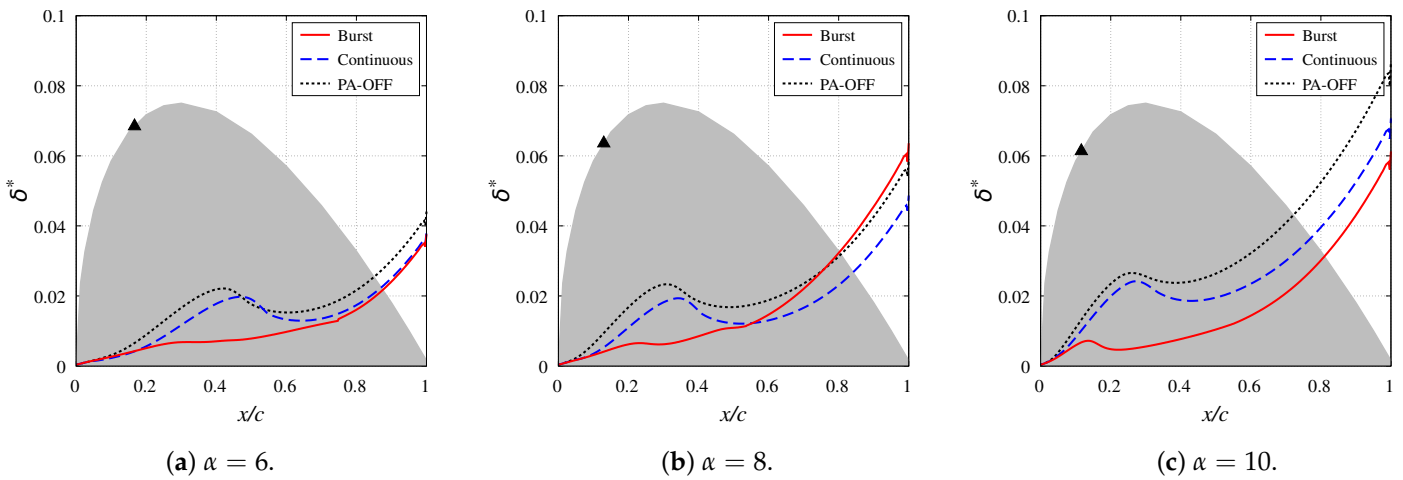


Figure 12. Displacement thickness (δ^*) on the airfoil’s upper surface.

The flow on the airfoil’s upper surface (suction side) generally accelerates due to the flow bending at the leading edge of the airfoil (the red region in Figure 11), creating the suction peak, as seen in Figure 9. In the present flow fields, the shape of the separation bubble existing in this acceleration region changes due to the PA control; thus, the value of the suction peak also changes in each case. The pressure distribution in the presence of the separated region on the airfoil surface can be predicted by assuming that the airfoil thickness increases as much as the thickness of the separated region. The smaller the displacement thickness, the lower the effect of the boundary layer and separated area, and the flow becomes closer to the potential flow of the NACA0015 airfoil.

In Figure 12, the displacement thicknesses of the Continuous and Burst cases are smaller than that of the PA-OFF case in the region of $0.1 \lesssim x/c \lesssim 0.4$ at any angle of attack. When the flow bends, the pressure inner side of the curved flow becomes lower as the radius of curvature becomes smaller. Therefore, in the Continuous and Burst cases with the thin displacement thickness, the radius of curvature of the flow near the leading edge of the airfoil is smaller than in the PA-OFF case, and the pressure is lower. However, in Figure 9b, the suction peak value of the burst case at $\alpha = 8$ is almost the same as that of the PA-OFF case. The exceptional suction value of the burst case at $\alpha = 8$ may be caused by the flow separation near the trailing edge on the suction side. At $x/c \simeq 0.9$ in Figure 10b, C_f is almost zero, and in Figure 11h, the low-speed region is larger near the trailing edge than in the other cases. Due to this trailing edge separation, in Figure 10b, the displacement thickness of the Burst case near the trailing edge ($0.8 \lesssim x/c \lesssim 1$) becomes the thickest, and the radius of curvature on the airfoil’s upper surface increases, resulting in weakening the acceleration of the flow near the leading edge and affecting the value of the suction peak.

4.4. Unsteady Flow Feature

In this section, we discuss the relationship between the instantaneous flow field for each case and the plots up to Section 4.3. Figure 13 shows the instantaneous flow fields of the PA-OFF and Continuous cases at $\alpha = 6$. The isosurface is the second invariant of the velocity gradient tensor ($Q = 6250$), colored by the chordwise velocity (u/U_∞). Figures 14 and 15 show the turbulent-kinetic-energy (TKE) distributions and the power spectral densities (PSDs) of the chordwise velocity fluctuations of the PA-OFF and Continuous cases, respectively. The PSD shows the value at the position where the TKE is the largest (indicated by the black cross symbol in Figure 14) at each cord length position. The gray dashed line indicates the slope of Kolmogorov’s $-5/3$ power law. As shown in Figure 13, the instantaneous flow fields of the PA-OFF and Continuous cases are similar. In

Figure 15, the spectrum shows a $-5/3$ power slope at $x/c = 0.5$ and downstream there in both PA-OFF and Continuous cases, indicating the flow transitions to turbulent flow. Although, at first glance, the instantaneous fields of the PA-OFF and Continuous cases are very similar, due to the momentum addition by PA, the laminar flow separation in the Continuous case is delayed more than that in the PA-OFF case, as shown in Figure 10, and the separated shear layer of the Continuous case is closer to the airfoil surface. As a result, as shown in Figure 12a, the displacement thickness of the Continuous case is thinner than that of PA-OFF in most regions. The position of the turbulent transition in the Continuous case is delayed, and a region where TKE is high is seen downstream compared to that in the PA-OFF case. Although only the case at $\alpha = 6$ was discussed here, the flow characteristics of the PA-OFF and Continuous cases are the same for other angles of attack.

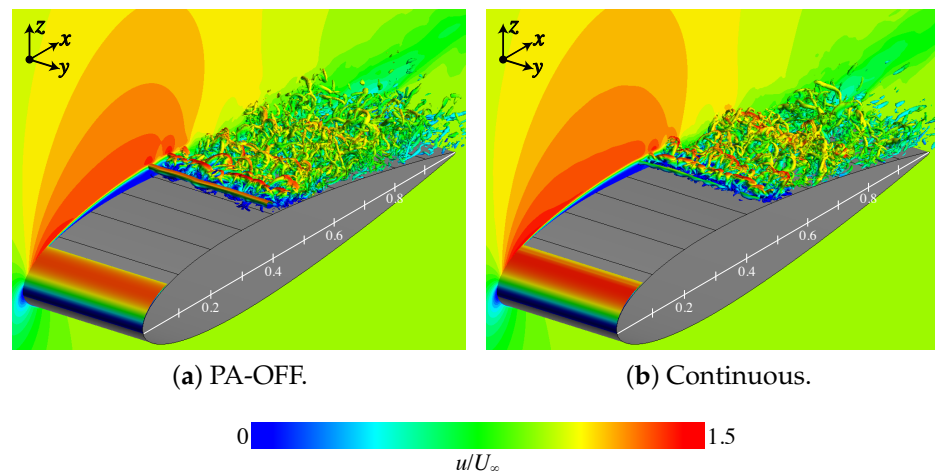


Figure 13. Instantaneous flows with the isosurface of the second invariant of the velocity gradient tensor colored with the chordwise velocity (u/U_∞) at $\alpha = 6$.

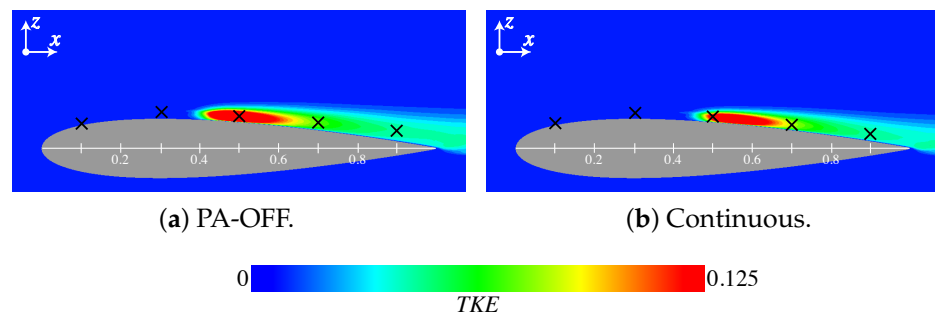


Figure 14. Turbulent kinetic energy (TKE) distributions at $\alpha = 6$.

Figure 16 shows the instantaneous flow fields of the burst case at each angle of attack. The isosurface is the second invariant of the velocity gradient tensor ($Q = 6250$), colored by the chordwise velocity (u/U_∞). The flow fields in the Burst cases differ from those in the PA-OFF and Continuous cases, where the large separated region is formed under the separated shear layer. At $\alpha = 6$ and 8 in Figure 16, two-dimensional vortex structures are induced by the burst drive of PA near the leading edge and move downstream. These two-dimensional vortex structures maintain their spanwise shape up to near the trailing edge. Such stable two-dimensional vortex structures are not observed in the controlled flows at post-stall angles. These two-dimensional vortex structures merge several times in the process of moving. Where large two-dimensional vortex structures merge, local variations of C_f and C_p are seen. Specifically, in the region of $0.4 \lesssim x/c \lesssim 0.5$, a small plateau region is seen in Figure 9a,b, and a local decrease in C_f is seen in Figure 10a,b.

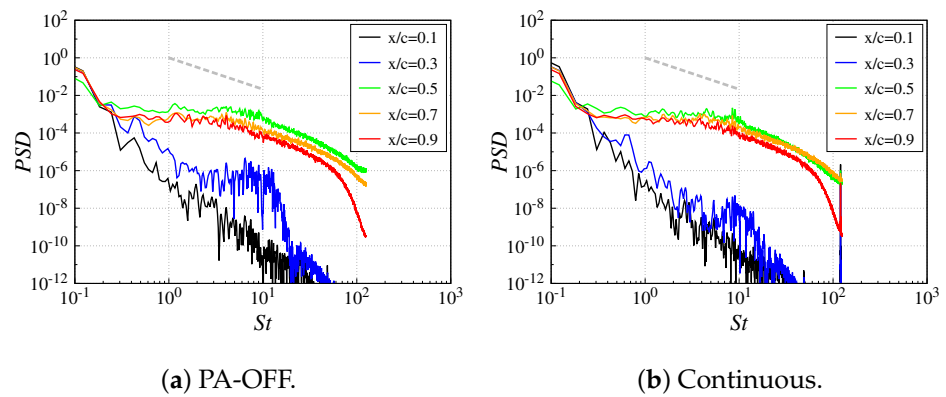


Figure 15. Power spectrum densities (PSDs) of the chordwise velocity fluctuations at the point of the maximum TKE directly above each cord length at $\alpha = 6$.

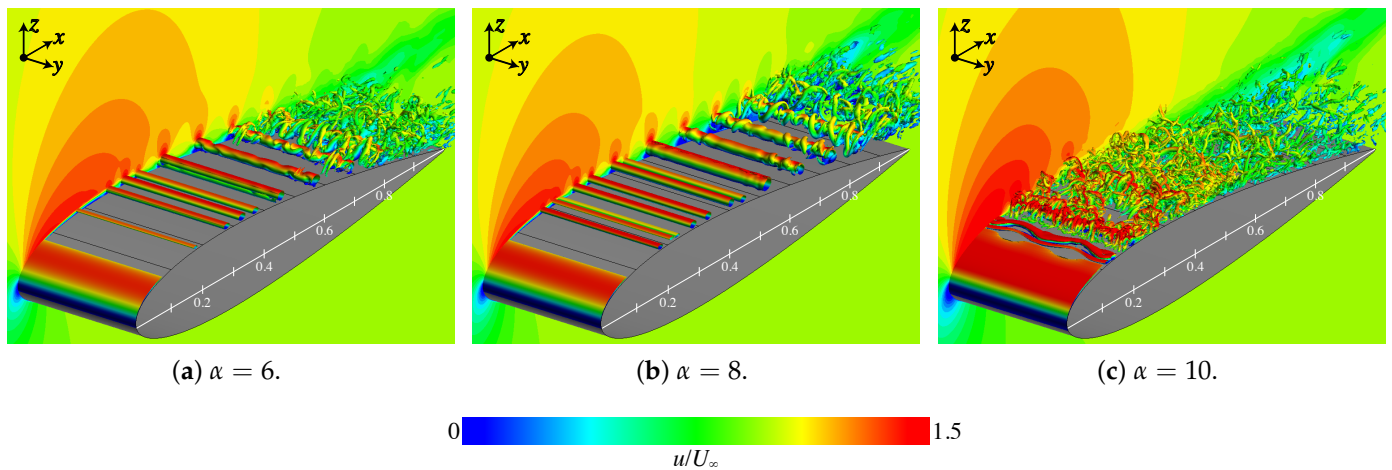


Figure 16. Instantaneous flows with the isosurface of the second invariant of the velocity gradient tensor colored with the chordwise velocity (u/U_∞) in the Burst cases.

The difference between the flow fields at $\alpha = 6$ and $\alpha = 8$ is remarkable near the trailing edge. As shown in Figure 16b, the flow at $\alpha = 8$ separates near the trailing edge while maintaining the two-dimensional vortex structures. The flow at $\alpha = 10$ is different from those at $\alpha = 6$ and 8, the two-dimensional vortex structures induced by PA rapidly collapse into the two-dimensional vortex structures (Figure 16c). This flow resembles the controlled flows investigated in the previous study [8] at the post-stall angles.

Figures 17 and 18 show the TKE distributions and the PSDs of the chordwise velocity fluctuations for the Burst case at each angle of attack. The PSD shows the value at the position where the TKE is the largest (indicated by the black cross symbol in Figure 17) at each cord length position. The TKE distribution differs at each angle of attack, reflecting the characteristics of the instantaneous flow fields. At $\alpha = 6$, the TKE increases from $x/c \simeq 0.3$ toward downstream due to the passing of the two-dimensional vortex structures. A turbulent transition occurs at $0.7 \lesssim x/c \lesssim 0.8$, and the region where TKE is particularly high (red region) locally spreads. In the PSD of Figure 18a, at $x/c = 0.3$, the frequency $St = 6$ and its harmonics are dominant due to the passing of the two-dimensional vortex structures induced by the burst drive of PA. At $x/c = 0.7$, the energy in the high-frequency range begins to increase due to the turbulent transition, and at $x/c = 0.9$, a PSD decay of the $-5/3$ slope can be confirmed. The position, where the $-5/3$ slope reveals, is downstream of that in the PA-OFF case (Figure 15a). These PSD characteristics indicate that transporting the two-dimensional vortex structures suppresses the turbulent transition. At $\alpha = 8$, the TKE increases from $x/c \simeq 0.2$ by the passing of the two-dimensional vortex structures, similar to that at $\alpha = 6$. At $x/c \simeq 0.8$, the two-dimensional vortex structures begin to move

away from the airfoil surface; thus, the high TKE region is also seen away from the airfoil surface. The two-dimensional vortex structures are relatively stable compared to those at the other angles of attack, and the turbulent transition is suppressed. Therefore, even at $x/c = 0.9$, the PSD decay of the $-5/3$ slope is not seen (Figure 18b). At $\alpha = 10$, TKE increases sharply at $0.1 \lesssim x/c \lesssim 0.3$ due to rapid turbulent transition. The PSD also has high energy in the high-frequency range at $x/c = 0.3$, and the slope of the energy decay is close to the $-5/3$ slope.

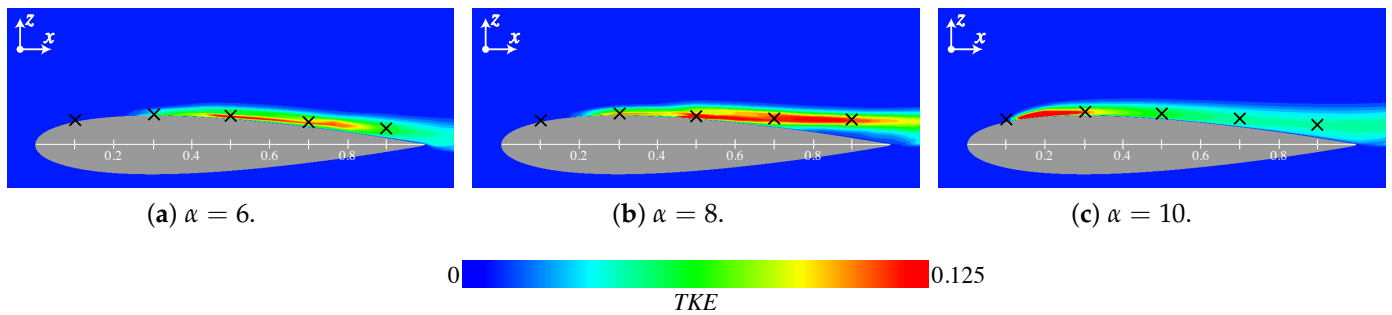


Figure 17. Turbulent kinetic energy (TKE) distributions in the Burst cases.

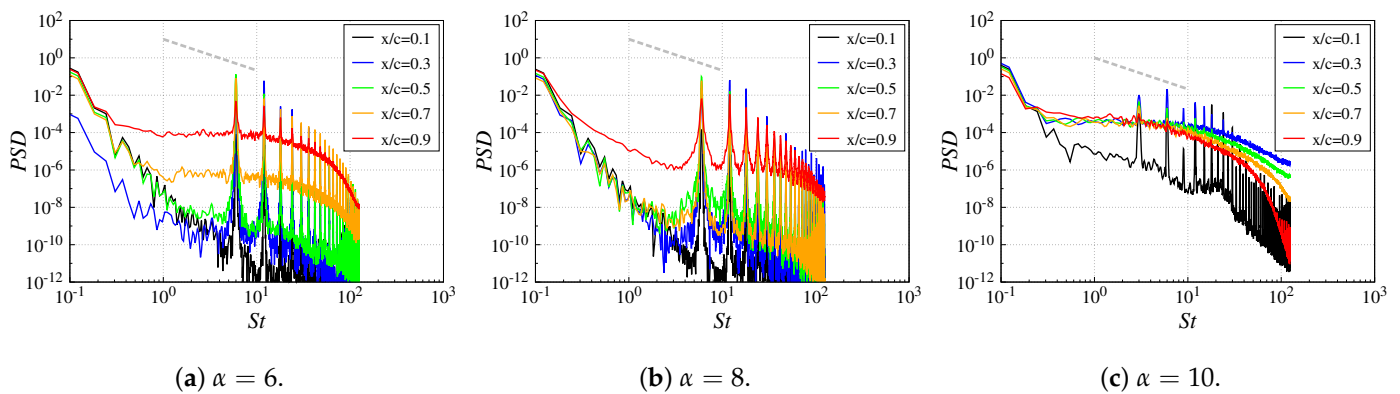


Figure 18. Power spectrum densities (PSDs) of the chordwise velocity fluctuation at the point of the maximum TKE directly above each code length in the Burst cases.

In Section 4.3, the possibility that the trailing edge separation affects the peak value of C_p at $\alpha = 8$ in the burst case is discussed. At $\alpha = 8$, as shown in Figures 16b and 18b, the two-dimensional vortex structures induced by PA keep their structure and move away from the airfoil surface, near the trailing edge, while the flows in the burst cases at $\alpha = 6$ and 8 occur as turbulent transitions and maintain attached near the trailing edge. Therefore, the promotion of turbulent transition at $\alpha = 8$ could suppress the trailing edge separation, the negative C_p peak value could become lower, and C_L could be improved.

In the previous study [27], the control effects of $F^+ = 1$ and 10 were discussed by performing LESs at the angle of attack of $\alpha = 6$. In the case of $F^+ = 1$, a turbulent transition occurred relatively upstream after a large-scale two-dimensional vortex structure shedding, while in the case of $F^+ = 10$, two-dimensional vortex structures keep their structures flowing up to the trailing edge of the airfoil. This result suggests the possibility of promoting a turbulence transition by using frequencies lower than the burst frequency, which induces stable two-dimensional structures, in a flow with a relatively small pressure gradient at low angles of attack. In other words, for the Burst case at $\alpha = 8$ of the present study, using frequencies lower than $F^+ = 6$ could promote the turbulent transition and reduce the low-velocity region at the trailing edge. The characteristics of the controlled flow at the pre-stall condition differ depending on the angle of attack and the PA drive condition. A method of dynamically changing the PA drive method depending on the flow

conditions at post-stall angles of attack to select an optimum PA drive is proposed [50]. If the optimum control method can be dynamically selected according to the flow conditions, even at pre-stall angles of attack, further improvements in aerodynamic characteristics could be expected.

4.5. Comparison with Controlled Flow at Post-Stall Angle of Attack

This section discusses the differences between the controlled flows at the pre- and post-stall angles of attack.

Figure 19 shows C_p and C_f distributions at the post-stall angle of attack ($\alpha = 12$). In the PA-OFF case, a massive separation occurs from the leading edge of the airfoil, and thus, the C_p shows a flat distribution on the suction side, and the C_f value takes a negative value on most of the airfoil surface. Because of the massive separation, the C_L of the PA-OFF case is significantly lower compared to the pre-stall angles (Figure 7a). The burst drive with F^+ can suppress the massive flow separation and create flow reattachment, while the continuous drive cannot. The flow reattachment in the Burst case increases the C_L and decreases the C_D significantly. Both the C_L increase and C_D decrease contribute to L/D improvement, as shown in Figures 6 and 7. The detailed discussion may be found in [15]. On the other hand, at the pre-stall angles of attack, in the PA-OFF case, a separation bubble, which does not exist at the post-stall angle of attack, is formed on the airfoil's upper surface, and its position and size affect the aerodynamic coefficients, as discussed in Section 4.3. The change in the separation bubble by PA control does not contribute much to the C_L increase but mainly reduces the C_D and contributes to the increase in L/D (Figures 6 and 7). At $\alpha = 4$ and 8, the C_L decreases due to the shrink of the separation bubble, but the C_D reduction is larger than the C_L decrease, so the L/D increases.

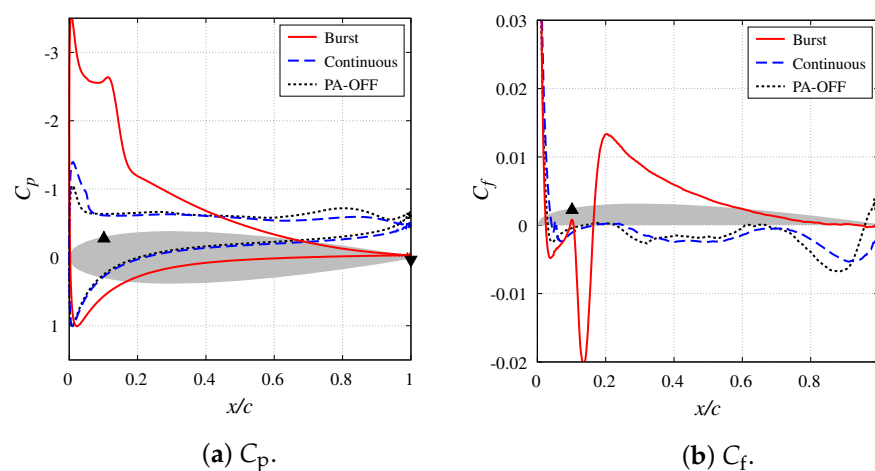


Figure 19. Pressure coefficient (C_p) and skin friction coefficient (C_f) distributions on the airfoil's upper surface at $\alpha = 12$.

The difference in the flows in the Burst case at each angle of attack becomes more apparent when the discussion includes the instantaneous flow at $\alpha = 12$. Figure 20 shows the instantaneous flow of the Burst case at $\alpha = 12$. This flow resembles that at $\alpha = 10$ shown in Figure 16c. The two-dimensional vortex structures induced by PA rapidly break down into fine vortices. Figures 21 and 22 show the TKE distributions and the PSDs of the chordwise velocity fluctuations for the Burst case at $\alpha = 12$. The PSD shows the value at the position where the TKE is the largest (indicated by the black cross symbol in Figure 21) at each chord length position. The region where TKE is locally high is seen at $0.1 \lesssim x \lesssim 0.4$, and a PSD decay of the $-5/3$ slope is seen at all stations in Figure 22 because the turbulent transition rapidly occurs. The turbulence growth shown by these TKE and PSDs also resembles those at $\alpha = 10$. The rapid turbulent transition draws the shear layer and reduces the separation region. On the other hand, as discussed in Section 4.4, at the lower angles of

attack ($\alpha = 4, 6, \text{ and } 8$), the burst actuation induces the two-dimensional vortices, which maintain their spanwise shape (Figure 16). The transport of the two-dimensional vortices draws the shear layer to the airfoil surface and shrinks the separation bubble. Additionally, those two-dimensional vortices suppress the turbulent transition. The suppression of turbulence transition can be confirmed by the spectrum in Figure 18.

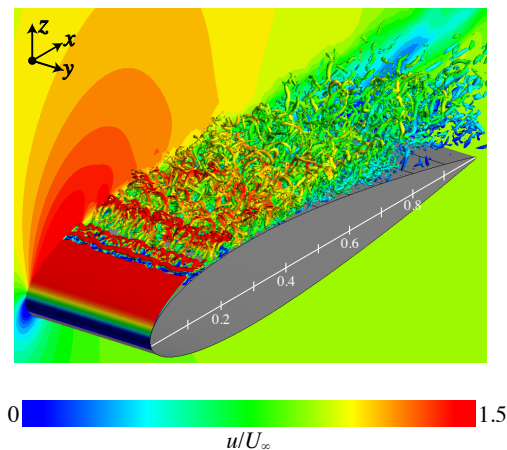


Figure 20. Instantaneous flows with the isosurface of the second invariant of the velocity gradient tensor colored with the chordwise velocity (u/U_∞) in the Burst cases at $\alpha = 12$.

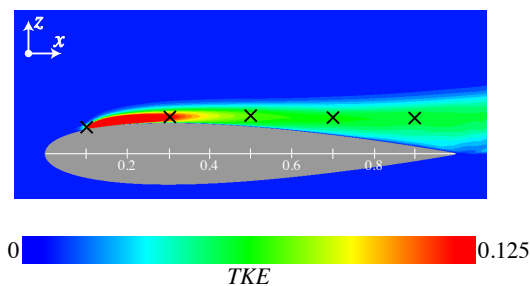


Figure 21. Turbulent kinetic energy (TKE) distribution in the Burst case at $\alpha = 12$.

As discussed above, the control mechanism is different between near the stall angle of attack ($\alpha = 10 \text{ and } 12$) and at lower angles of attack ($\alpha = 4, 6, \text{ and } 8$). This may be because the pressure gradient on the airfoil surface increases as the angle of attack increases. The pressure gradient may promote the collapse of the two-dimensional vortices induced by PA near the stall angle of attack. For post-stall angle flows, previous studies [15,21] have shown that using $F^+ \simeq 1$ maintains large two-dimensional vortex structures up to downstream. On the other hand, in the case of $F^+ = 6$, the two-dimensional vortex structures are maintained up to downstream at the low angles of attack in the present study. Whether or not the two-dimensional vortex structure is maintained may be determined by the relationship with the pressure gradient on the airfoil surface, and further research on this relationship is required.

Note that the magnitude of the pressure gradient on an airfoil surface depends on not only the angle of attack but also the curvature of the airfoil surface. For relatively thin airfoils, the flow control mechanism may differ from the cases of the NACA0015 airfoil. Further research on the relationship between the airfoil geometry and the flow control mechanism is required.

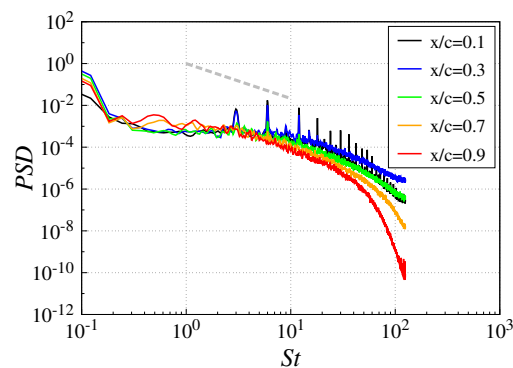


Figure 22. Power spectrum densities (PSDs) of the chordwise velocity fluctuation at the point of the maximum TKE directly above each chord length in the Burst case at $\alpha = 12$.

5. Conclusions

LES of the flows controlled by PA over an NACA0015 airfoil was performed at angles of attack before a stall. The flow control authority of PA was investigated, and the relationship between the aerodynamic coefficient and the flow field was clarified through the LES results.

The Continuous and Burst cases using PA at the angles of attack before the stall improved L/D compared to PA-OFF. The improvement in L/D is mainly owing to the reduction in C_{D_p} in addition to the improvement in C_L . The primary causes of the reduction in C_{D_p} are (1) lower pressure at the suction peak and (2) reduction in the plateau region of C_p as the separation bubble is moved or shrunk on the upper surface of the airfoil. The second effect is remarkable in the Burst cases with $F^+ = 6$. Although, in the Burst case, the lift-to-drag ratio is improved at all angles of attack, the phenomena leading to the improvement differ between near-stall angles ($\alpha = 10$ and 12) and other lower angles ($\alpha = 4, 6$, and 8). At near-stall angles, the turbulent transition is rapidly promoted by PA, and the flow is reattached. Whereas, at lower angles, the transport of two-dimensional vortex structures, which maintain their structures downstream and suppress the turbulent transition, creates flow reattachment. At $\alpha = 4$ and 8 , the L/D of the Continuous case was higher than that of the Burst case because the suction peak value of C_p in the Burst case was not improved compared to the PA-OFF case due to the trailing edge separation. The trailing edge separation may be caused by the suppression of the turbulent transition by the two-dimensional vortices whose structures are maintained even near the trailing edge in addition to the reverse pressure gradient. Therefore, applying flow control methods that promote turbulence transition could possibly suppress the trailing separation and improve aerodynamic characteristics. Based on the results of the previous study [27], frequencies lower than $F^+ = 6$ may be effective, and further investigation is required. In addition, a control method that dynamically changes the PA drive conditions according to the angle of attack is needed for robust control.

It should be noted that these phenomena in the present study would depend on the airfoil geometry and flow conditions. Future studies on the influence of the airfoil geometry such as a thin airfoil and the flow conditions such as freestream turbulence are required.

Author Contributions: Conceptualization, T.O. and K.F.; Data curation, T.O.; Formal analysis, T.O.; Funding acquisition, K.F.; Investigation, T.O.; Methodology, T.O.; Project administration, T.O.; Resources, T.O. and M.S.; Software, T.O., K.A., T.T. and K.F.; Supervision, K.A. and K.F.; Validation, T.O.; Visualization, T.O.; Writing—original draft, T.O.; Writing—review & editing, K.A. and K.F. All authors have read and agreed to the published version of the manuscript.

Funding: This research was supported by a JSPS Grant-in-Aid for Scientific Research No. 18H03816 in Japan.

Acknowledgments: The flow field computations presented in the present study are performed on the “JAXA Supercomputer System Generation 2 and 3 (JSS2 and JSS3)” in the Japan Aerospace Exploration Agency (JAXA) and on the “SX-Aurora TSUBASA” in the Cyberscience Center, Tohoku University. Supports by the system and center staffs are very much acknowledged. The authors would like to thank Satoshi Sekimoto of Tokyo University of Agriculture and Technology for conducting the experiments to validate the present simulations.

Conflicts of Interest: The authors declare no conflict of interest.

References

1. Corke, T.C.; Enloe, C.L.; Wilkinson, P.S. Dielectric Barrier Discharge Plasma Actuators for Flow Control. *Annu. Rev. Fluid Mech.* **2010**, *42*, 505–529. [CrossRef]
2. Jukes, T.N.; Choi, K.S. Control of unsteady flow separation over a circular cylinder using dielectric-barrier-discharge surface plasma. *Phys. Fluids* **2009**, *21*, 094106. [CrossRef]
3. Greenblatt, D.; Schneider, T.; Schuele, C.Y. Mechanism of flow separation control using plasma actuation. *Phys. Fluids* **2012**, *24*, 077102. [CrossRef]
4. Post, M.L.; Corke, T.C. Separation Control on High Angle of Attack Airfoil Using Plasma Actuators. *AIAA J.* **2004**, *42*, 2177–2184. [CrossRef]
5. Jukes, T.N.; Choi, K.S.; Johnson, G.A.; Scott, S.J. Turbulent Drag Reduction by Surface Plasma through Spanwise Flow Oscillation. In Proceedings of the 3rd AIAA Flow Control Conference, San Francisco, CA, USA, 5–8 June 2006; AIAA-2006-3693. [CrossRef]
6. Visbal, M.R.; Gaitonde, D.V.; Roy, S. Control of Transitional and Turbulent Flows Using Plasma-Based Actuators. In Proceedings of the 36th AIAA Fluid Dynamics Conference and Exhibit, San Francisco, CA, USA, 5–8 June 2006; AIAA-2006-3230. [CrossRef]
7. Bénard, N.; Jolibois, J.; Moreau, E. Lift and drag performances of an axisymmetric airfoil controlled by plasma actuator. *J. Electrostat.* **2009**, *67*, 133–139. [CrossRef]
8. Sato, M.; Nonomura, T.; Okada, K.; Asada, K.; Aono, H.; Yakeno, A.; Abe, Y.; Fujii, K. Mechanisms for laminar separated-flow control using dielectric-barrier-discharge plasma actuator at low Reynolds number. *Phys. Fluids* **2015**, *27*, 1–29. [CrossRef]
9. Thomas, F.O.; Corke, T.C.; Duong, A.; Midya, S.; Yates, K. Turbulent drag reduction using pulsed-DC plasma actuation. *J. Phys. D Appl. Phys.* **2019**, *52*, 434001. [CrossRef]
10. Wang, J.J.; Choi, K.S.; Feng, L.H.; Jukes, T.N.; Whalley, R.D. Recent developments in DBD plasma flow control. *Prog. Aerosp. Sci.* **2013**, *62*, 52–78. [CrossRef]
11. Vernet, J.A.; Orlu, R.; Soderblom, D.; Elofsson, P. Plasma Streamwise Vortex Generators for Flow Separation Control on Trucks. *Flow Turbul. Combust.* **2018**, *100*, 1101–1109. [CrossRef]
12. Zhang, Z.; Wu, Y.; Jia, M.; Song, H.; Sun, Z.; Zong, H.; Li, Y. The multichannel discharge plasma synthetic jet actuator. *Sens. Actuators A Phys.* **2017**, *253*, 112–117. [CrossRef]
13. Bhattacharya, S.; Gregory, J.W. Effect of Three-Dimensional Plasma Actuation on the Wake of a Circular Cylinder. *AIAA J.* **2015**, *53*, 958–967. [CrossRef]
14. Feng, L.H.; Jukes, N.T.; Choi, K.S.; Wang, J.J. Flow control over a NACA 0012 airfoil using dielectric-barrier-discharge plasma actuator with a Gurney flap. *Exp. Fluids* **2012**, *52*, 1533–1546. [CrossRef]
15. Fujii, K. Three Flow Feature behind the Flow Control Authority of DBD Plasma Actuator: Result of High-Fidelity Simulations and the Related Experiments. *Appl. Sci.* **2018**, *8*, 546. [CrossRef]
16. Wang, L.; Wong, C.W.; Alam, M.M.; Zhou, Y. Post-stall flow control using a sawtooth plasma actuator in burst mode. *Aerosp. Sci. Technol.* **2020**, *107*, 106251. [CrossRef]
17. Riherd, M.; Roy, S. Serpentine geometry plasma actuators for flow control. *J. Appl. Phys.* **2013**, *114*, 083303. [CrossRef]
18. Segawa, T.; Matsunuma, T. Applications of String-type DBD Plasma Actuators for Flow Control in Turbomachineries. In Proceedings of the 52nd Aerospace Sciences Meeting, National Harbor, Md, USA, 13–17 January 2014; AIAA 2014-1126. [CrossRef]
19. Kolbakir, C.; Hu, H.; Liu, Y.; Hu, H. An experimental study on different plasma actuator layouts for aircraft icing mitigation. *Aerosp. Sci. Technol.* **2020**, *107*, 106325. [CrossRef]
20. Visbal, M.R. Strategies for control of transitional and turbulent flows using plasma-based actuators. *Int. J. Comput. Fluid Dyn.* **2010**, *24*, 237–258. [CrossRef]
21. Ebrahimi, A.; Hajipour, M. Flow separation control over an airfoil using dual excitation of DBD plasma actuators. *Aerosp. Sci. Technol.* **2018**, *79*, 658–668. [CrossRef]
22. Wu, B.; Gao, C.; Liu, F.; Xue, M.; Zheng, B. Simulation of NACA0015 flow separation control by burst-mode plasma actuation. *Phys. Plasmas* **2019**, *26*, 063507. [CrossRef]
23. Sato, M.; Aono, H.; Yakeno, A.; Nonomura, T.; Fujii, K.; Okada, K.; Asada, K. Multifactorial Effects of Operating Conditions of Dielectric-Barrier-Discharge Plasma Actuator on Laminar-Separated-Flow Control. *AIAA J.* **2015**, *53*, 2544–2559. [CrossRef]
24. Liu, R.; Niu, Z.; Wang, M.; Hao, M.; Lin, Q. Aerodynamic control of NACA 0021 airfoil model with spark discharge plasma synthetic jets. *Sci. China Technol. Sci.* **2015**, *58*, 1949–1955. [CrossRef]
25. Erfani, R.; Kontis, K. MEE-DBD Plasma Actuator Effect on Aerodynamics of a NACA0015 Aerofoil: Separation and 3D Wake. *Comput. Methods Appl. Sci.* **2019**, *28*. [CrossRef]

26. Cui, Y.; Zhao, Z.; Zheng, J.; Li, J.M.; Khoo, B.C. Separation Control over a NACA0015 Airfoil Using Nanosecond Pulsed Plasma Actuator. In Proceedings of the 55th AIAA Aerospace Sciences Meeting, Grapevine, TX, USA, 9–13 January 2017; AIAA-2017-0715. [CrossRef]
27. Asano, K.; Sato, M.; Nonomura, T.; Oyama, A.; Fujii, K. Control of Airfoil Flow at Cruise Condition by DBD Plasma Actuator-Sophisticated Airfoil vs. Simple Airfoil with Flow Control. In Proceedings of the 8th AIAA Flow Control Conference, Washington, DC, USA, 13–17 June 2016; AIAA-2016-3624. [CrossRef]
28. Ogawa, T.; Asada, K.; Tatsukawa, T.; Fujii, K. Computational Analysis of the Control Authority of Plasma Actuators for Airfoil Flows at Low Angle of Attack. In Proceedings of the AIAA Scitech 2020 Forum, Orlando, FL, USA, 6–10 January 2020; AIAA 2020-0578. [CrossRef]
29. Asada, K.; Ninomiya, Y.; Oyama, A.; Fujii, K. Airfoil Flow Experiment on the Duty Cycle of DBD Plasma Actuator. In Proceedings of the 47th AIAA Aerospace Sciences Meeting including The New Horizons Forum and Aerospace Exposition, Orlando, FL, USA, 5–8 January 2009; AIAA-2009-531. [CrossRef]
30. Sekimoto, S.; Nonomura, T.; Fujii, K. Burst-Mode Frequency Effects of Dielectric Barrier Discharge Plasma Actuator for Separation Control. *AIAA J.* **2017**, *55*, 1385–1392. [CrossRef]
31. Sekimoto, S.; Fujii, K.; Hosokawa, S.; Akamatsu, H. Flow-control capability of electronic-substrate-sized power supply for a plasma actuator. *Sens. Actuators A Phys.* **2020**, *306*, 111951. [CrossRef]
32. Aono, H.; Sekimoto, S.; Sato, M.; Yakeno, A.; Nonomura, T.; Fujii, K. Computational and experimental analysis of flow structures induced by a plasma actuator with burst modulations in quiescent air. *Mech. Eng. J.* **2015**, *2*, 1–16. [CrossRef]
33. Sato, M.; Okada, K.; Aono, H.; Asada, K.; Yakeno, A.; nd Kozo Fujii, T.N. LES of Separated-flow Controlled by DBD Plasma Actuator around NACA 0015 over Reynolds Range of 10^4 – 10^6 . In Proceedings of the 53rd AIAA Aerospace Sciences Meeting, Kissimmee, FL, USA, 5–9 January 2015; AIAA 2015-0308. [CrossRef]
34. Suzen, Y.B.; Huang, P.G. Simulations of Flow Separation Control using Plasma Actuator. In Proceedings of the 44th AIAA Aerospace Sciences Meeting and Exhibit, Reno, NV, USA, 9–12 January 2006; AIAA-2006-877. [CrossRef]
35. Font, G.I.; Enloe, C.L.; McLaughlin, T.E. Plasma Volumetric Effects on the Force Production of a Plasma Actuator. *AIAA J.* **2010**, *48*, 1869–1874. [CrossRef]
36. Chen, D.; Asada, K.; Sekimoto, S.; Fujii, K.; Nishida, H. A high-fidelity body-force modeling approach for plasma-based flow control simulations. *Phys. Fluids* **2021**, *33*, 037115. [CrossRef]
37. Pereira, R.; Ragni, D.; Kotsonis, M. Effect of external flow velocity on momentum transfer of dielectric barrier discharge plasma actuators. *J. Appl. Phys.* **2014**, *103*, 301. [CrossRef]
38. Kawai, S.; Fujii, K. Analysis and Prediction of Thin-Airfoil Stall Phenomena Using Hybrid Turbulent Methodology. *AIAA J.* **2005**, *43*, 953–961. [CrossRef]
39. Kojima, R.; Nonomura, T.; Oyama, A.; Fujii, K. Large-Eddy Simulation of Low-Reynolds-Number Flow Over Thick and Thin NACA Airfoils. *J. Aircr.* **2013**, *50*, 187–196. [CrossRef]
40. Lee, D.; Kawai, S.; Nonomura, T.; Anyoji, M.; Aono, H.; Oyama, A.; Asai, K.; Fujii, K. Mechanisms of surface pressure distribution within a laminar separation bubble at different Reynolds numbers. *Phys. Fluids* **2015**, *27*, 023602. [CrossRef]
41. Lele, S.K. Compact Finite Difference Schemes with Spectral-like Resolution. *J. Comput. Phys.* **1992**, *103*, 16–42. [CrossRef]
42. Gaitonde, D.V.; Visbal, M.R. Padé-Type Higher-Order Boundary Filters for the Navier-Stokes Equations. *AIAA J.* **2000**, *38*, 2103–2112. [CrossRef]
43. Visbal, M.R.; Rizzetta, D.P. Large-Eddy Simulation on Curvilinear Grids Using Compact Differencing and Filtering Schemes. *J. Fluids Eng.* **2002**, *124*, 836–847. [CrossRef]
44. Fujii, K. Simple Ideas for the Accuracy and Efficiency Improvement of the Compressible Flow Simulation Methods. In Proceedings of the International CFD Workshop on Supersonic Transport Design, Tokyo, Japan, 16 March 1998; pp. 20–23. (later published as JAXA-SP-06-029E, pp. 25–28).
45. Choi, H.; Moin, P. Effects of the Computational Time Step on Numerical Solutions of Turbulent Flow. *J. Comput. Phys.* **1994**, *113*, 1–4. [CrossRef]
46. Visbal, M.R.; Rizzetta, D.P. Large-eddy Simulation on General Geometries Using Compact Differencing and Filtering Schemes. In Proceedings of the 40th AIAA Aerospace Sciences Meeting & Exhibit, Reno, NV, USA, 14–17 January 2002; AIAA-2002-288. [CrossRef]
47. Rizzetta, D.P.; Visbal, M.R.; Gaitonde, D.V. Large-Eddy Simulation of Supersonic Compression-Ramp Flow by High-Order Method. *AIAA J.* **2001**, *39*, 2283–2292. [CrossRef]
48. Kawai, S.; Fujii, K. Compact Scheme with Filtering for Large-Eddy Simulation of Transitional Boundary Layer. *AIAA J.* **2008**, *46*, 690–700. [CrossRef]
49. Fujii, K. Unified Zonal Method Based on the Fortified Solution Algorithm. *J. Comput. Phys.* **1995**, *118*, 92–108. [CrossRef]
50. Ogawa, T.; Asada, K.; Sekimoto, S.; Tatsukawa, T.; Fujii, K. Dynamic Burst Actuation to Enhance the Flow Control Authority of Plasma Actuators. *MDPI Aerospace* **2021**, *8*, 396. [CrossRef]

Article

A New Flow Control Method of Slat-Grid Channel-Coupled Configuration on High-Lift Device

Jingyi Yu and Baigang Mi *

School of Aeronautics, Northwestern Polytechnical University, Xi'an 710072, China

* Correspondence: mibaigang@163.com

Abstract: A slot formed between the slat and the main wing of the 2D high-lift device is used to accelerate the convergence of the flow to the upper surface of the main wing to improve the flow field quality. In order to further enhance flow characteristics, this paper proposes a design method for multi-channel leading-edge slats based on grid flow channels. On the one hand, a specific shape of a shrinking expansion tube is formed to improve the lift characteristics of the leading slat. On the other hand, the newly formed slot plays a similar role to that of the jet stream, delaying the separation on the upper surface of the main wing, making the separation point move back and helping to improve the lift characteristics of the main wing. The optimization of coupled slat-grid channel configuration is developed by using the DOE algorithm. The geometric parameters, such as coordinates and curve slope, are considered as design variables, and the maximum lift–drag ratio is taken as the optimization objective required to obtain the optimal configuration. The simulation and optimization results show that the lift coefficient increases by 3.3%, the drag coefficient decreases by 12.7%, and the lift–drag ratio increases by 18.4% of the optimal configuration compared with the original airfoil at an angle of attack of 16.3°.

Keywords: grid-fin; multi-element configuration; flow control; aerodynamic optimization; DOE optimization algorithm

Citation: Yu, J.; Mi, B. A New Flow Control Method of Slat-Grid Channel-Coupled Configuration on High-Lift Device. *Appl. Sci.* **2023**, *13*, 3488. <https://doi.org/10.3390/app13063488>

Academic Editors: Francesca Scargiali, Gabriel Bugeđa Castellort and Josep Maria Bergada

Received: 30 December 2022

Revised: 22 February 2023

Accepted: 6 March 2023

Published: 9 March 2023



Copyright: © 2023 by the authors. Licensee MDPI, Basel, Switzerland. This article is an open access article distributed under the terms and conditions of the Creative Commons Attribution (CC BY) license (<https://creativecommons.org/licenses/by/4.0/>).

1. Introduction

For the commonly used three-stage high-lift device, the flow characteristic is that the leading slat and trailing-edge flaps work together to improve the lift–drag characteristics of the entire airfoil. Van Dam [1] reviewed the recent developments in aerodynamic design and analysis methods for multi-element high-lift systems in transport airplanes, including necessity, the major design objectives, and constraints. For the commonly used three-stage high-lift device, the flow characteristic is that the leading slat and trailing-edge flaps work together to improve the lift–drag characteristics of the entire airfoil. In 1970, A. Smith [2] analyzed the aerodynamic principle of the multi-element configuration, and believed that it was affected by the slat effect, circulation effect, off-the-surface pressure recovery, and boundary layer effect of each wing segment. It is well recognized that the usual function of the slot is that of a boundary layer control device, permitting highly adverse upper-surface pressure gradients to be sustained without incurring severe separation. There appear to be five primary effects of gaps, and here we speak of properly designed aerodynamic slots. According to the current classical active and passive flow control theories, the mechanism of the three-segment high-lift device can be classified into the passive control method. The passive flow control technology does not add energy to the flow, but changes the flow boundary or pressure gradient through some methods to control the flow, such as optimizing the geometric parameters of the airfoil, adding or combining flow control devices, and through fixed-point displacement or deformation under specific working conditions. Compared with active flow control technology [3], it is widely valued for its advantages of simple structure, lack of additional energy consumption or lower energy

consumption, and low cost. For the three-stage high-lift device, the leading-edge slat can accelerate the airflow through the slots formed with the main wing, forming a similar effect to the jet flow, which can favorably disturb the airflow of the main wing and improve its wind resistance. However, the practical application of this three-element high-lift device has many limitations. For example, the aircraft is significantly affected by the ground effect during takeoff and landing. For the high-lift device, the flaps are deflected closer to the ground [4], meaning that the impact is greater. For amphibious aircraft [5,6], flap failure may even occur due to body splash. In order to further improve the aerodynamic characteristics and practical value of the high-lift device, slats are the preferred component for optimization and improvement.

The basic principle of slat lift enhancement is that there is a gap between the slat and the leading-edge surface of the main wing. Specifically, the velocity of the airflow on the lower surface of the airfoil increases in the gap and flows to two places, respectively. Part of the airflow accelerates from the gap between the tail of the slat and the leading edge of the main wing, flows backwards with the airflow on the upper surface of the airfoil, and accelerates the flow to the convergence of the upper surface of the main wing. Moreover, the velocity of airflow in the boundary layer on the upper surface of the wing is increased to eliminate a large number of vortices [7]; the other part flows to the cavity of the concave pressure surface of the slat, forming a recirculation zone. The velocities of these two streams differ greatly; a strong free shear layer is, therefore, formed at the interface. This shear layer originates from the sharp lower trailing edge and develops downstream with the separation vortex. When the separation vortex hits the trailing edge wall of the slat, a part of the vortex will flow back into the concave cavity of the slat, interfering with the new shear layer near the lower trailing edge [8] and forming return feedback [9]. In order to improve the lift–drag characteristics, grid flow channels can be added to the slats to improve the flow field in the slats. Grid fins [10], as multi-surface control systems consisting of an external frame and an internal grid partition, originate from the lift device composed of multiple elements used in the early design of aircraft, and have the advantages of high control efficiency, a large stall angle of attack, small hinge torque, and easy folding. In particular, their lift characteristics are good, and it is not easy to stall the devices with a high angle of attack, meaning they maintain good linearity. However, due to the defects in the structure, weight, resistance and technology of multi-element lift devices under the technical conditions of the time, single-element lift devices have been dominant in aircraft design for a long time. With the development of technology, the performance characteristics of grid fins derived from multi-element lift devices are increasingly understood, and their advantages as aerodynamic stabilizing and controlling surfaces for various types of aircraft continue to be highlighted. Research from Russia, the United States, Germany, and China has strengthened the understanding of grid fins; as a result, theoretical and applied achievements have been realized [11–15].

Wang Long et al. [16] carried out a numerical simulation on four different slotting positions of wind turbine blades by means of a computational fluid dynamic method, and obtained the flow field and lift coefficient of the blades at different angles of attack. They found that, under high angles of attack, the jet formed by slots can effectively inhibit flow separation, and the aerodynamic performance was better when the slotting position was near the separation point. Hui Zenghong et al. [17] studied the aerodynamic characteristics of multi-element leading slat lift devices using the pressure measurement method and obtained a better leading slat scheme by comparing the influence of different configuration slats on the airfoil lift effect and aerodynamic efficiency. Zhang Lijun et al. [18] proposed a scheme of symmetrical slitting in the wind separation zone for the vertical axis wind wing NACA0012 studied, which delayed the separation of the airfoil boundary layer and improved the aerodynamic performance of the airfoil. Liu Zhongyuan et al. [19], taking the L1T2 three-element airfoil as the research object, proposed carrying out slot control on the leading-edge slat to slow down the boundary layer separation and reduce its impact on the wake. They focused on the slot location, the flow direction at the slot outlet, and the

flow control technology in order to improve the stall characteristics of the lift enhancement device. Although there is a lot of research on the flow control of slats, most of this research focuses on the slot position and slot angle. There is relatively little optimization research on the slot layout scheme, slot width, and slot and chord angles of slotted airfoils of multi-element configuration, which limits the potential of the flow control effect of slats.

In this paper, a grid-slat flow control configuration is proposed to increase lift, reduce drag and suppress flow separation. The quadratic curve parametric modeling method is used for the slot, and the design of the experiment aims to optimize its design. The optimal design parameters of the grid-slat configuration under the given design space and flow conditions are determined through numerical simulation. Moreover, the flow control mechanism of the optimal configuration and the influence and correlation of each design parameter on the lift–drag coefficient are analyzed. It provides a new idea and method for the design of three-dimensional grid multi-element airfoil lift devices in the future.

2. Flow Control Optimization Strategy for Leading-Edge Slot of the Airfoil 30P30N Based on Grid Fin

The grid-slat configuration can improve the flow field level of the slot by increasing grid flow channels. Its basic principle is that, in addition to increasing the flow path of the leading-edge slats, the slats themselves generate additional lift. More importantly, a new additional slot is formed on the basis of the original single channel, which can enhance the flow characteristics of the original slot, improve its disturbance characteristics to the flow of the main wing, and thus enhance the flow control effect. However, since there are many design parameters involved due to the addition of slots in the slats, this paper constructs an aerodynamic optimization design method for grid-slat flow control based on the DOE algorithm.

2.1. Design of Grid Fin–Slat Composite Configuration

The grid-slat configuration is designed on the multi-section airfoil 30P30N of the high-lift device, and the configuration is parameterized to facilitate the transformation of the original optimization of the geometric model of the configuration into the optimization of the configuration design parameters.

Analytic geometric curves can be expressed using explicit functions with few design variables. For example, in the typical conic curve method, section control can be realized by the beginning and end coordinates of curves, as well as by the tangent slope and shape parameters. It has fewer control parameters, which is conducive to the optimal design of the aerodynamic shape. The general equation of a conic curve is: $y^2 + ax^2 + bxy + cx + dy + e = 0$. The conic curve can be regarded as a conic obtained by performing plane oblique cutting. By changing the angle of the tangent plane, conic curves such as circle, ellipse, parabola and hyperbola can be obtained [20].

The slot at the leading edge is separately described by two curve equations, as shown in Figure 1, curves 1-2-3 and 4-5-6, respectively. Assuming that point 2 is the origin of the curve coordinate system, where the slope of the curve is infinite, the 1-2-3 elliptic equation can be simplified as $y^2 + ax^2 + bxy + cx = 0$. Then, the equation can be obtained according to the coordinates and slope of the curve at point 1 and the tangent equation of the curve at point 3.

Among them, the designer gives the x coordinates of point 1, and the x and y coordinates of point 2. The method to determine the tangent equation at point 3 is shown in the figure above. First, a straight line should be made through the two points denoted as AB. The angle between AB and the horizontal direction is k_3 ; then, the distance of y_3 is offset upward, where k_3 and y_3 are also given by the designer. The curve 4-5-6 is determined in the same way with the parameters x_4 , x_5 , y_5 and k_6 . In conclusion, the chord length direction is assumed to be the x axis and the direction perpendicular to the chord length is assumed to be the y axis. Considering the calculation time and cost as well as the

configuration changes, the control variables of the slot at the leading edge are shown in Table 1:

Table 1. Design variable and value range.

Design Variable	x_1 (mm)	x_2 (mm)	y_2 (mm)	y_3 (mm)	k_3 (°)
value range	$11 \pm 30\%$	$9 \pm 15\%$	$11 \pm 15\%$	0–6	$40 \pm 15\%$
Design Variable	x_4 (mm)	x_5 (mm)	y_5 (mm)	y_6 (mm)	k_6 (°)
value range	$16 \pm 30\%$	$9 \pm 15\%$	$11 \pm 15\%$	0–6	$35 \pm 15\%$

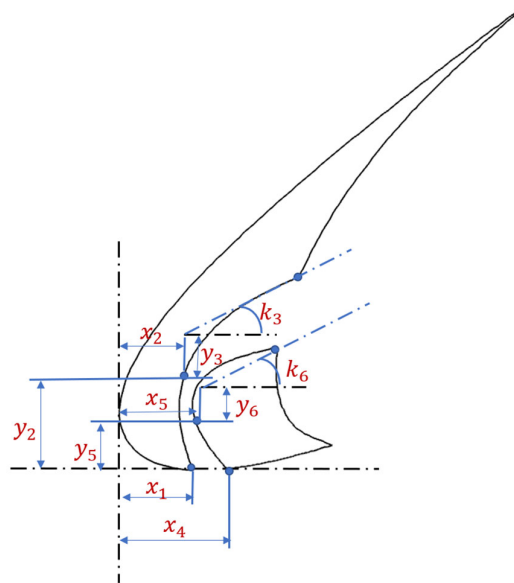


Figure 1. Grid-Slat configuration parameterization diagram.

The position and size of the slot inlet can be adjusted by adjusting x_5 and x_4 . The degree of shrinkage can be adjusted by adjusting x_2 and x_5 . Adjusting y_2 and y_5 can change the longitudinal position of the transition between the contraction and expansion of the joint. The position of the slot outlet position can be adjusted by adjusting x_3 and x_6 . The shape of the expansion segment can be controlled by adjusting k_3 , y_3 , k_6 and y_6 .

2.2. Aerodynamic Optimization Model of Grid-Slat Composite Configuration

The DOE module in the Isight-integrated platform is adopted, and the numerical optimization of control design parameters is used to replace the optimization of grid-slat configuration geometry. It is a structured research method used to systematically study the relationship between the independent variable and the dependent variable. This method studies the effect of one or more input parameters (factors) on multiple output results (responses) by arranging experiments scientifically and reasonably and replacing comprehensive tests with partial tests. The seven steps of the DOE experiment design are target determination, process analysis, factor screening, fast approach, factorial experiment, regression experiment, and robust design. The optimized design variables are parameters in the parameterized expression of grid-slat curve configuration ($x_1, x_2, y_2, y_3, k_3, x_4, x_5, y_5, y_6, k_6$). The objective of optimization is to obtain the maximum lift–drag ratio K . The calculation formula is as follows:

$$C_l = \frac{L}{0.5\rho U_\infty^2 c} \tag{1}$$

$$C_d = \frac{D}{0.5\rho U_\infty^2 c} \tag{2}$$

$$K = C_l/C_d \tag{3}$$

As shown in Figure 2, the optimization process of grid-slat configuration is as follows:

- (1) The optimization module assigns values to ten design variables for the first time according to the constraints, and Catia establishes a two-dimensional parametric model of grid-slat configuration according to the assignment;
- (2) The pointwise divides the structural grid and output of the case file for Fluent calculation;
- (3) The flow field of the grid-slat configuration is calculated at an angle of attack of 16.3°, and outputs the corresponding lift coefficient C_l and drag coefficient C_d ;
- (4) The Calculator module feeds back the lift–drag ratio K into the optimization platform according to the formula;
- (5) The DOE algorithm reassigns design variables according to the calculation results, and then enters the next round of optimization calculations.

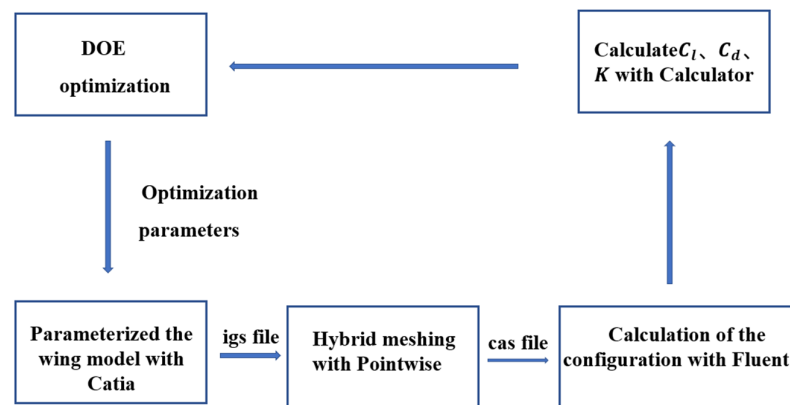


Figure 2. Optimization flow chart of grid-slat configuration.

3. Verification

3.1. Calculation Method and Verification of Aerodynamic Characteristics of the Multi-Section Airfoil 30P30N

In the present simulation, the flow field was assumed to be described by the 2D Reynolds-averaged Navier–Stokes (RANS) equations. The turbulence model adopted was the $k - \omega$ SST model. This turbulence model uses the damping function in the vortex viscosity model. It is more accurate at simulating the aerodynamic characteristics and pressure distribution of multi-section airfoil [21,22]. This has wide applicability and good prediction performance for separation flows with high-lift configurations.

The $k - \omega$ SST model formula is given as:

$$\begin{aligned} \mu_t &= \frac{\rho a_1 k}{\max(a_1 \omega; \Omega F_2)} \\ \frac{\partial(\rho k)}{\partial t} + u_i \frac{\partial(\rho k)}{\partial x_i} &= P_k - \beta_k \rho k \omega + \frac{\partial}{\partial x_i} \left[\left(\mu_l + \frac{\mu_t}{\sigma_k} \right) \frac{\partial k}{\partial x_i} \right] \\ \frac{\partial(\rho \omega)}{\partial t} + u_i \frac{\partial(\rho \omega)}{\partial x_i} &= C_\omega P_\omega - \beta_\omega \rho \omega^2 + \frac{\partial}{\partial x_i} \left[\left(\mu_l + \frac{\mu_t}{\sigma_\omega} \right) \frac{\partial \omega}{\partial x_i} \right] + 2\rho(1 - F_1) \frac{1}{\sigma_\omega} \frac{1}{\omega} \frac{\partial k}{\partial x_i} \frac{\partial \omega}{\partial x_i} \end{aligned} \quad (4)$$

The modified $k - \omega$ SST turbulence model constructs the model coefficient in the vortex viscosity coefficient of the equation as the following equation:

$$\alpha^* = \alpha_\infty^* \left[\frac{\alpha_0^* + \frac{Re_t}{R_k}}{1 + \frac{Re_t}{R_k}} \right] \quad (5)$$

where $Re_t = \rho k / \mu \omega$ is the turbulent Reynolds number.

A numerical simulation of the 30P30N airfoil is taken as an example to verify the numerical simulation method of the two-dimensional lifting device adopted in this paper. The multi-section airfoil 30P30N of the high-lift device is widely used by CFD workers [23,24]. The deflection angle of the leading-edge slat and trailing-edge flap of this airfoil is 30°, the

slot width of the leading-edge slat is 2.95%, and the overhang is -2.5% . The trailing-edge flap slot width is 1.27%, and the extension is 0.25% [23], as shown in Figure 3.



Figure 3. Geometry profile of 30P30N.

The comparative test data are the wind tunnel test results of McDonnell Douglas Aerospace and NASA Langley [25,26]. According to actual wind tunnel test conditions, the attack angles of the incoming flow are $-0.17^\circ \sim 21^\circ$. The Reynolds number is 9×10^6 . The Mach number is 0.2. All the calculations provided here were obtained using the coupled solver of Fluent code. A second-order upwind difference scheme was chosen for momentum and turbulent kinetic energy, respectively. The incoming flow pressure is the standard atmospheric pressure. The mesh is generated as shown in Figure 4. For the component grid, we used a hybrid mesh with 40,792 cells. Wall spacing of the first layer is 1.71×10^{-3} , which satisfies $y^+ \leq 1$.

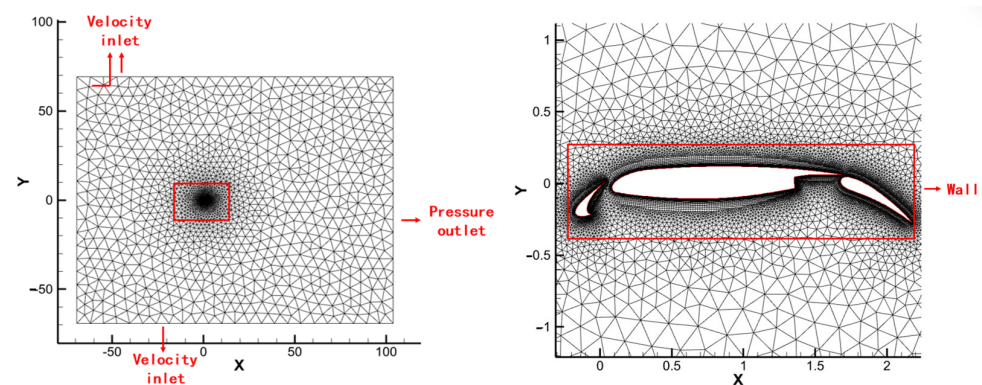


Figure 4. Computational mesh.

In the process of calculation, we monitored the convergence of residuals on the one hand, and found that the energy item decreases to 10^{-9} and other residuals except the energy item decrease to 10^{-4} . On the other hand, the calculation results c_l or c_d basically do not change with the increase in iteration steps. In Figure 5a, it seems that good agreement is achieved by comparing the calculated lift coefficient of the airfoil with the wind tunnel test results and that the deviation is large only near the stall angle of attack. As shown in Figure 5c,d, the surface pressure coefficients distribution of the main wing and flap coincide very well, and the pressure coefficients of the slats are basically consistent with the experimental data.

3.2. Grid Independence Verification

In order to ensure the accuracy of numerical calculation and reduce the calculation cost, the multi-section airfoil 30P30N is taken as an example to verify the independence of the computational grid. Three-grid generation schemes are used for simulation calculation. Table 2 shows the grid convergence verification results at an attack of 8° . The lift coefficient C_l converges with the increase in the number of grid cells. The drag coefficients, shown in Figure 6a, are basically the same using 2- and 3-grid generation schemes at different angles of attack. As shown in Figure 6c,d, the surface pressure coefficient distribution of the main wing and flap coincide very well. Using 2- and 3-grid generation schemes, the calculation results are similar, which meets the requirements of grid independence. Therefore, the grid division scheme of Case2 is adopted for subsequent calculations of cost.

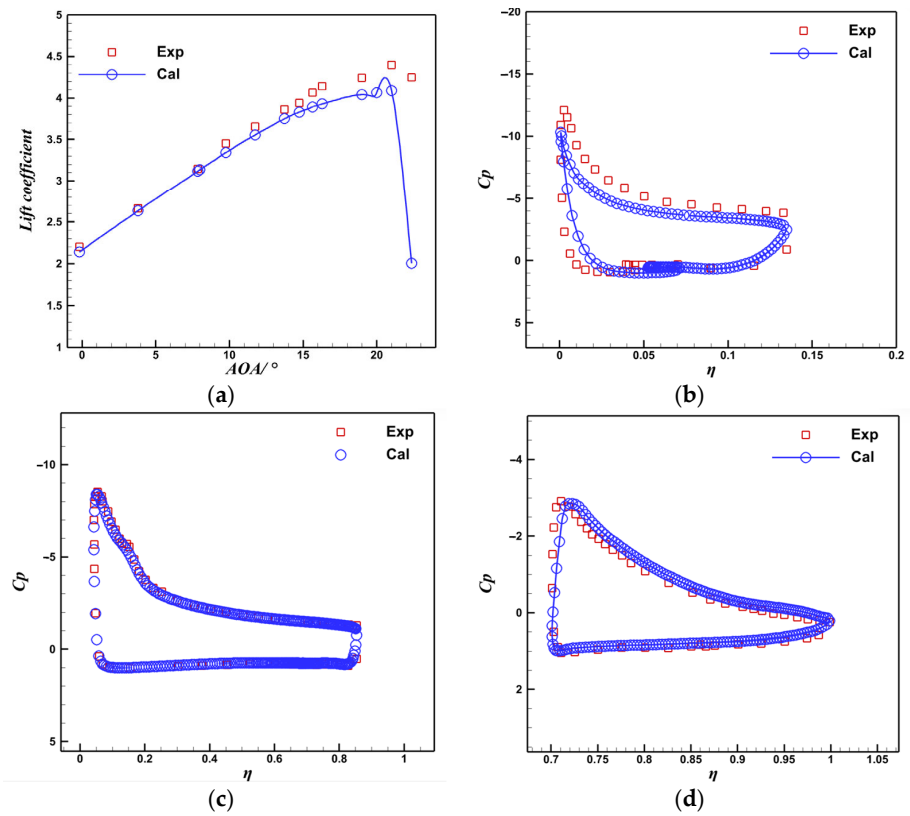


Figure 5. Verification results of 30P30N airfoil. (a) Lift Coefficient; (b) Slat Pressure Distribution [18,19]; (c) Main Pressure Distribution; (d) Flap Pressure Distribution.

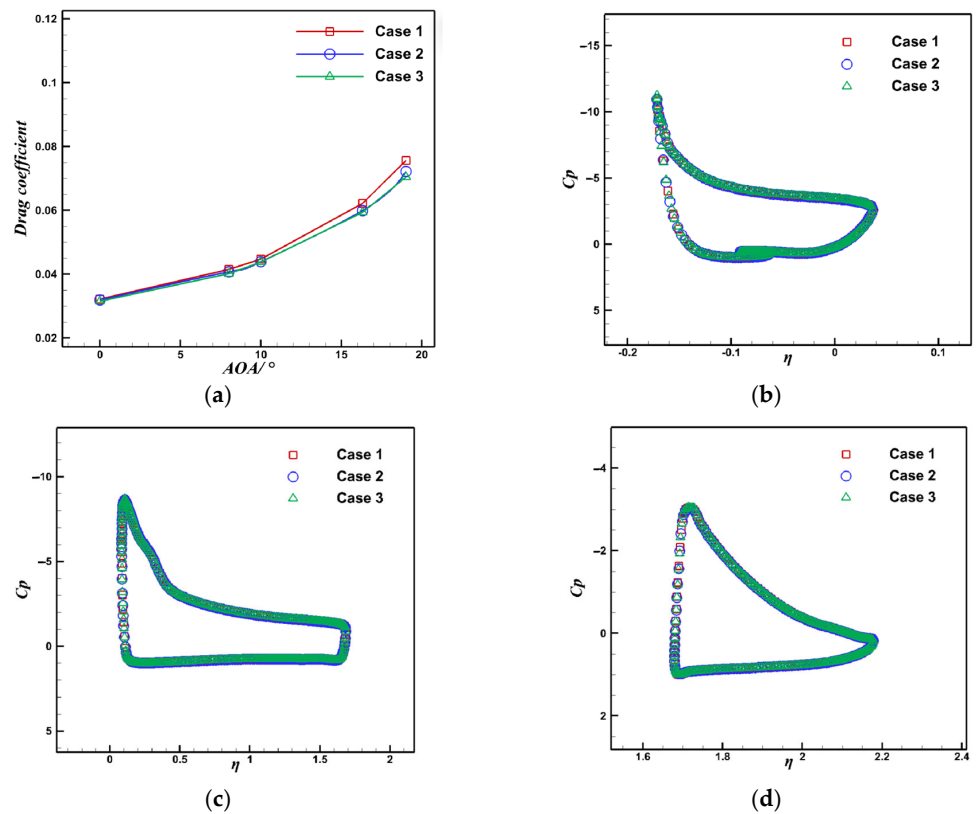


Figure 6. Grid independence verification. (a) Drag Coefficient; (b) Slat Pressure Distribution; (c) Main Pressure Distribution; (d) Flap Pressure Distribution.

Table 2. Grid independence verification.

Case	Grid Cell	Lift Coefficient
Case1	28,947	3.14498
Case2	40,792	3.13469
Case3	61,923	3.144985

4. Optimization Example and Analysis

Through optimization design, the values of design variables are shown in Table 3, and the configuration at this time is shown in Figure 7a. The grid-slat configuration plays a role in increasing lift and reducing drag through calculations. Figure 7b–d show the comparison of the lift coefficient, drag coefficient and lift–drag ratio between the original airfoil and the new configuration at different angles of attack. The simulation and optimization results show that the lift coefficient increases by 3.3%, the drag coefficient decreases by 12.7%, and the lift–drag ratio increases by 18.4% of the optimal configuration compared with the original airfoil at an angle of attack of 16.3°.

Table 3. Value of design variable.

Design Variable	x_1 (mm)	x_2 (mm)	y_2 (mm)	y_3 (mm)	k_3 (°)
optimal value	11	9	11	0	45
Design Variable	x_4 (mm)	x_5 (mm)	y_5 (mm)	y_6 (mm)	k_6 (°)
optimal value	16	11	11	0	30

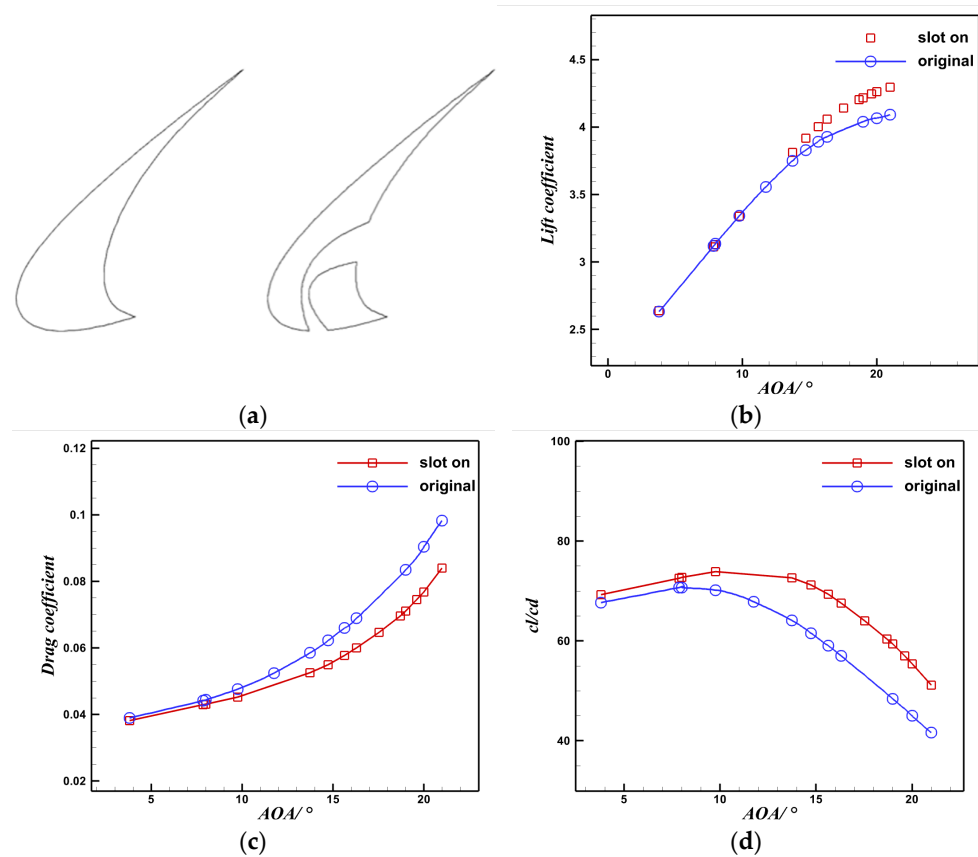


Figure 7. Numerical simulation comparison between original airfoil and optimal configuration. (a) Lift coefficient of slat; (b) Total lift coefficient; (c) Drag Coefficient; (d) Lift-drag ratio.

In order to further clarify the mechanism of increasing lift and reducing drag of grid-slat configuration, Figure 8 describes the total lift coefficients of the original airfoil and the optimized airfoil at different angles of attack. The lift coefficients, extracted separately from the slats, show that the configuration not only improves the lift of the slat itself but also improves the lift of the main wing.

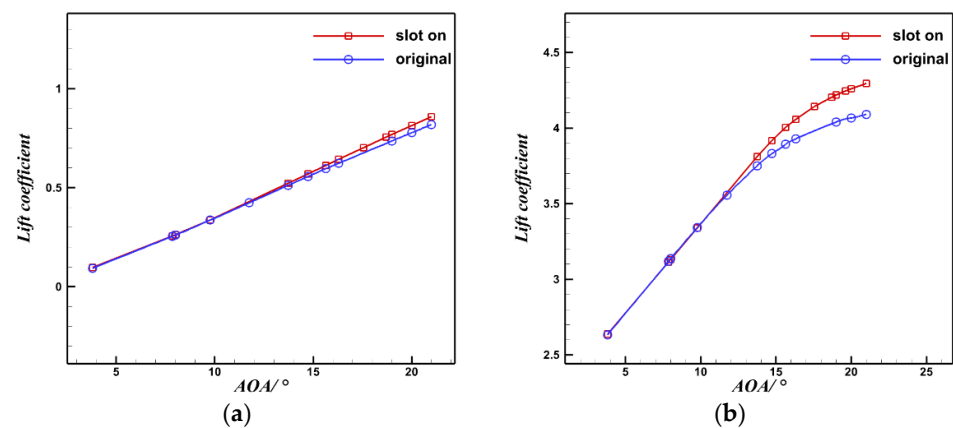


Figure 8. Comparisons of lift coefficients between original airfoil and optimal configuration. (a) Lift coefficient of slat; (b) Total lift coefficient.

The simulation results of the original airfoil and the optimized configuration at four typical angles of attack ($\alpha = 8^\circ, 16.3^\circ, 19^\circ, 22.36^\circ$) are compared and analyzed. The development process of wake flow is shown in Figure 9. For the original airfoil at an angle of attack of 22.36° , the wake flow area generated by the separation bubble is strongly mixed with the slot jet and the boundary layer of the main wing section, so that the rear section of the main airfoil and trailing-edge flap are in the mixed wake flow area. After optimization, the separation of grid-slat configuration is weakened, and the wake area is greatly reduced.

Superimposed contour plots of velocity magnitude and instantaneous streamlines at different angles are shown in Figure 10. Although the jet velocity has not yet reached the peak value, the velocities near the upper trailing edge are improved to varying degrees. The downstream flow-separated area near the upper trailing edge becomes a flow-attached area.

Figure 11 shows the surface pressure coefficient C_p of the original airfoil and the optimized layout under two operating conditions. For the convenience of differentiation, blue represents the original airfoil and red represents the optimal grid-slat configuration. The negative pressure value in the figure represents the suction on the upper surface of the wing. The positive pressure value represents the pressure on the lower surface of the wing. The pressure surface curve is located below the suction surface curve, indicating that the pressure on the lower surface is greater than that on the upper surface, which means the lift of the airfoil is positive [27,28]. The area enclosed by the pressure coefficient curve can roughly reflect the lift coefficient.

As is shown in Figure 11a, at an angle of attack of 19° , each suction peak of optimized configuration for each wing is slightly higher than that of the original wing, while the pressure surface curve is basically the same, so the optimal grid-slat configuration has a higher lift. As can be seen in Figure 11b, the suction peak of the original airfoil decreases sharply, and the area enclosed by the pressure coefficient curve decreases. However, the pressure coefficient curve of the optimized configuration is significantly different from that of the original airfoil, indicating that stall status had not been reached. Therefore, it can be concluded that the optimized configuration improves the aerodynamic characteristics at a high angle of attack and additionally increases the stall angle of attack.

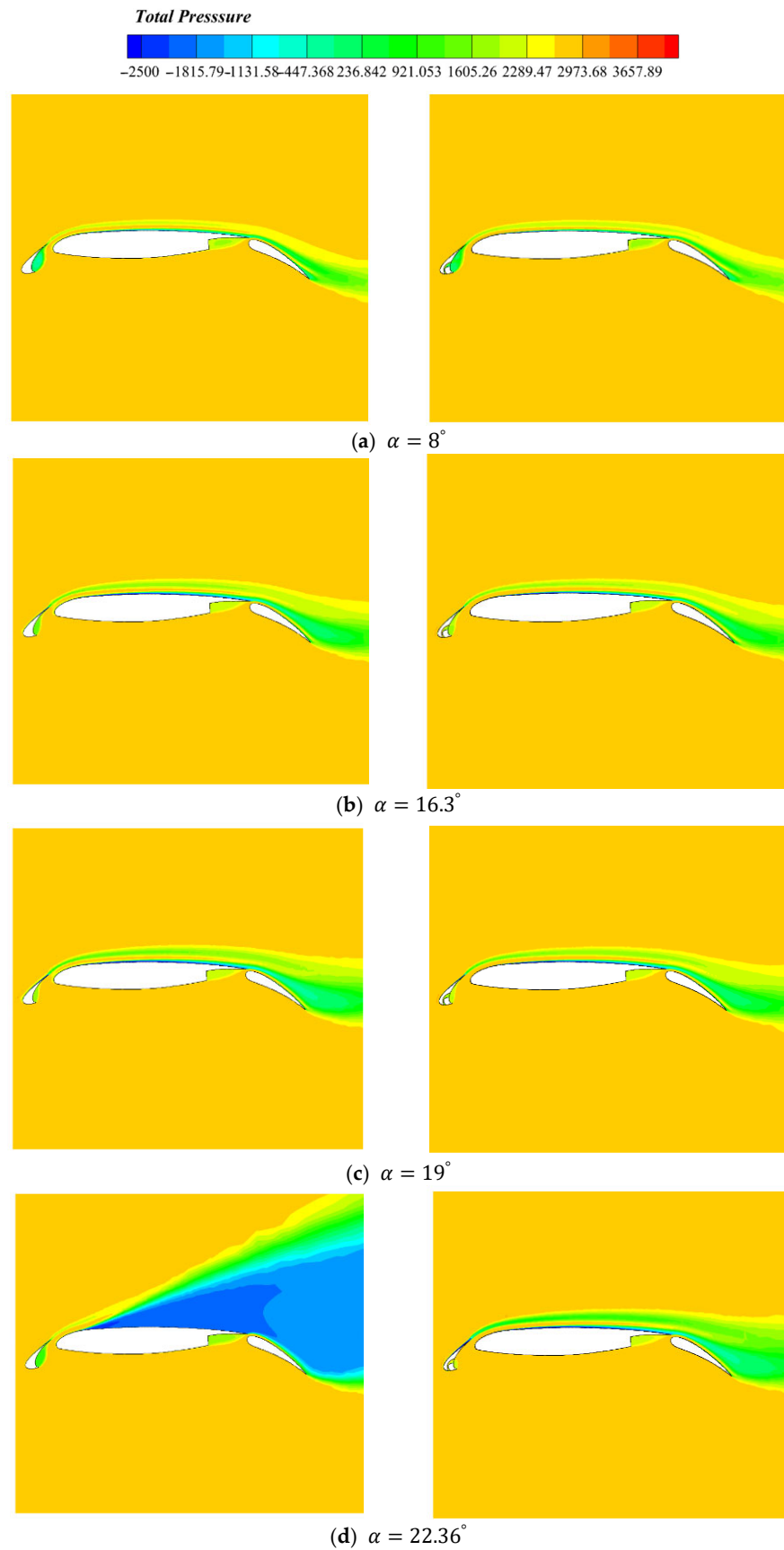


Figure 9. Comparison of wake flow development of the original airfoil and optimal grid-slat configuration.

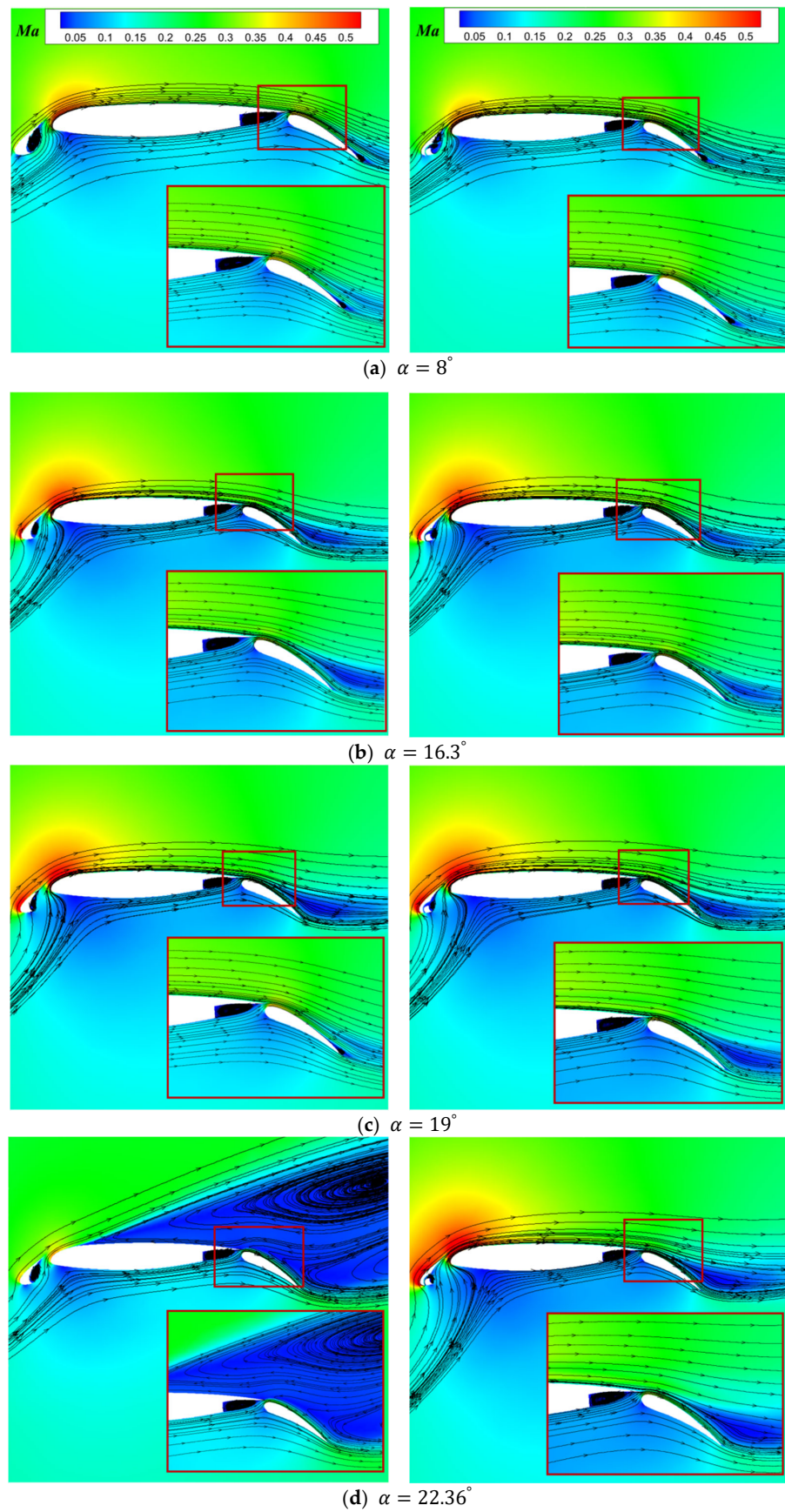


Figure 10. Contour comparison of the original airfoil and optimal grid-slat configuration at different attack angles.

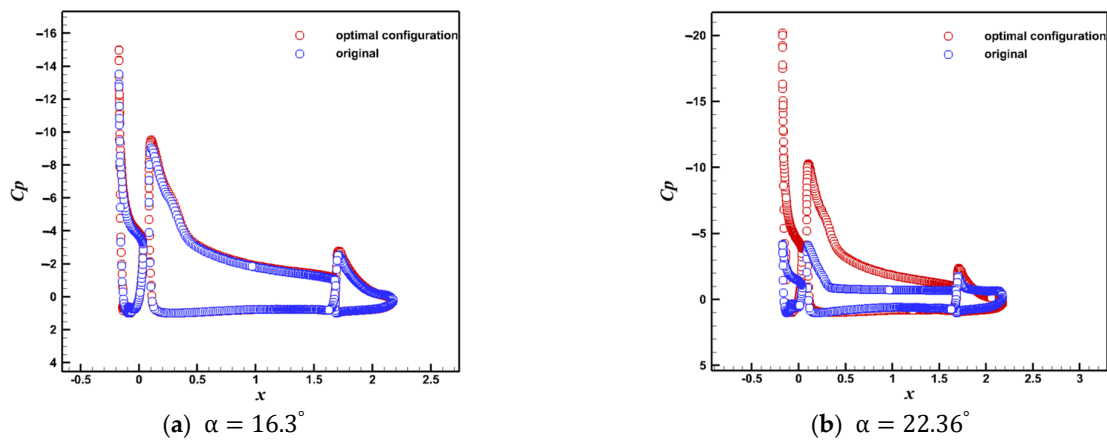


Figure 11. Comparison of pressure coefficient between the original airfoil and optimal grid-slat configuration at different attack angle.

5. Influence Analysis of Design Parameters

In order to further clarify the design method of grid-slat configuration, the influence of each parameter on lift–drag coefficient and lift–drag ratio is analyzed according to the calculation results under the different design parameters calculated in the optimization process. First, the Pearson correlation coefficient [29] is selected to calculate and analyze the correlation between design parameters, lift–drag coefficient and lift–drag ratio, as shown in Table 4. The results show that the five design parameters are significantly related to the lift–drag ratio K , where x_1, k_3, k_6 are positively correlated with K , y_3, y_6 are negatively correlated with K .

Table 4. The correlation analysis results between design parameters and lift–drag coefficient.

		x_1	x_2	y_2	y_3	k_3
C_l	Pearson correlation	0.036	−0.048	−0.097	−0.164 **	123 *
	Sig. (2-tailed)	0.500	0.373	0.070	0.002	0.021
C_d	Pearson correlation	−0.113 *	0.010	−0.028	0.260 **	−0.277 **
	Sig. (2-tailed)	0.034	0.857	0.607	0.000	0.000
K	Pearson correlation	0.112 *	−0.019	0.004	−0.300 **	0.305 **
	Sig. (2-tailed)	0.036	0.720	0.948	0.000	0.000
		x_4	x_5	y_5	y_6	k_6
C_l	Pearson correlation	0.063	0.109 *	0.174 **	−0.123 *	0.287 **
	Sig. (2-tailed)	0.241	0.041	0.001	0.021	0.000
C_d	Pearson correlation	0.007	0.082	−0.017	0.279 **	−0.240 **
	Sig. (2-tailed)	0.902	0.123	0.747	0.000	0.000
K	Pearson correlation	0.000	−0.055	0.057	−0.308 **	0.311 **
	Sig. (2-tailed)	0.997	0.302	0.284	0.000	0.000

** . At 0.01 level (2-tailed), the correlation is significant. * . At 0.05 level (2-tailed), the correlation is significant.

Pearson’s formula [30] is:

$$\rho_{X,Y} = \frac{\text{cov}(X,Y)}{\sigma_X \sigma_Y} = \frac{E(XY) - E(X)E(Y)}{\sqrt{E(X^2) - (E(X))^2} \sqrt{E(Y^2) - (E(Y))^2}} \tag{6}$$

where $\text{cov}(X, Y)$ is the covariance of X and Y , and σ_X, σ_Y is the standard deviation of X and Y , respectively.

This shows that within the given range of variables, the shape of the slot changes with the change in five design parameters, which will greatly change the flow field. The change of x_1 results in the change of seam entry position, while the change of the other four design parameters y_3 , y_6 , k_3 and k_6 results in the change in seam shape. The design parameter x_1 is positively correlated, indicating that the lift force is better when the inlet position of the slot is closer to the right. The design parameters k_3 and k_6 are positively correlated, indicating that as the expansion degree of the slot increases, the acceleration degree of the slot to the flow is greater, and the lift force is better.

6. Conclusions

In this article, a flow control method of grid-slat configuration was proposed, and its optimal design was configured using the DOE algorithm. The optimal configuration was obtained and verified through numerical simulation, and we analyzed the flow control mechanism and the influence of design parameters. Two main conclusions were drawn from this study.

(1) By slitting the leading-edge slats, the lift–drag characteristics of the multi-element configuration can be effectively improved, which shows the feasibility and effectiveness of conducting flow control through the leading-edge slats. The simulation and optimization results show that the lift coefficient increases by 3.3%, the drag coefficient decreases by 12.7%, and the lift–drag ratio increases by 18.4% of the optimal configuration compared with the original airfoil at an angle of attack of 16.3° . The grid-slat can effectively improve the flow field level, and the flow always remains attached.

(2) The analysis of the correlation between the design parameters and the configuration of aerodynamic performance shows that the slot design parameters are highly sensitive to the final flow control effect, which also indicates that the flow control potential of the slats is very good.

In this paper, a flow control model and design optimization method based on slat slitting have only been constructed for a single grid slot. In future work, we expect to build a more effective slot scheme with the possibility of three-dimensional applications.

Author Contributions: Conceptualization, B.M.; Methodology, J.Y.; Writing—original draft, J.Y.; Writing—review & editing, B.M. All authors have read and agreed to the published version of the manuscript.

Funding: This research was funded by [National Natural Science Foundation of China] grant number [12202363] and [Natural Science Basic Research Program of Shaanxi] grant number [2021]Q-084].

Institutional Review Board Statement: Ethical review and approval were waived for this study because this article does not involve human or animal research.

Informed Consent Statement: Informed consent was obtained from all subjects involved in the study.

Data Availability Statement: The data is unavailable due to privacy.

Acknowledgments: The authors would like to acknowledge the support of National Natural Science Foundation of China (Grant No. 12202363) and the support of Natural Science Basic Research Program of Shaanxi (Program No. 2021]Q-084).

Conflicts of Interest: The authors declared no potential conflict of interest with respect to the research, authorship, and/or publication of this article.

References






1. Dam, C. The aerodynamic design of multi-element high-lift systems for transport airplanes. *Prog. Aerosp. Sci.* **2002**, *38*, 101–144.
2. Hammond, A.D. High-lift aerodynamics. In Proceedings of the Vehicle Technology for Civil Aviation, NASA SP-292, Hampton, VA, USA, 2–4 November 1971.
3. Shi, Q. Research on Flow Control of Wing for Increasing Lift and Reducing Drag. Ph.D. Thesis, National University of Defense Technology, Changsha, China, 2017.
4. Sun, R.M. Experimental Investigation on Aerodynamics Characteristics and Tip Vortices, of a Wing in Ground Effect. Ph.D. Thesis, Shanghai University, Shanghai, China, 2011.

5. Gross, J.; Traub, L.W. Experimental and Theoretical Investigation of Ground Effect at Low Reynolds Numbers. *J. Aircr.* **2015**, *49*, 576–586. [CrossRef]
6. Zhang, Q.Y.; Wang, Z.H.; Wei, M.; Lin, W. Review of high-lift devices design for amphibious aircraft. *Acta Aerodyn. Sin.* **2019**, *37*, 19–32.
7. Lin, Y.X. Design and Research of Flap Wing Sail for Wind-Assisted Vessel. Ph.D. Thesis, Dalian Maritime University, Dalian, China, 2013. (In Chinese)
8. Huang, H. Slat Noise Suppression with Upstream Mass Injection. Ph.D. Thesis, Shanghai Jiao Tong University, Shanghai, China, 2013. (In Chinese)
9. Sun, K.X. Study on Implicit Large Eddy Simulation Based on High-order Discontinuous Galerkin Method. Master's Thesis, Nanjing University of Aeronautics and Astronautics, Nanjing, China, 2019. (In Chinese)
10. Peng, K.; Hu, F.; Zhang, W.H.; Zhou, Z. Review of aerodynamic characteristics and application of grid fin. *J. Solid Rocket Technol.* **2015**, *38*, 8.
11. Washington, W.D.; Miller, M. S.O-I Experimental investigations of grid fin aerodynamics: A synopsis of nine wind tunnel and three flight tests. In Proceedings of the RTO AVT Symposium on Missile Aerodynamics, Sorrento, Italy, 11–14 May 1998.
12. Kretzschmar, R.W.; Burkhalter, J.E. 1-l Aerodynamic Prediction Methodology for Grid Fins. In Proceedings of the US Army Aviation and Missile Command, RTO Applied Vehicle Technology Panel Symposium, Sorrento, Italy, 11–14 May 1998.
13. Li, H.H.; Shi, Y.H. Current Status and Development Trend of Grid Fin. *Missile Space Vehicle* **2008**, *6*, 27. (In Chinese)
14. Fanucci, J.P.; King, M.J.; Gorman, J.J. Method for Producing Lattice Fin for Missiles or Other Fluid-Born Bodies. U.S. Patent No. 6,928,715, 16 August 2005.
15. Pruzan, D.A.; Mendenhall, M.R.; Rose, W.C.; Schuster, D. Grid Fin Stabilization of the Orion Launch Abort Vehicle. In Proceedings of the 29th AIAA Applied Aerodynamics Conference, Honolulu, HI, USA, 27–30 June 2011; American Institute of Aeronautics and Astronautics: Reston, VA, USA, 2011.
16. Wang, L.; Sun, L.; Zhang, J. Study of the impact of the change of slotted position at high angle of attack on wind turbine blades. *J. Hefei Univ. Technol. (Nat. Sci.)* **2017**. (In Chinese) [CrossRef]
17. Hui, Z.H.; Zhu, Z.X.; Zhang, L. Experimental investigation of aerodynamics performance of multi-element airfoil with leading-edge slat. *J. Exp. Fluid Mech.* **2007**, *21*, 17–20.
18. Zhang, L.J.; MA, D.C.; GU, J.W. Influence of shape of slotted airfoil on aerodynamic performance of vertical axis wind turbine. *J. Cent. South Univ. (Sci. Technol.)* **2019**. (In Chinese) [CrossRef]
19. Liu, Z.Y.; Chu, H.B.; Chen, Y.C.; Mao, J.; Zhang, B. Stall characteristics of high-lift device improved by slotting on leading-edge slat. *Acta Aerodyn. Sin.* **2022**, *40*, 21–28. (In Chinese) [CrossRef]
20. Dong, B.B. Design and Optimization of Two-Element Airfoil. Master's Thesis, Nanjing University of Aeronautics and Astronautics, Nanjing, China, 2012.
21. Halila, G.; Antunes, A.P.; Da Silva, R.; Azevedo, J.L.F. Effects of boundary layer transition on the aerodynamic analysis of high-lift systems. *Aerosp. Sci. Technol.* **2019**, *90*, 233–245. [CrossRef]
22. Zhang, Y.; Wang, S.; Sun, G.; Mao, J. Aerodynamic surrogate model based on deep long short-term memory network: An application on high-lift device control. *Proc. Inst. Mech. Eng. Part G J. Aerosp. Eng.* **2022**, *236*, 1081–1097. [CrossRef]
23. Wang, Y.T.; Wang, G.X.; Zhang, Y.L. Numerical study of complex flow over 30P-30N multi-element. *Acta Aerodyn. Sin.* **2010**, *28*, 5. (In Chinese)
24. Qin, P.G.; Liu, P.Q.; Qu, Q.L.; Peng, G. Influence of gap parameters on aerodynamics of multi-element airfoil. *J. Beijing Univ. Aeronaut. Astronaut.* **2011**, *37*, 4.
25. Valarezo, W.O.; Dominik, C.J.; Mcghee, R.J.; Goodman, W.L.; Paschal, K.B. Multi-Element Airfoil Optimization for Maximum Lift at High Reynolds Numbers. Available online: <https://arc.aiaa.org/doi/10.2514/6.1991-3332> (accessed on 29 December 2022).
26. Chin, V.D.; Peters, D.W.; Spaid, F.W.; McGhee, R. Flowfield measurements about a multi-element airfoil at high Reynolds numbers. In Proceedings of the 23rd Fluid Dynamics, Plasmadynamics, and Lasers Conference, Orlando, FL, USA, 6–9 July 1993.
27. AI, G.Y. Numerical Simulation of Separated Flows around Isolated Airfoil at Different Reynolds Numbers. Master's Thesis, Chongqing University, Chongqing, China, 2017.
28. Cai, C.; Zuo, Z.G.; Liu, S.H.; Wang, X.; Wu, Y.L. Numerical Analysis on the Influence of Wavy Leading Edge on Stall Characteristics of a Wind Turbine Airfoil. *J. Eng. Thermophys.* **2015**, *3*, 531–534. (In Chinese)
29. Jin, L.; Li, Y. Discrimination of several correlation coefficients and their implementation in R software. *Stat. Inf. Forum* **2019**, *34*, 3–11. (In Chinese)
30. Xiao, X.; Jiang, B.; Ren, Q.; Yin, X.; Lu, J. Photovoltaic data cleaning based on interpolation and Pearson correlation. *Inf. Technol.* **2019**, *5*, 19–22. (In Chinese)

Disclaimer/Publisher's Note: The statements, opinions and data contained in all publications are solely those of the individual author(s) and contributor(s) and not of MDPI and/or the editor(s). MDPI and/or the editor(s) disclaim responsibility for any injury to people or property resulting from any ideas, methods, instructions or products referred to in the content.

Article

A New Hybrid Optimization Method, Application to a Single Objective Active Flow Control Test Case

Martí Coma^{1,2,*}, Navid Monshi Tousi³, Jordi Pons-Prats^{1,4}, Gabriel Bugeada^{1,5} and Josep M. Bergada³

- ¹ Centre Internacional de Mètodes Numèrics a l'Enginyeria (CIMNE), Edifici C1, Gran Capitan, 08034 Barcelona, Spain; jordi.pons-prats@upc.edu (J.P.-P.); bugeda@cimne.upc.edu (G.B.)
- ² Department of Physics, Aeronautics Division, Universitat Politècnica de Catalunya, Barcelona Tech (UPC), Edifici GAIA, Rambla de Sant Nebridi, 22, 08222 Terrassa, Spain
- ³ Department of Fluids Mechanics, Universitat Politècnica de Catalunya, Barcelona Tech (UPC), Edifici TR4, C/Colom, 9, 08222 Terrassa, Spain; navid.monshi.tousi@upc.edu (N.M.T.); josep.m.bergada@upc.edu (J.M.B.)
- ⁴ Department of Physics, Aeronautics Division, Universitat Politècnica de Catalunya, Barcelona Tech (UPC), Edifici C3, Esteve Terrades, 5, 08860 Castelldefels, Spain
- ⁵ Department of Civil and Environmental Engineering, Universitat Politècnica de Catalunya, Barcelona Tech (UPC), Edifici C1, Gran Capitan, 08034 Barcelona, Spain
- * Correspondence: mcoma@cimne.upc.edu; Tel.: +34-932057016; Fax: +34-934016517

Abstract: Genetic Algorithms (GA) are useful optimization methods for exploration of the search space, but they usually have slowness problems to exploit and converge to the minimum. On the other hand, gradient based methods converge faster to local minimums, although are not so robust (e.g., flat areas and discontinuities can cause problems) and they lack exploration capabilities. This article presents a hybrid optimization method trying to combine the virtues of genetic and gradient based algorithms, and to overcome their corresponding drawbacks. The performance of the Hybrid Method is compared against a gradient based method and a Genetic Algorithm, both used alone. The rate of convergence of the methods is used to compare their performance. To take into account the robustness of the methods, each one has been executed more than once, with different starting points for the gradient based method and different random seeds for the Genetic Algorithm and the Hybrid Method. The performance of the different methods is tested against an optimization Active Flow Control (AFC) problem over a 2D Selig–Donovan 7003 (SD7003) airfoil at Reynolds number 6×10^4 and a 14 degree angle of attack. Five design variables are considered: jet position, jet width, momentum coefficient, forcing frequency and jet inclination angle. The objective function is defined as minus the lift coefficient ($-C_l$), so it is defined as a minimization problem. The proposed Hybrid Method enables working with N optimization algorithms, multiple objective functions and design variables per optimization algorithm.

Citation: Coma, M.; Tousi, N.M.; Pons-Prats, J.; Bugeada, G.; Bergada J.M. A New Hybrid Optimization Method, Application to a Single Objective Active Flow Control Test Case. *Appl. Sci.* **2022**, *12*, 3894. <https://doi.org/10.3390/app12083894>

Academic Editor: Vincent A. Ciciello

Received: 15 March 2022

Accepted: 9 April 2022

Published: 12 April 2022

Publisher's Note: MDPI stays neutral with regard to jurisdictional claims in published maps and institutional affiliations.



Copyright: © 2022 by the authors. Licensee MDPI, Basel, Switzerland. This article is an open access article distributed under the terms and conditions of the Creative Commons Attribution (CC BY) license (<https://creativecommons.org/licenses/by/4.0/>).

Keywords: Hybrid Methods; Genetic Algorithms; gradient-based methods; optimization; Active Flow Control; Synthetic Jets

1. Introduction

Optimization methods usually excel in exploration or exploitation, they have to make a trade-off between those characteristics. The balance between exploration and exploitation capabilities will affect the usability of the optimization method. A method that excels in exploitation may lack the capacity to find the candidate regions and get stuck in local minima. On the other hand, a method that excels in exploration may lack the capacity to quickly converge to a refined solution, but it can find the candidate regions efficiently. Evolutionary bio-inspired methods usually excel in exploration capabilities and gradient based methods usually excel in exploitation capabilities.

Traditionally, bio-inspired optimization methods provide good exploration capabilities with robustness in providing global minimum. Nevertheless, this requires a large number

of evaluations of the objective functions, this being its main drawback, especially when dealing with applications to industry and engineering. We can see examples of this type of solution using particle swarm optimization algorithms in microwave engineering at A. Lalbakhsh and Smith [1], or resonator antennas at A. Lalbakhsh and Esselle [2]. Genetic Algorithms have also been used on environmental sensing problems at Lalbakhsh et al. [3], or improving satellite darkness at Lalbakhsh et al. [4]. Gray Wolf Optimization has been used for the solution of flow measurement and instrumentation problems at [5].

In practice, one could think in a sequential combination of different optimization methods in order to combine their main advantages and to overcome the different limitations of each one. For instance, first use an evolutionary algorithm (e.g., a Genetic Algorithm) to perform an exploration and, next, use its results to start a gradient based method (e.g., a conjugate gradient) to exploit the interesting regions found by the evolutionary algorithm. If we do that with all the individuals provided by the evolutionary method, the total computational cost would be even more prohibitive. However, one could also think of applying a deterministic improvement with only a reduced set of promising individuals. This is considered a form of hybridization. An example of this kind of hybridization can be found at Kelly Jr and Davis [6], which proposes a combination of a Genetic Algorithm and a k-nearest neighbors classification algorithm. Another example of hybridization with multiple algorithms is proposed at Jih and Hsu [7]. In this case, a Genetic Algorithm and dynamic programming is used to address vehicle routing optimization problems. Other examples can be found at El-Mihoub et al. [8], Kulcke and Lorenz [9].

Other forms of hybridization are the definition of new operators, including multi-population methods. A multi-population Hybrid Method was proposed in Lee et al. [10] where games strategies were combined with bio-inspired optimization methods. In this approach there are different players, all of them using Genetic Algorithms applied to the solution of different complementary optimization problems.

This approach was used for the optimization of aeronautic shape configurations in Lee et al. [10], Lee et al. [11] and D. S. Lee and Srinivas [12]. This was applied in the optimization of composite structure design at Lee et al. [13].

In this paper, an extended implementation of this approach combining a player using a Genetic Algorithm with another player using a conjugate gradient is presented and tested against a single objective problem on an Active Flow Control device optimization. The performance of this approach is compared with the use of the Genetic Algorithm and the conjugate gradient methods used alone.

There are two players:

- One population-based for exploration, which could be an evolutionary algorithm or swarm intelligence.
- One which tries to improve a selection of the most promising individuals coming from the population of the bio-inspired algorithm which uses a deterministic gradient based method.

2. Hybrid Method Description

In this section, the proposed Hybrid Method is described. Hybrid Methods have been researched by Lee et al. [10] among others. In the work of Lee et al. [10], there are different optimization algorithms inside the Hybrid Method that are also called *players*, as it uses the Nash games concepts and hybridizes a Nash game with a global Pareto player. In Lee et al. [10], the authors use Genetic Algorithms for all optimization algorithms (i.e., players) which compound the Hybrid Method. When working with two objective functions, it uses three players. The first one is the Pareto player or global player and it deals with the whole problem, two objective functions and all design variables. The other two players are the Nash players, and each one only deals with one objective function. The design variables are also split between the two Nash players, resulting in each Nash player working with a subset of the search space.

The proposed Hybrid Method, which has been derived from the one proposed by Lee et al. [10], enables working with N players, multiple objective functions and design variables per player, and a different optimization algorithm for each player. The structure of the method is divided into three main components:

- **General Algorithm:** It contains the initialization of the player, the main optimization loop and the post-process of the optimization. It is not intended to be changed for different variants of the Hybrid Method.
- **Migration epoch algorithm:** It is the function that defines the exchange of information between the different players. It defines which individuals are migrated between players, under which circumstances, etc.
- **Immigrate methods:** The immigrate method is a function that has to be defined for each type of player. The way each optimization algorithm used as a player can incorporate and use an individual highly depends on the internal algorithm of each type of player. This function defines how each type of player incorporates the individuals that emigrate into them.

The Hybrid Method interlaces the execution of its internal optimization algorithms. Each player runs one iteration of its optimization algorithm, then a migration epoch occurs before the other method runs one iteration of its own algorithm. The migration epoch is the mechanism that allows the exchange of information between players. The information exchanged by the players are the design variables of a selection of individuals. The migration epoch implementation is what defines the main functionality of the Hybrid Method. The general algorithm of the Hybrid Method is described in Algorithm 1.

Algorithm 1: General algorithm of the Hybrid Method

```

foreach player do
  | player-Initialize;
while not stop criteria is met do
  | foreach player do
  | | player-Generate;
  | | player-Compute;
  | | MigrationEpoch(players[i]);
foreach player do
  | player-PostProcess;
PostProcess;

```

In this article, the optimization method selected to perform the exploration is a Genetic Algorithm based on the NSGAI [14]. Other population based optimization algorithms, such as differential evolution, particle swarm optimization, etc., could also be used here. The Genetic Algorithm is known for its robustness and exploration capabilities and it is one of the most widely used optimization algorithms for complex problems. It should perform the task well in exploring the full search space. On the other hand, the method selected for the exploitation is a conjugate gradient [15]. As shown in Algorithm 1, first of all, the *Initialize* process for each player is called. These methods are called once and are used to initialize each optimization algorithm. After the initialization of each optimization algorithm, the optimization loop is started. Inside the loop, as mentioned above, each optimization player runs one iteration before the migration epoch. One iteration consists of generating a set of new individuals (i.e., a set of design variables) and computing them. For the Genetic Algorithm player, the genetic operators of selection, crossover and mutation are performed inside the *Generate* process, which yields a new population, known as the offspring. After the population is computed, the *MigrationEpoch* process is called, and after

that the conjugate gradient runs an iteration of its algorithm starting with the migrated individual, and the process repeats until the stop criteria is met.

The *MigrationEpoch* process is responsible for managing the exchange of information between the different players. The definition of this process is what defines most of the hybrid algorithm. For example, it defines the criteria of which individuals migrate between players, how often they migrate, etc. The internal algorithm of the *MigrationEpoch* process that describes the Hybrid Method presented and tested in this article is detailed in Algorithm 2.

Algorithm 2: Hybrid Method With Gradient Game

After computing a full iteration of a player the MigrationEpoch(this-player) function does:

```

if iter = 0 then
  foreach player do
    | player-Immigrate(this-player-Bestfits);
else
  if this-player-Bestfits < players[0]-Bestfits then
    | foreach player do
      | | player-Immigrate(this-player-Bestfits);
  else
    | GetMinBestfits;
    | this-player-Immigrate(Bestfit);

```

The tested Hybrid Method combines two players (i.e., optimization algorithms). One player is intended to perform the exploration of the full search space. The second player is responsible for the exploitation of the promising regions found by the first one. The Hybrid Method shares information between the two players, in a bidirectional way, to overcome the main drawbacks of the optimization algorithms that is formed of. It tries to achieve a fast rate of convergence and to avoid getting stuck at local minimums.

The Hybrid Method initially runs the Genetic Algorithm player. After the first iteration, the best individual found by the Genetic Algorithm is transferred to the conjugate gradient player (first *if* of the Algorithm 2). The *player-Bestfits* is the individual with the best objective function found so far, and it is stored for each player. It is updated every time a better individual is found. The conjugate gradient player will use this individual as the starting point of its internal algorithm for its own iteration. The iteration of the conjugate gradient consists of computing the gradient at the location of the starting point and performing a line search in the direction of the gradient. After the iteration of the conjugate gradient, another migration epoch occurs. If the best individual found by the conjugate gradient outperforms the best individual found by the Genetic Algorithm, then the best individual of the conjugate gradient is sent to the Genetic Algorithm.

If the first conditional is not met, a second *if* condition is evaluated, taking into account the values of the objectives functions achieved so far. The inner *if* condition compares the objective function of the last evaluated player (*this-player*) against the objective function of the first player, which in this case is a Genetic Algorithm. The condition *this-player-Bestfits < players[0]-Bestfits* is clear in a single-objective optimization case, as it is a direct comparison between values of the objective function. If the objective function of *this-player* is better (lower) than the first player, this individual is migrated to the other player.

If the objective function of *this-individual* is not better, the inner *else* part of the algorithm is conducted. In the function *GetMinBestfits*, a search for the best individual (*Bestfit*) among all players is performed, and the individual is migrated to *this-player*, the last player that was executed.

For the full comprehension of the hybrid algorithm, it is important to specify the *Immigrate* process. This process is defined for each player, and its implementation depends on the type of optimization algorithm, and it affects the general hybrid algorithm. It has one input parameter, the individual that has been selected to migrate into this player. The *Immigrate* process is responsible for incorporating the individual into the player. The *Immigrate* process of the Genetic Algorithm substitutes the design variables of the last individual of its internal population with the one that comes from the conjugate gradient. This introduces the genetic information of this individual into the population. In the next iteration, the design variables of this individual will be used in the genetic operators.

In order not to repeat computations, the conjugate gradient player only performs a new iteration when the Genetic Algorithm one provides a best individual different than in the previous global iteration.

On the other hand, the Genetic Algorithm player always incorporates to the population the best individual coming from the conjugate gradient, even if it is the same as in any previous global iteration. The stochastic nature of the Genetic Algorithm can benefit from maintaining the best individual in the population at each iteration. There is a probability that the best individual is not selected in the genetic operators, and to keep the best individual in the population, keeping its genetic information can help to converge in that region. One could think about problems with elitism, but the method only forces one individual to remain in the population, the absolute best so far. If this happens for too long, most probably the optimization has converged, and in case it is not converged, the algorithm should still be capable to explore other regions with the mutation operator and the stochastic nature of the Genetic Algorithm.

For more clarity, the general algorithm with two players, the Genetic Algorithm as the first player and the conjugate gradient as the second one, is schematized at Figure 1. As mentioned previously, a migration epoch occurs after each iteration of each player. This executes the process detailed in the Algorithm 2, enabling the possibility of exchanging information between the two players.

The configuration of the Genetic Algorithm is specified in Table 1 and the configuration of the conjugate gradient is specified in Table 2. The configuration of both optimization algorithms is the same when running alone and when running as a player of the Hybrid Method.

Table 1. Parameters of the Genetic Algorithm.

Parameter	Value
Crossover operator	Simulated Binary Crossover [16]
Mutation operator	Polynomial Mutation [17]
Selection operator	$\mu + \lambda$ & Crowded-Comparison Operator [14]
Probability of crossover	0.9
Probability of mutation	0.1
Population size	20

Table 2. Parameters of the conjugate gradient algorithm.

Parameter	Value
Search Direction Method	Fletcher-Reeves [18]
Optimal Step Size Method	Golden Section [19]
Epsilon for numerical differentiation	1.0×10^{-6}
First step size	1.0×10^{-3}
Optimal step size tolerance	1.0×10^{-3}

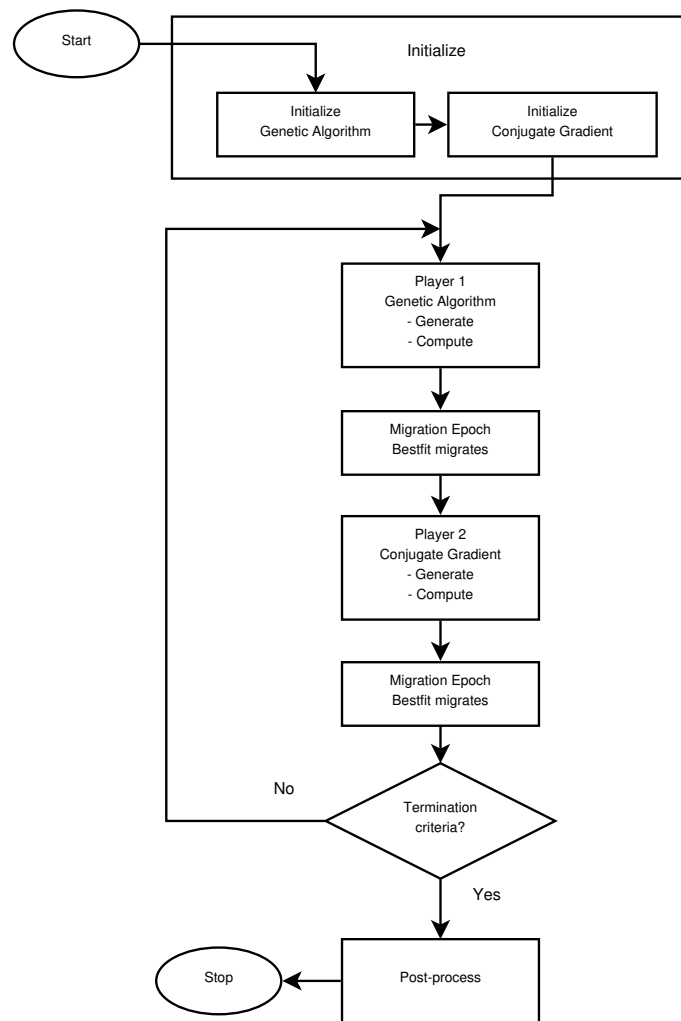


Figure 1. General algorithm of the tested Hybrid Method.

One of the main drawbacks of the proposed Hybrid Method, using both population and gradient-based optimization methods, is that it requires the independent configuration of each optimization method for each player. In this case, the configuration of the Hybrid Method requires the configuration of the Genetic Algorithm and the conjugate gradient players. On the other hand, it also enables the possibility to fine tune the players to perform better, but in cases with high computational costs, it is difficult to perform tests with different configuration values. Another drawback of the Hybrid Method is that the parallelization of the evaluations of the individuals can become more ineffective because each method may have its optimum number of CPUs which may be different for each method. For example, in this case, the evaluation of the Genetic Algorithm population can benefit from using 20 CPUs, one for each individual of the population because they can be computed at the same time. On the other hand, to evaluate the individuals of the conjugate gradient, the parallelization is not that clear. The individuals to compute the gradient can be evaluated at the same time, in this case there are eleven individuals, the central point plus two for each design variable. The line search could also be parallelized, but it is not in the implementation used in this study. The difference in the parallelization capabilities between players could result in an under utilization of the computational resources at some stages of the process.

3. Numerical Results

In order to evaluate the performance of the proposed Hybrid Method, it has been compared against two classical optimization methods, a plain conjugate gradient and a

plain Genetic Algorithm. The conjugate gradient method is the same as that which forms part of the Hybrid Method, but running on its own. The Genetic Algorithm used to compare the hybrid algorithm is also the same that forms part of the Hybrid Method, but also running alone. To take into account the random component of the Genetic Algorithm and the strong dependence on the starting point of the conjugate gradient, multiple optimizations with each algorithm have been conducted.

Two optimizations have been conducted with the Genetic Algorithm, starting with different random populations. The Hybrid Method was also run twice, starting with the same random populations as the Genetic Algorithm, so both methods started with the same populations. Finally, the conjugate gradient was run six times, starting with six individuals of the first random population generated by one of the Genetic Algorithms.

All the optimization methods have been tested against the same test case. The test case consists of a single objective optimization of an Active Flow Control optimization problem based on the work of Tousi et al. [20]. The objective of that work is to determine the optimum parameters of the Synthetic Jet actuator design at different angles of attack in a multiple objective optimization problem. The test case details for the comparison of optimization algorithms are presented in Section 3.1.

3.1. Test Case Description

The test case focuses on the optimization of an Active Flow Control device, more precisely, a Synthetic Jet actuator. The device is tested on a SD7003 airfoil at an angle of attack of 14 degrees. For the comparison between the optimization algorithms, which is the main objective of this work, a single optimization problem with five design variables has been used. The objective function is to maximize the lift coefficient, and to do so the objective function is set to:

$$f = -C_l$$

At high angles of attack, the Synthetic Jet can greatly affect the flow structure, improving the lift coefficient. The Synthetic Jet actuator, if set properly, can help to reattach the flow to the airfoil or to almost avoid the detachment of the flow.

The design variables are the same as the previous work by Tousi et al. [20]. For a full explanation and detail of the Synthetic Jet actuator design variables meaning refer to [20]. The five design variables are:

- F^+ Non-dimensional frequency.
- C_μ Momentum coefficient.
- θ Jet inclination angle.
- x/C Non-dimensional jet position.
- h/C Non-dimensional jet width.

The evaluation range of each design variable is shown in Table 3. The same ranges are used with all optimization algorithms.

Table 3. Active Flow Control design variables and their evaluation ranges.

Design Variable	Minimum Value	Maximum Value
F^+	0.1	10
C_μ	0.0001	0.02
θ°	5	175
x/C	0.001	0.3
h/C	0.005	0.015

The flow has been solved with an unsteady Reynolds averaged Navier–Stokes model (URANS), using the OpenFOAM software. Other models, like direct numerical simulation (DNS) or large eddy simulation (LES) could be used to solve the Synthetic Jet simulation, but their computational cost is too high to perform so many optimizations with the avail-

able resources. In addition, there is no need to use such precise solvers to evaluate the performance of the Hybrid Method. More details on the solver used can be consulted at [20], as this study uses the same model.

The mesh used, see Figure 2a, is one of the meshes previously evaluated in [20], although having a smaller number of cells (34,448) than the final one employed in that paper, the maximum y^+ after the simulation was $y^+ = 1$. The mesh nearby the Synthetic Jet actuator is presented in Figure 2b. The run time of the simulation has been adjusted to 30 time units, which as shown in [20] is sufficient to reach convergence. It is important to note that this study is not about the Synthetic Jet actuator optimization, but to compare the optimization algorithms in a real world application with a significant computational cost and complexity. The study of the physical problem is not the main purpose of this study, which justifies reducing the precision of each CFD simulation in order to reduce the overall computational cost.

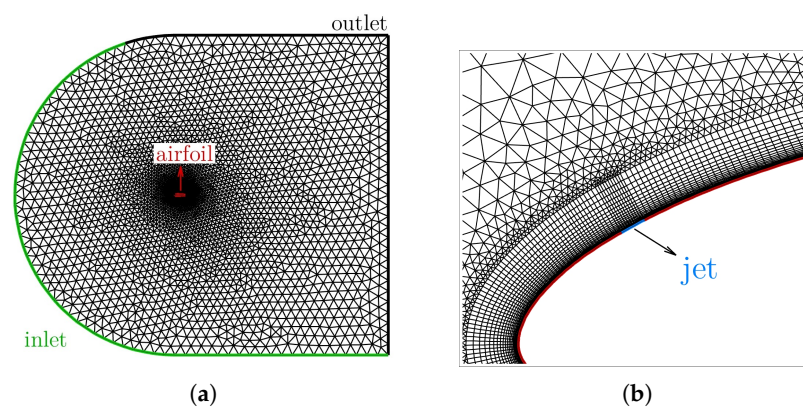


Figure 2. Full mesh of the domain (a) and Mesh nearby the Synthetic Jet actuator (b).

In Figure 3, the temporal averaged streamlines and pressure field for the non-actuated case is presented. This configuration is called the baseline. From the streamlines, it can be seen that the flow is fully separated and the airfoil is under stall conditions.

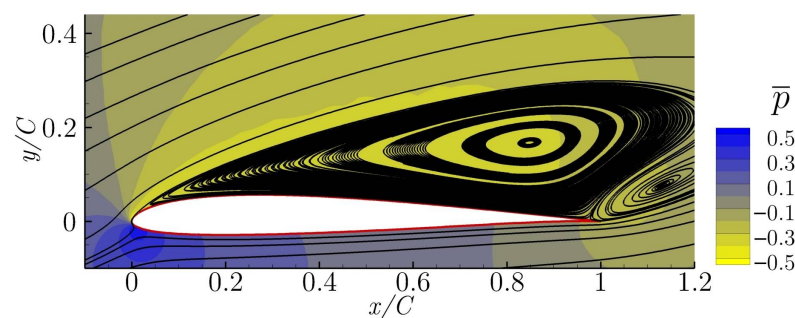


Figure 3. Averaged streamlines and pressure field of baseline case ($C_l = 0.80$).

3.2. Results from the Optimizations Methods

This section introduces the results obtained for the proposed comparison. The convergence of the different optimization algorithms are shown in Figure 4. The results shown in the graph of Figure 4 reflect the problems encountered by the gradient based method. Most runs of the conjugate gradient initially improve faster than the Genetic Algorithm but then get stuck between $C_l \approx 1.35$ and $C_l \approx 1.45$ (except for two runs that get stuck at $C_l \approx 0.8$ and $C_l \approx 1.25$, respectively). Those lift coefficient values are achieved with almost 100 evaluations of the objective function for each optimization of the conjugate gradient. The strong dependence of the conjugate gradient on the starting point is also reflected on these results, as it presents very different solutions between runs than the other methods.

In all cases, the conjugate gradient method was stopped because the algorithm found a local minimum and could not compute the gradient to further improve the results.

On the other hand, the Genetic Algorithm provides optimal solutions similar to the conjugate gradient, but with a higher computational cost, approximately four times higher. Both runs of the Genetic Algorithm achieve values of the objective function in the range of the conjugate gradient results. One of the runs achieves a better objective function than all of the conjugate gradient runs, with a value of $C_l = 1.49$. It is important to note that the Genetic Algorithm optimizations could run additional iterations and achieve better results, but with a high computational cost.

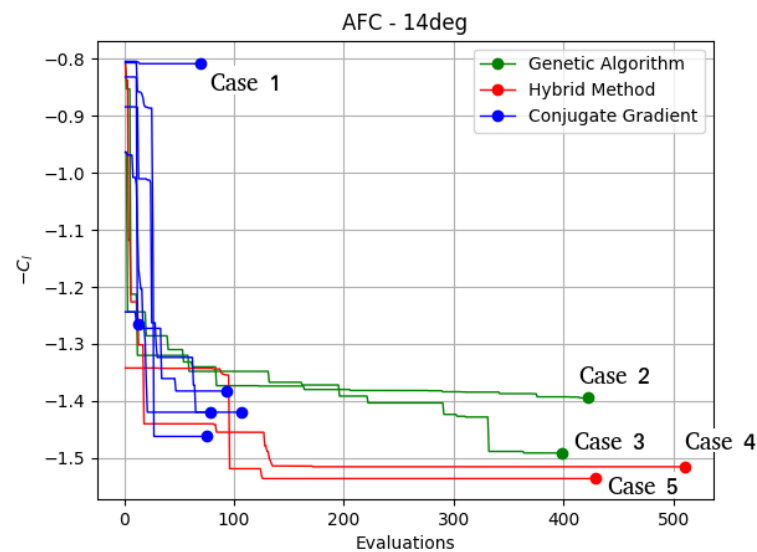


Figure 4. Comparative of the convergence of the different optimization methods.

The Hybrid Method is the method that achieved better results, outperforming all runs of the other algorithms in both of its runs. During the first iterations, it achieved a convergence rate similar to the conjugate gradient. However, the improvement of the solution has continued, avoiding being trapped in any local minimum. It is also the most robust, as both runs are very similar in their performance. Both Hybrid Method runs outperformed all the other optimization methods with a $C_l = 1.52$ and $C_l = 1.54$. One run of the Genetic Algorithm achieved a comparable solution ($C_l = 1.49$), but it took more than twice the computational cost of the Hybrid Method. Case 3, with a lift coefficient of $C_l = 1.49$, obtained by the Genetic Algorithm with around 375 objective function evaluations, improves the baseline lift coefficient by 86%. Cases 4 and 5, obtained by the Hybrid Method runs, achieved a lift coefficient of $C_l = 1.52$ and $C_l = 1.54$, respectively. Both runs needed around 125 objective function evaluations, which is 67% the number of evaluations of case 3, with an increase in the lift coefficient of 90% and 93%, respectively, from the baseline. The best lift coefficient achieved by each optimization is presented in Table 4. The mean (\bar{C}_l) and standard deviation (σ) of the lift coefficient achieved by each optimization method is also presented. The Hybrid Method presents the best lift coefficient mean ($C_l = 1.53$) followed by the Genetic Algorithm ($C_l = 1.44$) and the conjugate gradient ($C_l = 1.29$). The conjugate gradient is the least robust, with a standard deviation of $\sigma = 0.2458$, but four of the six optimizations achieved similar results than the Genetic Algorithm with less computational effort.

Looking at these results, one can conclude that the proposed Hybrid Method performs much more robustly than the conjugate gradient method and much faster than the Genetic Algorithm.

Table 4. Best lift coefficient of each optimization case, means and standard deviation.

	Genetic Algorithm	Hybrid Method	Conjugate Gradient
C_l	1.39	1.52	0.81
			1.26
	1.49	1.54	1.38
			1.42
			1.42
1.46			
$\overline{C_l}$	1.44	1.53	1.29
σ	0.07071	0.01414	0.2458

3.3. Results Based on the Fluid Flow Performance

This subsection provides a comparison between the characteristics of the flow field corresponding to each of the optimal solutions labeled in Figure 4. The lift coefficient and design variables of each of the optimal solutions are presented in Table 5. For a full explanation of the flow structure and details on the Synthetic Jet actuator performance, the reader is directed to [20].

Table 5. Values of the lift coefficient and design variables of the five labeled cases.

Case	C_l	F^+	C_μ	θ°	x/C	h/C
1	0.81	8.6	1×10^{-4}	136	3×10^{-1}	5×10^{-3}
2	1.39	0.3	1.47×10^{-2}	24	1×10^{-3}	1.4×10^{-2}
3	1.49	3.2	1.92×10^{-2}	8	2×10^{-2}	5×10^{-3}
4	1.52	6.7	2×10^{-2}	7	2.6×10^{-2}	5×10^{-3}
5	1.54	9.9	2×10^{-2}	5	1.97×10^{-2}	5×10^{-3}

As explained in the Section 3.1, the flow without the Synthetic Jet actuator is fully detached, see Figure 3. The objective of the Synthetic Jet actuator is to prevent or minimize flow separation. The averaged streamlines and pressure field of the optimized cases are presented and discussed in this section. The flow field corresponding to Case 1 is presented in Figure 5. Despite the fact that the flow separation is slightly delayed versus the baseline case, a large vortical structure is still observed over the airfoil.

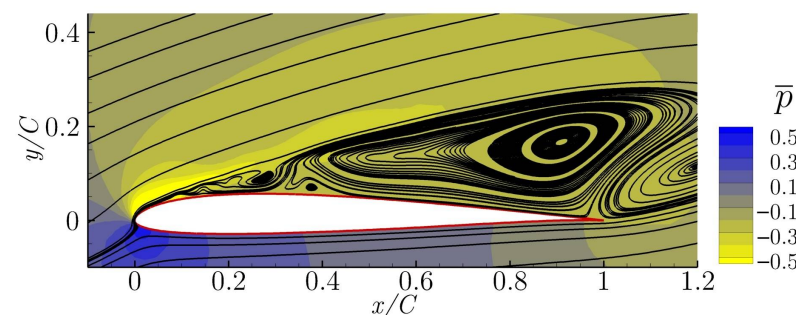


Figure 5. Averaged streamlines and pressure field of the Case 1 ($C_l = 0.81$).

In Figure 6, the averaged streamlines and pressure field obtained from case 2 is presented. It shows a late reattachment of the flow, which improves the lift coefficient of the baseline by 74%. This solution has been obtained by one of the Genetic Algorithm’s runs, with around 400 evaluations of the objective function. The resulting lift coefficient is $C_l = 1.39$.

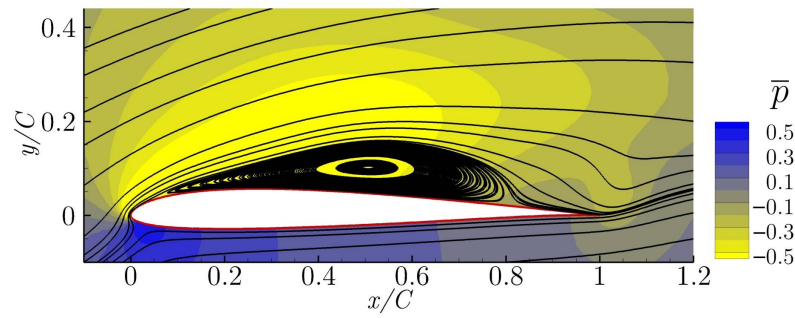


Figure 6. Averaged streamlines and pressure field of case 2 ($C_l = 1.39$).

The averaged streamlines and pressure fields of cases 3, 4 and 5 are presented in Figures 7–9, respectively. All of them show a complete flow reattachment, with very minor differences in the size of the laminar bubble appearing close to the airfoil leading edge. The bubbles are in fact located near the Synthetic Jet position, just downstream of it, as can be seen in the above mentioned figures. The optimization of the flow control actuation parameters has managed to successfully reattached the flow along the entire airfoil chord.

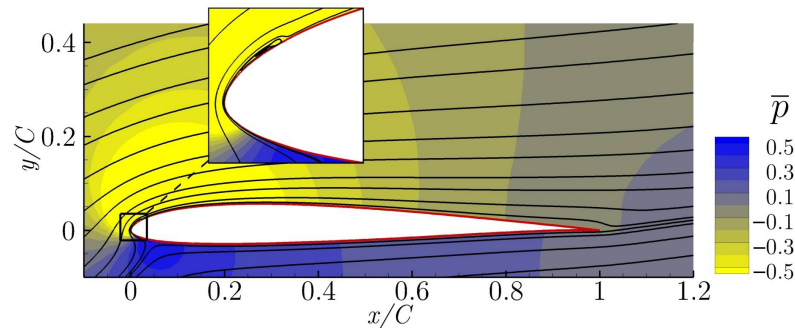


Figure 7. Averaged streamlines and pressure field of case 3 ($C_l = 1.49$).

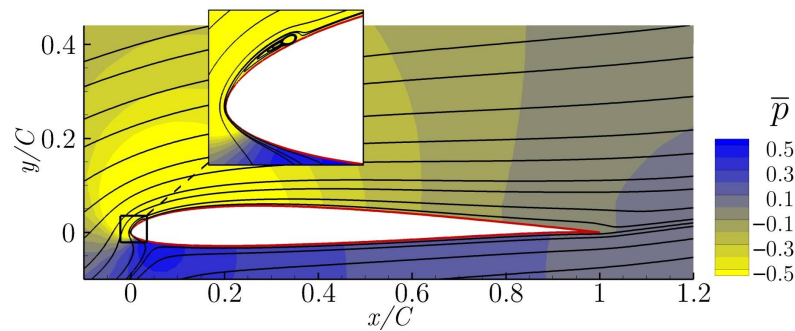


Figure 8. Averaged streamlines and pressure field of case 4 ($C_l = 1.52$).

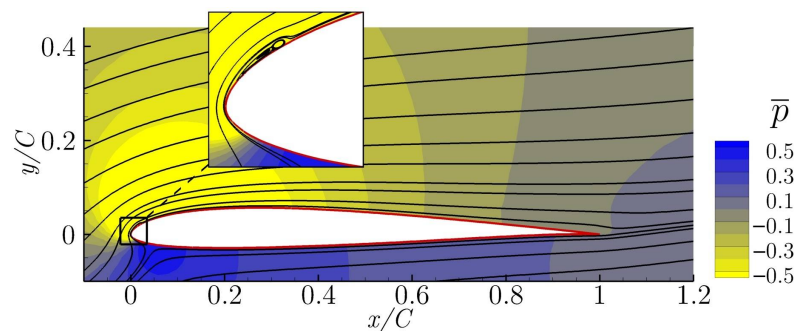


Figure 9. Averaged streamlines and pressure field of case 5 ($C_l = 1.54$).

4. Discussion

This article presents a new Hybrid Method which combines two optimization methods (a Genetic Algorithm and a conjugate gradient) of a very different nature. The test case used to evaluate the performance of the new Hybrid Method is a single objective optimization with five design variables associated with a Synthetic Jet actuator. The CFD simulations are solved using a URANS model, which has proven precise enough to capture the active flow actuator effect and to compare between different designs. For the test case of the Synthetic Jet actuator, the Hybrid Method has outperformed both of the traditional optimization algorithms. The new Hybrid Method successfully combines the best characteristics of both optimization algorithms. It shows a great convergence rate, like a gradient based method, but without the lack of robustness that usually comes with gradient based methods and complex applications. The increase in robustness is provided by the Genetic Algorithm player which avoids local minimums. The strategy to exchange information between the two optimization algorithms proposed in this Hybrid Method has proven efficient to overcome the main drawbacks of both classical optimization methods, and the result is an optimization method capable of exploring and exploiting the full search space.

The future work aims to further test the new Hybrid Method in a multi-objective optimization problem such as the one introduced in Tousi et al. [20]. In high CPU demanding applications, such a Synthetic Jet actuator optimization is important when working with optimization algorithms that require a low number of evaluations of the physical model, and the new Hybrid Method has proven a good option.

Author Contributions: Conceptualization, M.C., N.M.T., J.P.-P., G.B. and J.M.B.; methodology, M.C. and N.M.T.; software, M.C. and N.M.T.; validation, M.C., N.M.T., J.P.-P., G.B. and J.M.B.; formal analysis, M.C., N.M.T., J.P.-P., G.B. and J.M.B.; investigation, M.C., N.M.T., J.P.-P., G.B. and J.M.B.; resources, N.M.T. and J.M.B.; data curation, M.C. and N.M.T.; writing—original draft preparation, M.C.; writing—review and editing, M.C., N.M.T., J.P.-P., G.B. and J.M.B.; visualization, M.C. and N.M.T.; supervision, J.P.-P., G.B. and J.M.B. All authors have read and agreed to the published version of the manuscript.

Funding: This research has been partially supported through the Severo Ochoa Centre of Excellence (2019-2023) under the grant CEX2018-000797-S funded by MCIN/AEI/10.13039/501100011033.

Acknowledgments: The third author, Jordi Pons-Prats, is a Serra Hunter Fellow.

Conflicts of Interest: The authors declare no conflict of interest.

References

1. Lalbakhsh, A.; Afzal, M.U.; Esselle, K.P.; Smith, S. Design of an artificial magnetic conductor surface using an evolutionary algorithm. In Proceedings of the 2017 International Conference on Electromagnetics in Advanced Applications (ICEAA), Verona, Italy, 11–15 September 2017; Volume 1, pp. 885–887.
2. Lalbakhsh, A.; Afzal, M.U.; Esselle, K.P. Multiobjective Particle Swarm Optimization to Design a Time-Delay Equalizer Metasurface for an Electromagnetic Band-Gap Resonator Antenna. *IEEE Antennas Wirel. Propag. Lett.* **2017**, *16*, 912–915. [CrossRef]
3. Lalbakhsh, A.; Simorangkir, R.B.; Bayat-Makou, N.; Kishk, A.A.; Esselle, K.P. Chapter 2—Advancements and artificial intelligence approaches in antennas for environmental sensing. In *Artificial Intelligence and Data Science in Environmental Sensing*; Asadnia, M., Razmjou, A., Beheshti, A., Eds.; Cognitive Data Science in Sustainable Computing, Academic Press: Cambridge, MA, USA, 2022; pp. 19–38. [CrossRef]
4. Lalbakhsh, A.; Pitcairn, A.; Mandal, K.; Alibakhshikenari, M.; Esselle, K.P.; Reisenfeld, S. Darkening Low-Earth Orbit Satellite Constellations: A Review. *IEEE Access* **2022**, *10*, 24383–24394. [CrossRef]
5. Karami, A.; Roshani, G.H.; Nazemi, E.; Roshani, S. Enhancing the performance of a dual-energy gamma ray based three-phase flow meter with the help of grey wolf optimization algorithm. *Flow Meas. Instrum.* **2018**, *64*, 164–172. [CrossRef]
6. Kelly, J.D., Jr.; Davis, L. A Hybrid Genetic Algorithm for Classification. *IJCAI* **1991**, *91*, 645–650.
7. Jih, W.R.; Hsu, J.Y.J. Dynamic vehicle routing using hybrid Genetic Algorithms. In Proceedings of the 1999 IEEE International Conference on Robotics and Automation (Cat. No. 99CH36288C), Detroit, MI, USA, 10–15 May 1999; Volume 1, pp. 453–458.
8. El-Mihoub, T.A.; Hopgood, A.A.; Nolle, L.; Battersby, A. Hybrid Genetic Algorithms: A Review. *Eng. Lett.* **2006**, *13*, 124–137.
9. Kulcke, M.; Lorenz, W.E. Utilizing Gradient Analysis within Interactive Genetic Algorithms. *eCAAD* **2016**, *2*, 359–364.

10. Lee, D.; Gonzalez, L.F.; Periaux, J.; Srinivas, K.; Onate, E. Hybrid-Game Strategies for multi-objective design optimization in engineering. *Comput. Fluids* **2011**, *47*, 189–204. [CrossRef]
11. Lee, D.; Periaux, J.; Pons-Prats, J.; Bugada, G.; Oñate, E. Double Shock Control Bump design optimization using hybridised evolutionary algorithms. In Proceedings of the IEEE Congress on Evolutionary Computation, Barcelona, Spain, 18–23 July 2010; Volume 1, pp. 1–8.
12. Lee, D.S.; Gonzalez, L.F.; Périaux, J.; Srinivas, K. Efficient Hybrid-Game Strategies Coupled to Evolutionary Algorithms for Robust Multidisciplinary Design Optimization in Aerospace Engineering. *IEEE Trans. Evol. Comput.* **2011**, *15*, 133–150. [CrossRef]
13. Lee, D.; Morillo, C.; Bugada, G.; Oller, S.; Onate, E. Multilayered composite structure design optimisation using distributed/parallel multi-objective evolutionary algorithms. *Compos. Struct.* **2012**, *94*, 1087–1096. [CrossRef]
14. Deb, K.; Pratap, A.; Agarwal, S.; Meyarivan, T. A fast and elitist multiobjective genetic algorithm: NSGA-II. *IEEE Trans. Evol. Comput.* **2002**, *6*, 182–197. [CrossRef]
15. Shewchuk, J.R. *An Introduction to the Conjugate Gradient Method without the Agonizing Pain*; Technical Report; Carnegie Mellon University, Pittsburgh, PA, USA, 1994.
16. Deb, K.; Agrawal, R.B. Simulated binary crossover for continuous search space. *Complex Syst.* **1995**, *9*, 115–148.
17. Deb, K. *Multi-Objective Optimization Using Evolutionary Algorithms*; John Wiley & Sons: Chichester, UK, 2001; Volume 16.
18. Fletcher, R. *Practical Methods of Optimization*; John Wiley & Sons: Hoboken, NJ, USA, 2013.
19. Brent, R.P. *Algorithms for Minimization without Derivatives*; Prentice-Hall: Englewood Cliffs, NJ, USA, 1973.
20. Tousi, N.; Coma, M.; Bergadà, J.; Pons-Prats, J.; Mellibovsky, F.; Bugada, G. Active Flow Control optimisation on SD7003 airfoil at pre and post-stall angles of attack using Synthetic Jets. *Appl. Math. Model.* **2021**, *98*, 435–464. [CrossRef]

Article

An Efficient Hybrid Evolutionary Optimization Method Coupling Cultural Algorithm with Genetic Algorithms and Its Application to Aerodynamic Shape Design

Xin Zhao ¹, Zhili Tang ^{1,*}, Fan Cao ¹, Caicheng Zhu ¹ and Jacques Periaux ²

¹ College of Aerospace Engineering, Nanjing University of Aeronautics and Astronautics (NUAA), Nanjing 210016, China; zhaoxin970314@nuaa.edu.cn (X.Z.); caofan@nuaa.edu.cn (F.C.); zhucaicheng@nuaa.edu.cn (C.Z.)

² International Center for Numerical Methods in Engineering (CIMNE), Universitat Politècnica de Catalunya, 08034 Barcelona, Spain; periaux@cimne.upc.edu

* Correspondence: tangzhili@nuaa.edu.cn

Abstract: Evolutionary algorithms have been widely used to solve complex engineering optimization problems with large search spaces and nonlinearity. Both cultural algorithm (CA) and genetic algorithms (GAs) have a broad prospect in the optimization field. The traditional CA has poor precision in solving complex engineering optimization problems and easily falls into local optima. An efficient hybrid evolutionary optimization method coupling CA with GAs (HCGA) is proposed in this paper. HCGA reconstructs the cultural framework, which uses three kinds of knowledge to build the belief space, and the GAs are used as an evolutionary model for the population space. In addition, a knowledge-guided *t*-mutation operator is developed to dynamically adjust the mutation step and introduced into the influence function. HCGA achieves a balance between exploitation and exploration through the above strategies, and thus effectively avoids falling into local optima and improves the optimization efficiency. Numerical experiments and comparisons with several benchmark functions show that the proposed HCGA significantly outperforms the other compared algorithms in terms of comprehensive performance, especially for high-dimensional problems. HCGA is further applied to aerodynamic optimization design, with the wing cruise factor being improved by 23.21%, demonstrating that HCGA is an efficient optimization algorithm with potential applications in aerodynamic optimization design.

Keywords: evolutionary algorithms; cultural algorithm; genetic algorithms; aerodynamic optimization design

Citation: Zhao, X.; Tang, Z.; Cao, F.; Zhu, C.; Periaux, J. An Efficient Hybrid Evolutionary Optimization Method Coupling Cultural Algorithm with Genetic Algorithms and Its Application to Aerodynamic Shape Design. *Appl. Sci.* **2022**, *12*, 3482. <https://doi.org/10.3390/app12073482>

Academic Editor: Vincent A. Cicirello

Received: 23 February 2022

Accepted: 23 March 2022

Published: 29 March 2022

Publisher's Note: MDPI stays neutral with regard to jurisdictional claims in published maps and institutional affiliations.



Copyright: © 2022 by the authors. Licensee MDPI, Basel, Switzerland. This article is an open access article distributed under the terms and conditions of the Creative Commons Attribution (CC BY) license (<https://creativecommons.org/licenses/by/4.0/>).

1. Introduction

Aircraft shape optimization is one of the key problems in aerodynamic configuration design. The traditional aerodynamic optimization design methods mainly rely on experience and trial-and-error methods, which require a lot of human, material and financial resources, and not only take a long time but also require a lot of computational resources [1]. In recent years, with the rapid development of computational fluid dynamics (CFD) technology, the combination of numerical methods and optimization algorithms for the aerodynamic shape optimization of aircraft can significantly shorten the development cycle and reduce the design cost [2]. Therefore, it is important to carry out research on efficient aerodynamic optimization design methods based on the combination of CFD technology and optimization algorithms for the development of aerodynamic optimization design.

Among numerous aerodynamic optimization studies, gradient-based methods and heuristic algorithms are two of the most widely used methods. Gradient-based methods are particularly attractive due to their ability to significantly improve the efficiency of high-dimensional optimization problems. The adjoint method proposed by Jameson [3] is

an effective sensitivity analysis method that evaluates sensitivity information by solving the adjoint problem regardless of the number of design variables. Therefore, the computational time of sensitivity analysis can be significantly reduced. By combining the adjoint method with the gradient method, the optimization efficiency can be greatly improved. In recent years, this technique has been widely used in aerodynamic optimization [4,5]. However, two reasons make this technique less attractive: one is its difficulty in dealing with constrained/multi-objective problems, and the other is that it is easy for it to fall into local optima.

Heuristic algorithms do not need to rely on information about a specific problem and have good global performance in finding the optima; they are thus particularly suitable for solving problems with complex multiple local optima. Among them, genetic algorithms (GAs), differential evolution (DE) algorithm and particle swarm optimization (PSO) algorithm are the most popular methods in the field of aerodynamic optimization, and they have all been successfully applied in aerodynamic optimization [6–9]. However, their evolutionary procedures require multiple calls to the CFD analysers, which significantly increases the computational cost. Therefore, it is necessary to improve the optimal efficiency and therefore to develop optimization algorithms in particular allowing for balanced exploitation and exploration capabilities [10].

Many engineering problems are complex high-dimensional multimodal problems, so that most algorithms converge slowly, easily fall into local optima and are inefficient in dealing with such problems. Aerodynamic optimization is a highly complex nonlinear problem with multi-parameter, high-dimensional and multimodal characteristics. In order to solve aerodynamic optimization problems effectively, it is undoubtedly necessary to develop new intelligent and knowledge-based algorithms with satisfactory performance. The genetic algorithm has good robustness and global search capability [11–15], and can be well adapted to solve various types of problems. The cultural algorithm is a knowledge-based super-heuristic algorithm, and its unique two-layer evolutionary mechanism can improve the evolutionary efficiency very well. The hybrid of genetic algorithms and cultural algorithm can combine the advantages of both, and then solve aerodynamic optimization problems efficiently.

Cultural algorithm (CA) [16] is an evolutionary algorithm based on the simulation of a two-layer evolutionary mechanism of human society, proposed by R.G. Reynolds in 1994. It was inspired by and developed from human sociology and aimed to model the evolution of the cultural component of evolutionary systems over time [17]. CA simulates the development of society and culture, which can be divided into two parts, the population space and the belief space, which are independent from each other but interconnected through communication protocols. CA extracts the implicit information carried by the population evolution process, such as the location of the optimal individuals or the range of the best individuals, into the belief space and stores it in knowledge sources. CA provides a new framework and mechanism for evolutionary models or swarm intelligence systems [18], such as genetic algorithms [19], ant colony algorithms [20], particle swarm algorithms [21] and differential evolution [22], etc. The two-layer evolutionary mechanism of CA improves the efficiency of the algorithm. Compared with other evolutionary algorithms, CA has stronger global optimization capability and higher optimization precision, and it has been successfully applied to optimization problems such as clustering analysis [23], sensor localization [24], multi-objective optimization [25] and vehicle routing [26]. Although the cultural algorithm can use knowledge sources to improve evolutionary efficiency, its global convergence and evolutionary efficiency are deficient due to its single mutation operator [27]. Therefore, the cultural algorithm needs to be improved for better performance of the optimization.

In this paper, an efficient hybrid evolutionary optimization method coupling CA with GAs (HCGA) is introduced with a validation background of the application of evolutionary algorithms to aerodynamic optimization design. Considering the features of CA and GAs, the proposed algorithm reconstructs the framework of cultural algorithms, which uses

GAs as a population space evolutionary model of the cultural framework, with the three types of knowledge, namely situational knowledge, normative knowledge and historical knowledge; these kinds of knowledge construct the knowledge sources of the belief space. In addition, HCGA introduces population variance and population entropy to determine population diversity, and it develops a new knowledge-guided t -mutation operator to dynamically adjust the mutation step based on the change of population diversity during the evolutionary process. It further introduces the t -mutation operator into the influence function to balance the exploration and exploitation ability of the algorithm and improve its optimization efficiency.

The rest of the paper is organized as follows. A brief introduction to the basic principles and framework of the cultural and genetic algorithms is given in Section 2. The proposed algorithm HCGA is introduced in Section 3. Numerical results and comparisons are presented and discussed in Section 4.2. The HCGA is applied in Section 5 to the aerodynamic optimization design of the wing cruise factor. Conclusions and perspectives are discussed in Section 6.

2. Brief Description of GAs and CA

2.1. Genetic Algorithms (GAs)

Genetic algorithms (GAs) proposed by Professor J. Holland [19] are among the evolutionary algorithms (EAs). GAs operate on the whole population with individuals, and their main operators include selection, crossover and mutation. For a particular problem, GAs define the search space as the solution space, and each feasible solution is encoded as a chromosome. Before the search starts, a set of chromosomes is usually randomly selected from the solution space to form the initial population. Next, the fitness value of each individual is evaluated according to the objective function, then the selection, crossover and mutation operators are applied sequentially to generate a new generation of populations. The process is repeated until the stopping criterion is reached.

2.2. Cultural Algorithm (CA)

The two-layer evolutionary mechanism used by the cultural algorithm consists of two main evolutionary spaces at the micro and macro levels, namely the population space and the belief space [28], and the basic structure of the cultural algorithm is shown in Figure 1. The evolution on the micro level refers to the internal evolution of the population space that realizes the evolution of individuals, and the evolution on the macro level refers to the evolution of the belief space that realizes the extraction and updating of knowledge sources. The evolutions between these two spaces are independent of each other, but they are connected through communication protocols (influence and acceptance functions). Figure 2 describes the basic pseudo-code of the CA. The figure shows how the process is executed in each generation. Firstly, the objective function $Obj()$ evaluates individuals in the population space, and the $Acceptance()$ function selects the best individuals for updating the belief space knowledge source. After that, the $Influence()$ function influences the evolution of the next generation of populations. More details on the knowledge sources used and how they affect the population of this proposed work are given in Section 3.

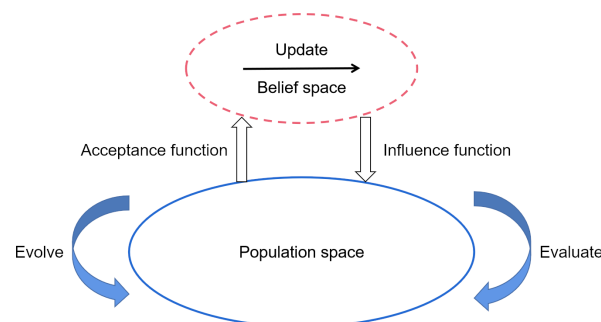


Figure 1. Framework of the cultural algorithm (CA).

```

Begin
  set  $g=0$ 
  initialize belief space,  $B^g$ 
  initialize population space,  $P^g$ 
  repeat
    evaluate  $P^g$  using  $Obj()$ 
    update  $B^g$  using  $Acceptance()$ 
    generate  $P^g$  using  $Influence()$ 
     $g=g+1$ 
    select  $P^{g+1}$  from  $P^g$ 
  until(termination condition met)
End
  
```

Figure 2. Pseudo-code of cultural algorithm.

3. The Hybrid Evolutionary Optimization Method Coupling CA with GAs

Cultural systems possess the ability to incorporate heterogeneous and diverse knowledge sources into their structures. As such, they are ideal frameworks within which to support hybrid amalgams of knowledge sources and population components [29]. In order to make full use of the advantages of CA and GAs, an efficient hybrid evolutionary optimization method coupling CA with GAs (HCGA) is proposed in this paper. The cultural framework of HCGA is shown in Figure 3, which includes population space, belief space and communication protocol, whose population space is modeled using GAs, and belief space includes situational knowledge, normative knowledge and historical knowledge. In addition, HCGA introduces population entropy and population variance to judge population diversity, and a knowledge-guided t -mutation operator is developed based on population diversity to balance the exploration and exploitation ability of the algorithm. In the remainder of this section, we describe each part of the HCGA in detail.

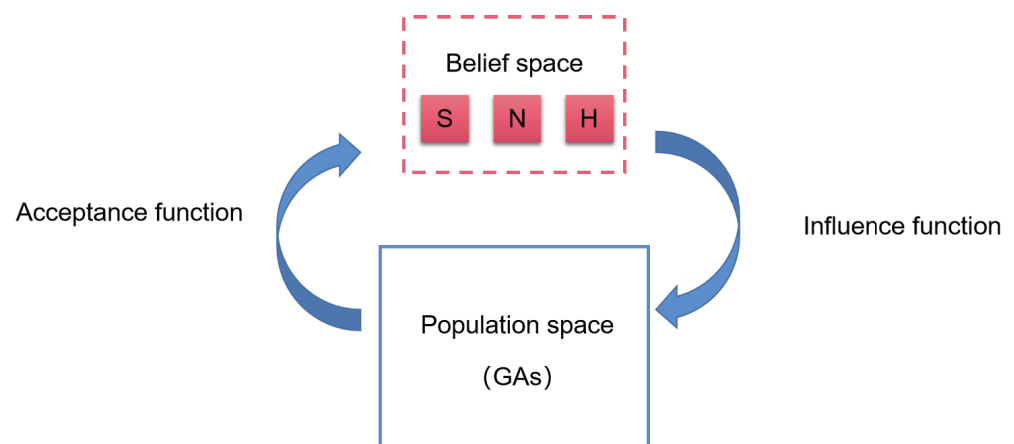


Figure 3. Framework of HCGA.

3.1. Population Space

In fact, the population space can support any population-based evolutionary algorithm or swarm intelligence algorithm, which can also interact and run simultaneously with the belief space. The standard cultural algorithm has only a single mutation operator in the population space, making its global convergence and exploration capability insufficient. The GAs has a strong global search capability and high robustness, which can effectively explore the search space with the increasing population convenience and global exploration capability of the algorithm, and thus the population space is evolved using the GAs in this paper. A detailed description of the genetic algorithms is given in Section 2.2 and will not be repeated here.

3.2. Belief Space

In this paper, according to the characteristics of genetic algorithms, combined with the manner of extracting and updating knowledge sources in the belief space, the knowledge sources are divided into situational knowledge, normative knowledge and historical knowledge. The manner of updating the knowledge sources in the belief space every K generations is adopted, so that the memory consumption brought by redundant information can be reduced. Different knowledge sources have different update strategies. Taking the maximization problem as an example, the update of the knowledge sources is described as follows:

- (1) Situational knowledge. Situational knowledge was proposed by Chung in 1997 [30] to record the excellent individuals with a guiding role in the evolutionary process and is structured as follows:

$$\langle E_1, E_2, \dots, E_n \rangle \tag{1}$$

where E_i is the i th best individual, and in this paper the best individual is selected to update the situational knowledge, that is, $s = 1$. The process of updating situational knowledge is described as follows:

$$\langle E(T + 1) \rangle = \begin{cases} \langle x_b \rangle & \text{if } f(x_b) > f(E(T)) \\ \langle E(T) \rangle & \text{else} \end{cases} \tag{2}$$

where x_b is the best individual in the T th generation of the population space.

- (2) Normative knowledge. Normative knowledge was also proposed by Chung [30] for limiting the search space and judging the feasibility of an individual. When an individual is outside the search space described by the normative knowledge, the normative knowledge will guide the individual into the dominant search space through the influence function, thus ensuring that evolution proceeds in the dominant region, and for the n -dimensional optimization problem, the structure of the normative knowledge is described as follows:

$$\langle V_1, V_2, \dots, V_n \rangle \tag{3}$$

where $V_i = [(l_i, u_i), (L_i, U_i)]$, $i \leq n$. u_i and l_i are the upper and lower bounds of the i th dimensional variables, and U_i and L_i are the upper and lower bounds of the fitness value, respectively. The normative knowledge is updated with the change of the dominant search region, and gradually approaches the region where the best individual is located. Therefore, when there is a better individual in the T th generation beyond the current search range described by the normative knowledge, the normative knowledge is updated as follows:

$$l_i(T + 1) = \begin{cases} x_j^i(T) & \text{if } x_j^i(T) \leq l_i(T) \text{ or } f(x_j(T)) > L_i(T) \\ l_i(T) & \text{otherwise} \end{cases} \tag{4}$$

$$L_i(T + 1) = \begin{cases} f(x_j(T)) & \text{if } x_j^i(T) \leq l_i(T) \text{ or } f(x_j(T)) > L_i(T) \\ L_i(T) & \text{otherwise} \end{cases} \tag{5}$$

$$u_i(T + 1) = \begin{cases} x_j^i(T) & \text{if } x_j^i(T) \geq u_i(T) \text{ or } f(x_j(T)) > U_i(T) \\ u_i(T) & \text{otherwise} \end{cases} \tag{6}$$

$$U_i(T + 1) = \begin{cases} f(x_j(T)) & \text{if } x_j^i(T) \geq u_i(T) \text{ or } f(x_j(T)) > U_i(T) \\ U_i(T) & \text{otherwise} \end{cases} \tag{7}$$

- (3) Historical knowledge. Historical knowledge was introduced into the belief space by Saleem [31] to record important events that occurred during the evolutionary process, and its main role is to adjust the offset distance and direction when the optimization falls into a local optima. The historical knowledge structure is divided as

shown in Figure 4, where e_i is the i th outstanding individual of historical knowledge preservation, W is its maximum capacity, and d_{sj} and d_{rj} are the average offset distance and the average offset direction of the j th design variable. The expressions of d_{sj} and d_{rj} are as follows:

$$d_{sj} = \frac{\sum_{k=1}^{w-1} |e_{k+1}x_j - e_kx_j|}{w - 1} \tag{8}$$

$$d_{rj} = \text{sgn}\left(\sum_{k=1}^{w-1} |e_{k+1}x_j - e_kx_j|\right) \tag{9}$$

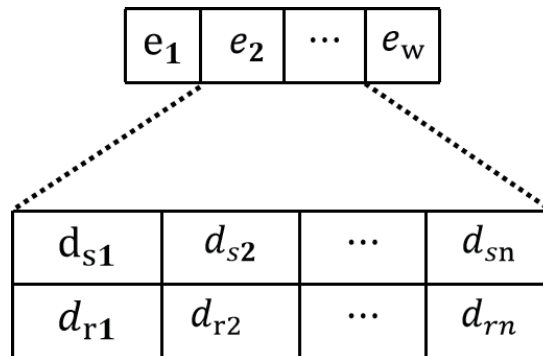


Figure 4. Structure of historical knowledge.

3.3. Proposed t -Mutation Operator

Evolutionary algorithms require good exploration capabilities in the early stages and good exploitation capabilities in the later stages of evolution. The t distribution contains the degree of freedom parameter n , which approaches the standard Gaussian distribution infinitely when $n \rightarrow +\infty$ and the t distribution is the standard Cauchy distribution when $n = 1$. That is, the standard Gaussian distribution and the standard Cauchy distribution are two boundary special cases of the t distribution. The probability density functions of the standard Gaussian distribution and the standard Cauchy distribution are shown in Figure 5. Obviously, the application of the Cauchy operator can produce a larger mutation step, which is conducive to the algorithm to guide individuals to jump out of the local optimal solution and ensure the exploration ability of the algorithm, and Gaussian distribution shows a better exploitation ability.

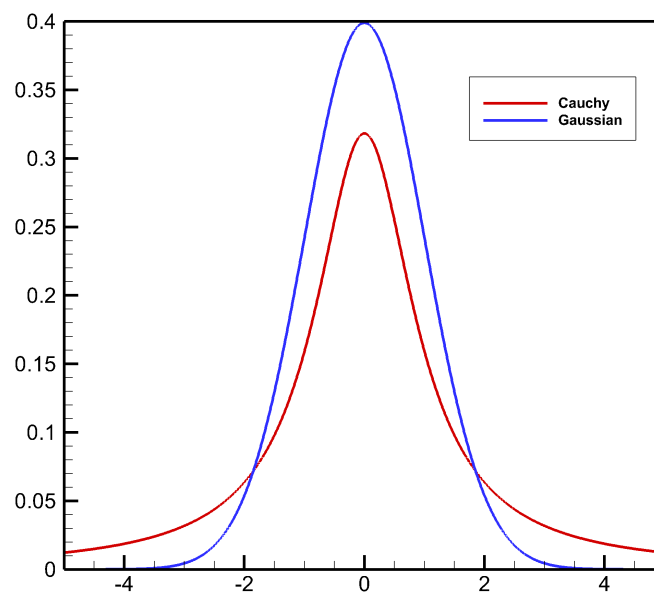


Figure 5. Probability density functions of the Cauchy and Gaussian distributions.

Population diversity is considered as the primary reason for premature convergence, which determines the search capability of the algorithm. In evolutionary algorithms, population diversity decreases over time as evolution proceeds. Therefore, population diversity can be used to determine the stage of evolution; we can thus use the population diversity to construct the degree of freedom n . By changing the degree of freedom parameter n , the mutation scale changes adaptively with evolution to balance the exploitation and exploration capabilities of the algorithm. In this paper, we introduce population variance and population entropy to determine population diversity. The expression of population variance D_T in the T th generation is as follows:

$$D_T = \frac{1}{N \times l} \left(\sum_{i=1}^N \sum_{j=1}^l x_i^j - \bar{x}^j \right) \tag{10}$$

where x_i^j is the j th gene value of the i th individual, N is the number of populations and l is the individual coding length. The expression of \bar{x}^j is as follows:

$$\bar{x}^j = \frac{1}{N} \left(\sum_{i=1}^N x_i^j \right) \tag{11}$$

The solution space A of the optimization problem is divided equally into L small spaces, and the number of individuals belonging to the i th space A_i in generation T is $|A_i|$. The expression of population entropy S_T in the T th generation is as follows:

$$S_T = - \sum_{i=1}^L p_i \log(p_i) \tag{12}$$

where

$$p_i = \frac{|A_i|}{N} \tag{13}$$

From the definitions of population variance and population entropy, it is clear that population variance reflects the degree of dispersion of individuals in the population and that population entropy reflects the number of individual types in the population. Therefore, the t -mutation operator $t(n)$ can be constructed based on the population variance and population entropy. The degree of freedom parameter n is expressed as follows:

$$n = \left[1 - \ln \left(\frac{D_T + S_T}{D_{max} + S_{max}} \right) \right] \tag{14}$$

where $[]$ is the least integer function, and D_{max} and S_{max} are the maximum values of population variance and population entropy, respectively. Obviously, the degree of freedom parameter n of the t -mutation operator is 1 in the first generation and increases gradually as evolution proceeds, then the degree of freedom parameter n converges to positive infinity in the late evolutionary stage, and the t distribution becomes a standard Gaussian distribution. The t -mutation operator can ensure the exploration capability of the algorithm in the early evolutionary stage and the exploitation capability of the algorithm in the late evolutionary stage.

3.4. Communication Protocol

The information interaction between the belief space and the population space is realized through the acceptance function and the influence function. The acceptance function passes the better individuals in the population space as samples to the belief space for knowledge sources extraction and update, and the influence function is the way to influence the population space by the belief space, which can use the knowledge sources in the belief space to guide the population space to complete and accelerate the evolution.

3.4.1. Acceptance Function

In this paper, a dynamic version of the acceptance function [31] is used. The number of accepted individuals is given as follows:

$$n_{Accept} = \left(p\% + \frac{p\%}{T} \right) \times N \tag{15}$$

where $[]$ is the least integer function, T is the current generation, N is the number of populations, $p\%$ is the preset fixed proportion and $p\% = 20\%$. In this paper, the acceptance function accepts n_{Accept} better individuals into the belief space. The dynamic acceptance function makes the number of individuals entering the belief space decrease with the depth of evolution, which increases the global search ability of the algorithm at the early stage of evolution, and reduces the number of individuals entering the belief space at the late stage of evolution because the population tends to converge and carries mostly similar information, which can maintain the diversity of knowledge sources and avoid the consumption of memory by redundant information.

3.4.2. Influence Function

The core of the influence function is the manner and proportion in which each type of knowledge affects the population. Knowledge acts on each type of influence function to control the number of individuals affected by each type of influence function. Therefore, the proportion by which each type of knowledge affects the population is the relative role that each type of influence function has in the population. The proportion of the effect of the influence function is determined by the success rate of the knowledge effect, and is expressed as follows:

$$P_k(T) = \begin{cases} 1/N_k & \text{if } T = 1 \\ \alpha + \beta \times \frac{v_k(T-1)}{v(T-1)} & \text{if } (T \bmod K) = 0 \\ P_k(T - 1) & \text{otherwise} \end{cases} \tag{16}$$

It satisfies the condition that $\beta + \alpha N_k = 1$, where N_k is the number of knowledge sources types, $v_k(T - 1)$ denotes the number of individuals influenced by knowledge k that are better than their parents in generation $T - 1$ and $v(T - 1)$ denotes the number of individuals influenced by all knowledge sources that are better than their parents in generation $T - 1$. The success rate of knowledge sources influenced in the previous generation determines the proportion of the effect of each knowledge source in the next generation. In order to allow each kind of knowledge source to always have the possibility of being used, we took $\alpha = 0.1, \beta = 0.7$, ensuring that the lower bound of P_k is 0.1 and the proportion of all knowledge sources in the first generation is the same, which is $1/N_k$.

Next, we introduced the proposed t -mutation operator into the influence function to develop a knowledge-guided t -mutation strategy.

- (1) Situational knowledge. Situational knowledge has a guiding role in the evolutionary process, and the effect of situational knowledge on the population space under the action of the t -mutation operator is noted as follows:

$$x'_{ij} = \begin{cases} x_{ij} + |(x_{ij} - E_j)t(n)| & \text{if } x_{ij} < E_j \\ x_{ij} - |(x_{ij} - E_j)t(n)| & \text{if } x_{ij} > E_j \\ x_{ij} + \gamma t(n) & \text{otherwise} \end{cases} \tag{17}$$

where x_{ij} is the j th dimensional design variable of the i th individual, x'_{ij} is the j th dimensional design variable of the newly generated i th individual, γ is a constant and E_j is the j th dimensional design variable of the situational knowledge.

- (2) Normative knowledge. The normative knowledge guides the population to search in the dominant region, and the effect of the normative knowledge on the population space under the action of the t -mutation operator is noted as follows:

$$x'_{ij} = \begin{cases} x_{ij} + |(u_j - l_j)t(n)| & \text{if } x_{ij} < l_j \\ x_{ij} - |(u_j - l_j)t(n)| & \text{if } x_{ij} > u_j \\ x_{ij} + \mu(u_j - l_j)t(n) & \text{otherwise} \end{cases} \quad (18)$$

where μ is a constant, and u_j and l_j are the upper and lower bounds of the j th dimensional design variables preserved by the normative knowledge of the current generation belief space, respectively.

- (3) Historical knowledge. Historical knowledge is used to adjust the offset distance and direction when the optimization is trapped in a local optima, and the effect of historical knowledge on the population space under the action of the t -mutation operator is noted as follows:

$$x'_{ij} = \begin{cases} ex_j + d_{rj}t(n) & \text{for 45\% of the time} \\ ex_j + d_{sj}t(n) & \text{for 45\% of the time} \\ \text{random}(l'_j, u'_j) & \text{for 10\% of the time} \end{cases} \quad (19)$$

where ex_j is the j th dimensional design variable of the best individual ex stored in the historical knowledge and u'_j and l'_j are the upper and lower bounds, respectively. Here a roulette wheel is used to determine how new individuals are generated, with a 45% probability that individuals produce a bias in direction, a 45% probability that individuals produce a bias in distance and a 10% probability that new individuals are generated randomly within the entire search space [32].

3.5. The Main Numerical Implementation of HCGA

The main numerical implementation of HCGA is described step-by-step as follows:

- Step 1:** Initialization of algorithm parameters ($N, l, P_m, P_c, T_{max}, l', u', K, \alpha, \beta, \gamma, \mu, p$).
- Step 2:** Initializing the population space. The initial population in the population space is generated randomly within the lower and upper bounds of the design variables, and the fitness of each individual in the initial population is evaluated. Set current generation $T = 1$.
- Step 3:** Initializing the belief space. Situational knowledge is initialized to the best individual in the initial population. In the normative knowledge, $U(1)$ and $L(1)$ are initialized to $-\infty$, and $u(1)$ and $l(1)$ are initialized to the upper and lower bounds of the design variables. In the historical knowledge, ex is initialized to the best individual in the initial population, while the average offset distance and the average offset direction are initialized to 0.
- Step 4:** Updating the population space. Evaluate the fitness of each individual and update the individuals in the population space by the genetic operation (selection, crossover, mutation). Calculate the population variance and population entropy and update the degree of freedom parameter n .
- Step 5:** If the current generation T is divisible by K , then go to Step 6; otherwise go to Step 8.
- Step 6:** Acceptance operation. Individuals are selected from the population space as samples to be passed to the belief space, and the number of acceptances is determined according to Equation (15).
- Step 7:** Updating the belief space. The update of knowledge in the belief space is performed according to Equation (2) and Equations (4)–(9).
- Step 8:** Influence operation. According to Equations (17)–(19), the influence operation is performed to update the individuals in the population space.

Step 9: Stop the algorithm if the stopping criterion is satisfied; otherwise $T = T + 1$ and go to Step 4.

4. Numerical Validation and Performance of Hybrid HCGA Algorithm

4.1. Parameter Discussion

Tuning parameters properly is very important for an evolutionary algorithm to achieve good performance. In HCGA, there are seven main parameters: $P_c, P_m, \alpha, \gamma, \mu, K, p$. In this section, we used the factorial design (FD) [16] approach in order to obtain a guideline on how to tune the designed parameters in HCGA.

Ten benchmark mathematical optimization problems were used to evaluate and compare optimization algorithms. These functions can be divided into unimodal functions and multimodal functions. Functions $F_1 - F_4$ are unimodal functions with only a global optimal value, which are mainly used to evaluate the exploitation ability and convergence speed of the algorithm. Functions $F_5 - F_{10}$ are multimodal functions, which have multiple local optimal values in the search space, and the number of local optima will increase with the increase of the problem size, which is an important reference for assessing the exploration capability of the algorithm. Seven of these test functions ($F_1 - F_7$) are dimension-wise scalable. The details of the test functions are listed in Table 1.

Table 1. Details of the mathematical optimization problems.

Test Function	D	Search Range	Optimal
$F_1 = \sum_{i=1}^n x_i^2$	10/30/100	$(-100, 100)^D$	0
$F_2 = \sum_{i=1}^n x_i + \prod_{i=1}^n x_i $	10/30/100	$(-10, 10)^D$	0
$F_3 = \sum_{i=1}^n \sum_{j=1}^i x_j$	10/30/100	$(-100, 100)^D$	0
$F_4 = \sum_{i=1}^n [(x_{4i-3} + 10x_{4i-2})^2 + 5(x_{4i-1} - x_{4i})^2 + (x_{4i-2} - 2x_{4i-1})^4 + 10(x_{4i-3} - x_{4i})^4]$	12/32/100	$(-4, 5)^D$	0
$F_5 = \sum_{i=1}^n (x_i^2 - 10 \cos(2\pi x_i) + 10)$	10/30/100	$(-5.12, 5.12)^D$	0
$F_6 = \sum_{i=1}^n \frac{x_i^2}{4000} - \prod_{i=1}^n \cos \frac{x_i}{\sqrt{i}} + 1$	10/30/100	$(-32, 32)^D$	0
$F_7 = -20 \exp\left(-0.2 \sqrt{\frac{1}{n} \sum_{i=1}^n x_i^2}\right) - \exp\left(\frac{1}{n} \cos(2\pi x_i)\right) + 20 + e$	10/30/100	$(-32, 32)^D$	0
$F_8 = -\frac{1 + \cos(12\sqrt{x_1^2 + x_2^2})}{0.5(x_1^2 + x_2^2) + 2}$	2	$(-5.12, 5.12)^D$	-1
$F_9 = 0.5 + \frac{\sin^2(x_1^2 - x_2^2) - 0.5}{(1 + 0.001(x_1^2 + x_2^2))^2}$	2	$(-100, 100)^D$	0
$F_{10} = (4 - 2.1x_1^2 + \frac{x_1^4}{3})x_1^2 + x_1x_2 + (-4 + 4x_2^2)x_2^2$	2	$(-3, 3)^D$	-1.031628

In the experiments, the population size was set to twice the dimension for the $F_1 - F_7$ function and five times the dimension for the $F_8 - F_{10}$ function, and the T_{max} was set to 5000. As shown in Table 2, we used seven parameters as factors for seven levels in an orthogonal experimental design. Table 3 shows the test results of the orthogonal parameter table with the $10D - f_1$ function. Trials of 30 times were performed for each set of parameters. The unabridged result tables, similarly to Table 3 of other experiments, were too large, and they were omitted here.

As shown in Table 3, to estimate the effects of each set of parameters, the mean fitness of the 30 runs were obtained and listed in in the last column of the table. K_i is the mean value of mean fitness for this column parameter at level i ($i = 1, 2, \dots, 7$). Std is the standard deviation of each column $K_1 - K_7$. The larger the Std value is, the more this column parameter influences the algorithm performance. Furthermore, for each column, if the value of K_i is the smallest K value in that column, then the best value of the

parameter is the parameter value on level i . The best parameters ($B-P$) are listed in the last row. Tables 4 and 5 show the Std and $B-P$ of all benchmark functions. The symbol \sim in Table 5 indicates that each set of parameters enables the algorithm to optimize to the same optimal value.

Table 2. Factors and levels for orthogonal experiment.

Factors	Levels						
	1	2	3	4	5	6	7
P_c	0.65	0.7	0.75	0.8	0.85	0.9	0.95
P_m	0.01	0.04	0.07	0.1	0.13	0.16	0.19
α	0.1	0.2	0.3	0.4	0.5	0.6	0.7
γ	0.1	0.2	0.3	0.4	0.5	0.6	0.7
μ	0.1	0.2	0.3	0.4	0.5	0.6	0.7
K	5	10	15	20	25	30	35
p	0.05	0.1	0.15	0.2	0.25	0.3	0.35

Table 3. Orthogonal parameter table of $L_{49}(7)^7$ and experimental results on f_1 (Dimension = 10).

No.	P_c	P_m	α	γ	μ	K	p	Mean Fitness
1	0.65	0.01	0.1	0.1	0.1	5	0.05	2.25×10^{-106}
2	0.65	0.04	0.3	0.4	0.5	35	0.1	1.50×10^{-157}
3	0.65	0.07	0.5	0.7	0.2	30	0.15	5.15×10^{-165}
4	0.65	0.1	0.7	0.3	0.6	25	0.2	6.04×10^{-197}
5	0.65	0.13	0.2	0.6	0.3	20	0.25	1.03×10^{-193}
6	0.65	0.16	0.4	0.2	0.7	15	0.3	1.82×10^{-201}
7	0.65	0.19	0.6	0.5	0.4	10	0.35	1.42×10^{-157}
8	0.7	0.01	0.7	0.6	0.5	15	0.35	7.77×10^{-236}
9	0.7	0.04	0.2	0.2	0.2	10	0.05	1.35×10^{-135}
10	0.7	0.07	0.4	0.5	0.6	5	0.1	1.21×10^{-132}
11	0.7	0.1	0.6	0.1	0.3	35	0.15	2.28×10^{-158}
12	0.7	0.13	0.1	0.4	0.7	30	0.2	6.61×10^{-205}
13	0.7	0.16	0.3	0.7	0.4	25	0.25	8.89×10^{-270}
14	0.7	0.19	0.5	0.3	0.1	20	0.3	1.68×10^{-218}
15	0.75	0.01	0.6	0.4	0.2	25	0.3	3.51×10^{-228}
16	0.75	0.04	0.1	0.7	0.6	20	0.35	8.97×10^{-261}
17	0.75	0.07	0.3	0.3	0.3	15	0.05	1.78×10^{-122}
18	0.75	0.1	0.5	0.6	0.7	10	0.1	2.06×10^{-144}
19	0.75	0.13	0.7	0.2	0.4	5	0.15	2.56×10^{-183}
20	0.75	0.16	0.2	0.5	0.1	35	0.2	2.52×10^{-258}
21	0.75	0.19	0.4	0.1	0.5	30	0.25	6.13×10^{-245}
22	0.8	0.01	0.5	0.2	0.6	35	0.25	3.85×10^{-232}
23	0.8	0.04	0.7	0.5	0.3	30	0.3	6.23×10^{-239}
24	0.8	0.07	0.2	0.1	0.7	25	0.35	1.08×10^{-273}
25	0.8	0.1	0.4	0.4	0.4	20	0.05	5.02×10^{-95}
26	0.8	0.13	0.6	0.7	0.1	15	0.1	7.55×10^{-133}
27	0.8	0.16	0.1	0.3	0.5	10	0.15	8.07×10^{-202}
28	0.8	0.19	0.3	0.6	0.2	5	0.2	5.27×10^{-230}
29	0.85	0.01	0.4	0.7	0.3	10	0.2	1.48×10^{-301}
30	0.85	0.04	0.6	0.3	0.7	5	0.25	0
31	0.85	0.07	0.1	0.6	0.4	35	0.3	0
32	0.85	0.1	0.3	0.2	0.1	30	0.35	0
33	0.85	0.13	0.5	0.5	0.5	25	0.05	6.59×10^{-103}
34	0.85	0.16	0.7	0.1	0.2	20	0.1	2.48×10^{-101}
35	0.85	0.19	0.2	0.4	0.6	15	0.15	3.36×10^{-248}

Table 3. Cont.

No.	P_c	P_m	α	γ	μ	K	p	Mean Fitness
36	0.9	0.01	0.3	0.5	0.7	20	0.15	0
37	0.9	0.04	0.5	0.1	0.4	15	0.2	1.90×10^{-295}
38	0.9	0.07	0.7	0.4	0.1	10	0.25	0
39	0.9	0.1	0.2	0.7	0.5	5	0.3	0
40	0.9	0.13	0.4	0.3	0.2	35	0.35	1.08×10^{-288}
41	0.9	0.16	0.6	0.6	0.6	30	0.05	5.37×10^{-100}
42	0.9	0.19	0.1	0.2	0.3	25	0.1	1.61×10^{-110}
43	0.95	0.01	0.2	0.3	0.4	30	0.1	0
44	0.95	0.04	0.4	0.6	0.1	25	0.15	4.75×10^{-308}
45	0.95	0.07	0.6	0.2	0.5	20	0.2	1.74×10^{-295}
46	0.95	0.1	0.1	0.5	0.2	15	0.25	7.46×10^{-306}
47	0.95	0.13	0.3	0.1	0.6	10	0.3	0
48	0.95	0.16	0.5	0.4	0.3	5	0.35	0
49	0.95	0.19	0.7	0.7	0.7	35	0.05	3.05×10^{-106}
K_1	3.21×10^{-107}	3.21×10^{-107}	3.21×10^{-107}	3.54×10^{-102}	3.21×10^{-107}	3.21×10^{-107}	7.18×10^{-96}	
K_2	1.73×10^{-133}	1.93×10^{-136}	1.93×10^{-136}	2.31×10^{-111}	3.54×10^{-102}	1.93×10^{-136}	3.54×10^{-102}	
K_3	2.54×10^{-123}	2.54×10^{-123}	2.54×10^{-123}	2.54×10^{-123}	2.31×10^{-111}	2.54×10^{-123}	3.26×10^{-159}	
K_4	7.18×10^{-96}	7.18×10^{-96}	7.18×10^{-96}	7.18×10^{-96}	7.18×10^{-96}	7.18×10^{-96}	8.62×10^{-198}	
K_5	3.64×10^{-102}	9.42×10^{-104}	9.42×10^{-104}	9.42×10^{-104}	9.42×10^{-104}	9.42×10^{-104}	1.48×10^{-194}	
K_6	7.67×10^{-101}	8.03×10^{-101}	7.67×10^{-101}	7.67×10^{-101}	7.67×10^{-101}	7.67×10^{-101}	2.60×10^{-202}	
K_7	4.35×10^{-107}	4.36×10^{-107}	3.54×10^{-102}	4.35×10^{-107}	4.35×10^{-107}	4.35×10^{-107}	2.02×10^{-158}	
Std	2.71×10^{-96}	2.71×10^{-96}	2.71×10^{-96}	2.71×10^{-96}	2.71×10^{-96}	2.71×10^{-96}	2.71×10^{-96}	
B-P	0.7	0.04	0.2	0.3	0.3	10	0.3	

Table 4. Standard deviations of orthogonal experiments.

F	D	P_c	P_m	α	γ	μ	K	p
F_1	10	2.71×10^{-96}	2.71×10^{-96}	2.71×10^{-96}	2.71×10^{-96}	2.71×10^{-96}	2.71×10^{-96}	2.71×10^{-96}
	30	1.74×10^{-95}	1.73×10^{-95}	1.73×10^{-95}	1.82×10^{-95}	1.73×10^{-95}	1.73×10^{-95}	1.73×10^{-95}
	100	7.17×10^{-20}	6.78×10^{-20}	6.83×10^{-20}	6.79×10^{-20}	6.78×10^{-20}	6.78×10^{-20}	7.81×10^{-20}
F_2	10	3.25×10^{-64}	3.25×10^{-64}	3.25×10^{-64}	3.25×10^{-64}	3.25×10^{-64}	3.25×10^{-64}	3.25×10^{-64}
	30	3.98×10^{-54}	2.62×10^{-54}	2.62×10^{-54}	2.62×10^{-54}	2.62×10^{-54}	2.62×10^{-54}	2.62×10^{-54}
	100	8.53×10^{-14}	5.98×10^{-14}	6.25×10^{-14}	6.08×10^{-14}	5.98×10^{-14}	5.98×10^{-14}	6.01×10^{-14}
F_3	10	2.96×10^{-99}	2.96×10^{-99}	2.96×10^{-99}	2.96×10^{-99}	2.96×10^{-99}	2.96×10^{-99}	3.02×10^{-99}
	30	3.66×10^{-90}	3.63×10^{-90}	3.63×10^{-90}	3.68×10^{-90}	3.63×10^{-90}	3.63×10^{-90}	3.63×10^{-90}
	100	4.76×10^{-17}	4.63×10^{-17}	4.67×10^{-17}	4.64×10^{-17}	4.63×10^{-17}	4.63×10^{-17}	5.02×10^{-17}
F_4	10	2.91×10^{-6}	1.35×10^{-6}	1.96×10^{-6}	9.89×10^{-7}	1.14×10^{-6}	1.04×10^{-6}	4.52×10^{-6}
	30	6.01×10^{-7}	2.30×10^{-7}	1.23×10^{-6}	2.07×10^{-7}	2.33×10^{-7}	2.81×10^{-7}	1.86×10^{-7}
	100	5.77×10^{-5}	6.78×10^{-5}	3.01×10^{-4}	5.91×10^{-5}	8.77×10^{-5}	7.14×10^{-5}	6.37×10^{-5}
F_5	10	1.23×10^{-15}	1.23×10^{-15}	1.23×10^{-15}	1.23×10^{-15}	1.23×10^{-15}	1.23×10^{-15}	1.23×10^{-15}
	30	4.32×10^{-2}	2.24×10^{-1}	4.47×10^{-2}	3.91×10^{-2}	3.73×10^{-2}	3.91×10^{-2}	4.32×10^{-2}
	100	1.47×10^{-1}	6.41×10^{-1}	1.47×10^{-1}	1.58×10^{-1}	1.29×10^{-1}	1.58×10^{-1}	1.63×10^{-1}
F_6	10	4.75×10^{-3}	6.52×10^{-3}	3.47×10^{-3}	5.71×10^{-3}	5.10×10^{-3}	3.48×10^{-3}	3.47×10^{-3}
	30	1.54×10^{-3}	1.38×10^{-3}	1.11×10^{-3}	2.00×10^{-3}	2.11×10^{-3}	2.77×10^{-3}	2.10×10^{-3}
	100	1.81×10^{-3}	2.23×10^{-3}	2.56×10^{-3}	2.63×10^{-3}	3.73×10^{-3}	3.24×10^{-3}	2.36×10^{-3}
F_7	10	1.21×10^{-13}	1.21×10^{-13}	1.21×10^{-13}	1.21×10^{-13}	1.21×10^{-13}	1.21×10^{-13}	1.21×10^{-13}
	30	5.46×10^{-16}	5.77×10^{-16}	1.37×10^{-15}	6.73×10^{-16}	1.51×10^{-15}	4.10×10^{-16}	7.33×10^{-16}
	100	4.43×10^{-11}	2.83×10^{-11}	3.16×10^{-11}	2.84×10^{-11}	2.82×10^{-11}	2.93×10^{-11}	3.02×10^{-11}
F_8	2	0	0	0	0	0	0	
F_9	2	0	0	0	0	0	0	
F_{10}	2	0	0	0	0	0	0	

Table 5. Best parameters (B–P) of orthogonal experiments.

<i>F</i>	<i>D</i>	<i>P_c</i>	<i>P_m</i>	α	γ	μ	<i>K</i>	<i>p</i>
<i>F</i> ₁	10	0.7	0.04	0.2	0.3	0.3	10	0.3
	30	0.75	0.13	0.2	0.5	0.1	10	0.2
	100	0.7	0.13	0.2	0.5	0.1	10	0.2
<i>F</i> ₂	10	0.75	0.04	0.2	0.3	0.3	10	0.35
	30	0.75	0.13	0.2	0.5	0.1	10	0.1
	100	0.7	0.13	0.1	0.5	0.1	25	0.1
<i>F</i> ₃	10	0.7	0.04	0.2	0.3	0.2	10	0.35
	30	0.75	0.1	0.2	0.6	0.1	10	0.1
	100	0.65	0.19	0.2	0.7	0.2	30	0.2
<i>F</i> ₄	10	0.95	0.19	0.6	0.6	0.4	25	0.3
	30	0.95	0.1	0.1	0.3	0.1	5	0.2
	100	0.9	0.04	0.1	0.4	0.1	5	0.1
<i>F</i> ₅	10	~	~	~	~	~	~	~
	30	0.85	0.13	0.1	0.3	0.1	5	0.1
	100	0.8	0.01	0.1	0.3	0.4	5	0.2
<i>F</i> ₆	10	0.8	0.16	0.3	0.1	0.3	35	0.35
	30	0.9	0.01	0.5	0.5	0.2	15	0.1
	100	0.7	0.01	0.2	0.3	0.1	5	0.2
<i>F</i> ₇	10	0.9	0.07	0.7	0.4	0.3	20	0.25
	30	0.95	0.19	0.1	0.3	0.1	30	0.05
	100	0.95	0.1	0.1	0.3	0.1	5	0.15
<i>F</i> ₈	2	~	~	~	~	~	~	~
<i>F</i> ₉	2	~	~	~	~	~	~	~
<i>F</i> ₁₀	2	~	~	~	~	~	~	~

From Table 4, it can be seen that for low-dimensional functions with unimodal functions, *P_c* has a greater influence on the algorithm performance, while for high-dimensional complex functions, it is *p*, α and *K* that have a greater influence. This indicates that when dealing with simple functions, the population space plays a major role, and when dealing with complex functions, the belief space plays a guiding role and has an influence on the evolution of the population space.

Some rules for adjusting parameters can be obtained from analyzing the results in Table 5. For simple functions, *P_c* and *P_m* can be set to a lower level, while for complex functions, they need to be set to a higher level. For most functions, α can be set to a level of about 0.2, and for multimodal functions with many local minima, α should be set to 0.1. For parameter γ , setting it to 0.3 is enough in most cases. μ has roughly the same rule as *P_c* and *P_m*. For high-dimensional multimodal functions, μ should be set to 0.1, but for unimodal or low-dimensional functions, setting it at 0.3–0.4 is enough. *K* should be set to a smaller value as the complexity of the function increases, which determines the frequency of updating the knowledge in the belief space. As for *p*, setting it at 0.1–0.2 should be enough for both unimodal and multimodal functions.

4.2. Validation in Numerical Experiments

In order to verify the performance of the algorithms, cultural algorithm (CA) [16], genetic algorithms (GAs) [11], differential evolution (DE, rand/1/L) [33] and HCGA were selected for comparison with numerical experiments. Ten mathematical functions optimization test problems shown in Table 1 were used to compare the performance of HCGA with GAs, CA and DE.

The parameters in HCGA were selected based on the results of the parameter discussion in Section 4.1, and the parameters of each algorithm in the experiments were set as shown in Table 6. Since evolutionary algorithms are essentially stochastic optimization algorithms, the solution found may not be the same each time. Therefore, each benchmark function was repeated 30 times.

Table 6. Main parameters of the HCGA, GAs, CA and DE.

Algorithm	Parameter Settings
HCGA	$P_c = 0.95, P_m = 0.1, T_{max} = 5000, \alpha = 0.1, \beta = 0.3, \gamma = 0.3, \mu = 0.1, K = 5, p = 20$
CA	$\alpha = 0.1, \beta = 0.3, \gamma = 0.3, \mu = 0.1, K = 5, p = 20, T_{max} = 500$
GAs	$P_c = 0.95, P_m = 0.1, T_{max} = 5000$
DE	$Cr = 0.95, F = 0.5, T_{max} = 5000$

The optimal values, means and standard deviations of HCGA, GAs, CA and DE for 30 independent runs are listed in Table 7, which were used to evaluate the optimization accuracy, average accuracy and stability of the algorithms. To obtain more reliable statistical conclusions, Wilcoxon nonparametric statistical tests were performed at $\alpha = 0.05$, and the symbols +, – or = mean that the optimization results of HCGA were significantly better, worse or similar to the comparison algorithm, respectively. Figure 6 shows the convergence curves of some of the benchmark test functions. The results are summarized as +/ – / = as the last row of each Table in Table 7.

As can be seen from Figure 6, HCGA shows a better performance for most functions. For unimodal functions, the convergence speed and accuracy of HCGA are significantly better than those of other algorithms. For multimodal functions, HCGA is able to achieve higher optimization accuracy in shorter iterations for all functions except for function F_{10} , which was slightly inferior to GAs and DE in terms of convergence speed in the initial search stages. This means that HCGA not only has good search ability and fast convergence, but also moderates quite well the conflict well between convergence speed and premature convergence, which means that it has a balanced exploitation and exploration ability.

The experimental results in Table 7 show that HCGA performs better for most of the tested functions compared with other algorithms, and can obtain higher optimization accuracy, average accuracy and better stability. This indicates that HCGA is less affected by randomness and that it can maintain optimization accuracy under multiple independent runs. The results of Wilcoxon nonparametric statistical tests for CA, GAs and DEs were 23/0/1, 22/1/1, and 21/3/0, respectively, indicating that the differences between the HCGA and the other three compared algorithms are statistically significant, implying that for all test functions, HCGA shows better performance or is close to the best performance of the other algorithms, which means that it is more robust.

In addition, HCGA shows an optimization capability for high-dimensional problems that cannot be matched by CA, GAs and DE. In high-dimensional optimization problems (100 dimensional $F_1 - F_7$), HCGA has significant advantages in optimization accuracy, average accuracy and stability. For the functions $F_4 - F_7$, the number of local optima will increase with the increase in the problem size, and the HCGA does not fall into dimensional disaster; it also scales well with the increasing dimensionality and converges in the proximity of the global optimum, which indicates its high level of performance in solving high-dimensional functions. HCGA can still maintain strong optimization accuracy and robustness in solving high-dimensional optimization problems, which lays the foundation for the application of HCGA in practical problems.

Table 7. Numerical experiment results.

Function	D	Opt	HCGA Mean	Std	Opt	CA Mean	Std	Opt	GAS Mean	Std	Opt	DE Mean	Std
F ₁	10	0	0	0	7.67 × 10 ⁻³⁷	1.62 × 10 ⁻⁹ (+)	8.92 × 10 ⁻⁹	5.68 × 10 ⁻⁸⁹	3.25 × 10 ⁻⁶⁷ (+)	1.78 × 10 ⁻⁶⁶	1.96 × 10 ⁻²⁶⁸	5.83 × 10 ⁻¹³ (+)	3.20 × 10 ⁻¹²
	30	1.76 × 10 ⁻²²⁶	2.68 × 10 ⁻²²⁰	0	1.80 × 10 ⁻¹⁸	1.35 × 10 ⁻¹⁰ (+)	7.10 × 10 ⁻¹⁰	4.03 × 10 ⁻⁴²	5.04 × 10 ⁻³⁸ (+)	2.11 × 10 ⁻³⁷	1.39 × 10 ⁻⁸¹	1.85 × 10 ⁻⁸⁰ (+)	2.19 × 10 ⁻⁸⁰
	100	1.75 × 10 ⁻⁶²	4.22 × 10 ⁻⁶⁰	4.54 × 10 ⁻⁶⁰	5.49 × 10 ⁻⁷	2.54 × 10 ⁻⁵ (+)	3.41 × 10 ⁻⁵	4.91 × 10 ⁻¹	1.45 × 10 ⁰ (+)	2.11 × 10 ¹	1.94 × 10 ⁻¹¹	3.81 × 10 ⁻¹¹ (+)	1.23 × 10 ⁻¹¹
F ₂	10	2.45 × 10 ⁻²⁴²	8.39 × 10 ⁻¹⁶¹	4.60 × 10 ⁻¹⁶⁰	1.07 × 10 ⁻¹⁷	2.07 × 10 ⁻⁶ (+)	1.13 × 10 ⁻⁵	3.99 × 10 ⁻⁴⁷	1.19 × 10 ⁻³³ (+)	6.54 × 10 ⁻³³	4.77 × 10 ⁻¹⁴⁸	4.15 × 10 ⁻¹⁴⁵ (+)	1.06 × 10 ⁻¹⁴⁴
	30	3.62 × 10 ⁻¹⁴¹	3.58 × 10 ⁻¹²⁶	1.25 × 10 ⁻¹²⁵	1.45 × 10 ⁻⁸	6.97 × 10 ⁻⁵ (+)	9.56 × 10 ⁻⁵	3.71 × 10 ⁻¹³	7.66 × 10 ⁻¹² (+)	1.62 × 10 ⁻¹¹	1.31 × 10 ⁻⁴⁵	8.54 × 10 ⁻⁴⁵ (+)	5.64 × 10 ⁻⁴⁵
	100	1.62 × 10 ⁻⁴²	2.59 × 10 ⁻³⁴	1.35 × 10 ⁻³³	4.58 × 10 ⁻³	1.71 × 10 ⁻¹ (+)	2.33 × 10 ⁻¹	4.79 × 10 ¹	6.45 × 10 ⁰ (+)	1.09 × 10 ¹	3.08 × 10 ²	3.61 × 10 ² (+)	2.60 × 10 ¹
F ₃	10	0	0	0	7.01 × 10 ⁻³⁵	6.70 × 10 ⁻²⁶ (+)	1.31 × 10 ⁻²⁵	6.76 × 10 ⁻⁸⁶	1.37 × 10 ⁻⁶⁷ (+)	7.50 × 10 ⁻⁶⁷	7.11 × 10 ⁻²⁶⁹	6.77 × 10 ⁻¹¹¹ (+)	3.71 × 10 ⁻¹¹⁰
	30	8.56 × 10 ⁻²¹⁵	8.56 × 10 ⁻²¹⁵	0	1.03 × 10 ⁻¹⁶	7.22 × 10 ⁻⁹ (+)	3.93 × 10 ⁻⁸	5.17 × 10 ⁻⁴⁰	3.53 × 10 ⁻³⁶ (+)	1.37 × 10 ⁻³⁵	7.57 × 10 ⁻⁸¹	1.76 × 10 ⁻⁷⁹ (+)	2.83 × 10 ⁻⁷⁹
	100	6.60 × 10 ⁻⁵⁷	4.43 × 10 ⁻⁵⁵	6.85 × 10 ⁻⁵⁵	5.35 × 10 ⁻⁵	2.54 × 10 ⁻³ (+)	5.91 × 10 ⁻³	2.39 × 10 ¹	4.99 × 10 ⁰ (+)	6.16 × 10 ³	9.99 × 10 ⁻¹⁰	1.62 × 10 ⁻⁹ (+)	4.90 × 10 ⁻¹⁰
F ₄	12	8.38 × 10 ⁻⁷	2.31 × 10 ⁻⁶	4.89 × 10 ⁻⁷	3.92 × 10 ⁻⁴	1.28 × 10 ⁻³ (+)	6.09 × 10 ⁻⁴	5.20 × 10 ⁻⁷	1.47 × 10 ⁻⁶ (-)	5.14 × 10 ⁻⁷	4.25 × 10 ⁻⁷	2.52 × 10 ⁻³ (+)	4.17 × 10 ⁻³
	32	1.62 × 10 ⁻⁷	3.65 × 10 ⁻⁷	1.09 × 10 ⁻⁷	6.14 × 10 ⁻⁴	4.21 × 10 ⁻³ (+)	2.38 × 10 ⁻³	2.31 × 10 ⁻⁴	3.56 × 10 ⁻⁴ (+)	9.31 × 10 ⁻⁵	2.00 × 10 ⁻⁴	5.02 × 10 ⁻⁴ (+)	4.21 × 10 ⁻⁴
	100	8.28 × 10 ⁻⁷	1.58 × 10 ⁻⁶	4.60 × 10 ⁻⁷	3.25 × 10 ⁻²	4.98 × 10 ⁻² (+)	1.52 × 10 ⁻²	2.40 × 10 ²	5.88 × 10 ² (+)	2.57 × 10 ²	3.66 × 10 ⁻²	5.74 × 10 ⁻² (+)	1.34 × 10 ⁻²
F ₅	10	0	0	0	1.14 × 10 ⁻¹³	8.87 × 10 ⁻⁷ (+)	4.46 × 10 ⁻⁶	1.44 × 10 ⁰	5.71 × 10 ⁰ (+)	2.28 × 10 ⁰	0	2.32 × 10 ⁻¹ (+)	4.28 × 10 ⁻¹
	30	0	2.19 × 10 ⁻¹³	4.15 × 10 ⁻¹⁴	2.38 × 10 ⁻⁷	1.38 × 10 ⁻¹ (+)	3.42 × 10 ⁻	1.17 × 10 ²	1.90 × 10 ² (+)	3.35 × 10 ¹	5.65 × 10 ¹	8.29 × 10 ¹ (+)	7.34 × 10 ⁰
	100	1.81 × 10 ⁻¹²	3.03 × 10 ⁻¹²	7.29 × 10 ⁻¹³	7.87 × 10 ⁻⁵	1.20 × 10 ⁰ (+)	1.56 × 10 ⁰	1.08 × 10 ³	1.23 × 10 ³ (+)	5.32 × 10 ¹	6.74 × 10 ²	7.16 × 10 ² (+)	1.82 × 10 ¹
F ₆	10	2.96 × 10 ⁻³	6.85 × 10 ⁻²	3.02 × 10 ⁻²	7.40 × 10 ⁻³	1.43 × 10 ⁻¹ (+)	9.36 × 10 ⁻²	5.34 × 10 ⁻¹	7.40 × 10 ⁻¹ (+)	1.08 × 10 ⁻¹	0	2.54 × 10 ⁻³ (-)	4.94 × 10 ⁻³
	30	0	3.78 × 10 ⁻¹³	1.72 × 10 ⁻¹³	3.23 × 10 ⁻¹⁰	3.77 × 10 ⁻² (+)	4.09 × 10 ⁻²	5.57 × 10 ⁰	8.58 × 10 ⁰ (+)	1.79 × 10 ⁰	0	0(-)	0
	100	3.63 × 10 ⁻¹²	6.00 × 10 ⁻¹²	1.18 × 10 ⁻¹²	1.01 × 10 ⁻⁷	1.00 × 10 ⁻² (+)	1.08 × 10 ⁻²	5.18 × 10 ²	6.38 × 10 ² (+)	7.65 × 10 ¹	1.25 × 10 ⁻¹¹	2.70 × 10 ⁻¹¹ (+)	9.68 × 10 ⁻¹²
F ₇	10	4.44 × 10 ⁻¹⁵	4.44 × 10 ⁻¹⁵	0	4.70 × 10 ⁻¹¹	9.06 × 10 ⁻⁷ (+)	2.87 × 10 ⁻⁶	8.88 × 10 ⁻¹⁶	4.32 × 10 ⁻¹⁵ (=)	6.48 × 10 ⁻¹⁶	0	3.20 × 10 ⁻¹⁵ (-)	1.08 × 10 ⁻¹⁵
	30	7.99 × 10 ⁻¹⁵	8.23 × 10 ⁻¹⁵	1.29 × 10 ⁻¹⁵	9.37 × 10 ⁻⁷	1.33 × 10 ⁻⁴ (+)	2.06 × 10 ⁻⁴	1.32 × 10 ⁻⁸	1.61 × 10 ⁻² (+)	8.81 × 10 ⁻²	3.55 × 10 ⁻¹⁵	3.55 × 10 ⁻¹⁵ (-)	0
	100	2.93 × 10 ⁻¹⁴	3.55 × 10 ⁻¹⁴	4.90 × 10 ⁻¹⁵	3.35 × 10 ⁻⁴	1.69 × 10 ⁻³ (+)	8.04 × 10 ⁻⁴	1.86 × 10 ¹	1.91 × 10 ¹ (+)	4.45 × 10 ⁻¹	7.24 × 10 ⁻⁷	1.07 × 10 ⁻⁶ (+)	1.94 × 10 ⁻⁷
F ₈	2	-1	-1	0	-1	-9.72 × 10 ⁻¹ (+)	3.21 × 10 ⁻²	-9.99 × 10 ⁻¹	-9.90 × 10 ⁻¹ (+)	1.97 × 10 ⁻²	-1	-9.95 × 10 ⁻¹ (+)	6.85 × 10 ⁻²
F ₉	2	0	0	0	0	8.90 × 10 ⁻¹⁴ (=)	3.39 × 10 ⁻¹³	3.64 × 10 ⁻¹¹	2.23 × 10 ⁻⁶ (+)	4.81 × 10 ⁻⁶	0	4.95 × 10 ⁻⁴ (+)	1.92 × 10 ⁻³
F ₁₀	2	-1.031628	-1.031628	0	-1.031628	-1.031628(+)	0	-1.031628	-1.03159(+)	4.85 × 10 ⁻⁵	-1.031628	1.38 × 10 ⁻¹⁴ (+)	7.54 × 10 ⁻¹⁴
+/-/=						23/0/1			22/1/1			21/3/0	

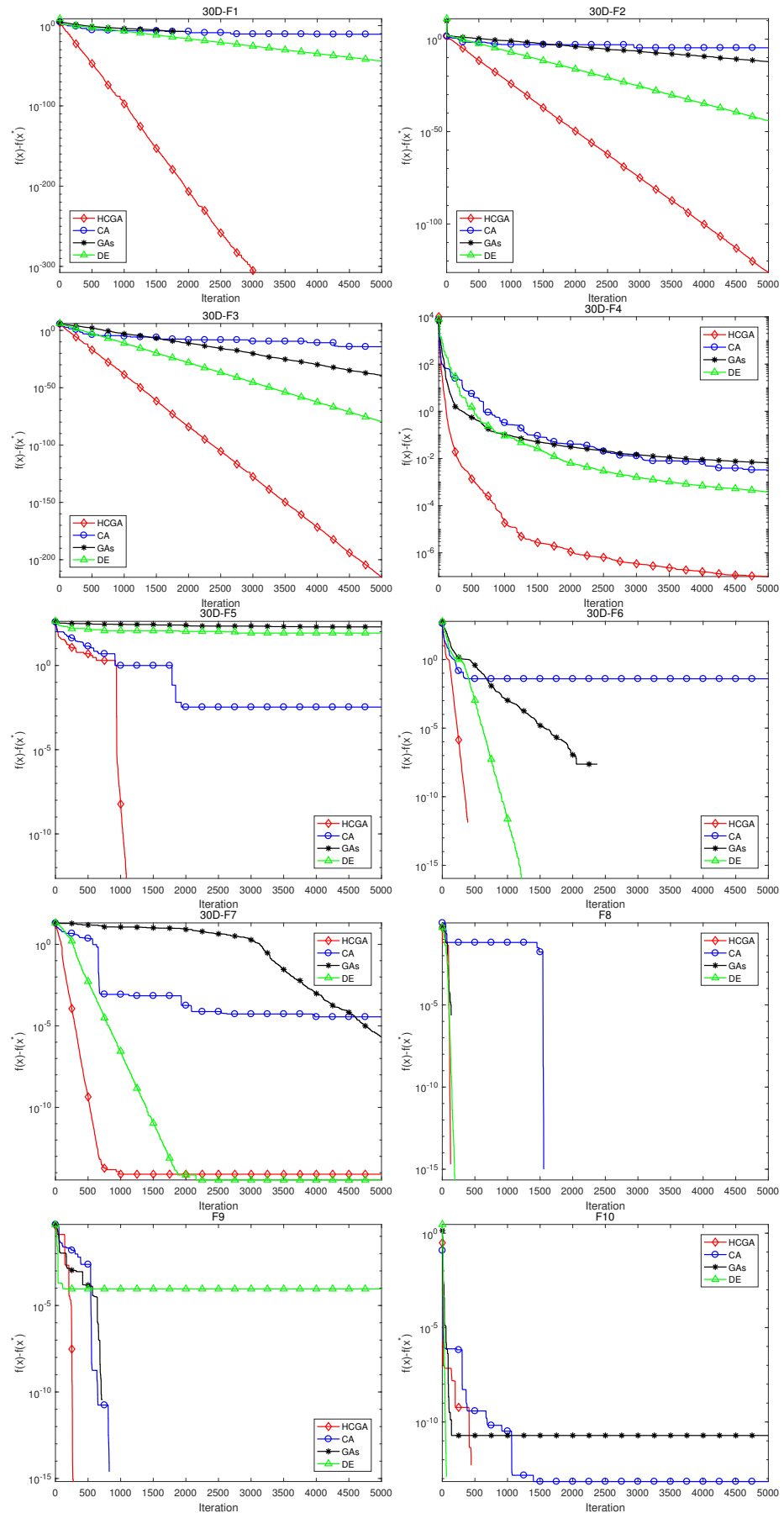


Figure 6. Convergence curves of the test functions.

4.3. Mechanistic Analysis of Improved Hybrid Algorithm Performance

Considering the benchmark function optimization results in Section 4.2, it is obvious that HCGA is superior compared to CA and GAs. The mechanistic analyses of improved hybrid algorithm performance are as follows:

- (1) Compared with the traditional CA population space with only a single mutation operator, HCGA uses GAs as a cultural framework for the population space evolution model, and the rich genetic operators of GAs can increase the population ergodicity and global exploration ability of the algorithm.
- (2) The belief space is constructed using situational knowledge, normative knowledge and historical knowledge, and used to guide the evolution of the population space, which effectively records the experience formed during the evolution of the algorithm and improves the evolutionary efficiency. The use of historical knowledge can also prevent the algorithm from falling into local optima to a certain extent.
- (3) A knowledge-guided t -mutation operator is developed to make the mutation step change adaptively with the evolutionary process, so that the algorithm can transition adaptively between global exploration and local exploitation. It does not depend on evolutionary generations but on population diversity to generate the adaptive step size. It can generate larger mutation steps in the early evolutionary stage, which increases the global exploration ability of the algorithm, and at the same time it can also avoid rapid loss of population diversity and make efficient use of the search space. It generates smaller mutation steps in the late evolutionary stage to enhance the local exploitation ability of the algorithm, which makes the algorithm converge rapidly.

The benchmark results obtained with mathematical functions and the above analysis demonstrate that HCGA is an efficient optimization algorithm with potential applications for complex optimization problems.

5. Applications to Aerodynamic Design Optimization of Wing Shapes

The aerodynamic shape optimization design of a wing is one of the important components of aircraft configuration design, and it has been the goal of researchers to design the aerodynamic shape of a wing for decades in terms of efficiency and quality to meet engineering objectives. Cruise factor is one of the most important aerodynamic characteristics that determine the performance of an aircraft. The objectives of this section are introducing and using HCGA for the aerodynamic design optimization of a wing to achieve the cruise factor optimization.

5.1. Parameterization Strategy

Airfoil parameterization is a crucial step in aerodynamic optimization, and its accuracy determines the accuracy and reliability of the optimized airfoil. The commonly used parameterization methods are the free-form deformation (FFD) technique [34], Bezier curves [35], the class/shape transformation (CST) method [36], etc. In this work, a four-order CST parameterization method is used to control the airfoil shape, and the parametric expressions of the upper and lower surface curves are defined in Equations (20) and (21).

The design variables are the leading-edge radius R_{le} of the airfoil, the inclination angles b_i and b'_i of the upper and lower surface curves at the trailing edge and the upper and lower surface shape function control parameters β and β' . For a total of nine airfoil design parameters, with the reference geometry being the RAE2822 airfoil, the design parameters and corresponding constraint ranges are shown in Table 8.

$$\frac{z}{c} = \sqrt{\frac{x}{c}}(1 - \frac{x}{c}) \left\{ \sqrt{\frac{2R_{le}}{c}}(1 - \frac{x}{c})^n + \tan \beta \left(\frac{x}{c}\right)^n + \sum_{i=1}^{n-1} \left[b_i \frac{n!}{i!(n-i)!} \left(\frac{x}{c}\right)^i (1 - \frac{x}{c})^{n-i} \right] \right\} \quad (20)$$

$$\frac{z}{c} = \sqrt{\frac{x}{c}}(1 - \frac{x}{c}) \left\{ -\sqrt{\frac{2R_{le}}{c}}(1 - \frac{x}{c})^n + \tan \beta' \left(\frac{x}{c}\right)^n - \sum_{i=1}^{n-1} \left[b'_i \frac{n!}{i!(n-i)!} \left(\frac{x}{c}\right)^i (1 - \frac{x}{c})^{n-i} \right] \right\} \quad (21)$$

Table 8. Range of design parameter.

Parameter	Range
R_{le}/c	(0.004, 0.012)
$\beta(rad)$	(0.14, 0.28)
$\beta'(rad)$	(0.00, 0.14)
b_1/c	(0.05, 0.20)
b_2/c	(0.10, 0.30)
b_3/c	(0.10, 0.30)
b'_1/c	(0.05, 0.30)
b'_2/c	(0.05, 0.30)

5.2. Wing Shape Optimization

In this design, eight sections were used to describe the whole wing geometry for its shape optimization, its configuration and control surface distribution, as shown in Figure 7. The parameterization method described in Section 5.1 was used to control the wing shape, with a total of 72 design variables. The optimal design of the wing for the cruise factor was considered in the cruising condition at the flow condition of Mach 0.785, a 1.92° angle of attack and a Reynolds number of 2×10^7 based on the aerodynamic mean chord. HCGA was used to optimize the shape with a population size of 150 and evolutionary iterations of 100. The objective was to maximize the cruise factor, and the constraints were that the maximum thickness of each control surface and the lift coefficient should not to be reduced. The mathematical optimization model is described as follows:

$$max : f(x) = Ma \frac{L}{D} \tag{22}$$

$$s.t : t_i \geq t_{Initial} (i = 1, 2, \dots, 8), C_L \geq C_{L0} \tag{23}$$

where Ma is Mach number, L is lift, D is drag, t_i is the maximum thickness of the i th section, $t_{initial}$ is the maximum thickness of the initial control surface, C_L is the lift coefficient and C_{L0} is the lift coefficient of the initial wing. The flow was modeled by the compressible full potential flow with viscous boundary layer correction, and the total number of mesh points was about 0.5 million. The pressure coefficient contours on the upper and lower surface of the initial and optimized wing are shown in Figure 8. The respective pressure distributions at each section are shown in Figure 9 and the wing section shapes before and after optimization are compared in Figure 10. It is seen that the shock waves were significantly smeared owing to the shape modification, which resulted in a considerable reduction of wave drag on the upper surface and therefore in better aerodynamic performance. The aerodynamic parameters of the wing before and after optimization are shown in Table 9. The cruise factor $Ma \times L/D$ was significantly increased from 21.863 to 26.938 because the drag coefficient C_D of the optimized wing was obviously reduced from 0.01605 to 0.01302. It can be seen that the cruise factor increased by 23.21%, while the drag coefficient decreased by 18.88% and the constraints of lift coefficient and thickness were satisfied. There was also no significant change in the induced drag coefficient C_{DIND} since there was no change in the lift coefficient C_L . The wave drag coefficient C_{Dwave} of the wing was reduced apparently from 0.00240 to 0.00030, and the profile drag coefficient C_{DPP} was also reduced from 0.00680 to 0.00602.

Table 9. Comparison of airfoil aerodynamic parameters.

	C_L	C_D	C_{Dwave}	C_{DPP}	C_{DIND}	$Ma \frac{L}{D}$
Baseline	0.447	0.01605	0.0024	0.0068	0.00685	21.863
Optimized	0.447	0.01302	0.0003	0.00602	0.0067	26.938
$\Delta(\%)$	0	-0.00303 (-18.88%)	-0.00210 (-87.50%)	-0.00078 (-11.47%)	-0.00015 (-2.19%)	5.075 (+23.21%)

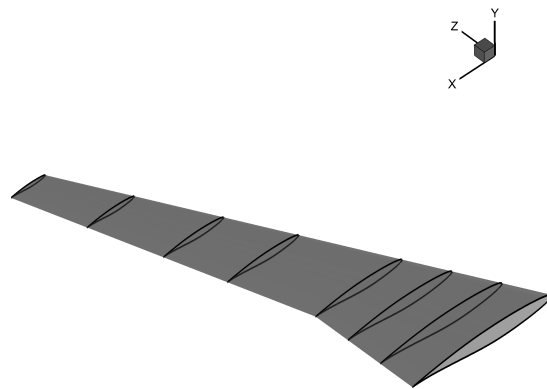


Figure 7. Distribution of the wing sections.

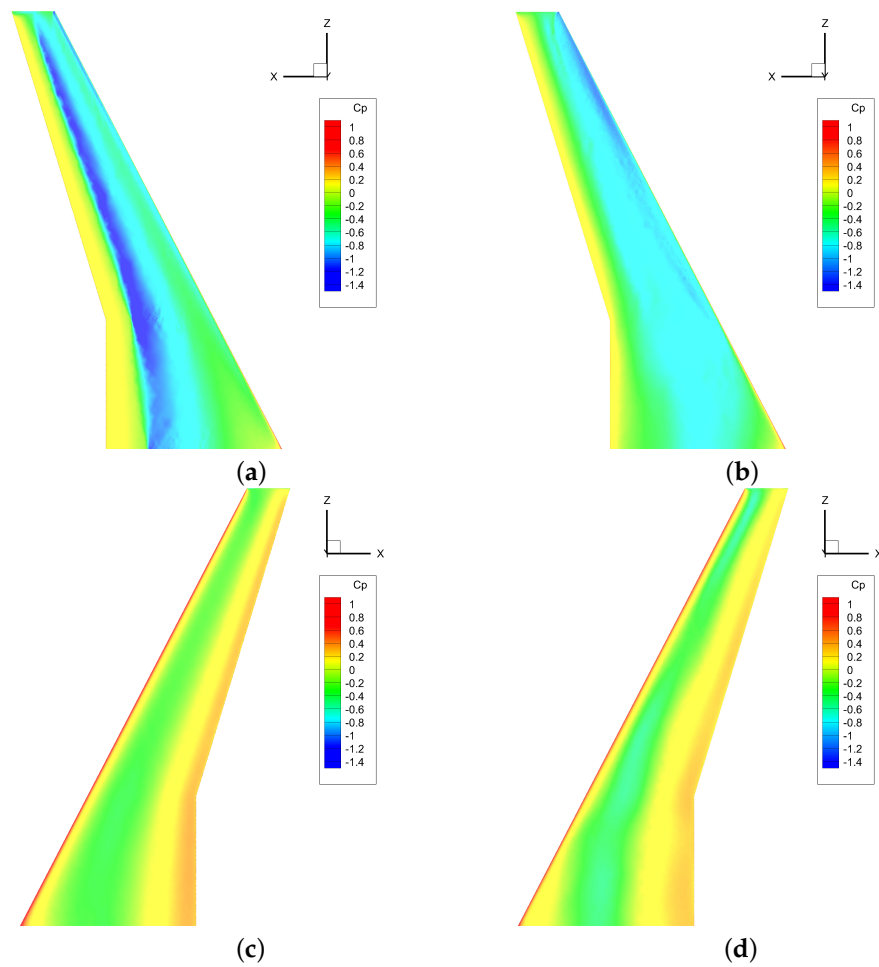


Figure 8. (a) Pressure coefficient contours on the wing upper surface of the initial wing; (b) Pressure coefficient contours on the wing upper surface of the optimized wing; (c) Pressure coefficient contours on the wing lower surface of the initial wing; (d) Pressure coefficient contours on the wing lower surface of the optimized wing.

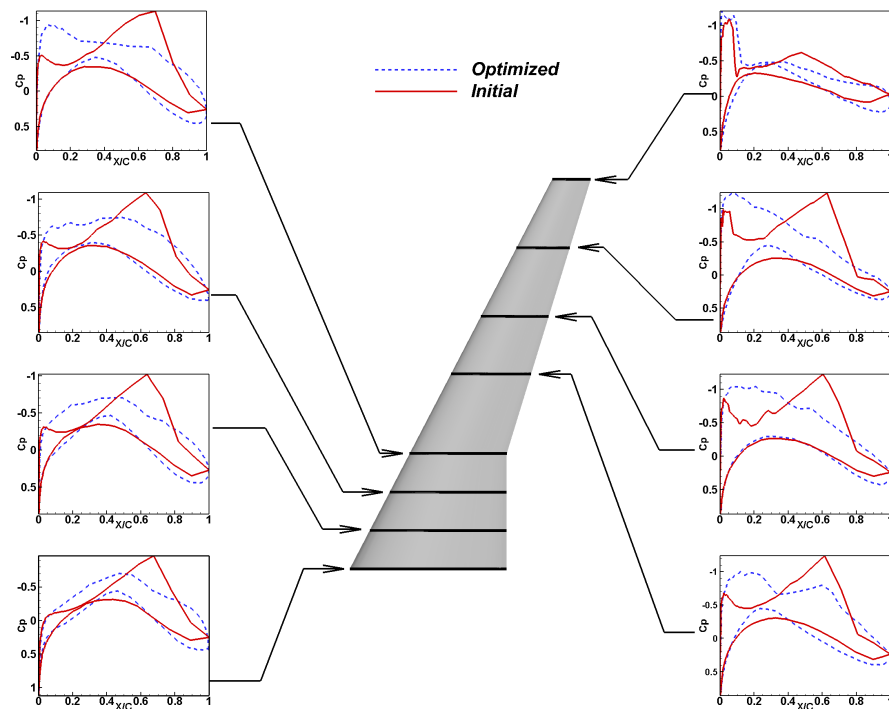


Figure 9. Comparison of surface pressure coefficient distributions for initial and optimized wings.

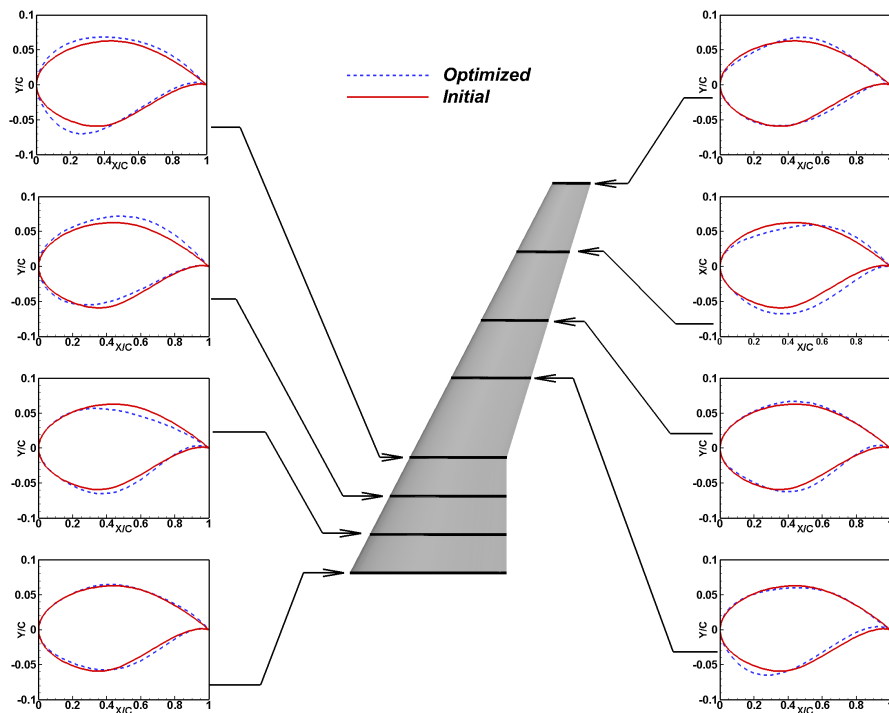


Figure 10. Comparison of initial and optimized wing-section shapes.

For a better comparison of values with the proposed HCGA algorithm in this engineering application, the commonly used GAs [11] and PSO [37] of the engineering optimization field were selected for comparison with HCGA. The parameter settings of HCGA were the same as for the numerical experiment, and all parameters of GAs and PSO were default parameters. The population size and maximum number of iterations for all three algorithms were 150 and 100, respectively. The cruise factor convergence curve is shown in Figure 11.

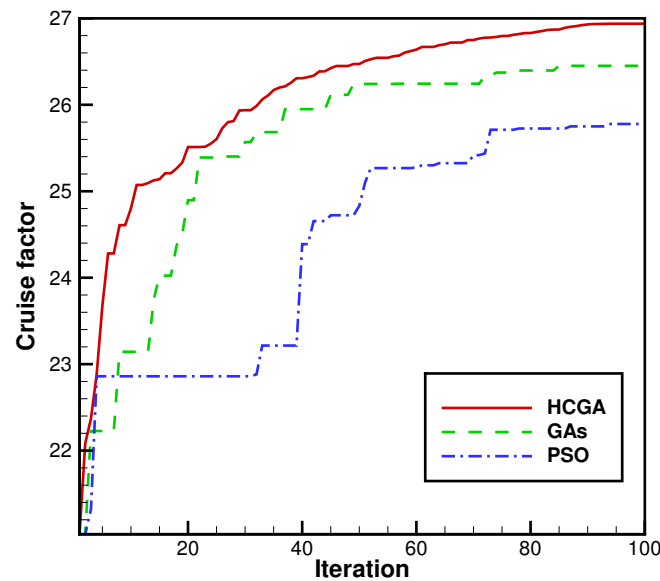


Figure 11. Convergence curves of cruising factor.

It can be seen that the optimization results of HCGA were significantly better than those of GAs and PSO for the same number of iterations. It can be observed that HCGA is obviously a more efficient algorithm for aerodynamic optimization problems, which can achieve better-quality optimized results with fewer flow field calculations and can significantly improve the efficiency of aerodynamic optimization.

6. Conclusions

In this paper, an efficient hybrid evolutionary optimization method coupling CA with GAs (HCGA) was proposed to improve the efficiency of the optimization procedure for the aerodynamic shape of an aircraft. HCGA aims to improve the ability to solve complex problems and increase the efficiency of optimization. To improve the robustness of the algorithm, HCGA uses GAs as an evolutionary model of the population space. HCGA constructs the belief space using three kinds of knowledge: situational knowledge, normative knowledge and historical knowledge. Meanwhile, the knowledge-guided t -mutation operator was developed to dynamically adjust the mutation step and balance the exploitation and exploration ability of the algorithm. The optimization performance of HCGA was demonstrated on many benchmark functions for which the global optima are known a priori. The optimization results obtained with the benchmark functions show that HCGA provides a better global convergence, a better convergence speed and a better optimization accuracy compared to CA and GAs. In particular, HCGA shows the potential for solving large-scale design variable optimization problems.

By combining HCGA with a CFD solver, an efficient decision-maker design tool for aerodynamic shape design optimization was developed to find the best aerodynamic shape to satisfy the design requirements. For the three-dimensional wing design problem, the proposed HCGA optimizer successfully reduced the wing drag computerized design, thus significantly improving the wing cruise factor. Compared with the baseline wing, the drag coefficient was reduced by 18.88%, which resulted in a 23.21% improvement in the cruise factor. This proves the capability and potential of HCGA for solving complex engineering design problems in aerodynamics. As a practical engineering application of the super-heuristic algorithm, the potential and value of such algorithms for engineering applications are further validated.

However, this study is only preliminary and further testing is needed to evaluate the performance of HCGA in complex engineering optimization. In addition, the practi-

cal application of HCGA only considered single-objective optimization. Multi-objective optimization problems should thus be the next step for investigation in future research.

Author Contributions: The contributions of the five authors in this paper are conceptualization, X.Z., Z.T. and J.P.; methodology, X.Z. and Z.T.; formal analysis, X.Z., Z.T. and F.C.; investigation, X.Z. and Z.T.; resources, F.C. and C.Z.; data curation, X.Z. and Z.T.; writing—original draft preparation, X.Z. and Z.T.; writing—review and editing, X.Z. and Z.T.; supervision, Z.T.; project administration, C.Z.; funding acquisition, Z.T. All authors have read and agreed to the published version of the manuscript.

Funding: This work was funded by the National Natural Science Foundation of China (NSFC-12032011, 11772154) and the Fundamental Research Funds for the Central Universities (NP2020102).

Institutional Review Board Statement: Not applicable.

Informed Consent Statement: Not applicable.

Data Availability Statement: The figures, tables and data that support the findings of this study are mentioned in the corresponding notes, with reference numbers and sources, and are publicly available in the repository.

Conflicts of Interest: The authors declare no potential conflicts of interest with respect to the research, authorship and/or publication of this article.

References

1. Tian, X.; Li, J. A novel improved fruit fly optimization algorithm for aerodynamic shape design optimization. *Knowl.-Based Syst.* **2019**, *179*, 77–91. [CrossRef]
2. Tang, Z.; Hu, X.; Périaux, J. Multi-level hybridized optimization methods coupling local search deterministic and global search evolutionary algorithms. *Arch. Comput. Methods Eng.* **2020**, *27*, 939–975. [CrossRef]
3. Jameson, A. Aerodynamic design via control theory. *J. Sci. Comput.* **1988**, *3*, 233–260. [CrossRef]
4. Lee, B.J.; Kim, C. Aerodynamic redesign using discrete adjoint approach on overset mesh system. *J. Aircr.* **2008**, *45*, 1643–1653. [CrossRef]
5. Luo, J.Q.; Xiong, J.T.; Liu, F. Aerodynamic design optimization by using a continuous adjoint method. *Sci. China Phys. Mech. Astron.* **2014**, *57*, 1363–1375. [CrossRef]
6. Antunes, A.P.; Azevedo, J.L.F. Studies in aerodynamic optimization based on genetic algorithms. *J. Aircr.* **2014**, *51*, 1002–1012. [CrossRef]
7. Mi, B.; Cheng, S.; Luo, Y.; Fan, H. A new many-objective aerodynamic optimization method for symmetrical elliptic airfoils by PSO and direct-manipulation-based parametric mesh deformation. *Aerosp. Sci. Technol.* **2022**, *120*, 107296. [CrossRef]
8. Bashir, M.; Longtin-Martel, S.; Botez, R.M.; Wong, T. Aerodynamic Design Optimization of a Morphing Leading Edge and Trailing Edge Airfoil-Application on the UAS-S45. *Appl. Sci.* **2021**, *11*, 1664. [CrossRef]
9. Zijiang, L.I.U.; Xuejun, L.I.U.; Xinye, C.A.I. A new hybrid aerodynamic optimization framework based on differential evolution and invasive weed optimization. *Chin. J. Aeronaut.* **2018**, *31*, 1437–1448.
10. Duan, Y.; Cai, J.; Li, Y. Gappy proper orthogonal decomposition-based two-step optimization for airfoil design. *AIAA J.* **2012**, *50*, 968–971. [CrossRef]
11. Sugisaka, M.; Fan, X. Adaptive genetic algorithm with a cooperative mode. In Proceedings of the 2001 IEEE International Symposium on Industrial Electronics Proceedings (Cat. No. 01TH8570), Pusan, Korea, 12–16 June 2001; IEEE: Piscataway, NJ, USA, 2001; Volume 3, pp. 1941–1945.
12. Srinivas, M.; Patnaik, L.M. Adaptive probabilities of crossover and mutation in genetic algorithms. *IEEE Trans. Syst. Man, Cybern.* **1994**, *24*, 656–667. [CrossRef]
13. Herrera, F.; Lozano, M. Adaptive genetic operators based on coevolution with fuzzy behaviors. *IEEE Trans. Evol. Comput.* **2001**, *5*, 149–165. [CrossRef]
14. Dong, H.; Li, T.; Ding, R.; Sun, J. A novel hybrid genetic algorithm with granular information for feature selection and optimization. *Appl. Soft Comput.* **2018**, *65*, 33–46. [CrossRef]
15. Li, X.; Gao, L.; Pan, Q.; Wan, L. An effective hybrid genetic algorithm and variable neighborhood search for integrated process planning and scheduling in a packaging machine workshop. *IEEE Trans. Syst. Man Cybern. Syst.* **2018**, *49*, 1933–1945. [CrossRef]
16. Reynolds, R.G. An introduction to cultural algorithms. In Proceedings of the Third Annual Conference on Evolutionary Pro-Gramming, San Diego, CA, USA, 24–26 February 1994; World Scientific: River Edge, NJ, USA, 1994; pp. 131–139.
17. dos Santos Coelho, L.; Souza, R.C.T.; Mariani, V.C. Improved differential evolution approach based on cultural algorithm and diversity measure applied to solve economic load dispatch problems. *Math. Comput. Simul.* **2009**, *79*, 3136–3147. [CrossRef]
18. Sun, Y.; Zhang, L.; Gu, X. A hybrid co-evolutionary cultural algorithm based on particle swarm optimization for solving global optimization problems. *Neurocomputing* **2012**, *98*, 76–89. [CrossRef]

19. Gao, F.; Liu, H.; Zhao, Q.; Cui, J. Hybrid model of genetic algorithms and cultural algorithms for optimization problem. In Proceedings of the Asia-Pacific Conference on Simulated Evolution and Learning, Hefei, China, 15–18 October 2006; Springer: Berlin/Heidelberg, Germany, 2006; pp. 441–448.
20. Azad, P.; Navimipour, N.J. An energy-aware task scheduling in the cloud computing using a hybrid cultural and ant colony optimization algorithm. *Int. J. Cloud Appl. Comput. (IJCAC)* **2017**, *7*, 20–40. [CrossRef]
21. Wang, X.; Hao, W.; Li, Q. An adaptive cultural algorithm with improved quantum-behaved particle swarm optimization for sonar image detection. *Sci. Rep.* **2017**, *7*, 1–16.
22. Awad, N.H.; Ali, M.Z.; Suganthan, P.N.; Reynolds, R.G. CADE: A hybridization of cultural algorithm and differential evolution for numerical optimization. *Inf. Sci.* **2017**, *378*, 215–241. [CrossRef]
23. Deng, L.; Yang, P.; Liu, W. Artificial Immune Network Clustering Based on a Cultural Algorithm. *EURASIP J. Wirel. Commun. Netw.* **2020**, *2020*, 168. [CrossRef]
24. Kulkarni, V.R.; Desai, V. Sensor Localization in Wireless Sensor Networks Using Cultural Algorithm. *Int. J. Swarm Intell. Res. (IJSIR)* **2020**, *11*, 106–122. [CrossRef]
25. Abdolrazzagh-Nezhad, M.; Radgozar, H.; Salimian, S.N. Enhanced cultural algorithm to solve multi-objective attribute reduction based on rough set theory. *Math. Comput. Simul.* **2020**, *170*, 332–350. [CrossRef]
26. Awad, N.H.; Ali, M.Z.; Duwairi, R.M. Cultural algorithm with improved local search for optimization problems. In Proceedings of the 2013 IEEE Congress on Evolutionary Computation, Cancun, Mexico, 20–23 June 2013; IEEE: Piscataway, NJ, USA, 2013; pp. 284–291.
27. Xue, H. Adaptive Cultural Algorithm-Based Cuckoo Search for Time-Dependent Vehicle Routing Problem with Stochastic Customers Using Adaptive Fractional Kalman Speed Prediction. *Math. Probl. Eng.* **2020**, *2020*, 7258780. [CrossRef]
28. Reynolds, R.G. The cultural algorithm: Culture on the edge of chaos. In *Culture on the Edge of Chaos*; Springer: Cham, Switzerland, 2018; pp. 1–11.
29. Ali, M.Z.; Awad, N.H.; Suganthan, P.N.; Reynolds, R.G. A modified cultural algorithm with a balanced performance for the differential evolution frameworks. *Knowl.-Based Syst.* **2016**, *111*, 73–86. [CrossRef]
30. Chung, C.J. *Knowledge-Based Approaches to Self-Adaptation in Cultural Algorithms*; Wayne State University: Detroit, MI, USA, 1997.
31. Saleem, S.M. *Knowledge-Based Solution to Dynamic Optimization Problems Using Cultural Algorithms*; Wayne State University: Detroit, MI, USA, 2001.
32. Becerra, R.L.; Coello, C.A.C. Culturizing differential evolution for constrained optimization. In Proceedings of the Fifth Mexican International Conference in Computer Science, ENC 2004, Colima, Mexico, 24 September 2004; IEEE: Piscataway, NJ, USA, 2004; pp. 304–311.
33. Opara, K.R.; Arabas, J. Differential Evolution: A survey of theoretical analyses. *Swarm Evol. Comput.* **2019**, *44*, 546–558. [CrossRef]
34. Samareh, J. Aerodynamic shape optimization based on free-form deformation. In Proceedings of the 10th AIAA/ISSMO Multidisciplinary Analysis and Optimization Conference, Albany, NY, USA, 30 August–1 September 2004; p. 4630.
35. Andersson, F.; Kvernes, B. *Bezier and B-Spline Technology*; Umea University Sweden: Umea, Sweden, 2003.
36. Straathof, M.H.; van Tooren, M.J.L. Extension to the class-shape-transformation method based on B-splines. *AIAA J.* **2011**, *49*, 780–790. [CrossRef]
37. Kennedy, J.; Eberhart, R. Particle swarm optimization. In Proceedings of the ICNN'95-International Conference on Neural Networks, Perth, WA, USA, 27 November–1 December 1995; IEEE: Piscataway, NJ, USA, 1995; Volume 4, pp. 1942–1948.

Review

A Review of Flow Control for Gust Load Alleviation

Yonghong Li ^{1,2} and Ning Qin ^{1,*}¹ Department of Mechanical Engineering, The University of Sheffield, Sheffield S1 3JD, UK² High Speed Aerodynamic Institute, China Aerodynamic Research and Development Center, Mianyang 621000, China

* Correspondence: n.qin@sheffield.ac.uk

Featured Application: Gust load control, aircraft weight reduction, aircraft drag reduction.

Abstract: Effective control of aerodynamic loads, such as maneuvering load and gust load, allows for reduced structural weight and therefore greater aerodynamic efficiency. After a basic introduction in the types of gusts and the current gust load control strategies for aircraft, we outline the conventional gust load alleviation techniques using trailing-edge flaps and spoilers. As these devices also function as high-lift devices or inflight speed brakes, they are often too heavy for high-frequency activations such as control surfaces. Non-conventional active control devices via fluidic actuators have attracted some attention recently from researchers to explore more effective gust load alleviation techniques against traditional flaps for future aircraft design. Research progress of flow control using fluidic actuators, including surface jet blowing and circulation control (CC) for gust load alleviation, is reviewed in detail here. Their load control capabilities in terms of lift force modulations are outlined and compared. Also reviewed are the flow control performances of these fluidic actuators under gust conditions. Experiments and numerical efforts indicated that both CC and surface jet blowing demonstrate fast response characteristics, capable for timely adaptive gust load controls.

Keywords: gust load alleviation; active flow control; blowing jet control; circulation control

Citation: Li, Y.; Qin, N. A Review of Flow Control for Gust Load Alleviation. *Appl. Sci.* **2022**, *12*, 10537. <https://doi.org/10.3390/app122010537>

Academic Editor: Josep Maria Bergada

Received: 26 September 2022

Accepted: 17 October 2022

Published: 19 October 2022

Publisher's Note: MDPI stays neutral with regard to jurisdictional claims in published maps and institutional affiliations.



Copyright: © 2022 by the authors. Licensee MDPI, Basel, Switzerland. This article is an open access article distributed under the terms and conditions of the Creative Commons Attribution (CC BY) license (<https://creativecommons.org/licenses/by/4.0/>).

1. Introduction

It is undeniable that air travel makes fast long-distance transportation possible and brings significant economic growth and improvement of quality of life. However, in the meantime, the negative impacts on the environment and climate [1] have become more and more pronounced and have posed a significant challenge to the aviation industry. For economic and ecological considerations, reduction in fuel consumption and exhaust emissions is very urgent task for future air transportation. For this purpose, the aviation industry is facing stringent 'Green Aviation' goals in their future product. For example, the primary goal of Europe's Flight-path 2050 is to reduce CO₂ emissions of aircraft by 75% relative to 2005 levels [2]. In the US, the N+3 goal proposed by NASA is to reduce Nitrogen oxides (NO_x) emission by up to 80% in the landing-take-off process and reduce fuel burn by 60% for an airliner entering service in 2030–2035 [3]. To achieve these objectives, a number of technologies, such as shock control [4–7], laminar flow control [8–14], turbulent drag reduction [15–18], as well as novel aircraft concepts, such as BWB or hybrid wing body (HWB) [19], 'double-bubble' [20], truss-braced wing (TBW) [21] and box-wing [22], have been proposed and investigated to explore a better aerodynamic performance. However, there are significant challenges in applying these technologies mentioned above on future aircraft, especially in terms of practical application. Meanwhile, with the increasing development and maturity in computational fluid dynamics (CFD) and aerodynamic design optimization, the aerodynamic efficiency of modern swept supercritical wings has almost reached its limit with diminishing return from large research investment. Therefore, it is urgent to explore game-changing technologies for drag reduction associated with the

reduction in exhaust emissions. Load control is an important topic in aerodynamics, as it can potentially provide an alternative way for drag reduction through decreasing the aircraft structure weight. Figure 1 shows the relationship among flow control, load control, aerodynamic performance and energy efficiency. It is well known that the structure mass is not determined by the cruise condition but the critical load cases such as gust and manoeuvring loads. Guo et al. [23] highlighted that the gust loads can be larger than the manoeuvring loads, and generate the most critical load cases that some aircraft will experience in flight. Figure 2 demonstrates the spanwise load distributions on a typical civil transport aircraft under cruise and gust encountering conditions, respectively.

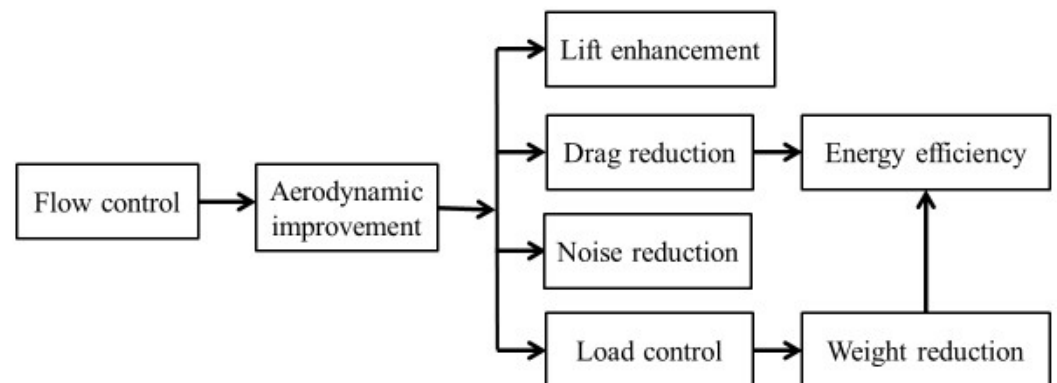


Figure 1. Relationship among flow control, load control and energy efficiency.

Compared to the cruise condition, the spanwise loading especially on the wing experiences a significant increase when the aircraft encounters a gust. This increase will affect the riding comfort of the passengers, and sometimes can be detrimental for the aircraft structure safety if the gust load is severe enough. For the safety of large commercial aircraft, airworthiness authorities have specified typical gust models as a requirement for the certification specifications of large commercial aircraft covered by European Union Aviation Safety Agency Certification Specifications (EASA CS-25) [24].

To cope with these critical load cases, aircraft structures need to withstand the forces and stress caused by gusts with a large amount of mass penalty, since it is challenging to build the structure that is both light and robust. However, if the load can be effectively alleviated through a control means, lighter structures may be used, resulting in the reduction in lift-induced drag and fuel consumption as shown in Figure 1. In the late 1970s, flaps, spoilers and ailerons were investigated to perform the additional task for gust load alleviation. Gust load alleviation (GLA) systems were studied and tested. The first commercial airplane to incorporate a GLA system using ailerons is the Tristar L-1011 from the 1980s [25] after the successful implementation of GLA technology on C-5A [26]. The effectiveness of GLA systems consisting ailerons and spoilers were tested on Airbus A300 [27] and firstly implemented on Airbus A320 [28]. The implementation of a GLA system on the Airbus A300 was shown to mitigate gust load significantly [25]. A baseline wing of a transonic transport aircraft integrated with a GLA system can lead to a reduction in the direct operating cost of nearly 6% and fuel savings of 9% [29]. A 15% wing root bending moment was relieved by the GLA system during unsteady wind encounters on A320 [28].

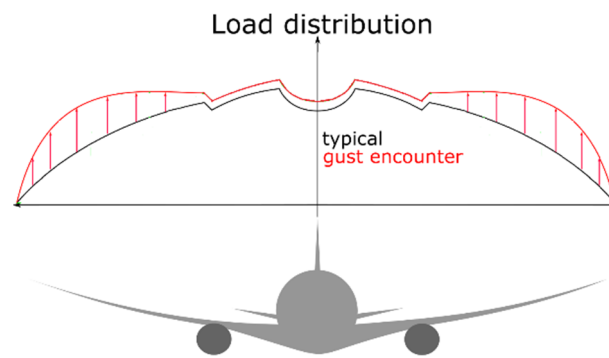


Figure 2. The sketch of the spanwise load distributions under cruise and gust encountering conditions (from [30]).

Currently, for gust load alleviation, active control flaps are deflected to create forces and moments to attenuate gust loads. Ailerons, elevators or spoilers are normally used as the control surfaces for gust load alleviation. Fluidic actuators, such as blowing or suction, synthetic jets and oscillating jets, have been studied for many decades in the field of active aerodynamic flow control. Most of the studies focused on changing the momentum balance in the boundary layer to achieve aerodynamic improvement, such as lift augmentation, drag reduction and stall delay.

Recently, there have been renewed interest in fluidic actuators for their potential application for modern aircraft flight control. Being able to fly and control aircraft without conventional control surfaces (namely flapless control) is one of the targets for future aircraft design with benefits including fewer moving parts, possibly less weight [31], less maintenance and enhanced stealth characteristics [32]. Apart from the steady load control capability, the dynamic responses of these fluidic actuators for unsteady load control, such as gust load, are the key factor for successively replacing the traditional flaps for flight control.

This paper focuses on an overview of the research progress of flow control on gust load alleviation. Gust load definitions and the types of gusts aircraft may be subjected to are introduced. Current gust load alleviation techniques are discussed, followed by a focus on the overview of the studies on gust load alleviation by fluidic actuators including the surface jet blowing and circulation control via Coanda effect. The effects on gust load alleviation through traditional flaps and fluidic actuators are compared and discussed.

2. Basics of Gust Load Alleviation

2.1. Gust Load Definition

Gust, being a complicated phenomenon, is often referred to as atmospheric turbulence. The following two idealized categories of gusts are generally considered in industry for aircraft design, namely [33]: (1) Discrete gusts: the instantaneous gust velocity profile is usually defined by a deterministic form, such as ‘one-minus-cosine’ and ‘sharp-edged’ shapes and (2) Continuous turbulence: the gust velocity varies randomly.

2.1.1. Discrete Gusts

‘One-minus-cosine’ gust is the typical discrete gust defined by the certification specifications of large commercial aircraft covered by the EASA CS-25 [24]. The gust profile is shown in Equation (1) and according to EASA CS-25, the gust shape can be expressed as

$$w_g(x_g) = \frac{w_{g0}}{2} \left(1 - \cos\left(\frac{2\pi x_g}{L_g}\right) \right), \quad 0 \leq x_g \leq L_g \quad (1)$$

where, w_{g0} is the magnitude of the peak gust velocity; L_g is the gust wavelength or twice the ‘gust gradient’ H_g . According to EASA CS-25, the gust wavelength is in the range from 9 to 107 m. In practice, the typical value is $12.5 \bar{c}$ (\bar{c} is the mean aerodynamic chord length).

The design gust velocity w_{g0} changes with gust wavelength and altitude which is expressed in relations of the gust gradient H_g (in m), the reference gust velocity w_{ref} and the flight profile alleviation factor F_g , as

$$w_{g0} = w_{ref} F_g \left(\frac{H_g}{106.17} \right)^{\frac{1}{6}} \quad (2)$$

where, w_{ref} decreases linearly from 17.07 m/s equivalent airspeed (EAS) at sea level to 13.41 m/s EAS at 4572 m and then again to 6.36 m/s EAS at 18,288 m. The flight profile alleviation factor F_g is related to the aircraft weight and the maximum operating altitude [33].

$$F_g = \frac{1}{2} [F_{gz} + F_{gm}] = \frac{1}{2} \left[\left(1 - \frac{Z_{m0}}{76,200} \right) + \sqrt{R_2 \tan \left(\frac{\pi R_1}{4} \right)} \right] \quad (3)$$

$$R_1 = \frac{W_{MLW}}{W_{MTOW}}, \quad R_2 = \frac{W_{MZFW}}{W_{MTOW}} \quad (4)$$

where, Z_{m0} is the maximum operating altitude, W_{MLW} is the maximum landing weight, W_{MZFW} is the maximum zero-fuel weight and W_{MTOW} is the maximum take-off weight.

Assuming an aircraft cruising with the speed U_∞ and encountering a one-minus-cosine gust, the gust penetrating distance is $x_g = U_\infty t$, and Equation (1) can be rewritten as

$$w_g(x_g) = \frac{w_{g0}}{2} \left(1 - \cos \left(\frac{2\pi U_\infty t}{L_g} \right) \right) = \frac{w_{g0}}{2} (1 - \cos(\omega t)) \quad (5)$$

An equivalent gust frequency can be obtained as $\omega = \frac{2\pi U_\infty}{L_g}$ in radians or $\omega = \frac{U_\infty}{L_g}$ in Hz.

2.1.2. Continuous Gusts

Unlike the discrete gusts with a deterministic-form gust velocity profile, the continuous gust velocity varies randomly. The spectrum is normally expressed as a power spectral density as:

$$\Phi(\omega) = \sigma^2 \frac{L_g}{\pi} \frac{1 + \frac{8}{3} (1.339 L_g \omega)^2}{\pi [1 + (1.339 L_g \omega)^2]^{11/6}} \quad (6)$$

where, the typical wavelength of the continuous gust is defined in EASA CS-25 [24] as 762 m and the frequency is given by ω , rad/m. σ is the root mean square value representing the fluctuations of the gust velocity.

2.2. Gust Load Control Strategies

As mentioned previously, flaps, such as ailerons, elevators or spoilers are normally used as the control surfaces for gust load alleviation. A complete gust load control system includes controllers, actuators and sensors. This control system is commonly called as Gust Load Alleviation (GLA) system. Sensors, such as air data sensors and accelerometers, are located on the aircraft body or wing to sense the incoming wind conditions and to provide feedback of dynamic loads. The general principle of gust load alleviation is to use sensors to provide motion feedback signals for the controllers. The controllers then initiate corresponding deflections of the control surfaces to create the aerodynamic forces and moments needed for attenuating the extra load induced by the gusts. Activating the control surfaces timely can determine the effectiveness of a GLA strategy. Detection of incoming gusts ahead of the aircraft to create a feedforward input is important. This provides control surfaces with additional time to respond. Currently, to compensate the lag of the control surface, it is common to locate the sensors ahead of the wings, along the fuselage, to provide the hydraulic actuators longer time to respond. A high-resolution

direct-measuring short-pulse ultraviolet (UV) Doppler lidar system was designed and tested on an Airbus A340 [34]. It was shown that a forward detection range of 50 m of the atmosphere disturbances was achieved, which translates to a lead time of 300 ms for control surfaces to perform.

Control methods can be categorized as either passive or active. Currently, the widely used gust load control system is active. Passive gust load control devices are more attractive as no extra energies are required compared to the active ones, and initial research has been conducted as being introduced in the following section. Open and closed-loop controls are commonly used by the GLA system. Closed-loop control utilizes feedback to compare the actual output with the desired output. For a successful closed-loop control system, the effective control laws [35,36] play an important role. Various control laws for GLA system have been investigated, such as the linear quadratic regulator theory [37,38], linear quadratic Gaussian method [39,40], and optimal control algorithms [41]. As this article focuses on the overview of the flow control devices for gust load alleviation, the progress in the control laws will not be covered further here.

3. Flow Control Devices for Gust Load Alleviation

Flow control devices for gust load alleviation are categorized into two parts here, i.e., control surfaces or control flaps and fluidic actuators. As being discussed in the following section, traditional control flaps have been revealed to be ineffective for typical high-frequency gust load controls [42,43]. More effective and novel gust load alleviation methods with fast response, such as passive control methods with control surfaces and active control methods using fluidic actuators have been explored and investigated.

3.1. Traditional Control Surfaces

The research on GLA systems was initially motivated by aircraft manufacturers to find ways for structural weight reduction so as to improve fuel efficiency. In 1975, the Lockheed-Georgia Company incorporated a GLA system using wing-outboard ailerons on the C-5A military aircraft. As shown in the flight tests, approximately half of the wing root bending moments was reduced under gust conditions. The dramatic effectiveness and benefits of the GLA system shown on C-5A attracted much attention of the commercial aircraft manufacturers. Later, the GLA system using ailerons was installed on Tristar L-1011 from the 1980s [25], making it the first commercial airplane to incorporate a GLA system. Implementation of a gust load alleviation system incorporating ailerons, spoilers and elevators was then studied for Airbus A300. The effectiveness of different control surfaces was investigated.

3.1.1. Trailing-Edge Flaps

Trailing-edge flaps, known as plain flaps such as ailerons and elevators encompass the aft portion of the wing [44]. The trailing-edge flaps operate by rotating up or down to achieve a desired change in camber, and thus results in a desired change in lift [45]. Lift enhancement is realized by rotating the flap downward, which can be considered as an effective increase in the airfoil camber. When the flap is rotated upwards instead, a negative camber with mitigating lift is realized. On the commercial aircrafts, these trailing-edge flaps play a more important role as the high-lift device. It has been shown that the change in lift achieved by the flaps depends on the chordwise extent of the flap. Unsurprisingly, larger flap sizes have been shown to create larger changes in lift [46]. Therefore, to make a significant lift change, they tend to be relatively large sized and therefore heavy, taking up a large portion of the wing. As a high-lift device, the capability of the steady-state lift augmentation under a constant flap deflection angle is the key. However, as a gust alleviation device, apart from the capability of the lift reduction achieved by the flaps, the characteristics of these flaps under dynamic activations are also vitally important.

On a supercritical airfoil equipped with a spoiler and a flap for a two-dimensional flow, Costes et al. [47] investigated the unsteady aerodynamic performance under subsonic

flow. It was found that for the trailing-edge flap, the lift coefficient decreases significantly with the flap rotating frequency, therefore reducing the range in lift coefficient change to the steady state. Bak et al. [48] also noted that the amplitude of lift change decreases with frequency. Hysteresis loops of the lift changes were present as a function of the flap deflection angle, indicating time lags in the dynamic responses. It was found that for the oscillating the aileron in a sinusoidal pattern, the range of lift coefficient change becomes smaller with angle of attack. For example, at a low angle of attack of $\alpha = 4.6^\circ$, the total lift change is 0.11, while this value is only 0.01 when the angle of attack is 19° , for a fixed reduced frequency of $k = 0.082$.

3.1.2. Spoilers

Spoilers are multifunctional control devices on the upper wing surface, serving a variety of tasks in the flight control system of modern airliners [49]. Spoilers are typically positioned along the upper surface of the wing. Unlike the high-lift devices mentioned above, spoilers are mainly used as an inflight speed brake by rotating to induce a controlled flow separation and thus reducing the lift and increasing the drag. For the inflight speed brake system, the deflection rate of spoilers is rather low, and the dynamic characteristic is not the key factor. However, for an effective GLA system, the deflection rate should be much higher to counteract the high-frequency gusts. Therefore, the dynamic performance of spoilers under unsteady activations requires better understanding. On a 2-D airfoil, Mack et al. [50] found that the incremental lift loss of the spoiler with the increasing deflection angle is quite nonlinear.

Wentz et al. [51] conducted parametric influences of the spoiler geometry on its aerodynamic characteristics. It was found that the vertical distance from the spoiler tip to the trailing edge of the airfoil acted a more important role than that of the chord or deflection angle of the spoiler. For the spoiler location, Maskell [52] found that placing the spoiler at $x/c = 0.4$ failed to reattach flow along the surface, unlike the spoiler at $x/c = 0.2$ for a given deflection angle of $\delta = 40^\circ$ at $\alpha = 4^\circ$. Croom et al. [53] suggested spoilers to be located downstream on swept wings in order to achieve analogous effects like that on unswept wings.

Siddalingappa and Hancock [54] conducted a comprehensive study of 2D and 3D spoilers on the unsteady flow patterns. Transient lag effects were observed during spoiler deployment and the lagging effects increased with the spoiler hinge line locating forward to the airfoil leading edge. Additionally, an initial lift overshoot rather than lift reduction was noticed during their experiments with fast spoiler deployment. This was later called as adverse lift effect by Mabey [55]. During their experiments, it was also found that spoilers on 3D wings had higher effectiveness than that of the 2D aerofoils. It was pointed out that it was due to reduced reattachment length behind the spoiler because of the interaction of vortices from spoiler tip and edges.

The time lag during dynamic spoiler deployment was also observed by Hancock [56], who also revealed a hysteresis effect. Mabey [55] introduced a non-dimensional time to quantify the spoiler deployment rate as $s = \frac{U_\infty t}{c}$, with c being the chord length of the airfoil and U_∞ the incoming flow velocity. It was found that the adverse lift effect is dependent to the non-dimensional time. When the non-dimensional time was less than 5, the adverse lift effect would be observed. However, during the experiments on harmonically oscillating spoilers by Consigny et al. [57], the adverse lift was observed for deployment times up to 9. During the experimental work to investigate the adverse lift by Kalligas [58], no adverse lift was observed for deployment times above 8.

Consigny et al. [59] also found that larger deflection angles did not mean greater changes in lift. It was found that lift remained relatively constant until the spoiler was sufficiently inclined to prevent separated flow downstream of the spoiler from reattaching. However, the low spoiler angle ($\delta = 1^\circ$) was shown to be ineffective at separating the flow. This is due to the height of the spoiler being too small, which is mentioned previously that the extent of the separated region being proportional to the spoiler height. The finding was

opposite by Costes et al. [47], as lower deflection angles produce greater force variation than larger deflection angles. Meanwhile, this statement was given under the result of the unsteady force variation with $\delta = 5^\circ$ which was greater than twice the amplitude observed at $\delta = 10^\circ$. From these findings, it can be seen that the deflection angle should be high enough to make sure a certain degree of spoiler height.

Harmonic oscillations of spoilers were also investigated by Nelson et al. [59]. During their studies, it was found that the nonlinearities of a rapidly deploying spoiler increased with reduced frequency (oscillating rate). The reduced frequency also has influence on the spoiler effectiveness. It was found by Consigny et al. [57] that the amplitude in change in lift coefficient became smaller with larger reduced frequencies, accompanied by greater phase delays. Mineck [60] extended the investigations of spoilers to transonic conditions with a consideration of Reynolds effects up to a flight Reynolds number of 30 million. It was found that the effectiveness of the spoiler increased with the Reynolds numbers increasing from 3 million up to 22 million. Meanwhile, a further Reynolds number increase up to 30 million saw almost no changes. To provide validation data of manoeuvring flaps for CFD methods, the German Aerospace Center (DLR) developed a wind tunnel model with an active spoiler [49,61] to investigate the aerodynamic characteristics of static and dynamic spoiler deflections.

3.2. Non-Traditional Control Surfaces

As mentioned previously, traditional control surfaces commonly take up a large portion of the wing section and thus tend to be heavy with slow responses. This prevents the control surfaces from high-frequency activations. Therefore, the effectiveness of the traditional control surfaces for high-frequency gust load alleviation is rather limited. As these control surfaces have other tasks for flight control, such as high-lift devices or inflight speed brakes, the size of these control surfaces should be balanced for their functions. Non-traditional control surfaces are relative to the above-mentioned flaps. These control surfaces use newer technology and 'smart' materials for fast activation. These control surfaces have been investigated mainly for wind turbines for gust load alleviation, such as the compact trailing-edge flap [62], the adaptive compliant wing [63], the adaptive trailing-edge geometry [48,64] and the microtabs [65,66]. Comprehensive overviews of these active flow control methods for wind turbines are presented by Johnson et al. [67,68].

3.3. Passive Control Devices

Comparing with the active control system, a passive control device is usually simpler and does not rely on extra energy. Guo et al. investigated the effects of a passive twist wingtip as a gust-load alleviation device on a flying-wing configuration [69] and a 200-seater airliner [23], respectively. This concept is to use a separate wing-tip section connected to the main wing by a spring. As the shaft is located ahead of the aerodynamic centre, this device will have a nose-down twist under the gust-induced aerodynamic force resulting in gust load alleviation. The results showed significant reduction in gust-induced wing-tip displacement and root bending moment. Compared to the current active control methods, this passive control concept is attractive as it requires no energy input.

Similar to the ideas by Guo et al., Castrichini et al. [70–72] investigated the effects for the alleviation on wing root bending moments at gust conditions by a flexible wing-fold device. The key idea was to introduce a hinge line which was not parallel to the incoming flow direction but was rotated outboard with a hinge orientation Λ to allow the wing tip to rotate. Therefore, folding the wingtip with the angle of θ will reduce the local angle of attack, which can be calculated as $\Delta\alpha = -\tan^{-1}(\tan\theta\sin\Lambda)$. The results indicated that suitable designs of the control device are capable for gust load alleviation. It was also observed that the load alleviation capabilities are highly sensitive to the stiffness of the hinge spring and the wing-tip mass. It will be a problem in application as it is very challenging practically to change the mass or the hinge spring stiffness according to different incoming flows.

3.4. Fluidic Actuators

As a means for active aerodynamic flow control, fluidic actuators, including synthetic jets, circulation control using Coanda effects, jet blowing and suction, have been investigated extensively. These methods have been shown to be effective for aerodynamic improvements through boundary-layer modulation, such as drag reduction [73,74], delay of transition [75,76] and flow separation control [10,77,78], flow improvement for air intakes [79,80], stall control and lift augmentation [81,82].

Flow control for load control is currently attractive for modern aircraft design, as it has the potential for flapless control with benefits including fewer moving parts, possibly less weight [31], less maintenance and enhanced stealth characteristics [32]. A few studies have been carried out to evaluate the capability of fluidic actuators known as jet flaps. The jet flap consists of a narrow slot extending across the wing surface, which ejects high momentum air [83]. For blowing tangentially near the trailing edge on an airfoil surface, the airflow will closely follow the profile of the surface due to the Coanda effect. The control method making use of the Coanda effect at the trailing edge can directly manipulate the airfoil circulation and is therefore called Circulation Control (CC).

3.4.1. Surface Jet Blowing

For normal surface jet blowing, the jet flow disrupts the main flow, leading to flow separation [84]. A separation bubble emerges to encompass the surface up to the trailing edge. An alteration in the Kutta condition is then realised as the separation bubble encourages flow to be entrained from the freestream flow around the wing surface, thereby modulating the circulation created by the wing [85]. Consequently, the load on the wing is modified.

Jet actuators have been investigated experimentally for load control on NACA0015 aerofoil for reshaping aeroelastic responses including limit cycle oscillation and flutter by Rao et al. [86]. The results showed an improvement of more than 15% of the flutter speed by the jet actuators using a PID controlled loop [87]. Microjets being small pneumatic jets using high-speed flow blowing normal to the aerofoil or wing surface have been studied as approaches for load control.

de Vries et al. [88] conducted numerical studies of a non-rotating NACA0018 aerofoil with microjets located near the trailing edge under freestream Mach number of 0.176. Significant changes in lift were observed for the angle of attack ranging from -10° to 10° . Moreover, the results also showed that approximately 50% of the total change in the lift could be obtained within the non-dimensional time $s = \frac{U_\infty \Delta t}{c} = 1$, indicating its rapid load control response characteristic. Blaylock et al. [66,85] compared the load control effects of microjets and microtabs deployed on the NACA0012 aerofoil trailing edge. The results showed that both concepts had a similar load control mechanism by affecting the trailing-edge flow, and therefore produced very similar aerodynamic load control effects.

Heathcote et al. [89] conducted wind tunnel tests for comparing the effects of blowing (microjets) and microtabs, and pointed out that blowing and microtabs were viable methods for load control but with very different behaviours: the blowing deflected the wake upwards thereby reducing lift, conversely the microtabs promoted separation over the upper surface resulting in lift reduction. They also noted the nearly constant lift change across all angles of attack by microjet blowing located at the trailing edge, which was constant with the result drawn by de Vries et al. [88].

However, for microtabs, optimal location varied according to the angle of attack. At small ones, it is preferable to place the microtabs near the trailing edge, while locations near the leading edge were better when the angle of attack is high. de Vries et al. [88] performed numerical studies at the steady condition on the NACA0018 aerofoil at $M_\infty = 0.176$ with a normal jet placed on the upper surface trailing edge and a significant lift reduction was obtained. Al-Battal et al. [43] assessed the capability of blowing for lift reduction experimentally. Two different blowing directions, normal and upstream, from the upper surface of the NACA0012 aerofoil under the steady incoming flow velocity of 20 m/s and a range of angles of attack from 0° to 20° were compared. The results indicated

that the chordwise location of normal blowing had a dramatic influence on the load control effectiveness in terms of lift reduction. Normal blowing at $x/c = 0.95$ induced a lift coefficient decrease of 0.15 under the maximum blowing momentum coefficient (momentum coefficient is defined as $C_\mu = \frac{\dot{m}U_{jet}}{q_\infty A}$, where, \dot{m} is the mass flow rate through the jet slot exit, q_∞ is the dynamic pressure of the freestream, A is the surface area of the wing and U_{jet} is the jet velocity). However, moving the microjet further forward, the lift change was negligible and even no lift decrease was induced when normal blowing was placed near the leading edge.

For the influence of jet-slot location and jet-slot width on the lift reduction effects by normal blowing, the authors conducted numerical studies based on the NACA0012 airfoil [30]. Figure 3 gives the results of lift coefficient reduction ($\Delta C_L = C_{L, with jet} - C_{L, without jet}$) against the jet-slot locations under $M_{jet} = M_\infty = 0.3$ at $\alpha = 0^\circ$ and 3° . It is clear that the magnitudes of the reduction in lift coefficient increase with microjets moving towards the trailing edge, and this trend is captured both at $\alpha = 0^\circ$ and 3° . The trend of positioning the jet towards the trailing edge enhancing lift is consistent to the findings by Lockwood and Vogler et al. [90], Mikolowsky and McMahon [91]. At $\alpha = 0^\circ$, the reduction in lift coefficient of $\Delta C_L = -0.09$ is obtained due to the microjet blowing at $x/c = 0.4$, and this value reaches to $\Delta C_L = -0.33$ when the microjet moves to $x/c = 0.95$. Noticeably, the magnitudes of lift coefficient reduction increase almost linearly with the microjet location moving from $x/c = 0.7$ to 0.95 for both $\alpha = 0^\circ$ and 3° . For the influence of jet-slot width, it is shown that the magnitude of lift reduction increases with the increase in jet slot width. It is more obvious when the jet slot width is below $0.5\%c$, as the value of lift reduction tends to be stable when the slot width increases from $0.5\%c$ to $1.0\%c$. Meanwhile, it is undeniable that a smaller width of the jet exit will be preferable since it is undeniable that the slots will bring discontinuity to the wing surfaces [92]. Figure 4 presents the comparisons of the surface pressure coefficients between the baseline model and the models with microjet blowing. Figure 5 displays the velocity flow fields of the models with microjets located at $x/c = 0.4$ and $x/c = 0.9$ at $\alpha = 0^\circ$.

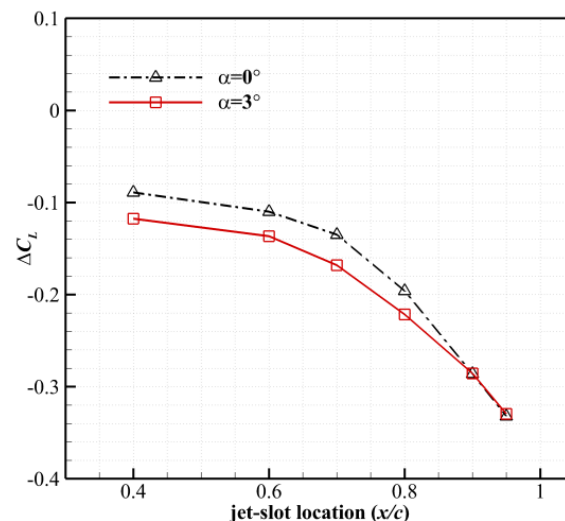


Figure 3. Influence of Microjet location on lift coefficient reduction with $M_{jet} = M_\infty = 0.3$ (from [30]).

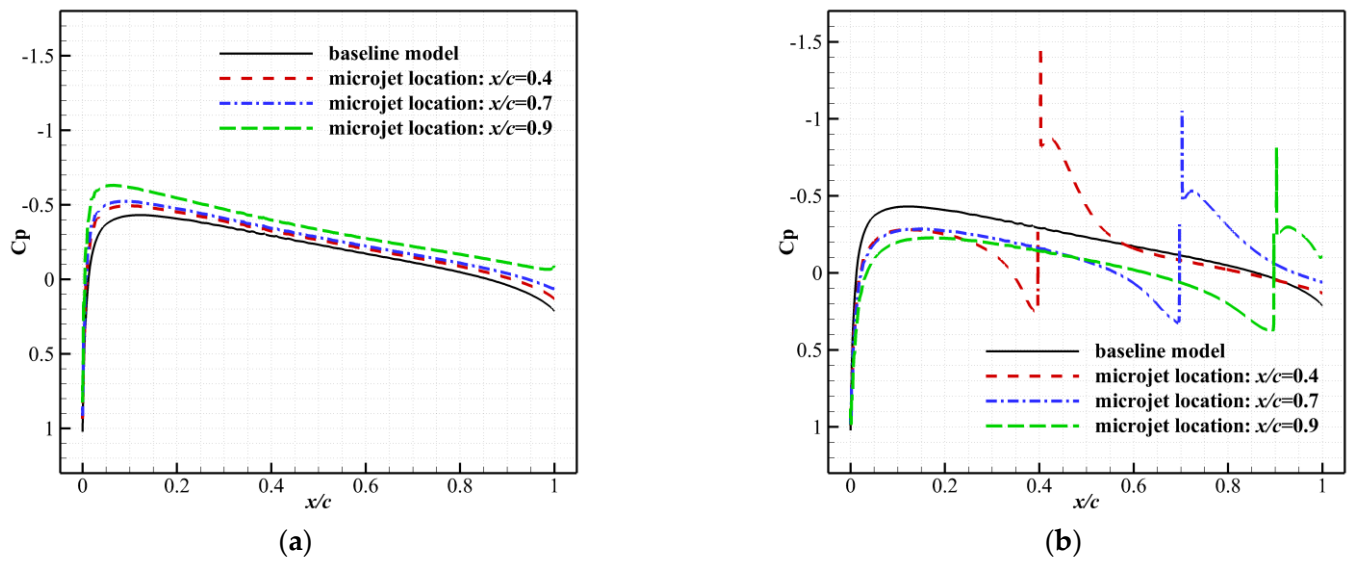


Figure 4. Comparisons of pressure coefficients between the baseline model and microjet blowing models at $M_\infty = 0.3$, $\alpha = 0^\circ$ (from [30]). (a) Lower surface; (b) Upper surface.

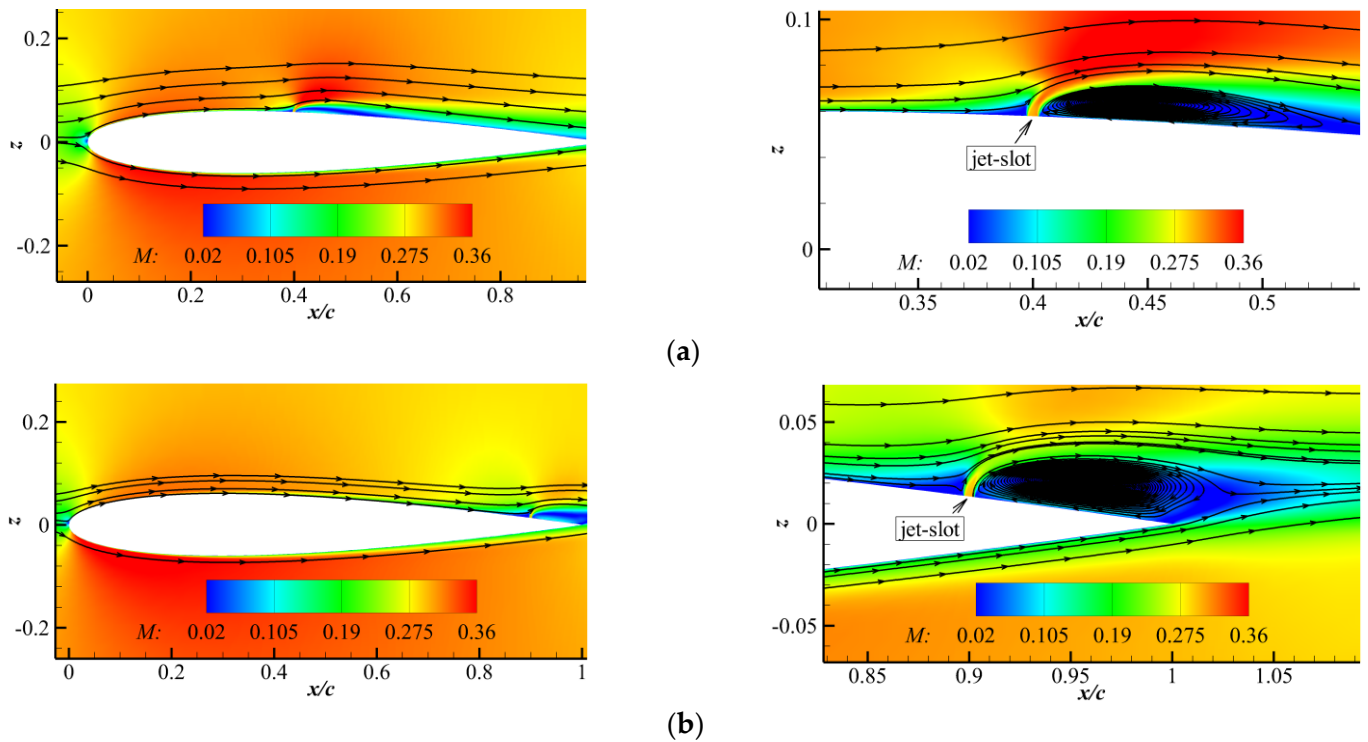


Figure 5. Velocity flow fields and streamlines of the baseline model and models with microjet blowing for $M_{jet} = M_\infty = 0.3$, at $\alpha = 0^\circ$ (from [30]). (a) Microjet blowing, $x/c = 0.4$; (b) microjet blowing, $x/c = 0.9$.

Also shown is the region of interest around the microjets and the trailing edges. From these results, it can be concluded that blowing generates a separation region near the jet location, and the separation region is more apparent after the jet location than that before it. This separation region deflects the streamlines upwards near the jet location and blocks the flow over the upper surface. This increases the upper surface pressure coefficients ahead the blowing slot. However, behind the jet slot, the pressure recovers rapidly. From Figure 5, it can be seen that this separation not only deflects the streamline above the upper surface, but also entrains the flow from the lower surface upwards. This entrainment accelerates the flow under the lower surface and results in a reduction in the pressure coefficients on the

lower surface. Also shown is that the entrainment capability is stronger when the blowing is placed towards the trailing edge, as slight decreases in pressure coefficients are noticed with blowing slot moving towards the trailing edge as demonstrated in Figure 4b. The combined effects explain the reduction in lift coefficient with the normal microjet blowing relative to the baseline model. In [92], the authors also demonstrated that normal microjet blowing has a stronger capability for load control at transonic incoming flow as normal microjet blowing show strong influence on the shock strength on the airfoil upper surface. For a 3D wing with jet slot only deployed near the wing tip, the effects of blowing have an extension to the whole wingspan.

For the properties of blowing under unsteady actuations, a further experiment of the upstream blowing was conducted by Al-Battal et al. [93]. The time lag in lift responses corresponding to blowing actuation frequency has been observed due to the change in the circulation and the vorticity shedding. The time delay became more significant with increasing angles of attack because of more separated flow. The effects of the slot blowing on unsteady aerodynamic load control with a freestream velocity from 6.7 m/s to 22.2 m/s on NACA0018 aerofoil was experimentally evaluated by Mueller-Vahl et al. [94]. The results showed that the lift oscillation due to the unsteady incoming flow can be effectively counteracted by dynamically adapting the slot blowing velocity. For the further understanding of the behaviour of the dynamic actuations, the responses of microjet blowing with periodic actuations are evaluated at by the authors in [92]. It was demonstrated that the microjet blowing is also effective under dynamic actuations. However, the load control effect is reduced with the increase in blowing frequency.

Based on the load control capabilities of microjet blowing under steady and unsteady actuations, its capabilities for gust load alleviation was evaluated by the authors in Ref. [92] on the 2-D NACA0012 and 3-D BAH wing. The test cases show that normal microjet blowing is a promising approach for gust load alleviation with a fast frequency response characteristic. The results of gust load alleviation on both the 2-D airfoil and the 3-D BAH wing verify that microjet blowing is able to suppress the gust load disturbances. Due to the fast response characteristics, it is capable for timely adaptive gust load control. For the test cases of rigid BAH wing, a significant reduction in gust-induced lift and root bending moment coefficients has been achieved. Because of the alleviation in gust load, significant suppression of the gust-induced disturbances in the displacement and acceleration has been obtained in the case study on the elastic BAH wing. Due to the fast-response characteristics of microjet blowing, a near constant lift response under gust condition is obtained by adaptively adjusting the blowing momentum coefficients. Another gust load alleviation study using synthetic jets on the NACA0012 aerofoil was conducted by De Breuker, et al. [95]. It was demonstrated that synthetic jets also have the potential for gust load control.

3.4.2. Circulation Control by Jet Blowing through the Trailing-Edge Coanda Device

Circulation Control (CC) using Coanda effect uses tangential surface jets to change the aerodynamic properties of the aerofoil or wing. The Coanda effect describes the tendency of a high-speed jet flow staying attached to a convex surface due to the balance between centrifugal forces and low static pressures created by the high-speed jet [96]. The high-speed jet flow entrains the external flow to follow it as to 'bend down' over the curved surface which generates the circulation increase, and thus results in lift augmentation. Similarly, lift reduction can be obtained through placing the jet slots on the lower surface. Conventionally, a CC device system consists of an air plenum, a rounded trailing edge and an orifice which is the slot exit of the CC jet.

The initial intention for the development of the CC system was for short landing and take-off capability, especially by the US Navy, looking for ways to improve aircraft operation from carriers [97]. Many tests including a full-scale flight test and design works have been carried out on the A-6 Intruder [98]. The effectiveness and efficiency of CC for manoeuvrability control of fixed and rotary-wing aircraft have also been researched

through various experiments and numerical studies. After the wind tunnel test on a diamond wing tailless aircraft, Cook et al. [99] pointed out that the CC device exhibited good aerodynamic performance similar to a traditional flap with an equivalent size on a fixed wing under modest blowing momentum coefficients, and the response characteristic was essentially linear.

Experimental and computational work seeking for a design using trailing-edge blowing to eliminate the trailing-edge flaps, or use leading-edge blowing to eliminate the need for leading-edge slats have been carried out on a Boeing 737 aircraft [97,100]. A joint project [32,101,102] has been carried out by University of Manchester, Cranfield University and BAE Systems to demonstrate new technologies for flapless control, and a drone has been designed named MAGMA which finished its first flight trial in 2017. Instead of traditional control surfaces, this project assessed the manoeuvrability of two novel technologies. One is to deploy CC on the wing sections and another one is to use the fluidic thrust vectoring (FTV) placed on the centre body. Engine bleed air is used for the pneumatic supply of the CC and fluidic thrust vectoring effectors. It is shown that the critical flight conditions are climb turns and descending flight where geometric and effort/power saturation limits are met, respectively [103].

To investigate the capability of CC for rolling control on the flying-wing configuration, Hoholis [104] extended a numerical study of CC as a roll effector on the generic SACCON UCAV configuration. This work was performed with a freestream Mach number 0.145 and was concluded that CC can produce similar rolling moments to flaps at low angles of attack. The effects for providing manoeuvrability by CC on a tailless vehicle was evaluated by Wilde et al. [105]. The results show that CC units could provide similar three-axis control effects relative to the split flap elevons.

To explore novel method for gust load alleviation to keep pace with the fast development in control system designs using CC. The feasibility and effects of gust load alleviation by means of CC is firstly numerically studied by Li and Qin [106]. The NACA0012 airfoil was chosen for the study from subsonic to transonic speeds. In this study, CC via steady blowing with different momentum coefficients are firstly tested for the gust load alleviation effects in terms of lift coefficients under a 'one-minus-cosine' gust. The results demonstrated that CC can effectively suppress the maximum gust-induced lift increment, but is not feasible for suppressing the unsteady gust-induced lift perturbations. Based on the verified fast-frequency response characteristics of CC, unsteady blowing with dynamically adaptive momentum coefficients proportional to the vertical gust velocities is proposed and tested. The results as shown in Figure 6 demonstrate that a near constant lift coefficient can be achieved under gust condition for subsonic incoming flow indicating its potential for real-time adaptive load control. This study also demonstrated that CC is able to reduce gust load at transonic speed, but it is less effective as compared with that at subsonic speed.

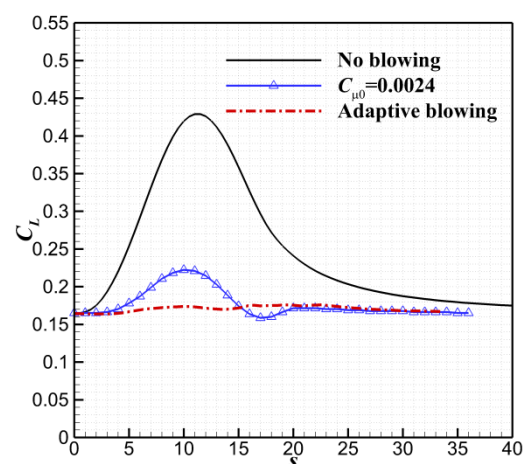


Figure 6. The gust response with and without Circulation Control (from [106]).

The study on the feasibility of gust load alleviation using CC is then extended to a three-dimensional wing including aerodynamic and structure interaction by Li and Qin [107]. Coanda device is deployed on the wing tip (from $\eta = y/l = 0.74$ to 0.98). The spanwise load control effects are firstly evaluated under steady CC jet blowing at different incoming flows as shown in Figure 7. Significant load control effect has been noticed around CC deployment region. Also shown is that apart from this region, CC also has influence on the span load towards the wing root, but with a reducing load control effect. Then, load control effects under dynamic CC jet blowing and gust load alleviation under typical ‘one-minus-cosine’ gust profiles from certification specification defined by European Aviation Safety Agency are tested. The results show a promising capability of CC for gust load alleviation as significant gust load alleviation effects have been achieved for both the rigid and elastic wings. For the wing considering aeroelasticity, the displacement oscillations induced by gusts have been effectively suppressed by CC.

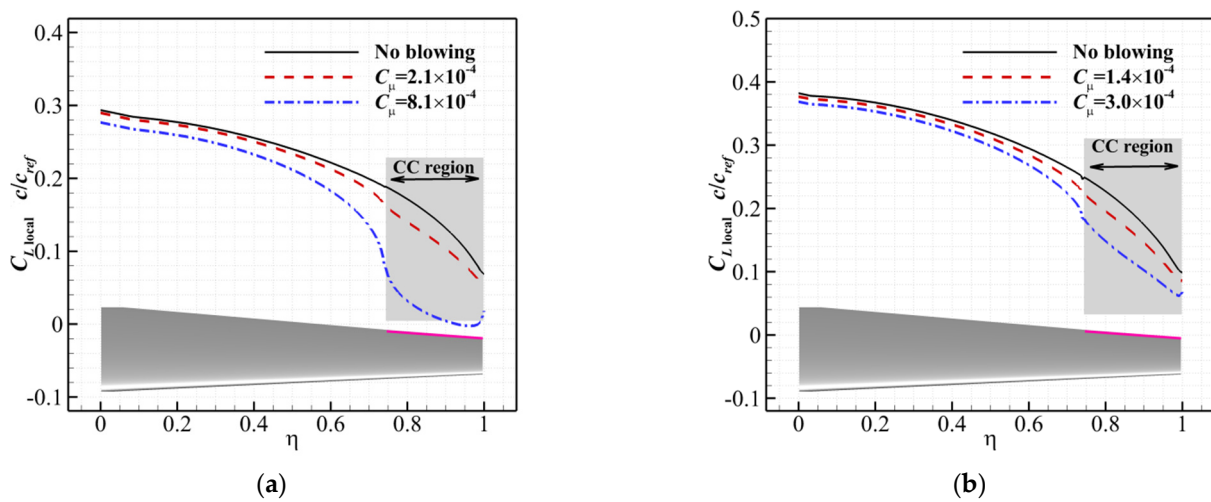


Figure 7. The influence of spanwise load distributions due to CC jet blowing. (a) $M_\infty = 0.3$; (b) $M_\infty = 0.7$.

3.5. Summary of the Characteristics of These Flow Control Devices

Table 1 gives a summary of the advantages and limitations of the flow control devices presented above. Although the traditional control surfaces have been applied to aircraft for gust load alleviations, these devices do not meet the requirements of fuel efficiency for future aircraft design due to their large size and structure weight. Although passive control technologies have been tested in the laboratories, it is still a challenge to improve the robustness and reliability. Active flow control using fluidic actuators show high efficiency and have great application potential for gust load alleviation. However, as it is still a novel technology, there is a lack of comprehensive understanding of flow control mechanism and in-depth research on their applications in the actual flight environment of aircraft.

Table 1. Comparisons of the characteristics of the flow control devices for gust load alleviation.

Flow Control Category	Typical Devices	Advantages	Limitations
Active flow control	Traditional control surfaces: Trailing-edge flaps and Spoilers	Robustness for a large range of incoming flow speeds	large size and heavy low-frequency responses
	Fluidic actuators: Surface jets and CC	high-frequency responses small size and less weight	decreases in gust load alleviation effects with increasing incoming flow speeds
Passive flow control	wingtip twist and flexible wing-fold devices	no extra energy required simple structural mechanism	Poor robustness away from design point

4. Concluding Remarks

In the context of growing concern for environmental protection and reduction in fuel consumption, flow control for gust load alleviation can play a vital role for future greener aircraft design. Some main conclusions can be drawn from the review.

Currently aircraft flow control for gust load control are achieved by deflecting control flaps, such as spoilers or trailing-edge flaps to create forces and moments that needed to alleviate the gust load. Being unsteady aerodynamic disturbances, gusts can have very high frequencies. For an effective gust load alleviation system, the capability of fast responses is the key factor. However, as the traditional flaps acting mainly for high-lift devices and flight manoeuvring, they are normally large sized and therefore heavy. These traditional flaps tend to exhibit low-frequency responses, which are ineffective for high-frequency gusts due to their large inertia.

In order to achieve faster responses, efforts towards smaller flap sizes have been made. However, these efforts have focused only on wind turbines up to now. To make a simpler system compared to the active flow control means which usually require complex actuating systems, passive wing-tip devices have also been studied for gust load alleviation. Passive control means can be designed to be reliable and effective at some flight conditions. It is hard to make them reliable and effective for a wide range of gust conditions.

The flow control methodologies using fluidic actuators are shown to have good potential for load control and flight control to replace the traditional flaps. This results in fewer moving parts, possibly less weight, less maintenance, high-frequency actuations and thus improved aerodynamic performance. This article has introduced two of the most promising actuators, i.e., surface jet blowing and circulation control. It has been demonstrated that both CC and surface jet blowing have a fast response characteristic and the capability for adaptive gust load controls. These actuators still face many engineering challenges. For CC, the main issue is the sharp decrease in load control capability with the increase in freestream velocities. For surface jet blowing including normal blowing and upstream blowing, the load control capability in terms of lift modulation is not as effective as CC at low speeds. Therefore, for industrial applications, more efforts are needed with in-depth investigations on these actuators.

Author Contributions: Conceptualization, N.Q. and Y.L.; Investigation, Y.L.; resources, N.Q.; writing—original draft preparation, Y.L.; writing—review and editing, N.Q. All authors have read and agreed to the published version of the manuscript.

Funding: This research received no external funding.

Institutional Review Board Statement: Not applicable.

Informed Consent Statement: Not applicable.

Data Availability Statement: Not applicable.

Conflicts of Interest: The authors declare no conflict of interest.

Nomenclature

s	non-dimensional time
C_L	lift coefficient
M_{jet}	the Mach number of the jet
C_μ	momentum coefficient
$C_{\mu 0}$	peak value of the momentum coefficient with the one-minus-cosine profile
M_∞	Mach number of the freestream flow
α	angle of attack
U_∞	freestream velocity
C_p	pressure coefficient
c	chord length
c_{ref}	mean aerodynamic chord length
x, y, z	Cartesian coordinates in streamwise, spanwise and vertical directions

References

1. Psarftis, H. *Green Transportation Logistics: The Quest for Win-Win Solutions*; International Series in Operations Research & Management Science; Springer: Berlin/Heidelberg, Germany, 2015; Volume 226.
2. Salam, I.R.; Bil, C. Multi-disciplinary analysis and optimisation methodology for conceptual design of a box-wing aircraft. *Aeronaut. J.* **2016**, *120*, 1315–1333. [CrossRef]
3. Chakraborty, I.; Nam, T.; Gross, J.R.; Mavris, D.N.; Schetz, J.A.; Kapania, R.K. Comparative Assessment of Strut-Braced and Truss-Braced Wing Configurations Using Multidisciplinary Design Optimization. *J. Aircr.* **2015**, *52*, 2009–2020. [CrossRef]
4. Colliss, S.P.; Babinsky, H.; Nöbler, K.; Lutz, T. Vortical structures on three-dimensional shock control bumps. *J. Aircr.* **2016**, *53*, 2338–2350. [CrossRef]
5. Bruce, P.J.K.; Babinsky, H. Experimental Study into the Flow Physics of Three-Dimensional Shock Control Bumps. *J. Aircr.* **2012**, *49*, 1222–1233. [CrossRef]
6. König, B.; Pätzold, M.; Lutz, T.; Krämer, E.; Rosemann, H.; Richter, K.; Uhlemann, H. Numerical and Experimental Validation of Three-Dimensional Shock Control Bumps. *J. Aircr.* **2009**, *46*, 675–682. [CrossRef]
7. Ogawa, H.; Babinsky, H.; Pätzold, M.; Lutz, T. Shock-Wave/Boundary-Layer Interaction Control Using Three-Dimensional Bumps for Transonic Wings. *AIAA J.* **2008**, *46*, 1442–1452. [CrossRef]
8. Messing, R.; Kloker, M.J. Investigation of suction for laminar flow control of three-dimensional boundary layers. *J. Fluid Mech.* **2010**, *658*, 117–147. [CrossRef]
9. Chernoray, V.G.; Dovgal, A.V.; Kozlov, V.V.; Lfdahl, L. Experiments on secondary instability of streamwise vortices in a swept-wing boundary layer. *J. Fluid Mech.* **2005**, *534*, 295–325. [CrossRef]
10. Krishnan, K.S.G.; Bertram, O.; Seibel, O. Review of hybrid laminar flow control systems. *Prog. Aerosp. Sci.* **2017**, *93*, 24–52. [CrossRef]
11. Brion, V.; Dandois, J.; Jacquin, L. Laminar buffet and flow control. In Proceedings of the 7th European Conference for Aeronautics and Space Sciences, Milano, Italy, 3–6 July 2017.
12. Ashill, P.R.; Fulker, J.L.; Hackett, K.C. A review of recent developments in flow control. *Aeronaut. J.* **2005**, *109*, 205–232. [CrossRef]
13. Joslin, R.D. *Overview of Laminar Flow Control*; NASA/TP-1998-208705; NASA Langley Research Center: Hampton, Virginia, USA, 1998.
14. *Hybrid Laminar Flow Control Study Final Technical Report*; NASA-CR-165930; NASA Langley Research Center: Hampton, VA, USA, 1982.
15. Murai, Y. Frictional drag reduction by bubble injection. *Exp. Fluids* **2014**, *55*, 1773. [CrossRef]
16. Fuaad, P.A.; Baig, M.F.; Khan, B.A. Turbulent drag reduction using active control of buoyancy forces. *Int. J. Heat Fluid Flow* **2016**, *61*, 585–598. [CrossRef]
17. Ahmad, H.; Baig, M.F.; Fuaad, P.A. Numerical investigation of turbulent-drag reduction induced by active control of streamwise travelling waves of wall-normal velocity. *Eur. J. Mech. B Fluids* **2015**, *49*, 250–263. [CrossRef]
18. Wang, Y.-S.; Huang, W.-X.; Xu, C.-X. Active control for drag reduction in turbulent channel flow: The opposition control schemes revisited. *Fluid Dyn. Res.* **2016**, *48*, 055501. [CrossRef]
19. Liebeck, R.H. Design of the Blended Wing Body Subsonic Transport. *J. Aircr.* **2004**, *41*, 10–25. [CrossRef]
20. Graham, W.R.; Hall, C.A.; Vera Morales, M. The potential of future aircraft technology for noise and pollutant emissions reduction. *Transp. Policy* **2014**, *34*, 36–51. [CrossRef]
21. Lebofsky, S.; Ting, E.; Nguyen, N.; Trinh, K. Optimization for Load Alleviation of Truss-Braced Wing Aircraft with Variable Camber Continuous Trailing Edge Flap. In Proceedings of the 33rd AIAA Applied Aerodynamics Conference, Dallas, TX, USA, 22–26 June 2015.
22. Jemitola, P.O.; Fielding, J.P. Box wing aircraft conceptual design. In Proceedings of the 28th International Congress of the Aeronautical Sciences, Brisbane, Australia, 23–28 September 2012.
23. Guo, S.; Los, J.; Liu, Y. Gust Alleviation of a Large Aircraft with a Passive Twist Wingtip. *Aerospace* **2015**, *2*, 135–154. [CrossRef]
24. European Aviation Safety Agency. *Certification Specifications for Large Aeroplanes CS-25*; European Aviation Safety Agency: Cologne, Germany, 2008.
25. Johnston, J.F. *Accelerated Development and Flight Evaluation of Active Controls Concepts for Subsonic Transport Aircraft. Volume 1: Load Alleviation/Extended Span Development and Flight Tests*; NASA-CR-159097; NASA Langley Research Center: Hampton, VA, USA, 1979.
26. Disney, T.E. C-5A Active Load Alleviation System. *J. Spacecr. Rocket.* **1977**, *14*, 81–86. [CrossRef]
27. Al-Battal, N. Flow Control for Loads Control. Ph.D. Thesis, University of Bath, Bath, UK, 2019.
28. Payne, B.W. Designing a Load Alleviation System for a Modern Civil Aircraft. In Proceedings of the 15th Congress of the International Council of the Aeronautical Sciences, London, UK, 7–12 September 1986. ICAS-86-5.2.3.
29. Xu, J.; Kroo, I. Aircraft Design with Maneuver and Gust Load Alleviation. In Proceedings of the 29th AIAA Applied Aerodynamics Conference, Honolulu, Hawaii, 27 June 2011. AIAA Paper 2011-3180.
30. Yonghong, L. Gust Load Alleviation by Fluidic Actuators on a Blended-Wing-Body Configuration. Ph.D. Thesis, Sheffield University, Sheffield, UK, 2020.
31. Paterson, E.; Baker, W.; Kunz, R.; Peltier, L. RANS and Detached-Eddy Simulation of the NCCR Airfoil. In Proceedings of the 2004 Users Group Conference (DOD_UGC'04), Williamsburg, VA, USA, 7–11 June 2004; pp. 112–122.

32. Anonymous. BAE Systems success in flapless flight. *Aircr. Eng. Aerosp. Technol.* **2006**, *78*. [CrossRef]
33. Wright, J.R. *Introduction to Aircraft Aeroelasticity and Dynamic Loads*, 2nd ed.; Cooper, J.E., Ed.; Wiley: Chichester, UK, 2015.
34. Rabadan, G.J.; Schmitt, N.P.; Pistner, T.; Rehm, W. Airborne Lidar for Automatic Feedforward Control of Turbulent In-Flight Phenomena. *J. Aircr.* **2010**, *47*, 392–403. [CrossRef]
35. Alam, M.; Hromcik, M.; Hanis, T. Active gust load alleviation system for flexible aircraft: Mixed feedforward/feedback approach. *Aerosp. Sci. Technol.* **2015**, *41*, 122–133. [CrossRef]
36. Liu, J.; Zhang, W.; Liu, X.; He, Q.; Qin, Y. Gust response stabilization for rigid aircraft with multi-control-effectors based on a novel integrated control scheme. *Aerosp. Sci. Technol.* **2018**, *79*, 625–635. [CrossRef]
37. Fazelzadeh, S.A.; Jafari, S.M. Active control law design for flutter suppression and gust alleviation of a panel with piezoelectric actuators. *Smart Mater. Struct.* **2008**, *17*, 035013. [CrossRef]
38. Patil, M.J.; Hodges, D.H. Output Feedback Control of the Nonlinear Aeroelastic Response of a Slender Wing. *J. Guid. Control Dyn.* **2002**, *25*, 302–308. [CrossRef]
39. Liu, X.; Sun, Q.; Cooper, J.E. LQG based model predictive control for gust load alleviation. *Aerosp. Sci. Technol.* **2017**, *71*, 499–509. [CrossRef]
40. Liu, X.; Sun, Q. Improved LQG Method for Active Gust Load Alleviation. *J. Aerosp. Eng.* **2017**, *30*, 04017006. [CrossRef]
41. Frost, S.; Taylor, B.; Bodson, M. Investigation of Optimal Control Allocation for Gust Load Alleviation in Flight Control. In Proceedings of the AIAA Atmospheric Flight Mechanics Conference, Minneapolis, MN, USA, 13–16 August 2012. AIAA 2012-4858.
42. Al-Battal, N.; Cleaver, D.; Gursul, I. Lift reduction by counter flowing wall jets. *Aerosp. Sci. Technol.* **2018**, *78*, 682–695. [CrossRef]
43. Al-Battal, N.; Cleaver, D.; Gursul, I. Aerodynamic Load Control through Blowing. In Proceedings of the 54th AIAA Aerospace Sciences Meeting, San Diego, CA, USA, 4–8 January 2016. AIAA 2016-1820.
44. Abbott, I.H.; Doenhoff, A.E. *Theory of Wing Sections: Including a Summary of Airfoil Data*; Dover Publications, Inc.: New York, NY, USA, 1959.
45. Anderson, J.D. *Introduction to Flight*, 8th ed.; McGraw-Hill Education: New York, NY, USA, 2016.
46. Frederick, M.; Kerrigan, E.C.; Graham, J.M.R. Gust alleviation using rapidly deployed trailing-edge flaps. *J. Wind Eng. Ind. Aerodyn.* **2010**, *98*, 712–723. [CrossRef]
47. Costes, M.; Gravelle, A.; Philippe, J.; Vogel, S.; Triebstein, H. Investigation of Unsteady Subsonic Spoiler and Flap Aerodynamics. *J. Aircr.* **1987**, *24*, 629–637. [CrossRef]
48. Bak, C.; Gaunaa, M.; Andersen, P.B.; Buhl, T.; Hansen, P.; Clemmensen, K. Wind tunnel test on airfoil Risø-B1-18 with an Active Trailing Edge Flap. *Wind Energy* **2010**, *13*, 207–219. [CrossRef]
49. Sven Geisbauer, T.L. Towards the Investigation of Unsteady Spoiler Aerodynamics. In Proceedings of the 35th AIAA Applied Aerodynamics Conference, Denver, CO, USA, 5–9 June 2017. A.A. Forum.
50. Mack, M.D.; Seetharam, H.D.; Kuhn, W.G.; Bright, J.T. Aerodynamics of Spoiler Control Devices. In Proceedings of the AIAA Aircraft Systems and Technology Meeting, New York, NY, USA, 20–22 August 1979. A.P. 1979-1873.
51. Wentz, J.W.; Ostowari, C.; Seetharam, H.C. Effects of Design Variables on Spoiler Control Effectiveness, Hinge Moments and Wake Turbulence. In Proceedings of the 19th AIAA Aerospace Sciences Meeting, Louis, MO, USA, 12–15 January 1981. AIAA Paper 1981-0072.
52. Maskell, E.C. *Pressure Distributions Illustrating Flow Reattachment behind a Forward Mounted Flap*; ARC-CP-211; Her Majesty's Stationery Office: London, UK, 1955.
53. Croom, D.R.; Shufflebarger, C.C.; Huffman, J.K. *An Investigation of Forward-Located Fixed Spoilers and Deflectors as Gust Alleviators on an Unswept-Wing Model*; NACA-TN-3705; NACA: Boston, MA, USA, 1956.
54. Siddalingappa, S.R.; Hancock, G.J. *An Introduction to the Aerodynamics of Spoilers*; Paper QMC EP-1034; Department of Aeronautical Engineering, Queen Mary College: London, UK, 1980.
55. Mabey, D.G. Experimental Methods to Determine Control Effectiveness in Wind Tunnels. In *AGARD Special Course on Aerodynamic Characteristics of Controls*; AGARD-R-711 Paper 5; AGARD: Neuilly sur Seine, France, July 1995.
56. Hancock, G.J. Dynamic Effects of Controls. In *AGARD Special Course on Aerodynamic Characteristics of Controls*; AGARD-R-711 Paper 4; AGARD: Neuilly sur Seine, France, July 1995.
57. Consigny, H.; Gravelle, A.; Molinaro, R. Aerodynamic Characteristics of a Moving Two-Dimensional Spoiler in Subsonic and Transonic Flow. *J. Aircr.* **1984**, *21*, 683–687. [CrossRef]
58. Kalligas, K. The Dynamic Characteristics of Two-Dimensional Spoilers at Low Speeds. Ph.D. Thesis, Department of Aeronautical Engineering, University of Bristol, Bristol, UK, 1986.
59. Nelson, C.F.; Koga, D.J.; Eaton, J.K. Unsteady, Separated Flow Behind an Oscillating, Two-Dimensional Spoiler. *AIAA J.* **1990**, *28*, 845–852. [CrossRef]
60. Mineck, R.E. Reynolds Number Effects on the Performance of Ailerons and Spoilers. In Proceedings of the 39th AIAA Aerospace Sciences Meeting and Exhibit, Reno, NV, USA, 8–11 January 2001. AIAA Paper 2001-0908.
61. Geisbauer, S. Numerical Simulation and Validation of Aerodynamics of Static and Dynamic Spoilers. *J. Aircr.* **2021**, *58*, 1187–1203. [CrossRef]
62. Roth, D.; Enenkl, B.; Dieterich, O. Active rotor control by flaps for vibration reduction—Full scale demonstrator and first flight test results. In Proceedings of the 32nd European Rotorcraft Forum, Maastricht, The Netherlands, 12–14 September 2006.

63. Kota, S.; Hetrick, J.A.; Osborn, R.; Paul, D.; Pendleton, E.; Flick, P.; Tilmann, C. Design and application of compliant mechanisms for morphing aircraft structures. In Proceedings of the SPIE, San Diego, CA, USA, 4–5 August 2003; pp. 24–33.
64. Buhl, T.; Gaunaa, M.; Bak, C. Potential Load Reduction Using Airfoils with Variable Trailing Edge Geometry. *J. Sol. Energy Eng.* **2005**, *127*, 503–516. [CrossRef]
65. Chow, R.; Dam, C.P.V. Unsteady Computational Investigations of Deploying Load Control Microtabs. *J. Aircr.* **2006**, *43*, 1458–1469. [CrossRef]
66. Blaylock, M.; Chow, R.; van Dam, C.P. Comparison of Microjets with Microtabs for Active Aerodynamic Load Control. In Proceedings of the 5th Flow Control Conference, Chicago, IL, USA, 28 June–1 July 2010. AIAA 2010-4409.
67. Johnson, S.J.; Baker, J.P.; Van Dam, C.P.; Berg, D. An overview of active load control techniques for wind turbines with an emphasis on microtabs. *Wind Energy* **2010**, *13*, 239–253. [CrossRef]
68. Van Dam, C.P.; Berg, D.E.; Johnson, S.J. *Active Load Control Techniques for Wind Turbines*; SAND2008-4809; Sandia National Laboratories (SNL): Albuquerque, NM, USA; Livermore, CA, USA, 2008.
69. Guo, S.; Jing, Z.W.; Li, H.; Lei, W.T.; He, Y.Y. Gust response and body freedom flutter of a flying-wing aircraft with a passive gust alleviation device. *Aerosp. Sci. Technol.* **2017**, *70*, 277–285. [CrossRef]
70. Castrichini, A.; Siddaramaiah, V.H.; Calderon, D.E.; Cooper, J.E.; Wilson, T.; Lemmens, Y. Preliminary investigation of use of flexible folding wing tips for static and dynamic load alleviation. *Aeronaut. J.* **2017**, *121*, 73–94. [CrossRef]
71. Castrichini, A.; Cooper, J.E.; Wilson, T.; Carrella, A.; Lemmens, Y. Nonlinear Negative Stiffness Wingtip Spring Device for Gust Loads Alleviation. *J. Aircr.* **2017**, *54*, 627–641. [CrossRef]
72. Castrichini, A.; Siddaramaiah, V.; Calderon, D.; Cooper, J.; Wilson, T.; Lemmens, Y. Nonlinear Folding Wing Tips for Gust Loads Alleviation. *J. Aircr.* **2016**, *53*, 1391–1399. [CrossRef]
73. Chan, D.T.; Jones, G.S.; Millholen, W.E.; Goodliff, S.L. Transonic Drag Reduction Through Trailing-Edge Blowing on the FAST-MAC Circulation Control Model. In Proceedings of the 35th AIAA Applied Aerodynamics Conference, Denver, CO, USA, 5–9 June 2017. AIAA AVIATION Forum, AIAA 2017-3246.
74. Cui, W.; Zhu, H.; Xia, C.; Yang, Z. Comparison of Steady Blowing and Synthetic Jets for Aerodynamic Drag Reduction of a Simplified Vehicle. *Procedia Eng.* **2015**, *126*, 388–392. [CrossRef]
75. Zahn, J.; Rist, U. Active and Natural Suction at Forward-Facing Steps for Delaying Laminar–Turbulent Transition. *AIAA J.* **2017**, *55*, 1343–1354. [CrossRef]
76. Guo, Z.; Kloker, M.J. Control of crossflow-vortex-induced transition by unsteady control vortices. *J. Fluid Mech.* **2019**, *871*, 427–449. [CrossRef]
77. Zhang, H.; Chen, S.; Meng, Q.; Wang, S. Flow separation control using unsteady pulsed suction through endwall bleeding holes in a highly loaded compressor cascade. *Aerosp. Sci. Technol.* **2018**, *72*, 455–464. [CrossRef]
78. Greenblatt, D.; Wagnanski, I.J. The control of flow separation by periodic excitation. *Prog. Aerosp. Sci.* **2000**, *36*, 487–545. [CrossRef]
79. Paul, A.R.; Joshi, S.; Jindal, A.; Maurya, S.P.; Jain, A. Experimental Studies of Active and Passive Flow Control Techniques Applied in a Twin Air-Intake. *Sci. World J.* **2013**, *2013*, 1–8. [CrossRef] [PubMed]
80. Paul, A.R.; Kuppa, K.; Yadav, M.S.; Dutta, U. Flow Improvement in Rectangular Air Intake by Submerged Vortex Generators. *J. Appl. Fluid Mech.* **2011**, *4*, 77–86.
81. Ebrahimi, A.; Hajipour, M.; Ghamkhar, K. Experimental study of stall control over an airfoil with dual excitation of separated shear layers. *Aerosp. Sci. Technol.* **2018**, *82–83*, 402–411. [CrossRef]
82. Amitay, M.; Glezer, A. Role of Actuation Frequency in Controlled Flow Reattachment over a Stalled Airfoil. *AIAA J.* **2002**, *40*, 209–216. [CrossRef]
83. Korbacher, G.K.; Sridhar, K. *A Review of the Jet Flap*; UTIA Review, No. 14; University of Toronto Press: Toronto, ON, CA, 1960.
84. Traub, L.W.; Miller, A.C.; Rediniotis, O. Comparisons of a Gurney and Jet-Flap for Hinge-Less Control. *J. Aircr.* **2004**, *41*, 420–423. [CrossRef]
85. Blaylock, M.; Chow, R.; Cooperman, A.; Dam, C.P. Comparison of pneumatic jets and tabs for Active Aerodynamic Load Control. *Wind Energy* **2014**, *17*, 1365–1384. [CrossRef]
86. Rao, P.; Strganac, T.; Rediniotis, O. Control of aeroelastic response via synthetic jet actuators. In Proceedings of the 41st Structures, Structural Dynamics, and Materials Conference and Exhibit, Atlanta, GA, USA, 3 April 2000; American Institute of Aeronautics and Astronautics: Reston, VA, USA, 2000. [CrossRef]
87. De Breuker, R.; Abdalla, M.; Marzocca, P.; Gürdal, Z. Flutter suppression using synthetic jet actuators: The typical section. In Proceedings of the 17th International Conference on Adaptive Structures and Technologies, Taipei, Taiwan, 16–19 October 2006; pp. 402–409.
88. De Vries, H.; Boeije, C.; Cleine, I.; van Emden, E.; Zwart, G.; Stobbe, H.; Hirschberg, A.; Hoeijmakers, H. Fluidic Load Control for Wind Turbine Blades. In Proceedings of the 47th AIAA Aerospace Sciences Meeting including the New Horizons Forum and Aerospace Exposition, Orlando, FL, USA, 5 January 2009. AIAA 2009-684. [CrossRef]
89. Heathcote, D.; Al-Battal, N.; Gursul, I.; Cleaver, D. Control of Wing Loads by Means of Blowing and Mini-Tabs. In Proceedings of the European Drag Reduction and Flow Control Meeting—EDRFCM 2015, Cambridge, UK, 23–26 March 2015.
90. Lockwood, V.E.; Vogler, R.D. *Exploratory Wind-Tunnel Investigation at High Subsonic and Transonic Speeds of Jet Flaps on Unswept Rectangular Wings*; NACA-TN-4353; NACA: Boston, MA, USA, 1958.

91. Mikolowsky, W.; McMahon, H. An Experimental Investigation of a Jet Issuing from a Wing in Crossflow. *J. Aircr.* **1973**, *10*, 546–553. [CrossRef]
92. Li, Y.; Qin, N. Gust load alleviation by normal microjet. *Aerosp. Sci. Technol.* **2021**, *117*, 106919. [CrossRef]
93. Al-Battal, N.H.; Cleaver, D.J.; Gursul, I. Unsteady actuation of counter-flowing wall jets for gust load attenuation. *Aerosp. Sci. Technol.* **2019**, *89*, 175–191. [CrossRef]
94. Mueller-Vahl, H.; Nayeri, C.; Paschereit, C.O.; Greenblatt, D. Control of Unsteady Aerodynamic Loads Using Adaptive Blowing. In Proceedings of the 32nd AIAA Applied Aerodynamics Conference, Atlanta, GA, USA, 16–20 June 2014.
95. De Breuker, R.; Abdalla, M.; Marzocca, P. Aeroelastic Control and Load Alleviation using Optimally Distributed Synthetic Jet Actuators. In Proceedings of the 48th AIAA/ASME/ASCE/AHS/ASC Structures, Structural Dynamics, and Materials Conference, Honolulu, Hawaii, 23 April 2007; American Institute of Aeronautics and Astronautics: Reston, VA, USA, 2007. [CrossRef]
96. Alexander, M.G.; Anders, S.G.; Johnson, S.K.; Florance, J.P.; Keller, D.F. *Trailing Edge Blowing on a Two-Dimensional Six-Percent Thick Elliptical Circulation Control Airfoil up to Transonic Conditions*; NASA/TM-2005-213545; Sponsoring Organization; NASA Langley Research Center: Hampton, VA, USA, 2005.
97. Ahuja, K.; Sankar, L.; Englar, R.J.; Munro, S.; Liu, Y. *Application of Circulation Control Technology to Airframe Noise Reduction*; GIT. Annual Performance Report; Georgia Institute of Technology: Atlanta, GA, USA, 2000; Volume 5928, pp. 1–2146.
98. Nichols, J.H.; Englar, R.J. Advanced circulation control wing system for navy stol aircraft. *J. Aircr.* **1981**, *18*, 1044–1050. [CrossRef]
99. Cook, M.V.; Buonanno, A.; Erbslöh, S.D. A circulation control actuator for flapless flight control. *Aeronaut. J.* **2008**, *112*, 483–489. [CrossRef]
100. Englar, R.; Smith, M.; Kelley, S. Application of circulation control to advanced subsonic transport aircraft. I—Airfoil development. II—Transport application. *J. Aircr.* **1994**, *31*, 1160–1177. [CrossRef]
101. Crowther, W.; Wilde, P.; Gill, K.; Michie, S.M. Towards Integrated design of fluidic flight controls for a flapless aircraft. *Aeronaut. J.* **2009**, *113*, 699–713. [CrossRef]
102. John, P. The flapless air vehicle integrated industrial research (FLAVIIR) programme in aeronautical engineering. *Proc. Inst. Mech. Eng. Part G J. Aerosp. Eng.* **2010**, *224*, 355–363. [CrossRef]
103. Wilde, P.; Buonanno, A.; Crowther, W.; Savvaris, A. Aircraft control using fluidic maneuver effectors. In Proceedings of the 26th AIAA Applied Aerodynamics Conference, Honolulu, Hawaii, 18–21 August 2008. AIAA 2008-6406.
104. Hoholis, G.; Steijl, R.; Badcock, K. Circulation Control as a Roll Effector for Unmanned Combat Aerial Vehicles. *J. Aircr.* **2016**, *53*, 1875–1889. [CrossRef]
105. Wilde, P.I.A.; Crowther, W.J.; Harley, C.D. Application of circulation control for three-axis control of a tailless flight vehicle. *Proc. Inst. Mech. Eng. Part G J. Aerosp. Eng.* **2010**, *224*, 373–386. [CrossRef]
106. Li, Y.; Qin, N. Airfoil gust load alleviation by circulation control. *Aerosp. Sci. Technol.* **2020**, *98*, 105622. [CrossRef]
107. Li, Y.; Qin, N. Gust load alleviation on an aircraft wing by trailing edge Circulation Control. *J. Fluids Struct.* **2021**, *107*, 103407. [CrossRef]

MDPI
St. Alban-Anlage 66
4052 Basel
Switzerland
www.mdpi.com

Applied Sciences Editorial Office
E-mail: applsci@mdpi.com
www.mdpi.com/journal/applsci



Disclaimer/Publisher's Note: The statements, opinions and data contained in all publications are solely those of the individual author(s) and contributor(s) and not of MDPI and/or the editor(s). MDPI and/or the editor(s) disclaim responsibility for any injury to people or property resulting from any ideas, methods, instructions or products referred to in the content.



Academic Open
Access Publishing

mdpi.com

ISBN 978-3-0365-8672-4